Oxidative Medicine and Cellular Longevity

Oxidative Stress and Pyroptosis in Heart Failure

Lead Guest Editor: Shao Liang
Guest Editors: Xinyong Cai and Chengxue Qin

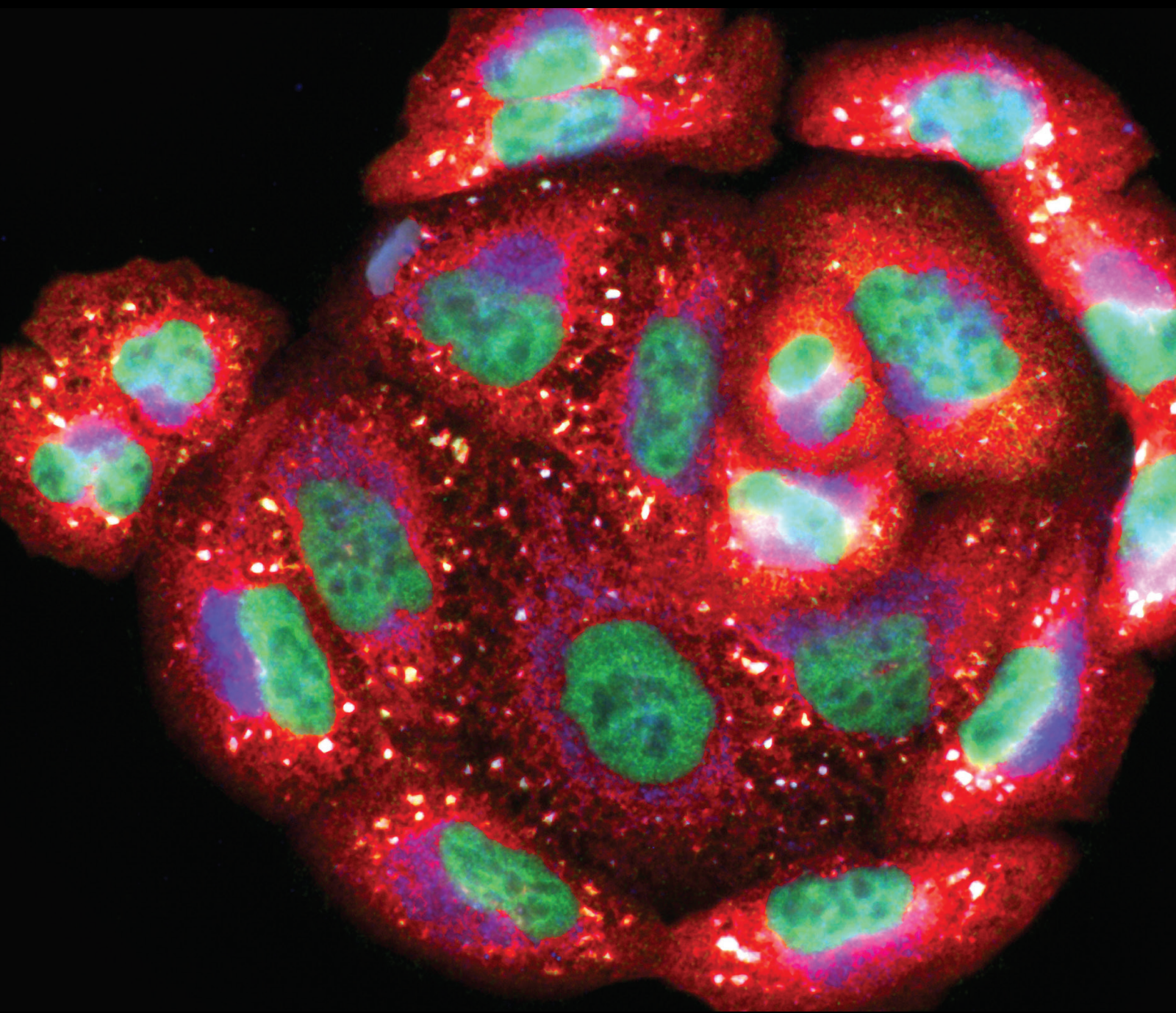

Oxidative Stress and Pyroptosis in Heart Failure

Oxidative Medicine and Cellular Longevity

Oxidative Stress and Pyroptosis in Heart Failure

Lead Guest Editor: Shao Liang
Guest Editors: Xinyong Cai and Chengxue Qin

Chief Editor

Jeannette Vasquez-Vivar, USA

Associate Editors

Amjad Islam Aqib, Pakistan
Angel Catalá, Argentina
Cinzia Domenicotti, Italy
Janusz Gebicki, Australia
Aldrin V. Gomes, USA
Vladimir Jakovljevic, Serbia
Thomas Kietzmann, Finland
Juan C. Mayo, Spain
Ryuichi Morishita, Japan
Claudia Penna, Italy
Sachchida Nand Rai, India
Paola Rizzo, Italy
Mithun Sinha, USA
Daniele Vergara, Italy
Victor M. Victor, Spain

Academic Editors

Ammar AL-Farga, Saudi Arabia
Mohd Adnan, Saudi Arabia
Ivanov Alexander, Russia
Fabio Altieri, Italy
Daniel Dias Rufino Arcanjo, Brazil
Peter Backx, Canada
Amira Badr, Egypt
Damian Bailey, United Kingdom
Rengasamy Balakrishnan, Republic of Korea
Jiaolin Bao, China
Ji C. Bihl, USA
Hareram Birla, India
Abdelhakim Bouyahya, Morocco
Ralf Braun, Austria
Laura Bravo, Spain
Matt Brody, USA
Amadou Camara, USA
Marcio Carocho, Portugal
Peter Celec, Slovakia
Giselle Cerchiaro, Brazil
Arpita Chatterjee, USA
Shao-Yu Chen, USA
Yujie Chen, China
Deepak Chhangani, USA
Ferdinando Chiaradonna, Italy
Zhao Zhong Chong, USA
Fabio Ciccarone, Italy
Alin Ciobica, Romania
Ana Cipak Gasparovic, Croatia
Giuseppe Cirillo, Italy
Maria R. Ciriolo, Italy
Massimo Collino, Italy
Manuela Corte-Real, Portugal
Manuela Curcio, Italy
Domenico D'Arca, Italy
Francesca Danesi, Italy
Claudio De Lucia, USA
Damião De Sousa, Brazil
Enrico Desideri , Italy
Francesca Diomede, Italy
Raul Dominguez-Perles, Spain
Joël R. Drevet, France
Grégory Durand, France
Alessandra Durazzo, Italy
Javier Egea, Spain
Pablo A. Evelson, Argentina
Mohd Farhan, USA
Ioannis G. Fatouros, Greece
Gianna Ferretti, Italy
Swaran J. S. Flora, India
Maurizio Forte, Italy
Teresa I. Fortoul, Mexico
Anna Fracassi , USA
Rodrigo Franco, USA
Juan Gambini, Spain
Gerardo García-Rivas, Mexico
Husam Ghanim, USA
Jayeeta Ghose, USA
Rajeshwary Ghosh, USA
Lucia Gimeno-Mallench , Spain
Anna M. Giudetti, Italy
Daniela Giustarini, Italy
José Rodrigo Godoy, USA
Saeid Golbidi, Canada
Guohua Gong, China
Tilman Grune, Germany
Solomon Habtemariam, United Kingdom
Eva-Maria Hanschmann, Germany
Md Saquib Hasnain, India
Md Hassan, India

Contents

Contents

Hindawi
Oxidative Medicine and Cellular Longevity
Volume 2023, Article ID 3492480, 11 pages
https://doi.org/10.1155/2023/3492480

Research Article

lncRNA PDCD4-AS1 Promotes the Progression of Glioma by Regulating miR-30b-3p/METTL7B Signaling

Zuowei Li,[1,2] **Yelin Song**,[3] **and Jimei Zhang**[1,4]

[1]*Shandong University of Traditional Chinese Medicine, Jinan 250011, China*
[2]*Department of Encephalopathy, Affiliated Hospital of Shandong University of Traditional Chinese Medicine, Jinan 250011, China*
[3]*Department of Cardiovascular Medicine, Qingdao Hospital of Traditional Chinese Medicine, Qingdao 266011, China*
[4]*The 960th Hospital of the PLA Joint Logistics Support Force (Tai'an), Tai'an 271099, China*

Correspondence should be addressed to Zuowei Li; zuowei_li@stu.cpu.edu.cn

Received 20 July 2022; Accepted 29 September 2022; Published 28 April 2023

Academic Editor: Shao Liang

Background. Gliomas are the most common and most malignant primary tumors of the adult central nervous system, but their etiology and pathogenesis remain unclear. This study was aimed at investigating the expression and function of lncRNA PDCD4-AS1 in glioma and elucidating the mechanism by which PDCD4-AS1 regulates the biological features of glioma. *Method*. The expression of PDCD4-AS1 was determined by bioinformatic analysis and qRT-PCR assay. PDCD4-AS1 was knocked down in glioma cells using siRNA transfection. The functional analysis of cells was conducted using CCK-8 proliferation, cell migration, and invasion assays, as well as cell cycle analysis. An *in vivo* tumorigenesis assay was performed to investigate the role of PDCD4-AS1 knockdown in glioma tumor growth. We performed bioinformatic analysis, RNA pull-down, and luciferase reporter assays to investigate the downstream targets of PDCD4-AS1. A rescue experiment was then performed to confirm the regulating mechanism. *Results*. PDCD4-AS1 was found to be significantly upregulated in glioma patients' tumor tissues and cell lines. The silencing of PDCD4-AS1 inhibited glioma cell proliferation, invasion, migration, and induced cell cycle arrest. *In vivo* experiments showed that silencing PDCD4-AS1 inhibited glioma tumor growth. An investigation of the underlying mechanism suggested that PDCD4-AS1 positively regulated METTL7B expression by sponging miR-30b-3. Both the knockdown of miR-30b-3p and the overexpression of METTL7B could, respectively, reverse the malignant phenotype of cells affected by silencing PDCD4-AS1. *Conclusion*. These results demonstrate that PDCD4-AS1 exerted an oncogenic role by regulating the miR-30b-3p/METTL7B axis.

1. Introduction

Glioma, located at the neuroepithelial origin of the central nervous system, is one of the most common causes of cancer-related death due to its highly aggressive and highly angiogenic features [1]. Multiple means of treatment have been applied for glioma, including radiotherapy, chemotherapy, and surgery. Glioma is divided into 4 grades, and as the grade of glioma increases, its malignancy increases. Glioblastoma is classed as grade 4 with the highest malignancy, and this accounts for 15% of all glioma cases [2]. Patients with glioblastoma often have a very poor prognosis, with a median survival time of 15 months and a 5-year survival rate of <10% [3]. Therefore, glioma represents a serious challenge to human health, and exploring novel treatment options is imperative for improving glioma therapy.

With the development of high-throughput sequencing and molecular biology, lncRNAs have been identified to participate in the occurrence and progression of various diseases [4, 5]. lncRNAs are RNAs < 200 bp in length which possess no protein-coding ability, most of which are derived from the intergenic regions (lincRNA) or from righteous and antisense gene transcription products. Initially, lncRNAs were considered to be biologically nonfunctional, as "junk" transcripts. However, research has since revealed lncRNAs to be involved in multiple biological processes, including epigenetic regulation, protein activity regulation, transcriptional regulation, and miRNA sponging [6–8]. Furthermore, lncRNAs have been

reported to be present in most tumor types, such as ovarian cancer, lung cancer, and glioma, where they function as important disease regulators in tumor progression. A previous study identified PDCD4-AS1 to be associated with a better prognosis in breast cancer [7]. Akbari F. et al. screened PDCD4-AS1 using TCGA-COAD data [9]. Wang D. et al. identified PDCD4-AS1 as an inhibitor of tumor growth in breast cancer via regulating miR-10b-5p/TNBC [10]. However, whether PDCD4-AS1 is involved in the progression of glioma remains unclear.

miRNAs are a category of evolutionarily conserved noncoding RNAs that are approximately 22 nucleotides in length [11]. miRNAs are involved in posttranscriptional regulation, whereby they bind to the target sequence of the mRNA 3′ untranslated region (UTR) and inhibit translation. One of the important mechanisms by which lncRNAs function is as competing endogenous RNAs (ceRNAs) to interact with miRNAs, thus regulating gene expression indirectly [12]. In recent years, many lncRNAs have been reported to either promote or inhibit tumor progression as a ceRNA. For example, Gu et al. reported that the knockdown lncRNA FOXD2-AS1 suppresses glioma progression and drug resistance via the microRNA-98-5p/CPEB4 axis [13]. The lncRNA MALAT1 was reported to promote glioma progression via sponging miR-613 [14].

In the present study, we investigated the expression and function of PDCD4-AS1 in glioma. Furthermore, we explored the downstream target of PDCD4-AS1, the miRNA/mRNA axis, to elucidate the mechanism of PDCD4-AS1 in glioma.

2. Materials and Methods

2.1. Sample Collection. Glioma and normal brain tissues were obtained by surgical excision. A total of 34 patients with pathologically confirmed glioma diagnosis and 34 control normal brain tissue specimens were collected from October 2019 to October 2021 at the Shandong University of Traditional Chinese Medicine Hospital, according to the WHO guidelines for the classification of central nervous system tumors. The inclusion and exclusion criteria were patients (i) under 70 years of age; (ii) receiving only surgical treatment without preoperative radiotherapy, chemotherapy, and other adjuvant treatments; (iii) with clinical pathological examination results clearly identified as glioma; and (iv) with no other types of malignant tumors, infectious diseases, autoimmune diseases, etc. Written informed consent was obtained from each patient with glioma. The collection and use of clinical samples was approved by the Ethics Committee of Shandong University of Traditional Chinese Medicine Hospital.

2.2. Cell Culture. Glioma cell lines (U251, U87, SHG44, and U373) and human brain glial cells (HEB cells) were purchased from the cell bank of the Chinese Academy of Sciences, Shanghai. Cell lines were cultured in DMEM medium containing 10% FBS and 1/1000 double anti-biotin. The cell culture conditions were 37°C and 5% CO_2 concentration.

2.3. Cell Transfection. The si-PDCD4-AS1, siNC, miR-NC, miR-30b-3p inhibitor, NC mimics, miR-30b-3p mimics, PDCD4-AS1-overexpression plasmid, control plasmid, and METTL7B-overexpression plasmid were purchased from GenePharma (Shanghai, China). Briefly, when cells were grown to 80% confluence, the above transfection plasmids, miRNA, or siRNA were, respectively, transfected into cells using Lipo2000 reagent for 48 h before the commencement of cell function experiments.

2.4. qRT-PCR Assay. Total RNA was obtained from glioma cells and tissues using the RNeasy Mini Kit (Qiagen, Valencia, CA). Then, 1 μg of RNA was used to synthesize cDNA using a High-Capacity Reverse Transcription Kit (Applied Biosystems, Foster City, CA). The resulting cDNA was then subjected to qRT-PCR with specific primer-probe mixtures. GAPDH was used as the internal reference gene. The PCR primers are as follows: PDCD4-AS1 (F: 5′-TTAGAAACG CAGCAGACAGC-3′, R: 5′-CAGAACCAAGGCCGAT CACC-3′) [10], METTL7B (F: 5′-CCTGCCTAGACCCA AATCCC-3′, R: 5′-AAACCGCTCATATTGGAGGTG-3′) [15], and miR-30b-3p (F: 5′-TGCGGAGAGGTTGCCC TTGGTGA-3′, R: 5′-TGCGGGTGCTCGCTTCGGCAGC-3′, RT: 5′-GTCGTATCCAGTGCAGGGTCCGAGGTGCA CTGGATACGACGAATTCAC-3′) [16]. The $2^{-\Delta\Delta Ct}$ method was used to calculate the gene expression of PDCD4-AS1 and METTL7B. The qRT-PCR of miR-30b-3p was performed using U6 as the internal reference gene.

2.5. Cell Proliferation Assay. The viability of U251 and U87 cells was determined using a CCK-8 kit. In brief, glioma cells were seeded into a 96-well plate with 3000 cells per well. After culturing for 48 h, each well was added with 10 μL of CCK8 solution and incubated at 37°C for 2 h. The absorbance values were then measured at $\lambda = 450$ nm using an enzyme marker, and three controls were set up in each group to reduce the error.

2.6. Transwell Assay. The Transwell assay was used to measure cell invasion. A Transwell membrane was first precoated with 100 μL of Matrigel gel for 6-10 h. Glioma cells (5×10^4 cells in 200 μL of serum-free medium) (initially transfected as described in the above section) were then seeded into each Transwell insert. Then, the lower chamber was added with 600 μL of cell culture medium containing 20% FBS. The cells were then cultured for 24 h, fixed with paraformaldehyde for 15 min, and stained with 0.01% crystal violet. For the cell migration assay, no Matrigel was added to Transwell inserts, while the remainder of the protocol remained the same.

2.7. Cell Cycle Assay. Transfected cells were harvested, washed with prechilled PBS, and then fixed in prechilled 95% ethanol for 13-20 h at 4°C in a refrigerator. The cells were then centrifuged at 1000 rpm for 5 min and washed with precooled PBS. After being stained with propidium iodide (PI; Sigma, St. Louis, MO) staining solution (RNase A 100 μg/mL and PI 500 μg/mL) for 30 minutes in the dark, the cell cycle distribution was analyzed using flow cytometry.

2.8. Subcutaneous Tumorigenesis Assay in Nude Mice. U87 cells were transfected with either siNC or si-PDCD4-AS1

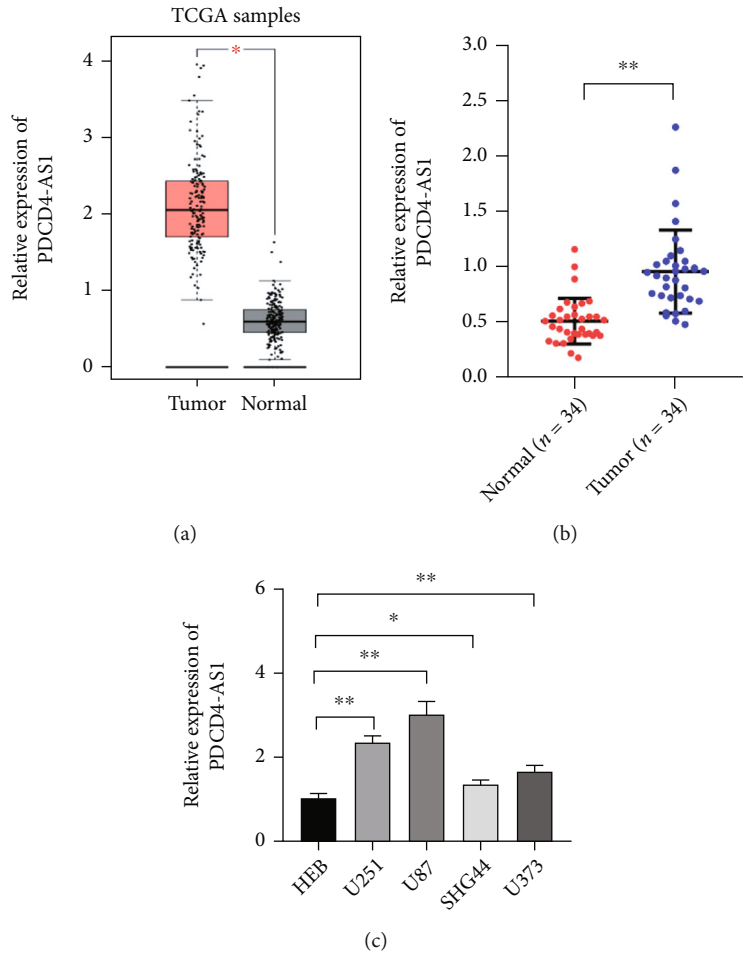

Figure 1: Increased expression of PDCD4-AS1 in glioma. (a) Obtaining PDCD4-AS1 expression in glioma by the GEPIA database (http://gepia2.cancer-pku.cn/#index) [17]. (b) Measuring PDCD4-AS1 expression in glioma tissues by qRT-PCR. (c) Detection of PDCD4-AS1 expression in glioma cell lines (U251, U87, SHG44, and U373) by qRT-PCR. $^{*}P < 0.05$ and $^{**}P < 0.01$.

for 48 h and then collected for live-cell counting. After being adjusted to a certain concentration with serum-free medium, the cells were injected into nude mice ($n = 6$ for each group) at the subcutaneous dorsal surface of the animal. The tumors were observed daily and their volumes were measured. After a month, the mice were executed by cervical dislocation, and their tumors were subsequently excised to be weighed and photographed.

2.9. Dual-Luciferase Reporter Assay. The binding site of the PDCD4-AS1 sequence with miR-30b-3p was inserted into the pmirGLO Vector (Promega, USA). The binding site was replaced with a mutated sequence to prepare mutant PDCD4-AS1 (PDCD4-AS1-MUT). HEK293T cells were transfected as follows: NC mimics+PDCD4-AS1-WT, miR-30b-3p mimics+PDCD4-AS1-WT, NC mimics+PDCD4-AS1-MUT, and miR-30b-3p mimics+PDCD4-AS1-MUT. After 24 h, luciferase activity was determined by the Dual-Luciferase Reporter Assay System (Promega).

2.10. Statistical Methods. Statistical analysis was conducted in GraphPad Prism 7. All experiment data were summarized as the mean ± SD. Statistical difference between two sets of data was determined by *T*-test, while one-way analysis of variance (ANOVA) was used to test the differences among multiple sets of groups. Dunnett's multiple comparison test was applied for multiple comparisons after ANOVA. $^{*}P < 0.05$ represented statistical significance.

3. Results

3.1. Increased Expression of PDCD4-AS1 in Glioma. Tumor suppressor genes or protumor genes typically exhibit abnormal expression patterns during tumor progression. In this study, the gene expression profile analysis database GEPIA was used to analyze the expression of PDCD4-AS1 in glioma tissues. The expression of PDCD4-AS1 was found to be higher in glioma tissues ($n = 163$) compared to normal brain tissue samples ($n = 207$ cases) (Figure 1(a)). Results of qRT-PCR obtained similar results (Figure 1(b)). Compared with normal glial cells (HEB cells), PDCD4-AS1 expression was significantly higher in glioma cell lines (U251, U87, SHG44, and U373) (Figure 1(c)). Taken together, these results reveal that PDCD4-AS1 exhibited abnormally high expression in glioma, thereby implying it to play an important role in the malignant progression of gliomas.

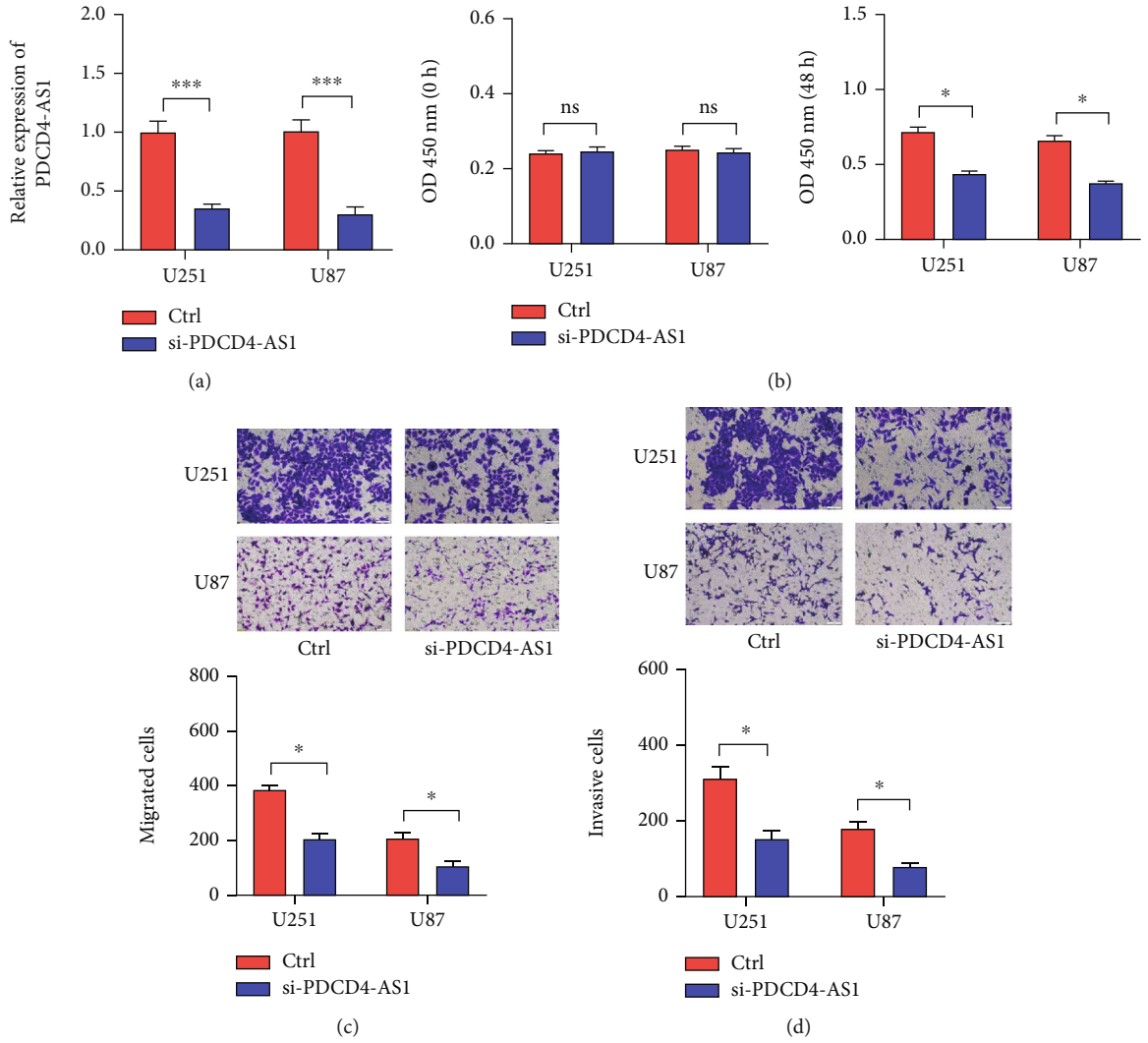

Figure 2: Continued.

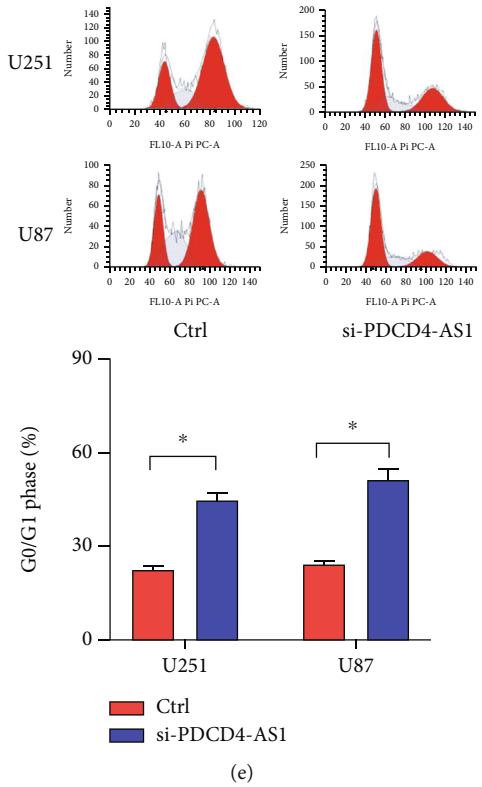

Figure 2: PDCD4-AS1 knockdown inhibited glioma progression. (a) qRT-PCR was used to verify the knockdown efficiency of PDCD4-AS1 expression. (b) CCK-8 assay was applied to detect cell vitality. (c, d) The Transwell assay was utilized to detect both cell migration (c) and invasion (d). (e) Flow cytometry was performed to characterize the cell cycle distribution. $^*P < 0.05$.

3.2. The Effects of PDCD4-AS1 Knockdown in Glioma Cell Malignant Phenotypes. Next, we synthesized a PDCD4-AS1-targeted siRNA and transfected it into U251 and U87 cells. As shown in Figure 2(a), the qRT-PCR results showed that the knockdown efficiency reached nearly 70% in both cell lines. Cell viability analysis showed that PDCD4-AS1 knockdown suppressed the vitality of the tumor cells (Figure 2(b)). In addition, results from the Transwell assay indicated that the knockdown of PDCD4-AS1 downregulated both cell migration and invasion (Figures 2(c) and 2(d)). The cell cycle distribution (Figure 2(e)) showed a significant increase in G1-phase-cell percentage following PDCD4-AS1 knockdown.

3.3. PDCD4-AS1 Directly Targeted miR-30b-3p in Glioma Cells. Mechanistic studies have revealed that lncRNAs regulate gene expression by competitively binding target miRNAs and blocking their functions. Here, we predicted the potential target miRNAs of PDCD4-AS1 using bioinformatic tools (lncRNASNP2). As shown in Figure 3(a), the prediction results showed that PDCD4-AS1 bound most tightly to miR-30b-3p. The dual-luciferase reporter assay showed that the miR-30b-3p mimics inhibited the luciferase activity of PDCD4-AS1 (Figure 3(b)). Furthermore, the RNA expression experiment also demonstrated that PDCD4-AS1 significantly decreased miR-30b-3p in glioma cells (Figure 3(c)).

3.4. METTL7B Is the Target Gene of miR-30b-3p. miRNAs regulate posttranscriptional translation via binding to mRNAs and blocking their interaction with the ribosome. Here, we found that METTL7B might be a downstream target miR-30b-3p by using the miRDB bioinformatic tool (Figure 3(a)). Next, we confirmed this interaction using the dual-luciferase reporter assay (Figure 3(d)). We also found that METTL7B was negatively regulated by miR-30b-3p mimics (Figure 3(e)). Meanwhile, the upregulation of METTL7B induced by PDCD4-AS1 overexpression was attenuated by miR-30b-3p (Figure 3(f)). We therefore suggest that METTL7B expression is regulated by PDCD4-AS1/miR-30b-3p signaling.

3.5. The Protumor Function of PDCD4-AS1 Is Mediated by miR-30b-3p/METTL7B. To investigate the role of miR-30b-3p/METTL7B in the oncogenic function of PDCD4-AS1 in glioma, a rescue experiment was performed. Based on our silencing of the expression of PDCD4-AS1, we subsequently inhibited the expression of miR-30b-3p and overexpressed METTL7B, respectively. It was found that miR-30b-3p inhibition and OV-METTL7B could each reverse the effects of glioma cell viability (Figure 4(a)), migration (Figure 4(b)), invasion (Figure 4(c)), and cell cycle arrest (Figure 4(d)) caused by PDCD4-AS1 knockdown.

3.6. PDCD4-AS1 Knockdown Inhibited Glioma In Vivo. To investigate whether PDCD4-AS1 could affect the growth of glioma tumors *in vivo*, we constructed a tumorigenesis model by subcutaneously injecting U87 cells (either PDCD4-AS1 knockdown or the negative control) into mice. It shows that

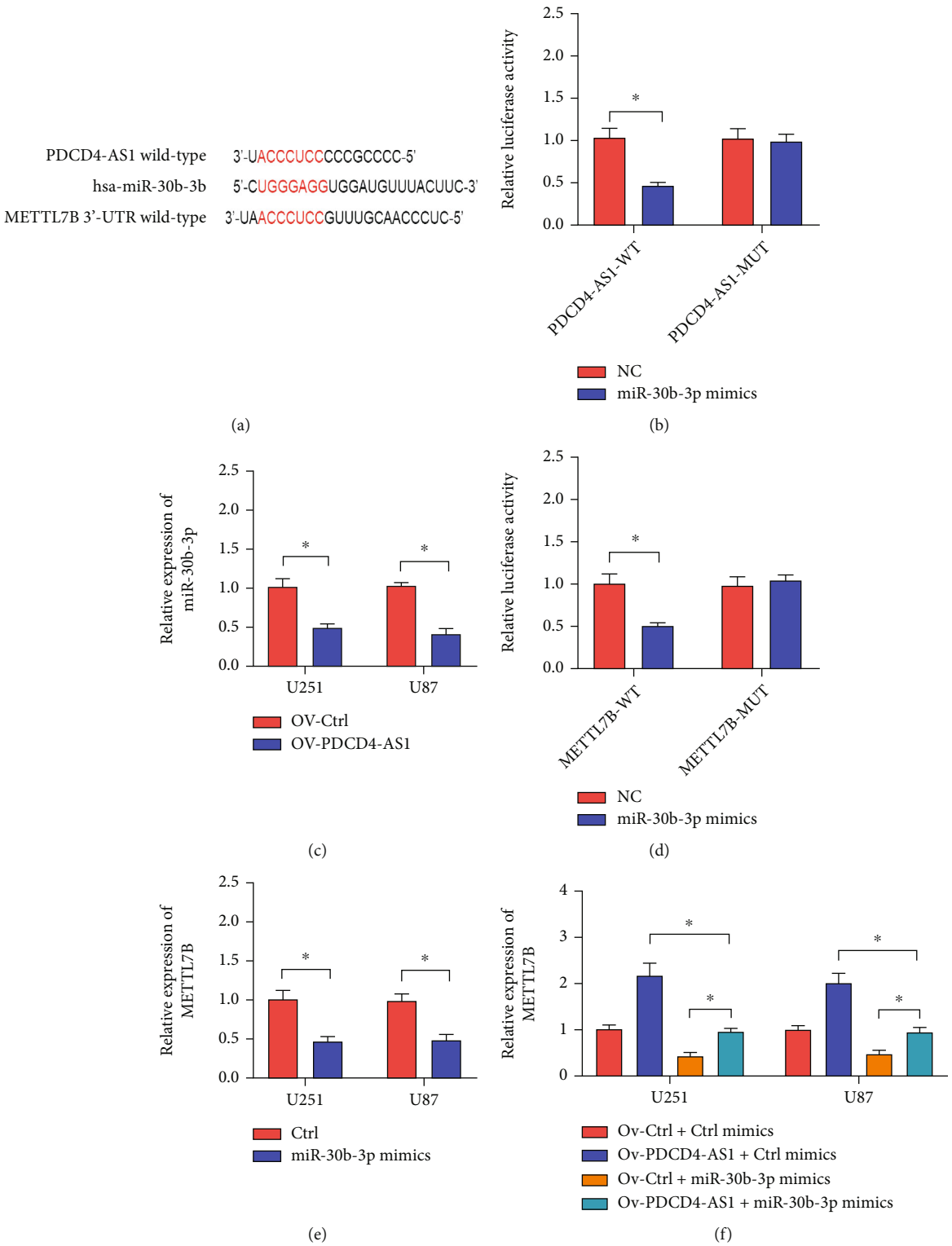

Figure 3: miR-30b-3p targets both PDCD4-AS1 and METTL7B. (a) Predicted complementary sequences of the miR-30b-3p targets PDCD4-AS1 and METTL7B. (b, d) Direct interaction was confirmed by the dual-luciferase reporter assay. (c) PDCD4-AS1 inhibited miR-30b-3p expression. (e) miR-30b-3p inhibited METTL7B expression. (f) The effects of the PDCD4-AS1/miR-30b-3p axis on the expression of METTL7B. $^*P < 0.05$.

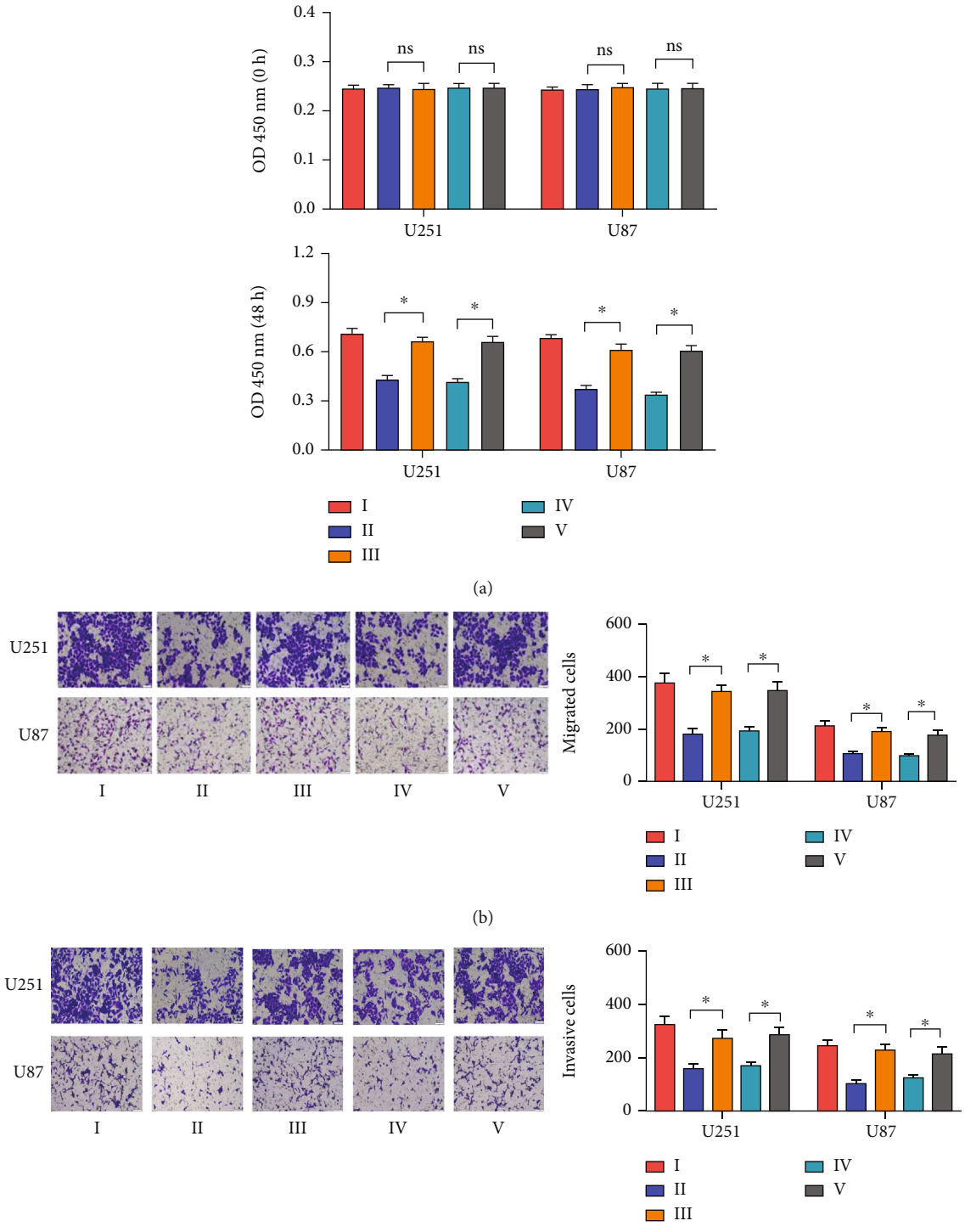

Figure 4: Continued.

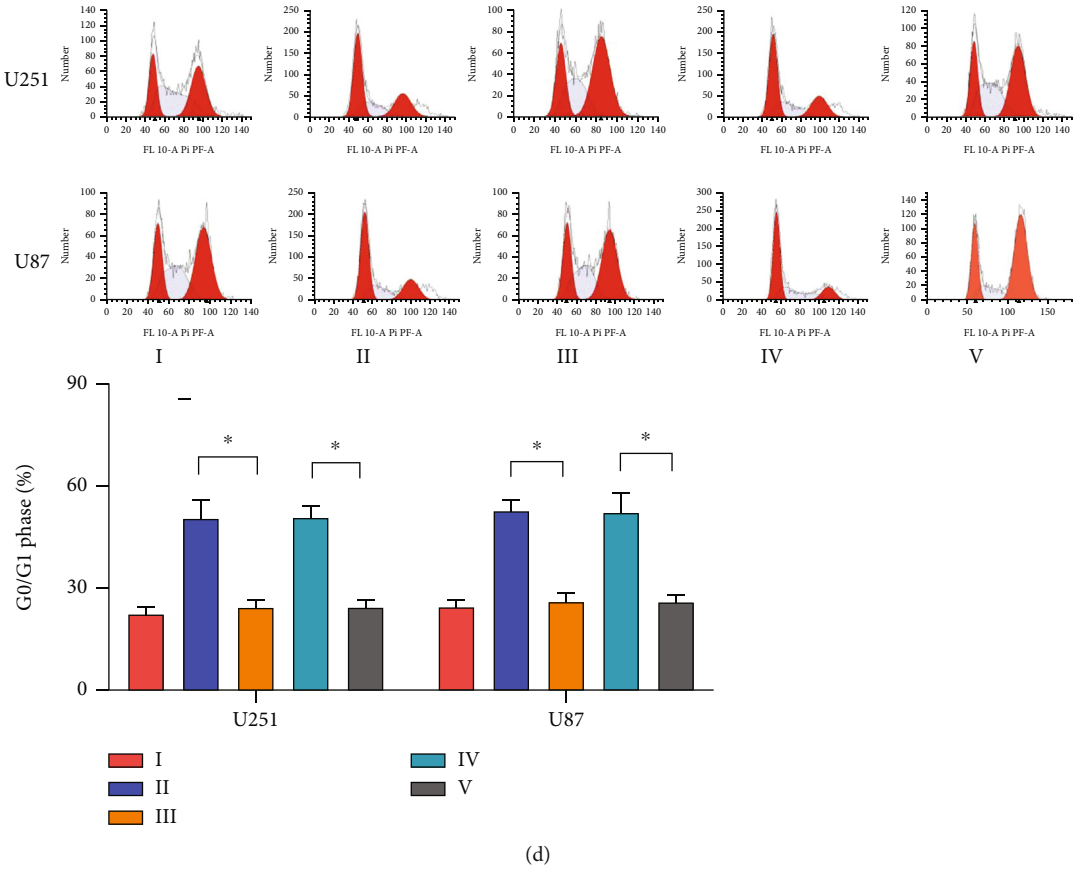

Figure 4: Oncogenic function of PDCD4-AS1 associated with miR-30b-3p/METTL7B. (a) The CCK-8 assay was applied to detect cell vitality. (b, c) The Transwell assay was utilized to measure both cell migration (b) and invasion (c). (d) Flow cytometry was performed to characterize the distribution of the cell cycle. Note: I: Ctrl; II: si-PDCD4-AS1+Ctrl-miR-30b-3p; III: si-PDCD4-AS1+miR-30b-3p inhibitor; IV: si-PDCD4-AS1+Ctrl-METTL7B; V: si-PDCD4-AS1+OV-METTL7B. $^*P < 0.05$.

the knockdown of PDCD4-AS1 significantly slowed the tumor growth (Figure 5(a)) of glioma compared with the negative group in tumor weight (Figure 5(b)) and volume (Figure 5(c)). Next, gene expression experiments showed that compared with the negative group, PDCD4-AS1-siRNA resulted in the downregulation of PDCD4-AS1 and METTL7B and the simultaneous upregulation of miR-30b-3p in glioma tumors (Figures 5(d)–5(f)). These results suggest that PDCD4-AS1 knockdown inhibited glioma in *vivo* and that this effect might be associated with the miR-30b-3p/METTL7B axis.

4. Discussion

Glioma is one of the most frequent tumor types in the human central nervous system; however, its treatment typically returns poor outcomes. Increasingly, research has made great achievements in developing target therapies for glioma [12, 13, 18, 19]. In the past few decades, evidence has revealed that lncRNAs and miRNAs are key regulators of tumor proliferation and progression. For example, numerous lncRNAs, including lncRNA MALAT1, LINC00525, PVT1, and LINC01094, have been shown to regulate tumor proliferation, metastasis, and other malignant phenotypes in glioma [14, 20–22].

Unlike miRNAs, the mechanisms of lncRNAs remain unclear. It is currently hypothesized that lncRNAs are involved in regulating biological processes through the regulation of chromosome structure and protein activity and the blocking of miRNA function [23–26]. lncRNA PDCD4-AS1 has been recently identified and reported to suppress the progression of triple-negative breast cancer either by regulating the miR-10b-5p/IQGAP2 axis or through positively regulating PDCD4 [10, 27]. However, whether lncRNA PDCD4-AS1 is involved in the progression of other tumor types remains unknown. Here, we found that lncRNA PDCD4-AS1 was significantly upregulated in glioma tumor tissues compared with normal brain tissues.

Furthermore, the functional cell analysis revealed that the knockdown of PDCD4-AS1 inhibited glioma progression. The animal model experiments also demonstrated that knockdown of PDCD4-AS1 slowed glioma tumor growth *in vivo*. These combined results reveal an oncogenic function of PDCD4-AS1 in glioma tumor progression which is inconsistent with its tumor suppressor function in triple-negative breast cancer. The tumor microenvironment and signal network exhibit a high degree of complexity and heterogeneity, and this can cause differential functions of a single gene in tumor progression.

One mechanism by which lncRNAs exert their function is by competitively binding with miRNAs. Indeed, lncRNAs

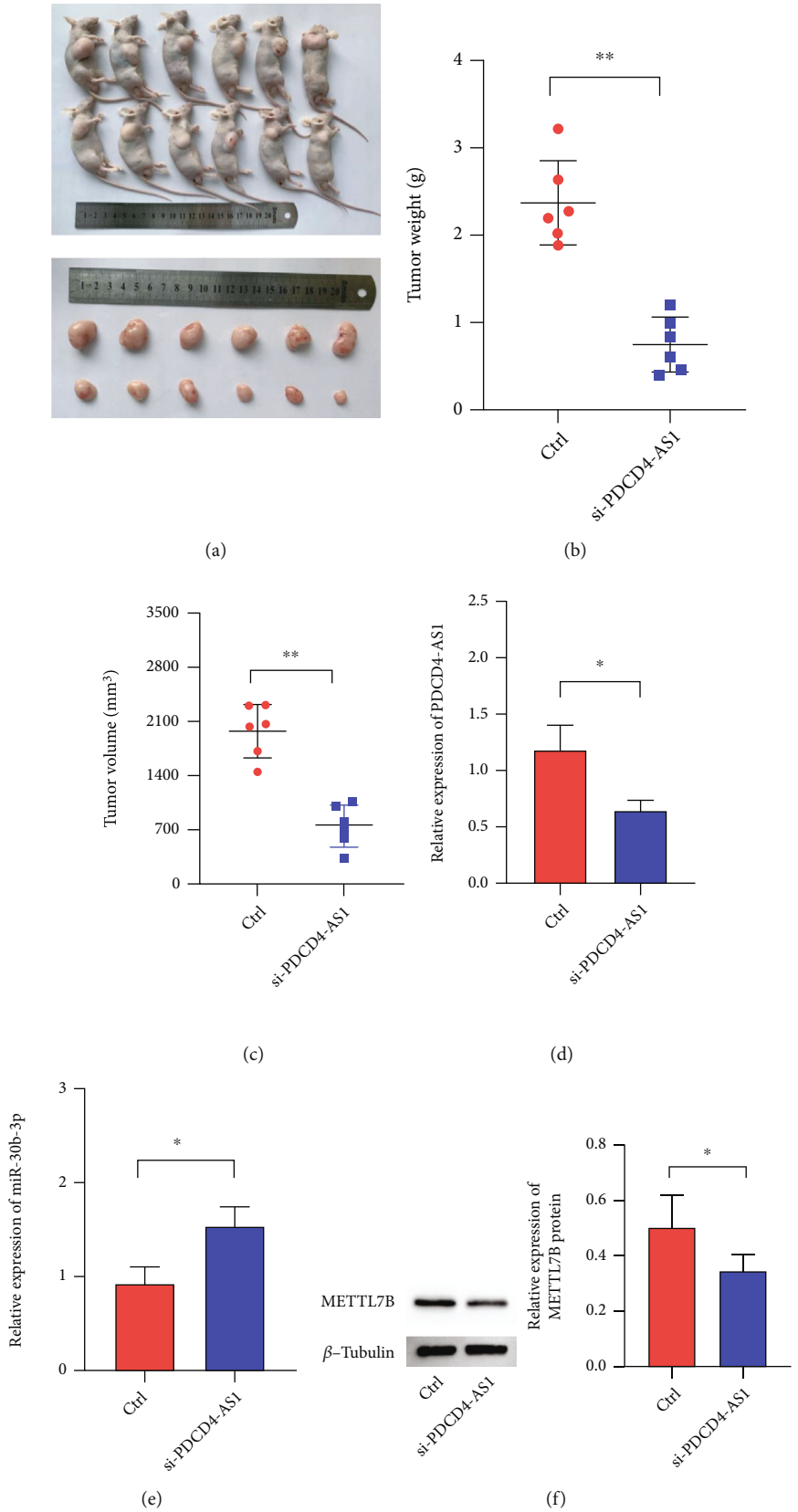

Figure 5: PDCD4-AS1 knockdown inhibited glioma *in vivo*. (a–c) Isolated tumors from mice were photographed (a), weighed (b), and measured for volume (c). (d) PDCD4-AS1 and (e) miR-30b-3p were detected by the qRT-PCR assay. (f) METTL7B protein expression in isolated tumors was detected by western blot. $^{*}P < 0.05$ and $^{**}P < 0.01$.

can bind to both DNA and RNA through a base-base pairing interaction. More importantly, lncRNAs can form secondary and tertiary structures with their target molecules, thereby endowing them with a high degree of affinity and specificity. lncRNAs can also affect the fate of mRNAs during the mRNA life cycle. Therefore, lncRNAs represent promising biological targets in tumor precision and personalized therapies. lncRNA PDCD4-AS1 can sponge miR-30b-3p to downregulate its expression. Previous studies have revealed miR-30b-3p to be downregulated in adenocarcinoma, ovarian cancer, and non-small-cell lung cancer and showed that it acted as a tumor suppressor [28–30]. In this work, we demonstrated that the downregulation of miR-30b-3p reversed the effects of PDCD4-AS1-siRNA on glioma cells and promoted glioma progression.

Finally, we have identified METTL7B to be a downstream target of miR-30b-3p in glioma. A previous study revealed that METTL7B was upregulated in glioma and was associated with a poor treatment outcome. Moreover, METTL7B is associated with tumor immune cell infiltration and immune regulation in glioma patients. The inhibition of METTL7B results in decreased cell proliferation and migration in glioma [31, 32]. Here, we demonstrated that the overexpression of METTL7B reversed the effects of PDCD4-AS1 knockdown on the proliferation, migration, and invasion of glioma cells. This study also has some limitations. Firstly, there are many potential binding miRNAs for lncRNA PDCD4-AS1, and only miR-30b-3p was selected for study in this study. Next, we did not perform a study targeting the downstream signaling of miR-30b-3p/METTL7B. Further, this study further needs to validate the function of PDCD4-AS1 in an in situ tumorigenic animal model.

In conclusion, the present study revealed that PDCD4-AS1 could promote glioma cell proliferation and tumor growth by regulating the miR-30b-3p/METTL7B axis. Our results, therefore, indicate a novel potential treatment target for glioma therapy.

Data Availability

No data were used to support this study.

Conflicts of Interest

We declare that we do not have any commercial or associative interests that represent a conflict of interest in connection with the work submitted.

Acknowledgments

This study was supported by the Special Education Fund of Shandong Province, Introduction and Training Team of Outstanding Young Talents of Shandong Province "Clinical Teaching Reform and Innovation Practice Team of Integrated Chinese and Western Medicine" (Project Number: 005-505012).

References

[1] L. L. Morgan, "The epidemiology of glioma in adults: a "state of the science" review," *Neuro-Oncology*, vol. 17, no. 4, pp. 623-624, 2015.

[2] D. Zhou, B. M. Alver, S. Li et al., "Distinctive epigenomes characterize glioma stem cells and their response to differentiation cues," *Genome Biology*, vol. 19, no. 1, p. 43, 2018.

[3] E. G. Van Meir, C. G. Hadjipanayis, A. D. Norden, H. K. Shu, P. Y. Wen, and J. J. Olson, "Exciting new advances in neuro-oncology: the avenue to a cure for malignant glioma," *CA: a Cancer Journal for Clinicians*, vol. 60, no. 3, pp. 166–193, 2010.

[4] C. Poulet, M. S. Njock, C. Moermans et al., "Exosomal long non-coding RNAs in lung diseases," *International Journal of Molecular Sciences*, vol. 21, no. 10, p. 3580, 2020.

[5] C. Bär, S. Chatterjee, and T. Thum, "Long noncoding RNAs in cardiovascular pathology, diagnosis, and therapy," *Circulation*, vol. 134, no. 19, pp. 1484–1499, 2016.

[6] J. Zhu, H. Fu, Y. Wu, and X. Zheng, "Function of lncRNAs and approaches to lncRNA-protein interactions," *Science China. Life Sciences*, vol. 56, no. 10, pp. 876–885, 2013.

[7] T. Ali and P. Grote, "Beyond the RNA-dependent function of LncRNA genes," *eLife*, vol. 9, article e60583, 2020.

[8] J. L. Charles Richard and P. J. A. Eichhorn, "Platforms for investigating LncRNA functions," *SLAS Technology*, vol. 23, no. 6, pp. 493–506, 2018.

[9] F. Akbari, M. Peymani, A. Salehzadeh, and K. Ghaedi, "Integrative in silico and in vitro transcriptomics analysis revealed new lncRNAs related to intrinsic apoptotic genes in colorectal cancer," *Cancer Cell International*, vol. 20, no. 1, p. 546, 2020.

[10] D. Wang, Z. Wang, L. Zhang, and S. Sun, "LncRNA PDCD4-AS1 alleviates triple negative breast cancer by increasing expression of IQGAP2 via miR-10b-5p," *Translational Oncology*, vol. 14, no. 1, article 100958, 2021.

[11] B. P. Towler, C. I. Jones, and S. F. Newbury, "Mechanisms of regulation of mature miRNAs," *Biochemical Society Transactions*, vol. 43, no. 6, pp. 1208–1214, 2015.

[12] Y. W. Deng, Y. G. Shu, and S. L. Sun, "LncRNA PART1 inhibits glioma proliferation and migration via miR-374b/SALL1 axis," *Neurochemistry International*, vol. 157, article 105347, 2022.

[13] N. Gu, X. Wang, Z. Di et al., "Silencing lncRNA FOXD2-AS1 inhibits proliferation, migration, invasion and drug resistance of drug-resistant glioma cells and promotes their apoptosis via microRNA-98-5p/CPEB4 axis," *Aging (Albany NY)*, vol. 11, no. 22, pp. 10266–10283, 2019.

[14] Y. Su, C. Liang, and Q. Yang, "LncRNA MALAT1 promotes glioma cell growth through sponge miR-613," *Journal of BUON*, vol. 26, no. 3, pp. 984–991, 2021.

[15] Z. Jiang, W. Yin, H. Zhu et al., "METTL7B is a novel prognostic biomarker of lower-grade glioma based on pan-cancer analysis," *Cancer Cell International*, vol. 21, no. 1, p. 383, 2021.

[16] D. Gao, Z. Zhou, and H. Huang, "miR-30b-3p inhibits proliferation and invasion of hepatocellular carcinoma cells via suppressing PI3K/Akt pathway," *Frontiers in Genetics*, vol. 10, p. 1274, 2019.

[17] Z. Tang, B. Kang, C. Li, T. Chen, and Z. Zhang, "GEPIA2: an enhanced web server for large-scale expression profiling and interactive analysis," *Nucleic Acids Research*, vol. 47, no. W1, pp. W556–W560, 2019.

[18] K. Wierzbicki, K. Ravi, A. Franson et al., "Targeting and Therapeutic Monitoring of H3K27M-Mutant Glioma," *Current Oncology Reports*, vol. 22, no. 2, pp. 1–9, 2020.

[19] Y. Cai, M. Wang, Y. Cui, Z. Tan, and Y. Jiang, "Differential expression profile of lncRNA in glioma cells and the effect of lncRNA NKX3-1 on glioma cells through Fem1b/SPDEF pathway," *Frontiers in Oncology*, vol. 11, article 706863, 2021.

[20] Y. Wan, F. Liang, M. Wei, and Y. Liu, "Long non-coding RNA LINC00525 regulates the proliferation and epithelial to mesenchymal transition of human glioma cells by sponging miR-338-3p," *AMB Express*, vol. 10, no. 1, p. 156, 2020.

[21] L. Liu, Q. Xu, Y. Xiong, H. Deng, and J. Zhou, "LncRNA LINC01094 contributes to glioma progression by modulating miR-224-5p/CHSY1 axis," *Human Cell*, vol. 35, no. 1, pp. 214–225, 2022.

[22] Z. Li, M. Li, P. Xia, L. Wang, and Z. Lu, "Targeting long non-coding RNA PVT1/TGF-β/Smad by p53 prevents glioma progression," *Cancer Biology & Therapy*, vol. 23, no. 1, pp. 225–233, 2022.

[23] Z. Cai, Y. Wu, Y. Li, J. Ren, and L. Wang, "BCAR4 activates GLI2 signaling in prostate cancer to contribute to castration resistance," *Aging (Albany NY)*, vol. 10, no. 12, pp. 3702–3712, 2018.

[24] P. Gu, X. Chen, R. Xie et al., "lncRNA HOXD-AS1 regulates proliferation and chemo-resistance of castration-resistant prostate cancer via recruiting WDR5," *Molecular Therapy*, vol. 25, no. 8, pp. 1959–1973, 2017.

[25] T. Bai, Y. Liu, and B. Li, "LncRNA LOXL1-AS1/miR-let-7a-5p/EGFR-related pathway regulates the doxorubicin resistance of prostate cancer DU-145 cells," *IUBMB Life*, vol. 71, no. 10, pp. 1537–1551, 2019.

[26] H. Jiang, W. Xiong, L. Chen, Z. Lv, C. Yang, and Y. Li, "Knockdown of the long noncoding RNA HOTTIP inhibits cell proliferation and enhances cell sensitivity to cisplatin by suppressing the Wnt/β-catenin pathway in prostate cancer," *Journal of Cellular Biochemistry*, vol. 120, no. 6, pp. 8965–8974, 2019.

[27] M. Jadaliha, O. Gholamalamdari, W. Tang et al., "A natural antisense lncRNA controls breast cancer progression by promoting tumor suppressor gene mRNA stability," *PLoS Genetics*, vol. 14, no. 11, article e1007802, 2018.

[28] S. Song, W. G. Bian, Z. Qin, D. Zeng, J. J. Xu, and H. C. Tang, "LncRNA BCYRN1 promotes cell migration and invasion of non-small cell lung cancer via the miR-30b-3p/ROCK1 axis," *Neoplasma*, vol. 69, no. 3, pp. 583–593, 2022.

[29] Y. Li, J. Zhou, J. Wang, X. Chen, Y. Zhu, and Y. Chen, "Mir-30b-3p affects the migration and invasion function of ovarian cancer cells by targeting the CTHRC1 gene," *Biological Research*, vol. 53, no. 1, p. 10, 2020.

[30] N. Li, R. Li, B. Song, H. Ge, and Y. Qu, "Downregulation of hsa-miR-30b-3p inhibits the oncogenicity of lung adenocarcinoma by targeting the METTL7B gene," *Journal of Oncology*, vol. 2022, Article ID 6883140, 15 pages, 2022.

[31] Y. Xiong, M. Li, J. Bai, Y. Sheng, and Y. Zhang, "High level of METTL7B indicates poor prognosis of patients and is related to immunity in glioma," *Frontiers in Oncology*, vol. 11, article 650534, 2021.

[32] R. Fu, X. Luo, Y. Ding, and S. Guo, "Prognostic potential of METTL7B in glioma," *Neuroimmunomodulation*, vol. 29, no. 3, pp. 186–201, 2022.

Hindawi
Oxidative Medicine and Cellular Longevity
Volume 2023, Article ID 3308725, 12 pages
https://doi.org/10.1155/2023/3308725

Research Article

MBNL1-AS1 Promotes Hypoxia-Induced Myocardial Infarction via the miR-132-3p/RAB14/CAMTA1 Axis

Yanbing Li,[1] Min Zong,[2] Xiaonan Guan,[2] Xuejiao Wu,[2] Guiling Ma,[2] Yu Wei,[2] and Zhi Li[3]

[1]*Department of Cardiology, Beijing Youan Hospital, Capital Medical University, Beijing 100069, China*
[2]*Department of Cardiology, Beijing Chaoyang Hospital, Capital Medical University, Beijing 100020, China*
[3]*Department of Cardiovascular Medicine, the First Affiliated Hospital of Shantou University Medical College, Shantou, 515041 Guangdong, China*

Correspondence should be addressed to Zhi Li; yuqian944326946184@163.com

Received 5 September 2022; Revised 19 October 2022; Accepted 25 November 2022; Published 4 February 2023

Academic Editor: Shao Liang

Background. Mounting evidence have indicated that long noncoding RNA (lncRNA) muscleblind like splicing regulator 1 antisense RNA 1 (MBNL1-AS1) play a crucial regulatory role in cardiovascular disease, myocardial infarction (MI) included. In this research, we sought to probe into the biological function and potential mechanism of MBNL1-AS1 in MI. *Methods.* Cardiomyocytes were treated under hypoxic conditions for 0–12 h. Functional assays including CCK-8 and flow cytometry were performed to assess hypoxia-stimulated cardiomyocyte viability and apoptosis, respectively. Moreover, bioinformatics analysis and mechanical assays were conducted to reveal the competitive endogenous RNA (ceRNA) mechanism of MBNL1-AS1. *Results.* The upregulation of MBNL1-AS1 was found in hypoxia-stimulated cardiomyocytes. Functionally, the downregulation of MBNL1-AS1 dramatically promoted hypoxia-induced cardiomyocyte viability and inhibited apoptosis. Mechanistically, miR-132-3p bound to MBNL1-AS1 in hypoxia-induced cardiomyocytes, and miR-132-3p directly targeted RAB14, member RAS oncogene family (RAB14) and calmodulin binding transcription activator 1 (CAMTA1). Furthermore, MBNL1-AS1 upregulates the expression of RAB14 and CAMTA1 in hypoxia-stimulated cardiomyocytes via targeting miR-132-3p. *Conclusions.* The current study revealed the critical role of the MBNL1-AS1/miR-132-3p/RAB14/CAMTA1 axis in MI, indicating MBNL1-AS1 as an innovative therapeutic target for MI.

1. Introduction

As a kind of ischemic heart disease, myocardial infarction (MI) is accompanied with high morbidity and mortality [1, 2]. Existing medicines and therapeutic methods can only retard the progression of the disease [3, 4]. As a consequence, it is urgent to explore and develop effective treatment strategies to prevent MI.

Noncoding RNAs (ncRNAs), a type of RNAs lack of the potential of protein-coding, were initially recognized as "junk DNAs" [5, 6]. Increasing researches have proved that about 98% of the human genome are ncRNAs, which have modulatory functions and can effectively couple back into a broader communication network [7, 8]. As the two main types of ncRNAs, long ncRNAs (lncRNAs) and microRNAs (miRNAs) have achieved extensive concern. Accumulating evidences have demonstrated that lncRNAs and miRNAs are important regulators in MI. Moreover, lncRNAs may act as competitive endogenous RNAs (ceRNA) to sequester miRNAs in MI development. At the same time, miRNAs usually function in MI through binding to the 3′-untranslated region (3′-UTR) of mRNAs, which affect the translation of mRNAs.

lncRNA MBNL1-AS1 has been widely documented to be implicated in multiple cancers, such as nonsmall cell lung cancer [9], bladder cancer, and retinoblastoma. Given the fact that the functions of MBNL1-AS1 in cancers have been well-studied, some studies have been devoted to exploring the role of MBNL1-AS1 in noncancerous diseases. A study proposed by Li et al. has indicated that MBNL1-AS1 targets KCNMA1 to enhance sevoflurane-pretreated ischemia-

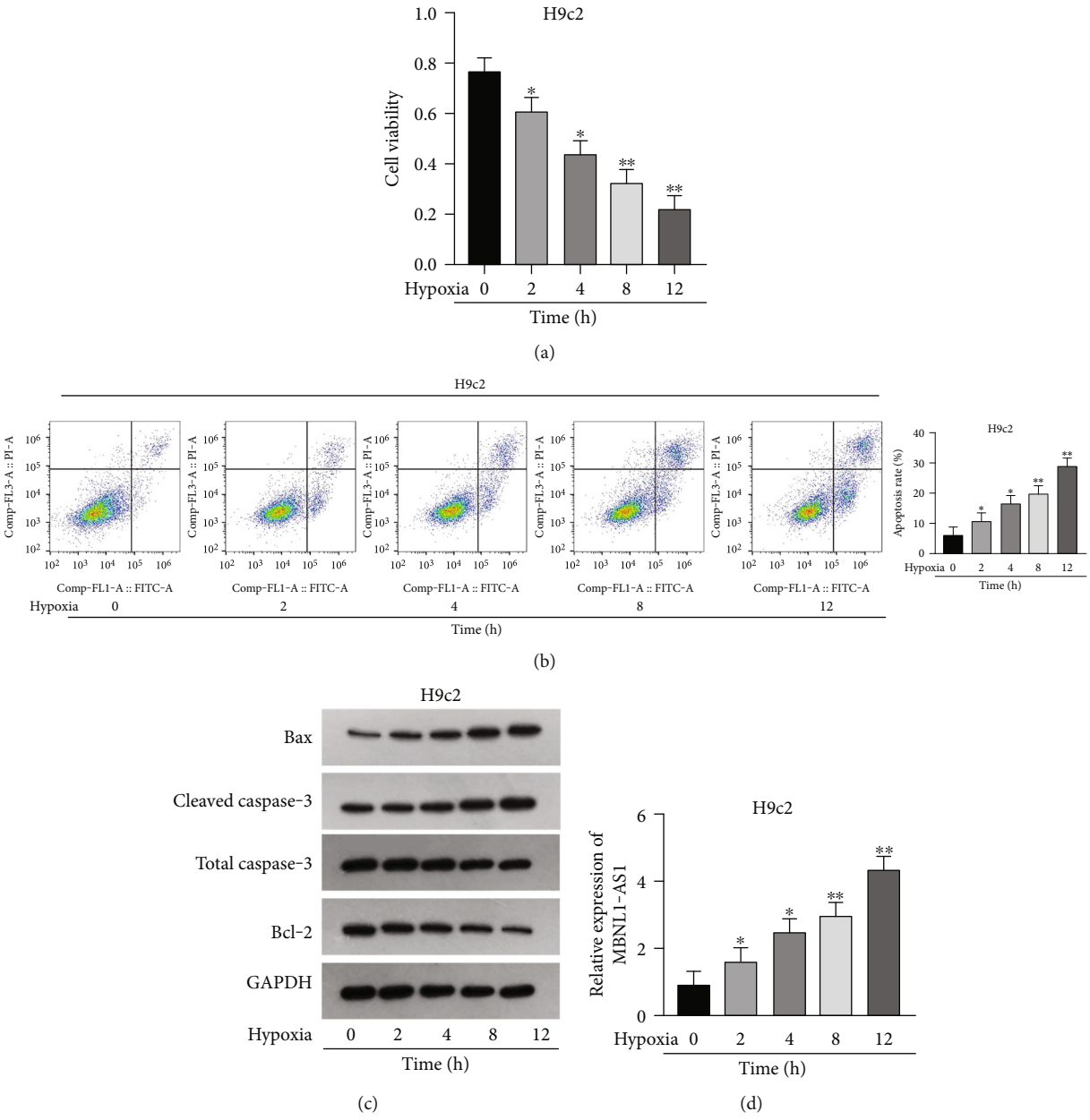

Figure 1: Continued.

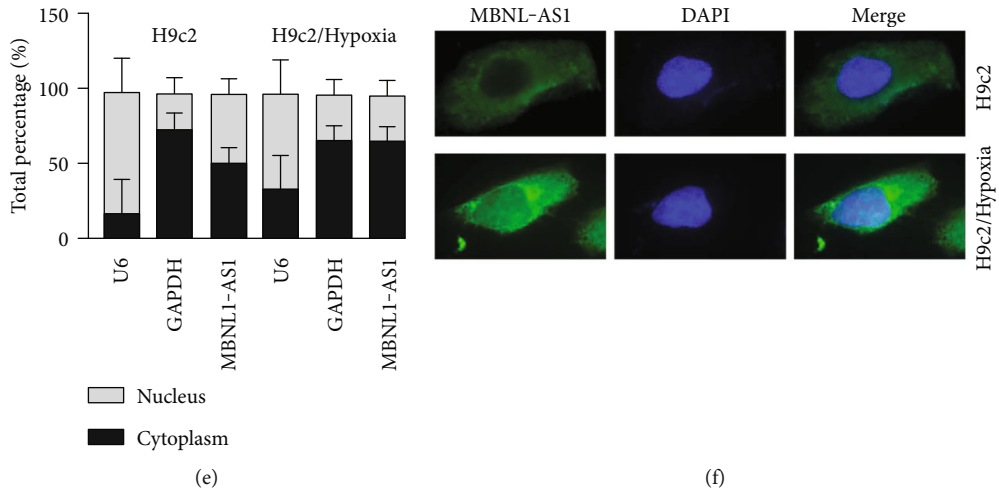

Figure 1: MBNL1-AS1 is highly expressed in hypoxia-induced H9c2 cells. (a) CCK-8 assay examined H9c2 cell viability after treatment of hypoxia for 0–12 h. (b) Flow cytometry analyzed H9c2 cell apoptosis after exposure of hypoxia for 0–12 h. (c) Levels of apoptosis-related proteins were measured in H9c2 cells after hypoxia treatment for 0–12 h via western blot. (d) MBNL1-AS1 expression was examined in H9c2 cells with exposure of hypoxia for 0–12 h by RT-qPCR. (e, f) Cellular location of MBNL1-AS1 was determined by subcellular fractionation and FISH assays. $^{*}P < 0.05$, $^{**}P < 0.01$.

reperfusion injury [10]. However, the role of MBNL1-AS1 in MI remains be investigated.

In this research, to reveal the function of MBNL1-AS1 in MI, we constructed an in vitro model of MI in H9c2 cells treated with hypoxia. Moreover, we explored the interaction between MBNL1-AS1 and miRNA as well as the downstream genes. Our study might provide a promising prospect for MI treatment.

2. Material and Methods

2.1. Cell Culture and Treatment. The rat embryonic ventricular cardiomyocyte H9c2 and human embryonic kidney cell (HEK293T) were procured from American Type Culture Collection. Both H9c2 and HEK293T cells were maintained in DMEM (A4192101, Gibco, Rockville, MD, USA) containing 10% fetal bovine serum with 5% CO_2 at 37°C. To mimic MI, H9c2 cells were maintained in a hypoxia incubator containing 1% O_2, 5% CO_2, and 94% N_2.

2.2. Cell Counting Kit-8 (CCK-8). Three independent experiments were performed. Cardiomyocytes were cultured with 10 μl CCK-8 solution procured from Dojindo (Gaithersburg, MD, USA) in 96-well plates. The absorbance was measured at 450 nm.

2.3. Flow Cytometry. The experiment was performed thrice independently. The FITC-annexin V/PI detection kit procured from Biosea Biotechnology (Beijing, China) was applied as per the user guide. Cardiomyocytes were collected and resuspended in 6-well plates, and then dyed with FITC-annexin V and PI, and assessed by the cytometry procured from Beckman Coulter (Fort Collins, CO, USA).

2.4. Western Blot. Three independent experiments were performed. Total protein was extracted via RIPA lysis buffer procured from Santa Cruz Biotechnology (CA, USA). After the proteins were assessed by SDS-PAGE (1610174, Bio-Rad Laboratories, Shanghai, China) and transferred to PVDF (Millipore, MA), 5% nonfat milk (QYR1330, Qualityard, Beijing qualityard biotechnology Co., Ltd.) were applied for membrane blocking. Next, the membranes were incubated with primary antibodies including Bax (Abcam, Cambridge, MA, USA, ab32503), Cleaved caspase-3 (Abcam, ab32042), total caspase-3 (Abcam, ab32351), Bcl-2 (Abcam, ab32124), RAB14 (Invitrogen, PA5-100175), CAMTA1 (Abcam, ab227713), and GAPDH (Abcam, ab181602). After washing, the secondary antibodies procured form Abcam were incubated. The blots were detected using the chemiluminescence detection kit (Pierce, WI, USA).

2.5. Quantitative Real-Time Polymerase Chain Reaction (RT-qPCR). Three experiments were performed independently. Total RNA was extracted from hypoxia-induced cardiomyocytes using the Trizol reagent procured from Life Technologies Corporation (Carlsbad, USA). After the application of First Strand cDNA Synthesis Kit (GeneCopoeia, USA), qPCR was implemented using Takara SYBR® PrimeScript™ PCR kit (11736051, Invitrogen, Carlsbad, CA, USA). Calculation of gene expression was performed using $2^{-\Delta\Delta Ct}$ method, with GAPDH or U6 as the internal control.

2.6. Subcellular Fractionation. Three experiments were performed independently. This assay was carried out via a Nuclear and Cytoplasmic Extraction Reagent (78835, Thermo Fisher Scientific, Rockford, IL, USA). Fractionated RNAs were detected by RT-qPCR analysis.

2.7. Fluorescent In Situ Hybridization (FISH). Three experiments were performed independently. Ribo™ Fluorescent In Situ Hybridization Kit procured from RiboBio (Guangzhou, China) was applied as per the user guide. The

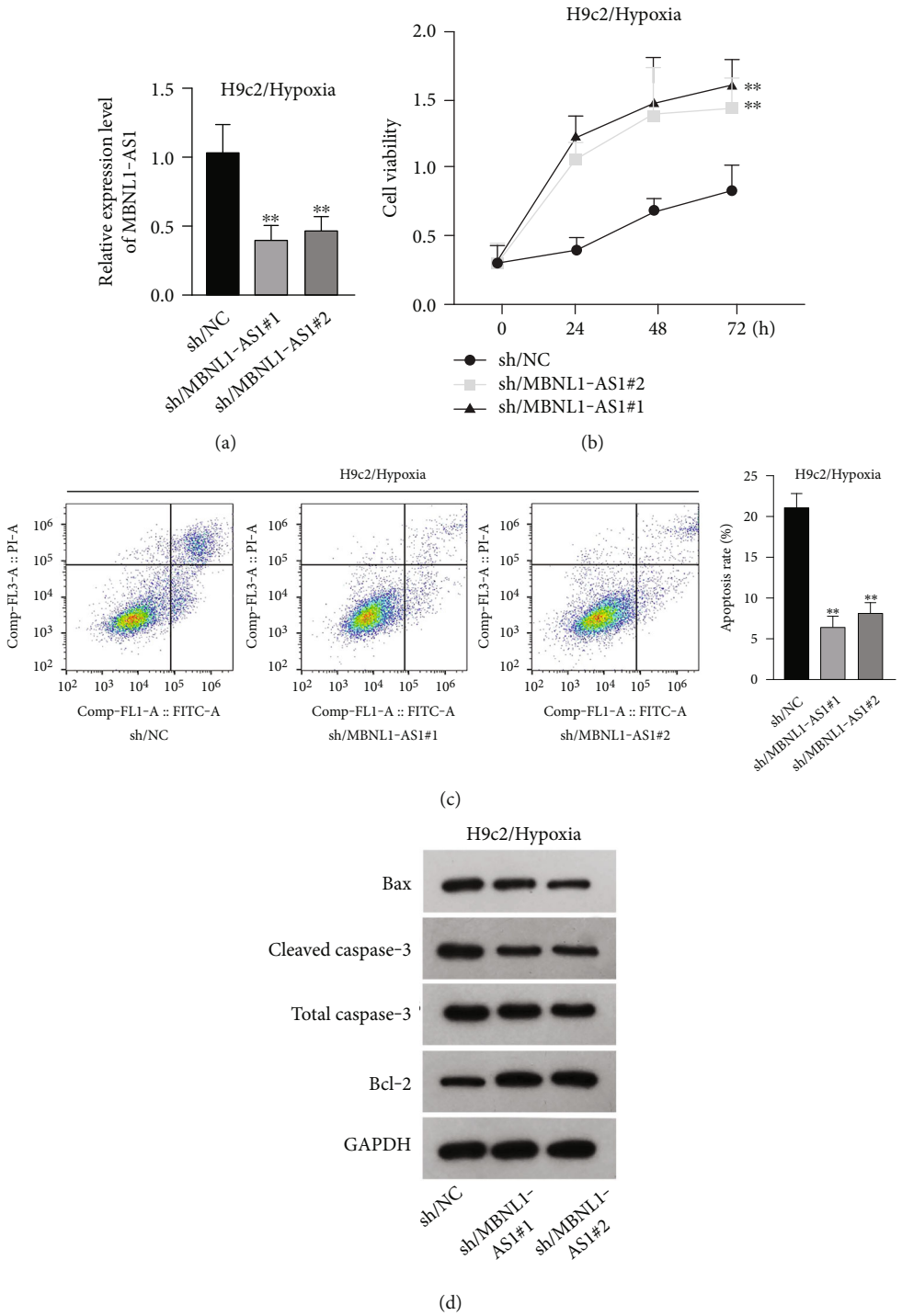

Figure 2: Impacts of MBNL1-AS1 depletion on hypoxia-induced H9c2 cell viability and apoptosis. (a) Silencing efficiency of MBNL1-AS1 was verified by RT-qPCR in hypoxia-induced H9c2 cells. (b) Viability of H9c2 cells after MBNL1-AS1 silencing was examined via CCK-8 assay with 8 h hypoxia treatment. (c) Apoptosis of H9c2 cells after MBNL1-AS1 silencing was examined by flow cytometry analysis, after exposure of hypoxia for 8 h. (d) Levels of apoptosis-related proteins were measured in MBNL1-AS1-depleted H9c2 cells after exposure of hypoxia for 8 h by western blot.** $P < 0.01$.

MBNL1-AS1 probe was purchased by RiboBio. DAPI (D9542, Sigma-Aldrich, St. Louis, MO, USA) was applied for nuclear staining. Images of both H9c2 and H9c2/Hypoxia cells were captured by confocal microscope (Axio-Imager_LSM-800, Zeiss, Oberkochen, Germany).

2.8. Cell Transfection. Three experiments were performed independently. Specific shRNAs for MBNL1-AS1, RAB14, and CAMTA1 were obtained by GenePharma (Shanghai, China) with the sh/NC being negative control. miR-132-3p mimics, miR-132-3p inhibitor, and the negative controls

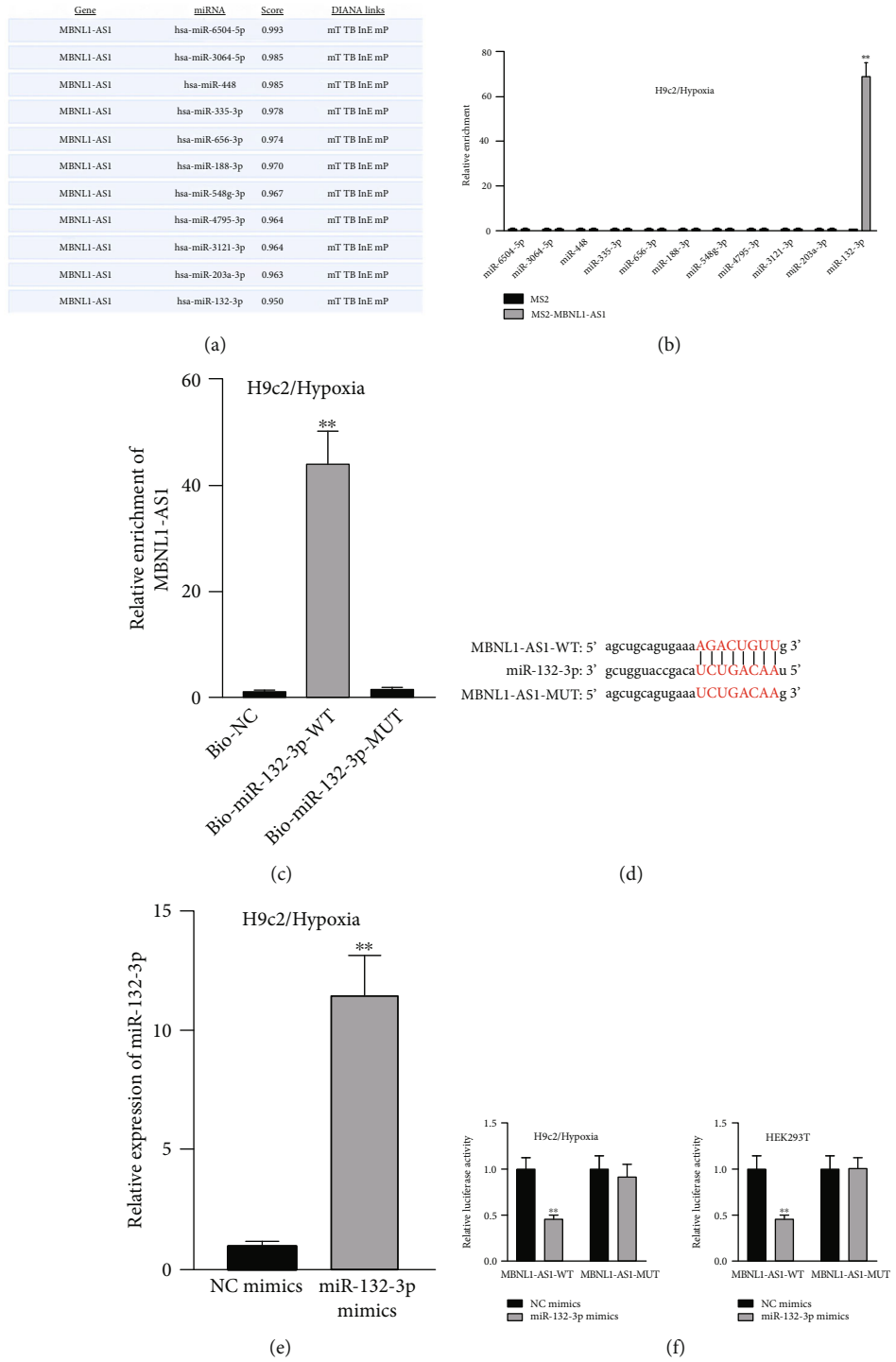

FIGURE 3: miR-132-3p interacts with MBNL1-AS1. (a) miRNAs bound to MBNL1-AS1 from DIANA database with the threshold value > 0.95. (b) MS2-RIP assay detected the combination between candidate miRNAs and MBNL1-AS1. (c) RNA pull down assay measured the combination between MBNL1-AS1 and miR-132-3p. (d) Binding sites between MBNL1-AS1 and miR-132-3p. (e) Upregulation efficiency of miR-132-3p was measured by RT-qPCR. (f) Luciferase activities of MBNL1-AS1-WT as well as MBNL1-AS1-MUT were detected in hypoxia-treated H9c2 and HEK293T cells after miR-132-3p elevation. $^{**}P < 0.01$.

(NC mimics and NC inhibitor) were also supplied by GenePharma. Cell transfection was performed using lipofectamine 3000 reagent (Life Technologies Corporation), and the transfection efficiency was verified by RT-qPCR.

2.9. MS2-RNA-Binding Protein Immunoprecipitation (RIP). Three independent experiments were performed. Maltose-binding protein (MBP)-affinity purification was employed to evaluate miRNAs that are related to MBNL1-AS1. Cells

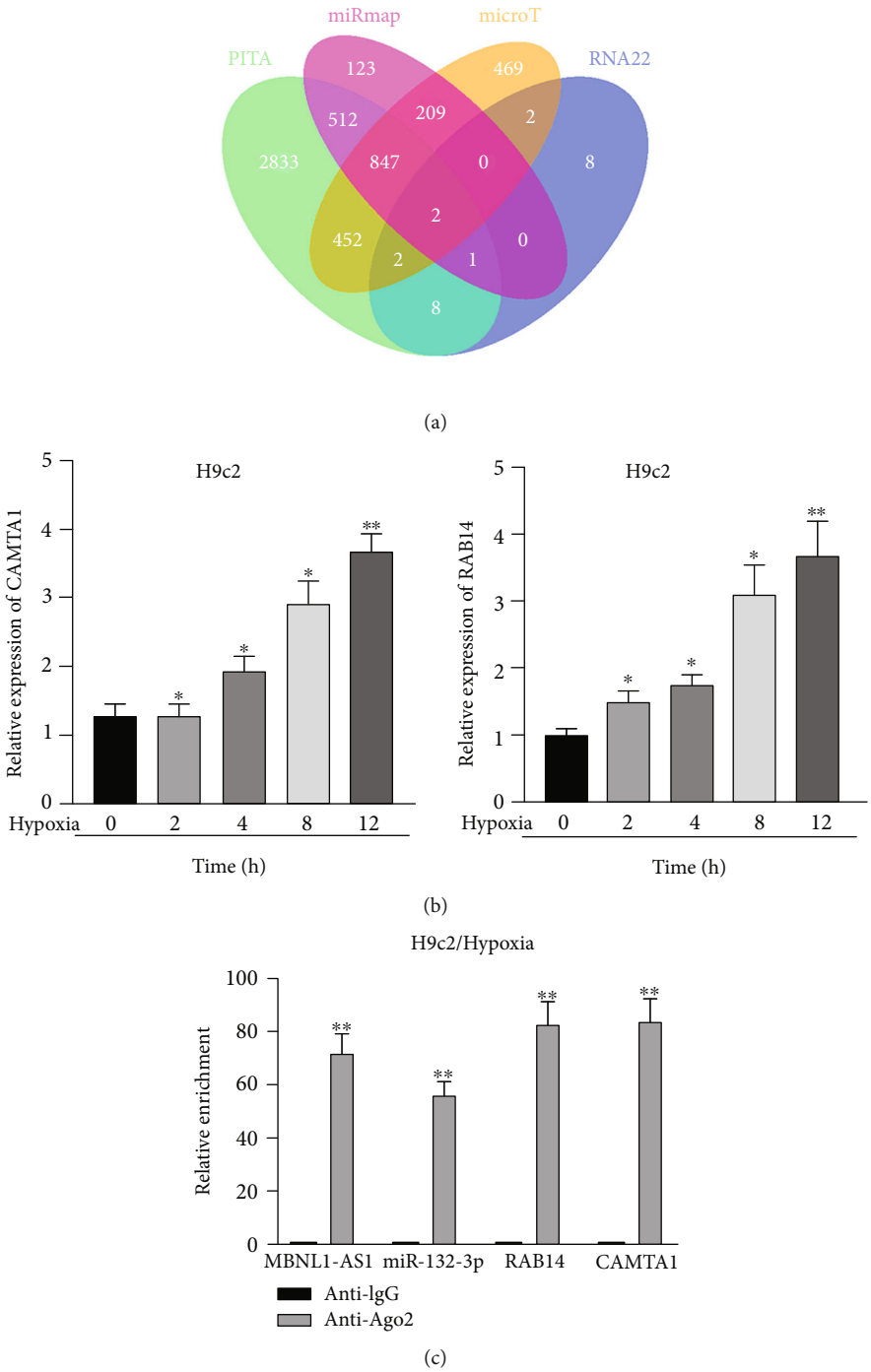

Figure 4: Continued.

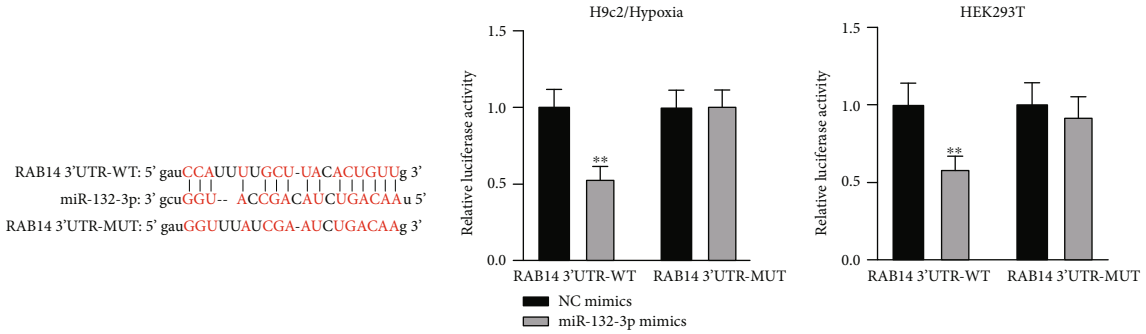

(d)

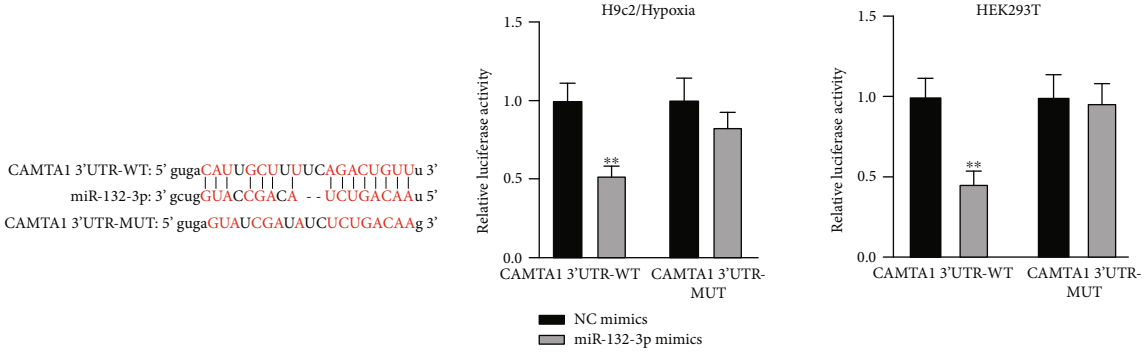

(e)

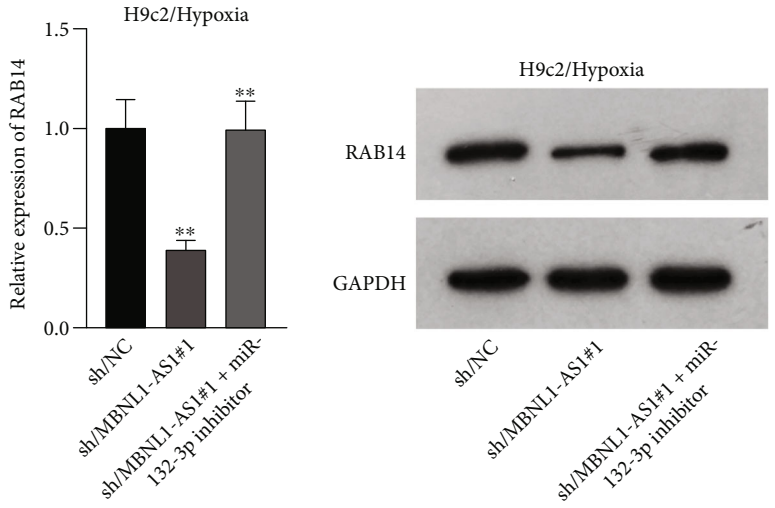

(f)

Figure 4: Continued.

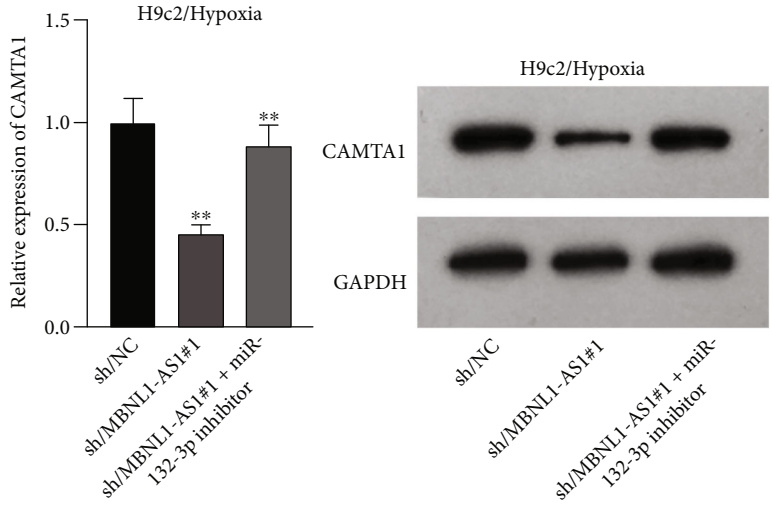

(g)

Figure 4: miR-132-3p directly targets CAMTA1 and RAB14. (a) Two mRNAs (CAMTA1 and RAB14) targeted by miR-132-3p were sifted out by four bioinformatics tools including PITA, miRmap, microT, and RNA22. (b) Expression of CAMTA1 and RAB14 were detected in H9c2 cells under hypoxia treatment for 0-12 h. (c) RIP assays detected the abundance of MBNL1-AS1, miR-132-3p, CAMTA1, and RAB14 in anti-Ago2 groups. (d, e) Binding sites between miR-132-3p and RAB14 3′UTR/CAMTA1 3′UTR, and luciferase activities of RAB14 3′ UTR-WT/MUT as well as CAMTA1 3′UTR-WT/MUT were assessed in hypoxia-treated H9c2 and HEK293T cells after miR-132-3p overexpression. (f, g) Expression of RAB14 and CAMTA1 were examined in hypoxia-treated H9c2 cells after the transfection of sh/NC, sh/MBNL1-AS1#1, and sh/MBNL1-AS1#1 + miR-132-3p inhibitor, respectively. $^{**}P < 0.01$.

were treated with MS2-tagged MBNL1-AS1 to acquire miRNAs related to MBNL1-AS1. The RIP assay was conducted as previously described [11]. The abundance of miRNAs was measured by RT-qPCR.

2.10. Luciferase Reporter Assay. Three experiments were performed independently. The fragment of RAB14 3′-UTR or CAMTA1 3′ UTR or MBNL1-AS1 containing the miR-132-3p binding site were inserted into pmirGLO dual luciferase vector (E1330, Promega, Madison, Wisconsin, USA). The luciferase reporter plasmids were cotransfected into hypoxia-induced cardiomyocytes or HEK293T cells with miR-132-3p mimics. The luciferase activity of wild-type MBNL1-AS1/RAB14/CAMTA1 (MBNL1-AS1-WT, MBNL1-AS1-WT, and CAMTA1-WT) and their mutant types (MBNL1-AS1-MUT, MBNL1-AS1-MUT, and CAMTA1-MUT) was measured by Dual Luciferase Reporter Assay System procured from Promega.

2.11. Statistical Analysis. Data of experimental results was presented as mean ± standard deviation and processed by Graphpad Prism 8 software (GraphPad Software, San Diego, United States). Statistical analyses were implemented with SPSS 19.0 software (IBM, Stanford University, United States). Statistical differences were tested by Student's t test or one-way analysis of variance (ANOVA). Statistical differences were considered significant when $P < 0.05$.

3. Results

3.1. Upregulation of MBNL1-AS1 in Hypoxia-Induced H9c2 Cells. Firstly, H9c2 cells were subjected to the exposure of hypoxia for 0–12 h, and the viability of H9c2 cells was declined in a time dependent manner (Figure 1(a)). Since cell viability was reduced to about 50% after 8 h of hypoxia treatment, 8 h was chosen as a hypoxia-stimulating condition to be applied in the subsequent assays. Besides, the results from flow cytometry manifested that the apoptosis rate of H9c2 cells was promoted with increasing duration of hypoxia treatment (Figure 1(b)). This phenomenon was further obtained from western blot analysis. As indicated in Figure 1(c), the levels of proapoptotic proteins (Bax and cleaved caspase-3) were significantly elevated whereas that of Bcl-2 (antiapoptotic protein) was decreased as the hypoxia treatment time increased. These data collectively suggested that the MI in vitro model was successfully established. Then, we assessed the expression of MBNL1-AS1 in H9c2 cells subjected to hypoxic treatment using RT-qPCR. The results indicated that MBNL1-AS1 expression was elevated with increasing duration of hypoxia treatment (Figure 1(d)). In addition, the results of subcellular fractionation and FISH assays indicated that MBNL1-AS1 was majorly distributed in the cytoplasm of both H9c2 and hypoxia-induced H9c2 cells (Figures 1(e) and 1(f)), suggesting that MBNL1-AS1 might exert critical functions in hypoxia-induced H9c2 cells via posttranscriptional regulation.

3.2. MBNL1-AS1 Depletion Increases the Viability and Decreases the Apoptosis of Hypoxia-Induced H9c2 Cells. To seek the functional impacts of MBNL1-AS1 in hypoxia-induced H9c2 cells, two specific shRNAs targeting MBNL1-AS1 were transfected into cells to silence MBNL1-AS1 expression. Then, RT-qPCR analysis verified the

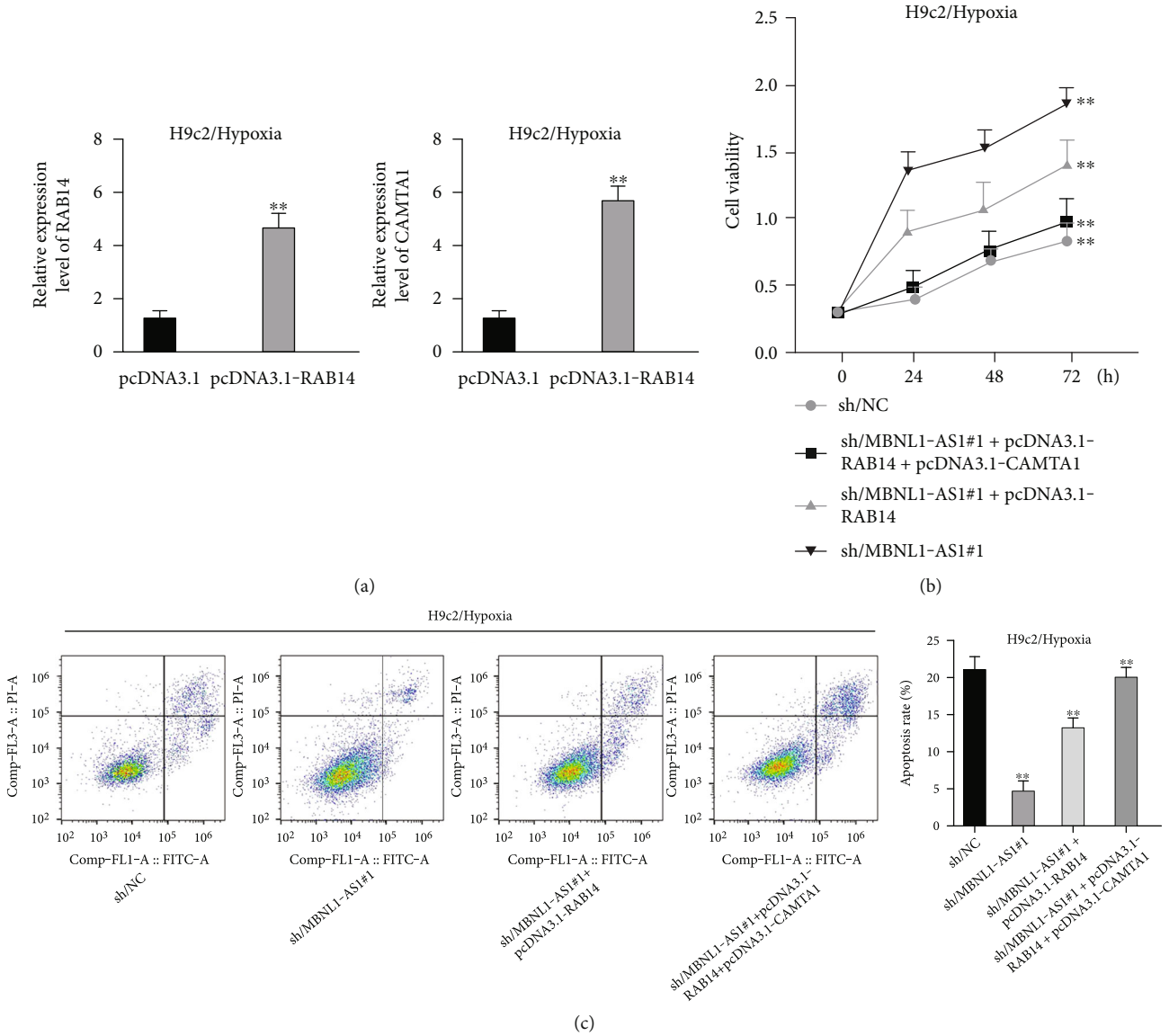

Figure 5: Continued.

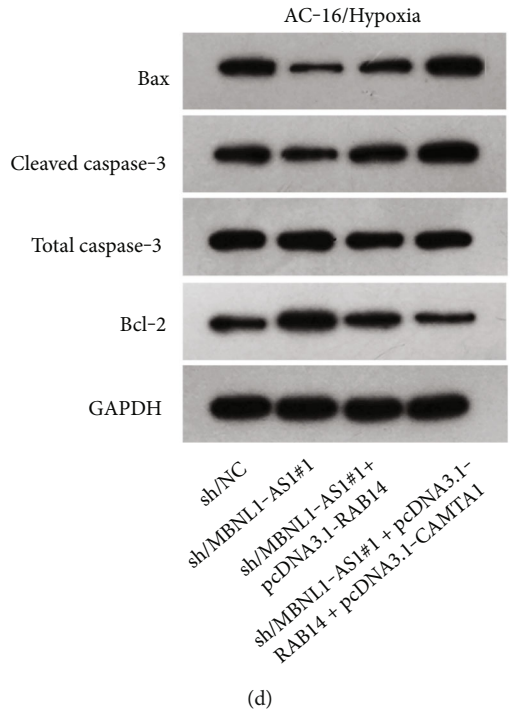

Figure 5: MBNL1-AS1 regulates hypoxia-induced H9c2 cell viability via upregulating RAB14 and CAMTA1. (a) Overexpression efficiency of RAB14 or CAMTA1 was certified by RT-qPCR. Rescue assays were implemented in H9c2 cells after the transfection of sh/NC, sh/MBNL1-AS1#1, sh/MBNL1-AS1#1 + pcDNA3.1-RAB14, and sh/MBNL1-AS1#1 + pcDNA3.1-RAB14 + pcDNA3.1-CAMTA1, respectively. (b) H9c2/Hypoxia cell viability was assessed by CCK-8 assay after different transfections. (c) H9c2/Hypoxia cell apoptosis was assessed through flow cytometry analysis after different transfections. (d) Protein levels of Bax, cleaved caspase-3, and Bcl-2 was measured by western blot. $^{**}P < 0.01$.

successful transfection (Figure 2(a)). The results of functional assays revealed that the viability of hypoxia-induced H9c2 cells was increased when MBNL1-AS1 was knocked down (Figure 2(b)). Meanwhile, MBNL1-AS1 depletion diminished the apoptosis rate of H9c2 cells under hypoxia treatment (Figure 2(c)). Additionally, the expression of apoptosis-linked proteins was detected by western blot analysis. The results showed that the expression of Bax and cleaved caspase-3 were decreased in hypoxia-induced H9c2 cells after MBNL1-AS1 deletion but that of Bcl-2 was enhanced (Figure 2(d)).

3.3. MBNL1-AS1 Binds to miR-132-3p. Given that MBNL1-AS1 was preferentially located in cell cytoplasm, we conjectured that MBNL1-AS1 might work as a ceRNA to sponge specific miRNA in MI progression. Based on DIANA (http://carolina.imis.athena-innovation.gr) tool, we predicted 11 miRNAs harboring binding sites of MBNL1-AS1 with the threshold value > 0.95 (Figure 3(a)). Then MS2-RIP assay was employed to determine the target miRNAs of MBNL1-AS1 in hypoxia-induced H9c2 cells. The results indicated that MS2-tagged MBNL1-AS1 vector was abundant for miR-132-3p (Figure 3(b)). Moreover, the data of RNA pull down assay indicated that MBNL1-AS1 was pulled down by biotin-labeled miR-132-3p wild-type rather than biotin-labeled miR-132-3p mutant-type (Figure 3(c)). In addition, the binding sites between MBNL1-AS1 and miR-132-3p were predicted by starBase (http://starbase.sysu.edu.cn) and presented in Figure 3(d). To further assess the interaction between MBNL1-AS1 and miR-132-3p, we firstly overexpressed miR-132-3p in H9c2/Hypoxia cells (Figure 3(e)). The data of luciferase reporter assay demonstrated that miR-132-3p mimics decreased the luciferase activity of MBNL1-AS1-WT in H9c2/Hypoxia and HEK293T cells, but had no changes on that of MBNL1-AS1-MUT (Figure 3(f)). To validate whether MBNL1-AS1 is involved in MI via interacting with miR-132-3p, RT-qPCR was firstly performed and data manifested that miR-132-3p was downregulated in miR-132-3p inhibitor group than that in the NC group (Figure S1A). Subsequently, rescue assays were carried out. The results indicated that miR-132-3p silencing reversed the increased viability and the reduced apoptosis caused by MBNL1-AS1 depletion in H9c2 cells under hypoxia treatment (Figure S1B-S1C). Similarly, the inhibited protein levels of Bax and cleaved caspase-3 as well as the elevated Bcl-2 levels in MBNL1-AS1-silenced H9c2 cells under hypoxia treatment were restored after cotransfection of miR-132-3p inhibitor (Figure S1D).

3.4. miR-132-3p Directly Targets CAMTA1 and RAB14. Applying four bioinformatics tools including PITA, miRmap, microT, and RNA22, 2 mRNAs (CAMTA1 and RAB14) targeted by miR-132-3p were sifted out (Figure 4(a)). Then we detected their expression in hypoxia-treated H9c2 cells for 0-12 h. We found that

CAMTA1 and RAB14 were upregulated in H9c2 cells in a time-independent manner (Figure 4(b)). Besides, we silenced CAMTA1 and RAB14 expression and found that knockdown of CAMTA1 and RAB14 significantly elevated the viability and inhibited the apoptosis of H9c2 cells under hypoxia treatment (Figure S2A-S2D). To test whether MBNL1-AS1, miR-132-3p, CAMTA1, and RAB14 coexisted in the RNA-induced silencing complex (RISC), RIP assay was performed using Ago2 antibody. It was revealed that these four RNAs were largely abundant in anti-Ago2 groups relative to anti-IgG groups (Figure 4(c)). Moreover, we severally predicted the binding sites of miR-132-3p on RAB14 3′UTR and CAMTA1 3′UTR, and found that miR-132-3p overexpression led to a reduction on the luciferase activities of RAB14 3′UTR-WT and CAMTA1 3′UTR-WT in H9c2/Hypoxia and HEK293T cells, while barely influenced those of RAB14 3′UTR-MUT and CAMTA1 3′UTR-MUT (Figures 4(d) and 4(e)). In addition, we revealed that MBNL1-AS1 silencing markedly declined the expression of RAB14 and CAMTA1, while this effect was counteracted by miR-132-3p silencing (Figures 4(f) and 4(g)).

3.5. MBNL1-AS1 Regulates the Viability of Hypoxia-Induced H9c2 Cells via Upregulating RAB14 and CAMTA1. We further upregulated RAB14 and CAMTA1 expression (Figure 5(a)), and then separately transfected sh/NC, sh/MBNL1-AS1#1, sh/MBNL1-AS1#1 + pcDNA3.1-RAB14, and sh/MBNL1-AS1#1 + pcDNA3.1-RAB14 + pcDNA3.1-CAMTA1 into hypoxia-treated H9c2 cells for rescue assays. The results indicated that the enhanced cell viability induced by MBNL1-AS1 knockdown under hypoxia treatment was partly offset after RAB14 overexpression, and was fully counteracted after the simultaneous overexpression of RAB14 and CAMTA1 (Figure 5(b)). Besides, the inhibited apoptosis rate in MBNL1-AS1-depleted H9c2 cells under hypoxia treatment was partially abolished when RAB14 was increased together, and was totally counteracted after overexpression of RAB14 and CAMTA1 simultaneously (Figure 5(c)). Likewise, the lessened Bax and cleaved caspase-3 levels as well as the increased Bcl-2 levels in hypoxia-treated H9c2 cells after MBNL1-AS1 downregulation were partly neutralized by RAB14 elevation, and was completely abrogated when RAB14 and CAMTA1 were upregulated together (Figure 5(d)).

4. Discussion

A large amount of lncRNAs have been identified to be associated with multiple kinds of cardiovascular diseases, MI included. lncRNA CAIF represses autophagy and improves MI via p53-mediated myocardin transcription [12]. lncRNA H19 inhibits MI-induced myocardial injury through regulating KDM3A [13]. lncRNA Gm2691 impedes apoptosis and inflammatory response after MI via the PI3K/Akt signaling pathway [14]. In this research, we found that lncRNA MBNL1-AS1, a wide coverage gene in cancer progression, was significantly highly expressed in H9c2 cells under hypoxia treatment. Moreover, functional assays proved that MBNL1-AS1 silencing significantly promoted the viability and restrained the apoptosis of hypoxia-induced H9c2 cells. These findings were in line with a previous study about ischemia-reperfusion injury [10], suggesting that lncRNA MBNL1-AS1 might contribute to MI progression.

Recent studies have revealed that lncRNAs interact with miRNAs and exert important functions in the development of diseases. Dysregulation of miRNAs was extensively reported in the progression of MI. miRNA-145 represses MI-induced apoptosis via Akt3/mTOR signaling pathway [15]. miRNA-488-3p impedes acute MI-induced cardiomyocyte apoptosis via modulating ZNF791 [16]. miR-124 influences cardiomyocyte apoptosis and MI via targeting Dhcr24 [17]. Moreover, the lncRNA-miRNA interaction in MI is emerged as an interest topic. In this study, we focused on the relation between MBNL1-AS1 and miRNAs, with the purpose of revealing a potential mechanism of which MBNL1-AS1 promoted MI. We found that MBNL1-AS1 directly bound to miR-132-3p. As reported previously, miR-132-3p is involved in ischemic myocardial injury by interacting with lncRNA TUG1 [18]. In our study, we further showed that MBNL1-AS1 regulates MI in hypoxia-induced H9c2 cells via targeting miR-132-3p. Additionally, miRNAs combines with their target mRNAs to block the mRNA translation. miR-132-3p has been registered to directly target SOX11 to inhibit mantle cell lymphoma progression [19]. In our research, we found that RAB14 and CAMTA1 were targeted by miR-132-3p. Moreover, we validated that MBNL1-AS1 served as a sponge for miR-132-3p, and subsequent regulated RAB14 and CAMTA1 expressions.

5. Conclusions

To sum up, we demonstrated that lncRNA MBNL1-AS1 promoted hypoxia-induced MI in H9c2 cells via the regulation of miR-132-3p/RAB14/CAMTA1 axis. Our study might provide an innovative target for the treatment of MI. However, our study also exist some limitations. First, our study did not explore the upregulation mechanism of MBNL1-AS1 in hypoxia-treated H9c2 cells. Moreover, our study did not investigate whether MBNL1-AS1 is involved in MI via the modulation of certain pathways. All of these deficiencies will be improved in the near future.

Abbreviations

3′-UTR: 3′-Untranslated region
ANOVA: Analysis of variance
CAMTA1: Calmodulin binding transcription activator 1
CCK-8: Cell counting kit-8
ceRNA: Competitive endogenous RNA
FISH: Fluorescent in situ hybridization
lncRNA: Long noncoding RNA
MBP: Maltose-binding protein
miRNAs: MicroRNAs
MBNL1-AS1: Muscleblind like splicing regulator 1 antisense RNA 1

MI: Myocardial infarction
ncRNAs: Noncoding RNAs
RT-qPCR: Quantitative real-time polymerase chain reaction
RAB14: RAB14, member RAS oncogene family
RIP: RNA-binding protein immunoprecipitation
RISC: RNA-induced silencing complex.

Data Availability

The data used to support the findings of this study are included within the article.

Conflicts of Interest

The authors declare that they have no conflicts of interest.

Authors' Contributions

Yanbing Li and Min Zong contributed equally to this work.

Acknowledgments

This work was supported by Guangdong Basic and Applied Basic Research Foundation [2018A030307056] of China by Zhi Li.

Supplementary Materials

Figure S1: MBNL1-AS1 regulates the viability and apoptosis in hypoxia-induced H9c2 cells via miR-132-3p. Figure S2: knockdown of RAB14 and CAMTA1 increase the viability and decrease the apoptosis in hypoxia-induced H9c2 cells. *(Supplementary Materials)*

References

[1] T. J. Pollard, "The acute myocardial infarction," *Primary Care*, vol. 27, no. 3, pp. 631–649, 2000.

[2] A. Sirajuddin, S. M. Mirmomen, S. J. Kligerman et al., "Ischemic heart disease: noninvasive imaging techniques and findings," *Radiographics*, vol. 41, no. 4, pp. 990–1021, 2021.

[3] K. Thygesen, J. S. Alpert, and H. D. White, "Universal definition of myocardial infarction," *Journal of the American College of Cardiology*, vol. 50, no. 22, pp. 2173–2195, 2007.

[4] V. Sucato, G. Testa, S. Puglisi, S. Evola, A. R. Galassi, and G. Novo, "Myocardial infarction with non-obstructive coronary arteries (MINOCA): intracoronary imaging-based diagnosis and management," *Journal of Cardiology*, vol. 77, no. 5, pp. 444–451, 2021.

[5] M. Wolfien, D. L. Brauer, A. Bagnacani, and O. Wolkenhauer, "Workflow development for the functional characterization of ncRNAs," *Methods in Molecular Biology*, vol. 1912, pp. 111–132, 2019.

[6] B. Chen, M. P. Dragomir, C. Yang, Q. Li, D. Horst, and G. A. Calin, "Targeting non-coding RNAs to overcome cancer therapy resistance," *Signal Transduction and Targeted Therapy*, vol. 7, no. 1, p. 121, 2022.

[7] M. Matsui and D. R. Corey, "Non-coding RNAs as drug targets," *Nature Reviews. Drug Discovery*, vol. 16, no. 3, pp. 167–179, 2017.

[8] B. Bartsch, P. R. Goody, M. R. Hosen et al., "ncRNAs in vascular and valvular intercellular communication," *Frontiers in Molecular Biosciences*, vol. 8, p. 749681, 2021.

[9] G. Cao, B. Tan, S. Wei et al., "Down-regulation of MBNL1-AS1 contributes to tumorigenesis of NSCLC via sponging miR-135a-5p," *Biomedicine & pharmacotherapy = Biomedecine & pharmacotherapie.*, vol. 125, p. 109856, 2020.

[10] X. F. Li, Z. Q. Wang, L. Y. Li, G. Q. Zhao, and S. N. Yu, "Down-regulation of the long noncoding RNA MBNL1-AS1 protects sevoflurane-pretreated mice against ischemia-reperfusion injury by targeting KCNMA1," *Experimental & Molecular Medicine*, vol. 50, no. 9, p. 115, 2018.

[11] W. Luan, L. Li, Y. Shi et al., "Long non-coding RNA MALAT1 acts as a competing endogenous RNA to promote malignant melanoma growth and metastasis by sponging miR-22," *Oncotarget*, vol. 7, no. 39, pp. 63901–63912, 2016.

[12] C. Y. Liu, Y. H. Zhang, R. B. Li et al., "lncRNA CAIF inhibits autophagy and attenuates myocardial infarction by blocking p53-mediated myocardin transcription," *Nature Communications*, vol. 9, no. 1, p. 29, 2018.

[13] B. F. Zhang, H. Jiang, J. Chen et al., "lncRNA H19 ameliorates myocardial infarction-induced myocardial injury and maladaptive cardiac remodelling by regulating KDM3A," *Journal of Cellular and Molecular Medicine*, vol. 24, no. 1, pp. 1099–1115, 2020.

[14] T. Li, H. Tian, J. Li et al., "Overexpression of lncRNA Gm2691 attenuates apoptosis and inflammatory response after myocardial infarction through PI3K/Akt signaling pathway," *IUBMB Life*, vol. 71, no. 10, pp. 1561–1570, 2019.

[15] L. Yan, N. Guo, Y. Cao et al., "miRNA-145 inhibits myocardial infarction-induced apoptosis through autophagy via Akt3/mTOR signaling pathway in vitro and in vivo," *International Journal of Molecular Medicine*, vol. 42, no. 3, pp. 1537–1547, 2018.

[16] H. F. Zheng, J. Sun, Z. Y. Zou, Y. Zhang, and G. Y. Hou, "miRNA-488-3p suppresses acute myocardial infarction-induced cardiomyocyte apoptosis via targeting ZNF791," *European Review for Medical and Pharmacological Sciences*, vol. 23, no. 11, pp. 4932–4939, 2019.

[17] F. Han, Q. Chen, J. Su et al., "MicroRNA-124 regulates cardiomyocyte apoptosis and myocardial infarction through targeting Dhcr24," *Journal of Molecular and Cellular Cardiology*, vol. 132, pp. 178–188, 2019.

[18] Q. Su, Y. Liu, X. W. Lv, R. X. Dai, X. H. Yang, and B. H. Kong, "lncRNA TUG1 mediates ischemic myocardial injury by targeting miR-132-3p/HDAC3 axis," *American Journal of Physiology. Heart and Circulatory Physiology*, vol. 318, no. 2, pp. H332–H344, 2020.

[19] B. Wu, J. Li, H. Wang, Q. Wu, and H. Liu, "miR-132-3p serves as a tumor suppressor in mantle cell lymphoma via directly targeting SOX11," *Naunyn-Schmiedeberg's Archives of Pharmacology*, vol. 393, no. 11, pp. 2197–2208, 2020.

Hindawi
Oxidative Medicine and Cellular Longevity
Volume 2023, Article ID 3612814, 9 pages
https://doi.org/10.1155/2023/3612814

Research Article

Emodin Regulates lncRNA XIST/miR-217 Axis to Protect Myocardial Ischemia-Reperfusion Injury

Shuai Huang[1], **Lailiang Xue**[2] **and Qiaona Mou**[3]

[1]*Shandong Yuncheng Center for Disease Control and Prevention, Heze, 274700 Shandong, China*
[2]*Department of Cardiology, Gaoxin District People's Hospital of Linyi, Linyi, 276000 Shandong, China*
[3]*Department of Cardiology, Yantai Laiyang Central Hospital, Yantai, 265200 Shandong, China*

Correspondence should be addressed to Qiaona Mou; mouqiaona@lyzxyy.org.cn

Received 20 September 2022; Revised 22 October 2022; Accepted 24 November 2022; Published 31 January 2023

Academic Editor: Xinyong Cai

Purpose. This study is aimed at investigating the effect of emodin on myocardial ischemia-reperfusion injury (MIRI) and mechanism. *Methods*. Eighty healthy adult male SD rats (weighing 230-250 g) were utilized to establish I/R model, which were randomly divided into five groups (16 rats in each group): sham operation group, myocardial ischemia-reperfusion injury group (I/R group), emodin group, emodin +NC group, and emodin +XIST group. The contents of CK, CK-MB, LDH, and HBDH in serum were determined by ELISA kit. LDH was detected by ELISA assay, SOD was detected by the xanthine oxidase method, and MDA was detected by the thiobarbituric acid method. The relative expression of XIST and miR-217 was evaluated by RT-qPCR. Western blot was applied to detect the protein expression. Flow cytometry was applied to detect cardiomyocyte apoptosis. *Results*. Myocardial infarction area was obviously increased in I/R model rats, while emodin decreased the myocardial infarction in I/R model rats. In addition, cardiac enzymes (CK, CK-MB, LDH, and HBDH) and apoptosis were obviously increased in MIRI model rats, while emodin obviously decreased cardiac enzymes and apoptosis. The ROS and MDA levels were raised while the activities of SOD were declined in the I/R model group. The ROS and MDA levels were decreased while the activities of SOD were raised in the emodin group. The XIST expression was markedly raised in the I/R model group while decreased in the emodin group, and the overexpression of XIST reversed the protective effect of emodin on myocardial infarction, oxidative stress, and cardiomyocyte apoptosis. In addition, XIST directly regulated the expression of miR-217, and si-XIST inhibited H/R-induced oxidative damage of cardiomyocytes via inhibiting miR-217. *Conclusion*. Emodin protected MIRI both in vitro and in vivo via inhibiting lncRNA XIST to upregulate miR-217.

1. Introduction

Although the current treatment of acute myocardial infarction (AMI) has some effect, AMI and frequent heart failure are still the main causes of death [1]. Therefore, new treatment strategies are needed to protect the heart from the harmful effects of acute ischemia/reperfusion (I/R) injury. Myocardial ischemia-reperfusion injury (MIRI) refers to a series of reactions such as enlargement of infarct area and low cardiac function after successful recovery of cardiac blood flow, which not only fails to restore its function but also aggravates the myocardial injury. A large number of studies have shown that drug preconditioning has a certain protective effect on myocardial ischemia/reperfusion injury. In contract to drugs with broad-spectrum mechanism of action, drugs specifically targeting mitochondrial function have not proved to have obvious clinical significance [2]. China is rich in traditional Chinese medicine resources. It is of great clinical value to find drugs that can effectively protect the heart against ischemia/reperfusion injury. Emodin is an anthraquinone derivative from the rhizome of Rheum palmatum, which is widely used as a laxative in traditional Chinese medicine [3–5]. Emodin significantly reduced the level of inflammatory factors in myocardial injury and relieved LPS-induced myocardial injury [6]. Emodin can alleviate MIRI and has a good anti-inflammatory effect [7].

MIRI is a common pathophysiological manifestation in clinic, and its pathogenesis may be closely related to many

factors, such as increased free radical production, metabolic disorder of myocardial fiber capacity, increased nitric oxide, and activation of neutrophils [8]. Relevant research reports have confirmed that reducing cardiomyocyte apoptosis is conducive to improving the prognosis of MIRI. Apoptosis is a way of cell death, that is, programmed cell death. More and more evidence shows that apoptosis is an important pathogenesis of MIRI [9, 10]. In the rat ischemia-reperfusion injury model, it can be found that the apoptosis rate is obviously higher than that in the normal group [11]. Heusch found that ischemia-reperfusion rats have typical DNA breakage and apoptotic body formation; that is, reperfusion injury can have typical apoptotic phenomenon [12]. Activation of reactive oxygen species, intracellular calcium overload, and mitochondrial energy metabolism disorder is the main mechanisms of apoptosis in MIRI [13]. The caspase family plays a major role in the executive stage of apoptosis [14]. Apoptosis is accomplished by a variety of caspases. Caspase-3 is considered to be the terminal shear enzyme that various apoptosis-stimulating factors promote apoptosis [15]. Some studies have shown that caspase-3 activation is the main mechanism of myocardial cell apoptosis leading to the aggravation of myocardial infarction after reperfusion [16, 17]. In the early stage of MIRI and during reperfusion, apoptosis will aggravate myocardial injury. The study of blocking the signal pathway of apoptosis may provide a new theoretical basis for the prevention and treatment of MIRI. However, the effects of emodin on oxidative stress and apoptosis in MIRI and its underlying mechanisms have not been reported.

This study is mainly aimed at exploring the effects and potential mechanisms of emodin on oxidative stress and apoptosis in MIRI.

2. Materials and Method

2.1. Animals. Healthy adult male SD rats (weighing 230-250 g) were purchased from SBF Biotechnology Co., Ltd. and fed in a sterile and quiet environment with a temperature of 18-26°C and a humidity of 40%-70%. Rats were fed with fresh and clean sterile feed at fixed time every week. All animal experiments were carried out in accordance with the Guidelines for Laboratory Animals of the Animal Experiment. After three days of feeding, they were randomly divided into five groups (16 rats in each group): sham operation group, myocardial ischemia-reperfusion injury group (I/R group), emodin group, emodin +NC group, and emodin +XIST group. The I/R model was constructed. The left anterior descending coronary artery was ligated, and the heart was reset after ligation. After ischemia for 30 min, the ligation line was cut and had reperfusion for 120 min. The heart was quickly cut and placed in ice normal saline. The heart was washed and stored in a refrigerator at -80°C. The sham operation group was operated in the same way without ligation. Rats were injected with emodin 1 hour before I/R treatment.

2.2. Cell Line and Transfection. Immortalized rat H9C2 cardiomyocytes were obtained from ATCC and were cultured in DMEM with 10% fetal bovine serum and penicillin/streptomycin (Gibco, USA) at 37°C with 5% CO_2. To establish a cellular hypoxia-reoxygenation (H/R) model, H9C2 cells were maintained in anaerobic conditions for 3 h and then underwent reoxygenation for 6 h in the normoxic incubator. The small interfering RNAs (siRNAs) specifically targeting lncRNA-XIST were purchased from Ribobio (China).

Table 1: Primer sequence.

Target	Primer sequence (5′-3′)
miR-217	F: CGCAGATACTGCATCAGGAA
	R: CTGAAGGCAATGCATTAGGAACT
U6	F: CTCGCTTCGGCAGCACA
	R: AACGCTTCACGAATTTGCGT
XIST	F: GGTTCTGTCAAGATACTTTCCT
	R: CAATGAAGAGCTTGACGTG
β-Actin	F: ACGTCACGAACTACTAGCAAT
	R: TGTGTGCATGAGTCTCTCCACG

2.3. Luciferase Reporter Assay. The starBase database (https://starbase.sysu.edu.cn/) was utilized to predict the relationship between XIST and miR-217. Luciferase reporter assay was conducted to confirm the regulatory relationship. After amplifying the full length, XIST-WT vector was constructed, and XIST-MUT vector was constructed by point mutation kit (Hanbio Biotechnology Co., Ltd. Shanghai, China). XIST-WT or XIST-MUT was cotransfected into H9C2 cells with miR-217 mimic or miR-NC, respectively, by TurboFect. The luciferase activity was determined by kit after 48 hours using a dual luciferase reporter system (Promega).

2.4. RNA Isolation and Quantitative Real-Time PCR Analysis. Heart tissue samples (50-100 mg) were collected, and total RNA of cells was extracted by the TRIzol method. RNA was reverse-transcribed to cDNA according to the instructions of reverse transcription kit. qPCR reaction was carried out with All in-one miRNA kit (GeneCopoeia, USA), and the relative expression was calculated by the $2^{-\Delta\Delta CT}$ method. Primer sequences for PCR were shown in Table 1.

2.5. ELISA Assay. The contents of CK, CK-MB, LDH, and HBDH in serum were determined by ELISA kit (Beyotime, China).

2.6. Measurement of Myocardial Infarct Volume. Myocardial infarction area was detected by 1% TTC staining. After the hearts of rats in each group were frozen at -20°C for 30 min, they were cut into 5 slices of equal thickness, put into 1% TTC dye solution, dyed in 37°C constant temperature water bath for 30 min, washed and sliced with PBS for 3 times, and fixed with 10% formaldehyde for 12 h. Images were collected and processed by ImageJ software.

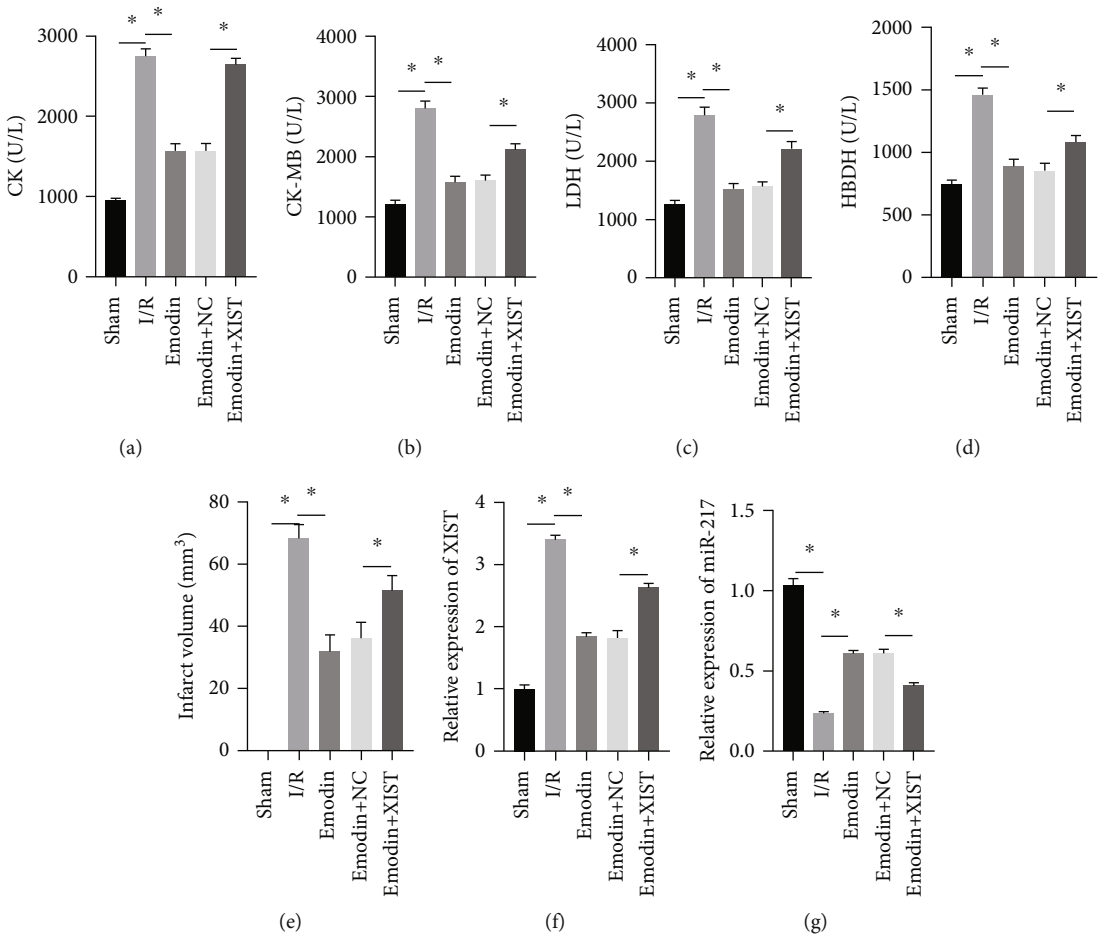

Figure 1: Emodin attenuated MIRI by inhibiting XIST. The contents of CK (a), CK-MB (b), LDH (c), and HBDH (d) in serum were determined by ELISA kit. Infarct volume (e) was detected via Image-Pro software. (e, g) The relative expression of XIST and miR-217 was evaluated by RT-qPCR. $n = 16$, $^*P < 0.05$.

2.7. Assessment of ROS, SOD, LDH, and MDA. The ROS were determined by ROS Assay Kit (DCFH-DA, Sigma-Aldrich, Merck KGaA) and were incubated with DCFH-DA (10 mM/L) for 30 min at 37°C in the dark. The ROS level was detected by flow cytometry. The concentrations of SOD, LDH, and MDA in rat myocardium were detected by chemical colorimetry. LDH was detected by ELISA assay, SOD was detected by the xanthine oxidase method, and MDA was detected by the thiobarbituric acid method. GAH-Px was detected by the colorimetric method. The relevant kits were purchased from Nanjing Jiancheng Bioengineering Institute.

2.8. Western Blot. Heart tissue samples (50-100 mg) and cardiomyocytes samples were collected and were fully lysed with RIPA lysate (Cell Signaling Technology, USA) for 30 min, and the protein concentration was detected with BCA protein detection kit. After 10% SDS-PAGE gel electrophoresis, the protein was transferred to PVDF membrane, and 5% skimmed milk powder blocked the protein at room temperature for 2 hours. The specific primary antibody (Abcam, UK) was incubated with PVDF membrane overnight at 4°C, and the corresponding secondary antibody (Abcam, UK) was incubated with PVDF membrane at room temperature. Chemiluminescence was developed using a hypersensitive ECL kit (Baiaosi, China).

2.9. Flow Cytometry Assay. After washing with PBS, the cells were resuspended, and 500 μL of binding buffer was added into suspension. 20 μL of annexin V-fluorescein isothiocyanate (Annexin V-FITC) was added into suspension, and cells were incubated at room temperature for 10 min. 20 μL of propidium iodide (PI) was added, and cells were incubated without light at room temperature for 5 min. FACScan flow cytometer (Becton, USA) was utilized for measurement.

2.10. Statistical Analysis. Statistical analysis was performed using SPSS 25.0 software. Mean between groups was compared with one-way ANOVA, and $P < 0.05$ was considered statistically significant.

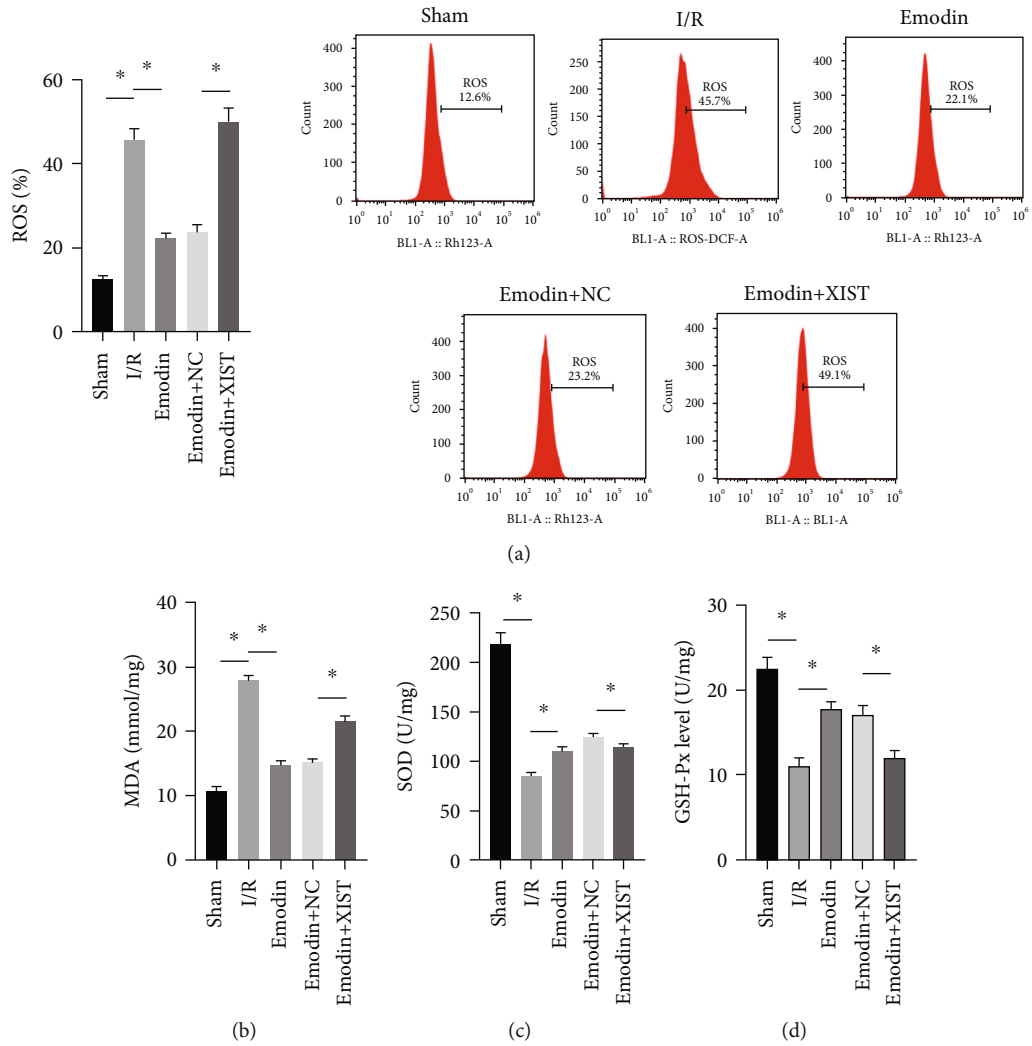

Figure 2: Emodin reduced oxidative stress by inhibiting XIST. (a) ROS was measured by flow cytometry. The contents of MDA (b), SOD (c), and GSH-Px (d) in myocardial tissues were determined. $n = 16$, $^*P < 0.05$.

3. Results

3.1. Emodin Attenuated Myocardial Ischemia-Reperfusion Injury by Inhibiting XIST. The activities of CK, CK-MB, LDH, and HNDH levels were increased in the I/R model group compared with the sham group, while the activities of CK, CK-MB, LDH, and HNDH levels were declined in the emodin group compared with the I/R model group (Figures 1(a)–1(d)). The activities of CK, CK-MB, LDH, and HNDH levels were increased in the emodin+XIST group compared with the emodin+NC group (Figures 1(a)–1(d)). Infarct size was obviously increased in the I/R model group compared with the sham group, while emodin declined the infarct size (Figure 1(e)). The relative expression of XIST was markedly raised in the I/R model group while decreased in the emodin group (Figure 1(f)). The relative expression of miR-217 was markedly decreased in the I/R model group while raised in the emodin group (Figure 1(g)).

3.2. Emodin Reduced Oxidative Stress by Inhibiting XIST. The ROS and MDA levels were increased in the I/R model group compared with the sham group, while the ROS and MDA levels were declined in the emodin group compared with the I/R model group (Figures 2(a) and 2(b)). In addition, the overexpression of XIST reversed the inhibitory effect of emodin on ROS and MDA levels. The activities of SOD were declined in the I/R model group compared with the sham group, while the activities of SOD were raised in the emodin group compared with the I/R model group (Figure 2(c)). The overexpression of XIST reversed the promoting effect of emodin on the activities of SOD (Figure 2(c)). The levels of GSH-Px were declined in the I/R model group compared with the sham group, while the levels of GSH-Px were raised in the emodin group compared with the I/R model group (Figure 2(d)). The overexpression of XIST reversed the promoting effect of emodin on the levels of GSH-Px.

3.3. Emodin Reduced Cardiomyocyte Apoptosis by Inhibiting XIST. The cardiomyocyte apoptosis (Figures 3(a) and 3(b)) and the expression of caspase-3 (Figure 3(d)) and Bax (Figure 3(e)) were increased in the I/R model group

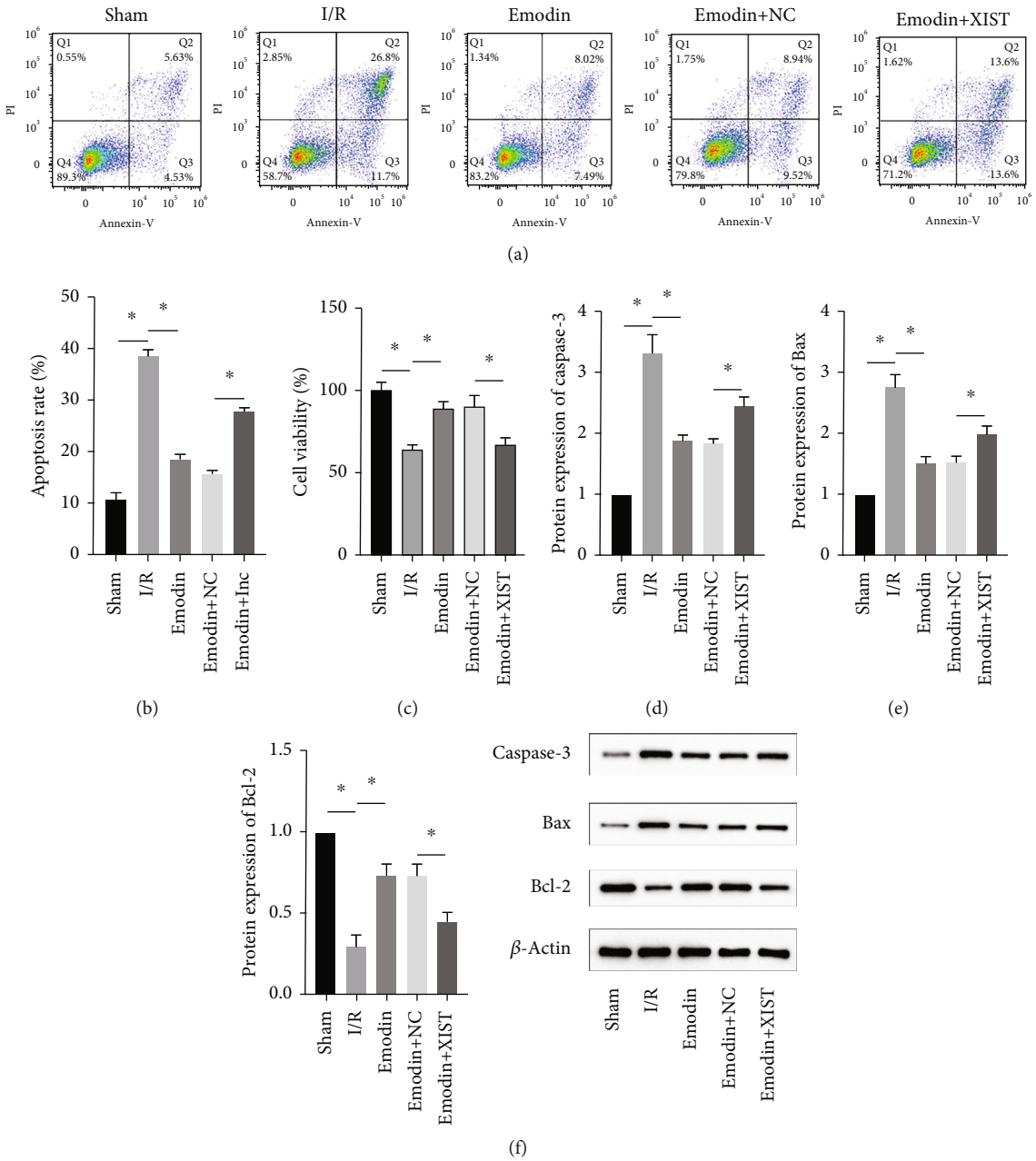

Figure 3: Emodin reduced cardiomyocyte apoptosis by inhibiting XIST. (a, b) Apoptosis was detected by flow cytometry. (c) CCK-8 assay was utilized to measure cell viability. (d–f) The protein expression of caspase-3 (d), Bax (e), and Bcl-2 (f) in myocardial tissues was determined. $n = 3$, $^*P < 0.05$.

compared with the sham group, while cardiomyocyte apoptosis and the expression of Bax and caspase-3 were declined in the emodin group compared with the I/R model group. In addition, the overexpression of XIST reversed the inhibitory effect of emodin on cardiomyocyte apoptosis and the expression of Bax and caspase-3. Cell viability was inhibited in the I/R model group compared with the sham group, while it was enhanced in the emodin group compared with the I/R model group. The overexpression of XIST reversed the promoting effect of emodin on cell viability (Figure 3(c)). The expression of Bcl-2 was decreased in the I/R model group compared with the sham group, while it was raised in the emodin group compared with the I/R model group (Figure 3(f)). The overexpression of XIST reversed the promoting effect of emodin on cardiomyocyte apoptosis and the expression of Bcl-2.

3.4. XIST Directly Regulated the Expression of miR-217. miR-217 was predicted to be regulated by XIST via TargetScan website (Figure 4(a)). The relative luciferase activity of XIST-WT was obviously decreased in miR-217 mimic while the relative luciferase activity of XIST-MUT was remained

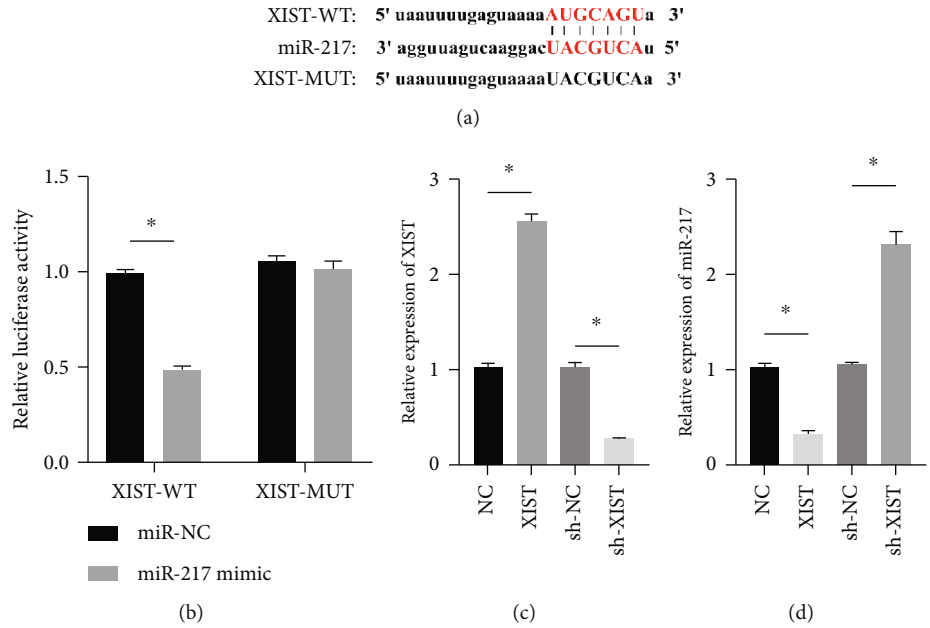

FIGURE 4: XIST directly regulated the expression of miR-217. (a) Predicted binding sites. (b) Inhibiting effect of miR-217 mimic on luciferase activity of XIST-WT. (c) The relative expression of XIST and miR-217 was evaluated by RT-qPCR (d). $n = 3$, $^*P < 0.05$.

unchanged (Figure 4(b)). The XIST expression was observably raised in the XIST group and was markedly decreased in the sh-XIST group (Figure 4(c)). Overexpressed XIST obviously inhibited the miR-217 expression while sh-XIST markedly raised the miR-217 expression (Figure 4(d)).

3.5. Si-XIST Inhibited H/R-Induced Oxidative Damage of Cardiomyocytes via Inhibiting miR-217. H/R treatment obviously decreased the miR-217 expression while si-XIST observably raised the miR-217 expression (Figure 5(a)). H/R treatment obviously raised ROS and MDA levels while si-XIST observably declined ROS and MDA levels, and miR-217 inhibitor markedly decreased ROS and MDA levels (Figures 5(b) and 5(c)). H/R treatment obviously inhibited the activities of SOD while si-XIST observably declined the activities of SOD, and miR-217 inhibitor markedly decreased ROS and MDA levels (Figure 5(d)).

3.6. miR-217 Directly Regulated the Expression of HDAC4. HDAC4 was predicted to be regulated by miR-217 via TargetScan website (Figure 6(a)). The relative luciferase activity of HDAC4-WT was obviously decreased in miR-217 mimic while the relative luciferase activity of HDAC4-MUT was remained unchanged (Figure 6(b)). The HDAC4 expression was observably raised in the miR-217 inhibitor group and was markedly decreased in the miR-217 mimic group (Figure 6(c)).

4. Discussion

Cardiovascular disease can cause reduced heart blood perfusion and insufficient oxygen supply to the heart, resulting in myocardial ischemia and hypoxia, abnormal cardiomyocyte metabolism, weak heart function, and threatening the life and health of patients [18]. The treatment for myocardial ischemia is blood flow reperfusion, which can restore cardiac oxygen supply and blood supply. However, studies reported that after ischemia and reperfusion, patients will have more serious arrhythmia, enlarged myocardial infarction, cardiac hypofunction, and even death, which is an obstacle in the clinical treatment of cardiovascular diseases [19].

The pathophysiological factors of MIRI include inflammatory stimulation, oxidative stress, cell necrosis, apoptosis, cardiomyocyte metabolism disorder, and other links, and MIRI is more closely related to reactive oxygen species free radicals and mitochondrial damage [20]. In MIRI, more oxygen free radicals form, and lipid peroxidation reacts with unsaturated fatty acids in membrane phospholipids, producing large amounts of toxic lipid peroxides, with impaired mitochondrial metabolism, and causing impaired cardiomyocyte structure [21]. Emodin can effectively prevent the expansion of inflammatory mediators and their biological effects and prevent serious complications mediated by inflammatory mediators. Present study demonstrated that the ROS and MDA levels were increased while the activities of SOD were decreased in the I/R model group. The ROS and MDA levels were decreased while the activities of SOD were raised in the emodin group. Therefore, emodin could improve the oxidative stress and cardiomyocyte apoptosis induced by MIRI, which is consistent with previous research results [22]. This study showed that ligation of the left anterior coronary artery in SD rats resulted in an increase in myocardial infarction area, while emodin decreased the myocardial infarction in MIRI model rats. In addition, emodin obviously decreased cardiac enzymes, oxidative stress, and apoptosis, which demonstrated that emodin exhibited

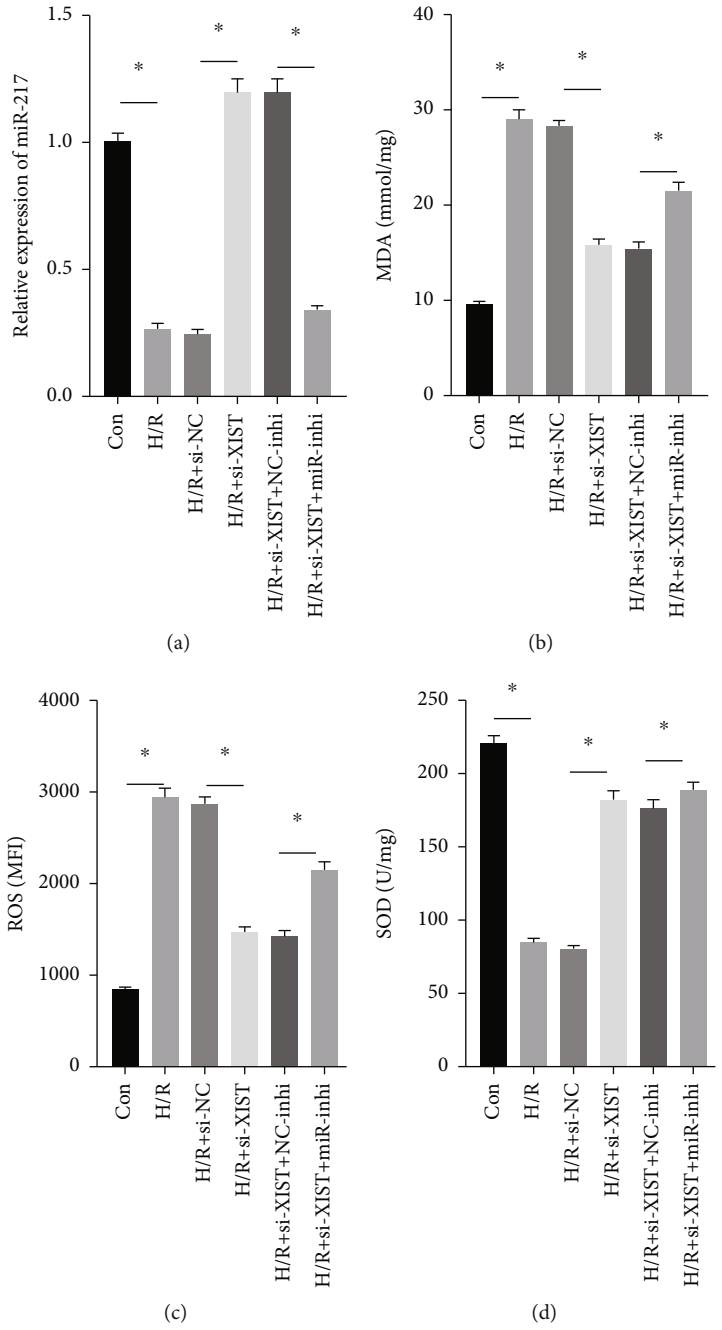

Figure 5: si-XIST inhibited H/R-induced oxidative damage of cardiomyocytes via inhibiting miR-217. (a) The relative expression of miR-217 was evaluated by RT-qPCR. The contents of MDA (b), ROS (c), and SOD (d) in myocardial tissues were determined. $n = 16$, $^*P < 0.05$.

protective functions against MIRI. This result is consistent with previous studies. Ye et al. had confirmed that emodin could alleviate MIRI [7]. Apoptosis may play a crucial role in the pathogenesis of myocardial ischemia-reperfusion injury. Relevant studies have confirmed that reducing the apoptosis of cardiomyocytes is beneficial to improve the prognosis of myocardial ischemia and reperfusion injury. Oxidative stress as well as the inflammatory response all play a crucial role in cardiomyocyte apoptosis.

Long chain noncoding RNA is a kind of RNA with a length of more than 200 nucleotides and does not encode proteins [23]. Although it does not have the ability to encode proteins, long chain noncoding RNA can regulate the expression level of target genes at the transcription and translation levels [24]. In MIRI, lncRNAs can regulate the activity of cardiomyocytes and the degree of reperfusion injury by targeting miRNA. Present study showed that the relative expression of XIST was markedly raised in the I/R model group while decreased in the emodin group, and the overexpression of XIST reversed the protective effect of emodin on myocardial infarction, oxidative stress, and cardiomyocyte apoptosis, which is similar to the results studied

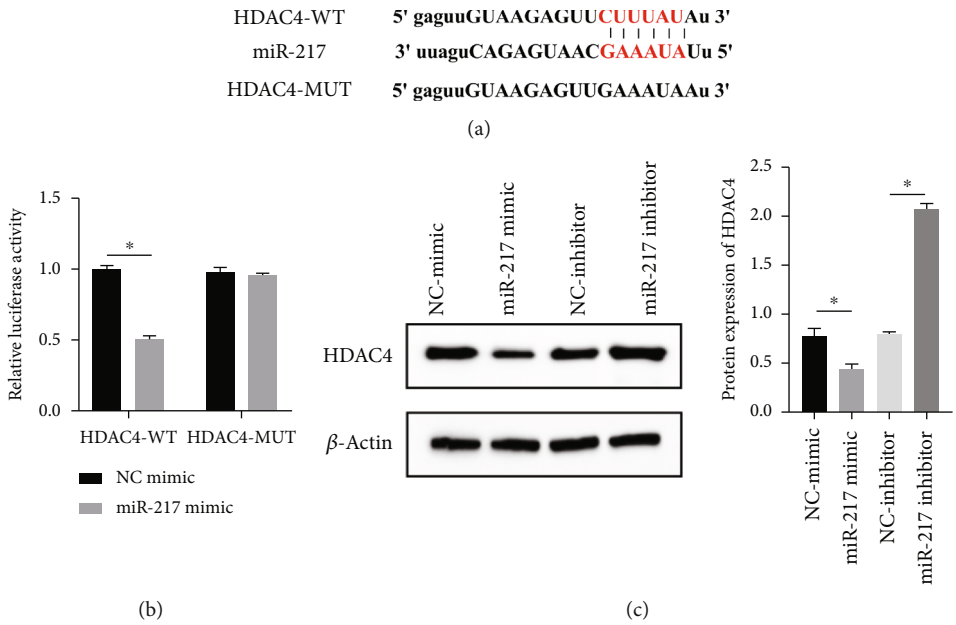

Figure 6: miR-217 directly regulated the expression of HDAC4. (a) Predicted binding sites. (b) Inhibiting effect of miR-217 mimic on luciferase activity of HDAC4-WT. (c) The protein expression of HDAC4 and miR-217 was evaluated by western blot. $n = 3$, $^*P < 0.05$.

by Wang et al. [25]. lncRNAs can regulate the occurrence and development of heart disease and play a role by transcriptional or posttranscriptional control or competitive binding to miRNAs. XIST directly regulated the expression of miR-217, and XIST inhibited H/R-induced oxidative damage of cardiomyocytes via inhibiting miR-217.

In conclusion, emodin protected MIRI both *in vitro* and *in vivo* via inhibiting lncRNA XIST to upregulate miR-217. This study has some limitations. However, whether emodin can affect myocardial infarction area through lncRNA XIST/miR-217 needs further study. Because there are many regulatory pathways of myocardial injury, other regulatory pathways still need further research and evidence.

Data Availability

Data to support the findings of this study is available on reasonable request from the corresponding author.

Conflicts of Interest

The authors do not have conflicts of interest to declare.

References

[1] H. A. Cabrera-Fuentes, J. Aragones, J. Bernhagen et al., "From basic mechanisms to clinical applications in heart protection, new players in cardiovascular diseases and cardiac theranostics: meeting report from the third international symposium on "new frontiers in cardiovascular research"," *Basic Research in Cardiology*, vol. 111, no. 6, p. 69, 2016.

[2] G. Campo, R. Pavasini, G. Morciano et al., "Clinical benefit of drugs targeting mitochondrial function as an adjunct to reperfusion in ST-segment elevation myocardial infarction: a meta-analysis of randomized clinical trials," *International Journal of Cardiology*, vol. 244, pp. 59–66, 2017.

[3] X. Dong, J. Fu, X. Yin et al., "Emodin: a review of its pharmacology, toxicity and pharmacokinetics," *Toxicity and Pharmacokinetics. Phytotherapy research: PTR*, vol. 30, no. 8, pp. 1207–1218, 2016.

[4] Y. Cui, L. J. Chen, T. Huang, J. Q. Ying, and J. Li, "The pharmacology, toxicology and therapeutic potential of anthraquinone derivative emodin," *Chinese Journal of Natural Medicines*, vol. 18, no. 6, pp. 425–435, 2020.

[5] M. Stompor-Gorący, "The health benefits of emodin, a natural anthraquinone derived from rhubarb-a summary update," *International Journal of Molecular Sciences*, vol. 22, no. 17, p. 9522, 2021.

[6] S. Dai, B. Ye, L. Chen, G. Hong, G. Zhao, and Z. Lu, "Emodin alleviates LPS-induced myocardial injury through inhibition of NLRP3 inflammasome activation," *Phytotherapy Research: PTR*, vol. 35, no. 9, pp. 5203–5213, 2021.

[7] B. Ye, X. Chen, S. Dai et al., "Emodin alleviates myocardial ischemia/reperfusion injury by inhibiting gasdermin D-mediated pyroptosis in cardiomyocytes," *Drug Design, Development and Therapy*, vol. Volume 13, pp. 975–990, 2019.

[8] W. K. Zhao, Y. Zhou, T. T. Xu, and Q. Wu, "Ferroptosis: opportunities and challenges in myocardial ischemia-reperfusion injury," *Oxidative Medicine and Cellular Longevity*, vol. 2021, Article ID 9929687, 12 pages, 2021.

[9] M. Zhai, B. Li, W. Duan et al., "Melatonin ameliorates myocardial ischemia reperfusion injury through SIRT3-dependent regulation of oxidative stress and apoptosis," *Journal of Pineal Research*, vol. 63, no. 2, article e12419, 2017.

[10] Y. Shen, X. Liu, J. Shi, and X. Wu, "Involvement of Nrf2 in myocardial ischemia and reperfusion injury," *International Journal of Biological Macromolecules*, vol. 125, pp. 496–502, 2019.

[11] A. I. Guaricci, G. Bulzis, G. Pontone et al., "Current interpretation of myocardial stunning," *Trends in Cardiovascular Medicine*, vol. 28, no. 4, pp. 263–271, 2018.

[12] G. Heusch, "Myocardial stunning and hibernation revisited," *Nature Reviews Cardiology*, vol. 18, no. 7, pp. 522–536, 2021.

[13] W. A. AlJaroudi and F. G. Hage, "Myocardial stunning by gated SPECT: an old tool reinvented in a stunning turn," *Journal of Nuclear Cardiology: Official Publication of the American Society of Nuclear Cardiology*, vol. 26, no. 3, pp. 841–844, 2019.

[14] T. J. Fan, L. H. Han, R. S. Cong, and J. Liang, "Caspase family proteases and apoptosis," *Acta Biochimica et Biophysica Sinica*, vol. 37, no. 11, pp. 719–727, 2005.

[15] A. A. Barrientos-Bonilla, R. Nadella, P. B. Pensado-Guevara et al., "Caspase-3-related apoptosis prevents pathological regeneration in a living liver donor rat model," *Advances in Medical Sciences*, vol. 66, no. 1, pp. 176–184, 2021.

[16] Z. Jiang, H. Tang, J. Shi et al., "Myocardial stunning-induced left ventricular dyssynchrony on gated single-photon emission computed tomography myocardial perfusion imaging," *Nuclear Medicine Communications*, vol. 39, no. 8, pp. 725–731, 2018.

[17] G. S. Choudhary, S. Al-Harbi, and A. Almasan, "Caspase-3 activation is a critical determinant of genotoxic stress-induced apoptosis," *Methods in Molecular Biology (Clifton, NJ)*, vol. 1219, pp. 1–9, 2015.

[18] E. A. Leonard and R. J. Marshall, "Cardiovascular disease in women," *Primary Care*, vol. 45, no. 1, pp. 131–141, 2018.

[19] M. Zhou, Y. Yu, X. Luo et al., "Myocardial ischemia-reperfusion injury: therapeutics from a mitochondria-centric perspective," *Cardiology*, vol. 146, no. 6, pp. 781–792, 2021.

[20] A. L. Moens, M. J. Claeys, J. P. Timmermans, and C. J. Vrints, "Myocardial ischemia/reperfusion-injury, a clinical view on a complex pathophysiological process," *International Journal of Cardiology*, vol. 100, no. 2, pp. 179–190, 2005.

[21] L. Tian, W. Cao, R. Yue et al., "Pretreatment with Tilianin improves mitochondrial energy metabolism and oxidative stress in rats with myocardial ischemia/reperfusion injury via AMPK/SIRT1/PGC-1 alpha signaling pathway," *Journal of Pharmacological Sciences*, vol. 139, no. 4, pp. 352–360, 2019.

[22] S. W. Leung, J. H. Lai, J. C. Wu et al., "Neuroprotective effects of emodin against ischemia/reperfusion injury through activating ERK-1/2 signaling pathway," *International Journal of Molecular Sciences*, vol. 21, no. 8, p. 2899, 2020.

[23] M. C. Bridges, A. C. Daulagala, and A. Kourtidis, "LNCcation: lncRNA localization and function," *The Journal of Cell Biology*, vol. 220, no. 2, 2021.

[24] W. Zhao, D. Geng, S. Li, Z. Chen, and M. Sun, "LncRNA HOTAIR influences cell growth, migration, invasion, and apoptosis via the miR-20a-5p/HMGA2 axis in breast cancer," *Cancer Medicine*, vol. 7, no. 3, pp. 842–855, 2018.

[25] J. Wang, Z. Fu, M. Wang, J. Lu, H. Yang, and H. Lu, "Knockdown of XIST attenuates cerebral ischemia/reperfusion injury through regulation of miR-362/ROCK2 axis," *Neurochemical Research*, vol. 46, no. 8, pp. 2167–2180, 2021.

Hindawi
Oxidative Medicine and Cellular Longevity
Volume 2022, Article ID 1526540, 6 pages
https://doi.org/10.1155/2022/1526540

Research Article

A Machine Learning Applied Diagnosis Method for Subcutaneous Cyst by Ultrasonography

Hao Feng,[1] Qian Tang,[1] Zhengyu Yu,[2] Hua Tang,[1] Ming Yin,[1] and An Wei[3]

[1]*Department of Dermatology, Hunan Provincial People's Hospital (The First Affiliated Hospital of Hunan Normal University), Changsha 410005, China*
[2]*Faculty of Engineering and IT, University of Technology, Sydney, Sydney, NSW 2007, Australia*
[3]*Department of Ultrasound, Hunan Provincial People's Hospital (The First Affiliated Hospital of Hunan Normal University), Changsha 410005, China*

Correspondence should be addressed to An Wei; weian1976@163.com

Received 24 August 2022; Revised 19 September 2022; Accepted 28 September 2022; Published 17 October 2022

Academic Editor: Xinyong Cai

For decades, ultrasound images have been widely used in the detection of various diseases due to their high security and efficiency. However, reading ultrasound images requires years of experience and training. In order to support the diagnosis of clinicians and reduce the workload of doctors, many ultrasonic computer aided diagnostic systems have been proposed. In recent years, the success of deep learning in image classification and segmentation has made more and more scholars realize the potential performance improvement brought by the application of deep learning in ultrasonic computer-aided diagnosis systems. This study is aimed at applying several machine learning algorithms and develop a machine learning method to diagnose subcutaneous cyst. Clinical features are extracted from datasets and images of ultrasonography of 132 patients from Hunan Provincial People's Hospital in China. All datasets are separated into 70% training and 30% testing. Four kinds of machine learning algorithms including decision tree (DT), support vector machine (SVM), *K*-nearest neighbors (KNN), and neural networks (NN) had been approached to determine the best performance. Compared with all the results from each feature, SVM achieved the best performance from 91.7% to 100%. Results show that SVM performed the highest accuracy in the diagnosis of subcutaneous cyst by ultrasonography, which provide a good reference in further application to clinical practice of ultrasonography of subcutaneous cyst.

1. Introduction

Subcutaneous cyst occurs especially at younger age, especially in the head, arms, and back in youth. It is a soft or a plurality of soft or firm balls with diameters ranging from 1 to approximately 3 cm. Subcutaneous cyst is buried in the skin or subcutaneous tissue and adheres to the skin and the base can move. There are small openings on the skin. When the cyst is pushed, it adheres tightly to the skin. Small pit appears when it is slightly depressed, which is the opening of the duct where the gland directly reaches the skin surface. Some openings are stuffed with a black pimple-like plug to squeeze out white wax-like substances [1–3]. The ultrasonic images of superficial epidermoid cyst have certain specificity. The advantages of ultrasound include high spatial resolution, portability, convenience, and low cost. It is important to be able to combine the physical examination results with the patient's medical history in ultrasonic examination. In addition, real-time imaging allows manual compression, limb movement, muscle contraction, and direct interaction with patients during scanning [4]. By summarizing and analyzing its acoustic features, it can effectively improve the correct rate of clinical diagnosis and reduce misdiagnosis and missed diagnosis [5, 6]. However, one disadvantage of ultrasound is when the disease occurs in deeper soft tissues. In these cases, the image resolution is reduced, and auxiliary information about the mass, such as physical examination results and medical history, may be blurred [7].

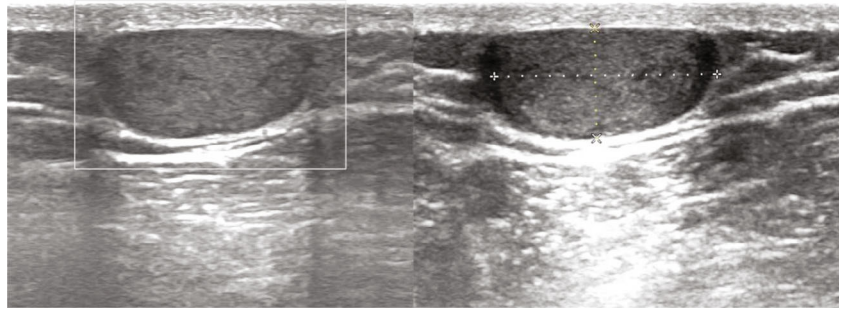

Figure 1: Sample ultrasound images of subcutaneous cyst.

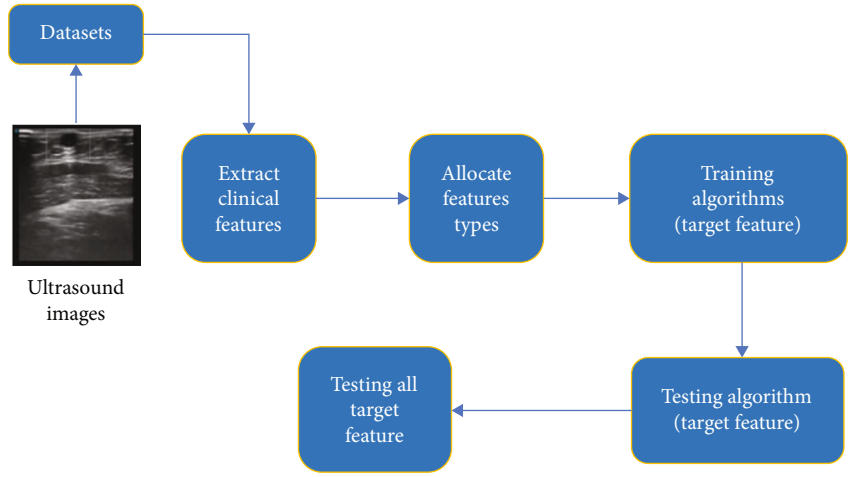

Figure 2: Workflow diagram for machine learning applied diagnosis method.

Machine learning is one of the branch in artificial intelligence and has been widely used in multidisciplinary research fields [8, 9], which is related to computer science, statistics, and information theory [10, 11]. Algorithms are used to analyze data and try to explore potential patterns hidden in data to predict new information in machine learning [8, 12], with high precision, high speed, and convenient expansion [13, 14]. The main application fields of deep learning in ultrasound computer-aided diagnosis system include breast disease diagnosis [15], liver disease diagnosis [16], fetal ultrasound standard plane detection [17], thyroid nodule diagnosis [18], and carotid artery ultrasound image classification [19]. In recent years, machine learning algorithms, such as decision tree (DT), support vector machine (SVM), *K*-nearest neighbors (KNN), and neural networks (NN), have been more and more frequently applied in medical field [20–23].

However, limited relative studies on machine learning in the diagnosis of subcutaneous cyst based on ultrasonography have been reported. Thus, the motivation and novelty of this study were to apply several machine learning algorithms to diagnose subcutaneous cyst from clinical features extracted from datasets and images of ultrasonography and find a powerful alternative method for ultrasonic diagnosis of subcutaneous cysts.

2. Materials and Methods

2.1. Data Acquisition. All datasets in this article are from Hunan Provincial People's Hospital in China. There are 133 patients that participated. Each patient has five ultrasound images record with 19 clinical features extracted including gender, age, none blood flow, dotted blood flow, dot-bar blood flow, rich blood flow, none echo, mixed echo, low echo, medium echo, high echo, uniform internal echo, nonuniform internal echo, clear boundary, unclear boundary, regular form, irregular form, strong spot, and changes of parenchyma echo. Figure 1 illustrates sample ultrasound images of subcutaneous cyst.

2.2. Data Preparation. A machine learning applied method is proposed to diagnose subcutaneous cyst in this article. Clinical features are extracted from datasets and images of ultrasonography. Figure 2 displays the workflow processes for the machine learning applied diagnosis method in several steps, which are presented in the following:

(1) Extract clinical features from datasets and ultrasound images

(2) Allocate feature types: there are two different feature types in our method, categorical and numerical. To

improve the accuracy of the diagnosis method, we allocated these features into two types, Table 1 presents all the features and types

(3) Training algorithms: machine learning algorithms, such as decision tree (DT), support vector machine (SVM), *K*-nearest neighbors (KNN), and neural networks (NN), had been approached to determine the best performance. The result indicated that the best accurate algorithm is SVM. Feature 1 (gender) and feature 2 (age) are excluded from target features, as they are basic information of the patient, they do not change or are not affected by cysts lesions. Therefore, the target features in this research are 17 features, which are from feature 3 to feature 19. In the training stage, we start from target feature 3, the results indicated that SVM provided the highest accuracy

(4) Testing algorithm: in this stage, the rest 30% of the datasets is processed by SVM. We use the same target feature as the previous training. SVM achieves 100% accuracy

(5) Testing target features: each target feature is trained and tested to validate the reliability of SVM. The rest target features are from feature 4 to feature 19. We compared with all the results from each feature, SVM still achieved the best performance from 91.7% to 100%. This is a significant accuracy in diagnosing subcutaneous cyst

Statistical Processing

3. Results

3.1. Training Process. Four different types of machine algorithms are applied. We separated datasets into two parts, 70% for training and 30% for testing. 19 features from 132 patients are computed. Since feature 1 and feature 2 are gender and age, they are general information of patients and will not be affected by any cyst lesions, and the target features in this research are from feature 3 to feature 19. Initially, we set feature 3, none blood flow, as the target feature, and the rest of the features are attributes. To avoid datasets overfitting, we use 5 cross-validation folds. After processing the training by using DT, SVM, KNN, and ANN, the accuracy results are 99.2%, 100%, 92.4%, and 98.5%, respectively. SVM provides best result for the diagnosis method. Table 2 indicates the accuracy result for the training process.

3.2. Testing Process. To validate the reliability of the method, SVM is tested by using the rest 30% of the datasets. The target features are the same as the previous training, which are from feature 3 to feature 19. We start setting the target feature from feature 3. We also use 5 cross validation folds to avoid datasets overfitting. As shown in Table 3, the testing results slightly changed to DT (96.2%), SVM (100%), KNN (95.5%), and ANN (98.5). Comparing with the results, SVM still achieves 100% accuracy. It is the best algorithm for the diagnosis method when we set the target feature as feature 3.

Table 1: 19 features extracted from datasets.

ID	Feature	Type
1	Gender	Categorical
2	Age	Numerical
3	None blood flow	Categorical
4	Dotted blood flow	Categorical
5	Dot-bar blood flow	Categorical
6	Rich blood flow	Categorical
7	None Echo	Categorical
8	Mixed Echo	Categorical
9	Low Echo	Categorical
10	Medium Echo	Categorical
11	High Echo	Categorical
12	Uniform internal Echo	Categorical
13	Nonuniform internal Echo	Categorical
14	Clear boundary	Categorical
15	Unclear boundary	Categorical
16	Regular form	Categorical
17	Irregular form	Categorical
18	Strong spot	Categorical
19	Changes of parenchyma Echo	Categorical

Table 2: Machine learning algorithms for training.

Algorithm	Accuracy (%)
Decision tree (DT)	99.2
Support vector machine (SVM)	100
K-nearest neighbors (KNN)	92.4
Artificial neural network (ANN)	98.5

Table 3: Machine learning algorithms for testing.

Algorithm	Accuracy (%)
Decision tree (DT)	96.2
Support vector machine (SVM)	100
K-nearest neighbors (KNN)	95.5
Artificial neural network (ANN)	98.8

3.3. Training and Testing for Each Target Feature. In the previous stage, we trained and tested feature 3 as a target feature, and the result indicated that SVM achieved the best accuracy. Further training and testing are approached for each target feature, from feature 4 to feature 19. Table 4 indicates the testing results for 17 target features. In Table 4, the target features are trained and tested by using DT, SVM, KNN, and ANN. Comparing with the results in each column, SVM achieved the best performance (from 91.7% to 100%) for all the target features. The lowest accuracy from SVM is 91.7% at target feature 19. The reason could be that the datasets for feature 19 contains noise and uncertainties that reduces the accuracy from all the algorithms. In that column, we can find that DT is 87.1%, KNN is 90.9, and ANN is 86.5. We compare the results, SVM (91.7) is still

Table 4: Testing results for target features.

Accuracy (%)	3	4	5	6	7	8	9	10
DT	96.2	97.0	98.5	93.9	98.5	97.0	95.6	98.5
SVM	100	99.2	99.2	99.2	99.2	99.2	98.8	99.2
KNN	95.5	95.5	93.9	94.7	97.0	95.5	90.2	97.0
ANN	98.8	97.7	96.2	97.0	98.5	97.7	97.7	98.5

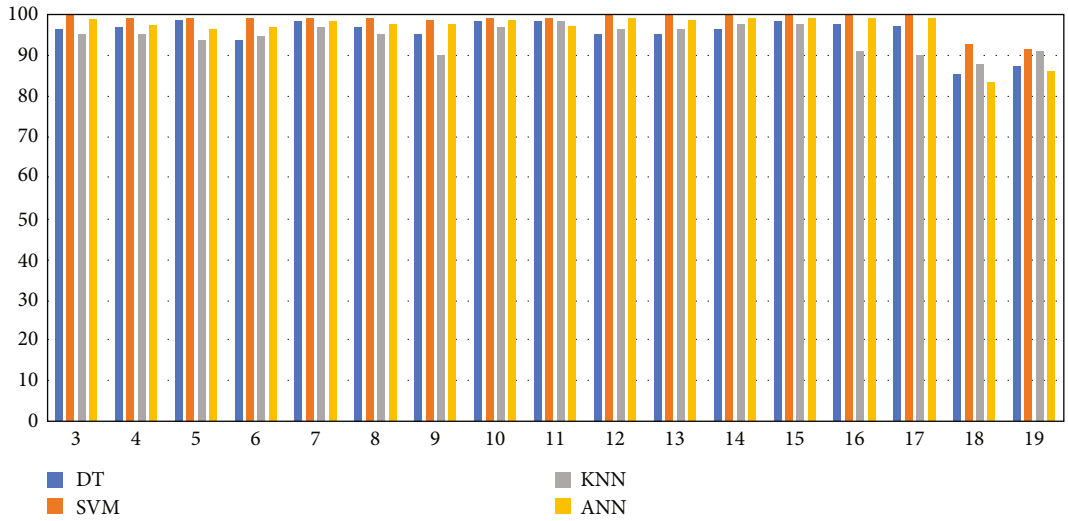

Figure 3: Column chart of testing results.

Table 5: Testing results for target features.

Accuracy (%)	11	12	13	14	15	16	17	18	19
DT	98.5	95.5	95.5	96.2	98.5	97.7	97.0	85.6	87.1
SVM	99.2	100	100	100	100	100	100	92.9	91.7
KNN	98.5	96.2	96.2	97.7	97.7	90.9	90.2	87.9	90.9
ANN	97.0	99.2	98.5	99.2	99.2	99.2	99.2	83.3	86.4

the best. Figure 3 is the column chart associated with Table 5. SVM is in orange and is the highest in each column. In this article, we found a machine learning method with SVM achieved the significant accuracy (from 91.7 to 100%) to diagnose subcutaneous cyst in addressing blood flow, echo, internal echo, boundary, strong spot, and changes of parenchyma echo.

4. Discussion and Conclusions

In this study, a total of 132 patients from Hunan Provincial People's Hospital in China participated. Four different types of machine algorithms including decision tree (DT), support vector machine (SVM), K-nearest neighbors (KNN), and neural networks (NN) in machine learning method are applied for the diagnose of subcutaneous cyst by ultrasonography. Decision tree is an effective ultrasonic image classification algorithm. It can learn classification rules from unordered data [24, 25]. The decision tree algorithm uses the divide and conquer strategy to divide the search space of the problem into several subsets. From top to bottom, each node determines the next node by calculating the eigenvalue of the input sample. In the leaf node, the final classification result is given [26]. In the case of small amount of data and nondiversified eigenvalues, the construction of decision tree is simple and fast. However, if the data volume is large and the eigenvalues are large, the complexity of the decision tree algorithm will be large. Support vector machine has good performance on both small datasets and large datasets. However, with the increase of dataset size, the complexity of support vector machine also increases. At the same time, the choice of kernel function will also affect the performance of support vector machine [27–29]. K-nearest neighbors is a lazy and nonparametric algorithm that has the good characteristics of being simple and easy to use and has a reasonable accuracy [30].

Our research has limitations. First of all, the training set data came from the same hospital, and we did not summarize the basic information of patients and cysts. Second, no matter training or testing datasets, the sample size is

relatively small. Therefore, these results need to be validated in a larger cohort to determine the value of our model in clinical practice.

All datasets are separated into two parts, which is 70% for training and 30% for testing. Results show that SVM achieved the best performance (from 91.7% to 100%) for all the target features. The machine learning method developed in this study can help doctors diagnose the ultrasonic images of patients with subcutaneous cysts more accurately. However, other prospective cohort studies should be conducted externally.

Data Availability

The labeled dataset used to support the findings of this study is available from the corresponding author upon request.

Ethical Approval

This retrospective study was approved by the Ethics Committee of Hunan Provincial People's Hospital as an exempt study without a registration number.

Conflicts of Interest

The authors declare no competing interests.

Acknowledgments

We would like to express our gratitude to all participants in this study. This study was supported by the Project of Education Department of Hunan Province (20C1164 General Project), Project of Finance Department of Hunan Province (2020CZT03), and Joint Project of Science and Health Departments (2021JJ70020).

References

[1] J. J. Krant and J. A. Carucci, "Benign subcutaneous lesions: cysts and lipomas," in *Surgery of the Skin*, pp. 767–776, Elsevier, 2005.

[2] R. D. Tyler, J. H. Meinkoth, R. L. Cowell, C. G. MacAllister, and K. J. Caruso, *Cutaneous and subcutaneous lesions: masses, cysts, and fistulous tracts*, Elsevier, 2002.

[3] S. R. Thaller and B. S. Bauer, "Cysts and cyst-like lesions of the skin and subcutaneous tissue," *Clinics in Plastic Surgery*, vol. 14, no. 2, pp. 327–340, 1987.

[4] J. A. Jacobson, W. D. Middleton, S. J. Allison et al., "Ultrasonography of superficial soft-tissue masses: Society of Radiologists in Ultrasound consensus conference statement," *Radiology*, vol. 304, no. 1, pp. 18–30, 2022.

[5] V. Quaresma, L. Marconi, M. Lopes et al., "Diagnostic performance of contrast-enhanced ultrasonography for the evaluation of malignancy in complex cystic masses," *European Urology Open Science*, vol. 33, pp. S172–S173, 2021.

[6] H. Athar, A. Q. Mir, M. B. Gugjoo, R. A. Ahmad, and H. M. Khan, "Ultrasonography: an affordable diagnostic tool for precisely locating coenurosis cyst in sheep and goats," *Small Ruminant Research*, vol. 169, pp. 19–23, 2018.

[7] L. H. Goldman, L. Perronne, E. F. Alaia et al., "Does magnetic resonance imaging after diagnostic ultrasound for soft tissue masses change clinical management?," *Journal of Ultrasound in Medicine*, vol. 40, no. 8, pp. 1515–1522, 2021.

[8] K.-Q. Li, Y. Liu, and Q. Kang, "Estimating the thermal conductivity of soils using six machine learning algorithms," *International Communications in Heat and Mass Transfer*, vol. 136, article 106139, 2022.

[9] M. Zhu, J. Wang, X. Yang et al., "A review of the application of machine learning in water quality evaluation," *Eco-Environment & Health*, vol. 1, no. 2, pp. 107–116, 2022.

[10] B. Ratner, *Statistical and Machine-Learning Data Mining: Techniques for Better Predictive Modeling and Analysis of Big Data*, CRC Press, 2017.

[11] C. Ma, H. H. Zhang, and X. Wang, "Machine learning for big data analytics in plants," *Trends in Plant Science*, vol. 19, no. 12, pp. 798–808, 2014.

[12] Y. Liu, T. Zhao, W. Ju, and S. Shi, "Materials discovery and design using machine learning," *Journal of Materiomics*, vol. 3, no. 3, pp. 159–177, 2017.

[13] N. Geetha and P. Bridjesh, "Overview of machine learning and its adaptability in mechanical engineering," Materials Today: Proceedings, 2020.

[14] Z. Zhang, Y. Wang, and K. Wang, "Intelligent fault diagnosis and prognosis approach for rotating machinery integrating wavelet transform, principal component analysis, and artificial neural networks," *The International Journal of Advanced Manufacturing Technology*, vol. 68, no. 1-4, pp. 763–773, 2013.

[15] S. Han, H.-K. Kang, J.-Y. Jeong et al., "A deep learning framework for supporting the classification of breast lesions in ultrasound images," *Physics in Medicine & Biology*, vol. 62, no. 19, pp. 7714–7728, 2017.

[16] T. M. Hassan, M. Elmogy, and E.-S. Sallam, "Diagnosis of focal liver diseases based on deep learning technique for ultrasound images," *Arabian Journal for Science and Engineering*, vol. 42, no. 8, pp. 3127–3140, 2017.

[17] Z. Yu, E.-L. Tan, D. Ni et al., "A deep convolutional neural network-based framework for automatic fetal facial standard plane recognition," *IEEE Journal of Biomedical and Health Informatics*, vol. 22, pp. 874–885, 2017.

[18] J. Ma, F. Wu, T. A. Jiang, J. Zhu, and D. Kong, "Cascade convolutional neural networks for automatic detection of thyroid nodules in ultrasound images," *Medical Physics*, vol. 44, no. 5, pp. 1678–1691, 2017.

[19] R.-M. Menchón-Lara, J.-L. Sancho-Gómez, and A. Bueno-Crespo, "Early-stage atherosclerosis detection using deep learning over carotid ultrasound images," *Applied Soft Computing*, vol. 49, pp. 616–628, 2016.

[20] B. Ambale-Venkatesh, X. Yang, C. O. Wu et al., "Cardiovascular event prediction by machine learning: the multi-ethnic study of atherosclerosis," *Circulation Research*, vol. 121, no. 9, pp. 1092–1101, 2017.

[21] N. Ludwig, T. Fehlmann, F. Kern et al., "Machine learning to detect Alzheimer's disease from circulating non-coding RNAs," *Genomics, Proteomics & Bioinformatics*, vol. 17, no. 4, pp. 430–440, 2019.

[22] P. Ferroni, F. M. Zanzotto, S. Riondino, N. Scarpato, F. Guadagni, and M. Roselli, "Breast cancer prognosis using a machine learning approach," *Cancers*, vol. 11, no. 3, p. 328, 2019.

[23] A. D. Hardie, J. H. Chamberlin, J. H. Boyum et al., "Multi-center follow-up study to develop a classification system which differentiates mucinous cystic neoplasm of the liver and

benign hepatic cyst using machine learning," *Academic Radiology*, vol. 29, no. 8, pp. 1149–1156, 2022.

[24] U. R. Acharya, P. Chowriappa, H. Fujita et al., "Thyroid lesion classification in 242 patient population using gabor transform features from high resolution ultrasound images," *Knowledge-Based Systems*, vol. 107, pp. 235–245, 2016.

[25] U. R. Acharya, S. V. Sree, M. M. R. Krishnan et al., "Computer-aided diagnostic system for detection of Hashimoto thyroiditis on ultrasound images from a polish population," *Journal of Ultrasound in Medicine*, vol. 33, no. 2, pp. 245–253, 2014.

[26] T. S. Rao, "Classification, parameter estimation and state estimation-an engineering approach using MATLAB," *Journal of Time Series Analysis*, vol. 32, pp. 194–194, 2011.

[27] L. Cai, X. Wang, Y. Wang, Y. Guo, J. Yu, and Y. Wang, "Robust phase-based texture descriptor for classification of breast ultrasound images," *Biomedical Engineering Online*, vol. 14, no. 1, pp. 1–21, 2015.

[28] P.-L. Yen, H.-K. Wu, H.-S. Tseng et al., "Vascular morphologic information of three-dimensional power Doppler ultrasound is valuable in the classification of breast lesions," *Clinical Imaging*, vol. 36, no. 4, pp. 267–271, 2012.

[29] Q. Zhang, J. Suo, W. Chang, J. Shi, and M. Chen, "Dual-modal computer-assisted evaluation of axillary lymph node metastasis in breast cancer patients on both real-time elastography and b-mode ultrasound," *European Journal of Radiology*, vol. 95, pp. 66–74, 2017.

[30] K. Li, Y. Xu, Z. Zhao, and M. Q.-H. Meng, "Automatic recognition of abdominal organs in ultrasound images based on deep neural networks and k-nearest-neighbor classification," in *2021 IEEE International Conference on Robotics and Biomimetics (ROBIO)*, pp. 1980–1985, Sanya, China, 2021.

Hindawi
Oxidative Medicine and Cellular Longevity
Volume 2022, Article ID 8445093, 19 pages
https://doi.org/10.1155/2022/8445093

Research Article

Nerve Growth Factor (NGF) Encourages the Neuroinvasive Potential of Pancreatic Cancer Cells by Activating the Warburg Effect and Promoting Tumor Derived Exosomal miRNA-21 Expression

Tao Peng,[1] Yao Guo,[1] Zheng Gan,[2] Yan Ling,[3] Jiongxin Xiong,[1] Xueyi Liang,[1] and Jing Cui[1]

[1]*Department of Pancreatic Surgery, Union Hospital, Tongji Medical College, Huazhong University of Science and Technology, Wuhan, Hubei 430022, China*
[2]*Department of Anesthesiology, Union Hospital, Tongji Medical College, Huazhong University of Science and Technology, Wuhan, Hubei 430022, China*
[3]*Medical Examination Center, Union Hospital, Tongji Medical College, Huazhong University of Science and Technology, Wuhan, Hubei 430022, China*

Correspondence should be addressed to Jing Cui; cuijing1266@hust.edu.cn

Received 8 July 2022; Revised 25 August 2022; Accepted 1 September 2022; Published 15 October 2022

Academic Editor: Shao Liang

Background. It has been reported that signaling from the nerve growth factor (NGF) pathway associated with peripheral nerves is able to contribute to perineural invasion (PNI) of pancreatic cancer (PC). Nevertheless, the underlying mechanism by which NGF leads to PNI remained poorly understood. *Methods*. Western blotting was employed to determine NGF level in PC and paracarcinoma tissues and in PC cell lines as well as pancreatic ductal epithelial cells. MiaPaCa-2 and CFPAC-1 cells were treated with 100 ng/ml of NGF or the NGF inhibitor Tanezumab for 24 h, CCK-8 and Transwell assays were employed to test cell proliferation, invasion, and migration, respectively. TrkA expression was knocked down in MiaPaCa-2 and dorsal root ganglion (DRG) cells treated with NGF to determine its effect on the Warburg effect. To reveal that the NGF-TrkA signaling pathway was closely associated with PC PNI, *in vitro* neuroinvasion model was established by using MiaPaCa-2 cells via coculturing DRG cells in Matrigel. Further, exosomes were extracted from PC cells and identified by examining the levels of specific markers for exosomes. Then RT-qPCR was applied to test miR-21-5p level in tumor derived exosomal (TDE-miR-21-5p). RIP assay was performed to validate NGF and miR-21 binding ability in MiaPaCa-2 cells. Rescue experiments were performed by using coprocessing of Tanezumab and miR-21-5p mimic on MiaPaCa-2 cells, followed by coculture with DRG cells. Subsequently, we used a model of neuroinvasion in nude mice to assess the effect of NGF *in vivo* on tumor nerve invasion as well as on nociceptive transmission. *Results*. NGF level was preeminently higher in PC tissues and cell lines than in paracarcinoma tissues and normal pancreatic epithelial cell lines. NGF promoted MiaPaCa-2 and CFPAC-1 cell invasion and migration, while Tanezumab treatment showed the opposite results. Besides, NGF binding to TrkA receptors encouraged the intracellular Warburg effect in PC and DRG cells. TrkA blocking-up could restrain NGF induced PC cell migration and neural invasion. Mechanistically, NGF could upregulate TDE-miR-21-5p levels, and DRG cells took up TDE to activate the Warburg effect and stimulate nociceptor gene expression. miR-21-5p inhibitor could abolish the facilitative effect of NGF on PNI in MiaPaCa-2 cells. *In vivo* tumorigenesis experiments, Tanezumab markedly alleviated nerve invasion of PC cells as well as relieved nociceptive conduction in animal models. *Conclusions*. These findings displayed that NGF/TrkA encouraged the neuroinvasive potential of PC cells by activating the Warburg effect in DRG cells through upregulation of TDE-miR-21-5p expression.

1. Introduction

Pancreatic cancer (PC) is a relatively common malignancy of the digestive system and one of the human malignancies with the worst prognosis [1]. Approximately 213,000 people worldwide die from PC each year [2]. Its pathogenesis remains unknown, and it is currently only well established that family history, smoking, diabetes mellitus, obesity as well as alcohol abuse are high risk factors for PC [3]. PC has an insidious onset and often has no obvious clinical manifestation in the early stage. However, the disease progresses more rapidly, and until the clinical symptoms appear or the diagnosis is confirmed, most cases lose the opportunity of surgical treatment because of local invasion or hematogenous, lymphatic, and distant metastasis. Surgery is accessible to only less than 20% of patients, with an additional 70% of cases being amenable to only palliative surgery [4]. Even radical surgical cases that achieve clinicopathological cure criteria, curative effects remain unsatisfactory.

Infiltration versus metastasis is one of the most characteristic biological properties of tumors [5]. Generally, it is believed that there are four main pathways between tumor invasion and metastasis, including local invasion, blood, lymphatic, and seeding metastasis [6]. In addition to these four pathways, tumors can undergo infiltration around nerve fibers and metastasis along nerves, that is, perineural invasion (PNI), which refers to the phenomenon of perineural invasion by tumor cells filling the perineurial space, wrapping around nerves in a continuous concentric sheath-like pattern, infiltration, and metastasis of extension along nerves around nerve fibers or into perineurium within the perineurium [7]. Although this more specific biological behavior is seen in biliary tract tumors, PC, parotid gland tumors, prostate cancer, and breast cancer, as well as basal and squamous cell carcinomas of the head and neck, perineural invasion is more common in PC. The fact that pancreatic tissue itself is rich in neural tissue determines the predisposition of PC to perineural invasion, which also constitutes the anatomical basis for the predisposition of pancreatic cancer to perineural tissue invasion. Perineural invasion, which starts within the pancreas, evolves to perineural invasion of the pancreas and subsequent metastasis to distant sites such as retroperitoneum, which is also thought to be an important cause of surgical margin remnant and persistent extra-pancreatic dissemination [8]. In the PNI of PC, a variety of genes or proteins are involved in the process of promoting tumor cell growth and inhibiting their apoptosis. Their interaction creates a favorable microenvironment for the invasiveness and neurotropic growth of tumor cells. Special growth factors produced by nerves or the cells associated with them are important reasons for promoting the growth and survival of cancer cells with a proneural nature [9].

Nerve growth factor (NGF) plays a very important role in this behavior. NGF, an important neuropeptide in the neurotrophin family with a molecular weight of about 140 KD, is composed of three peptide chains, α, β, and γ, bound noncovalently at the ratio of $\alpha 2 \beta \gamma 2$. Subunit β, which consists of an identical skin chain containing 188 amino acid residues each, is the active zone of NGF and the only of the three subunits to have the biological activities of NGF. Under normal circumstances, NGF exerts regulatory effects on neuronal survival, growth and development, differentiation, regeneration, and functional maintenance. Numerous studies have shown that high level of NGF in PC are closely associated with tumor cell migration and perineural invasion. For example, NGF activated the ERK1/2 signaling pathway in PC by regulating CD133 to accelerate cell migration and invasion [10]. Further, tyrosine kinase receptor A (TrkA) is the functional receptor for NGF and when bound to NGF can activate tyrosine kinase signaling systems that initiate cellular activity to produce biological effects. NGF and TrkA are its high affinity receptors that play a crucial role in cancer pathogenesis through cell proliferation, angiogenesis, invasion, and migration. Vera et al. [11] demonstrated that NGF/TrkA could promote the malignant behavior of ovarian cancer cells by upregulating oncogenic proteins such as vascular endothelial growth factor and c-myc expression during ovarian cancer progression. Further, NGF acts by binding to receptors on the surface of target cells, which are divided into a high affinity TrkA and a low affinity receptor p75. NGF/TrkA facilitated PC cell proliferation and invasion in coculture system by activating the PI3K/Akt/GSK signaling cascade [12]. However, the specific mechanism by which the NGF/TrkA pathway leads to PNI in PC remains to be further explored.

Tumor cells consume far more glucose than normal cells. More importantly, even under aerobic conditions glucose in tumor cells is not oxidized exhaustively but is broken down to produce lactate, a phenomenon that was discovered by the German biochemist O.H. Warburg and is therefore called the Warburg effect [13]. Although the capacity rate of glycolysis is lower than that of oxidative phosphorylation, glycolysis can meet the energy demand of rapid tumor cell growth [14]. Moreover, high levels of glycolysis within tumor cells would consume a large amount of glucose in the tumor microenvironment and lead to the accumulation of lactate, which in turn inhibits lymphocytes and tumor infiltration [15]. An increasing number of studies have shown that an excessive level of glycolysis is closely associated with PC progression and invasion [16]. The molecular mechanism by which cancer cells achieve metabolic reorganization is still unclear. Therefore, elucidating the molecular mechanism of metabolic reorganization of tumor cells will provide a new and effective way for tumor targeted therapy.

In this study, an *in vitro* model generated by coculturing mouse dorsal root ganglion (DRG) neuronal cells and PC cells, and an *in vivo* PNI model were applied to investigate the function and underlying mechanisms of NGF/TrkA signaling in the progression and pathogenesis of PNI, contributing to the development of therapeutic regimens for PC.

2. Materials and Methods

2.1. Patients and Clinical Samples. A total of 90 cases were selected and included at the Union Hospital attended patients with PC. The pathological diagnosis of PC was carried out according to the standards of the World Health

Organization. Written informed consent was signed by each patient.

2.2. Cell Lines and Culture. Panc-1, AsPc-1, MiaPaCa-2, BxPC-3, Capan-2, CFPAC-1, and HPDE cell lines were obtained from Shanghai Huiying biotech Co., Ltd, Shanghai, China. Subsequently, cells were subjected to mycoplasma testing, isoenzyme testing, and cell viability assays were performed by the biological company (GeneCreate Biological Engineering Co., Ltd., Wuhan, China). All cells were cultured in DMEM medium containing 10% fetal bovine serum, 100 U/mL penicillin and 100 μg/mL streptomycin. All cell lines were maintained at 37°C in a humidified incubator with 5% CO_2. MiaPaCa-2 and CFPAC-1 cells were treated with 100 ng/ml NGF or NGF inhibitor Tanezumab for 24 hours, and cells were collected for further experiments.

2.3. Genetic Overexpression and Knockdown. The shRNAs were designed by Qiagen to knock down TrkA. The miR-21-5p mimic and miR-21-5p inhibitor, and corresponding controls NC mimic and NC inhibitor were purchased from Geneseed (Shanghai, China). TrkA shRNA constructs were produced using the following target sequences: 5′- GCTT GGCTGATACTGGCATCT-3′ for sh70 and 5′-ACCTGA CTGAGCTCTACATCG-3′ for sh200. Stable infections were performed for lentiviral constructs: plv-hu6-EF1a-puro-negative control shRNA, plv-hu6-TrkAsh70, and plv-hu6-EF1a-puro-TrkAsh200. Confluent cells were diluted in DMEM medium, and the cells were observed to grow to about 70% confluence when the cell monolayer was covered with serum-free DMEM medium. The plasmid transfection was performed by using Lipofectamine®3000 transfection reagent, all cells in each group were collected for subsequent experiments after incubating in an incubator at 37°C with 5% CO_2 for a specified period of times.

2.4. RNA Extraction and PCR Assays. The cells from each group after transfection were collected, and Trizol (ThermoFisher, USA) was added to extract total cellular RNA according to the instructions of total RNA extraction reagent. After measurement of A260/A280 between 1.8-2.0. Total cellular RNA was reverse transcribed into cDNA using a reverse transcription Kit (Qiagen, Germany), with a 20 μL of reverse transcription reaction system including 0.2 μL of MMLV (200 U/μL), 1.2 μL of miR-RT primer (1 μmol/L), 0.75 μL of dNTP (10 mmol/L), 4 μL of 5 × RT buffer, 10 μL of total RNA and 3.85 μL of RNase free ddH2O. The reaction conditions were as follows: 37°C for 30 min and 85°C for 10 min. PCR products were detected with steponeplus real time PCR system (Thermo Fisher, USA). The real time PCR reaction system was 20 μL, including 1 μL of cDNA template, 0.5 μl each of upstream and downstream primers (10 μmol/L), 10 μL of SYBR GREEN mastermix, and 8 μL of RNase free ddH2O. GAPDH and U6 served as internal references. The relative expression levels were calculated by using $2^{-\Delta\Delta CT}$ method. The efficiency of the PCR should be between 90-110% ($3.6 > \text{slope} > 3.1$). miR-21-5p forward, 5′- GCC GCT AGC TTA TCA GAC TGA TGT -3′; and reverse, 5′-CGA CAG TGG GAG TGA CGC CCT TA -3′; NGF forward: 5′- CTG GCC ACA CTG AGG TCG AT-3′; and reverse, 5′- TCC TGC AGG GAC ATT GCT CTC-3′. U6 forward, 5′- TGCGGGTGCTCGCTTCGGCAGC-3′; and reverse, 5′- CCA GTG CAG GGT CCG AGG T-3′; GAPDH forward, 5′- GCA CCG TCA AGG CTG AGA AC -3′; and reverse, 5′- TGG TGA AGA CGC CAG TGG A -3′.

2.5. Western Blotting. Total cell protein was extracted with RIPA lysate, and the protein concentration was determined using a BCA protein assay kit (Thermo Fisher Scientific, Waltham, MA, USA) in a microplate reader. After denaturation for 10 min with the addition of loading buffer, 50 μg of protein samples were subjected to SDS-PAGE and transferred onto PVDF membranes. The membrane was blocked with blocking solution (5% nonfat dry milk) for 2 h and subsequently washed three times using TBST. Specific primary and secondary antibodies were next added separately, followed by incubation on a shaker. ImageJ software was applied to detect and analyze the gray values of protein bands on the membrane. The following primary antibodies: β-actin (1 : 1000, Abcam, ab8227, Cambridge, UK), NGF (1 : 1000, ab52918, Abcam), TrkA (1 : 1000, ab109010, Abcam), PI3K (1 : 1000, ab32089, Abcam), p-AKT (phospho T308) (1 : 500, ab38449, Abcam), AKT (1 : 1000, ab8805, Abcam), mTOR (1 : 1000, ab109268, Abcam), p-mTOR (phospho S2481) (1 : 1000, ab137133, Abcam), CD63 (1 : 1000, ab134045, Abcam), TSG101 (1 : 1000, ab125011, Abcam), ALIX (1 : 500, ab88388, Abcam), CD9 antibody (1 : 2000, ab92726, Abcam), TRPV1 (1 : 1000, ab6166, Abcam).

2.6. Glucose, Lactate, Adenosine Triphosphate (ATP) Levels, and Extracellular Acidification Rate (ECAR). The medium was collected after cell transfection. Simply put, glucose levels are measured with a glucose test kit (Thermo Fisher, USA). The lactic acid content was measured with a lactic acid meter (Thermo Fisher, USA). The content of ATP was determined using the Cell Titer-Glo Cell Viability Assay (Thermo Fisher, USA). ECAR was determined using the Seahorse XF96 Cell Efflux Analyzer according to the manufacturer's instructions.

2.7. Exosome Isolation and Identification. Exosomes were isolated by precipitation using exoquick reagent (SBI) according to the manufacturer's instructions. Briefly, conditioned medium was incubated with exoquick reagent (5 : 1) for 12 h or longer, followed by centrifugation at 1500 g for 30 min, and the precipitated exosomes were suspended in 100 mL of PBS, then stored at -80°C. In addition, total exosome isolation (Magen) was performed using serum exosomes. Reagents were added to serum samples and incubated at 4°C for 30 min, followed by centrifugation of 1 ml of serum samples at 2000 g for 30 min to remove cells and debris. Alternatively, exudates observed by transmission electron microscopy were suspended in glutaraldehyde, dripped onto carbon-containing copper mesh and stained with 2% uranyl acetate, then dried and imaged.

2.8. Co-Immunoprecipitation (co-IP). MiaPaCa-2 and DRG cells were lysed with RIPA buffer (Thermo Fisher, USA), and the supernatant was collected and incubated with NGF and TrkA antibodies overnight at 4°C. This mixture was incubated with 100 microliters of A/G agarose beads overnight at 4°C. Then, the agarose sphere-antigen-antibody complexes were collected by transient centrifugation and washed 3 times with PBS. Next, the complex with protein-added buffer for 5 minutes. Intracellular interacting proteins were analyzed by immunoblotting technique.

2.9. RNA Immunoprecipitation (RIP) Assay. Protease inhibitor EDTA as well as RNase inhibitor (Qiagen, Hilden, Germany) were added to IP lysis buffer to lyse cells. After the addition of magnetic beads preclearing for 30 min, IgG antibody and NGF antibody (Abcam, USA) were added, respectively, and then the added magnetic beads were rotated to mix for 2 h at room temperature. Aspirate supernatant on magnetic stand and wash beads with IP lysis buffer. After removal of proteins by addition of proteinase K, Trizol LS was added to extract RNA and finally subjected to subsequent analysis.

2.10. Assessment of Neural Cancer Cell Interactions. PNI model was used to simulate the tumor and surrounding neural microenvironment. DRGs were placed on ice in DMEM in 24 wells containing 25 μL of Matrigel at a distance of approximately 1 mm from tumor colonies suspended in 25 μL of matrix. To rule out nonspecific metastasis of tumor cells, another 25 microliters of DRG-free male basement membrane was placed on its back. The incubator was placed in an incubator at 37°C and saturated with 5% CO_2 for 20 minutes in a humid environment to perform Matrigel polymerization. After solidification, the DMEM medium was added every 2 days. The cell suspensions on adjacent sides were photographed by using an inverted microscope technique. To quantitatively study the growth of tumor cells, we determined the tumor boundary and tumor boundary as the γ parameter, the tumor cell metastasis distance as the α parameter, and the direction of the DRG as the tumor growth length. Invasion index was α/γ, and DRG growth index was β/γ. The moving distance is performed by the image analysis software of the microscope imaging system (NIS-Elements, Nikon Instruments Inc., China).

2.11. Cell Migration and Invasion Assay. The ability of cell invasion and migration was detected by treatment with 8.0-μm chamber plates. The upper surface of the Transwell filter we used was coated with or without Matrigel (BD, New Jersey, USA). Firstly, cells were planted into the 8.0 μm chamber plates, then 300 μL of serum-free DMEM medium was added to the upper compartment of the chamber, and then 500 μL of DMEM medium supplemented with 10% FBS was added to the lower chamber for 48 h incubations. Then, the noninvasive cells on the upper side of the chamber were suspended with a cotton swab, and then the invasive cells were fixed in 4% paraformaldehyde and stained with a crystal violet solution. We stained infiltrating cells by using an Olympus IX70 inverted microscope (Olympus Corp, Tokyo, Japan) and randomly selected the best six fields of view, and each experiment was repeated three times.

2.12. Cell Proliferation Assay. The treated cells from each group were seeded in 96 well culture plates at a cell number per well of 3×103, and 5 replicate wells were set in each group. Cell culture supernatants were removed at 0 h, 24 h, 48 h, and 72 h after seeding, and 10 μl of CCK-8 solution was added to each well according to the CCK-8 cell proliferation activity assay kit instructions (Sigma-Aldrich, USA). After incubation at 37°C in 5% CO2 for 1 h, the OD value at 450 nm was measured by using a microplate reader (Bio-Rad, USA), and the cell growth curve was plotted.

2.13. Immunohistochemistry. S-100, CK19, and NGF were detected by immunohistochemistry by using SABC kit according to the manufacturer's requirements. Briefly, incubate with S-100 (1 : 100), NGF (1 : 50) primary antibodies overnight, with an appropriate biotin secondary antibody for 30 min at room temperature, then with streptavidin peroxidase Incubation (Dako LSAB + HRP kit). Slides were stained with DAB and counterstained with hematoxylin.

2.14. In Vivo PNI Model. Animal experiments were approved and supervised by the Animal Ethics Committee of Huazhong University of Science and Technology. 5 week old male athymic BALB/C nude mice were obtained from Experimental animal center of Huazhong University of Science and Technology, and subsequently randomly divided into 2 groups, including PNI + PBS and PNI + Tanezumab. MiaPaCa-2 cell suspension was injected subcutaneously into the midline of the back of the mice. Tanezumab was then administered at 10 mg/kg/kg/d, and tumors were excised within 8 weeks and histologically examined to determine neural PNI. In order to evaluate the role of NGF in tumors that invade along nerves, the nerve invasion model is basically performed in this way. Under the microscope, MiaPaCa-2 cells were injected into the sciatic nerve of paralyzed rats separated from the tibial and peroneal nerve bifurcations. 3 ml of normal saline was injected into the right sciatic nerve as a sham-operated control group. 3 microliters of cytoplasm were microinjected with a 5 microliter microsyringe at a concentration of 1×10^5 cells per microliter. In order to evaluate the function of the sciatic nerve innervating the paw muscles of the hindlimbs, we measured the following parameters: rough movements, 10 minutes per week, and repeated bite marks on the hindlimbs; limb function, according to the degree of response of the hindlimb paws to manual stretching, divided into 4-1 (total paw paralysis), sciatic nerve function index, the unit of elongation (mm) between the 1st and 5th toes of the hind legs of mice, 7 weeks per week.

2.15. Statistical Analysis. SPSS 22.0 and GraphPad Prism 7.0 were used for data analysis and mapping. The pairwise comparisons were analyzed using the chi-square test. The measurement data were represented as mean ± SEM with normal distribution and homogeneity of variance. Student's t-test was performed for the comparison between two groups. The means of the different groups were compared

using one-way or two-way analysis of variance (ANOVA) following Tukey's post hoc test. $P < 0.05$ was considered as statistically significant difference. All experiments were repeated 3 times ($n = 3$).

3. Results

3.1. NGF Indicated the Unfavorable Prognosis of PC Patients. To explore the potential involvement of NGF in PC, we analyzed the differential level of NGF in PC samples with the aid of a bioinformatics. Figure 1(a) was shown as differential genes on chromosomes in the PC samples, and the differential expression genes on chromosome 1, where NGF was located, were found to be most enriched. Figure 1(b) revealed that NGF was prominently higher in pancreatic cancer than in normal samples. Subsequently, we performed RT-qPCR to determine the level of NGF in 80 paired PC tissues and matched with normal tissues, and three groups of samples were randomly selected to detect the NGF protein expression level by using western blotting. As shown in Figure 1(c)–(d), the NGF level was higher in tumor tissues of PC patients than that in the corresponding normal tissues. Similarly, NGF was overexpressed in human PC cell lines compared with that of normal pancreatic epithelial cell lines, especially in MiaPaCa-2 cells (Figure 1(e)–1(f)).

3.2. NGF Promoted PC Cell Migration and Invasion In Vitro. Next, we sought to analyze the effect of NGF on the proliferation and invasive capacity of PC cells. MiaPaCa-2 and CFPAC-1 cells were treated with 100 ng/ml of NGF or the NGF inhibitor Tanezumab for 24 h. The Western blotting results revealed that NGF level was effectively modulated in MiaPaCa-2 and CFPAC-1 cells (Figure 2(a)–2(b), $p < 0.01$). As shown in Figures 2(c)–2(f), NGF promoted MiaPaCa-2 and CFPAC-1 cell invasion and migration, while Tanezumab treatment inhibited cell invasion and migration. Differently, we found that NGF or Tanezumab treatment had insignificant effects on cell proliferation (Figure 2(g)–2(h), $p > 0.05$). These results suggest that NGF functions by promoting migration and invasion of PC cells.

3.3. NGF Binding to TrkA Receptors Encouraged the Intracellular Warburg Effect in PC Cells and DRG Cells. It has been reported that Warburg effect is able to participate in regulating neural function [17]. First, we detected and validated NGF and TrkA receptor binding in PC and DRG cells by using protein co-immunoprecipitation (Figure 3(a)). Subsequently, to understand the role of NGF-TrkA signaling in PC and DRG cells, we knocked down TrkA expression in MiaPaCa-2 and DRG cells treated with NGF to determine its effect on the Warburg effect. The efficiency of TrkA siRNA on its level in PC and DRG cells was confirmed by Western blotting (Figure 3(b), $p < 0.01$). Glucose uptake analysis, lactate production analysis, and ATP analysis discovered that NGF overexpression increased the glucose uptake, lactate production, and ATP accumulation. Further, TrkA knockdown partially reversed the facilitative effects of NGF on glucose uptake, lactate production, and ATP accumulation (Figure 3(c)–3(e), $p < 0.05$). ECAR analysis discovered that NGF promoted the glycolytic capacity, which was reversed by TrkA inhibition (Figure 3(f), $p < 0.01$). In short, these findings revealed that NGF could encourage the Warburg effect of PC and DRG cells.

We knocked down TrkA expression in MiaPaCa-2 and DRG cells treated with 100 ng/ml of NGF for 48 h to determine its effect on the Warburg effect. (a) Co-IP was employed to test the interaction between NGF and TrkA in MiaPaCa-2 and DRG cells. (b) Western blotting was employed to test the level of TrkA in MiaPaCa-2 DRG cells transfected with TrkA siRNA. (c-e) Glucose uptake, lactate production, and ATP assays were employed to test glucose uptake, lactate production, and ATP accumulation in MiaPaCa-2 DRG cells treated with 100 ng/ml of NGF or/and transfected with TrkA siRNA for 48 h. (f) Extracellular acidification rate (ECAR) was employed to test and detects the glycolytic capacity of DGR cells treated with 100 ng/ml of NGF or/and transfected with TrkA siRNA for 48 h. $N = 3$, $^{*}P < 0.05$, $^{**}P < 0.01$.

3.4. NGF/TrkA Activated the PI3K/AKT/mTOR Signaling Pathway and Enhanced the Interaction between PC Cells and DRG Cells. To investigate potential regulators of NGF/TrkA signaling that induce cell invasion and migration, we focused our attention on downstream pathways. We used western blot assay to detect PI3K/AKT/mTOR pathway-related proteins. The results demonstrated that PI3K, p-AKT, and p-mTOR were upregulated in NGF overexpression PC cells, whereas transfection of TrkA siRNA reversed the results (Figure 4(a), $p < 0.01$). Moreover, PC and DRG cell migration and invasion numbers were increased after NGF treatment, and this result was partially counteracted by TrkA downregulated (Figure 4(b)–4(e), $p < 0.01$). Signaling through the NGF-TrkA pathway was involved not only in PC cell growth but also in the process of PNI in PC cells [18]. To confirm whether the NGF/TrkA axis is involved in the PNI of PC cells, a model of neuroinvasion was constructed *in vitro* by culturing rat DRG cells and MiaPaCa-2 cells using a Matrigel coculture system. The invasion schematic is shown in Figure 4(f). The results revealed that overexpression of NGF memorably increased the MiaPaCa-2 invasion index and DRG growth index, whereas TrkA knockdown impaired the MiaPaCa-2 invasion index and DRG growth ability. Furthermore, TrkA knockdown was also able to partially reverse the promoting effect of NGF overexpression on the MiaPaCa-2 invasion index and DRG growth index (Figure 4(g)–4(h), $p < 0.01$). In a word, these findings reveal that TrkA blockade attenuates NGF induced PC cell migration and neuroinvasion as well as PI3K/Akt/mTOR pathway activation.

3.5. NGF Could Upregulate Tumor Derived Exosomal miRNA-21-5p (TDE-miR-21-5p) Expression Level. PC cells derived exosomes were collected and cultured for several days. Transmission electron microscopy was used to assess the morphology and size of exosomes extracted from PC cells (Figure 5(a)). Besides, surface markers of exosomes were observed to be significantly expressed in the extracts, including CD9, CD63, TSG101, and Alix (Figure 5(b)). In

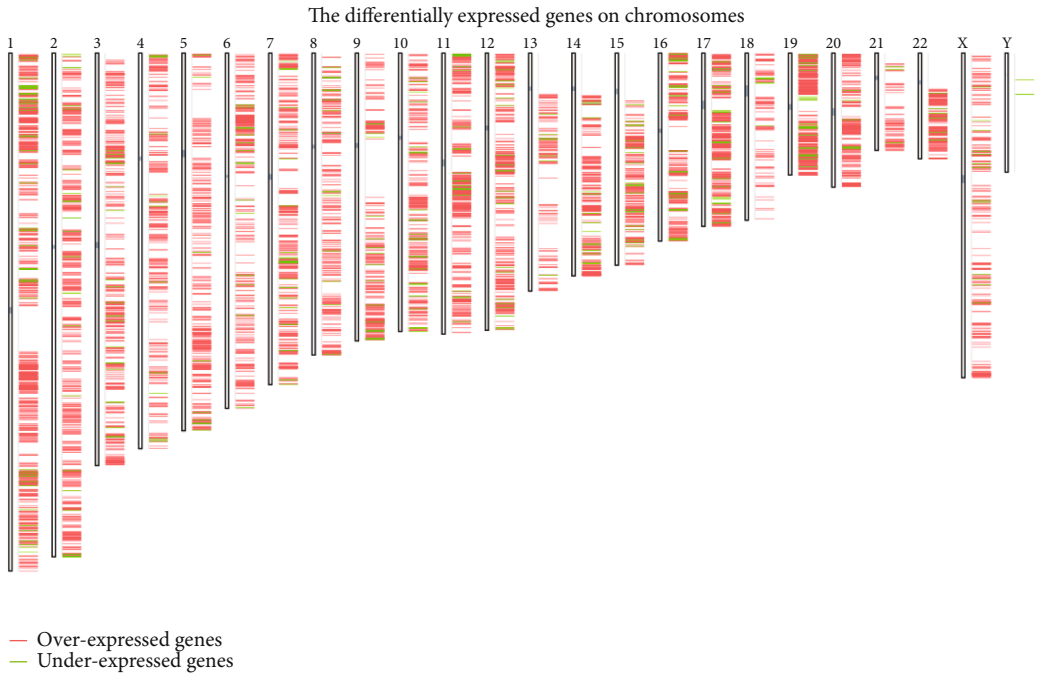

(a)

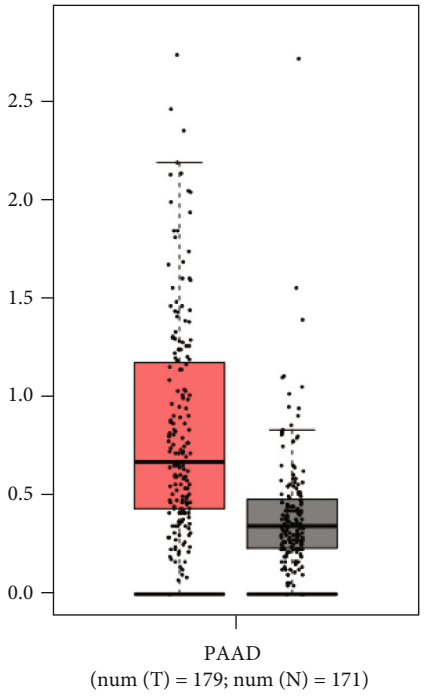

(b)

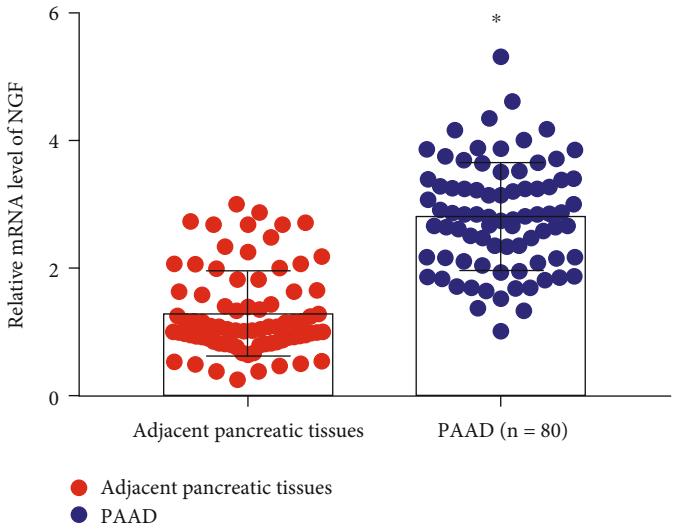

(c)

Figure 1: Continued.

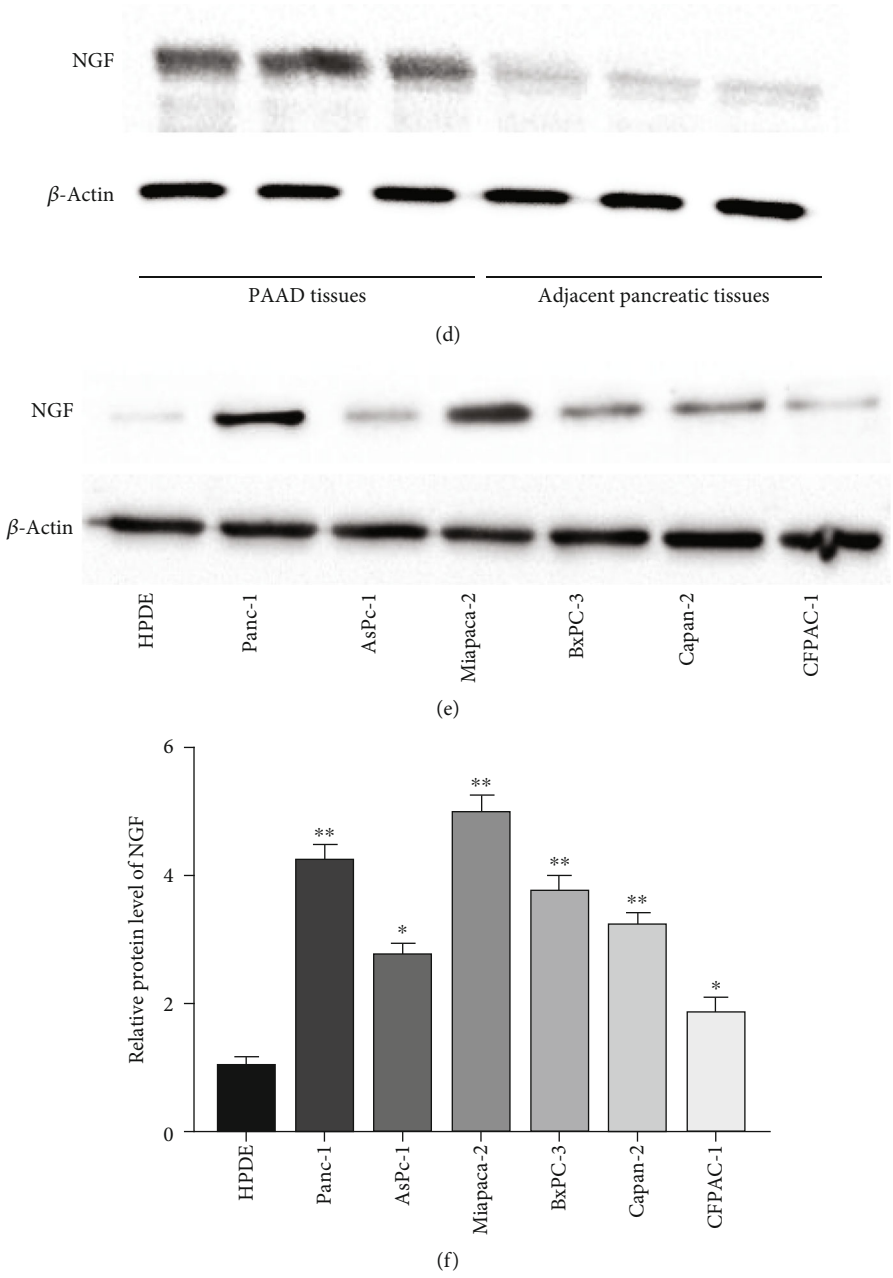

Figure 1: NGF was increased in PC tissues and cell lines. (a) Differentially expressed genes on chromosomes in PC. (b) GEPIA database analysis of NGF expression in PC samples and normal samples. (c) NGF level in PC tissues and adjacent tissue samples collected from 80 patients was tested by RT-qPCR. $^{**}P < 0.01$, unpaired t-test. (d) Differential of NGF was assessed by Western blotting in three randomly selected pairs of 80 samples. (e-f) Relative level of NGF in PC cell lines (Panc-1, AsPc-1, MiaPaCa-2, BxPC-3, Capan-2, CFPAC-1) and pancreatic ductal epithelial cells HPDE was tested by Western blotting. Data were presented as mean ± SEM. $N = 3$, $^{*}P < 0.05$ compared with adjacent pancreatic tissues. $^{**}P < 0.01$ compared with adjacent pancreatic tissues or HDPE.

the GEO dataset we found that miR-21-5p expression was significantly reduced in NGF deficiency (Figure 5(c)). Additionally, we found that miRNA-21-5p expression was highly enriched in PS cells-derived exosomes (Figure 5(d) , $p < 0.01$). A study validated differential miRNA expression by RT-qPCR after NGF treatment and discovered that miR-21-5p level was memorably decreased in NGF deprivation [19]. We further authenticated the binding between NGF and miR-21-5p by using RIP assay (Figure 5(e) , $p < 0.01$). In addition, NGF could promote miR-21-5p, while Tanezumab treatment repressed miR-21-5p levels (Figure 5(f)–5(g), $p < 0.01$).

3.6. miR-21-5p Inhibitor Suppressed PNI in PC Cells to Relieve Nociceptive Transmission. To further investigate whether miR-21-5p has an effect on PNI in PC cells, MiaPaCa-2 cells were transfected with miR-21-5p inhibitor cocultured with DRG cells. Figure 6(a) is shown as a

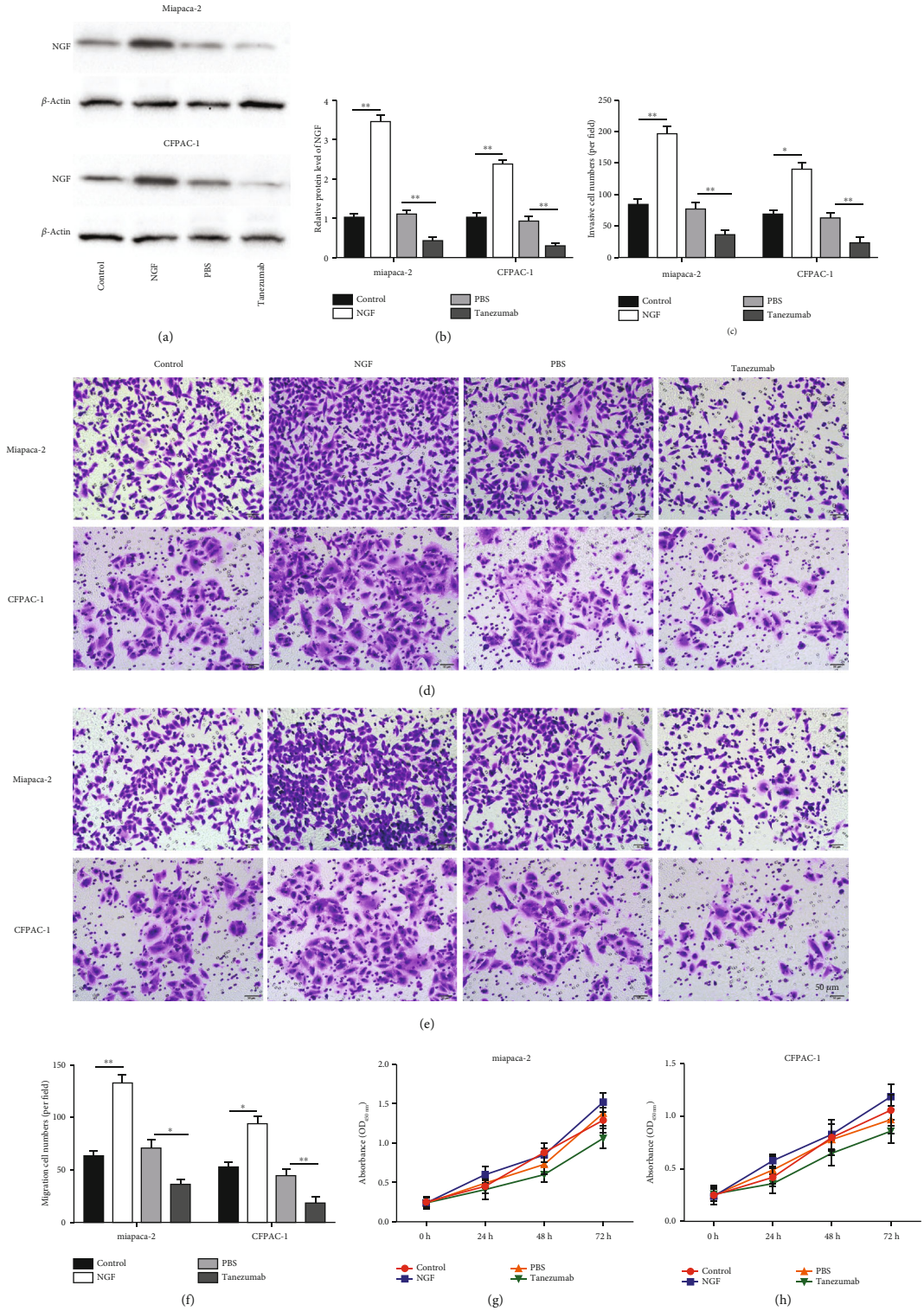

Figure 2: NGF promoted PC cell migration and invasion *in vitro*. MiaPaCa-2 and CFPAC-1 cells were treated with 100 ng/ml of NGF or the NGF inhibitor Tanezumab for 48 h. (a-b) Western blot analysis was employed to test the level of NGF in Miapaca-2 and CFPAC-1 cells treated with NGF or the NGF inhibitor Tanezumab. (c-f) Transwell assay was employed to test migration and invasion of MiaPaCa-2 and CFPAC-1 cells treated with NGF or the NGF inhibitor Tanezumab. (g-h) CCK8 was used to detect cell proliferation of MiaPaCa-2 and CFPAC-1 cells treated with NGF or the NGF inhibitor Tanezumab. $N = 3$, $^{*}P < 0.05$, $^{**}P < 0.01$.

coculture system schematic. We discovered that miR-21-5p level, cell migration number, ATP accumulation, glucose absorption, lactate production, and glycolytic capacity, as well as pain state dependent protein TRPV1 expression, were observably increased in DRG cells under coculture conditions, which could be partially reversed by inhibition of

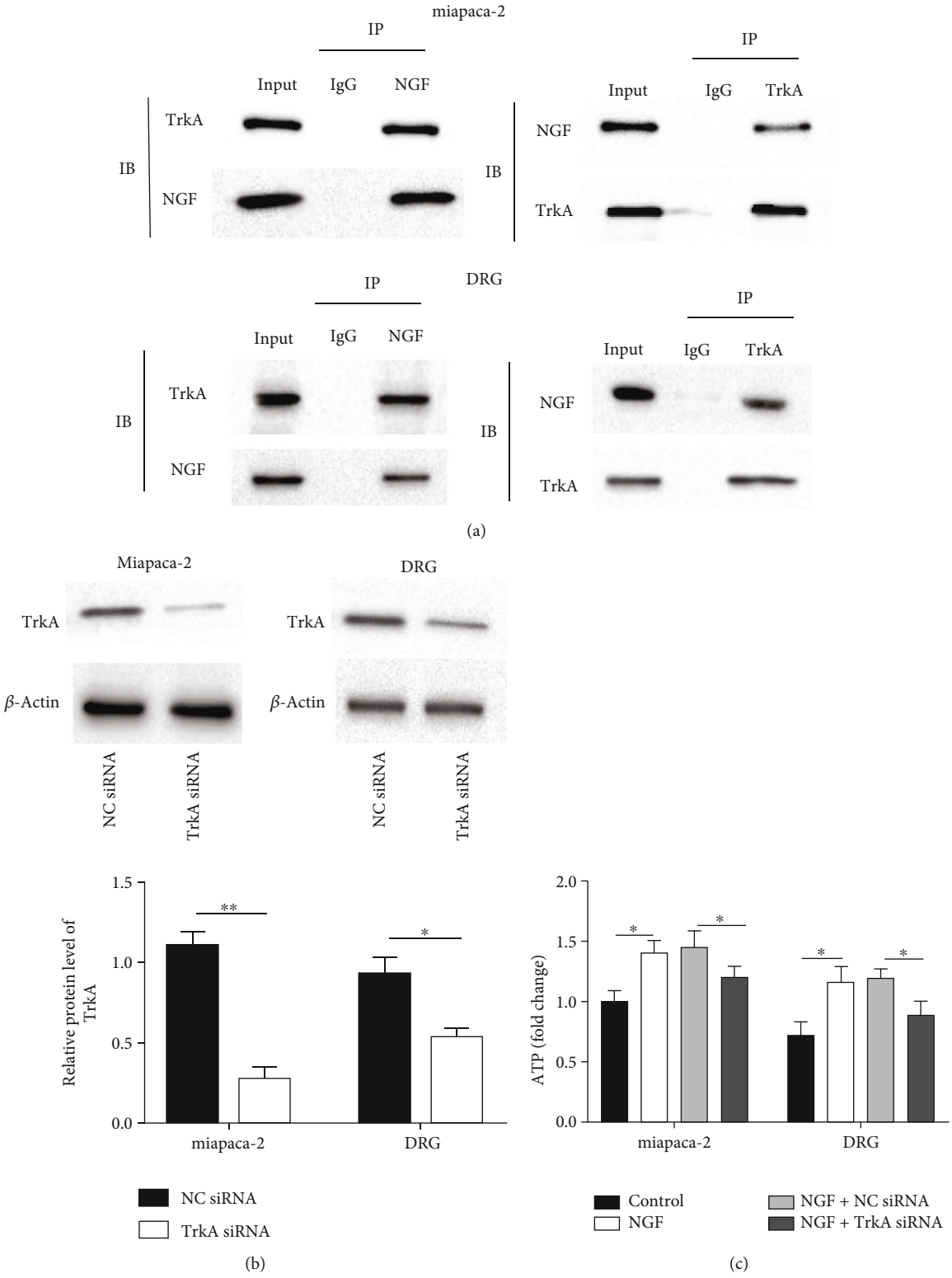

Figure 3: Continued.

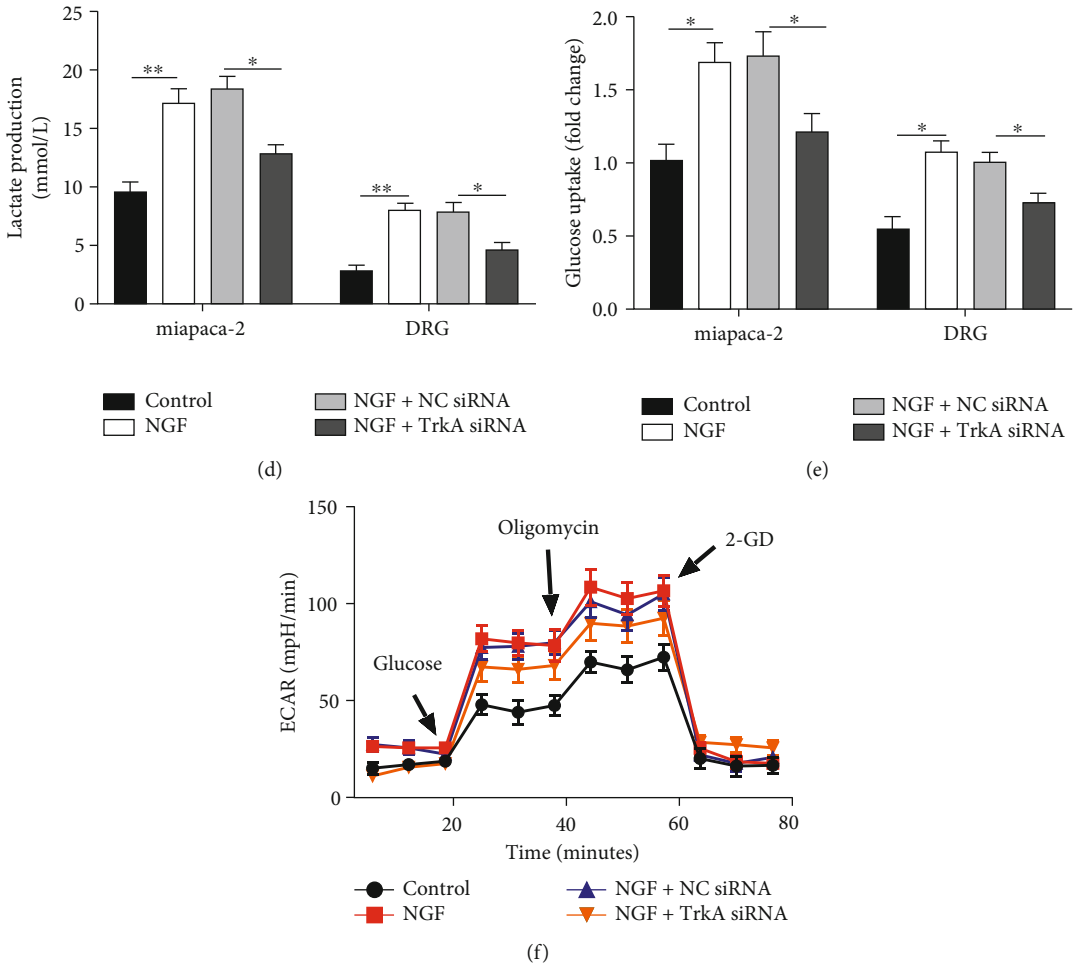

Figure 3: NGF binding to TrkA receptors encouraged the intracellular Warburg effect in PC cells and DRG cells.

miR-21-5p (Figure 6(b)–6(i), $P < 0.05$). Therefore, we hypothesized that TDE-miR-21-5p is an important regulator of PNI in PC cells.

3.7. NGF Encouraged PC Cell Neuroinvasive Potential by Activating the Warburg Effect and Upregulating TDE-miR-21-5p Expression. To further explore whether NGF and miR-21-5p are functionally relevant in regulating PC, rescue experiments were performed by using cotreatment of Tanezumab and miR-21-5p mimic on MiaPaCa-2 cells, followed by coculture with DRG cells. Figure 7(a) is presented as the overexpression efficiency of mir-21-5p mimic. Subsequently, intracellular miR-21-5p level also decreased in DRG cells of the Tanezumab-treated MiaPaCa-2 cell group after coculture, and the miR-21-5p level was reversed after transfection of miR-21-5p mimic (Figure 7(a) , $p < 0.01$). Furthermore, Tanezumab treatment significantly decreased the invasion index and DRG growth index of MiaPaCa-2 cells, and the invasion number, cell migration number, ATP accumulation, glucose absorption, lactate production, and glycolytic capacity of MiaPaCa-2 and DRG cells, and TRPV1 protein level in MiaPaCa-2 cells, which were reversed by miR-21-5p upregulation (Figure 7(b)–7(m) , $p < 0.05$). In conclusion, inhibition of miR-21-5p expression in MiaPaCa-2 cells was able to abolish the promoting effect of NGF on PNI in PC cells.

3.8. NGF Knockout Markedly Alleviated Nerve Invasion by PC Cells as Well as Relieved Nociceptive Conduction in Animal Models. Subsequently, we used a model of neuroinvasion in nude mice. A total of 15 nude mice were randomly divided into 3 groups: Sham, PNI + PBS, and PNI + Tanezumab. The cell suspension was injected into the middle of the back of the mouse. Eight weeks after injection, tumors were obtained histologically to observe whether the nerves had PNI. The relationship between NGF and PNI was studied by western blot analysis. Using immunohistochemical methods, nerve tissue marker (S100), and tumor marker (CK19) was evaluated in the neural invasion model (Figure 8(a)). Next, mice in the Tanezumab group developed hindlimb dysfunction after 15 days and left hindlimb paralysis by week 7, which was significantly prolonged compared with the PBS group. Seven of the ten mice in the PNI + PBS group became completely paralyzed at week 7, whereas only two mice in the Tanezumab group became paralyzed. All mice in the sham group had normal hindlimb function (Figure 8(b)). Sciatic nerves were excised for HE staining after mice were sacrificed at 8 weeks. HE staining displayed

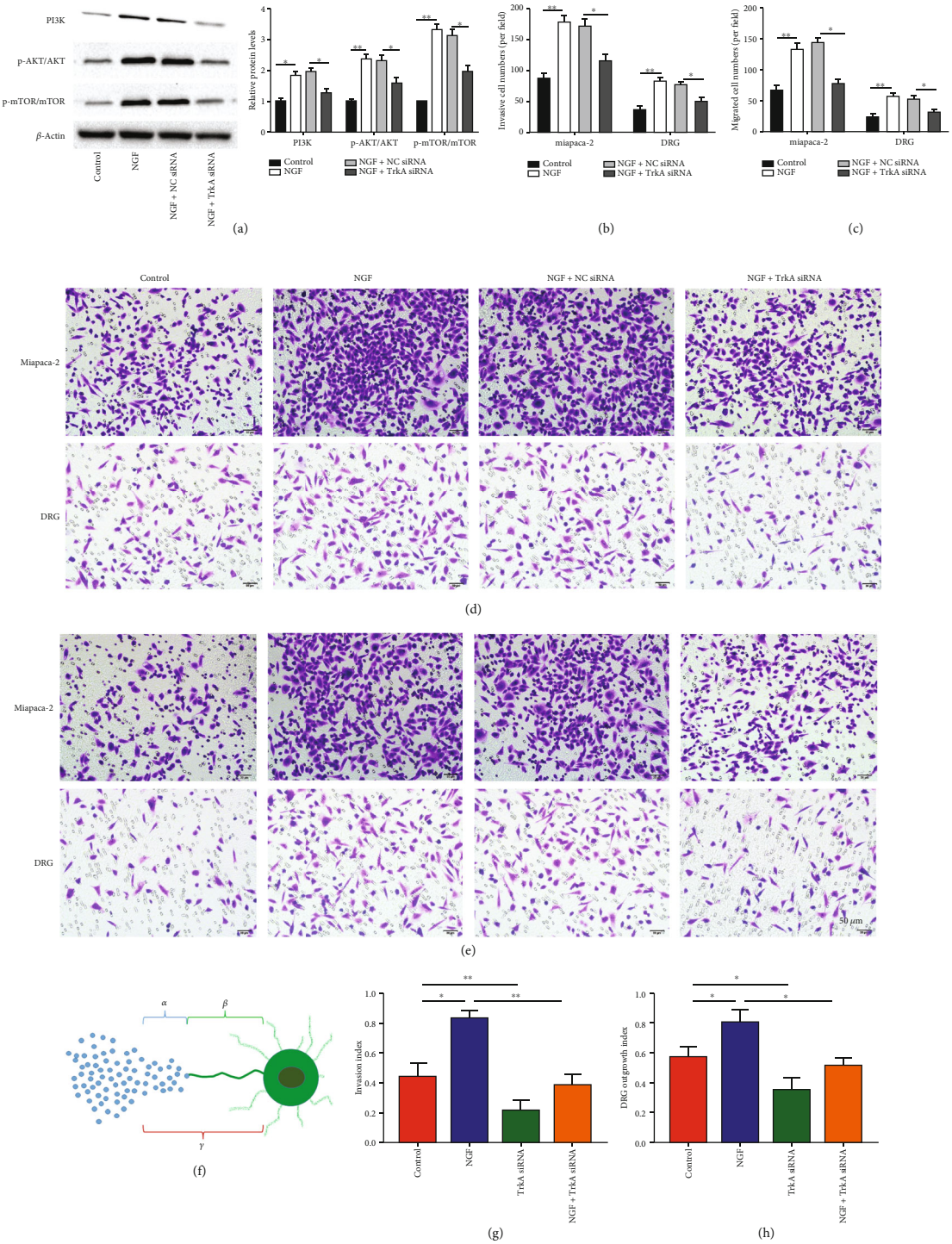

Figure 4: NGF/TrkA activated the PI3K/AKT/mTOR signaling pathway and enhanced the interaction between PC cells and DRG cells. (a)Western blotting was employed to test the levels of PI3K, p-AKT, and p-mTOR in MiaPaCa-2 cells treated with 100 ng/ml of NGF or/and transfected with TrkA siRNA for 48 h. (b-e) Transwell was used to detect migration and invasion of DGR or MiaPaCa-2 cells treated with 100 ng/ml of NGF or/and transfected with TrkA siRNA for 48 h. (f) Schematic of MiaPaCa-2 and DGR invasion. (g) DRG growth index. (h) Neuroinvasion index. $N = 3$, $^{*}P < 0.05$, $^{**}P < 0.01$.

that the diameter of sciatic nerve at the site of primary tumor and 5 mm along the proximal end of sciatic nerve was prominently reduced in PNI + Tanezumab mice compared with PNI + PBS (Figure 8(c)). Tumor volume and invasive nerve diameter were prominently decreased in the Tanezumab group compared with the PNI + PBS control group (Figure 8(d)–8(e)). Sciatic nerve scores and sciatic nerve index were evidently reduced in the PNI + PBS group

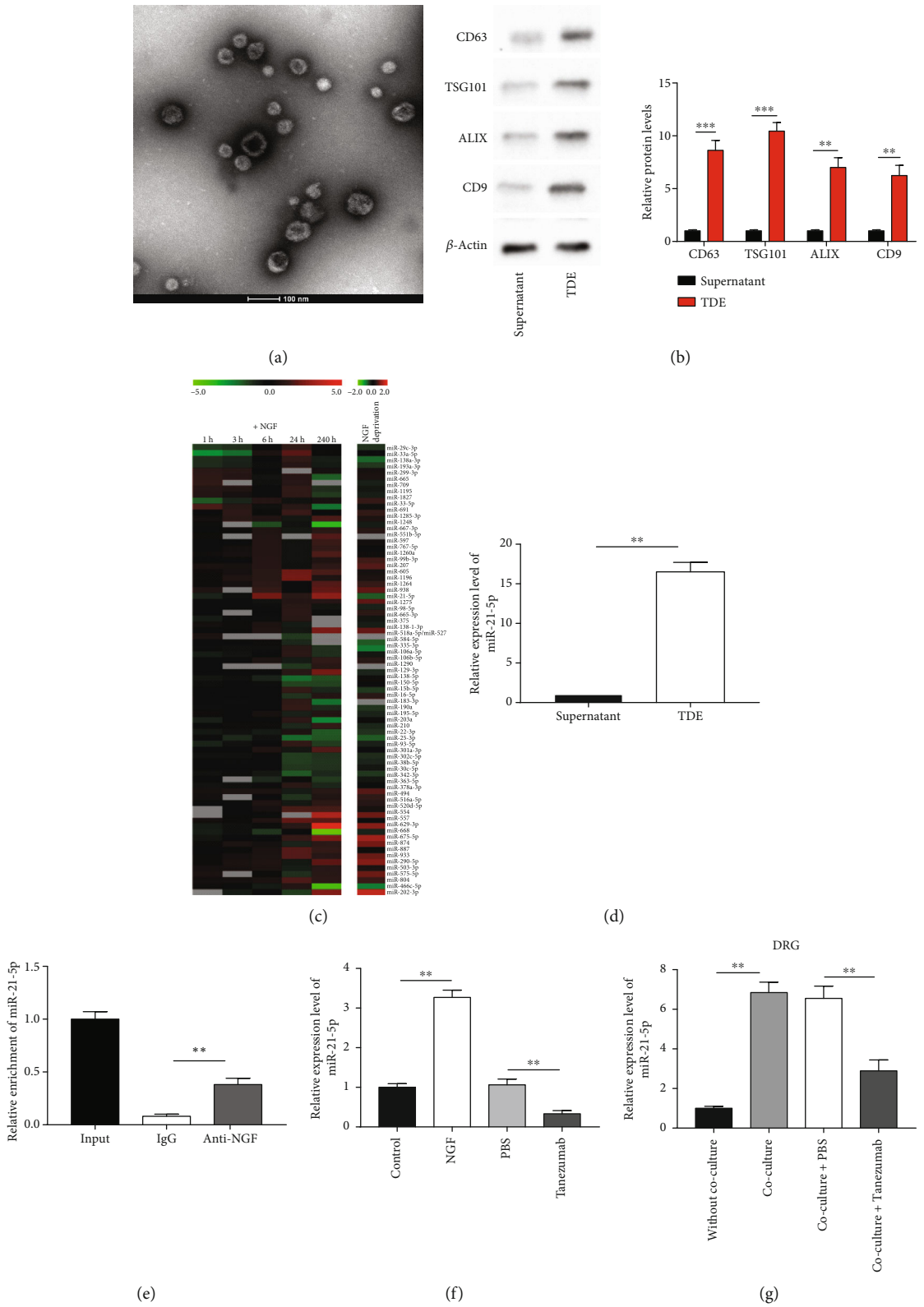

Figure 5: NGF could upregulate TDE-miR-21-5p expression level. (a) Characterization of PC cells-derived exosomes was tested by transmission electron microscopy. Scale bar, 100 nm. (b) The markers of exosomes were tested by western blotting. (c) Heat map analysis of NGF regulated differentially expressed miRNAs in GEO database. (d) RT-qPCR was employed to test miR-21-5p expression in PC cells-derived exosomes. (e) miR-21-5p level in the 3′UTR region of NGF was assessed by RIP assay. (f-g) RT-qPCR was employed to test miR-21-5p expression in MiaPaCa-2 cells treated with NGF or Tanezumab. $N = 3$, $^{*}P < 0.05$, $^{**}P < 0.01$.

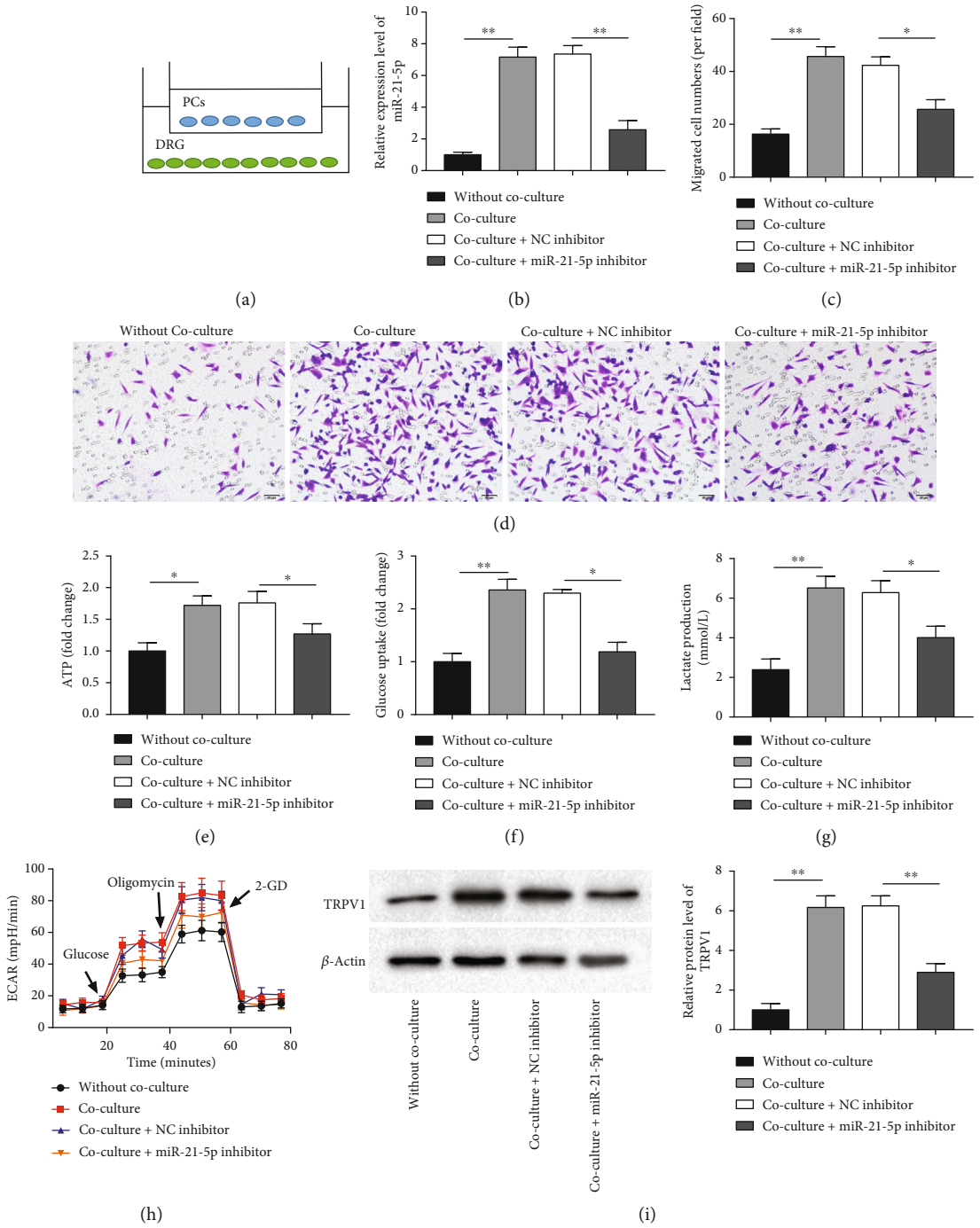

FIGURE 6: miR-21-5p inhibitor suppressed PNI in PC cells to relieve nociceptive transmission. MiaPaCa-2 cells transfected with miR-21-5p inhibitor were cocultured with DRG cells for 48 h. (a) Diagrammatic sketch of MiaPaCa-2 and DGR cell coculture. (b) RT-qPCR was employed to test miR-21-5p level in DGR cells. (c-d) Transwell was used to detect migration of DGR cells. (e-g) Glucose uptake, lactate production, and ATP assays were employed to test glucose uptake, lactate production, and ATP accumulation. (h) Extracellular acidification rate (ECAR) was employed to test and detect the glycolytic capacity of DGR cells. (i) Western blotting was employed to test TRPV1 expression in DGR cells. $N = 3$, $^{*}P < 0.05$, $^{**}P < 0.01$.

compared to the sham group, and were back increased after treatment with Tanezumab (Figure 8(f)–8(g)). Further, the results revealed that NGF inhibition could reduce tumor volume and invasive nerve diameter. Additionally, compared with the sham group, PNI + PBS substantially promoted NGF and miR-21-5p expression in mouse tumor tissues, which were dramatically reversed by Tanezumab treatment (Figure 8(h)–8(i)). These data suggest that elimination of NGF can inhibit tumor growth and sciatic nerve invasion into the spinal cord.

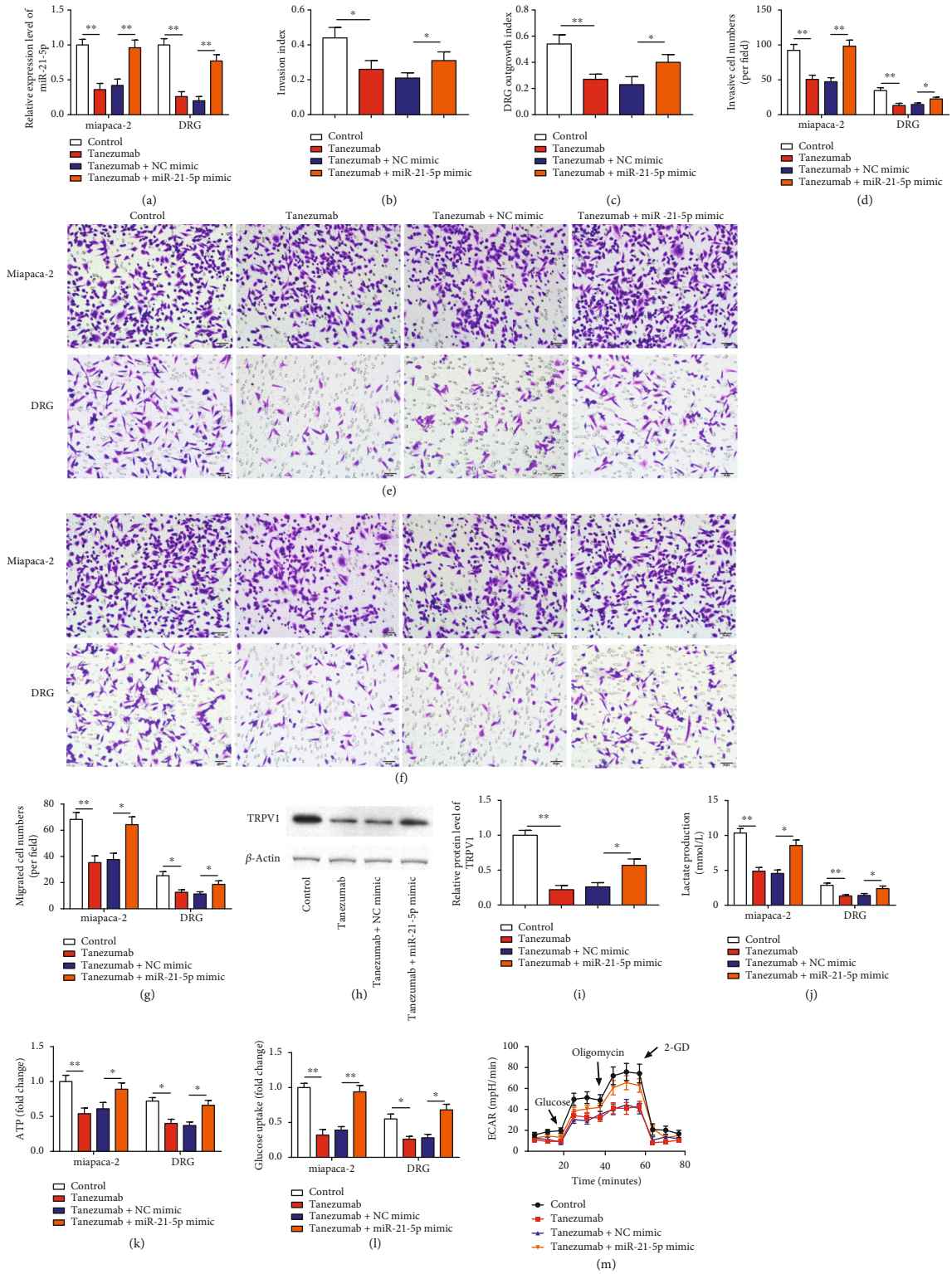

Figure 7: NGF encouraged PC cell neuroinvasive potential by activating the Warburg effect and upregulating TDE-miR-21-5p. Rescue experiments were performed by using cotreatment of 100 ng/ml of Tanezumab and miR-21-5p mimic on MiaPaCa-2 cells for 48 h, followed by coculture with DRG cells. (a) RT-qPCR was employed to test miR-21-5p expression in MiaPaCa-2 and DGR cells cotreatment of Tanezumab and miR-21-5p mimic. (b-c) Neuroinvasion index and DRG growth index are illustrated. (d-g) Transwell was used to detect invasion and migration of MiaPaCa-2 and DGR cells cotreatment of Tanezumab and miR-21-5p mimic. (h-i) Western blotting was employed to test TRPV1 expression in DGR cells. (j-l) Glucose uptake, lactate production, and ATP assays were employed to test glucose uptake, lactate production, and ATP accumulation. (m) Extracellular acidification rate (ECAR) was employed to test and detect the glycolytic capacity of DGR cells. (m) $N = 3$, $^{*}P < 0.05$, $^{**}P < 0.01$.

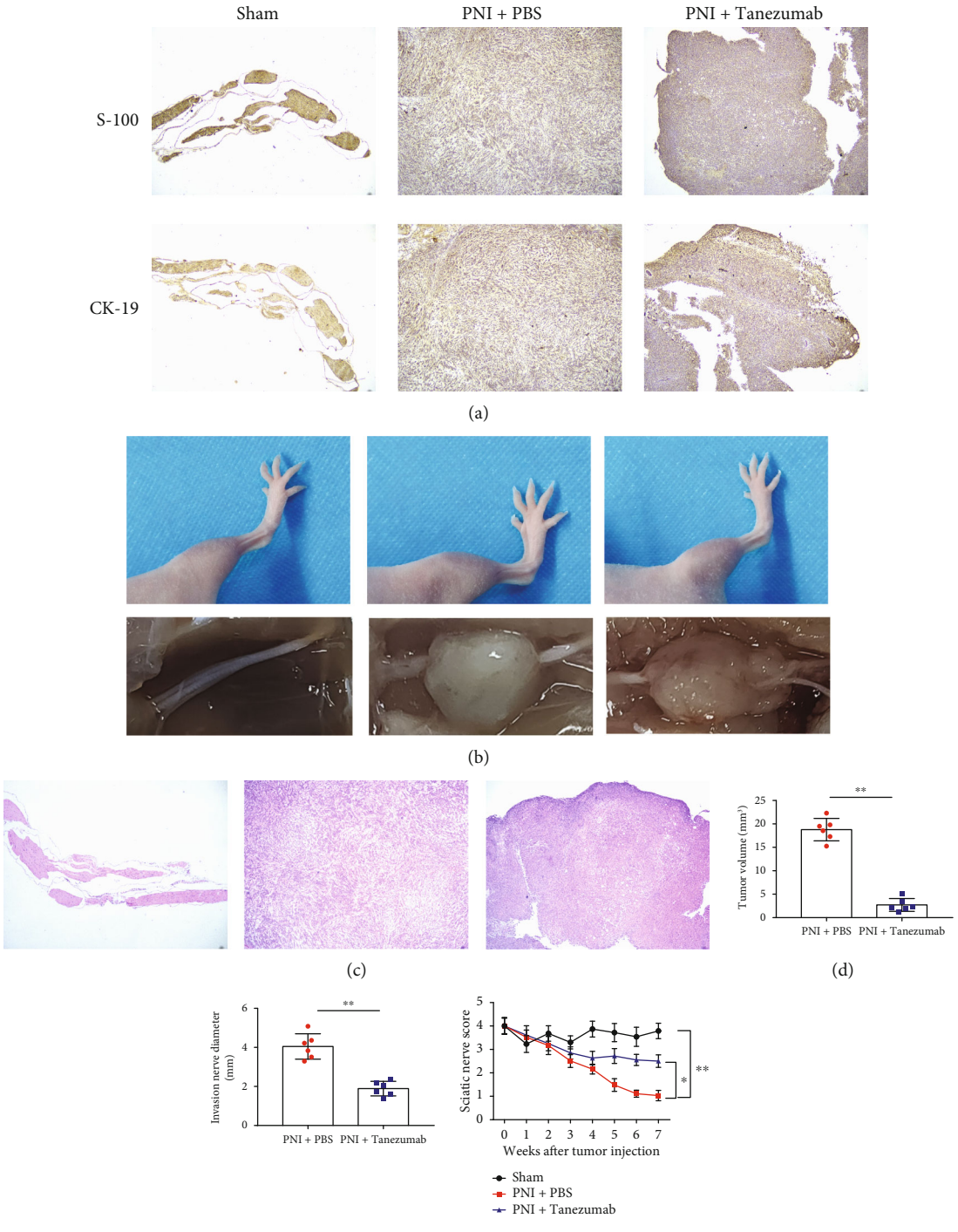

Figure 8: Continued.

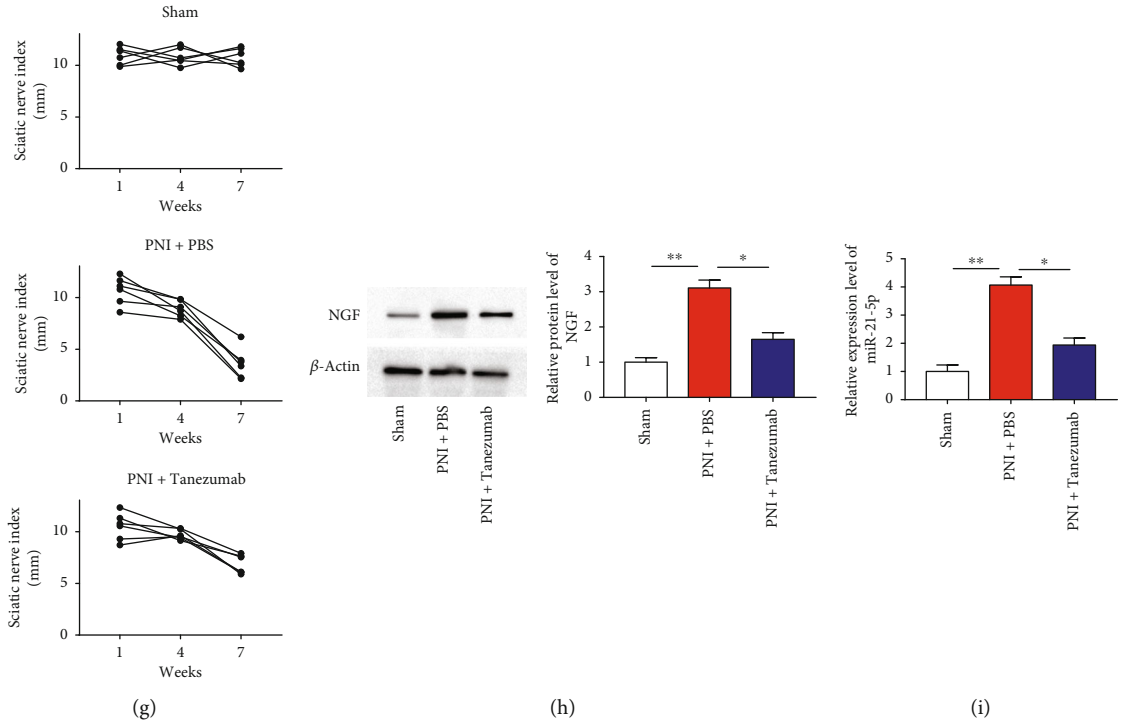

FIGURE 8: NGF knockout markedly alleviated nerve invasion by PC cells as well as relieved nociceptive conduction in animal models. (a) The expression of S100 (a neural tissue marker) and CK19 (a cancer cell marker) was detected immunohistochemically (scale bar, 1 mm). (b) The mean left sciatic nerve scores and sciatic nerve index in different groups were measured weekly for 7 weeks. (c) Xenograft tumors and corresponding HE staining of orthotopic sciatic nerves from the mouse hindlimbs. (d-g) Tumor volume, invasive nerve diameter, sciatic nerve score, and sciatic nerve index were tested in each group at 7 weeks after injection. (h) Western blotting was employed to test the protein level of NGF in in mouse tumor tissues. (i) RT-qPCR was employed to test the level of miR-21-5p in mouse tumor tissues. $N = 3$, $^{*}P < 0.05$, $^{**}P < 0.01$.

4. Discussion

PNI is one of the most characteristic biological behaviors of pancreatic cancer and is also one of the leading causes of local recurrence and poor prognosis after curative resection [20]. At present, it is generally accepted that neuroinvasion refers to the existence of reciprocal chemotactic interactions between tumor cells and nerve cells, resulting in the infiltrative growth of nerve bundles with tumor cell extension [21]. In this experiment, Matrigel/DRG and mouse sciatic nerve infiltration models were used to investigate the effect of NGF on the formation of PNI in PC cells and preliminarily explore the paracrine loop of NGF/TrkA/miR-21-5p. Normally, NGF regulates neuronal survival, growth and development, differentiation, and regeneration and functional maintenance [22]. First, we determined NGF expression in PC. NGF level in PC tissues and cell lines was prominently upregulated than in normal tissues and normal pancreatic epithelial cell lines. Besides, NGF promoted MiaPaCa-2 and CFPAC-1 cell invasion and migration, while Tanezumab treatment inhibited cell invasion and migration. Zhu et al. revealed that the mRNA levels of NGF and TrkA in PC were increased by 2.7- and 5.6-fold compared with normal pancreatic tissue, respectively. Moreover, mRNA levels of NGF and TrkA were higher in tumors with perineural invasion than in those without perineural invasion, and perineural invasion was more likely to occur in tumors with high expression of NGF and TrkA, suggesting that NGF released by cancer cells does not act on itself through paracrine or autocrine actions, but rather acts on TrkA presented at the perineurium to bring nerves into contact with cancer cells, which in turn leads to TrkA-mediated perineural invasion [23]. Thus, it illustrates that the NGF/TrkA pathway plays a role in the dissemination and invasion of neural processes along nerves in PC.

In 1920, the German biochemist Warburg discovered that liver cancer cells, in contrast to normal hepatocytes, were more active in their glycolytic activity, leading to the discovery that the programmed metabolism of cancer cells differed from that of other normal cells [24]. Even under oxygen replete conditions, cancer cells metabolize glucose through anaerobic glycolysis to generate the energy needed for cell survival, a metabolic feature of aerobic glycolysis known as the Warburg effect, which is manifested by a high rate of glucose uptake, active glycolysis, and high levels of metabolite lactate [25]. A research found that circ_03955 through miR-3662/HIF-1α Axis activation of the Warburg effect functions as a tumor promoter, which may provide a new perspective for PC treatment [26]. ARF6 may contribute to pancreatic cancer development by promoting the Warburg effect [27]. Li et al. [28] displayed that silencing of PKM2 exhibited suppressive effects on pancreatic cancer tumor growth and invasion by altering the Warburg effect. Ye et al. [29] confirmed that lncRNA FEZF1-AS1 made an

indispensable contribution to the invasion of pancreatic cancer cells by maintaining the Warburg effect. Additionally, the Warburg effect has been reported to participate in tumor development and also accelerate the neurological diseases. Formaldehyde upregulates the Warburg effect in hippocampal tissue, as evidenced by increased ATP, glucose, and lactate production [30]. Therefore, we speculate that NGF/TrkA signaling may contribute to PC and DRG cell migration and PNI by activating the Warburg effect. TrkA knockdown partially reversed the facilitative effects of NGF on glucose uptake, lactate production, and ATP accumulation. Accumulating evidence has established that the PI3K/AKT/mTOR pathway is one of the key intracellular signaling pathways, and its activation has recently been found to be frequently aberrantly activated in many tumors and plays a critical role in regulating key physiological and pathological cellular processes, including cell proliferation, invasion, cancer progression, and chemoresistance as well as angiogenesis [31]. Currently, many studies have shown that Akt/mTOR signaling promotes the Warburg effect and tumor development by increasing GLUT1 trafficking and activation of glycolytic enzymes, as well as by inducing glycolysis [32]. In this study, we further tested the level of the PI3K/AKT/mTOR pathway proteins under NGF/TrkA pathway stimulation and blockade, and the results showed that PI3K, p-AKT, and p-mTOR protein expression were upregulated in NGF overexpression PC cells, whereas transfection of TrkA siRNA reversed the results.

Exosomes, small extracellular vesicles with a diameter of 30-150 nm that are secreted by almost all living cells in the body and have a phospholipid bilayer resembling the structure of the cell membrane, have been closely followed by researchers in recent years [33]. Exosomes carry a variety of biologically active substances such as DNA, RNA, proteins, liposomes, and metabolic small molecules associated with their cell of origin, which reflect the body's physiopathological state and suggest disease-related biological information, including tumors [34]. Tumor cell or other cells in the tumor microenvironment create a microenvironment suitable for tumor survival and progression by secreting exosomes and transporting tumor related active substances such as DNA, RNA, or proteins into the target cells via exosomes, which in turn regulate the biological functions of the target cells, thereby promoting the occurrence and development of tumors [35]. High baseline miR-21 plasma concentrations are associated with clinical outcomes in cancer patients after induction chemotherapy [36]. Exosomal miR-21-5p could increase the tumor volume, size, and weight of ovarian cancer *in vivo* and promote the development of ovarian cancer [37]. Tang et al. [38] showed that miR-21-5p may encourage cell proliferation, migration, and invasion by disrupting Smad7 expression in lung cancer cells. Besides, high expression of miR-21-5p was demonstrated to be associated with rectal tumor TNM stage and lymph node metastasis [39]. A study using nanomedicines to codeliver miR-21-5p antisense oligonucleotides and gemcitabine for PC treatment showed that the integration of miR-21-5p gene inhibition and gemcitabine treatment by using single-chain variable fragment functionalized nanoparticle carriers exerted synergistic antitumor effects on PC cells [40]. miR-21-5p was obviously increased in PC cells and tissues [41]. Besides, the effect of miR-21-5p on the Warburg effect is positively correlated with the activity of the Wnt/β-catenin pathway [42, 43]. The results of this study demonstrate that miR-21-5p is highly enriched in MiaPaCa-2-derived exosomes. We discovered that TDE-miR-21-5p is a considerable regulator of PNI in PC cells. Our results confirmed that NGF was able to upregulate miR-21-5p expression. Furthermore, knocking down the expression of miR-21-5p in MiaPaCa-2 cells was able to abolish the promoting effect of NGF on PNI in PC cells. Because, we speculated that NGF/TrkA promoted neuroinvasion in pancreatic cancer may be associated with upregulation of miR-21-5p by NGF.

As mentioned above, NGF and miR-21-5p levels were prominently overexpressed in PC tissues and cell lines. NGF/TrkA promotes the neuroinvasive potential of PC cells by activating the Warburg effect in DRG cells through upregulation of TDE-miR-21-5p expression. Collectively, this study demonstrates that a paracrine loop between PC cells and the DRG mediated by NGF/TrkA/miR-21-5p contributes to PNI.

Data Availability

The datasets used during the present study are available from the corresponding author on reasonable request.

Conflicts of Interest

The authors declare that they have no competing interests.

Authors' Contributions

Tao Peng and Yao Guo designed this study. Zheng Gan and Yan Ling performed the experimental work and wrote the manuscript. Jiongxin Xiong, Xueyi Liang, and Jing Cui provided the majority of statistical analysis as well as provided the figures and tables for the manuscript. All authors read and approved the final manuscript.

References

[1] L. D. Wood, M. I. Canto, E. M. Jaffee, and D. M. Simeone, "Pancreatic cancer: pathogenesis, screening, diagnosis, and treatment," *Gastroenterology*, vol. 163, no. 2, pp. 386–402.e1, 2022.

[2] V. Goral, "Pancreatic cancer: pathogenesis and diagnosis," *Asian Pacific Journal of Cancer Prevention*, vol. 16, no. 14, pp. 5619–5624, 2015.

[3] S. Yu, C. Zhang, and K. P. Xie, "Therapeutic resistance of pancreatic cancer: Roadmap to its reversal," *Biochimica Et Biophysica Acta. Reviews on Cancer*, vol. 1875, no. 1, article 188461, 2021.

[4] L. C. Chu, M. G. Goggins, and E. K. Fishman, "Diagnosis and detection of pancreatic cancer," *Cancer Journal*, vol. 23, no. 6, pp. 333–342, 2017.

[5] J. A. Eble and S. Niland, "The extracellular matrix in tumor progression and metastasis," *Clinical & Experimental Metastasis*, vol. 36, no. 3, pp. 171–198, 2019.

[6] E. R. Murray, S. Menezes, J. C. Henry et al., "Disruption of pancreatic stellate cell myofibroblast phenotype promotes pancreatic tumor invasion," *Cell Reports*, vol. 38, no. 4, article 110227, 2022.

[7] W. Alrawashdeh, R. Jones, L. Dumartin et al., "Perineural invasion in pancreatic cancer: proteomic analysis and in vitro modelling," *Molecular Oncology*, vol. 13, no. 5, pp. 1075–1091, 2019.

[8] I. Lohse and S. P. Brothers, "Pathogenesis and treatment of pancreatic cancer related pain," *Anticancer Research*, vol. 40, no. 4, pp. 1789–1796, 2020.

[9] J. Wang, Y. Chen, X. Li, and X. Zou, "Perineural invasion and associated pain transmission in pancreatic cancer," *Cancers*, vol. 13, no. 18, p. 4594, 2021.

[10] B. Xin, X. He, J. Wang et al., "Nerve growth factor regulates CD133 function to promote tumor cell migration and invasion via activating ERK1/2 signaling in pancreatic cancer," *Pancreatology*, vol. 16, no. 6, pp. 1005–1014, 2016.

[11] D. B. Vera, A. N. Fredes, M. P. Garrido, and C. Romero, "Role of mitochondria in interplay between NGF/TRKA, miR-145 and possible therapeutic strategies for epithelial ovarian cancer," *Life*, vol. 12, no. 1, p. 8, 2022.

[12] J. Jiang, J. Bai, T. Qin, Z. Wang, and L. Han, "NGF from pancreatic stellate cells induces pancreatic cancer proliferation and invasion by PI3K/AKT/GSK signal pathway," *Journal of Cellular and Molecular Medicine*, vol. 24, no. 10, pp. 5901–5910, 2020.

[13] L. Schwartz, C. T. Supuran, and K. O. Alfarouk, "The Warburg effect and the hallmarks of cancer," *Anti-Cancer Agents in Medicinal Chemistry*, vol. 17, no. 2, pp. 164–170, 2017.

[14] P. Vaupel and G. Multhoff, "Revisiting the Warburg effect: historical dogma versus current understanding," *The Journal of Physiology*, vol. 599, no. 6, pp. 1745–1757, 2021.

[15] P. Icard, S. Shulman, D. Farhat, J. M. Steyaert, M. Alifano, and H. Lincet, "How the Warburg effect supports aggressiveness and drug resistance of cancer cells?," *Drug Resistance Updates*, vol. 38, pp. 1–11, 2018.

[16] J. Yang, B. Ren, G. Yang et al., "The enhancement of glycolysis regulates pancreatic cancer metastasis," *Cellular and Molecular Life Sciences*, vol. 77, no. 2, pp. 305–321, 2020.

[17] Y. Hou, Q. Zhang, W. Pang et al., "YTHDC1-mediated augmentation of miR-30d in repressing pancreatic tumorigenesis via attenuation of RUNX1-induced transcriptional activation of Warburg effect," *Cell Death and Differentiation*, vol. 28, no. 11, pp. 3105–3124, 2021.

[18] A. A. Bapat, R. M. Munoz, D. D. Von Hoff, and H. Han, "Blocking nerve growth factor signaling reduces the neural invasion potential of pancreatic cancer cells," *PLoS One*, vol. 11, no. 10, article e0165586, 2016.

[19] E. Montalban, N. Mattugini, R. Ciarapica et al., "MiR-21 is an Ngf-modulated MicroRNA that supports Ngf signaling and regulates neuronal degeneration in PC12 cells," *Neuromolecular Medicine*, vol. 16, no. 2, pp. 415–430, 2014.

[20] G. H. You, Y. J. Wang, L. Y. Zhang, and M. Zhang, "Research progression in neural invasion model of pancreatic cancer," *Zhonghua Zhong Liu Za Zhi*, vol. 42, no. 4, pp. 346–350, 2020.

[21] D. Liang, S. Shi, J. Xu et al., "New insights into perineural invasion of pancreatic cancer: More than pain," *Biochimica et Biophysica Acta*, vol. 1865, no. 2, pp. 111–122, 2016.

[22] N. K. Isaev, E. V. Stelmashook, and E. E. Genrikhs, "Role of nerve growth factor in plasticity of forebrain cholinergic neurons," *Biochemistry*, vol. 82, no. 3, pp. 291–300, 2017.

[23] Z. Zhu, H. Friess, F. F. diMola et al., "Nerve growth factor expression correlates with perineural invasion and pain in human pancreatic cancer," *Journal of Clinical Oncology*, vol. 17, no. 8, pp. 2419–2428, 1999.

[24] P. Vaupel, H. Schmidberger, and A. Mayer, "The Warburg effect: essential part of metabolic reprogramming and central contributor to cancer progression," *International Journal of Radiation Biology*, vol. 95, no. 7, pp. 912–919, 2019.

[25] V. Fresquet, M. J. Garcia-Barchino, M. Larrayoz et al., "Endogenous retroelement activation by epigenetic therapy reverses the Warburg effect and elicits mitochondrial-mediated cancer cell death," *Cancer Discovery*, vol. 11, no. 5, pp. 1268–1285, 2021.

[26] A. Liu and J. Xu, "Circ_ 03955 promotes pancreatic cancer tumorigenesis and Warburg effect by targeting the miR-3662/HIF-1α axis," *Clinical and Translational Oncology*, vol. 23, no. 9, pp. 1905–1914, 2021.

[27] C. Liang, Y. Qin, B. Zhang et al., "ARF6, induced by mutant Kras, promotes proliferation and Warburg effect in pancreatic cancer," *Cancer Letters*, vol. 388, pp. 303–311, 2017.

[28] C. Li, Z. Zhao, Z. Zhou, and R. Liu, "PKM2 promotes cell survival and invasion under metabolic stress by enhancing Warburg effect in pancreatic ductal adenocarcinoma," *Digestive Diseases and Sciences*, vol. 61, no. 3, pp. 767–773, 2016.

[29] H. Ye, Q. Zhou, S. Zheng et al., "FEZF1-AS1/miR-107/ZNF312B axis facilitates progression and Warburg effect in pancreatic ductal adenocarcinoma," *Cell Death & Disease*, vol. 9, no. 2, p. 34, 2018.

[30] X. N. Li, S. Q. Yang, M. Li et al., "Formaldehyde induces ferroptosis in hippocampal neuronal cells by upregulation of the Warburg effect," *Toxicology*, vol. 448, article 152650, 2021.

[31] Y. Peng, Y. Wang, C. Zhou, W. Mei, and C. Zeng, "PI3K/Akt/mTOR pathway and its role in cancer therapeutics: are we making headway?," *Frontiers in Oncology*, vol. 12, article 819128, 2022.

[32] X. Yang, Y. Cheng, P. Li et al., "A lentiviral sponge for miRNA-21 diminishes aerobic glycolysis in bladder cancer T24 cells via the PTEN/PI3K/AKT/mTOR axis," *Tumour Biology*, vol. 36, no. 1, pp. 383–391, 2015.

[33] L. Zhang and D. Yu, "Exosomes in cancer development, metastasis, and immunity," *Biochimica Et Biophysica Acta. Reviews on Cancer*, vol. 1871, no. 2, pp. 455–468, 2019.

[34] L. Mashouri, H. Yousefi, A. R. Aref, F. Molaei, and S. K. Alahari, "Exosomes: composition, biogenesis, and mechanisms in cancer metastasis and drug resistance," *Molecular Cancer*, vol. 18, no. 1, p. 75, 2019.

[35] R. Kalluri, "The biology and function of exosomes in cancer," *The Journal of Clinical Investigation*, vol. 126, no. 4, pp. 1208–1215, 2016.

[36] K. Khan, D. Cunningham, C. Peckitt et al., "miR-21 expression and clinical outcome in locally advanced pancreatic cancer: exploratory analysis of the pancreatic cancer Erbitux, radiotherapy and UFT (PERU) trial," *Oncotarget*, vol. 7, no. 11, pp. 12672–12681, 2016.

[37] J. Cao, Y. Zhang, J. Mu, D. Yang, X. Gu, and J. Zhang, "Exosomal miR-21-5p contributes to ovarian cancer progression by regulating CDK6," *Human Cell*, vol. 34, no. 4, pp. 1185–1196, 2021.

[38] J. Tang, X. Li, T. Cheng, and J. Wu, "miR-21-5p/SMAD7 axis promotes the progress of lung cancer," *Thorac Cancer*, vol. 12, no. 17, pp. 2307–2313, 2021.

[39] X. H. Jin, S. Lu, and A. F. Wang, "Expression and clinical significance of miR-4516 and miR-21-5p in serum of patients with colorectal cancer," *BMC Cancer*, vol. 20, no. 1, p. 241, 2020.

[40] Y. Li, Y. Chen, J. Li et al., "Co-delivery of microRNA-21 antisense oligonucleotides and gemcitabine using nanomedicine for pancreatic cancer therapy," *Cancer Science*, vol. 108, no. 7, pp. 1493–1503, 2017.

[41] T. Moriyama, K. Ohuchida, K. Mizumoto et al., "MicroRNA-21 modulates biological functions of pancreatic cancer cells including their proliferation, invasion, and chemoresistance," *Molecular Cancer Therapeutics*, vol. 8, no. 5, pp. 1067–1074, 2009.

[42] J. Li, T. Han, Z. Li et al., "A novel circRNA hsa_circRNA_002178 as a diagnostic marker in hepatocellular carcinoma enhances cell proliferation, invasion, and tumor growth by stabilizing SRSF1 expression," *Journal of Oncology*, vol. 2022, Article ID 4184034, 15 pages, 2022.

[43] Z. Wu, Z. Zhou, W. Zhang, and Y. Yu, "MiR-21-5p inhibition attenuates Warburg effect and stemness maintenance in osteosarcoma cells via inactivation of Wnt/β-catenin signaling," *Acta Biochimica Polonica*, vol. 68, no. 4, pp. 725–732, 2021.

Hindawi
Oxidative Medicine and Cellular Longevity
Volume 2022, Article ID 7056283, 18 pages
https://doi.org/10.1155/2022/7056283

Research Article

Transcription Factor p300 Regulated miR-451b Weakens the Cigarette Smoke Extract-Induced Cellular Stress by Targeting RhoA/ROCK2 Signaling

Wen Shen, Shukun Wang, Ruili Wang, Yang Zhang, Hong Tian, Xi Wang, Xin Wu, Xiaolei Yang, and Wei Wei

Department of Respiratory Medicine, The Second Affiliated Hospital of Kunming Medical University, Kunming, China

Correspondence should be addressed to Wen Shen; shenwen@kmmu.edu.cn

Received 18 August 2022; Revised 22 September 2022; Accepted 28 September 2022; Published 14 October 2022

Academic Editor: Shao Liang

Background. A previous study identified miR-451b as a potential biomarker in smoker with or without chronic obstructive pulmonary disease (COPD). However, the function and molecular mechanisms of miR-451b in the pathogenesis of COPD remain elusive. *Methods*. Macrophages and lung fibroblasts were exposed to 10% cigarette smoke extract (CSE) solution for 24 h. Expression miR-451b and its potential transcription factor p300 were detected. The association between p300 and miR-451b, miR-451b and RhoA was validated by luciferase reporter assay. The release of IL-12 and TNF-$\alpha$by macrophages was measured by ELISA assay, and Transwell assay was performed to analyze its migration and invasion. Collagen protein of fibroblasts was detected by Western blotting. *Results*. Results showed that p300 and miR-451b was downregulated, while RhoA was upregulated in CSE-induced macrophages and lung fibroblasts. The stimulation of CSE promoted the degradation of p300 by ubiquitination, and RhoA was confirmed as the target gene of miR-451b. MiR-451b overexpression significantly decreased the release of IL-12 and TNF-α, downregulated the expression of RhoA, ROCK2, and p65, and suppressed cell migration and invasion in CES-induced macrophages. In addition, miR-451b overexpression decreased the expression of RhoA, ROCK2, COL1A1, and COL2A1 in lung fibroblasts. *Conclusions*. Our data suggest that p300/miR-451b protects against CSE-induced cell stress possibly through downregulating RhoA/ROCK2 pathway.

1. Background

Chronic obstructive pulmonary disease (COPD) is widely considered an incurable but preventable respiratory disease with a rise in prevalence and mortality, which has been the third most frequent cause of death worldwide [1, 2]. The main symptoms of COPD include chronic cough, expectoration, emphysema, chronic airway obstruction, and airway remodeling [3]. Cigarette smoke extract (CSE) induced inflammatory disorder [4, 5] and impaired functional properties of lung fibroblasts [6, 7], are the important mechanisms underlying COPD. Although the association between CSE and COPD development has been reported [8–10], the cellular and molecular mechanism underlying COPD remains largely unclear.

MicroRNAs (miRNAs/miRs) are small non-coding RNA molecules that could regulate the transcriptional or translational gene expression via binding the 3′-untranslated region of multiple target mRNAs [11]. In recent years, some studies have shown that alterations in miRNA expression are closely associated with progression of smoking-induced patients with COPD [12, 13]. For example, miR-34a plays a key role in CSE-induced endothelial cell apoptosis by directly regulating its target gene Notch-1 [14]. Tang et al. [15] reported that miR-29b may participate in the airway inflammation in COPD by regulating inflammatory cytokine expression through targeting bromodomain protein 4 (BRD4). In addition, miR-146a is significantly downregulated in lung fibroblasts of COPD patients [16] and miR-26a acts as a regulator of the nuclear factor-κB (NF-κB) pathway in alveolar macrophages [17]. It is worth noting that our previous work identified several potential biomarkers, including miR-3202, miR-451b, and miR-149-3p in smokers with or without COPD and all their expression

levels were downregulated in COPD group compared with control group [18]. In functional experiments, we demonstrated that reducing miR-149-3p may increase the inflammatory response in COPD patients through the regulation of the TLR-4/NF-κB signaling pathway [18]. Similarly, our data provided support for the protective role of miR-3202 in CSE-stimulated T lymphocytes and human bronchial epithelial cells through targeting Fas apoptotic inhibitory molecule 2 (FAIM2) [19]. However, whether miR-451 plays an important role in suppressing CSE-induced lung injury has not been reported yet.

The small G-protein RhoA, as the master regulator of actin dynamics, is necessary for cell morphology, adhesion, proliferation, and migration [20]. Rho-kinase (ROCK-I or ROCKβ and ROCK-II or ROCKα) is the downstream effector of RhoA and constitutes the RhoA/ROCK signal pathway involved in pulmonary endothelial dysfunction in healthy smokers [21] and patients with COPD [22]. In diabetic nephropathy, the RhoA/ROCK pathway might regulate NF-κB activity to upregulate inflammatory genes [23]. In rheumatoid arthritis, blockade of ROCK inhibits the activation of NF-κB and the production of pro-inflammatory cytokines [24]. Interestingly, CSE-induced p120-catenin- (p120-) mediated NF-κB activation in human epithelial cells is dependent on the RhoA/ROCK pathway [25]. The online bioinformatics analysis suggests that RhoA was the target of miR-451b, which makes us hypothesize that the function of miR-451b in CSE-induced lung injury might through targeting RhoA/ROCK pathway.

To validate our hypothesis, CSE was first used to treat the macrophages and lung fibroblasts as useful *in vitro* models to evaluate smoking-related COPD pathogenesis. Then, we examined transcriptional regulation of miR-451b and its effects on inflammatory mediators, RhoA/ROCK pathway, extracellular matrix (ECM) components, migration, and invasion.

2. Materials and Methods

2.1. Sample Collection. Blood samples from non-smoking healthy volunteers (NS-H, $n=10$), smoking healthy volunteers (S-H, $n=10$), and smoking COPD patients (S-COPD, $n=10$) were collected from September 2019 to January 2020 at the Second Affiliated Hospital of Kunming Medical University. Total of 4 mL of peripheral blood was collected at fasting and half of it was used to isolate peripheral blood mononuclear cells (PBMCs) through gradient centrifugation with Ficoll-Hypaque (Ficoll-Paque PLUS; GE Healthcare Bio-Sciences AB, Uppsala, Sweden). The rest is used to separate serum.

2.2. Cell Culture. Macrophages (RAW264.7), rat pulmonary microvascular endothelial cells (rPMECs), rat alveolar epithelial cells (rAECs), rat bronchial epithelial cells (rBECs), and rat lung fibroblasts (rLFs) were purchased from Procell Life Science & Technology Co., Ltd. (Wuhan, China), which were both cultured in Dulbecco's Modified Eagle's Medium (DMEM) supplemented with 10% fetal bovine serum, 2 mM/L glutamine, 100 units/mL penicillin, and 0.1 mg/mL streptomycin at a humidified incubator containing 5% CO_2 at 37°C.

2.3. Preparation of CSE. Preparation of CSE was performed using commercial cigarettes (Marlboro; Philip Morris USA, Richmond, VA, USA) by a modified method as previously described [26]. In brief, one cigarette was bubbled through 25 mL of DMEM at a constant rate, which was considered 100% CSE solution. Then, CSE solution was sterilized and diluted to a final working concentration (10%) before use.

2.4. Cell Transfection. MiR-451b mimics and inhibitor, specifically targeting RhoA small interference sequence, were synthesized by RiboBio (Guangzhou, China) (Table S1). Coding sequence was cloned and inserted into pcDNA 3.1 plasmid vector. For cell transfection, cells were seeded into six-well plates at a density of 3.0×10^7 cells per well and cultured overnight at 37°C. Next day, cells were transfected with 25 nM above material for 48 h with Lipofectamine 2000 (Invitrogen, Carlsbad, CA), followed by 10% CSE exposure for an additional 48 h.

2.5. Quantitative Reverse Transcription PCR. Total RNA extraction was performed by Trizol reagent (Invitrogen) and cDNA was synthesized using a Reverse Transcription Kit (Applied Biosystems, Foster City, CA, USA) according to the manufacturer's instructions. Quantitative reverse transcription PCR was conducted with TaqMan Gene Expression Assays and the ABI Prism 7500 (Applied Biosystems) according to the thermal cycling conditions: 37°C for 10 min, 95°C for 5 min, followed by 50 cycles of 95°C for 15 s, 60°C for 20 s, and 68°C for 20 s. The primer sequences used in this study are showed in Table S1. Relative expression levels of miR-451b or RhoA were calculated by the $2^{-\Delta\Delta Ct}$ method with U6 or GAPDH as endogenous controls.

2.6. Western Blot Analysis. Total protein samples were extracted from cell samples with RIPA buffer (CWBio, Beijing, China) and protein concentration was measured using BCA protein assay kit (Beyotime, Shanghai, China). Equal amount of protein sample was separated on 12% SDS-PAGE gels followed by transferred to nitrocellulose membranes. Then, the membranes were blocked in 5% non-fat milk dissolved in TBST solution and incubated with primary antibodies against p300 (Abcam, Cambridge, MA, USA; ab275378, 1:1000 diluted), RhoA (ab187027, 1:2000 diluted), ROCK (ab134181, 1:1000 diluted), NF-κB p65(ab207297, 1:1000 diluted), HDAC1 (ab109411, 1:4000 diluted), COL1A1 (ab270993, 1:3000 diluted), COL2A1 (ab34712, 1:3000 diluted), and GAPDH (ab8245, 1:5000 diluted) overnight at 4°C. After washing with TBST, membranes were incubated with HRP-conjugated secondary antibodies for 2 h. The protein bands were visualized using an enhanced chemiluminescence reagent (Pierce Biotech, Inc., Rockford, IL, USA).

2.7. Immunofluorescence. Cells from different groups were fixed with 4% paraformaldehyde, washed with PBS, and permeabilized with 0.5% Triton X-100 dissolved in PBS. After blocked with 3% bovine serum albumin (BSA) for 1 h, the cells were incubated with primary antibodies against RhoA (ab187027, 1:500 diluted) or p300 (ab275378, 1:500 diluted) overnight at 4°C. Subsequently, cells were washed with PBS twice and incubated with appropriate secondary

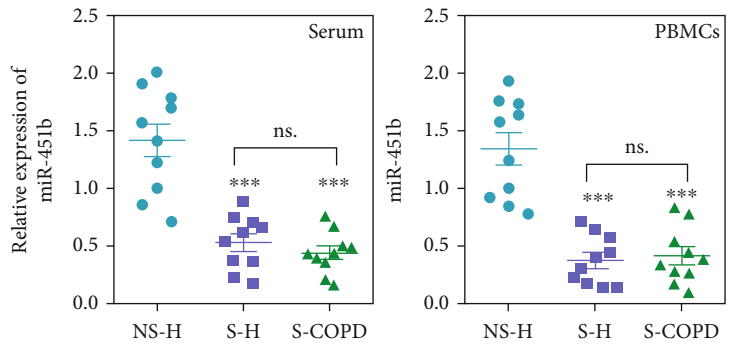

(a)

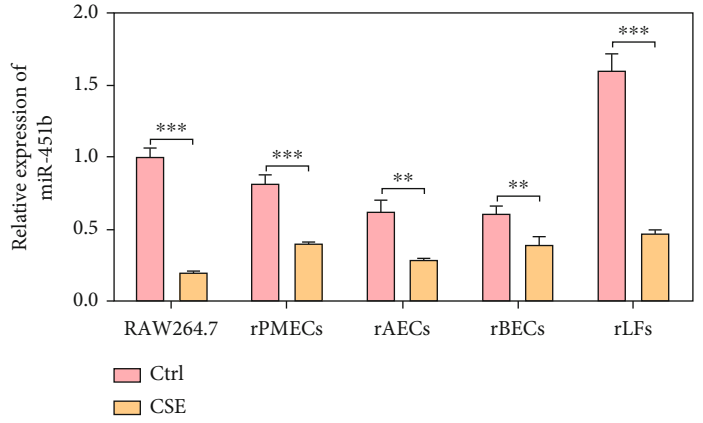

(b)

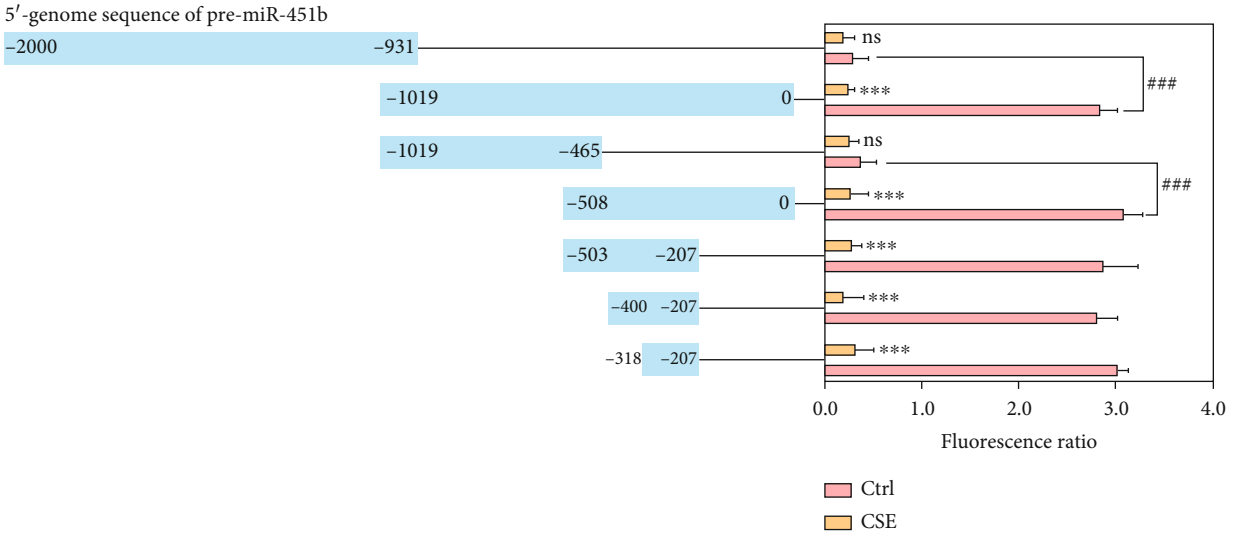

(c)

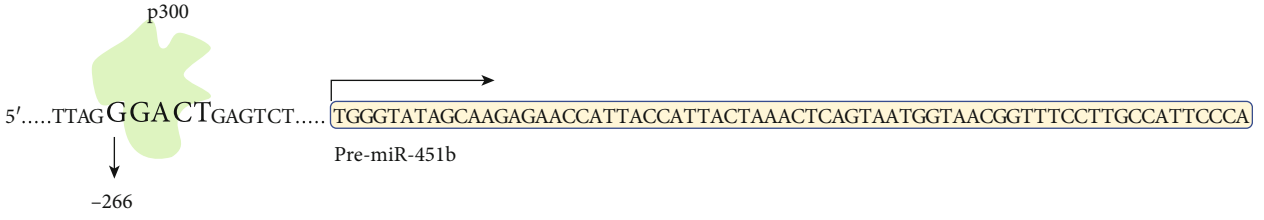

(d)

Figure 1: Continued.

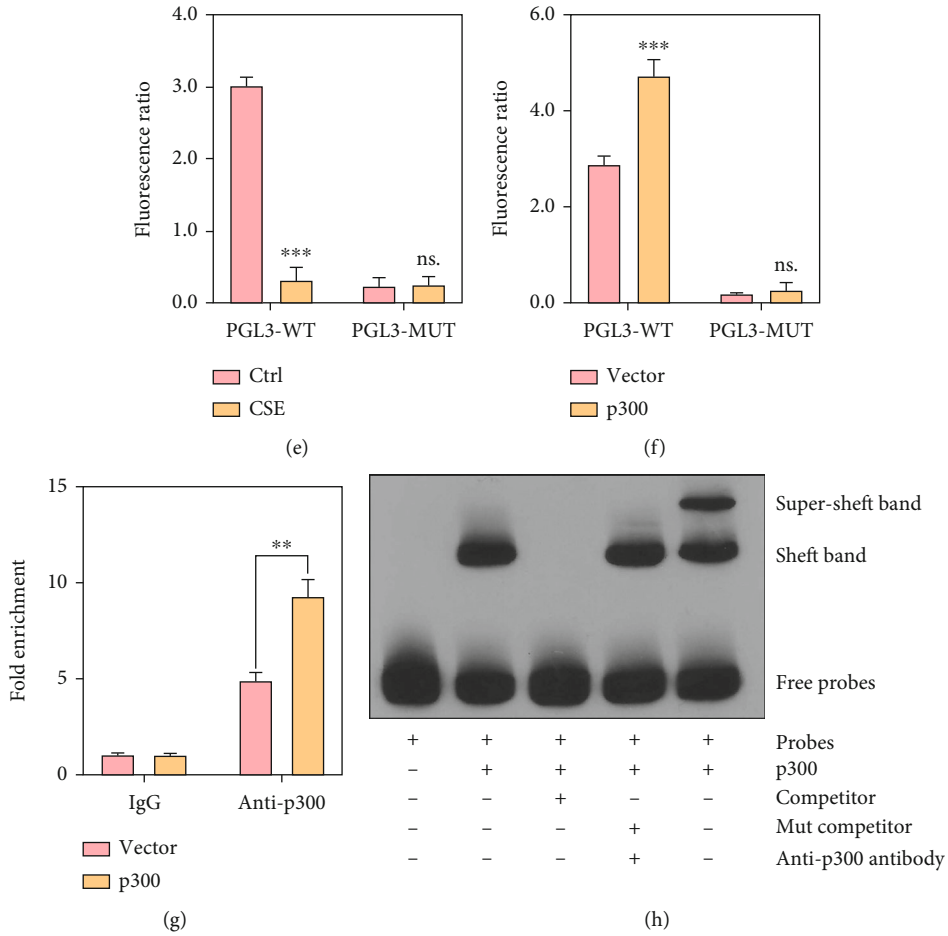

Figure 1: CSE inhibited expression of miR-451b through regulating RhoA. (a) Blood samples from non-smoking healthy volunteers (NS-H), smoking healthy volunteers (S-H), and smoking COPD patients (S-COPD) were collected and the expressions of miR-451b were detected by QPCR. $^{***}P < 0.001$, compared with NS-H group. (b) Macrophages (RAW264.7), rat pulmonary microvascular endothelial cells (rPMECs), rat alveolar epithelial cells (rAECs), rat bronchial epithelial cells (rBECs), and rat lung fibroblasts (rLFs) were stimulated with 10% CSE, and the expressions of miR-451b were detected by QPCR. (c) The 5′-upstream sequence of pre-miR-451b was segmented, cloned, and inserted into pGL3-Basic plasmid, followed by transfecting to RAW264.7 cells and fluorescence detection. $^{***}P < 0.001$, compared with Ctrl group (no CSE treatment). (d) Predicted binding site of p300 on miR-451b's promoter sequence. (e) The binding site of p300 was mutated and applied to luciferase reporter assay. (f) Luciferase reporter assay was repeated in p300 overexpressed RAW264.7 cells. (g, h) Chromatin Immunoprecipitation assay and Electrophoretic Mobility Shift assay were performed in p300 overexpressed RAW264.7 cells. $^{**}P < 0.01$, $^{***}P < 0.001$; $^{\#\#\#}P < 0.001$; ns: no significance.

antibodies. The nucleus was labeled with 4′,6-diamidino-2-phenylindole for 5 min. All staining images were viewed under a fluorescence microscope (Thermo Fisher Scientific, Waltham, MA, USA).

2.8. Enzyme-Linked Immunosorbent Assay (ELISA). The release concentration of IL-12 and TNF-α was measured in cell culture media by commercial ELISA according to the manufacturer's instructions (R&D Systems) according to the manufacturer's protocol. All samples were assayed in duplicate. Results are expressed as picograms of cytokine per milligram (pg/mL) of total protein in the homogenate.

2.9. Transwell Assay. The migrated and invasive ability of macrophages was assessed using Transwell chamber (Corning Inc., Corning, NY, USA). In brief, approximately macrophages prepared in serum-free medium were added into the upper chamber (normal chamber for migration assay and matrigel-coated chamber for invasion assay). Meanwhile, complete medium (500 μL) containing 10% FBS was added into the lower chamber. After 24 h incubation at 37°C, the macrophages that migrated into the lower chamber were fixed with methanol and stained with crystal violet, which were further counted with a microscope.

2.10. Luciferase Reporter Assay. Briefly, the oligonucleotides containing wild-type or mutated RhoA-3′UTR of the predicted binding site were synthesized and subcloned into psiCHECK-2 vector (Promega, Madison, Wisconsin) to construct WT or MUT RhoA plasmids, respectively. Then, co-transfection of WT or MUT RhoA plasmid and miR-451b mimics or NC was performed in RAW264.7 cells using

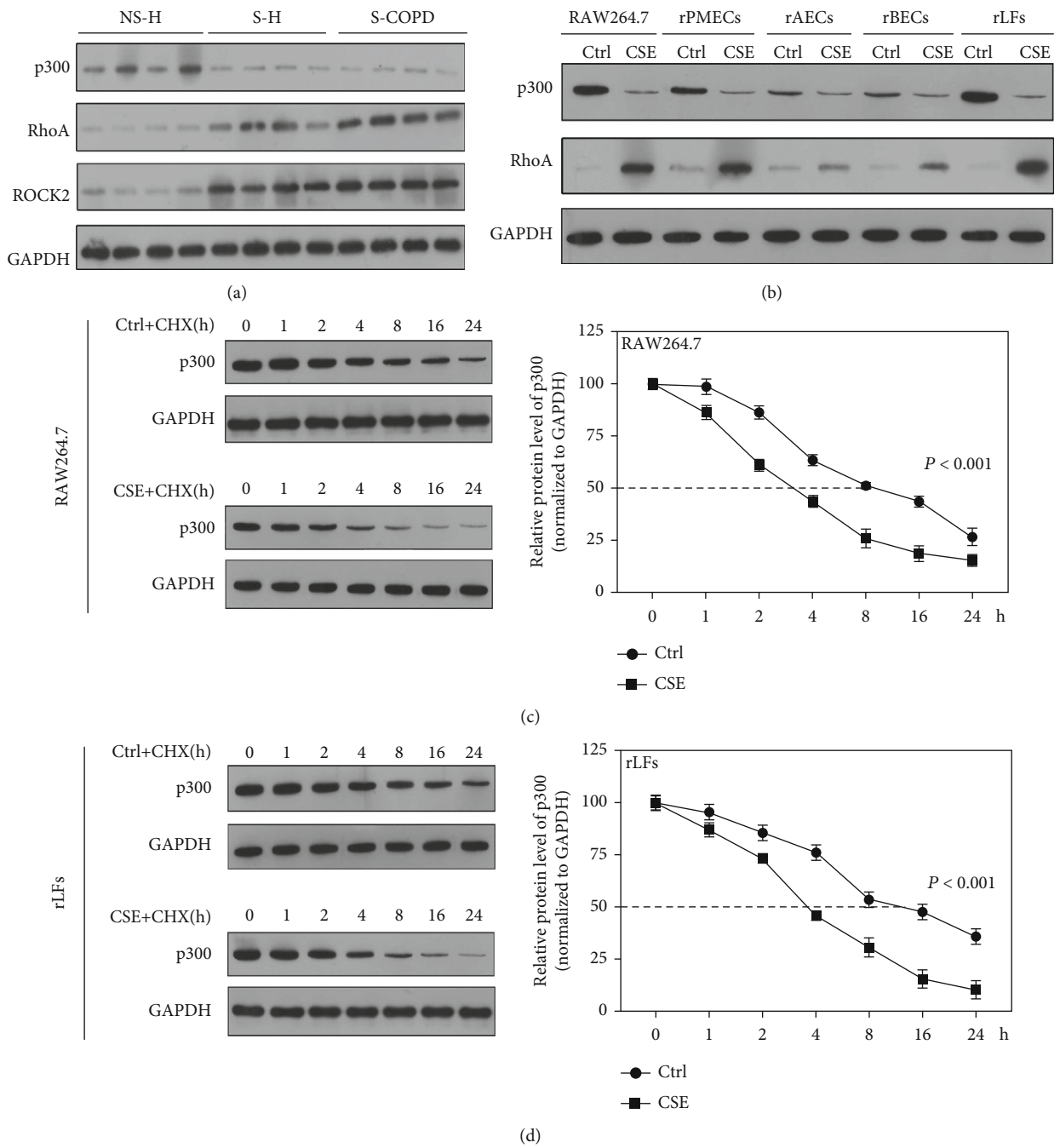

Figure 2: CSE induced the degradation of p300. (a) Western blotting was used to detect p300, RhoA, and ROCK2 in PBMCs. (b) Levels of p300 and RhoAin the CSE-stimulated RAW264.7, rPMECs, rAECs, rBECs, and rLFs. (c, d) The level of p300 at 0 h, 1 h, 2 h, 4 h, 8 h, 16 h, and 24 h after stimulation with CSE and cycloheximide (CHX) (100 μg/mL) in RAW264.7 and rLFs was measured. NS-H: non-smoking healthy volunteers; S-H: smoking healthy volunteers; S-COPD: smoking COPD patients; Ctrl: no CSE treatment.

Lipofectamine 2000. After 48 h, luciferase activity was determined using the dual-luciferase reporter assay system (Promega). Relative luciferase activity was reported as luciferase activity/Renilla luciferase activity. In addition, the 5′-upstream sequence of pre-miR-451b was segmented, cloned, and inserted into pGL3-Basic plasmid, followed by transfecting to RAW264.7 cells and fluorescence detection. To test and verify p300 regulating transcription of pre-miR-451b, the binding site sequence (5′-TTAGGGACTGAGTCT-3′) was mutated (5′-TTAATGCGGGAGTCT-3) and used to repeat fluorescence detection.

2.11. Chromatin Immunoprecipitation. Chromatin immunoprecipitation was performed according to the instruction of a ChIP Assay Kit (Beyotime). In brief, cells were lysed with ice-treated SDS lysis buffer and ultrasonication, and

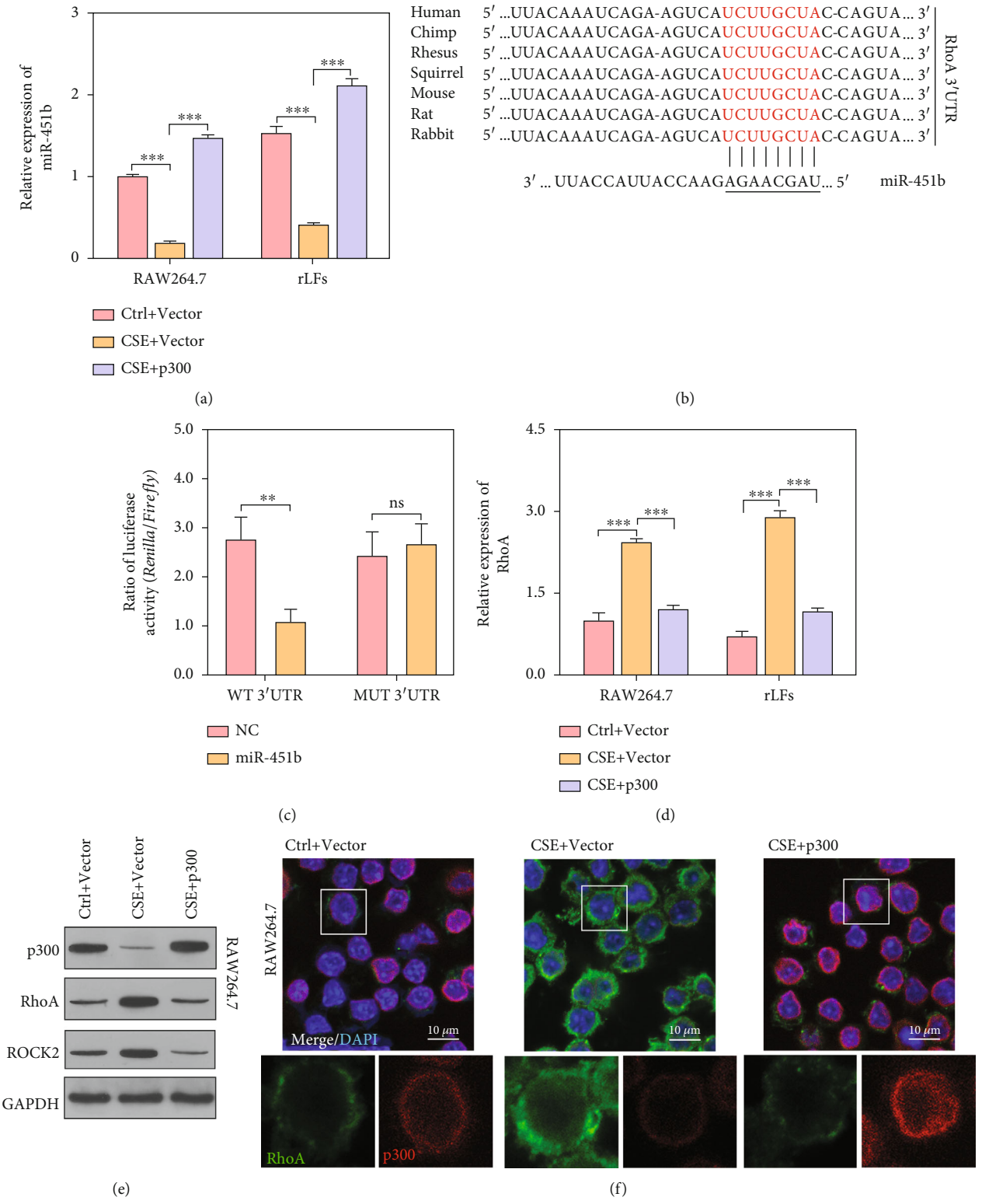

Figure 3: Continued.

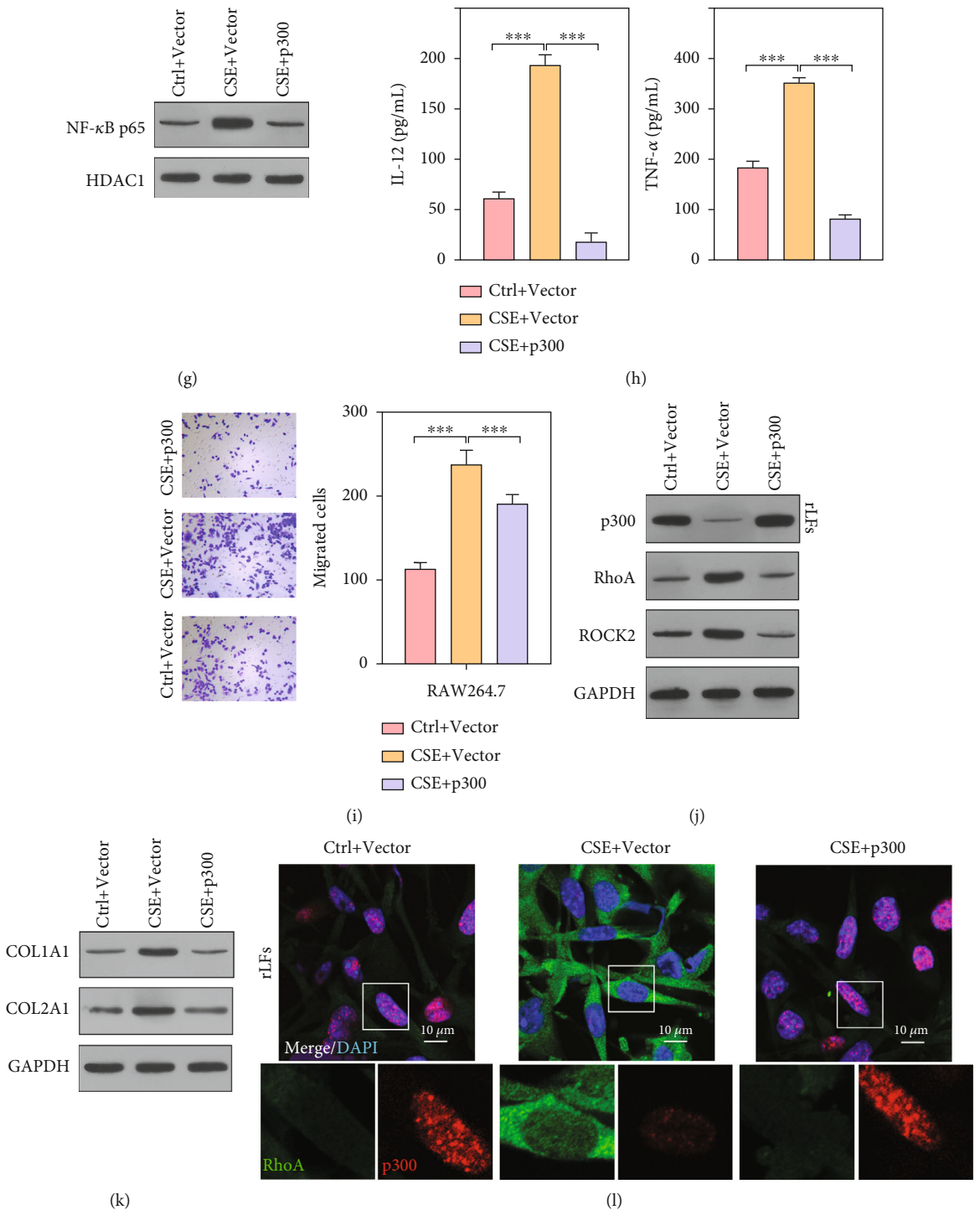

Figure 3: MiR-451b targeted the 3′-UTR regions of RhoA mRNA. The p300 was overexpressed in CSE-stimulated RAW264.7 and rLFs. (a) Expression of miR-451b was detected by QPCR. (b) Bioinformatics analysis shows that miR-451b binds to 3′-UTR regions of RhoA through base-complementary pairing. (c) RAW264.7 cells were co-transfected with psi-CHECK2-RhoA-3′-UTR (WT or MUT) and miR-451b mimics (or NC). After 48 h, luciferase activity was calculated as the ratio of Renilla luciferase activity to Firefly luciferase. (d) Expression of RhoA was detected by QPCR. (e) Western blot analysis was performed to analyze the protein of p300, RhoA, and ROCK2 in RAW264.7. (f) Protein level of p300 and RhoA in RAW264.7 was showed by immunofluorescence assay. (g) Nuclear NF-κB p65 (normalized to HDAC1) in RAW264.7 was detected by Western blotting. (h) The pro-inflammatory cytokine IL-12 and TNF-α levels were detected by ELISA assay. (i) Cell migration was assessed in RAW264.7 by Transwell assay. (j, k) Protein of p300, RhoA, ROCK2, COL2A1, and COL1A1 in rLFs was showed by Western blotting. (l) Protein level of p300 and RhoA in rLFs was showed by immunofluorescence assay. $^{**}P < 0.01$, $^{***}P < 0.001$. NC: negative control. Ctrl: no CSE treatment; CSE+ p300: CSE treatment plus p300-overexpression; DAPI: 4′,6-diamidino-2-phenylindole.

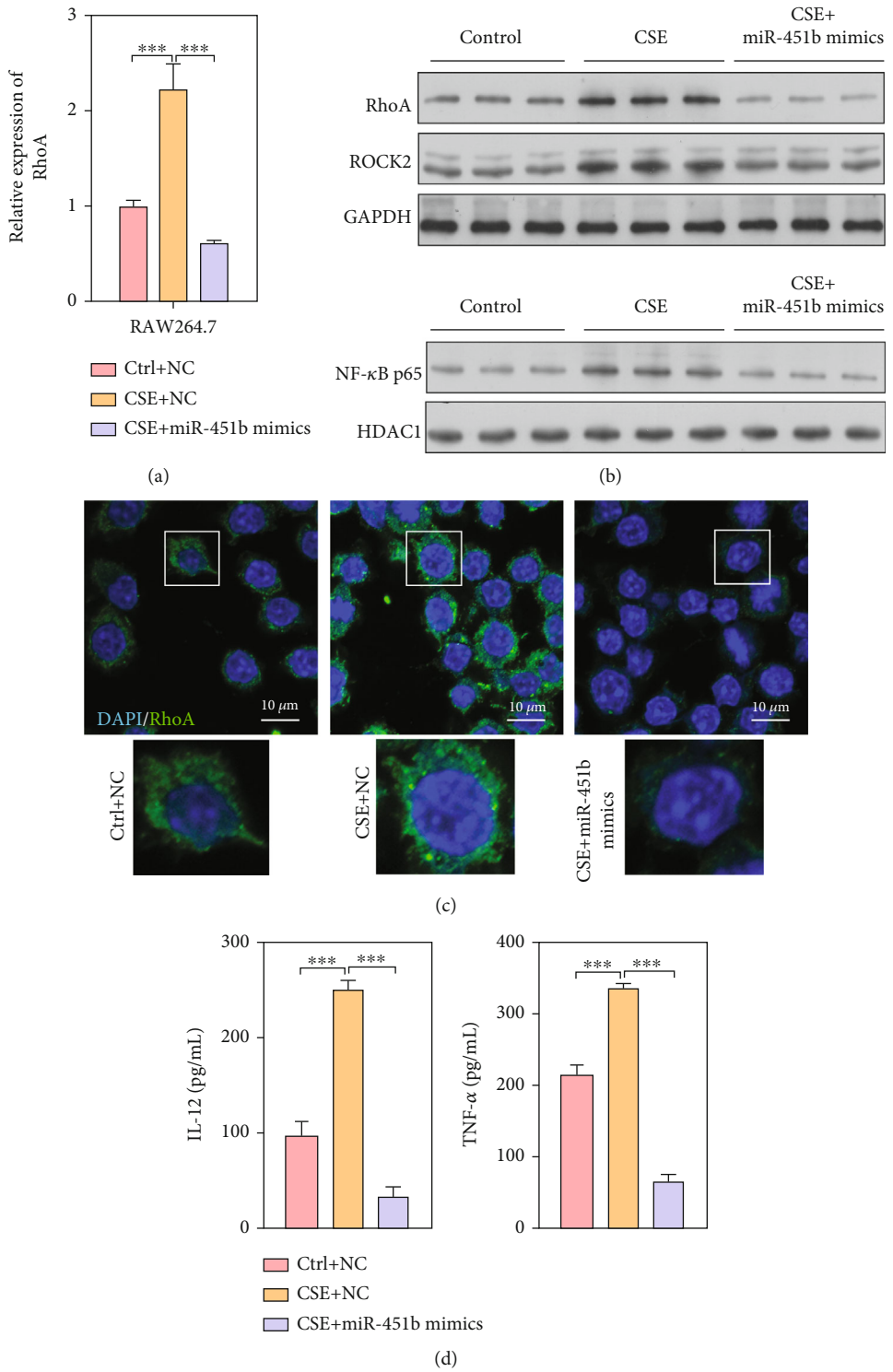

Figure 4: Continued.

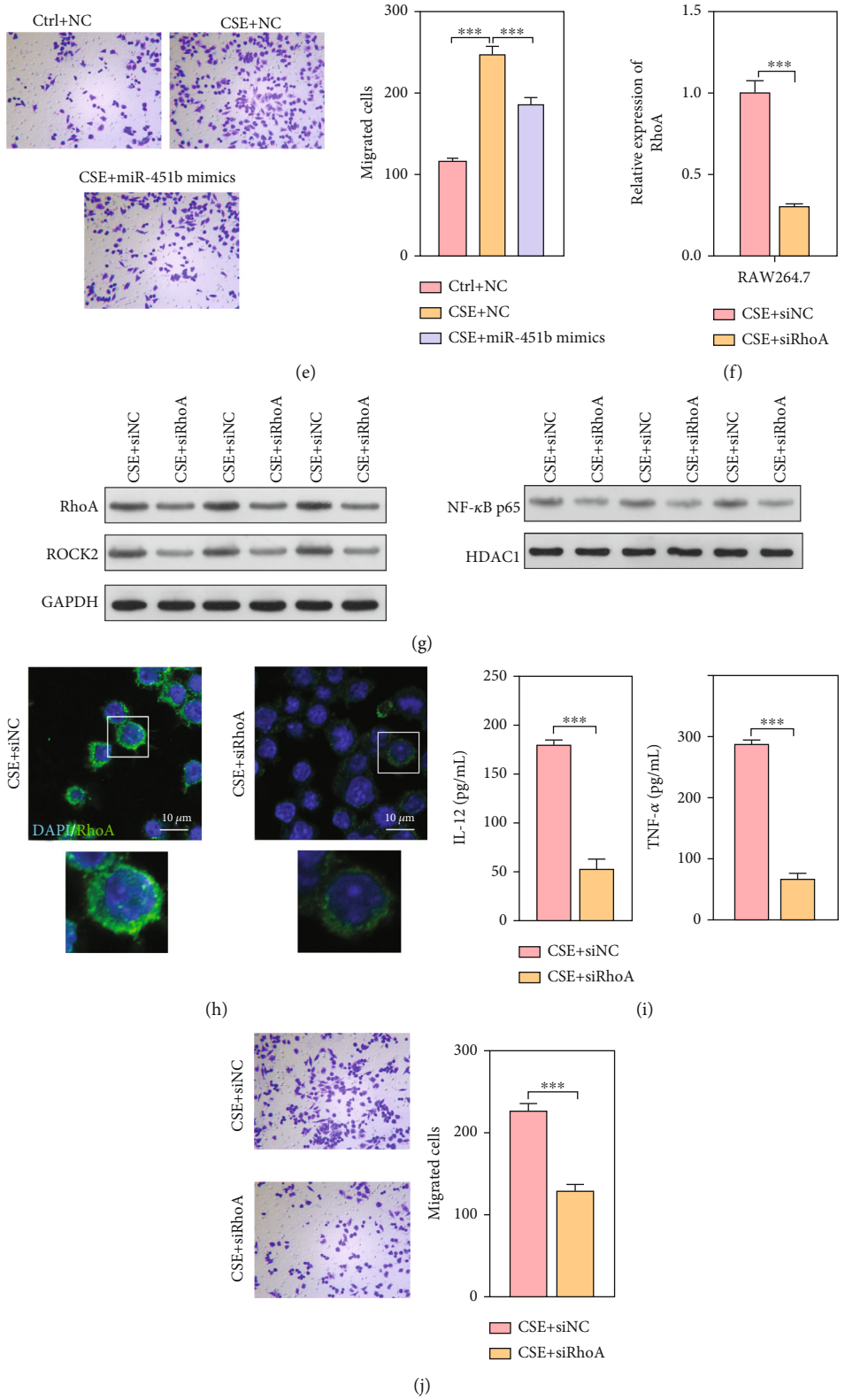

Figure 4: Overexpression of miR-451b or knockdown of RhoA decreased the effect of CSE on macrophages. RAW264.7 was transfected with miR-451b mimics or specifically targeting RhoA small interference sequence, followed by 10% CSE exposure. (a, f) The expression of RhoA mRNA was determined by QPCR. (b) Western blot analysis was performed to analyze the protein expression of RhoA, ROCK2, and nuclear NF-κBp65. (c, h) Immunofluorescence staining demonstrated the labeling intensity of RhoA. (d, i) The pro-inflammatory cytokine IL-12 and TNF-α levels were detected by ELISA assay. (e, g) Cell migration was assessed by Transwell assay. $^{***}P < 0.001$. NC: negative control. Ctrl: no CSE treatment; CSE+ siRhoA: CSE treatment plus RhoA knockdown; DAPI: 4′,6-diamidino-2-phenylindole.

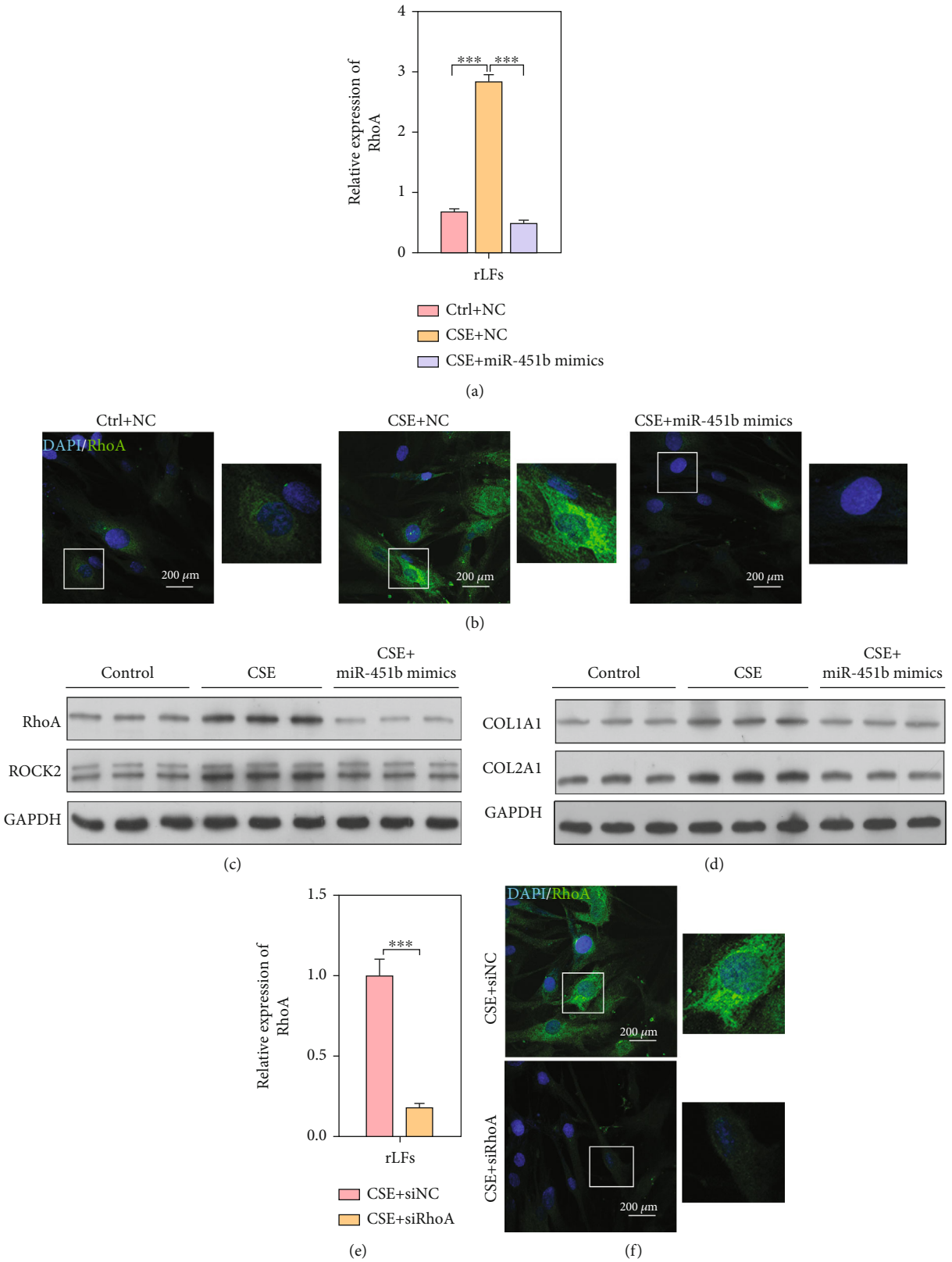

Figure 5: Continued.

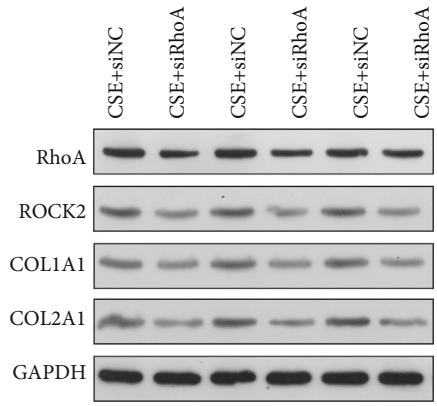

(g)

Figure 5: Overexpression of miR-451b or knockdown of RhoA decreased the effect of CSE on lung fibroblasts. The rLFs were transfected with miR-451b mimics or specifically targeting RhoA small interference sequence, followed by 10% CSE exposure. (a, e) The expression of RhoA mRNA was determined by QPCR. (b, f) Immunofluorescence staining demonstrated the labeling intensity of RhoA. (c, d, g) Western blot analysis was performed to analyze the protein expression of RhoA, ROCK2, COL1A1, and COL2A1. $^{***}P < 0.001$. NC: negative control. Ctrl: no CSE treatment; CSE+ siRhoA: CSE treatment plus RhoA-knockdown; DAPI: 4′,6-diamidino-2-phenylindole.

deoxyribonucleic acid (DNA) was extracted. Then, the sample was treated with ChIP dilution buffer and incubated with primary antibody targeted to p300. Subsequently, protein A agarose/salmon sperm DNA was added to precipitate the immune complex. Finally, wash the sediment, de crosslink, and recover DNA fragments. The 5′-upstream sequence of pre-miR-451b was detected by real-time quantitative PCR.

2.12. Electrophoretic Mobility Shift Assays. Promoter of pre-miR-451b-p300 banding was detected by probes that has been Biotin-labeled in the presence or absence of anti-p300 antibody. Prokaryotic expressed p300 protein was purified by gel filtration chromatography, followed by incubation with DNA probes in binding buffer. Anti-p300 antibody or specific mutant competitors were pre-incubated with p300. Finally, 4% PAGE gel was used to finish the electrophoretic separation to products.

2.13. Statistical Analysis. Each experiment was performed in triplicates and data were expressed as mean ± SD. Statistical analyses were carried out with GraphPad Prism version 6.0 (GraphPad Software, San Diego, CA, USA). Different comparisons were performed by Student's *t* test between two groups and one-way analysis of variances (ANOVA) followed by Tukey's test for three groups. Statistical significance was accepted when the *P*-value less than 0.05.

3. Results

3.1. Smoking Inhibits the miR-451b Expression through Regulating p300. To verify whether miR-451b is related to smoking, blood samples from non-smoking healthy volunteers (NS-H), smoking healthy volunteers (S-H), and smoking COPD patients (S-COPD) were collected and the expressions of miR-451b in which were detected. Results showed that the expression of miR-451b was significantly downregulated in serum and peripheral mononuclear cells (PBMCs) from both S-H group and S-COPD group, when compared with that from NS-H group (Figure 1(a)). Meanwhile, *in vitro* 10% CSE inhibited the expression of miR-451b in macrophages (RAW264.7), rat pulmonary microvascular endothelial cells (rPMECs), rat alveolar epithelial cells (rAECs), rat bronchial epithelial cells (rBECs), and rat lung fibroblasts (rLFs) (Figure 1(b)). Further, fluorescence report experiment in RAW264.7 showed that the core promoter sequence of miR-451b responding to CSE was region from -318 site ~ -207 site (Figure 1(c)). Through ALGGEN-PROMO database (http://alggen.lsi.upc.es/cgi-bin/promo_v3/promo/promoinit.cgi?dirDB=TF_8.3), the transcription factor, p300, could bind to the core promoter sequence of miR-451b (Figure 1(d)), and fluorescence report showed that there was no significant difference in fluorescence ratio between with or without CSE stimulation, when we mutated banding site of p300 in the core promoter sequence of miR-451b (Figure 1(e)). In addition, we overexpressed p300 in RAW264.7 cells, and fluorescence report showed that the fluorescence ratio was significantly increased (Figure 1(f)). Furthermore, the combined relationship between p300 and the core promoter sequence of miR-451b was confirmed by Chromatin Immunoprecipitation assay (Figure 1(g)) and Electrophoretic Mobility Shift assay (Figure 1(h)). Above results revealed that CSE may inhibited the expression of miR-451b in respiratory system related cells by regulating p300.

3.2. CSE Promoted Degradation of p300 by Ubiquitination Pathway. To explore the mechanism of miR-451b, we further detected the levels of p300 and miR-451b's potential downstream proteins, RhoA and ROCK2 in above PBMCs. Results showed that p300 in S-H and S-COPD group was decreased when compared with NS-H group, while RhoA and ROCK2 were increased in PBMCs derived from smokers (Figure 2(a)). In CSE-stimulated RAW264.7, rPMECs, rAECs, rBECs, and rLFs, we found that the protein levels of p300 were inhibited, and levels of RhoA were

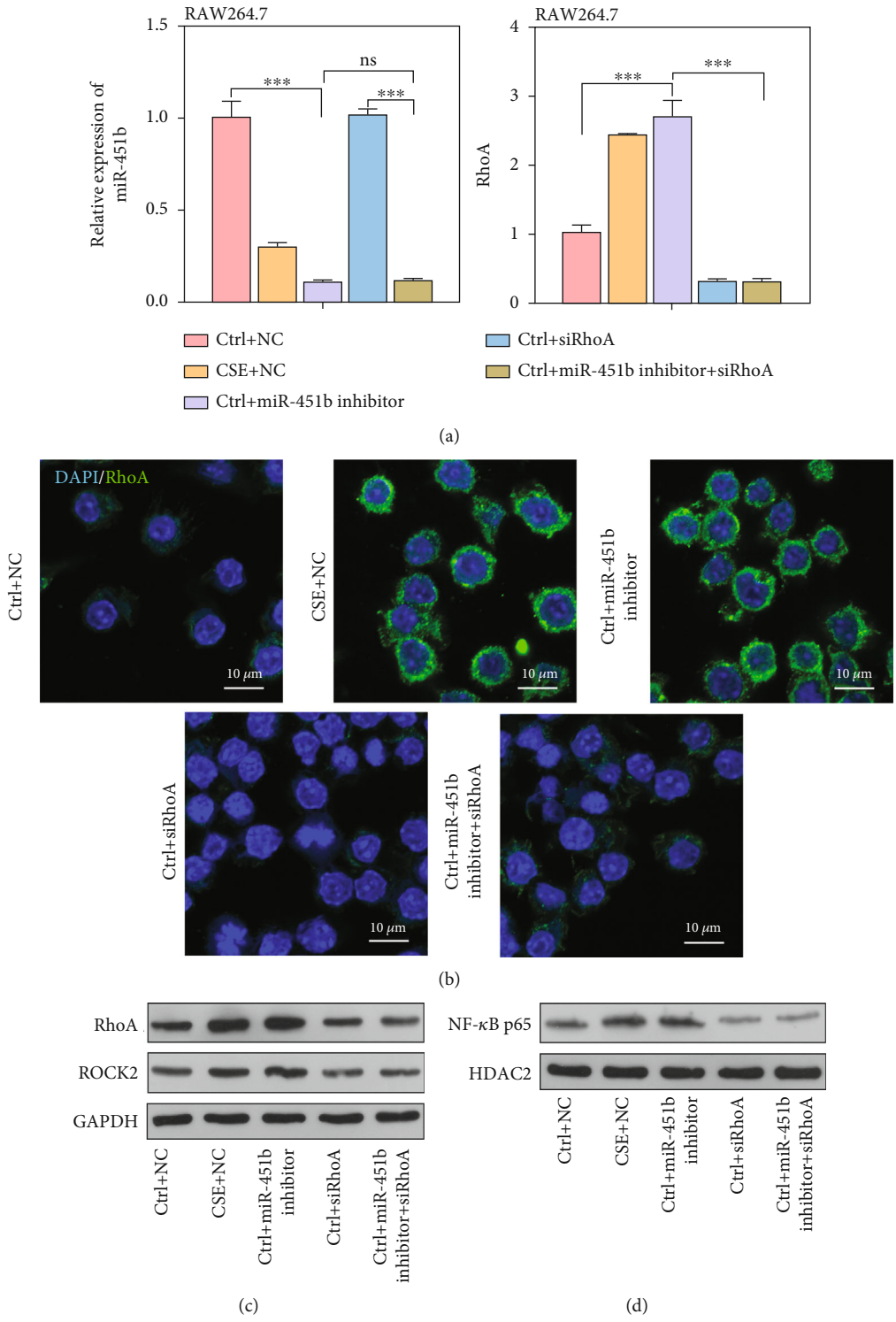

Figure 6: Continued.

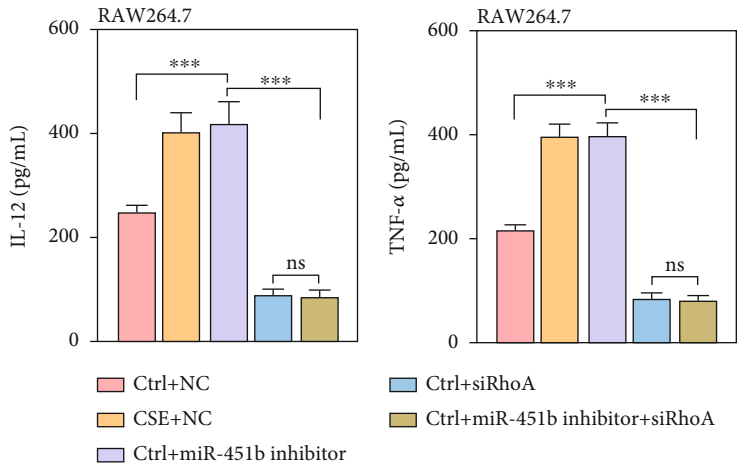

(e)

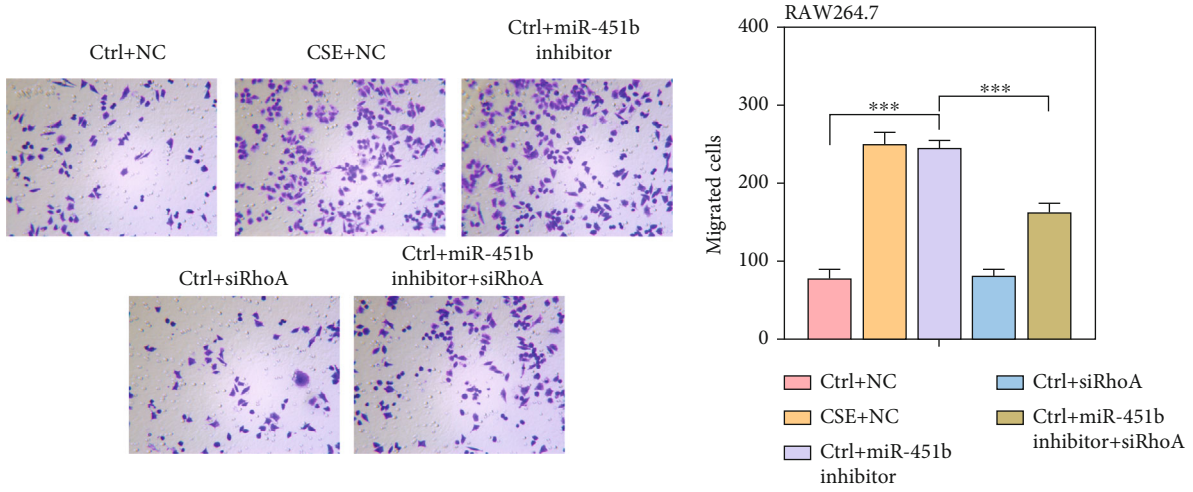

(f)

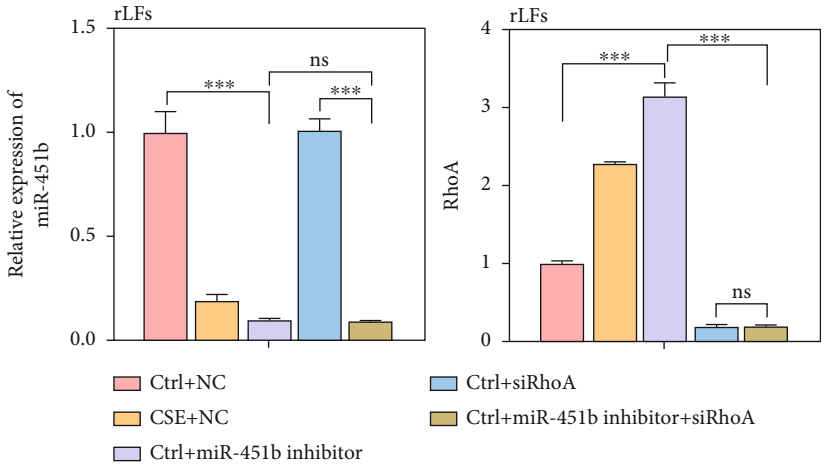

(g)

Figure 6: Continued.

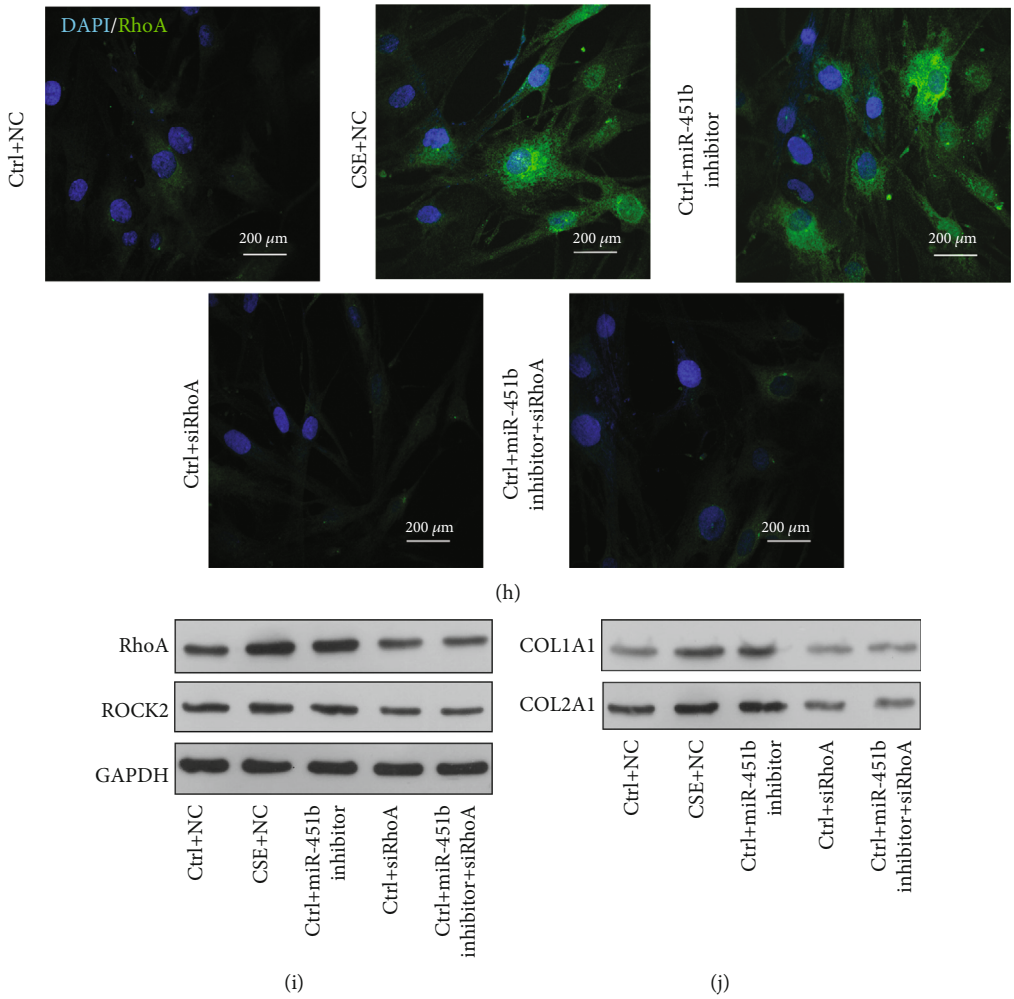

Figure 6: Knockdown of miR-451b activated the RhoA/ROCK2 signaling in RAW264.7 and rLFs. The RAW264.7 and rLFs were transfected with miR-451b inhibitor and specifically targeting RhoA small interference sequence. (a, g) The expression of miR-451b and RhoA mRNA was determined by QPCR. (b, h) Immunofluorescence staining demonstrated the labeling intensity of RhoA. (c, i) Western blot analysis was performed to analyze the protein expression of RhoA, ROCK2. (d) Protein level of nuclear NF-κB p65 in RAW264.7. (e) IL-12 and TNF-α levels were detected by ELISA assay. (f) Cell migration was assessed by Transwell assay. (j) Protein level of COL1A1 and COL2A1 in rLFs. $^{***}P < 0.001$. NC: negative control. Ctrl: no CSE treatment; CSE+ siRhoA: CSE treatment plus RhoA-knockdown; DAPI: 4′,6-diamidino-2-phenylindole; ns: no significance.

increased (Figure 2(b)). Further, we stimulated RAW264.7 and rLFs with CSE and cycloheximide (CHX), and cells were collected 0 h, 1 h, 2 h, 4 h, 8 h, 16 h, and 24 h after stimulation, followed by Western blotting to p300. Results showed that CSE stimulation significantly reduced the half-life of protein p300 (Figures 2(c) and 2(d)).

3.3. MiR-451b Targeted the 3′-UTR Regions of RhoA mRNA. In p300-overexpressed RAW264.7 and rLFs, we found that the decreased expressions of miR-451b induced by CSE stimulation were reversed (Figure 3(a)). Then, the online bioinformatics software was used to predict downstream target gene of miR-451b. As shown in Figure 3(b), miR-451b could bind to 3′-UTR regions of RhoA gene, which has been associated with pulmonary endothelial dysfunction in patients with COPD [22]. Subsequently, we performed luciferase report assay to confirm the association between miR-451b and RhoA. The results (Figure 3(c)) showed that miR-451b mimics transfection significantly suppressed the relative luciferase activity of the WT RhoA 3′-UTR compared with NC transfection in RAW264.7cells. In contrast, co-transfection of miR-451b mimics did not affect the luciferase activity of the binding site mutant RhoA 3′-UTR reporter. Further, we found that the expression of RhoA mRNA and protein was markedly increased by CSE stimulation, while it was reverted to low level by overexpression of p300 in RAW264.7 and rLFs (Figures 3(d)–3(f), 3(j), and 3(l)). Meanwhile, the level of ROCK2 and nuclear NF-κB p65 was consistent with that of RhoA in RAW264.7 (Figures 3(e) and 3(g)), as well as the level of interleukin 12 (IL-12) and tumor necrosis factor-α (TNF-α) in culture supernatant (Figure 3(h)). Furthermore, CSE stimulation induced

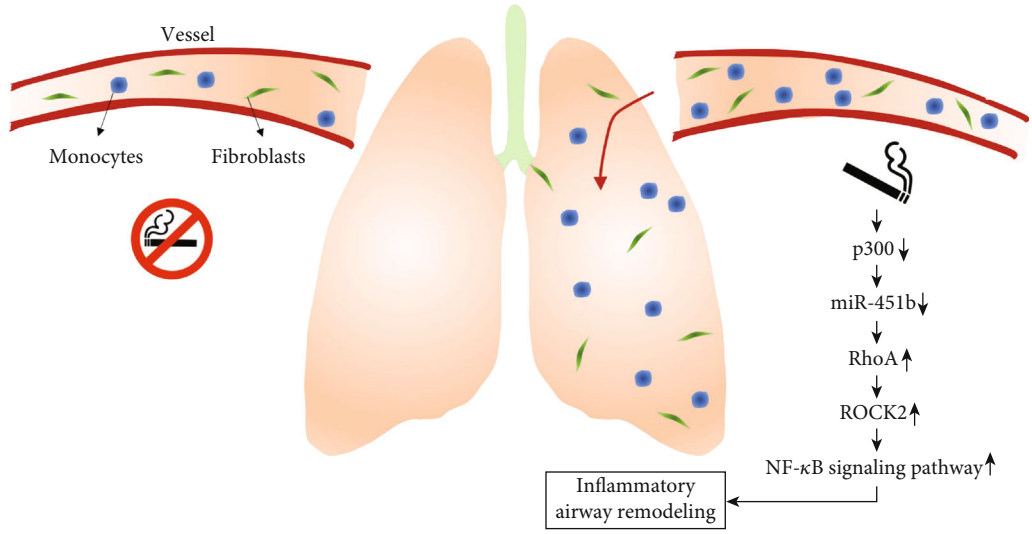

Figure 7: Schematic diagram of smoking-induced inflammatory and airway remodeling through regulating miR-451b.

increasing migration ability of RAW264.7, and accumulation of proteins COL1A1 and COL2A1 in rLFs was both suppressed by overexpression of p300 (Figure 3(i)). These data suggest that RhoA might be a downstream target of miR-451b.

3.4. Overexpression of miR-451b and Knockdown of RhoA Inhibited Cell Migration and Inflammatory Factor Release in RAW264.7 Cells. Since miR-451b was downregulated in RAW264.7 after CSE exposure, miR-451b mimics was transfected into RAW264.7 to investigate its impact on CSE-induced injury. At first, the expression of RhoA mRNA was demonstrated to be significantly upregulated in CSE exposure, which was notably decreased after miR-451b mimics transfection using quantitative reverse transcription PCR (Figure 4(a)). Results of Western blot analysis showed that miR-451b overexpression obviously downregulated the expression of RhoA, ROCK2, and nuclear NF-κBp65 in CSE-treated macrophages (Figure 4(b)). The immunofluorescence staining of RhoA (Figure 4(c)) also revealed similar result. Subsequently, the IL-12 and TNF-α levels (Figure 4(d)) were significantly decreased after miR-451b mimics transfection in CSE-treated RAW264.7, and the increased migratory cells in CSE group were remarkedly reduced after miR-451b overexpression (Figure 4(e)). In addition, we knockdown RhoA in CSE-stimulated RAW264.7 cells and results showed that RhoA mRNA and protein were both decreased (Figures 4(f)–4(h)). The protein level of ROCK2, concentration of IL-12 and TNF-α in culture supernatant, and cell migration ability were also suppressed by knockdown of RhoA (Figures 4(g), 4(i), and 4(j)).

3.5. Overexpression of miR-451b and Knockdown of RhoA Decreased Extracellular Collagen Accumulation in rLFs. Similarly, rLFs were transfected with miR-451b mimics and siRNA-specific targeting RhoA, followed by 10% CSE exposure. As shown in Figures 5(a) and 5(e), CSE-induced upregulation of RhoA mRNA in rLFs was significantly reduced after miR-451b mimics or siRhoA transfection. Consistently, immunofluorescence staining of RhoA further confirmed that upregulation of RhoA in CSE treatment was obviously impaired in rLFs after miR-451b mimics r siRhoA transfection (Figures 5(b) and 5(f)). What's more, we observed the obviously elevated protein expression of RhoA and ROCK2 induced by CSE was abolished by miR-451b mimics or siRhoA transfection (Figures 5(c) and 5(g)). We further found that accumulation of extracellular matrix (ECM) components (COL1A1 and COL2A1) in CSE group was significantly attenuated after miR-451b overexpression and knockdown of RhoA in rLFs (Figures 5(d) and 5(g)).

3.6. Knockdown of miR-451b Activated RhoA/ROCK2 Signaling in RAW264.7 and rLFs. To further verify the role of miR-451b in cells and its targeted regulation to RhoA, we directly inhibited the expression of miR-451b using its inhibitor, and knock of RhoA down at the same time. Results found that both in RAW264.7 and rLFs, the expression of miR-451b was significantly downregulated by its inhibitor, while the RhoA mRNA and protein level was increased (Figures 6(a)–6(c) and 6(g)–6(i)). The protein level of ROCK2 and nuclear NF-κB p65 was also increased by miR-451b inhibitor (Figures 6(c) and 6(d)). The IL-12 and TNF-α levels in RAW264.7 culture supernatant were significantly increased in the miR-451b inhibitor group (Figure 6(d)), as well as the cell migration ability (Figure 6), which was both reversed by knockdown of RhoA. Furthermore, the accumulation of COL1A1 and COL2A1 in rLFs was induced by miR-451b inhibitor, and which was also reversed by knockdown of RhoA, too (Figure 6(j)). These results confirm miR-451b functions through regulating RhoA.

4. Discussion

In the present study, we reported that miR-451b was downregulated in macrophages after CSE exposure. Overexpression of miR-451b significantly decreased the pro-

inflammatory mediators (IL-12 and TNF-α), downregulated the expression of RohA, ROCK2, and NF-κB p65, and suppressed migration and invasion ability. Macrophages are mononuclear leukocyte-derived inflammatory cells, which are correlated with the inflammatory response and alveolar wall destruction in COPD [27]. Macrophages respond to cigarette smoke by producing pro-inflammatory mediators, including IL-8, IL-12, IL-1β, and TNF-α [28]. Previous work has reported the important role of IL-12 and TNF-α in inflammatory airway diseases [29, 30]. In addition, macrophages are also an important source of MMP production that contributes to alveolar wall destruction [31]. Moreover, activation of RhoA/ROCK signaling could mediate macrophage differentiation induced by PMA [32]. Here, we thus selected RAW264.7 to stimulate with CSE to study the role of miR-451b on CSE-induced inflammation, migration, and invasion.

Much of the research has examined whether smoking influenced the expression of miRNAs in airway, and it is known that there is an association between differentially expressed miRNAs and COPD [33, 34]. The interactions between miRNA-mRNA-lncRNA expanded our understanding of the disease mechanism in smoking COPD [35]. As for the miR-451b in COPD pathogenesis, our previous work demonstrated that miR-451b expression was downregulated in the smoker without COPD, smoker with stable COPE, and smoker with acute exacerbation COPD groups compared with non-smoker non-COPD group [18]. Here, stimulation of CSE results in a decrease in miR-451b expression and in increase in the expression of its target gene, RhoA. Furthermore, transfection of miR-451b mimics induced the downregulation of RhoA. MiR-451b overexpression reversed the effects of CSE on macrophages. Similarly, a previous study indicated that miR-451b was associated with both childhood asthma and adult COPD exacerbations [36]. Our data further showed that increased miR-451b expression caused the alteration of RhoA/ROCK signaling and p65 protein levels. Accumulating evidence has indicated RhoA plays a crucial role on the development of COPD. For instance, CSE may impair efferocytosis through oxidant-dependent activation of RhoA [37]. CSE-induced p120-catenin- (p120-) mediated NF-κB activation in human epithelial cells is dependent on the RhoA/ROCK pathway [25]. Activity of RhoA/Rho-kinase was increased in pulmonary arteries of COPD patients as compared with control subjects [22]. Furthermore, miR-133a/RhoA axis has been reported to participate in the elevation of carbon dioxide in tissues in patients with severe lung diseases, including COPD [38].

Lung fibroblasts have been previously reported to play a significant role in orchestrating inflammatory responses and responding to cigarette smoke by increasing pro-inflammatory prostaglandins and other pro-inflammatory mediators [39]. Here, we showed that CSE exposure increased the expression of RhoA, ROCK2, COL1A1, and COL2A1 in lung fibroblasts. Importantly, miR-451b mimics transfection abolished these effects of CSE on lung fibroblasts. COL1A1 and COL2A1, as the ECM components, have been demonstrated to be the downstream of transforming protein RhoA and Rho-associated protein kinase 1 for the regulation of osteogenesis [40]. Wang et al. [41] further manifested that ECM proteins promoted proliferation, migration, and adhesion of ASMCs from rat models of COPD through activation of the PI3K/AKT signaling pathway. Based on these facts, we thus speculated that overexpression of miR-451b could attenuate the impaired functional properties of lung fibroblasts, as key players in maintaining tissue homeostasis, are believed to be an important mechanism underlying COPD (Figure 7). However, there is a lack of verification by animal experiment and which is one of the limitations in the presented study.

5. Conclusions

In summary, our results suggest that transcription factor p300 regulated the expression of miR-451b and the latter suppressed CSE-induced inflammation and impaired functional properties in macrophages and lung fibroblasts. These effects may be associated with the regulation of its target gene RhoA-mediated RhoA/ROCK2 signaling pathway. This study therefore identifies p300/miR-451b/RhoA axis as a potential therapeutic target for CSE-induced injury in COPD.

Data Availability

The data that support the findings of this study are available on request from the corresponding author.

Ethical Approval

All participants provided their written informed consent for study participation, and the study protocol was approved by the Ethics Committee of the Second Affiliated Hospital of Kunming Medical University (Med-Eth-Re [20180302]).

Conflicts of Interest

The authors declare no competing interests.

Authors' Contributions

Wen Shen and Shukun Wang wrote the manuscript and operated the experiments; Ruili Wang, Yang Zhang, Hong Tian, and Xi Wang collected clinical samples and operated molecular experiments; Xin Wu, Xiaolei Yang, and Wei Wei analyzed the data; Wen Shen designed the experiments and edited the manuscript.

Acknowledgments

This work was supported by research grant from Applied Basic Research Foundation of Yunnan Province (2019FB090), Applied Basic Research (Kunming Medical Joint Special Project) Foundation of Yunnan Province (2017FE468[-058]), and Yunnan Provincial Health Committee Medical Reserve Talent Training Plan (H-2018096).

Supplementary Materials

Table S1 Sequences of transfected substance and primers used in QPCR. *(Supplementary Materials)*

References

[1] P. J. Barnes, "Chronic obstructive pulmonary disease: a growing but neglected global epidemic," *PLoS Medicine*, vol. 4, no. 5, article e112, 2007.

[2] G. B. D. Disease, I. Injury, and C. Prevalence, "Global, regional, and national incidence, prevalence, and years lived with disability for 310 diseases and injuries, 1990-2015: a systematic analysis for the Global Burden of Disease Study 2015," *Lancet*, vol. 388, no. 10053, pp. 1545–1602, 2016.

[3] B. R. Celli, W. MacNee, and A. E. T. Force, "Standards for the diagnosis and treatment of patients with COPD: a summary of the ATS/ERS position paper," *The European Respiratory Journal*, vol. 23, no. 6, pp. 932–946, 2004.

[4] S. R. Yang, J. Wright, M. Bauter, K. Seweryniak, A. Kode, and I. Rahman, "Sirtuin regulates cigarette smoke-induced proinflammatory mediator release via RelA/p65 NF-kappaB in macrophages in vitro and in rat lungs in vivo: implications for chronic inflammation and aging," *American journal of physiology Lung cellular and molecular physiology*, vol. 292, no. 2, pp. L567–L576, 2007.

[5] P. J. Barnes, "New anti-inflammatory targets for chronic obstructive pulmonary disease," *Nature Reviews Drug Discovery*, vol. 12, no. 7, pp. 543–559, 2013.

[6] S. Carnevali, S. Petruzzelli, B. Longoni et al., "Cigarette smoke extract induces oxidative stress and apoptosis in human lung fibroblasts," *American journal of physiology Lung cellular and molecular physiology*, vol. 284, no. 6, pp. L955–L963, 2003.

[7] S. Togo, O. Holz, X. Liu et al., "Lung fibroblast repair functions in patients with chronic obstructive pulmonary disease are altered by multiple mechanisms," *American Journal of Respiratory and Critical Care Medicine*, vol. 178, no. 3, pp. 248–260, 2008.

[8] A. Higham, D. Bostock, G. Booth, J. V. Dungwa, and D. Singh, "The effect of electronic cigarette and tobacco smoke exposure on COPD bronchial epithelial cell inflammatory responses," *International Journal of Chronic Obstructive Pulmonary Disease*, vol. Volume 13, pp. 989–1000, 2018.

[9] A. Hulina-Tomašković, A. Somborac-Bačura, M. Grdić Rajković, M. Bosnar, M. Samaržija, and L. Rumora, "Effects of extracellular Hsp70 and cigarette smoke on differentiated THP-1 cells and human monocyte-derived macrophages," *Molecular Immunology*, vol. 111, pp. 53–63, 2019.

[10] Y. Wang, J. Liu, J. S. Zhou et al., "MTOR suppresses cigarette smoke-induced epithelial cell death and airway inflammation in chronic obstructive pulmonary disease," *Journal of immunology (Baltimore, Md: 1950)*, vol. 200, no. 8, pp. 2571–2580, 2018.

[11] K. Rolle, M. Piwecka, A. Belter et al., "The sequence and structure determine the function of mature human miRNAs," *PLoS One*, vol. 11, no. 3, article e0151246, 2016.

[12] E. T. Osei, L. Florez-Sampedro, W. Timens, D. S. Postma, I. H. Heijink, and C. A. Brandsma, "Unravelling the complexity of COPD by microRNAs: it's a small world after all," *The European Respiratory Journal*, vol. 46, no. 3, pp. 807–818, 2015.

[13] M. Kara, G. Kirkil, and S. Kalemci, "Differential expression of microRNAs in chronic obstructive pulmonary disease," *Advances in clinical and experimental medicine : official organ Wroclaw Medical University*, vol. 25, no. 1, pp. 21–26, 2016.

[14] Y. J. Long, X. P. Liu, S. S. Chen, D. D. Zong, Y. Chen, and P. Chen, "miR-34a is involved in CSE-induced apoptosis of human pulmonary microvascular endothelial cells by targeting Notch-1 receptor protein," *Respiratory Research*, vol. 19, no. 1, p. 21, 2018.

[15] K. Tang, J. Zhao, J. Xie, and J. Wang, "Decreased miR-29b expression is associated with airway inflammation in chronic obstructive pulmonary disease," *American journal of physiology Lung cellular and molecular physiology*, vol. 316, no. 4, pp. L621–L629, 2019.

[16] T. Sato, X. Liu, A. Nelson et al., "Reduced miR-146a increases prostaglandin E2 in chronic obstructive pulmonary disease fibroblasts," *American Journal of Respiratory and Critical Care Medicine*, vol. 182, no. 8, pp. 1020–1029, 2010.

[17] L. Zhang, C. Huang, Y. Guo et al., "MicroRNA-26b modulates the NF-κB pathway in alveolar macrophages by regulating PTEN," *Journal of immunology (Baltimore, Md: 1950)*, vol. 195, no. 11, pp. 5404–5414, 2015.

[18] W. Shen, J. Liu, G. Zhao et al., "Repression of Toll-like receptor-4 by microRNA-149-3p is associated with smoking-related COPD," *International Journal of Chronic Obstructive Pulmonary Disease*, vol. 12, pp. 705–715, 2017.

[19] W. Shen, J. Liu, M. Fan et al., "MiR-3202 protects smokers from chronic obstructive pulmonary disease through inhibiting FAIM2: an _in vivo_ and _in vitro_ study," *Experimental Cell Research*, vol. 362, no. 2, pp. 370–377, 2018.

[20] S. Etienne-Manneville and A. Hall, "Rho GTPases in cell biology," *Nature*, vol. 420, no. 6916, pp. 629–635, 2002.

[21] S. Duong-Quy, P. Dao, T. Hua-Huy, C. Guilluy, P. Pacaud, and A. T. Dinh-Xuan, "Increased rho-kinase expression and activity and pulmonary endothelial dysfunction in smokers with normal lung function," *The European Respiratory Journal*, vol. 37, no. 2, pp. 349–355, 2011.

[22] Y. Bei, S. Duong-Quy, T. Hua-Huy, P. Dao, N. N. Le-Dong, and A. T. Dinh-Xuan, "Activation of RhoA/Rho-kinase pathway accounts for pulmonary endothelial dysfunction in patients with chronic obstructive pulmonary disease," *Physiological Reports*, vol. 1, no. 5, article e00105, 2013.

[23] X. Xie, J. Peng, X. Chang et al., "Activation of RhoA/ROCK regulates NF-κB signaling pathway in experimental diabetic nephropathy," *Molecular and Cellular Endocrinology*, vol. 369, no. 1-2, pp. 86–97, 2013.

[24] Y. He, H. Xu, L. Liang et al., "Antiinflammatory effect of Rho kinase blockade via inhibition of NF-κB activation in rheumatoid arthritis," *Arthritis and Rheumatism*, vol. 58, no. 11, pp. 3366–3376, 2008.

[25] C. Zhang, S. Qin, L. Qin et al., "Cigarette smoke extract-induced p120-mediated NF-kappaB activation in human epithelial cells is dependent on the RhoA/ROCK pathway," *Scientific Reports*, vol. 6, article 23131, 2016.

[26] T. Higashi, Y. Mai, Y. Mazaki, T. Horinouchi, and S. Miwa, "A standardized method for the preparation of a gas phase extract of cigarette smoke," *Biological & Pharmaceutical Bulletin*, vol. 39, no. 6, pp. 898–902, 2016.

[27] S. Arora, K. Dev, B. Agarwal, P. Das, and M. A. Syed, "Macrophages: their role, activation and polarization in pulmonary diseases," *Immunobiology*, vol. 223, no. 4-5, pp. 383–396, 2018.

[28] S. R. Yang, A. S. Chida, M. R. Bauter et al., "Cigarette smoke induces proinflammatory cytokine release by activation of

NF-kappaB and posttranslational modifications of histone deacetylase in macrophages," *American journal of physiology Lung cellular and molecular physiology*, vol. 291, no. 1, pp. L46–L57, 2006.

[29] S. M. Bal, J. H. Bernink, M. Nagasawa et al., "IL-1β, IL-4 and IL-12 control the fate of group 2 innate lymphoid cells in human airway inflammation in the lungs," *Nature Immunology*, vol. 17, no. 6, pp. 636–645, 2016.

[30] B. Shyam Prasad Shetty, S. K. Chaya, V. S. Kumar et al., "Inflammatory biomarkers interleukin 1 beta (IL-1β) and tumour necrosis factor alpha (TNF-α) are differentially elevated in tobacco smoke associated COPD and biomass smoke associated COPD," *Toxics*, vol. 9, no. 4, p. 72, 2021.

[31] J. Xu, B. Tao, X. Guo et al., "Macrophage-restricted Shp2 tyrosine phosphatase acts as a rheostat for MMP12 through TGF-beta activation in the prevention of age-related emphysema in mice," *Journal of immunology (Baltimore, Md: 1950)*, vol. 199, no. 7, pp. 2323–2332, 2017.

[32] L. Yang, F. Dai, L. Tang, Y. Le, and W. Yao, "Macrophage differentiation induced by PMA is mediated by activation of RhoA/ROCK signaling," *The Journal of Toxicological Sciences*, vol. 42, no. 6, pp. 763–771, 2017.

[33] G. Conickx, F. Avila Cobos, M. van den Berge et al., "microRNA profiling in lung tissue and bronchoalveolar lavage of cigarette smoke-exposed mice and in COPD patients: a translational approach," *Scientific Reports*, vol. 7, no. 1, p. 12871, 2017.

[34] S. Paul, L. M. Ruiz-Manriquez, H. Ambriz-Gonzalez et al., "Impact of smoking-induced dysregulated human miRNAs in chronic disease development and their potential use in prognostic and therapeutic purposes," *Journal of Biochemical and Molecular Toxicology*, vol. 36, no. 9, article e23134, 2022.

[35] Y. Qian, Z. D. Mao, Y. J. Shi, Z. G. Liu, Q. Cao, and Q. Zhang, "Comprehensive analysis of miRNA-mRNA-lncRNA networks in non-smoking and smoking patients with chronic obstructive pulmonary disease," *Cellular Physiology and Biochemistry*, vol. 50, no. 3, pp. 1140–1153, 2018.

[36] A. Tiwari, B. Hobbs, J. Li et al., "Blood miRNAs are linked to frequent asthma exacerbations in childhood asthma and adult COPD," *Noncoding RNA*, vol. 8, no. 2, p. 27, 2022.

[37] T. R. Richens, D. J. Linderman, S. A. Horstmann et al., "Cigarette smoke impairs clearance of apoptotic cells through oxidant-dependent activation of RhoA," *American Journal of Respiratory and Critical Care Medicine*, vol. 179, no. 11, pp. 1011–1021, 2009.

[38] M. Shigemura, E. Lecuona, M. Angulo et al., "Hypercapnia increases airway smooth muscle contractility via caspase-7-mediated miR-133a-RhoA signaling," *Science translational medicine*, vol. 10, no. 457, 2018.

[39] C. A. Martey, S. J. Pollock, C. K. Turner et al., "Cigarette smoke induces cyclooxygenase-2 and microsomal prostaglandin E2 synthase in human lung fibroblasts: implications for lung inflammation and cancer," *American journal of physiology Lung cellular and molecular physiology*, vol. 287, no. 5, pp. L981–L991, 2004.

[40] C. B. Khatiwala, P. D. Kim, S. R. Peyton, and A. J. Putnam, "ECM compliance regulates osteogenesis by influencing MAPK signaling downstream of RhoA and ROCK," *Journal of Bone and Mineral Research: the Official Journal of the American Society for Bone and Mineral Research*, vol. 24, no. 5, pp. 886–898, 2009.

[41] Z. Wang, R. Li, and R. Zhong, "Extracellular matrix promotes proliferation, migration and adhesion of airway smooth muscle cells in a rat model of chronic obstructive pulmonary disease via upregulation of the PI3K/AKT signaling pathway," *Molecular Medicine Reports*, vol. 18, no. 3, pp. 3143–3152, 2018.

Hindawi
Oxidative Medicine and Cellular Longevity
Volume 2022, Article ID 9264852, 9 pages
https://doi.org/10.1155/2022/9264852

Research Article

Clinical Analysis of Minimally Invasive Percutaneous Treatment of Severe Lumbar Disc Herniation with UBE Two-Channel Endoscopy and Foraminal Single-Channel Endoscopy Technique

Cuihua Yuan, Baojun Wen, and Hongkuan Lin

Department of Orthopaedics, Mindong Hospital Affiliated to Fujian Medical University, Fuan, 355000 Fujian, China

Correspondence should be addressed to Hongkuan Lin; linhongkuan7017@163.com

Received 21 July 2022; Revised 13 September 2022; Accepted 23 September 2022; Published 13 October 2022

Academic Editor: Shao Liang

For surgical treatment, herniation of traditional open surgery is the traditional approach and the representative operation for lamina windowing excision of nucleus pulposus. In recent years, the unilateral dual channel spine endoscopic technology (UBE/BESS) has caused extensive concern of spine surgery performer. This research compared the results of minimally invasive percutaneous treatment of severe lumbar disc herniation with foraminal single-channel endoscopy and unilateral biportal endoscopy (UBE). A retrospective study was conducted on 50 patients with severe disc herniation treated with minimally invasive percutaneous treatment in MinDong Hospital affiliated to Fujian Medical University from September 2019 to September 2021. According to different surgical methods, they were divided into two groups: foraminal single-channel endoscopic group and UBE dual-channel endoscopic group. There were 22 cases in the UBE surgery group and 28 cases in the interforaminal endoscopic group. The comparison included operation time, postoperative hospital stays, preoperative and postoperative pain scale (VAS), and postoperative MRI to observe the residual condition of prolapsed nucleus pulposus and the occurrence of complications. There were no significant differences between the UBE group and the interforaminal endoscopic group in incision length, operation time, postoperative hospital stays, and improvement of VAS score before and after surgery. In terms of postoperative nucleus pulposus residual rate and postoperative recurrence rate, the two-channel UBE group was significantly better than the single-channel interforaminal endoscopic group. The incidence of postoperative anemia in the interforaminal endoscopic group was significantly lower than that in the UBE group. In the treatment of severe disc herniation, UBE two-channel endoscopy has the advantages of lower recurrence rate, lower nucleus pulposus residual rate, shorter learning curve, and better field of vision than foraminal single-channel endoscopy, which is worth promoting in primary hospitals.

1. Introduction

Lumbar disc herniation (LDH), a local displacement of intervertebral disc material beyond the normal intervertebral disc space edge, usually causes low back pain and radiculopathy [1]. It is the most common cause of sciatica, affecting 1% to 5% of the population every year [2]. Lumbar disc herniation often dissolves over time, and the spontaneous resorption rate is 60% or above [3]. The first-line treatment for sciatica is non-surgical treatment, including physical therapy, drug therapy, and epidural steroid injection [4, 5], whereas surgery can relieve symptoms faster than continuous conservative treatment [6]. However, after a long follow-up, the differences between the groups tended to converge, but they still preferred surgical treatment.

For surgical treatment, herniation of traditional open surgery is the traditional approach and the representative operation for lamina windowing excision of nucleus pulposus. In traditional open surgery, there are many possible complications, such as excessive loss of intraoperative verte-

bral side, long-time muscle exertion, cerebrospinal fluid leakage, vertebral instability, low back pain and recurrence [7, 8]. Spinal endoscopy is a new minimally invasive spinal technology. Yeung [9] first proposed the Yeung endoscopy spine system (YESS) technology through the kambin triangle safety zone [10] in 1998. In 2002, Hoogl-and et al. proposed the technique of Transforaminal Endoscopic Spine System (TESSYS) [11, 12].

In recent years, the Unilateral Biportal Endoscopic (UBE/BESS) technology has caused extensive concern of spine surgery performer. UBE is unilateral dual-channel endoscopic technology (unlateral biportal endoscopic technique); the technology is usually set up two channels, a channel for observation and an instrument operating channels. Observation channels generally use 0° or 30° of arthroscopy, now can be very good completed the mirror through UBE technology fusion surgery under [13, 14].

At present, there are few comparative reports in the literature on the efficacy of UBE two-channel endoscopy and foraminal single-channel endoscopy technique in the treatment of severe intervertebral disc herniation. Thus, the motivation and novelty of this paper is to compare the efficacy of the above two minimally invasive endoscopic techniques in the treatment of severe intervertebral disc herniation.

2. Materials and Methods

2.1. General Information. The spine surgery retrospective comparative analysis of MinDong Hospital between September 2019 and September 2021 of patients with severe disc herniation percutaneous minimally invasive treatment included a total of 50 cases. The ratio of male to female is 4 : 6. The age was 28–66 years old, with an average age of 38.6 years: responsible intervertebral space distribution: 8 cases of L3/4 space; L4/5 space 22 cases; L5/S1 space in 20 cases. According to the operation plan, 28 cases underwent nucleus pulposus extraction assisted by foraminal single-channel endoscopy, and 22 cases underwent UBE two-channel endoscopy-assisted nucleus pulposus extraction. There was no significant difference in gender, age, BMI, and prominent responsibility gap between the two groups. Details are shown in Table 1.

2.2. Case Selection

(1) Case Inclusion Criteria: Our spine team operation cases showed that severe intervertebral disc hernia and hernia of nucleus pulposus arrived after the upper and lower adjacent vertebral bodies (arrived at 1 and 4 and beyond)

(2) Case Exclusion Criteria: Severe osteoporosis, spinal instability, or slippage patients always received spinal open surgery. Patient age is high and accompanied by severe basic diseases, which cannot tolerate surgery

2.3. Case Grouping

(1) UBE Group: UBE under arthroscopy-assisted technology, unilateral double channel endoscopic technique, percutaneous nucleus pulposus enucleation, preoperative signed informed consent UBE technology, preoperative examination lumbar positive side, a song, ghost piece of lumbar vertebra CT, preoperative check lumbar MR know I of nucleus pulposus, and postoperative lumbar MRI review about removal of nucleus pulposus and residue are included in this group.

(2) Interforaminal Endoscopic Group: Percutaneous enucleation of nucleus pulposus was performed by spinal foraminal endoscope-assisted single-channel endoscopy. Preoperative signed informed consent intervertebral foramen lens technology, preoperative signed informed consent UBE technology, preoperative examination lumbar positive side, a ghost piece, lumbar CT, lumbar MRI, and postoperative lumbar MRI review about removal of nucleus pulposus and residue are included in this group. Intraoperative operation and visual field are shown in Figures 1 and 2

2.4. Method

2.4.1. Interforaminal Endoscopic Group (Foraminal Single-Channel Endoscopy Technology Group). In L3 and L4/4/5 clearance, 12 cases were treated with topical anesthesia in 5 cases with local anesthesia plus intravenous reinforcement; 11 cases adopted general anesthesia. All patients took the prone position, and L5/S1 clearance do vertebral plate gap into the way, according to the conventional uniaxial intervertebral foramen mirror assisted surgery and according to the observation of intraoperative nerve root beat situation to judge the nerve root decompression are in good condition.

2.4.2. UBE Group (UBE Two-Channel Technology Group). All cases underwent endotracheal intubation anesthesia and surgery in the prone position. Two skin incisions were made under C-arm fluoroscopic guidance. The initial target point of the mirror instrument is located at the junction of the spinous process and the lamina, so as to make a horizontal marking line and draw a marking line along the inner edge of the pedicle. Intersection of two lines and 1.5 cm, respectively, to observe incision and incision operation point of the body surface. And we made 2 portals, layer by layer, the lumbar and dorsal fascia was cut longitudinally, and the soft tissue covered by the bony surface of the lamina was gradually expanded and bluntly separated to form the observation portals and the working portals. In the observation portals, the arthroscopic system was inserted and use salt water irrigation, under the hydraulic pressure to make tiny intra-spinal canal vein, does not ooze blood; it keeps to the field of vision clear; smooth flow of water is the key to UBE to get clear operative field. In the working portals, the soft tissue on the surface of the intervertebral space was treated under the 90° plasma scalpel and hemostasis was performed. Lamina rongeur and arthroscopy of the operating system dynamic power drill were used to remove the target intervertebral disc under the upper edge of vertebral lamina and a vertebral lamina edge, the edge of exposure on the yellow ligament, and the removal of yellow ligament. Using nerve hook open, nerve root, and dural sac

Table 1: Comparison of two groups of general data.

Group	Age (year, $x \pm s$)	Gender(male/female)	Protruding space		
			L3/4 and L2/3	L4/5	L5/S1
UBE group ($n = 22$)	40.0 ± 7.22	10/12	3	10	9
Interforaminal endoscopic group ($n = 28$)	38.0 ± 6.71	13/15	5	12	11
t/χ^2	1.012	0.005	0.164		
P value	0.317	0.945	0.921		

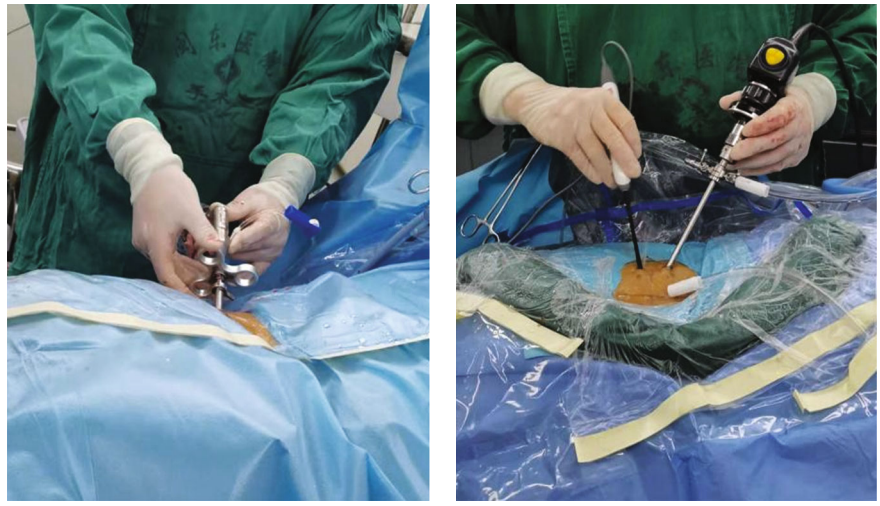

(a) (b)

Figure 1: Intraoperative operation of the two approach (a: foraminal single-channel endoscopy; b: two-channel UBE.).

intervertebral disc, preoperative MRI image data suggest peering into spinal canal and vertebral bodies with nucleus pulposus clamp fall off removal of nucleus pulposus, under endoscopic direct from removed off to the nucleus pulposus in the back part of the vertebral bodies.

Typical Case 1: Patient, male, 46 years old, L4 5. After intervertebral disc prolapse and intervertebral foraminal endoscopic nucleus pulposus extraction (Figures 3 and 4), MRI lost its shape and position before and after operation. It can be seen that there are still some residual compression nerve roots of nucleus pulposus after operation.

Typical case 2: Patients, male, 60 L2.3 slipped disc, line UBE dual channel after percutaneous minimally invasive nucleus pulposus enucleation (Figure 5), preoperative and postoperative MRI 3 loss with coronary, visible after removal of nucleus pulposus thoroughly, and no leave of nucleus pulposus.

2.5. Observation Index

(1) Effect of Evaluation Method: namely, operation time, intraoperative blood loss (loss with Hgb hemoglobin before and after operation situation assessment), incision length, operation rate, and hospital stay after operation

(2) Postoperative Review: magnetic resonance imaging (MRI) watch out residue and complications of nucleus pulposus; cerebrospinal fluid leakage after operation was compared between the two groups

(3) Follow-Up Records: VAS score (visual analogue pain score) was recorded before operation, after discharge, and 3 months and 6 months after operation. On a scale of 10, 0 indicates no pain and 10 indicates severe pain, with the end of the month being less painful

2.6. Statistical Analysis. The SPSS 16.0 statistical software was used for data analysis, and the measurement data were expressed in $x \pm s$. Rank sum test or t-test was used for measurement data, and intergroup comparison and counting data used χ^2 inspection. When the statistical result is $P < 0.05$, it is considered that the difference is statistically significant.

3. Results

3.1. Clinical Information. Two groups of operation time, postoperative hospitalization days, preoperative and postoperative VAS score difference have no obvious statistical significance ($P > 0.05$). Two groups of postoperative incision length difference were statistically significant ($P < 0.05$) (see Table 2).

3.2. Intraoperative Operation and Postoperative Complications. The UBE group under the dual-channel operation, wide field of vision, and flexible operating instrument freedom is not restricted. The UBE group of cerebrospinal fluid leakage in the postoperative complications occurred in 2 cases, The interforaminal endoscopic group was 0 cases; the occurrence of infection in the two groups was 0 cases; nucleus pulposus

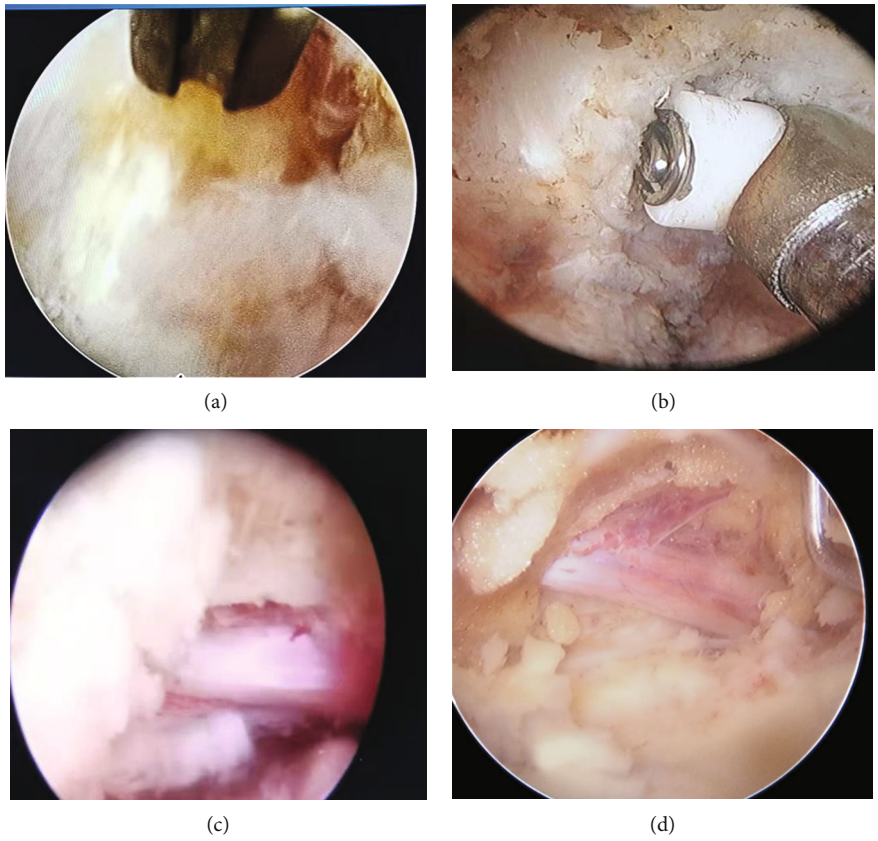

(a) (b) (c) (d)

Figure 2: Visual field during operation (a: visual field under radiofrequency cauterization in poroscopy; b: visual field under radiofrequency ablation during UBE; c: visual field after decompression of nerve was obtained during poroscopy; d: visual field after decompression of nerve was obtained during UBE.).

(a) (b)

Figure 3: Incision of two approach (a: incision after single-channel endoscopy; b: incision after two-channel UBE.).

residues in the UBE group occurred in 0 cases; the interforaminal endoscopic group occurred in 7 cases. The complication rate of two groups showed no significant difference ($P = 0.384$); however, there were significant differences in the incidence of anemia and residual nucleus pulposus between the two groups (as shown in Table 3).

4. Discussion

4.1. Advantages and Disadvantages of UBE Compared with Interforaminal Endoscopic. Compared with UBE two-channel endoscopic technique and foraminal single-channel endoscopy technique, the two techniques have the

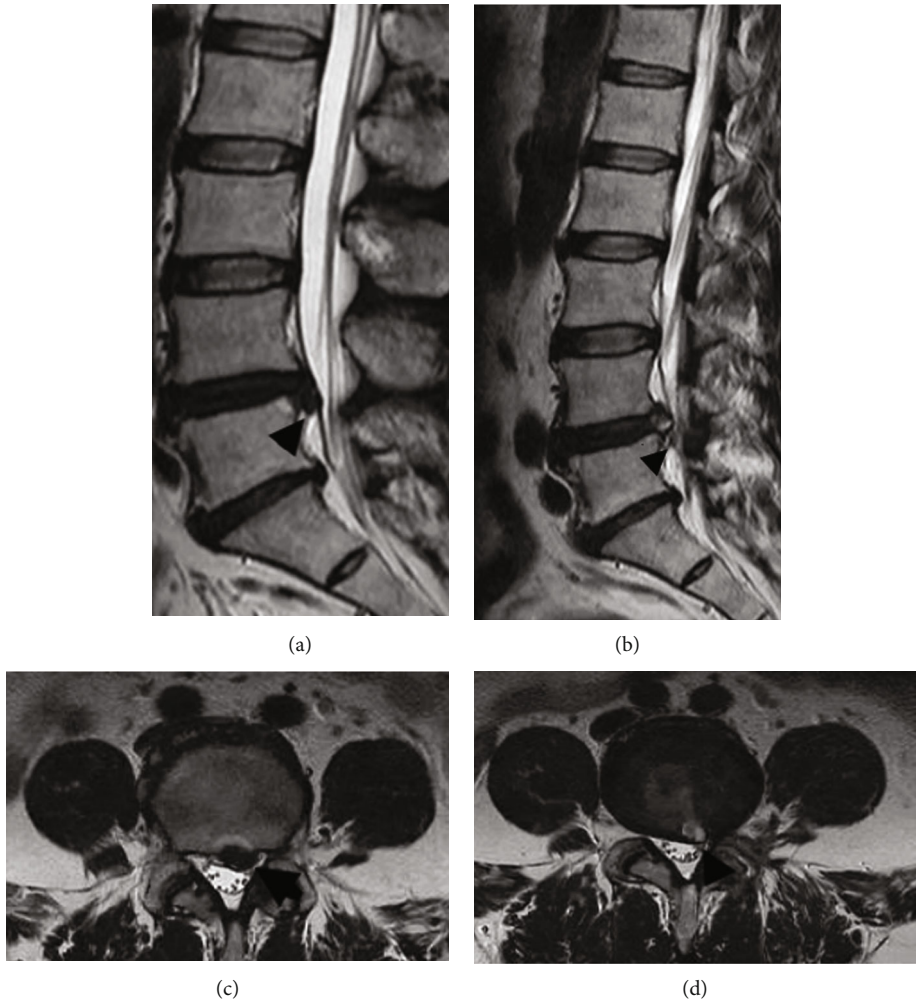

Figure 4: MRI imaging of typical case 1 (a: MRI sagittal of L4. Five intervertebral disc herniation before operation; b: MRI sagittal of L4. Five intervertebral disc after prolapse poroscopy; c: coronal MRI of L4. Five intervertebral disc herniation before operation; d: coronal MRI of L4. Five intervertebral disc herniation after prolapse poroscopy.).

following advantages and disadvantages: The advantages of percutaneous minimally invasive technique with uniaxial foraminal endoscope in the treatment of spinal diseases are minimally invasive, less intraoperative bleeding, and no need to place drainage ball after operation. The probability of postoperative anemia is low. The operation can be completed under local anesthesia.

Compared with UBE technology, the shortcomings of uniaxial foraminal endoscopic percutaneous minimally invasive technology are as follows: Uniaxial intervertebral foraminal mirror equipment is relatively expensive and has a long learning curve. Most grass-roots county-level hospitals have not purchased the equipment and still cannot master the technology in most hospitals. In addition, the field of vision of single-channel intervertebral foraminal endoscopy is relatively limited, and the use of posterior approach is generally limited to L5S1 segment. In the segment above L5S1, posterior surgery cannot be performed because the posterior lamina space is relatively narrow. If posterior surgery is required, a special large channel (delta channel) needs to be used. Therefore, the lateral intervertebral foramen approach is generally used in clinic. When the severe intervertebral disc prolapses to the back of the vertebral body (when the nucleus pulposus falls off to zone 1 and zone 4), it is often very difficult to completely remove the prolapsed nucleus pulposus by using the lateral intervertebral foramen mirror, which requires superb endoscopic technology. Generally, it is based on the experience of the operator and the observation of the pulsation of the nerve root during the operation to judge whether the nucleus pulposus is completely removed, and there is a high possibility of residual nucleus pulposus. High iliac crest should be considered in lateral foraminal endoscopy. If there is high iliac crest obstruction, it is difficult to place the tube at the target point of lateral approach and operate under the microscope.

The advantages of UBE two-channel endoscopy compared with the interforaminal endoscopic technology are as follows: First, because the two-channel spinal endoscopy technology uses the arthroscopic operating system, the equipment is cheap, and the equipment is available in most grass-roots county hospitals. Second, UBE percutaneous minimally invasive technology itself is a microscopic surgical posterior spinal operation technology under the guidance of water medium.

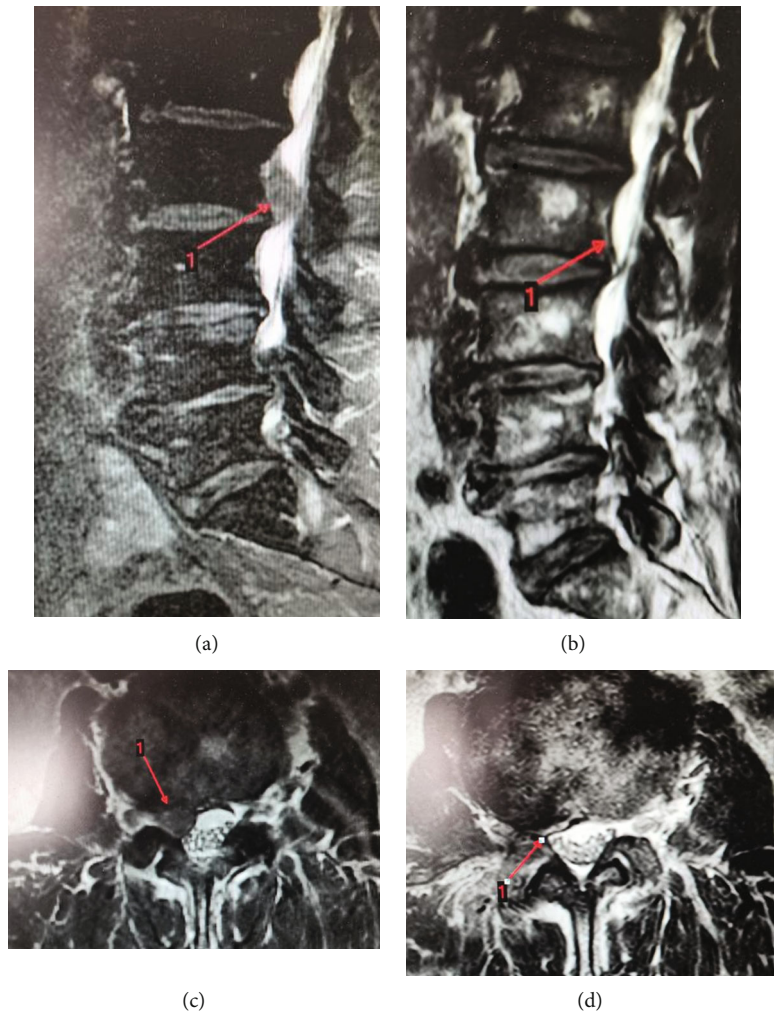

Figure 5: MRI imaging of typical case 1 (a: MRI sagittal of L2. Three intervertebral disc herniation before operation; b: MRI sagittal of L2. Three intervertebral disc after prolapse poroscopy; C: coronal MRI of L2. Three intervertebral disc herniation before operation; D: coronal MRI of L2. Three intervertebral disc herniation after prolapse poroscopy.).

The intraoperative anatomy is almost the same as that of the traditional posterior spinal technology. The technology can be carried out after a short training of spinal surgeons on the basis of arthroscopy. Therefore, the learning curve of UBE is relatively flat, and the learning cycle is short. Third, the essence of UBE is the surgical posterior spinal technique under the microscope. The field of vision under the double-channel microscope is more comprehensive, and the nucleus pulposus can be removed completely under direct vision. The surgical field of vision is wide, and the probability of residual nucleus pulposus is very low. Especially when the nucleus pulposus is prolapsed to the back of the vertebral body (nucleus pulposus falls off to zone 1 and zone 4) in the treatment of severe intervertebral disc herniation, UBE has obvious advantages, Tian, Zhu, and others also proposed that UBE has a good effect in the treatment of prolapsed free disc herniation [15, 16]. Fourth, UBE has many advantages, such as more flexible operation and more choice of instruments, which has more advantages in the treatment of lumbar spinal stenosis. In the future, it can enable more and more complex spinal degenerative diseases to achieve minimally invasive and endoscopic treatment. Fifth, the posterior approach of UBE operation does not need to consider the blocking factor of high iliac crest.

UBE has the following disadvantages compared with intervertebral foramen technology: First, the trauma of UBE is relatively larger than that of poroscopy: two incisions should be made during the operation. During the operation, the muscle attached to the lamina needs to be stripped under the microscope, and the artificial creation of two operation spaces needs to damage and destroy the anatomical structure of multifidus muscle and longissimus pectoralis muscle. Part of the vertebral lamina needs to be chiseled during the operation, and there is iatrogenic injury. There is relatively more bleeding during the operation than the hole mirror technology. After the operation, it is often necessary to place a drainage ball to prevent intraspinal hematoma. Second, UBE technology is relatively traumatic, and the probability of postoperative anemia is higher than that of poroscopy. Third, UBE technology generally needs to be carried out under general anesthesia, and lateral intervertebral foramen technology can be carried out under local anesthesia. UBE posterior surgery is a microscopic posterior spinal surgery.

Table 2: Comparison of intraoperative and postoperative conditions between the two groups ($\bar{x} \pm s$).

Group	Case	Operation time (min)	Postoperative hospital stay (d)	Preoperative/postoperative VAS score	Surgical incision (cm)
UBE group	22	65.6 ± 10.2	3.0 ± 1.5	7.02 ± 0.35/1.05 ± 0.54 *	2.26 ± 1.05
Interforaminal endoscopic group	28	62.3 ± 8.7	3.6 ± 1.2	8.13 ± 0.67/1.12 ± 0.36 *	1.8 ± 1.54
P	/	0.216	0.583	0.0169/0.218	0.006

Note: $^*P < 0.05$ *vs* preoperative VAS score.

Table 3: Comparison of postoperative complication rates of patients with different surgical methods between the two groups (%).

Group	Cerebrospinal fluid leakage	Incision infection	Anemia	Residual nucleus pulposus	Incidence rate
UBE group ($n = 22$)	2 (9.1)	0 (0)	6 (27.3)	0 (0)	8 (36.4)
Interforaminal endoscopic group ($n = 28$)	0 (0)	0 (0)	0 (0)	7 (25.0)	7 (25.0)
χ^2	2.652	/	8.678	6.395	0.758
P	0.104	/	0.003	0.011	0.384

During the operation, it is often necessary to chisel out the lamina and remove the ligamentum flavum. The probability of cerebrospinal fluid leakage caused by dural injury is relatively high.

4.2. Progress of UBE. De Antoni et al. [17] first reported UBE in 1996 and achieved good curative effect. In 1996, they performed discectomy under dual channel arthroscopy and achieved good clinical effect. They proposed dual channel technology to improve the vision and flexibility of operation.

Soliman first proposed the application of this technology to the minimally invasive treatment of intervertebral disc herniation in 2013 [18]. He proposed that the operation uses water as the medium, and the two-channel percutaneous minimally invasive technology expands the surgical field of vision, with less vascular bleeding in the spinal canal under the pressure of water medium. Eum et al. [19] applied the percutaneous dual-channel spinal endoscopic decompression technology to the treatment of lumbar spinal stenosis and found that under the assistance of percutaneous dual-channel endoscopic technology, the vertebral lamina can be windowed and decompressed through one incision, and the bottom of spinous process base can be bitten off through lamina gun pliers to the opposite side and bilateral decompression and ULBD can be performed without bilateral incision, and there is less vascular bleeding and less trauma under water pressure. In 2017, Heo et al. [13] first proposed the concept of unilateral dual channel endoscopy. At present, unilateral and dual-channel endoscopy is widely used in the treatment of lumbar spinal stenosis and lumbar disc herniation, with good curative effect [20, 21].

4.3. Surgical Techniques of UBE Single-Side Dual-Channel Spinal Endoscopy. The following points should be paid attention to in the operation of UBE percutaneous minimally invasive technique in the treatment of severe lumbar disc herniation:

(1) During preoperative positioning, the target space should be perpendicular to the ground, and the two channels should be V-shaped

(2) Before the operation, the C-arm machine transmission was clear and the operation gap was correct. During the operation, the operation space was created and the operation gap was clear again

(3) Keeping the water flowing smoothly and maintaining the stability of water pressure is the key to obtain a clear surgical field. During the operation, it is necessary to completely cut the low back fascia with a sharp knife and make a "cross" incision on the low back fascia under the incision with a sharp knife, which can keep the water flowing smoothly. At the same time, during the operation, pay attention to remove the soft tissue near the channel outlet to avoid the soft tissue blocking the water outlet, resulting in blurred vision. Especially at the beginning of the operation, the soft tissue attached to the upper and lower edges of the vertebral lamina needs to be stripped with a plasma knife. At this time, the detached soft tissue will block the water outlet, resulting in blurred vision at the beginning of the operation, so that the north and south cannot be distinguished during the operation. At this time, the operator should be calm and completely remove the soft tissue near the water outlet channel with nucleus pulposus forceps to keep the water outlet unobstructed and the field of vision variable and clear

(4) MRI and other imaging data should be carefully read before operation to clarify the location of the detached free nucleus pulposus, so that we can know well when exploring and removing the detached nucleus pulposus during operation

4.4. Limitations and Prospects. This study still has room for improvement. First, the sample size of the study is too small to detect a difference between both groups. Second, the follow-up time was too short to obtain long-term efficacy of the two surgical approaches. Besides, relatively few measures have been used to evaluate efficacy, and patient functional measures have not been discussed. Consequently, a well-designed, randomized, and controlled trial with prospective data collection and sample size calculation is needed to confirm the findings in our study and to examine the long-term efficacy of two approaches with clinical outcomes.

5. Conclusion

In the treatment of severe disc herniation, UBE unilateral two-channel percutaneous minimally invasive technology has wider field of vision, low residual rate of nucleus pulposus, and short learning curve compared with foraminal single-channel endoscopy. In the UBE group compared with the interforaminal endoscopic group, intraoperative on bone and soft tissue damage is bigger; the intraoperative bleeding is more, a high incidence of postoperative anemia; the damage of epidural cerebrospinal fluid leak rate is relatively high.

Data Availability

The labeled dataset used to support the findings of this study are available from the corresponding author upon request.

Conflicts of Interest

The authors declare no competing interests.

Authors' Contributions

Cuihua Yuan and Baojun Wen contributed equally to this work and are co-first authors.

Acknowledgments

This study was funded by the 2021 Fujian Provincial Natural Fund Health Industry Joint Fund General Project (2021J011453).

References

[1] D. S. Kreiner, S. W. Hwang, J. E. Easa et al., "An evidence-based clinical guideline for the diagnosis and treatment of lumbar disc herniation with radiculopathy," *The Spine Journal*, vol. 14, no. 1, pp. 180–191, 2014.

[2] J.-H. Kim, R. M. van Rijn, M. W. van Tulder et al., "Diagnostic accuracy of diagnostic imaging for lumbar disc herniation in adults with low back pain or sciatica is unknown; a systematic review," *Chiropractic & manual therapies*, vol. 26, no. 1, pp. 1–14, 2018.

[3] M. Zhong, L. Jin-Tao, H. Jiang et al., "Incidence of spontaneous resorption of lumbar disc herniation: a meta-analysis," *Pain Physician*, vol. 20, pp. E45–E52, 2017.

[4] P. C. Vroomen, M. De Krom, and J. Knottnerus, "Predicting the outcome of sciatica at short-term follow-up," *British Journal of General Practice*, vol. 52, pp. 119–123, 2002.

[5] J. Ashbrook, N. Rogdakis, M. J. Callaghan, G. Yeowell, and P. C. Goodwin, "The therapeutic management of back pain with and without sciatica in the emergency department: a systematic review," *Physiotherapy*, vol. 109, pp. 13–32, 2020.

[6] W. C. Peul, H. C. Van Houwelingen, W. B. van den Hout et al., "Surgery versus prolonged conservative treatment for sciatica," *New England Journal of Medicine*, vol. 356, no. 22, pp. 2245–2256, 2007.

[7] G. Datta, K. K. Gnanalingham, D. Peterson et al., "Back pain and disability after lumbar laminectomy: is there a relationship to muscle retraction?," *Neurosurgery*, vol. 54, no. 6, pp. 1413–1420, 2004.

[8] G. Kohlboeck, K. V. Greimel, W. P. Piotrowski et al., "Prognosis of multifactorial outcome in lumbar Discectomy," *The Clinical Journal of Pain*, vol. 20, no. 6, pp. 455–461, 2004.

[9] A. T. Yeung, "Minimally invasive disc surgery with the yeung endoscopic spine system (yess)," *Surgical Technology International*, vol. 8, pp. 267–277, 1999.

[10] P. Kambin, "Arthroscopic microdiskectomy. The Mount Sinai journal of medicine," *New York*, vol. 58, pp. 159–164, 1991.

[11] M. Schubert and T. Hoogland, "Endoscopic transforaminal nucleotomy with foraminoplasty for lumbar disk herniation," *Operative Orthopädie und Traumatologie*, vol. 17, no. 6, pp. 641–661, 2005.

[12] T. Hoogland, M. Schubert, B. Miklitz, and A. Ramirez, *Transforaminal Posterolateral Endoscopic Discectomy with or without the Combination of a Low-Dose Chymopapain: A Prospective Randomized Study in 280 Consecutive Cases*, vol. 31, no. 24, 2006LWW, 2006.

[13] D. H. Heo, S. K. Son, J. H. Eum, and C. K. Park, "Fully endoscopic lumbar interbody fusion using a percutaneous unilateral biportal endoscopic technique: technical note and preliminary clinical results," *Neurosurgical Focus*, vol. 43, no. 2, article E8, 2017.

[14] H.-J. Park, S.-K. Kim, S.-c. Lee, W. Kim, S. Han, and S.-S. Kang, "Dural tears in percutaneous biportal endoscopic spine surgery: anatomical location and management," *World Neurosurgery*, vol. 136, pp. e578–e585, 2020.

[15] D. Tian, J. Liu, B. Zhu et al., "Unilateral biportal endoscopic technique for lumbar disc herniation and lumbar spinal stenosis," *Chinese Journal of Orthopaedics*, vol. 12, pp. 1155–1164, 2020.

[16] B. Zhu, D. Tian, L. Chen et al., "Development and application of unilateral biportal endoscopy in lumbar diseases," *Chinese Journal of Orthopaedics*, pp. 1030–1038, 2020.

[17] D. J. De Antoni, M. L. Claro, G. G. Poehling, and S. S. Hughes, "Translaminar lumbar epidural endoscopy: anatomy, technique, and indications," *Arthroscopy: The Journal of Arthroscopic & Related Surgery*, vol. 12, no. 3, pp. 330–334, 1996.

[18] H. M. Soliman, "Irrigation endoscopic discectomy: a novel percutaneous approach for lumbar disc prolapse," *European Spine Journal*, vol. 22, no. 5, pp. 1037–1044, 2013.

[19] J. H. Eum, D. H. Heo, S. K. Son, and C. K. Park, "Percutaneous biportal endoscopic decompression for lumbar spinal stenosis: a technical note and preliminary clinical results," *Journal of Neurosurgery: Spine*, vol. 24, no. 4, pp. 602–607, 2016.

[20] L. Zhu, T. Cai, Y. Shan, W. Zhang, L. Zhang, and X. Feng, "Comparison of clinical outcomes and complications between percutaneous endoscopic and minimally invasive transforaminal lumbar interbody fusion for degenerative lumbar disease: a systematic review and meta-analysis," *Pain Physician*, vol. 24, no. 6, pp. 441–452, 2021.

[21] J. Liang, L. Lian, S. Liang et al., "Efficacy and complications of unilateral biportal endoscopic spinal surgery for lumbar spinal stenosis: a meta-analysis and systematic review," *World Neurosurgery*, vol. 159, 2022.

Hindawi
Oxidative Medicine and Cellular Longevity
Volume 2022, Article ID 4320809, 13 pages
https://doi.org/10.1155/2022/4320809

Research Article

Cancer-Associated Fibroblasts Hinder Lung Squamous Cell Carcinoma Oxidative Stress-Induced Apoptosis via METTL3 Mediated m^{6}A Methylation of COL10A1

Yuchan Li,[1] **Xiaoxue Li**,[2] **Muwen Deng**,[3,4] **Changda Ye**,[3,4] **Yuanhong Peng**,[3,4] **and Yan Lu**[5]

[1]*Department of 2nd Oncology, Guangdong Second Provincial General Hospital, Guangzhou, 510317 Guangdong, China*
[2]*Institute of Pathology, University Medical Center, Göttingen, Germany*
[3]*Department of Gastrointestinal Surgery, Shunde Hospital, Southern Medical University (The First People's Hospital of Shunde Foshan), Foshan, 528300 Guangdong, China*
[4]*The Second School of Clinical Medicine, Southern Medical University, Guangzhou, 510080 Guangdong, China*
[5]*GCP Center, Shunde Hospital, Southern Medical University (The First People's Hospital of Shunde Foshan), Foshan, 528300 Guangdong, China*

Correspondence should be addressed to Yan Lu; veryan0532@163.com

Received 11 July 2022; Revised 8 August 2022; Accepted 28 August 2022; Published 6 October 2022

Academic Editor: Shao Liang

Background. Cancer-associated fibroblasts (CAFs) within the tumor microenvironment are key players in tumorigenesis and tumor development. Nevertheless, the regulatory mechanisms of CAFs on lung squamous cell carcinoma- (LUSC-) associated remain poorly elucidated. *Methods*. The microarray dataset GSE22874, containing 30 specimens of primary culture of normal fibroblasts (NFs) and 8 specimens of cancer-associated fibroblasts (CAFs) samples derived from LUSC, was retrieved from the Gene Expression Omnibus (GEO) database and then calculated by using the R language (limma package) to identify differentially expressed genes (DEGs). CAF-conditioned medium (CAF-CM) was collected and used to culture LUSC cells, followed by assessment of cell proliferation, apoptosis, and oxidative stress levels by using CCK-8, annexin V-FITC/PI double staining and ELISA assays. Subsequently, COL10A1 was knocked down in CAFs to assess the role of COL10A1 in CAF regulation of LUSC behavior. Bioinformatics online analysis and MeRIP were applied to predict and test the m^{6}A modification of COL10A1 mRNA and the regulatory relationship with METTL3. Rescue experiments were next performed to explore the effects of METTL3 and COL10A1 in CAFs on LUSC cell proliferation, apoptosis, and oxidative stress. LUSC tumor cells with or without (COL10A1-silenced) CAFs were subcutaneously inoculated in nude mice to evaluate the effect of COL10A1 in CAFs on LUSC tumor growth. *Results*. Elevated expression of COL10A1 was found in LUSC-derived CAFs by GSE22874 dataset analysis. We discovered that COL10A1 and METTL3 was expressed in both LUSC cells and matched CAFs, while COL10A1 expression was prominently higher in CAFs than in LUSC cells. CAF-CM memorably encouraged LUSC cell proliferation and suppressed apoptosis-induced oxidative stress, which was reversed by interfering with COL10A1 expression in CAFs, suggesting that COL10A1 might be secreted by CAFs into the culture medium to exert its effects inside LUSC cells. Global m^{6}A modification was decreased in METTL3 knocked down CAFs. M^{6}A modification, expression levels, and stability of COL10A1 mRNA were impaired upon METTL3 knockdown in CAFs. Overexpression of COL10A1 in CAFs partially reversed the effect of METTL3 knockdown on the malignant behavior of LUSC cells. *In vivo* studies confirmed that CAFs accelerated LUSC tumor growth, and this effect was counteracted by COL10A1 silencing. *Conclusions*. COL10A1 secreted by CAFs could facilitate LUSC cell proliferation and repress apoptosis-induced oxidative stress, and the mechanism was due to elevated expression mediated by METTL3 promoting its mRNA m^{6}A modification, thereby accelerating tumor growth.

1. Introduction

Lung cancer is one of the most common malignant diseases with high morbidity and mortality, and the incidence is increasing with each passing year [1]. Depending on the pathological type, lung cancer can be divided into non-small-cell lung cancer (NSCLC) and small cell lung cancer (SCLC), of which 85% of lung cancer patients belong to NSCLC [2]. NSCLC in turn includes two main pathological types, lung adenocarcinoma (LUAD) and lung squamous cell carcinoma (LUSC). LUSC, as one of the major pathological types of non-small-cell lung cancer, leads to the death of approximately 400000 patients annually worldwide [3]. Despite the tremendous advances in existing medical treatments for the diagnosis, treatment, and care of LUSC, the mortality rate of LUSC has risen rapidly over the past few decades, and the overall survival rate is still very low. The reason for the poor survival rate and poor prognosis is that a large proportion of LUSC patients are already in the middle to advanced stages of lung cancer at the time of diagnosis and may already present with cancer metastasis [4]. It follows that the key to improving the survival rate of LUSC patients is the screening and detection of early stage.

Tumors are complex structures composed of malignant cells and a large number of non-neoplastic cells that interact with each other to create a tumor microenvironment (TME) [5]. The TME is mainly composed of blood vessels, extracellular matrix (ECM), and other non-neoplastic cells (including fibroblasts, adipocytes, and vascular endothelial cells, as well as immune cells such as T lymphocytes, B lymphocytes, NK cells, and tumor associated macrophages) surrounding the tumor, as well as cytokines and exosomes secreted by the cells [6]. Among them, cancer-associated fibroblasts (CAFs) are an important class of cellular components in TME, which have a wide range of origins and can be transformed by resident fibroblasts, BMSCs and HSCs, adipose stem cells, endothelial cells, and stellate cells in hepatocytes [7]. In addition to producing growth factors and inflammatory factors to modulate fibroblast activation in an autocrine manner, CAFs have been found to regulate the behavior of tumor cells and other stromal cells in a paracrine manner, to recruit them to the primary lesion or metastatic lesions of cancer, and to remodel the ECM and build the TME, ultimately promoting tumor cell proliferation, invasion, metastasis, drug resistance, and so on [8]. A study found that CAF-derived exosomes could suppress peripheral blood mononuclear cell-induced lung cancer cell killing and promote lung cancer progression [9]. Further, HIF-1α in CAFs could activate the NF-κB signaling pathway and enhance the subsequent secretion of CCL5, thereby promoting lung cancer tumor growth [10]. A data displayed that conditioned medium (CM) of CAFs could raise lung cancer cell proliferation, migration, and invasion, whereas blocking VCAM-1 in CAF-CM attenuated cancer cell proliferation and invasion [11].

Oxidative stress is an imbalance between free radicals and reactive metabolites that produces a large number of oxidative intermediates, leading to damage of important biomolecules and cells with potential implications for the whole organism [12]. Since oxidative stress can increase DNA mutations or induce DNA damage leading to genomic instability and cell proliferation, cancer initiation and progression are associated with oxidative stress [13]. From the whole apoptotic process, initial stress-induced cell damage cannot kill cells directly, but is able to trigger apoptotic signaling that leads to cell death [14]. Liu et al. found that oxidative stress inhibited the growth and induced apoptosis of human U251 glioma cells through a caspase-3-dependent pathway [15]. Tor et al. demonstrated that ethyl acetate extract induced apoptosis of breast cancer cells and its chemical features through oxidative stress generating, mitochondria dependent, and caspase independent pathways [16]. ROS appear to be important regulatory signals, as proposed by the growth suppressive role of SOD [17]. In fibroblasts, SOD inhibitors seem to favor apoptosis over cell proliferation. Recombinant adenoviral vectors expressing the radical scavenging enzymes Mn SOD and Cu, Zn SOD were able to reduce the level of apoptosis [18]. SOD has been reported to provide protection against tumor necrosis factor (TNF) cytotoxicity in hematopoietic cells [19]. TNF-induced antiproliferative effects, caspase-3 activation as well as other indicators of apoptosis were also completely inhibited by SOD activity [20]. Hypoxia-induced CAFs convey cisplatin resistance to sensitive NSCLC cells by delivering PKM2, which in turn inhibits oxidative stress-induced apoptosis [21]. Nevertheless, whether oxidative stress is involved in CAF involvement in LUSC progression remains to be investigated.

The aim of this study was to investigate the effects and molecular mechanisms of LUSC-associated CAFs on LUSC (SW900 and LOU-NH91 cells) in terms of cell proliferation, oxidative stress, and apoptosis and to identify the key genes in CAFs combined with bioinformatics software and biological experiment validation.

2. Materials and Methods

2.1. Tissue Specimens. This study enrolled 43 LUSC patients in The First People's Hospital of Shunde Foshan from May 2019 to August 2021. None of these patients received preoperative chemotherapy or radiotherapy. Subsequently, isolation and culture of CAFs and NFs were performed in cancer tissues and corresponding noncancerous tissues. Informed consent was obtained from patients accordingly to established protocols approved by the institutional review board of The First People's Hospital of Shunde Foshan. This study conformed to the declaration of Helsinki.

2.2. Ethics Approval. Both human and animal studies were conducted after approval from the committees of clinical ethics of The First People's Hospital of Shunde Foshan.

2.3. Cell Culture. LUSC cell lines SW900 and LOU-NH91 (ATCC, Manassas, VA, USA) were cultured at 37°C in a 5% CO_2 saturated humidified cell culture incubator with 10% fetal bovine serum (FBS, Gibco, CA). CAFs were cultured until 70-90% confluent, at which time the medium used was collected and passed through a 0.22 μM filter and

diluted 1 : 1 with RPMI-1640 containing 10% FBS. RPMI1640 medium supplemented with 10% FBS as the control medium. LUSC cells were cultured in conditioned media from CAFs cells for 21 days.

2.4. Bioinformatics Analysis. Microarray data are available with the accession numbers GSE22874 from Gene Expression Omnibus database (GEO, https://www.ncbi.nlm.nih.gov/geo/). The datasets GSE22874 was based on the platform GPL5175, including 30 normal fibroblasts (NFs) primary culture samples and 8 carcinoma-associated fibroblasts (CAFs) primary culture samples derived from LUSC. The difference analysis was performed using the limma package based on the R software, which employs the classical Bayesian's t-test analysis method with filtering criteria: $|\log \text{fold change}| \geq 0.5$, adjust $P < 0.05$. Targeted visualization of differential sites. The volcano plot was drawn by using the R language ggplot2 package to demonstrate the differentially expressed genes. Then, the Heatmap was plotted against the significantly upregulated versus significantly downregulated differentially expressed genes using the pHeatmap package in the R language, and samples were clustered on the upper part of the Heatmap, and sites were clustered on the left side of the Heatmap. In addition, m^6A modification sites of COL10A1 were predicted by online analysis website (http://www.cuilab.cn/sramp).

2.5. RT-qPCR Assay. Each group of differently treated cells were collected, and then TRIzol (Thermo Fisher, USA) was added to extract total cellular RNA. Total cellular RNA was reverse transcribed into cDNA by using a reverse transcription kit. RT-qPCR was performed by using cDNA as template, and then PCR products were detected with real time PCR system (Thermo Fisher, USA) with three replicate wells set for each group. The primer sequences were as follows: COL10A1 forward, 5′-TAT CCC GGC CCT ACT CCA AA-3′; and reverse, 5′-TTC AGC ACA GAG TCA GGC AG-3′. The relative expression levels were calculated by using $2^{-\Delta\Delta CT}$ method. We used GAPDH as endogenous control.

2.6. Western Blotting. Total cell protein was extracted with RIPA lysate, and the protein concentration was determined using a BCA protein assay kit (Thermo Fisher, USA) in a microplate reader. After denaturation for 10 min with the addition of loading buffer, 50 μg of protein samples were subjected to SDS-PAGE and transferred onto PVDF membranes. The membrane was blocked with blocking solution (5% nonfat dry milk) for 2 h and subsequently washed three times by using TBST buffer. Then, the membranes were incubated with horseradish peroxidase- (HRP-) conjugated goat antirabbit IgG (1 : 3000, Abcam, ab6721) for 1 h at room temperature. The secondary antibody was added by using TBST washing three times. This was followed by incubation on a shaker and protein exposure. ImageJ software was applied to detect and analyze the gray values of protein bands on the membrane. β-Actin was used as an endogenous control.

2.7. Cell Apoptosis Assay. Cell apoptosis was detected by using flow cytometry. The cells to be tested were washed 2 times with phosphate buffered saline, then 5 μl of annexin V dye solution and 10 μl of propidium iodide dye solution were added to stain for 30 min in the dark at 4°C. The apoptosis rate was detected by using flow cytometry.

2.8. Genetic Overexpression and Knockdown. The COL10A1 full sequence was ligated into pcDNA3.1 plasmid (GenePharma, China). The shRNAs were designed by QIAGEN to knock down METTL3 and COL10A1. Confluent cells were diluted in DMEM medium, and the cells were observed to grow to about 70% confluence when the cell monolayer was covered with serum-free DMEM medium. The plasmid transfection was performed using TurboFect Transfection Reagent as required for the experiments. All cells in each group were collected for subsequent experiments after incubating in an incubator at 37°C with 5% CO_2 for a specified period of times.

2.9. CCK-8 Assay. Cells were seeded in 96 well culture plates at a cell number per well of 3×10^3, and 5 replicate wells were set in each group. Transfection was performed after incubation at 37°C in 5% CO_2 until the cells became adherent. Then, the cells were incubated at 37°C in a 5% CO_2 incubator for 0, 24, 48, and 72 h after which the supernatant was discarded and 100 μl of complete medium and 10 μl of CCK-8 (Sigma-Aldrich, St. Louis, MO, USA). After incubation at 37° C in 5% CO_2 for 1 h, the optical density (OD) value at 450 nm was measured using a microplate reader (Bio-Rad, Hercules, CA, USA).

2.10. RNA Stability Assay. Actinomycin D (act D, 5 μg/ml) was added to the cells. Total RNA was isolated and RT-PCR was performed to measure relative levels of COL10A1 as previously described.

2.11. Total m^6A Measurement. Total RNA from cells in each group was isolated using TRIzol (Thermo Fisher, USA) according to the manufacturer's instructions. M^6A content was subsequently quantified using the EpiQuik m^6A RNA Methylation Quantification Kit (EpiGentek, USA).

2.12. M^6A RNA Immunoprecipitation Assay (MeRIP). Total RNA from cells of each group was isolated, and an mRNA purification kit (Thermo Fisher, USA) was used to further enrich poly (A)+RNA, which was then treated using DNase I (Thermo Fisher, USA). Subsequently, the Magna methylated RNA immunoprecipitation (MeRIP) m^6A kit (Thermo Fisher, USA) is employed to incubate global RNA with m^6A antibodies for immunoprecipitation. Finally, RT-PCR was performed on extracted RNA using mRNA primers of COL10A1 and then normalized to input.

2.13. Enzyme-Linked Immunosorbent Assay (ELISA). Cells were assayed for ROS, SOD, and GPX contents with ELISA kits (Thermo Fisher Scientific, Waltham, Ma, USA) according to the manufacturer's instructions.

2.14. In Vivo Experiments. 5-week-old male athymic BALB/C nude mice were obtained from experimental animal center

of Southern Medical University, and subsequently randomly divided into four groups, including SW900, SW900+CAFs, and SW900+CAFs^{COL10A1shRNA}. First, we stably transfected CAFs with COL10A1 shRNA. For xenograft experiments, SW900 or/and CAFs (5×10^5 cells/mouse) were subcutaneously injected into the right armpits of mice. Tumor length and width were calculated with vernier calipers every 7 days. After 35 days, the mice were humanely sacrificed, and the subcutaneous tumors were excised and removed. Experimental protocols were performed in accordance with the National Institute of Health guidelines for the Care and Use of Laboratory Animals.

2.15. Statistical Analysis. SPSS 22.0 and GraphPad prism 7.0 were used for data analysis and mapping. The pairwise comparisons were analyzed using the chi-square test. The measurement data were represented as mean ± SEM with normal distribution and homogeneity of variance. Student's *t*-test was used for comparison of two samples. The means of the different groups were compared using one-way or two-way analysis of variance (ANOVA) following Tukey's post hoc test. $P < 0.05$ was considered as statistically significant difference. All experiments were repeated 3 times ($N = 3$).

3. Results

3.1. Elevated Expression of COL10A1 in CAFs of LUSC Based on GEO Dataset Mining. Analysis of dataset GSE22874 downloaded from the Gene Expression Omnibus (GEO) database, including 30 normal fibroblasts (NFs) primary culture samples and 8 carcinoma-associated fibroblasts (CAFs) primary culture samples derived from LUSC. In addition, GSE22874 dataset was found to have a total of 20 differentially expressed genes (DEGs) by screening (Figure 1(a)). The gene expression profile was next analyzed in the GSE22874 dataset, generating a volcano plot and Heatmap of DEGs, which revealed 2 significantly upregulated DEGs and 18 significantly downregulated DEGs in CAFs (Figures 1(b) and 1(c)). We found that COL10A1 was prominently highly expressed in CAFs (Figure 1(d)). Subsequently, to further confirm the predicted results, we isolated and primary cultured LUSC-derived CAFs and matched NFs *in vitro*. Validation of CAF surface markers revealed that the expression of fibroblast-activating protein (FAP) and alpha-smooth muscle actin (*α*-SMA) was substantially elevated in CAFs compared with NFs (Figure 1(e)). In addition, we also discovered that both COL10A1 and C12orf54 were significantly upregulated in CAFs, with COL10A1 being more differentially expressed (Figures 1(f) and 1(g)).

3.2. CAF-CM Prominently Encouraged LUSC Cell Proliferation and Suppressed Apoptosis-Induced Oxidative Stress. Next, we employed the conditioned medium of CAFs (CAF-CM) to culture different cell lines of l LUSC to explore whether CAFs had an effect on the malignant behavior of LUSC cells SW900 and LOU-NH91. The growth curve generated by the CCK-8 assay displayed a significant elevation of the cell OD value after culturing the SW900 and LOU-NH91 cells by using CAF-CM, indicating cell proliferation was increased (Figure 2(a)). Further, apoptosis results revealed that the apoptotic rate of SW900 and LOU-NH91 cells were prominently decreased after CAF-CM treatment (Figure 2(b)). Subsequently, we detected ROS, SOD, and GPX contents in cell supernatants using ELISA to evaluate the regulation of CAFs on oxidative stress levels in LUSC cells. The results revealed that CAF-CM treatment significantly inhibited ROS content and facilitated SOD and GPX generation (Figures 2(c)–2(e)).

3.3. Knockdown of COL10A1 in CAFs Impedes the Promotion of LUSC Cell Growth by CAF-CM and Restraint of Apoptosis-Induced Oxidative Stress. Subsequently, to further confirm whether the CAFs effects on LUSC cells were through the involvement of COL10A1, COL10A1 shRNA was transfected into CAFs, and then CAF^{COL10A1shRNA}-CM were collected and treated with SW900 and LOU-NH91 cells. ELISA results showed that COL10A1 expression was significantly reduced within CAFs after COL10A1 shRNA transfection (Figure 3(a)). In addition, COL10A1 expression was apparently lower in SW900 and LOU-NH91 cells than in CAFs (Figure 3(a)). Further, compared with CAF^{NCshRNA}-CM, CAF^{COL10A1shRNA}-CM was able to reduce the expression of COL10A1 in SW900 and LOU-NH91 cells (Figure 3(b)), suggesting that COL10A1 may be secreted by CAFs into the culture medium and then into SW900 and LOU-NH91 cells. Next, we further discovered that CAF^{COL10A1shRNA}-CM treatment dramatically repressed cell proliferation, and contents of SOD and GPX in the cell supernatant, as well as accelerated cell apoptosis and ROS levels (Figures 3(c)–3(g)).

3.4. METTL3 Stabilizes COL10A1 Expression by Elevating its m^{6}A Modification in CAFs. Next, we aimed at exploring the underlying mechanism by which COL10A1 is highly expressed in CAFs. Prediction of whether COL10A1 is modified via m^{6}A on mRNA by online bioinformatics tools (http://www.cuilab.cn/sramp). Figure 4(a) displayed that there were m^{6}A binding sites ′GGACT′ on mRNA of COL10A1, among them, the highest confidence binding sites were at 12151-12155 on COL10A1. To further demonstrate whether m^{6}A methylation on COL10A1 is regulated by RNA methyltransferases, we obtained the binding motifs of METTL3, METTL14, and WTAP at Starbase website (https://starbase.sysu.edu.cn/) and retrieved the mRNA 3′ UTR sequences of COL10A1. The results displayed that the possible binding sites of METTL3 and COL10A1 were ATACCACCCT (Figure 4(b)). Because no binding sites were found for COL10A1 with METTL4 and WTAP, they are not shown in figures. Interestingly, we found that METTL3 level was elevated in LUSC derived CAFs compared with NFs (Figure 4(c)). Subsequently, METTL3 was knocked down in CAFs to assess its effect on COL10A1 expression and mRNA stability. Figure 4(d), shown as the interference efficiency of METTL3 shRNA, indicates that METTL3 shRNA can suppress the METTL3 expression. MeRIP results confirmed that m^{6}A antibody enrichment on COL10A1 mRNA was significantly reduced when

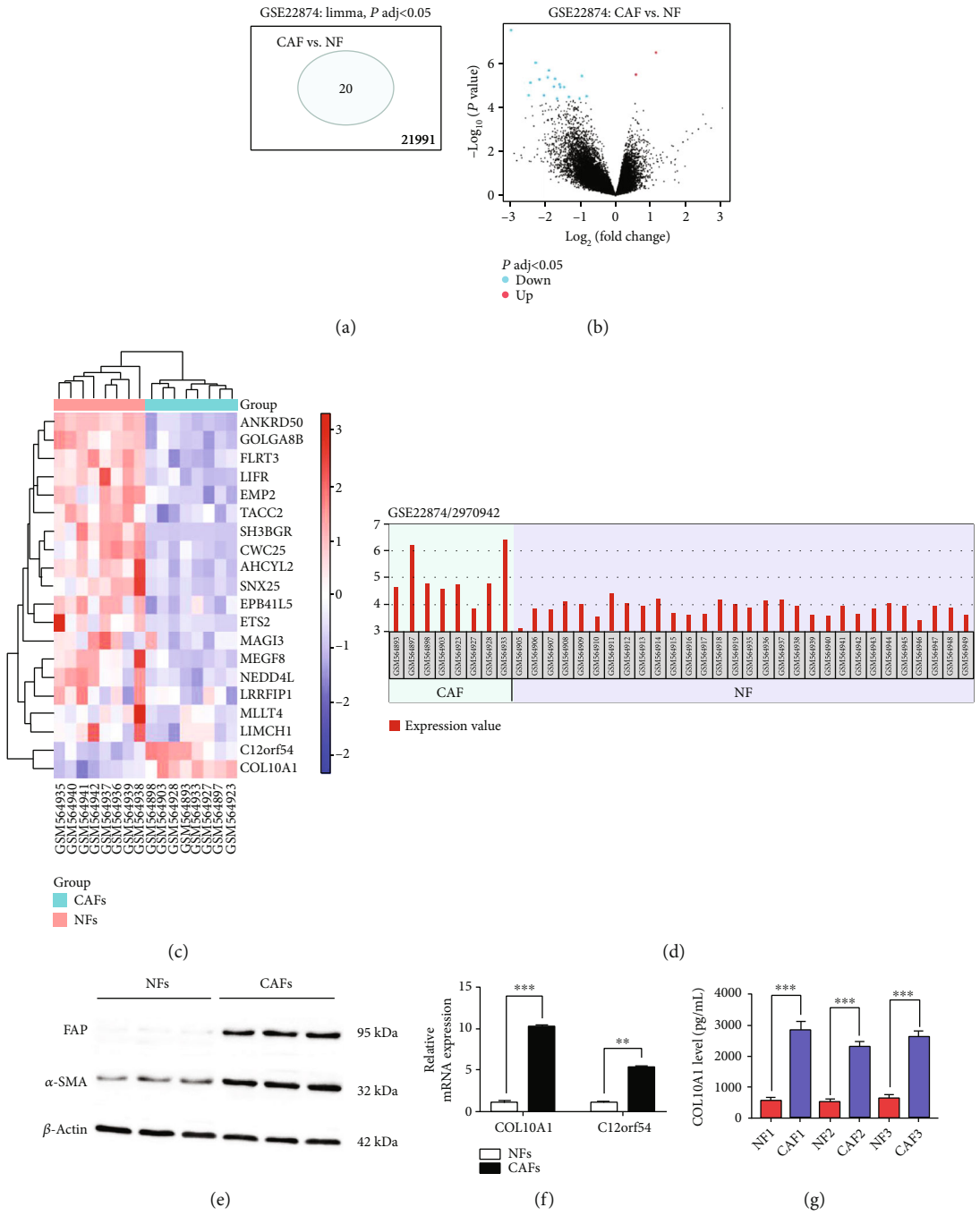

Figure 1: Elevated expression of COL10A1 in CAFs of LUSC based on GEO dataset mining. (a and b) Volcano plot of differentially expressed genes (DEGs) in GSE22874 dataset, which included 30 normal fibroblasts (NFs) primary culture samples and 8 carcinoma-associated fibroblasts (CAFs) primary culture samples derived from LUSC. (c) Heatmap visualization analysis of 20 DEGs. (d) Expression of COL10A1 in individual samples of the GSE22874 dataset. (e) Western blotting was employed to examine the expression of FAP and α-SMA in CAFs and NFs derived from three different LUSC samples. (f) RT-qPCR was used to test the expression of COL10A1 and C12orf54 in CAFs and NFs. (g) ELISA was employed to examine the expression of COL10A1 in CAFs and NFs derived from three different LUSC samples. Data were presented as mean ± SEM. $N = 3$. $^{**}P < 0.01$, $^{***}P < 0.001$.

METTL3 was downregulated (Figure 4(e)). Moreover, we also found that global m^{6}A modification levels were reduced, COL10A1 protein expression and mRNA stability were all suppressed in CAFs upon METTL3 knockdown (Figures 4(d)–4(g)). Taken together, we speculate that the increased expression of COL10A1 in CAFs may be due to METTL3 stabilizing its expression by increasing m^{6}A modification of COL10A1 mRNA.

3.5. METTL3 in CAFs Facilitates Malignant Behavior of SW900 by Mediating m^{6}A Methylation of COL10A1. Next, we will further analyze whether the effects of CAFs on LUSC

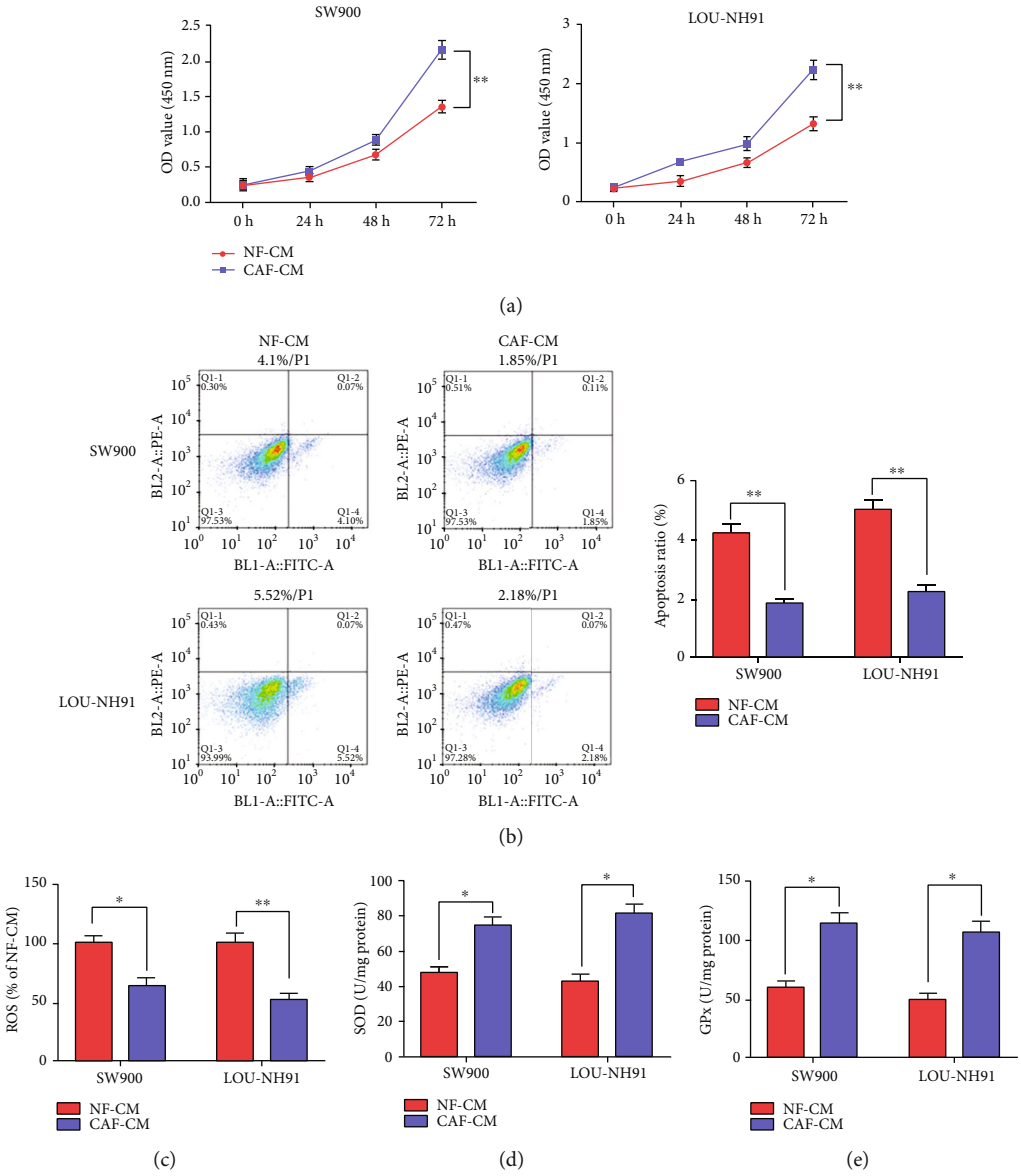

Figure 2: CAF-CM prominently encouraged LUSC cell proliferation and suppressed apoptosis-induced oxidative stress. (a) The CCK-8 kit was used to assess cell proliferation after CAF-CM treatment of SW900 and LOU-NH91 cells for 72 h. (b) The annexin V-FITC/PI double staining assay was used to test cell apoptosis after CAF-CM treatment of SW900 and LOU-NH91 cells for 48 h. (c–e) ELISA was employed to examine contents of ROS, SOD, and GPX after CAF-CM treatment of SW900 and LOU-NH91 cells for 48 h. Data were presented as mean ± SEM. $N = 3$. $^{*}P < 0.05$, $^{**}P < 0.01$.

cells are through the METTL3/COL10A1 axis. METTL3 shRNA was transfected into CAFs alone or together with pcDNA-COL10A1, and SW900 cells were then cultured with CAF-CM. The results demonstrated that COL10A1 expression was downregulated (Figure 5(a)), cell proliferation (Figure 5(b)) and SOD (Figure 5(e)), and GPX (Figure 5(f)) contents were decreased, and the rate of apoptosis (Figure 5(c)) and ROS production (Figure 5(d)) were increased in SW900 cells after knockdown of METTL3 in CAFs, these above results being partially counteracted by COL10A1 overexpression.

3.6. COL10A1 Interference Impairs CAF Acceleration of LUSC Xenograft Tumor Growth in Nude Mice. Based on the *in vitro* findings, we confirmed that COL10A1 played a crucial role in CAFs promoting LUSC cell growth. Nude mice were subcutaneously injected with SW900 cells or/and CAFs stably transfected with a COL10A1 shRNA plasmid vector to further evaluate the effect of $CAF^{COL10A1}$ on LUSC cell growth *in vivo* (Figure 6(a)). SW900 and CAFs injection significantly increased tumor volume and mass compared with SW900 transplanted tumors, whereas tumor growth was inhibited after $CAF^{COL10A1shRNA}$ injection, with a size close to that of the untreated group (Figures 6(b)–6(d)). Besides, the results of HE staining of mouse lung tissues suggested that large clumps were found in the SW900 +CAFs group, whereas the clumps became smaller in the SW900+$CAFs^{COL10A1shRNA}$ group (Figure 6(e)). Consistent

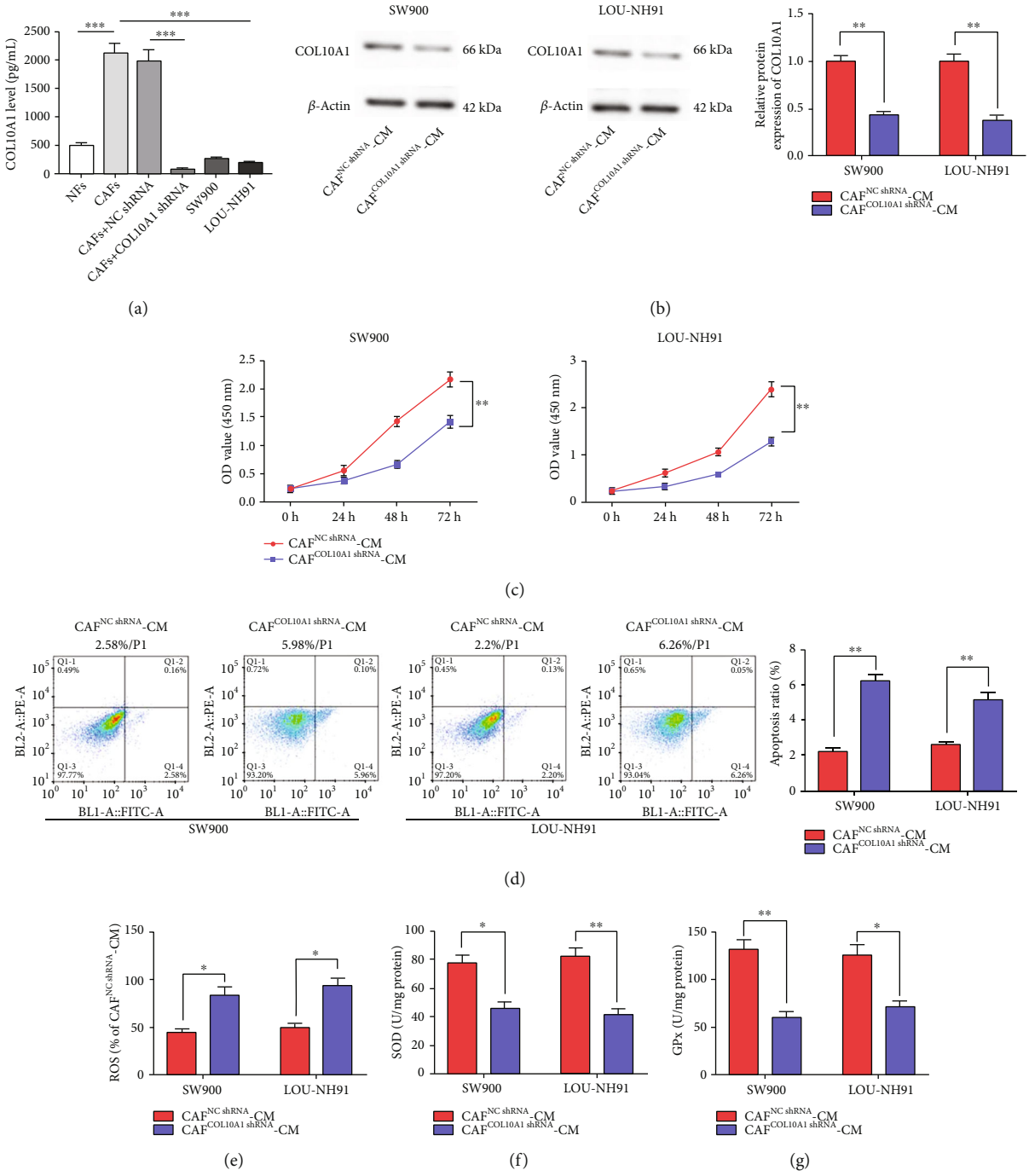

Figure 3: Knockdown of COL10A1 in CAFs impedes the promotion of LUSC cell growth by CAF-CM and restraint of apoptosis-induced oxidative stress. (a) ELISA was employed to examine COL10A1 level in NFs, CAFs, CAFs transfected with NC shRNA or COL10A1 shRNA, SW900 cells, and LOU-NH91 cells. (b) Western blotting was applied to test COL10A1 protein level in SW900 and LOU-NH91 cells treated with $CAF^{NCshRNA}$-CM and $CAF^{COL10A1shRNA}$-CM. (c) The CCK-8 kit was used to assess cell proliferation, which treated with $CAF^{NCshRNA}$-CM and $CAF^{COL10A1shRNA}$-CM. (d) The annexin V-FITC/PI double staining assay was used to test cell apoptosis in SW900 and LOU-NH91 cells treated with $CAF^{NCshRNA}$-CM and $CAF^{COL10A1shRNA}$-CM. (e–g) ELISA was employed to examine contents of ROS, SOD and GPX in SW900 and LOU-NH91 cells treated with $CAF^{NCshRNA}$-CM and $CAF^{COL10A1shRNA}$-CM. Data were presented as mean ± SEM. $N = 3$. $^{*}P < 0.05$, $^{**}P < 0.01$, $^{***}P < 0.001$.

with the *in vitro* results, ROS production was decreased and contents of SOD and GPX were increased in the SW900 +CAFs group compared with the SW900 group, whereas the above results were significantly reversed after knockdown of COL10A1 in CAFs (Figures 6(f)–6(h)).

4. Discussion

LUSC is one of the most common malignant tumors of the lung tissues. Despite continuous improvements in medical technology in recent years, the 5-year survival rate of LUSC

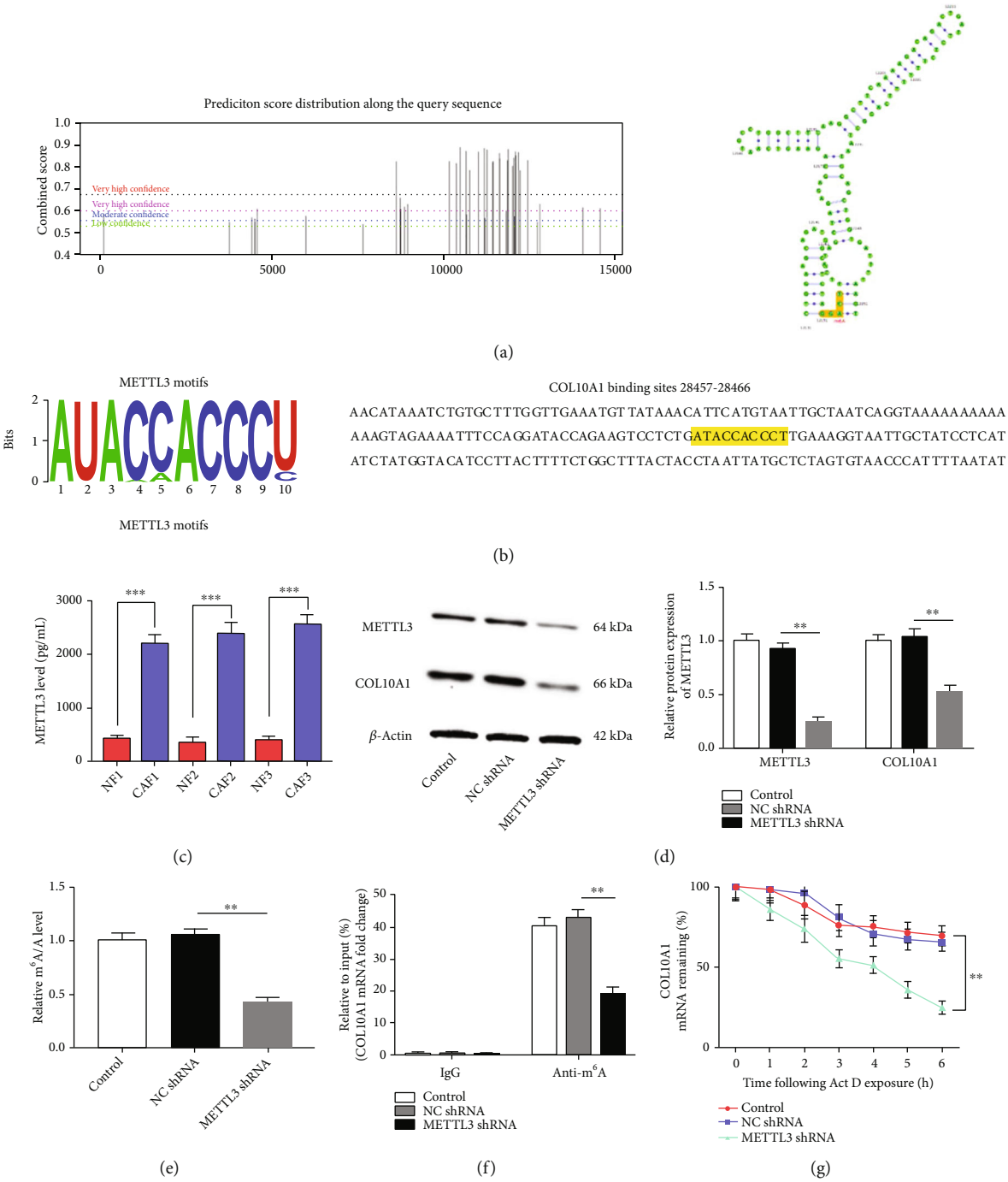

Figure 4: METTL3 stabilizes COL10A1 expression by elevating its m^{6}A modification in CAFs. (a) Diagram of m^{6}A modification peaks on COL10A1 mRNA, and schematic of the most likely binding sites. (b) Motifs of METTL3 and the binding sequences of its on COL10A1 3′ UTR. (c) Protein content of METTL3 in NFs and CAFs was detected by ELISA. (d) The protein levels of METTL3 and COL10A1 in CAFs after transfection with METTL3 shRNA were tested by Western blotting. (e) MeRIP was used to analyze m^{6}A modification levels on COL10A1 in CAFs. (f) m^{6}A quantitative analysis was applied to analyze m^{6}A global levels in CAFs. (g) Actinomycin D (5 μg/ml) was added to the cells to assess mRNA stability of COL10A1. Data were presented as mean ± SEM. $N = 3$. $^{**}P < 0.01$, $^{***}P < 0.001$.

remains less than half [22]. Therefore, it is still an important task to study its specific mechanism. In recent years, researchers have gradually found that TME as an 'inner person' rather than an 'outer person' is involved in most stages of tumor progression during the development of tumors [23]. Among them, CAFs, the most predominant stromal cells in the TME, can directly or indirectly affect surrounding parenchymal tumors. Currently, CAFs are commonly identified by the combined detection of several of the following proteins, including α-SMA, asporin, FAP, PDGFR, and

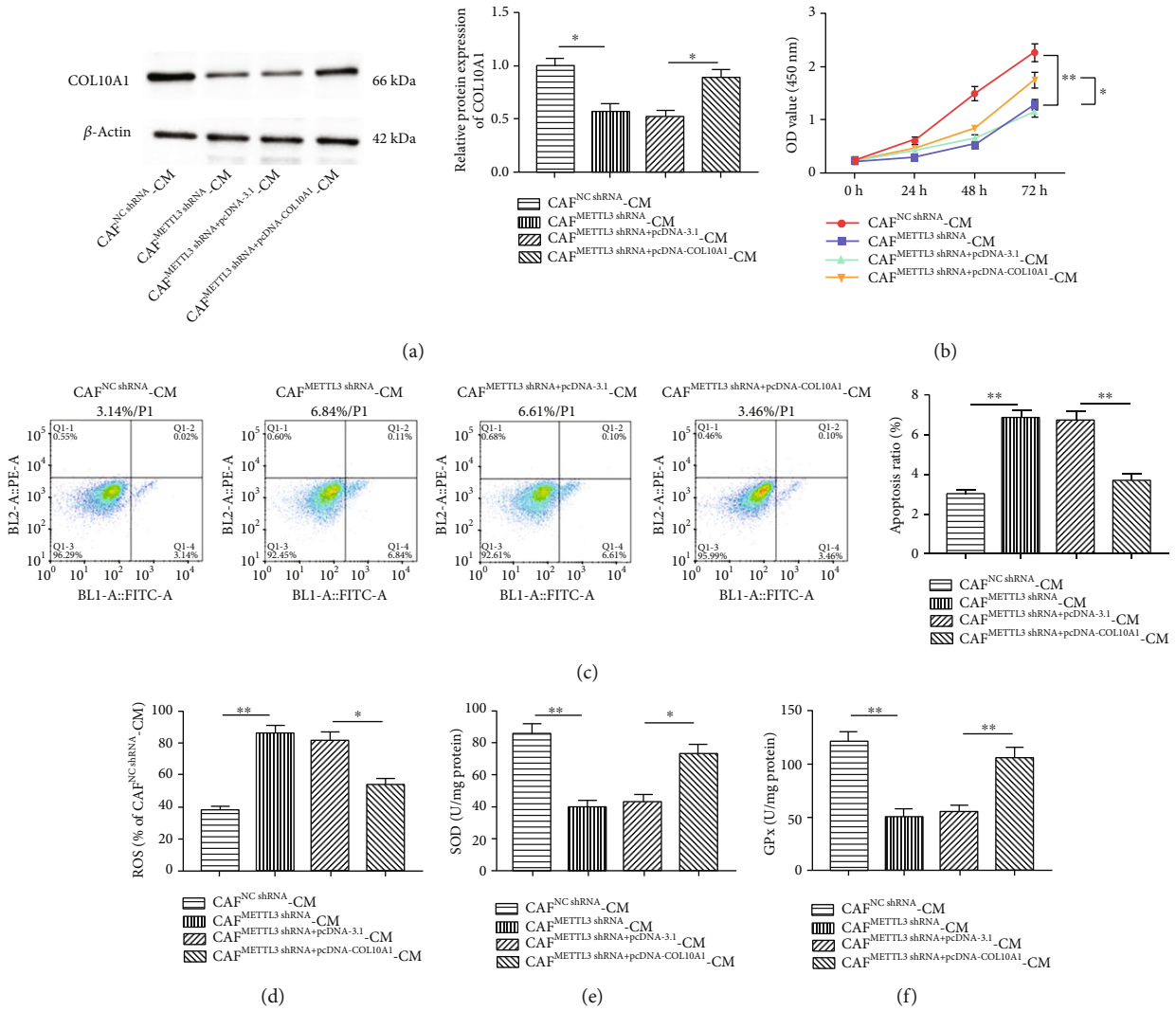

Figure 5: METTL3 in CAFs facilitates malignant behavior of SW900 by mediating m^{6}A methylation of COL10A1. (a) Western blotting was applied to test COL10A1 protein level in SW900 cells treated with CAF^{METTL3shRNA}-CM or/and CAF$^{METTL3shRNA+pcDNA-COL10A1}$-CM. (b) CCK-8 assay was employed to test SW900 cell proliferation treated with CAF^{METTL3shRNA}-CM or/and CAF$^{METTL3shRNA+pcDNA-COL10A1}$-CM. (c) The annexin V-FITC/PI double staining assay was used to detect cell apoptosis in SW900 cells treated with CAF^{METTL3shRNA}-CM or/and CAF$^{METTL3shRNA+pcDNA-COL10A1}$-CM. (d–f) ELISA was employed to examine contents of ROS, SOD, and GPX in SW900 cells treated with CAF^{METTL3shRNA}-CM or/and CAF$^{METTL3shRNA+pcDNA-COL10A1}$-CM. Data were presented as mean ± SEM. $N = 3$. $^*P < 0.05$, $^{**}P < 0.01$.

FSP1 [24]. In this study, we compared extracted primary CAFs and NFs and found that expression of FAP and α-SMA were substantially increased in CAFs. CAFs have been shown to enhance squamous cell carcinoma (SCC) growth, but it is unclear whether they promote SCC lung metastasis. One data showed that TRAP1, an important regulatory molecule for glucose metabolism in CAFs, was able to promote oral squamous cell carcinoma progression by regulating OXPHOS in CAFs [25]. LAMC1 promoted CXCL1 secretion, which stimulated inflammatory CAF formation via CXCR2-pSTAT3, which in turn accelerates esophageal squamous cell carcinoma progression [26]. Ba et al. demonstrated that CAF-CM facilitated proliferation of tongue squamous cell carcinoma cells, and xenograft models confirmed this effect [27]. Subsequently, co-culturing the cells with NF/CAF-CM revealed that the proliferative capacity of the SW900 and LOU-NH91 cells was significantly enhanced, and the apoptotic rate and oxidative stress levels were reduced after treatment with CAF-CM, indicating that CAFs can encourage the proliferation of LUSC.

COL10A1 belongs to the α-chain of the collagen family collagen X. In mammals, collagen is one of the most abundantly expressed proteins [28]. It has been reported in the literature that the collagen superfamily consists of 28 types of collagens, including collagen I to collagen XXVIII [29]. COL10A1 plays a considerable role in endochondral ossification, possibly related to matrix degradation, calcification, vascular invasion, and mutations in this gene are associated with metaphyseal chondrodysplasia [30]. It was demonstrated that COL10A1 expression preceded the development of bone vascularization and then altered the properties of the extracellular matrix contributed to the invasion of blood

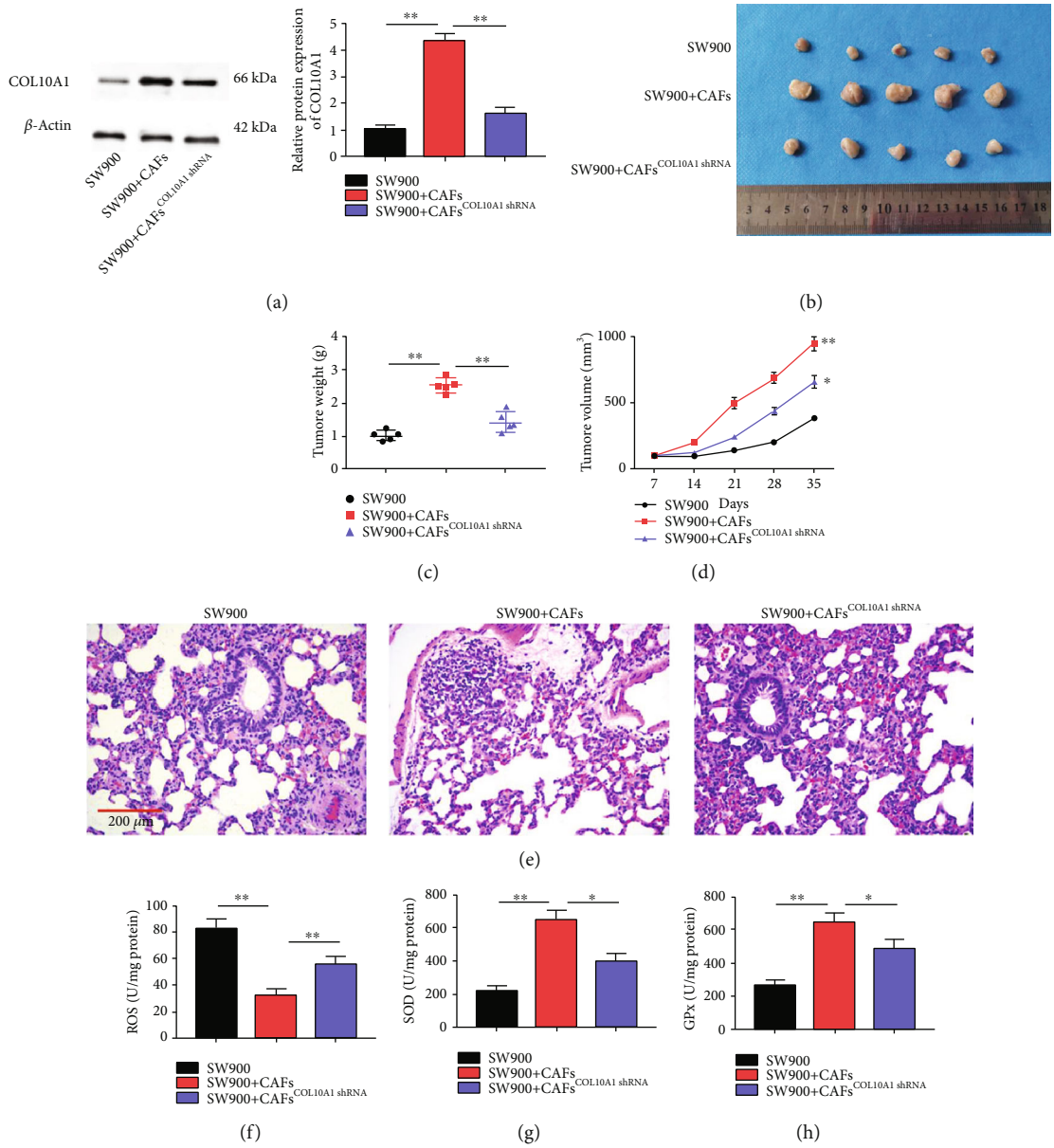

FIGURE 6: COL10A1 interference impairs CAF acceleration of LUSC xenograft tumor growth in nude mice. (a) Western blotting was applied to test COL10A1 protein level in mice from each group. (b) Representative images of tumors from each group; (c) Tumor growth curves; (d) Tumor mass of each group; (d) HE staining was applied to detect lung injury in mice from each group. (f–h) ELISA was used to test the production of ROS, SOD, and GPX in mice serum. Data were presented as mean ± SEM. $N = 3$. $^{*}P < 0.05$, $^{**}P < 0.01$.

vessels, and angiogenesis was particularly important for tumor tissues [31]. Thus, COL10A1 is a specific marker potentially involved in tumor angiogenesis [32]. It has been reported that COL10A1 is highly expressed in most tumor tissues, such as breast cancer [33], colorectal cancer [34], and gastric cancer [35] and so on. Up-regulation of COL10A1, a molecular marker of early colorectal cancer, encouraged colorectal cancer cell proliferation, migration, and invasion [36]. Logistic regression analysis indicated that high expression of COL10A1 in gastric cancer was largely associated with pathological stage, tumor differentiation, and T classification [37]. Bidirectional communication between tumor cells and CAFs regulates extracellular matrix (ECM) deposition and remodeling. As a result of this dynamic process, soluble ECM proteins can be released into the bloodstream and may represent novel circulating biomarkers for cancer diagnosis. Circulating COL11A1 expression is elevated in plasma samples of breast cancer patients and may be helpful in the diagnostic evaluation of suspicious breast nodules [38]. Moreover, a research confirmed that the expression of circulating protein COL10A1 was substantially elevated in the plasma of lung cancer patients compared with lung cancer cells [39]. In the present research, with the help of GEO dataset analysis and screening possible key genes, COL10A1 was found to be significantly higher expressed in LUSC patient plasma-derived CAFs compared

with NF and LUSC cells. Furthermore, knockdown of COL11A1 was able to counteract the accelerating effect of CAF-CM on the malignant behavior of the cells.

Epigenetics refers to the study of heritable and reversible phenotypic changes that do not involve alterations in the nuclear DNA sequence [40]. It mainly includes DNA methylation, RNA modification, noncoding RNAs, and histone modification. RNA methylation includes N1 methyladenine (m^1A), 5-methylcytosine (m^5C), N6 methyladenine (m^6A), and N7 methylguanine (m^7G) [41]. Among these, m^6A is the most common and most abundant RNA modifier in eukaryotic cells and can occur in messenger RNA (mRNA), ribosome RNA (rRNA), transfer RNA (tRNA), and noncoding RNA (ncRNA) [42]. M^6A refers to the methyl modification that occurs at the sixth position of adenine (a) under the action of methyltransferases, and is the most abundant modification occurring post transcriptionally in mRNA, accounting for about 50%, mainly occurring near stop codons and 3 'untranslated regions' [43]. A research demonstrated that chronic Cr exposure could alter cellular epi transcriptome by adding m^6A RNA modification through elevating the RNA methyltransferase METTL3 expression, which plays an important role in chronic Cr exposure-induced cell transformation, cancer stem cell-like property, and lung tumorigenesis [44]. METTL3 acts as an oncogene in NSCLC by mediating Bcl-2 mRNA m^6A modification, suggesting that targeting METTL3 may be an effective therapeutic strategy for the clinical management of NSCLC [45]. Further, Pan et al. demonstrated that CAFs derived exosomes suppress 5-Fluorouracil sensitivity in colorectal cancer cells via the METTL3/miR-181d-5p axis [46]. Combined with the above findings, this experiment confirmed that the expression of METTL3 increased in LUSC derived CAFs. Besides, we speculate that the increased expression of COL10A1 in CAFs may be due to METTL3 stabilizing its expression by increasing m^6A modification of COL10A1 mRNA. METTL3 in CAFs promotes proliferation and inhibits oxidative stress-induced apoptosis in LUSC cells by mediating m^6A methylation of COL10A1.

Taken together, the results of this study indicate that LUSC-derived CAFs have the ability to accelerate cell proliferation and repress oxidative stress-induced apoptosis *in vitro* and *in vivo*. The main mechanism is upregulation of m^6A modification of COL10A1 by an increase in METTL3 expression, which stabilizes COL10A1 expression for subsequent delivery into LUSC cells. These findings contribute to a better understanding of the molecular biological mechanisms by which CAFs promote LUSC and hopefully provide new molecular targets and theoretical basis for LUSC therapy. Nevertheless, this research content is mainly based on the conditioned medium of CAFs and lacks further confirmation on exosomes, which will be the focus of our subsequent studies.

Data Availability

The labeled dataset used to support the findings of this study is available from the corresponding author upon request.

Conflicts of Interest

The authors declare no competing interests.

Authors' Contributions

Yuchan Li and Xiaoxue Li contributed equally to this work.

Acknowledgments

This work was supported by the National Natural Science Foundation of China (No. 81802879), the Natural Science Foundation of Guangdong Province (No. 2022A1515012315), the Southern Medical University Scientific Research Startup Plan (No. PY2018N110), and the Foshan 13th Five-Year Key Specialty Project (No. FSGSP2D135051).

References

[1] A. A. Thai, B. J. Solomon, L. V. Sequist, J. F. Gainor, and R. S. Heist, "Lung Cancer," *The Lancet*, vol. 398, no. 10299, pp. 535–554, 2021.

[2] F. Wu, L. Wang, and C. Zhou, "Lung cancer in China: current and prospect," *Current Opinion in Oncology*, vol. 33, no. 1, pp. 40–46, 2021.

[3] E. O'Dowd, J. Mackenzie, and H. Balata, "Lung cancer for the non-respiratory physician," *Clinical Medicine*, vol. 21, no. 6, pp. e578–e583, 2021.

[4] F. Passiglia, V. Bertaglia, M. L. Reale et al., "Major breakthroughs in lung cancer adjuvant treatment: looking beyond the horizon," *Cancer Treatment Reviews*, vol. 101, article 102308, 2021.

[5] T. Wu and Y. Dai, "Tumor microenvironment and therapeutic response," *Cancer Letters*, vol. 387, pp. 61–68, 2017.

[6] S. Peng, F. Xiao, M. Chen, and H. Gao, "Tumor-microenvironment-responsive nanomedicine for enhanced cancer immunotherapy," *Advanced Science*, vol. 9, no. 1, article e2103836, 2022.

[7] G. Biffi and D. A. Tuveson, "Diversity and biology of cancer-associated fibroblasts," *Physiological Reviews*, vol. 101, no. 1, pp. 147–176, 2021.

[8] Y. Chen, K. M. Mcandrews, and R. Kalluri, "Clinical and therapeutic relevance of cancer-associated fibroblasts," *Nature Reviews Clinical Oncology*, vol. 18, no. 12, pp. 792–804, 2021.

[9] Y. Jiang, K. Wang, X. Lu, Y. Wang, and J. Chen, "Cancer-associated fibroblasts-derived exosomes promote lung cancer progression by OIP5-AS1/ miR-142-5p/ PD-L1 axis," *Molecular Immunology*, vol. 140, pp. 47–58, 2021.

[10] Y. Zhang, Y. Bian, Y. Wang et al., "HIF-1α is necessary for activation and tumour-promotion effect of cancer-associated fibroblasts in lung cancer," *Journal of Cellular and Molecular Medicine*, vol. 25, no. 12, pp. 5457–5469, 2021.

[11] Z. Zhou, Q. Zhou, X. Wu et al., "VCAM-1 secreted from cancer-associated fibroblasts enhances the growth and invasion of lung cancer cells through AKT and MAPK signaling," *Cancer Letters*, vol. 473, pp. 62–73, 2020.

[12] H. Sies, "Oxidative stress: a concept in redox biology and medicine," *Redox Biology*, vol. 4, pp. 180–183, 2015.

[13] M. S. Cooke, M. D. Evans, M. Dizdaroglu, and J. Lunec, "Oxidative DNA damage: mechanisms, mutation, and disease," *The FASEB Journal*, vol. 17, no. 10, pp. 1195–1214, 2003.

[14] L. Cao, J. Zhang, Y. Du et al., "Selenite induced breast cancer MCF7 cells apoptosis through endoplasmic reticulum stress and oxidative stress pathway," *Chemico-Biological Interactions*, vol. 349, p. 109651, 2021.

[15] X. R. Liu, Y. Q. Li, C. Hua et al., "Oxidative stress inhibits growth and induces apoptotic cell death in human U251 glioma cells via the caspase-3-dependent pathway," *European Review for Medical and Pharmacological Sciences*, vol. 19, no. 21, pp. 4068–4075, 2015.

[16] Y. S. Tor, L. S. Yazan, J. B. Foo et al., "Induction of apoptosis in MCF-7 cells via oxidative stress generation, mitochondria-dependent and caspase-independent pathway by ethyl acetate extract of dillenia suffruticosa and its chemical profile," *PLoS One*, vol. 10, no. 6, article e0127441, 2015.

[17] M. Islam, "Oxidative stress and mitochondrial dysfunction-linked neurodegenerative disorders," *Neurological Research*, vol. 39, no. 1, pp. 73–82, 2017.

[18] M. A. Pahlavani, J. F. Mele, and A. Richardson, "Effect of overexpression of human cu/Zn-SOD on activation-induced lymphocyte proliferation and apoptosis," *Free Radical Biology & Medicine*, vol. 30, no. 11, pp. 1319–1327, 2001.

[19] J. Zuo, M. Zhao, B. Liu et al., "TNF-α-mediated upregulation of SOD-2 contributes to cell proliferation and cisplatin resistance in esophageal squamous cell carcinoma," *Oncology Reports*, vol. 42, no. 4, pp. 1497–1506, 2019.

[20] S. Carta, S. Tassi, I. Pettinati, L. Delfino, C. A. Dinarello, and A. Rubartelli, "The rate of interleukin-1β secretion in different myeloid cells varies with the extent of redox response to toll-like receptor triggering," *The Journal of Biological Chemistry*, vol. 286, no. 31, pp. 27069–27080, 2011.

[21] D. Wang, C. Zhao, F. Xu et al., "Cisplatin-resistant NSCLC cells induced by hypoxia transmit resistance to sensitive cells through exosomal PKM2," *Theranostics*, vol. 11, no. 6, pp. 2860–2875, 2021.

[22] E. N. Imyanitov, A. G. Iyevleva, and E. V. Levchenko, "Molecular testing and targeted therapy for non-small cell lung cancer: current status and perspectives," *Critical Reviews in Oncology/Hematology*, vol. 157, article 103194, 2021.

[23] D. C. Hinshaw and L. A. Shevde, "The tumor microenvironment innately modulates cancer progression," *Cancer Research*, vol. 79, no. 18, pp. 4557–4566, 2019.

[24] X. Chen and E. Song, "Turning foes to friends: targeting cancer-associated fibroblasts," *Nature Reviews Drug Discovery*, vol. 18, no. 2, pp. 99–115, 2019.

[25] X. Li, Q. Hu, Y. Peng et al., "TRAP1 suppresses oral squamous cell carcinoma progression by reducing oxidative phosphorylation metabolism of cancer-associated fibroblasts," *BMC Cancer*, vol. 21, no. 1, p. 1329, 2021.

[26] L. Fang, Y. Che, C. Zhang et al., "LAMC1 upregulation via TGFβ induces inflammatory cancer-associated fibroblasts in esophageal squamous cell carcinoma via NF-κB-CXCL1-STAT3," *Molecular Oncology*, vol. 15, no. 11, pp. 3125–3146, 2021.

[27] P. Ba, M. Xu, M. Yu et al., "Curcumin suppresses the proliferation and tumorigenicity of Cal27 by modulating cancer-associated fibroblasts of TSCC," *Oral Diseases*, vol. 26, no. 7, pp. 1375–1383, 2020.

[28] M. Zhang, H. Chen, M. Wang, F. Bai, and K. Wu, "Bioinformatics analysis of prognostic significance of COL10A1 in breast cancer," *Bioscience Reports*, vol. 40, no. 2, 2020.

[29] J. C. Brown and R. Timpl, "The collagen superfamily," *International Archives of Allergy and Immunology*, vol. 107, no. 4, pp. 484–490, 2004.

[30] H. Wu, S. Wang, G. Li et al., "Characterization of a novelCOL10A1variant associated with schmid-type metaphyseal chondrodysplasia and a literature review," *Molecular Genetics & Genomic Medicine*, vol. 9, no. 5, article e1668, 2021.

[31] Y. Liang, W. Xia, T. Zhang et al., "Upregulated collagen COL10A1 remodels the extracellular matrix and promotes malignant progression in lung adenocarcinoma," *Frontiers in Oncology*, vol. 10, p. 573534, 2020.

[32] A. M. Moreira, R. M. Ferreira, P. Carneiro et al., "Proteomic identification of a gastric tumor ECM signature associated with cancer progression," *Frontiers in Molecular Biosciences*, vol. 9, article 818552, 2022.

[33] W. Yang, X. Wu, and F. Zhou, "Collagen type X alpha 1 (COL10A1) contributes to cell proliferation, migration, and invasion by targeting prolyl 4-hydroxylase beta polypeptide (P4HB) in breast cancer," *Medical Science Monitor*, vol. 27, article e928919, 2021.

[34] C. He, W. Liu, Y. Xiong et al., "VSNL1 promotes cell proliferation, migration, and invasion in colorectal cancer by binding with COL10A1," *Annals of Clinical and Laboratory Science*, vol. 52, no. 1, pp. 60–72, 2022.

[35] H. H. Li, J. D. Wang, W. Wang, H. F. Wang, and J. Q. Lv, "Effect of miR-26a-5p on gastric cancer cell proliferation, migration and invasion by targeting COL10A1," *European Review for Medical and Pharmacological Sciences*, vol. 24, no. 3, pp. 1186–1194, 2020.

[36] H. Huang, T. Li, G. Ye et al., "High expression of COL10A1 is associated with poor prognosis in colorectal cancer," *Oncotargets and Therapy*, vol. 11, pp. 1571–1581, 2018.

[37] S. Chen, Y. Wei, H. Liu et al., "Analysis of collagen type X alpha 1 (COL10A1) expression and prognostic significance in gastric cancer based on bioinformatics," *Bioengineered*, vol. 12, no. 1, pp. 127–137, 2021.

[38] M. Giussani, E. Landoni, G. Merlino et al., "Extracellular matrix proteins as diagnostic markers of breast carcinoma," *Journal of Cellular Physiology*, vol. 233, no. 8, pp. 6280–6290, 2018.

[39] F. Andriani, E. Landoni, M. Mensah et al., "Diagnostic role of circulating extracellular matrix-related proteins in non-small cell lung cancer," *BMC Cancer*, vol. 18, no. 1, p. 899, 2018.

[40] L. Zhang, Q. Lu, and C. Chang, "Epigenetics in health and disease," *Advances in Experimental Medicine and Biology*, vol. 1253, pp. 3–55, 2020.

[41] M. A. Dawson and T. Kouzarides, "Cancer epigenetics: from mechanism to therapy," *Cell*, vol. 150, no. 1, pp. 12–27, 2012.

[42] T. Wang, S. Kong, M. Tao, and S. Ju, "The potential role of RNA N6-methyladenosine in cancer progression," *Molecular Cancer*, vol. 19, no. 1, p. 88, 2020.

[43] Y. An and H. Duan, "The role of m6A RNA methylation in cancer metabolism," *Molecular Cancer*, vol. 21, no. 1, p. 14, 2022.

[44] Z. Wang, M. B. Uddin, J. Xie et al., "Chronic hexavalent chromium exposure upregulates the RNA methyltransferase

METTL3 expression to promote cell transformation, cancer stem cell-like property, and tumorigenesis," *Toxicological Sciences*, vol. 187, no. 1, pp. 51–61, 2022.

[45] Y. Zhang, S. Liu, T. Zhao, and C. Dang, "METTL3-mediated m6A modification of Bcl-2 mRNA promotes non-small cell lung cancer progression," *Oncology Reports*, vol. 46, no. 2, 2021.

[46] S. Pan, Y. Deng, J. Fu, Y. Zhang, Z. Zhang, and X. Qin, "N6-methyladenosine upregulates miR-181d-5p in exosomes derived from cancer-associated fibroblasts to inhibit 5-FU sensitivity by targeting NCALD in colorectal cancer," *International Journal of Oncology*, vol. 60, no. 2, 2022.

Hindawi
Oxidative Medicine and Cellular Longevity
Volume 2022, Article ID 9033342, 12 pages
https://doi.org/10.1155/2022/9033342

Research Article

AKAP12 and RNF11 as Diagnostic Markers of Fibromyalgia and Their Correlation with Immune Infiltration

Xiaowen Lin,[1] **Kangda Zhang**,[2] **and Tao Meng**[2]

[1]*Department of Pain Management, Shandong Provincial Hospital Affiliated to Shandong First Medical University, Jinan, China*
[2]*Department of Anesthesiology, Qilu Hospital of Shandong University, Jinan, China*

Correspondence should be addressed to Tao Meng; mengtao@sdu.edu.cn

Received 16 August 2022; Accepted 13 September 2022; Published 4 October 2022; Published October 2022

Academic Editor: Shao Liang

Fibromyalgia (FM) is a chronic nonarticular rheumatic disease mainly characterized by diffuse disseminated skeletal muscle pain, with varied symptoms including anxiety, sleep disturbance, and fatigue. Due to its unknown etiology and pathogenesis, FM is easily ignored in clinical practice, resulting in unclear diagnosis and difficult treatment. This study is aimed at investigating whether AKAP12 and RNF11 can be used as biomarkers for the diagnosis of FM and at determining their correlation with immune infiltration. The FM dataset in Gene Expression Omnibus (GEO) database was downloaded and was randomly divided into the training and test sets. Differentially expressed genes (DEGs) were screened, and functional correlation analysis was performed. Diagnostic markers of FM were screened and validated by random forest (RF). The least absolute shrinkage and selection operator (LASSO) logistic regression algorithm was then used to evaluate immune cell infiltration in the FM patients' peripheral blood. Finally, Spearman's rank correlation analysis was used to identify correlation between the diagnostic indexes and immune cell infiltration. A total of 69 DEGs were selected. Results indicated that AKAP12 and RNF11 can be used as diagnostic markers of FM, and CD8 + T cells might contribute in the pathogenesis of FM. In addition, AKAP12 was positively correlated with CD8 + T cells, while RNF11 was negatively correlated with CD8 + T cells. In conclusion, AKAP12 and RNF11 can be used as diagnostic indicators of FM, and CD8 + T cells may be involved in the occurrence and development of FM.

1. Introduction

Fibromyalgia (FM) is a chronic, painful, nonarticular rheumatic disease characterized by diffuse pain and often accompanied by multiple symptoms, including fatigue, sleep disturbances, emotional abnormalities, and cognitive dysfunction [1]. So far A kinase anchoring protein-12 (AKAP12) and RNF11 have not shown any abnormal expression in any osteoarthritis and rheumatoid arthritis. FM is considered the third most common musculoskeletal disorder, and its incidence increases with age [2]. Due to improved diagnosis techniques, the current FM prevalence is about 2%-8% [3]. A great controversy still exists regarding FM assessment and diagnosis. Initially, the diagnosis of FM proposed by the American College of Rheumatology (ACR) in 1990 mainly consisted of counting 18 tenderness points at the same anatomical site on the left and right sides of the body [4]. Although widespread chronic pain lasting more than 3 months is the main symptom of FM, there are still about 70%-80% of patients with specific manifestations such as sleep disturbance and lethargy, which cannot be ignored [5].

Later, in 2010, the ACR updated its diagnostic criteria, which assessed the presence and severity of fatigue, cognitive difficulties, sleep deprivation, degree of other somatic symptoms, and considered the painful body parts [6]. The ACR 2010 criteria, which rely on Symptom Severity Scale (SSS) and the Widespread Pain Index (WPI), are more sensitive than the ACR 1990 criteria and are presently widely used in clinical practice [7]. Routine clinical laboratory diagnoses of FM do not reveal objective abnormalities, and diagnosis is usually done based on complex clinical manifestations after excluding other diseases. Due to the delayed diagnosis, progression of FM in most patients leads to poor prognosis and

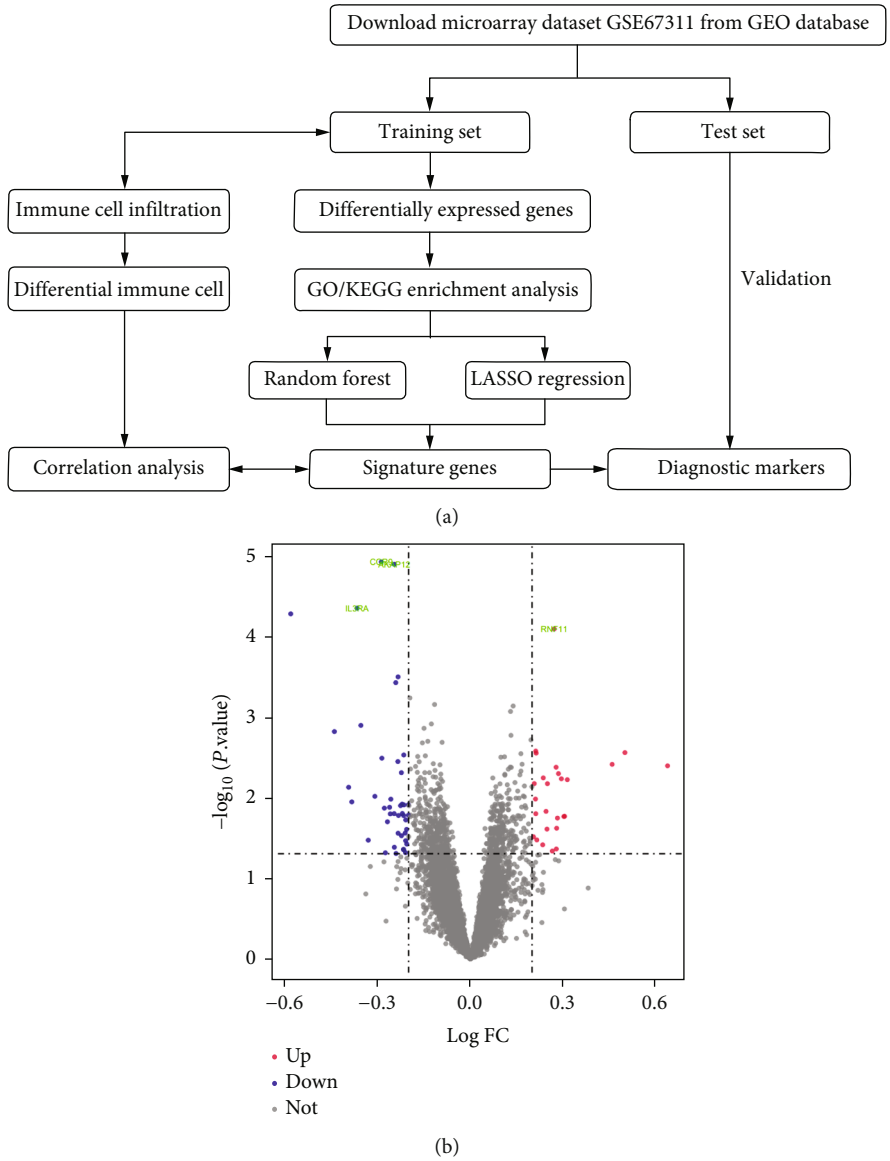

Figure 1: Volcano map of DEGs. Red represents high expression, blue represents low expression, and gray represents no difference.

ineffective treatment options. Consequently, exploring biomarkers might help in early diagnosis and improve prognosis.

The underlying mechanisms of FM are complex and result from the interaction of mental stress, neuroendocrine abnormalities, immune dysfunction, and behavioral and psychological factors [8, 9]. Recent studies have shown that immune cell infiltration is essential in FM occurrence and development. Blood sample immunophenotypic analysis from patients revealed the role of Mu opioid receptors on B lymphocytes as specific biomarkers for FM [10]. From the immune system perspective, it is important to evaluate the differences in immune cell components infiltrated in peripheral blood of FM patients compared to healthy people to elucidate the molecular mechanism and develop possible immunotherapeutic targets. With the widespread use of microarray and high-throughput sequencing, bioinformatics analysis can identify novel genes and biomarkers associated with various disease development, including systemic lupus erythematosus, osteoarthritis, and rheumatoid arthritis [11–13]. CIBERSORT is an analytical tool that uses gene expression profiles to assess the expression and composition of immune cells [14].

The present investigation is aimed at investigating whether AKAP12 and RNF11 can be used as biomarkers for the diagnosis of FM and at determining their correlation with immune infiltration. A microarray dataset of FM was downloaded from Gene Expression Omnibus (GEO) database to identify Differentially Expressed Genes (DEGs). After DEG screening, the functional correlation was analyzed by Gene Ontology (GO) and Kyoto Encyclopedia of Genes and Genomes (KEGG), and machine learning algorithms were used to further screen and determine diagnostic markers of FM. Subsequently, CIBERSORT was used to analyze the differences in immune cell subsets' infiltration

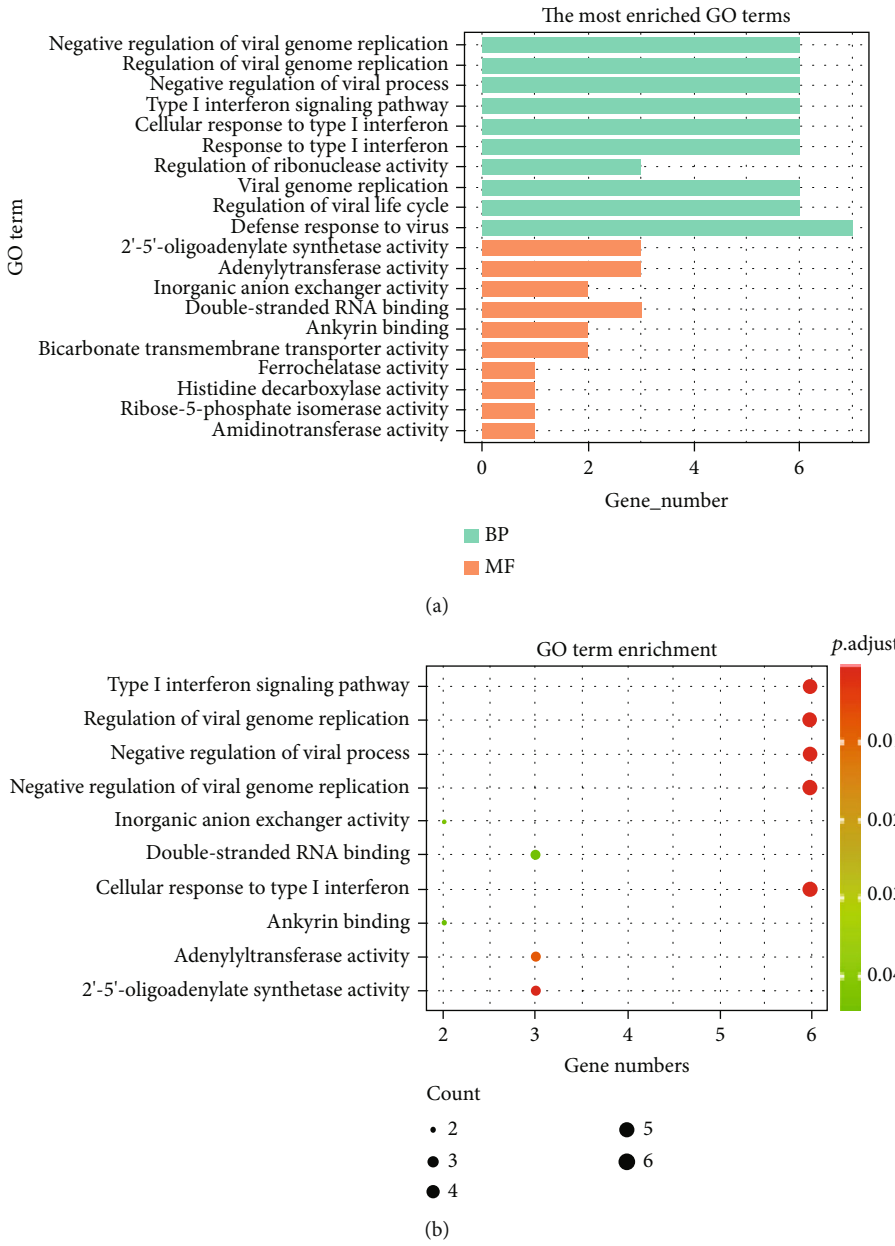

Figure 2: Continued.

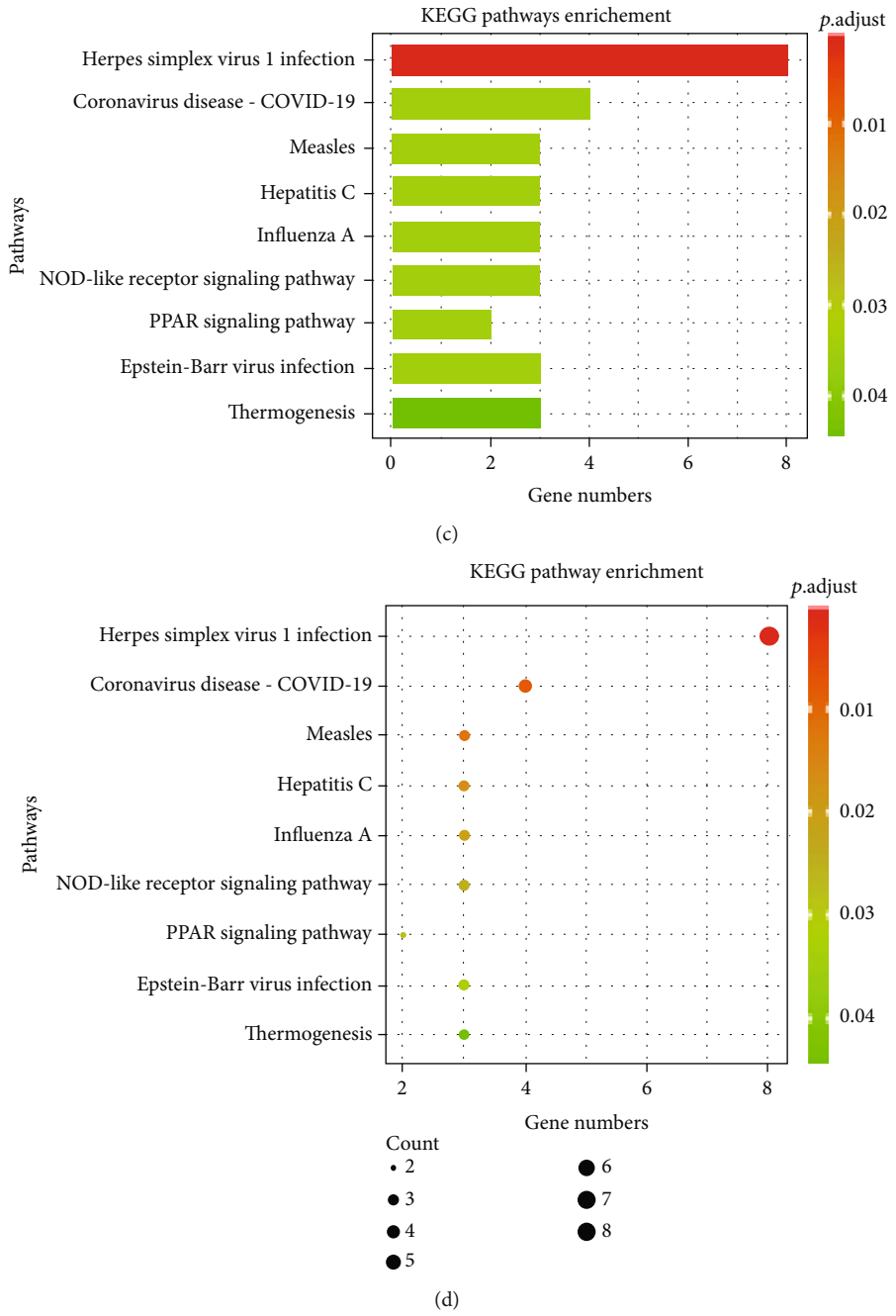

Figure 2: GO and KEGG functional enrichment analyses of DEGs. (a) Histogram of GO enrichment analysis. (b) Bubble plot for GO enrichment analysis. (c) Histogram of KEGG enrichment analysis. (d) Bubble plot for KEGG enrichment analysis.

between FM patients and healthy subjects. Finally, we investigated the relationship between diagnostic markers and infiltrating immune cells.

2. Materials and Methods

2.1. Data Download and Preprocessing. The GEO database (http://www.ncbi.nlm.nih.gov/geo) is an open-source platform created by the National Biotechnology Information Center of the United States (NCBI) to retrieve gene expression data. The GSE67311 dataset consisted of 142 whole blood samples from 67 patients with fibromyalgia syndrome and 75 healthy controls, and the results were published in 2016 by Jones et al. [15]. All subjects were genotyped using the GPL11532 Affymetrix Human Gene 1.1 ST Array. After downloading the raw gene expression data, it was standardized using a robust multiarray averaging (RMA) algorithm, and 142 samples were randomly divided into the training and test sets. The training set consisted of 95 samples for screening differential and characteristic genes. The test set

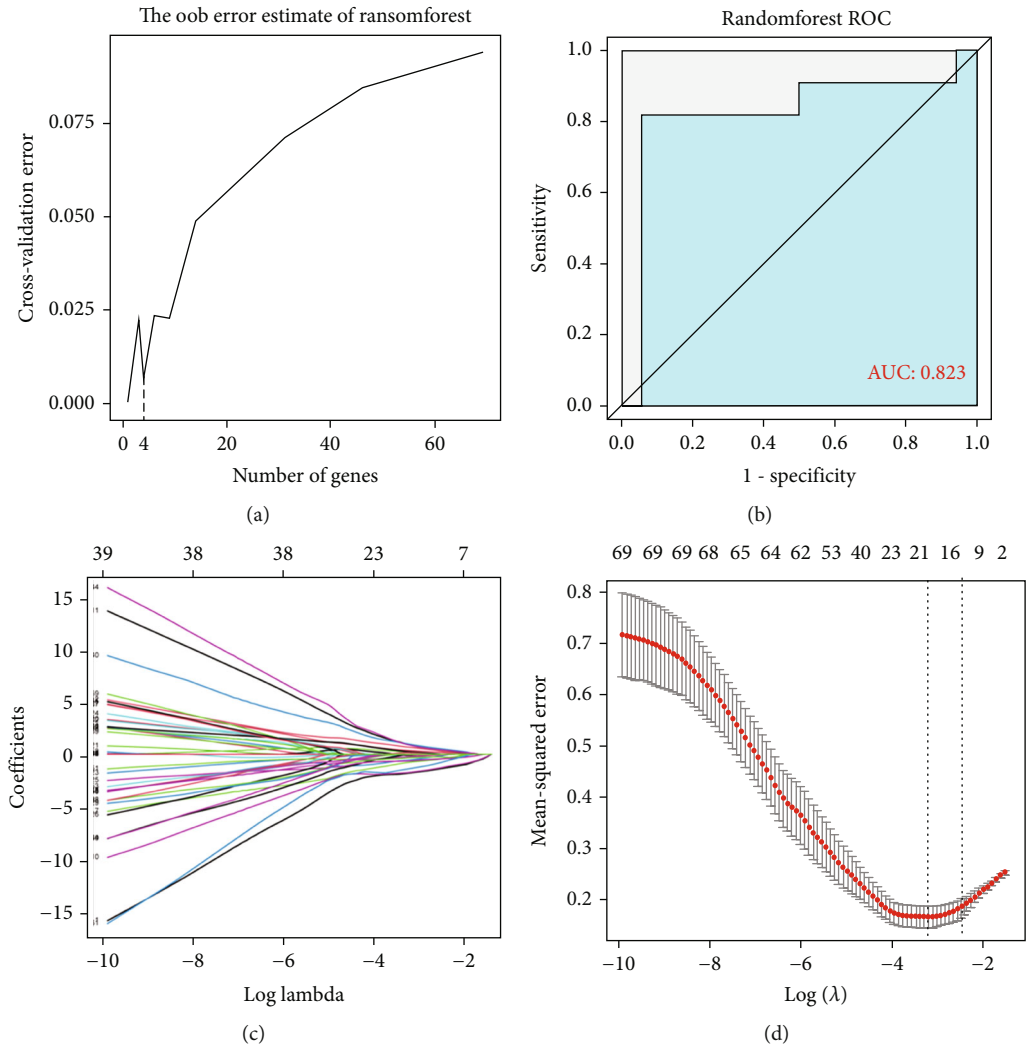

Figure 3: Diagnostic gene screening process. (a) The cross-validation curve of the relationship between model error and the number of genes used for fitting. (b) The ROC curve of signature genes is screened by a random forest algorithm. (c) LASSO coefficient profiles of the nineteen potential genes. (d) The partial likelihood deviation curve of the minimum number of signature genes.

had 47 samples for validating the analysis results. All statistical analyses were performed using the R software (version 3.6.3).

2.2. DEG Identification. After data were standardized, the "limma" package was used to identify DEGs between FM patients and healthy controls [16]. DEGs with $P < 0.05$ and $|\log_2 FC| > 0.2$ were considered statistically significant [17]. The volcano map of DEGs was drawn using the "ggplot2" package.

2.3. Functional Enrichment Analysis. The "clusterProfiler" package was used for GO and KEGG enrichment analyses to explore the potential biological functions of DEGs in patients and healthy controls [18]. GO terms include biological process (BP), cellular component (CC), and molecular function (MF). The significance threshold of GO analysis was set as an adjusted P value < 0.05, and KEGG analysis was set as P value < 0.05. The above analysis results are presented as a bar chart and bubble chart by the "ggplot2" package.

2.4. Screening and Verification of Diagnostic Markers. As a technical means to achieve artificial intelligence (AI), machine learning can automatically analyze existing data to obtain rules or models and use the guidelines to predict unknown data [19]. Here, we applied a computational method combining random forest (RF) and least absolute shrinkage and selection operator (LASSO) logistic regression algorithms to screen genetic biomarkers of FM and construct diagnostic models. We specifically used "glmnet" package for LASSO analysis and the "randomForest" package for random forest algorithm analysis [20, 21]. We obtained diagnostic marker genes that overlapped with LASSO and the random forest algorithm. The sensitivity and specificity of the diagnostic prediction model were analyzed by the receiver operating characteristic (ROC) curve and quantified by the area under ROC curve (AUC). Next,

we verified the test set and reserved the gene with AUC greater than 0.6 as the final diagnostic marker gene.

2.5. Evaluation of Immune Cell Subtype Distribution. CIBERSORT (http://CIBERSORT.stanford.edu/) was used to evaluate the proportion of 22 subtypes of immune cells in the human body, while the LM22 signature matrix was used to define 22 infiltrating immune cells components. After obtaining the immune cell infiltration matrix, the Wilcoxon test was used to screen different immune cell infiltration between FM patients and normal controls. $P < 0.05$ was considered statistically significant, and the results were presented in a boxplot. The correlations of 22 infiltrating immune cells were analyzed using the "corrplot" package [22].

2.6. Correlation Analysis between Diagnostic Biomarkers and Immune Cells. Spearman correlation test was used to analyze the correlation between the immune score of characteristic immune cells and the expression level of diagnostic marker genes. The results were visualized by the "ggplot2" package.

3. Results

3.1. Identification of DEGs. DEGs were shown in the volcano map (Figure 1). Compared with healthy controls, FM patients had 26 upregulated DEGs and 43 downregulated DEGs.

3.2. Functional Enrichment Analysis. The high-throughput data analysis allows us to obtain several candidate genes. To better understand the function of these genes, we used enrichment analysis, which reflects them as a whole. GO analysis results showed that DEGs were mainly related to defense response to the virus, regulation of viral genome replication, type I interferon (IFN) signaling pathway, and cellular response to type I IFN (Figures 2(a) and 2(b)). Furthermore, the KEGG enrichment analysis suggested that the map05167 pathways of herpes simplex virus 1 (HSV-1) infection might be the biological pathways altered in FM patients compared with healthy controls (Figures 2(c) and 2(d)).

3.3. Screening and Verification of Diagnostic Markers. We first used a random forest algorithm to identify 4 genes from DEGs as diagnostic markers of FM (Figure 3(a)) and made a ROC curve (Figure 3(b)). Nineteen DEGs were then screened by the LASSO regression algorithm (Figures 3(c) and 3(d)). The marker genes obtained by the two algorithms were overlapped to obtain 4 diagnostic characteristic genes, namely, AKAP12, CCR9, IL3RA, and RNF11. In order to further test the diagnostic efficacy of the above genes, test sets were used to verify them. ROC analysis was performed by the R software to predict the diagnostic effectiveness of biomarkers, and only genes with AUC > 0.6 were retained as the final marker genes. The results showed that AKAP12 (AUC = 0.628) and RNF11 (AUC = 0.663) had high diagnostic values. We combined genes and observed that AUC was also greater than 0.6 when CCR9 was combined with RNF11 (AUC = 0.643) and AKAP12 was combined with IL3RA (AUC = 0.617) (Figure 4).

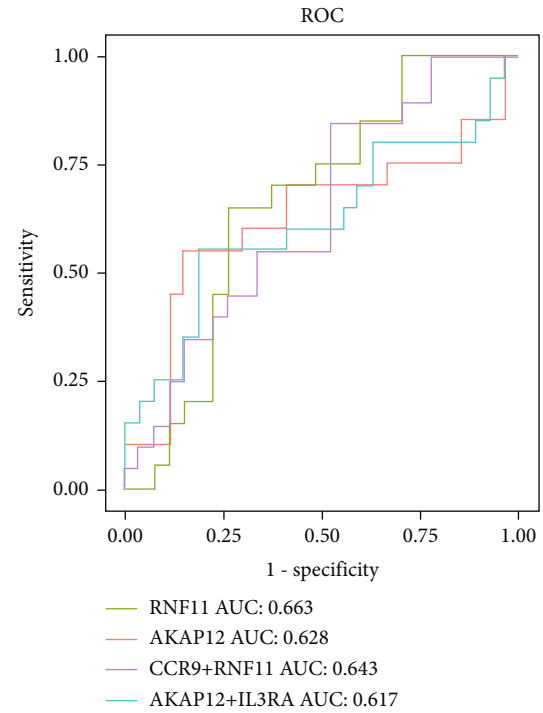

Figure 4: ROC curve to verify the diagnostic efficacy of candidate genes.

3.4. Immune Cell Infiltration in FM and Its Relationship with Diagnostic Markers. The correlation of 22 groups of immune cells in the blood of FM patients was first evaluated (Figure 5(a)). According to the results, M1 macrophages, activated mast cells, resting mast cells, plasma cells, regulatory T cells, M2 macrophages, activated dendritic cells, memory B cells, Th cells, activated NK cells, and resting dendritic cells had a significant positive correlation. Resting CD4 memory T cells and neutrophils had a significant negative correlation. The Wilcoxon test was then used to evaluate significant differences in immune cell infiltration in peripheral blood between FM patients and the control group. Figure 5(b) shows the different immune cell occupation in peripheral blood of FM patients and healthy controls. CD8+ T cells were significantly reduced in FM patients compared with the control group, confirming the importance of reducing this cell type in the FM immune microenvironment. Furthermore, the correlation among four effective biomarkers (AKAP12, CCR9, IL3RA, and RNF11) and one significantly differential immune cell (CD8+ T cells) is presented in Figure 6(a). Correlation analysis showed that AKAP12 was positively correlated with CD8+ T cells ($R = 0.33$, $P = 0.0012$), while RNF11 was negatively correlated with CD8+ T cells ($R = -0.34$, $P = 0.00066$) (Figures 6(b) and 6(c)).

4. Discussion

Fibromyalgia has been broadly described as a multifaceted disease, including autoimmune, infectious, and somatic disorders [23]. Due to the various symptoms and lack of early diagnostic indicators, FM patients are often only diagnosed

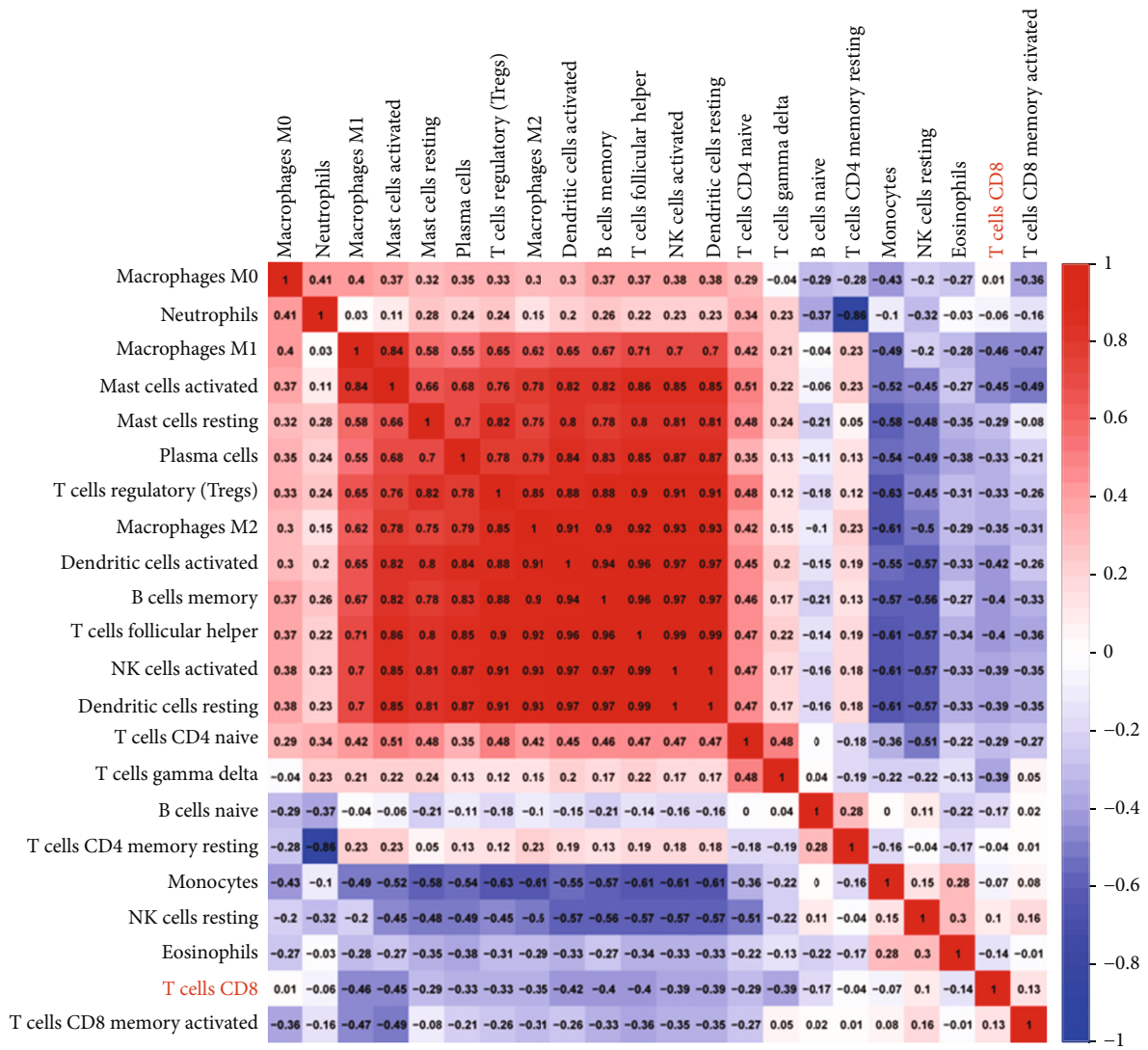

(a)

Figure 5: Continued.

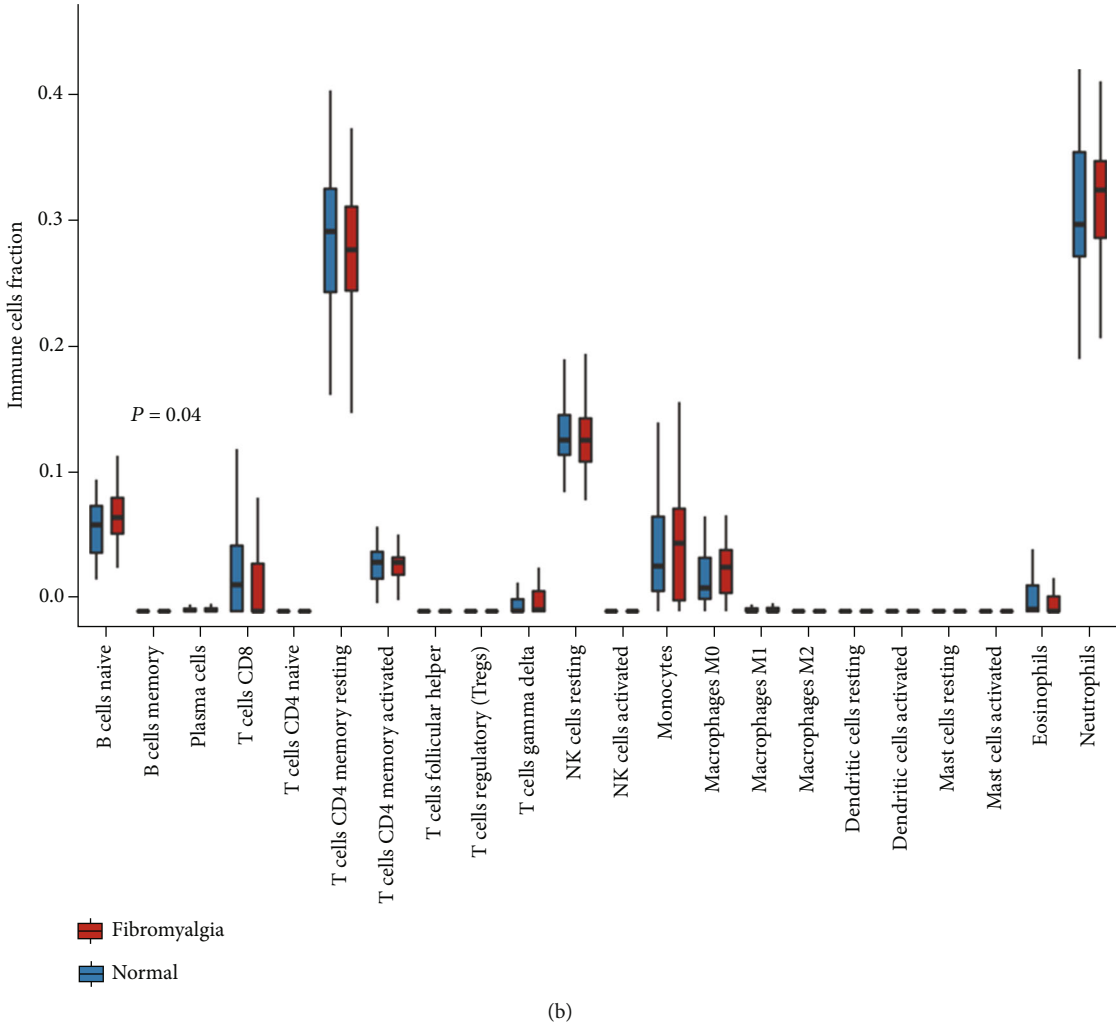

(b)

Figure 5: Immune cell infiltration. (a) The correlation of 22 immune cells in peripheral blood of patients with FM was evaluated. Red is positive, and blue is negative. (b) The box diagram shows the proportion of 22 groups of immune cells in the peripheral blood of FM patients and healthy persons.

after excluding other diseases, leading to late treatment. According to evidence, inflammation plays a role in fibromyalgia pathogenesis [24–26]. Research on suitable specific diagnostic markers and the infiltrating immune cell landscape identification helps consolidate the prognosis of FM patients. In this study, bioinformatics was used to screen molecular markers of FM. CIBERSORT analysis facilitated the analysis of immune cell infiltration patterns in the disease. We focused on identifying the diagnostic markers and exploring the role of immune cell infiltration in FM.

The FM gene expression dataset from the GEO database was downloaded and randomly divided into the training and test sets to select the optimal model. Under the differential expression threshold, 69 DEGs were identified. GO and KEGG analyses were performed on DEGs to decipher the underlying biological mechanisms contributing to FM progression. The results of GO analysis showed that DEGs were mainly involved in virus defense response and IFN signaling pathway. KEGG analysis showed that enriched pathways mainly involved the HSV-1 infection pathway. Sarzi-Puttini et al. evaluated the efficacy of an antiherpetic drug in combination with a COX-2 inhibitor (famciclovir + celecoxib, IMC-1) in FM patients in a 16-week double-blind, placebo-controlled trial conducted at 12 centers [2]. Compared with placebo, the IMC-1-treated patients had a significantly reduced FM-related pain, improved Patient's Global Impression of Change (PGIC) response rates, better self-reported function as measured by the Revised Fibromyalgia Impact Questionnaire (FIQ-R), and reduced fatigue as measured by the NIH Patient-Reported Outcomes Measurement Information System (PROMIS). In contrast, neither drug alone seemed to relieve symptoms of FM. Their results support the hypothesis that HSV infection may cause FM and are consistent with our analysis.

In order to improve the accuracy of the results, two independent machine learning algorithms (RF and LASSO logistic regression) were used to screen various variables and establish the optimal classification model. Finally, four

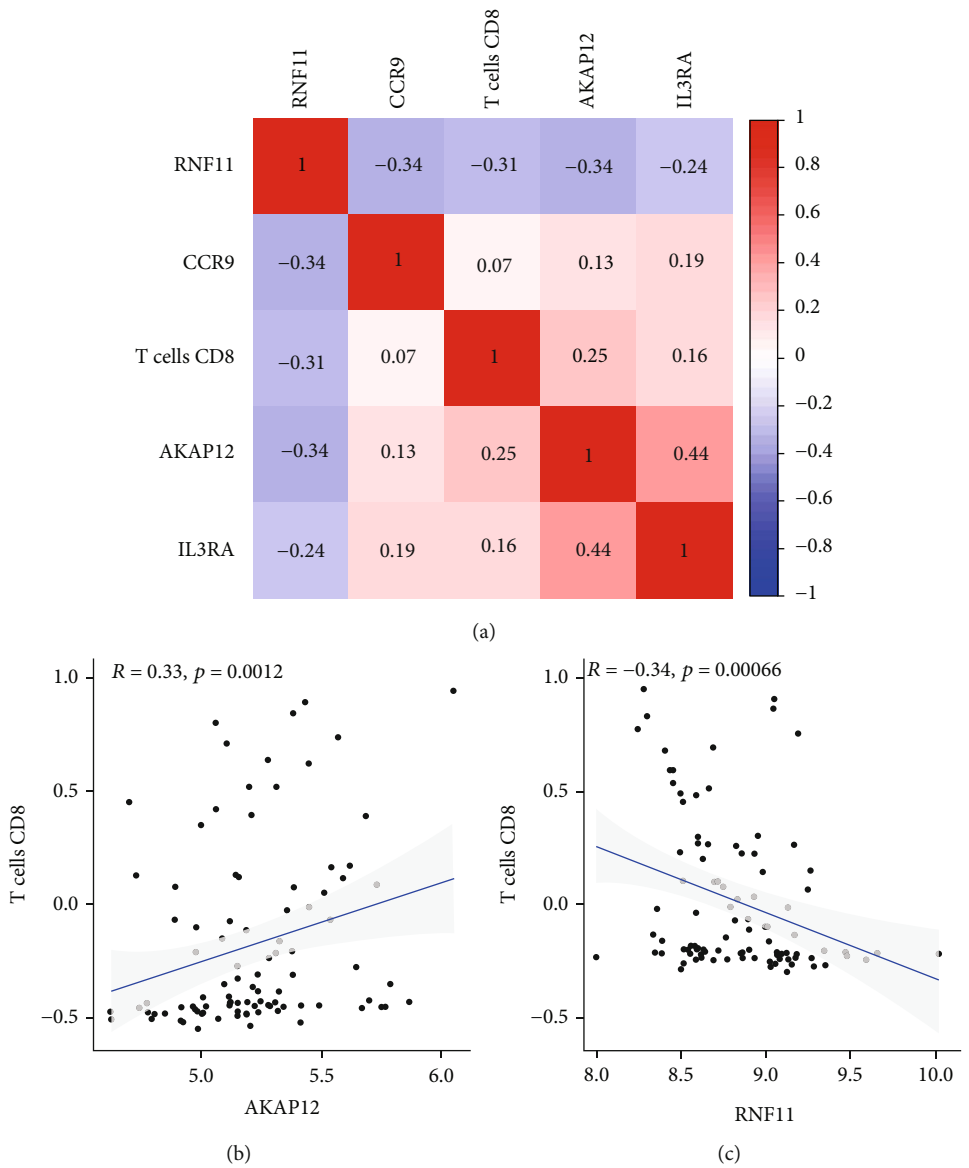

Figure 6: Correlation between diagnostic markers and differential immune cells in FM. (a) Correlation among 4 diagnostic biomarkers and CD8+ T cells. (b) Correlation between CD8+ T cells and AKAP12. (c) Correlation between CD8+ T cells and RNF11. $P < 0.01$.

DEGs (AKAP12, CCR9, IL3RA, and RNF11) were identified and verified by the test set as diagnostic markers of FM. The validation of AKAP12 and RNF11 seems to be reliable, indicating that the strategy for modeling is feasible. According to previous reports, RING finger protein 11 (RNF11), a 154 amino acid protein belonging to the E3 ubiquitin ligase family, is strongly associated with human breast cancer and hepatocellular carcinoma [27–29]. As a posttranslational modification of proteins, ubiquitination controls almost all cellular processes, explaining the diversity of ubiquitination in different cellular pathways. Ubiquitination requires sequence action of E1 ubiquitin-activating enzyme, E2 ubiquitin-conjugating enzyme, and E3 ubiquitin-protein ligase to bind the ubiquitin chain to the target protein, resulting in protein degradation or protein stabilization [30]. However, the mechanism used by RNF11 to regulate protein ubiquitination remains unclear because the RNF11 promotes ubiquitination in some cases but inhibits substrate ubiquitination in other instances [31]. Hsu et al. conducted a metabolomic and proteomic analysis of serum samples from patients with FM, and the results showed that FM patients had metabolic disorders and produced numerous NF-κB-dependent cytokines [32]. RNF11 has been reported as a negative regulator of NF-κB and Jun N-terminal kinase (JNK) signaling pathways [33]. Another study reported that RNF11 negatively regulates the inflammatory signaling pathway of microglia, which may be a potential target for regulating neuroinflammatory responses [34]. RNF11 upregulation may protect neurons from nonregulated inflammation [35]. In our study, the increased expression of RNF11 in peripheral blood cells of FM patients might have upregulated inflammation.

AKAP12, an anchor gene that mediates the subcellular compartmentation of protein kinase A (PKA) and protein kinase C (PKC), was initially identified as a molecule associated with poor prognosis in myasthenia gravis [36]. Subsequently, AKAP12 was found to inhibit malignant tumor metastasis and progression, regulate the formation of blood-brain and blood-retinal barriers, and resensitize β2-adrenergic pain receptors [37]. Since sleep dysfunction has been shown to reduce descending spinal inhibition of pain signals [38], a significant difference in the frequency of Gly16Arg polymorphism in the β2-adrenergic receptor gene was observed in FM patients with varying degrees of sleep disorders compared to the controls [39]. AKAP12 expression may be negatively correlated with estrogen levels, and in granulosa cells with estrogen receptor- (ER-) β deletion, AKAP12 is upregulated after FSH treatment [40]. In our study, AKAP12 was downregulated in FM patients, which seems to confirm that FM prevalence is higher in females than males. However, big cohort studies are still needed to confirm the diagnostic value of AKAP12 and RNF11 in peripheral blood.

Previous works of literature are inconclusive on the role of immune cell infiltration in FM development and maintenance. Consequently, this investigation used CIBERSORT online tool to evaluate immune infiltration of FM comprehensively. CD8 + T cells were significantly downregulated in FM patients compared to the control group. In addition, the correlation analysis showed that CD8 + T cells were positively correlated with RNF11 and AKAP12. Nishikai et al. reported antibodies against 68/48 kDA protein in some patients with chronic fatigue syndrome and primary FM, which might confirm FM as an immune-mediated disease [41]. The coexistence of endometriosis and FM is associated with a high burden of autoimmune diseases, depression, and anxiety [42].

Further, B or T cell-mediated cross-reactive responses may occur in chronic pain and systemic inflammation, but recent research on the association between FM and adaptive immunity seems to focus on CD4 + T cells [43]. However, serum CD8 + T cell levels were lower in chronic pain patients than in healthy subjects [44]. A study investigating the effects of pain and stress on lymphocyte count and lymphocyte subsets showed that the number of cytotoxic CD8+ lymphocytes was significantly reduced in patients with chronic pain, while the CD4/CD8 ratio was not significantly changed. Posttraumatic stress score was negatively correlated with the number of CD8 + T cells in FM patients [45]. Therefore, the immune system is no longer a bystander in the occurrence and maintenance of FM. The pathophysiological mechanism of FM and the formation of general inflammation may also involve adaptive immune cells, especially T cells, which need further study.

We innovatively adopted machine learning methods based on current sample GitHub to screen and verify the diagnostic markers of FM, which need to further improve the predictive algorithms. CIBERSORT was used to analyze the infiltration of immune cells in the peripheral blood of FM. However, we acknowledge that this study has some limitations. Firstly, our analysis is secondary mining of previously published data sets, and different conclusions may be drawn due to the differences in analytical ideas and perspectives. Secondly, this study lacks relevant clinical information and self-sequencing test, which will be the direction of our future clinical research on FM. Thirdly, the CIBERSORT algorithm is only based on limited transcriptome data, and the distribution of some low abundance expressed immune cell subsets in FM has not been fully revealed. As a result, our research results are not only consistent with some previous studies but also contradictory to some of them. The limitations of this study require further laboratory validation.

5. Conclusion

In summary, bioinformatics analysis confirmed that peripheral blood RNF11 and AKAP12 might be used as diagnostic markers of FM. In addition, CD8 + T lymphocytes might play a role in the occurrence and development of FM and are significantly correlated with RNF11 and AKAP12. Therefore, this study may provide a new perspective on the diagnosis of FM, especially from the aspects of immune cells and immune regulation.

Data Availability

All data, models, and code generated or used during the study appear in the submitted article.

Ethical Approval

The studies involving human participants were reviewed and approved by the ethics committee of the Qilu Hospital of Shandong University.

Consent

Written informed consent was obtained from the individual for the publication of any potentially identifiable images or data included in this article. The participants provided their written informed consent to participate in this study.

Conflicts of Interest

The authors declare that the research was conducted in the absence of any commercial or financial relationships that could be construed as a potential conflict of interest.

Authors' Contributions

Tao Meng and Kangda Zhang were responsible for the conceptualization. Xiaowen Lin was responsible for the methodology. Kangda Zhang was responsible for the software. Tao Meng, Xiaowen Lin, and Kangda Zhang validated the manuscript. Xiaowen Lin was responsible for the formal analysis. Kangda Zhang was responsible for the investigation. Kangda Zhang was responsible for the resources. Xiaowen Lin was responsible for the data curation. Xiaowen Lin was responsible for the writing—original draft preparation. Tao Meng was responsible for the writing—review and editing. Tao Meng was responsible for the visualization. Tao Meng

supervised the manuscript. Xiawen Lin was responsible for the project administration. Tao Meng was responsible for the funding acquisition. All authors have read and agreed to the published version of the manuscript.

Acknowledgments

This research was supported by the National Natural Science Foundation of China (81900394).

References

[1] M. J. Bair and E. E. Krebs, "Fibromyalgia," *Annals of internal medicine*, vol. 172, no. 5, pp. Itc33–itc48, 2020.

[2] P. Sarzi-Puttini, V. Giorgi, D. Marotto, and F. Atzeni, "Fibromyalgia: an update on clinical characteristics, aetiopathogenesis and treatment," *Nature reviews Rheumatology*, vol. 16, no. 11, pp. 645–660, 2020.

[3] D. J. Clauw, "Fibromyalgia," *Journal of the American Medical Association*, vol. 311, no. 15, pp. 1547–1555, 2014.

[4] F. Wolfe, H. A. Smythe, M. B. Yunus et al., "The American College of Rheumatology 1990 criteria for the classification of fibromyalgia," *Arthritis and Rheumatism*, vol. 33, no. 2, pp. 160–172, 1990.

[5] E. H. Choy, "The role of sleep in pain and fibromyalgia," *Nature reviews Rheumatology*, vol. 11, no. 9, pp. 513–520, 2015.

[6] F. Wolfe, D. J. Clauw, M. A. Fitzcharles et al., "The American College of Rheumatology preliminary diagnostic criteria for fibromyalgia and measurement of symptom severity," *Arthritis care & research*, vol. 62, no. 5, pp. 600–610, 2010.

[7] M. E. Maffei, "Fibromyalgia: recent advances in diagnosis, classification, pharmacotherapy and alternative remedies," *International journal of molecular sciences*, vol. 21, no. 21, p. 7877, 2020.

[8] M. Di Franco, C. Iannuccelli, and G. Valesini, "Neuroendocrine immunology of fibromyalgia," *Annals of the New York Academy of Sciences*, vol. 1193, no. 1, pp. 84–90, 2010.

[9] V. A. Ryabkova, L. P. Churilov, and Y. Shoenfeld, "Neuroimmunology: what role for autoimmunity, neuroinflammation, and small fiber neuropathy in fibromyalgia, chronic fatigue syndrome, and adverse events after human papillomavirus vaccination?," *International journal of molecular sciences*, vol. 20, no. 20, p. 5164, 2019.

[10] W. Raffaeli, V. Malafoglia, A. Bonci et al., "Identification of MOR-positive B cell as possible innovative biomarker (Mu Lympho-Marker) for chronic pain diagnosis in patients with fibromyalgia and osteoarthritis diseases," *International journal of molecular sciences*, vol. 21, no. 4, p. 1499, 2020.

[11] Y. J. Deng, E. H. Ren, W. H. Yuan, G. Z. Zhang, Z. L. Wu, and Q. Q. Xie, "GRB10 and E2F3 as diagnostic markers of osteoarthritis and their correlation with immune infiltration," *Diagnostics*, vol. 10, no. 3, p. 171, 2020.

[12] X. Zhao, L. Zhang, J. Wang et al., "Identification of key biomarkers and immune infiltration in systemic lupus erythematosus by integrated bioinformatics analysis," *Journal of Translational Medicine*, vol. 19, no. 1, p. 35, 2021.

[13] S. Zhou, H. Lu, and M. Xiong, "Identifying immune cell infiltration and effective diagnostic biomarkers in rheumatoid arthritis by bioinformatics analysis," *Frontiers in immunology*, vol. 12, p. 726747, 2021.

[14] A. M. Newman, C. L. Liu, M. R. Green et al., "Robust enumeration of cell subsets from tissue expression profiles," *Nature Methods*, vol. 12, no. 5, pp. 453–457, 2015.

[15] K. D. Jones, T. Gelbart, T. C. Whisenant et al., "Genome-wide expression profiling in the peripheral blood of patients with fibromyalgia," *Clinical and experimental rheumatology*, vol. 34, 2 Suppl 96, pp. S89–S98, 2016.

[16] M. E. Ritchie, B. Phipson, D. Wu et al., "limma powers differential expression analyses for RNA-sequencing and microarray studies," *Nucleic acids research*, vol. 43, no. 7, p. e47, 2015.

[17] Y. Qiu, T. J. Zhang, L. B. Meng, X. T. Cheng, and Z. Hua, "Bioinformatics analysis of gene and microRNA targets for fibromyalgia," *Clinical and experimental rheumatology*, vol. 39, no. 1, pp. 21–31, 2021.

[18] G. Yu, L. G. Wang, Y. Han, and Q. Y. He, "clusterProfiler: an R package for comparing biological themes among gene clusters," *Omics: a journal of integrative biology*, vol. 16, no. 5, pp. 284–287, 2012.

[19] E. Kawakami, J. Tabata, N. Yanaihara et al., "Application of artificial intelligence for preoperative diagnostic and prognostic prediction in epithelial ovarian cancer based on blood biomarkers," *Clinical cancer research*, vol. 25, no. 10, pp. 3006–3015, 2019.

[20] J. Friedman, T. Hastie, and R. Tibshirani, "Regularization paths for generalized linear models via coordinate descent," *Journal of statistical software*, vol. 33, no. 1, pp. 1–22, 2010.

[21] R. Díaz-Uriarte and S. Alvarez de Andrés, "Gene selection and classification of microarray data using random forest," *BMC bioinformatics*, vol. 7, no. 1, p. 3, 2006.

[22] A. M. Newman, C. B. Steen, C. L. Liu et al., "Determining cell type abundance and expression from bulk tissues with digital cytometry," *Nature Biotechnology*, vol. 37, no. 7, pp. 773–782, 2019.

[23] A. T. Borchers and M. E. Gershwin, "Fibromyalgia: a critical and comprehensive review," *Clinical reviews in allergy & immunology*, vol. 49, no. 2, pp. 100–151, 2015.

[24] B. I. Coskun, "Role of inflammation in the pathogenesis and treatment of fibromyalgia," *Rheumatology international*, vol. 39, no. 5, pp. 781–791, 2019.

[25] S. Metyas, T. Rezk, D. Arkfeld, and T. Leptich, "Autoinflammation and immunomodulation in inflammatory fibromyalgia syndrome- a review," *Current rheumatology reviews*, vol. 13, no. 2, pp. 98–102, 2017.

[26] G. Littlejohn and E. Guymer, "Neurogenic inflammation in fibromyalgia," *Seminars in Immunopathology*, vol. 40, no. 3, pp. 291–300, 2018.

[27] A. Burger, Y. Amemiya, R. Kitching, and A. K. Seth, "Novel RING E3 ubiquitin ligases in breast cancer," *Neoplasia*, vol. 8, no. 8, pp. 689–695, 2006.

[28] V. Subramaniam, H. Li, M. Wong et al., "The RING-H2 protein RNF11 is overexpressed in breast cancer and is a target of Smurf2 E3 ligase," *British journal of cancer*, vol. 89, no. 8, pp. 1538–1544, 2003.

[29] D. Rao, S. Guan, J. Huang, Q. Chang, and S. Duan, "miR-425-5p acts as a molecular marker and promoted proliferation, migration by targeting RNF11 in hepatocellular carcinoma," *BioMed research international*, vol. 2020, Article ID 6530973, 11 pages, 2020.

[30] D. Komander and M. Rape, "The ubiquitin code," *Annual Review of Biochemistry*, vol. 81, no. 1, pp. 203–229, 2012.

[31] R. Budhidarmo, J. Zhu, A. J. Middleton, and C. L. Day, "The RING domain of RING finger 11 (RNF11) protein binds

Ubc13 and inhibits formation of polyubiquitin chains," *FEBS letters*, vol. 592, no. 8, pp. 1434–1444, 2018.

[32] W. H. Hsu, D. S. Han, W. C. Ku, Y. M. Chao, C. C. Chen, and Y. L. Lin, "Metabolomic and proteomic characterization of sng and pain phenotypes in fibromyalgia," *European journal of pain*, vol. 26, no. 2, pp. 445–462, 2022.

[33] N. Shembade, K. Parvatiyar, N. S. Harhaj, and E. W. Harhaj, "The ubiquitin-editing enzyme A20 requires RNF11 to down-regulate NF-kappaB signalling," *The EMBO journal*, vol. 28, no. 5, pp. 513–522, 2009.

[34] N. V. Dalal, E. L. Pranski, M. G. Tansey, J. J. Lah, A. I. Levey, and R. S. Betarbet, "RNF11 modulates microglia activation through NF-κB signalling cascade," *Neuroscience Letters*, vol. 528, no. 2, pp. 174–179, 2012.

[35] A. Mattioni, L. Castagnoli, and E. Santonico, "RNF11 at the crossroads of protein ubiquitination," *Biomolecules*, vol. 10, no. 11, p. 1538, 2020.

[36] T. Gordon, B. Grove, J. C. Loftus et al., "Molecular cloning and preliminary characterization of a novel cytoplasmic antigen recognized by myasthenia gravis sera," *The Journal of clinical investigation*, vol. 90, no. 3, pp. 992–999, 1992.

[37] I. H. Gelman, "Emerging roles for SSeCKS/Gravin/AKAP12 in the control of cell proliferation, cancer malignancy, and barriergenesis," *Genes & cancer*, vol. 1, no. 11, pp. 1147–1156, 2010.

[38] M. T. Smith, R. R. Edwards, U. D. McCann, and J. A. Haythornthwaite, "The effects of sleep deprivation on pain inhibition and spontaneous pain in women," *Sleep*, vol. 30, no. 4, pp. 494–505, 2007.

[39] Y. Xiao, W. He, and I. J. Russell, "Genetic polymorphisms of the beta2-adrenergic receptor relate to guanosine protein-coupled stimulator receptor dysfunction in fibromyalgia syndrome," *The Journal of rheumatology*, vol. 38, no. 6, pp. 1095–1103, 2011.

[40] A. K. Binder, K. F. Rodriguez, K. J. Hamilton, P. S. Stockton, C. E. Reed, and K. S. Korach, "The absence of ER-β results in altered gene expression in ovarian granulosa cells isolated from in vivo preovulatory follicles," *Endocrinology*, vol. 154, no. 6, pp. 2174–2187, 2013.

[41] M. Nishikai, S. Tomomatsu, R. W. Hankins et al., "Autoantibodies to a 68/48 kDa protein in chronic fatigue syndrome and primary fibromyalgia: a possible marker for hypersomnia and cognitive disorders," *Rheumatology*, vol. 40, no. 7, pp. 806–810, 2001.

[42] H. Greenbaum, C. Weil, G. Chodick, V. Shalev, and V. H. Eisenberg, "Evidence for an association between endometriosis, fibromyalgia, and autoimmune diseases," *American journal of reproductive immunology*, vol. 81, no. 4, article e13095, 2019.

[43] G. Banfi, M. Diani, P. D. Pigatto, and E. Reali, "T cell subpopulations in the physiopathology of fibromyalgia: evidence and perspectives," *International journal of molecular sciences*, vol. 21, no. 4, p. 1186, 2020.

[44] C. Ye, G. Xiao, J. Xu et al., "Differential expression of immune factor between patients with chronic prostatitis/chronic pelvic pain syndrome and the healthy volunteers," *International urology and nephrology*, vol. 50, no. 3, pp. 395–399, 2018.

[45] I. Kaufmann, C. Eisner, P. Richter et al., "Lymphocyte subsets and the role of TH1/TH2 balance in stressed chronic pain patients," *Neuroimmunomodulation*, vol. 14, no. 5, pp. 272–280, 2008.

Hindawi
Oxidative Medicine and Cellular Longevity
Volume 2022, Article ID 5413035, 11 pages
https://doi.org/10.1155/2022/5413035

Research Article

Expression of eIF4E Gene in Glioma and Its Sensitivity to Oxidative Stress

Jian Liang,[1] Yaoqiang Yang,[2] Xing Li,[1,3] Guangmou Cai,[1] Jianxuan Cao,[1] and Bo Zhang[4,5]

[1]*Department of Neurosurgery, Shenzhen People's Hospital (The Second Clinical Medical College, Jinan University; The First Affiliated Hospital, Southern University of Science and Technology), Shenzhen, Guangdong 518020, China*
[2]*First Clinical Medical College of Jinan University, Jinan University, Guangzhou 510630, China*
[3]*School of Medicine, Southern University of Science and Technology, Shenzhen, Guangdong 518055, China*
[4]*Department of Neurosurgery, The Shenzhen Luohu Hospital Group, The Third Affiliated Hospital of Shenzhen University, Shenzhen 518001, China*
[5]*Neurosurgery Department of School of Medicine, The Chinese University of Hong Kong, Shenzhen 518172, China*

Correspondence should be addressed to Bo Zhang; zhang.bo@szhospital.com

Received 21 July 2022; Accepted 13 September 2022; Published 3 October 2022

Academic Editor: Shao Liang

Objective. Increased expression of eIF4E has been observed in various cancers, which makes eIF4E an attractive target of anticancer drugs. This study mainly discussed eIF4E gene expression in glioma and its sensitivity to oxidative stress (OS). *Methods*. Relevant data from The Cancer Genome Atlas (TCGA) database regarding eIF4E gene expression and its prognostic significance in glioma samples were analyzed. Additionally, we measured eIF4E at mRNA and protein levels in clinical samples collected between July 2019 and September 2021, as well as glioma cell strains. U251 cells cultured in vitro were treated with OS injury induced by hydrogen peroxide (H_2O_2) and then transfected with si-eIF4E to determine changes in cell multiplication, invasiveness, and migration capacities as well as apoptosis rate. ELISA quantified cell malondialdehyde (MDA), superoxide dismutase (SOD), and glutathione peroxidase (GSH-Px) concentrations, and flow cytometry measured reactive oxygen species (ROS) level. *Results*. In glioma samples from the TCGA database, eIF4E showed obviously elevated levels in LGG and GBM patients, which was usually associated with adverse patient prognosis ($P < 0.05$). eIF4E was also upregulated in glioma cell strains than in HBE cells. In comparison with the blank control group, transfection of si-eIF4E statistically suppressed the capacity of U251 cells to proliferate, invade and migrate, and enhance apoptosis rate, while reducing SOD and GSH-Px and increasing MDA and ROS. In addition, H_2O_2 induced the upregulation of eIF4E in U251 cells. H_2O_2 + si-eIF4E exhibited reduced multiplication and number of clone cell formation, invasion, and migration of U251 cells, as well as increased apoptosis rate than H_2O_2 + si-NC group. *Conclusions*. eIF4E is highly expressed in glioma. Knocking down eIF4E can effectively inhibit the capacity of U251 to proliferate, invade and migrate, and significantly increase apoptosis. In addition, eIF4E knock-down is able to lower OS reaction under H_2O_2 inducement and enhance U251 cells' sensitivity to OS.

1. Introduction

Glioma, an aggressive primary cerebral tumor most frequently occurring in the central nervous system, accounts for about four-fifths of primary malignant cerebral tumors and is the major inducement of death in children and adults [1, 2]. Although the molecular mechanisms underlying the occurrence of glioma have been gradually revealed over the years and innovative therapeutic strategies have been proposed, no successful clinical methodology has been found [3, 4]. Improved survival and quality of life have been realized, attributing to advances in molecular and genetic technology and the

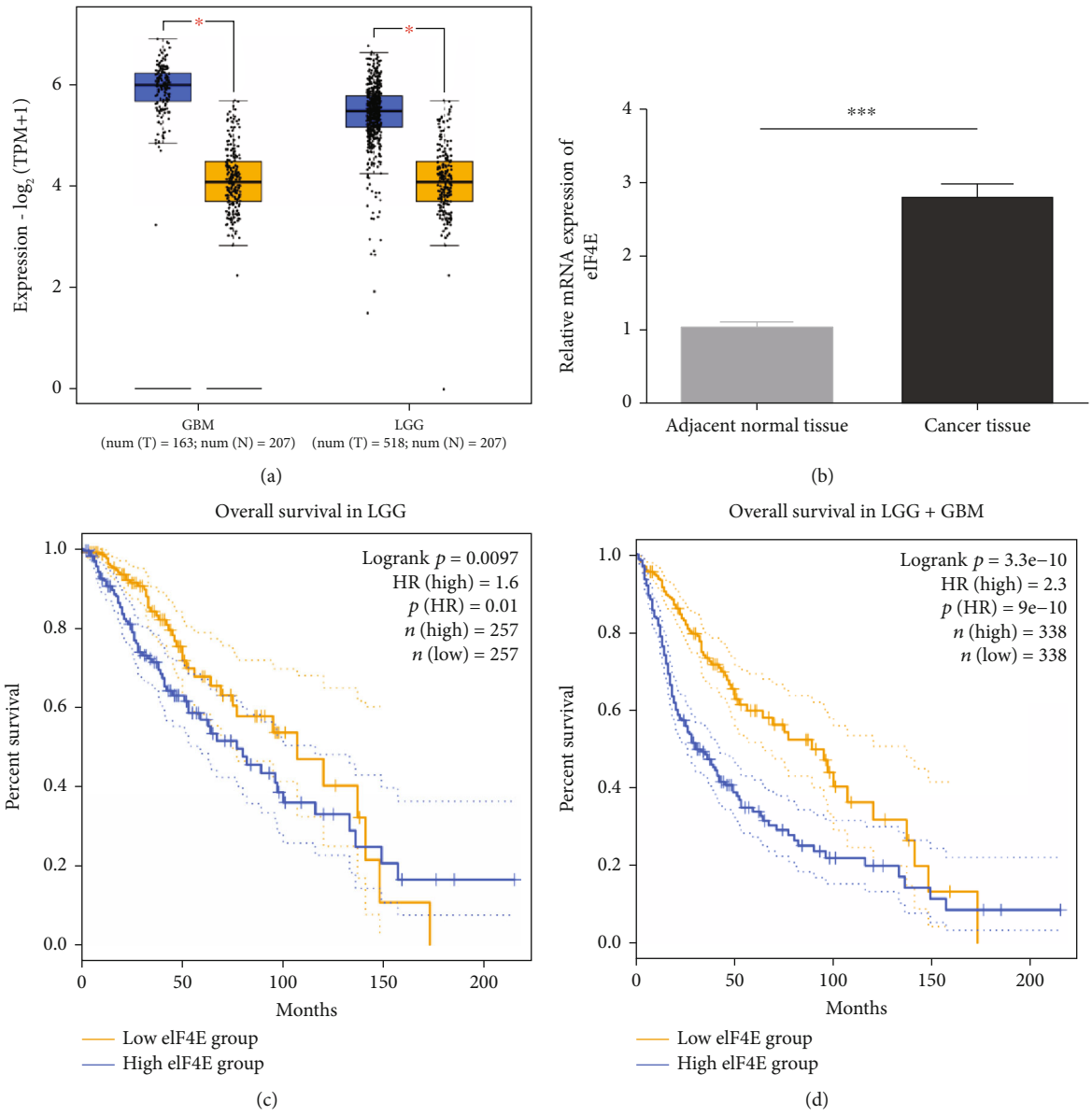

Figure 1: Expression profiling and prognostic significance of eIF4E in glioma patients. (a: eIF4E expression in LGG and GBM patients. b: eIF4E expression in clinical glioma samples. c: Survival analysis of LGG patients' eIF4E expression levels. d: Survival analysis of LGG and GBM patients' eIF4E expression levels; $*P < 0.05$, $***P < 0.001$.).

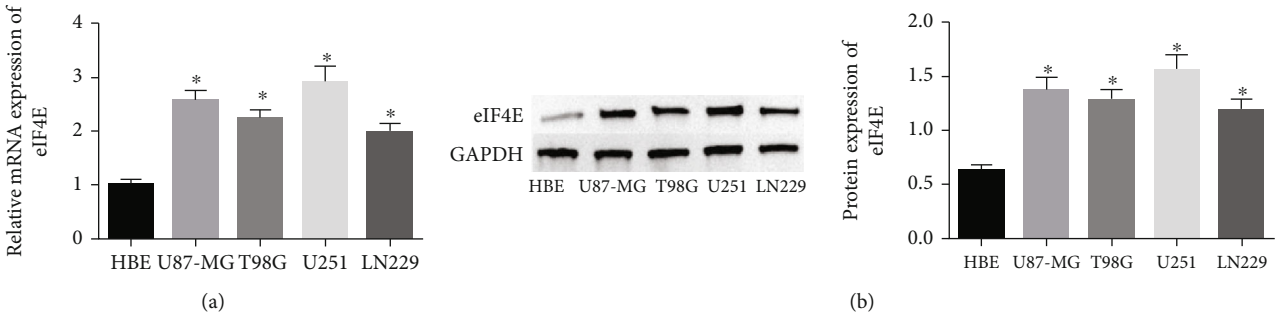

Figure 2: eIF4E expression in glioma cells. (a: eIF4E mRNA expression in glioma cells by qRT-PCR. b: eIF4E protein in glioma cells by Western blot; $*P < 0.05$ *vs* HBE cells.).

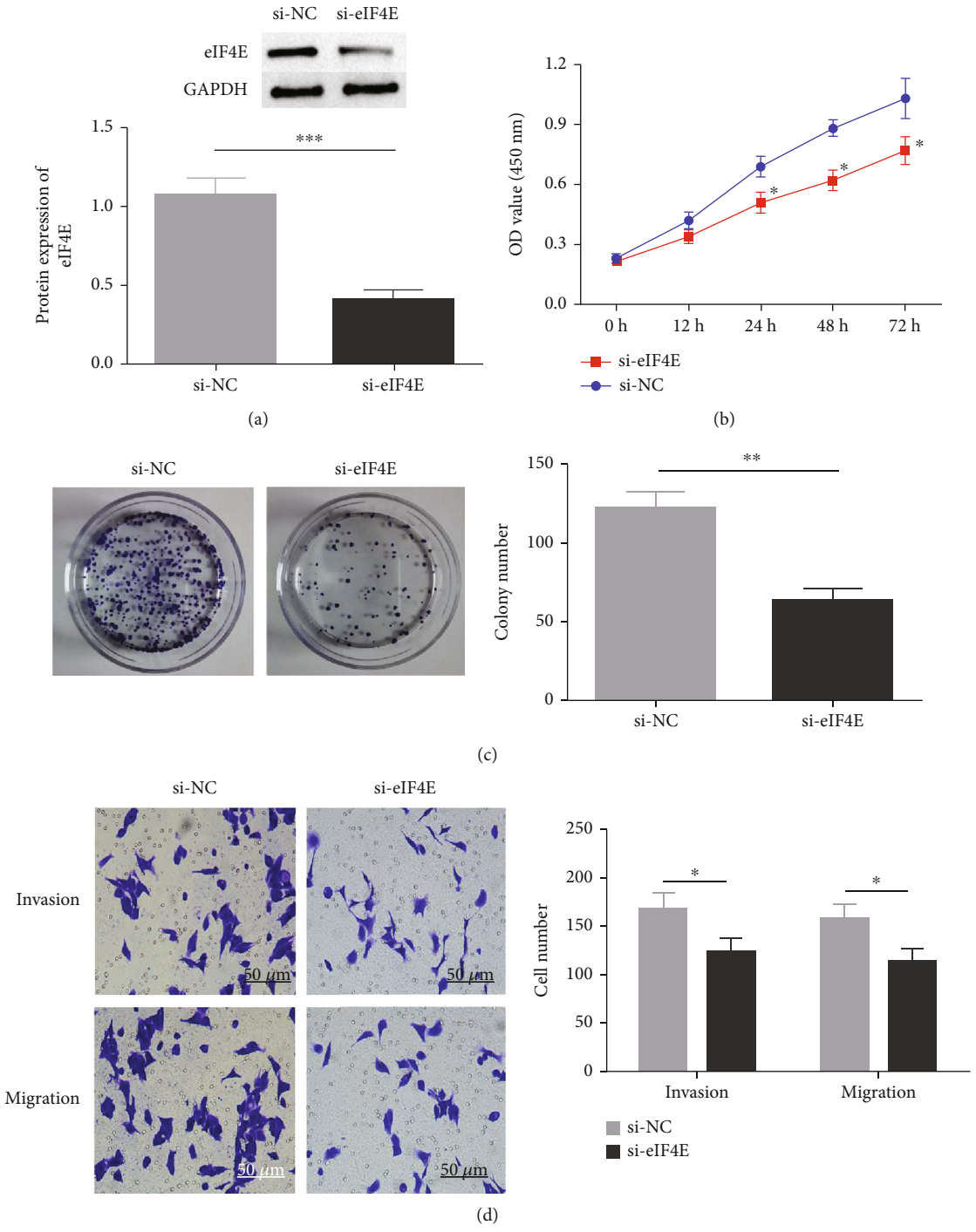

Figure 3: Continued.

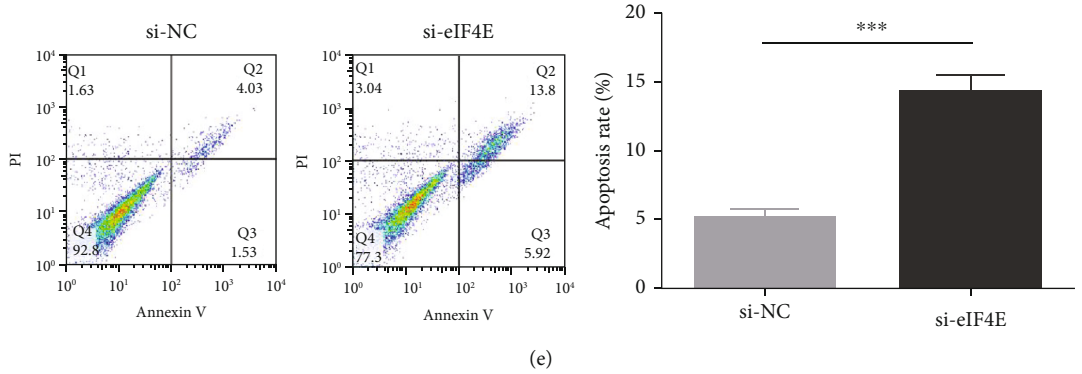

Figure 3: Impact of eIF4E knock-out on U251 cell biological function. (a: eIF4E protein expression. b: Cell proliferation by CCK-8 assay. c: Cell clone number. d: Invading and migrating cell number. e: Apoptosis rate; $*P < 0.05$, $**P < 0.01$, $*** P < 0.001$.).

understanding of physiological and biochemical pathways of the disease [5, 6]. However, the overall survival of glioma patients is merely 12–15 months [7, 8].

The uncontrolled reactive oxygen species (ROS) production and the products produced by their interactions with biomolecules and cells have contributed to several pathological etiologies, among which cancer is the most reported one [9–11]. Oxidative stress (OS) and ROS are closely related to cancer genesis and progression. OS refers to the relative ROS excess compared to antioxidants [12]. Carcinoma cells exhibit aberrant redox homeostasis, while ROS is tumor-promoting and high-level ROS is cytotoxic [13]. To be specific, there is high ROS production during the hyperproliferation of tumor cells, but the cells get adapted to grow in a reduced state where this oxidation load pushes the redox balance away. Tumor cells optimize ROS-driven proliferation by increasing their antioxidant status while avoiding senescence, apoptosis, or ferroptosis triggered by ROS thresholds [14, 15]. Over the past few decades, antioxidant molecules have been recognized as one of the most effective alternative and complementary therapies for diseases, combining treatment with prevention [16]. Therefore, we believe that based on this, enhancing the sensitivity of cancer cells to OS may improve the therapeutic effect of OS inducers.

Translation control, which plays a vital part in regulating gene expression in eukaryotes, influences various crucial cell processes such as differentiation, multiplication, and apoptosis. In most cases, translation control takes place in the initial step of ribosome recruitment into mRNA [17]. As a part of the eIF4F complex, the eucaryotic translation initiation factor 4E (eIF4E) first establishes interactions with mRNAs to promote the 40S ribosome subunit recruitment [18]. eIF4E is essential in a wide spectrum of human tumors, including carcinomas of the breast [19], head and neck [20], urinary bladder [21], and cervix [22]. eIF4E overexpression or knockout provides clues for its functional significance in tumorigenesis. Studies have shown that knocking down eIF4E can inhibit cancer cell proliferation and angiogenesis [23, 24]. In addition, increased eIF4E can lead to drug resistance to multiple chemotherapeutic drugs. Moreover, the combined use of eIF4E-silencing chemotherapy enhanced sensitivity to chemotherapeutics (paclitaxel, cisplatin, adriamycin, docetaxel, etc.) [25–27]. Truitt et al. found that the dose of eIF4E in mice is crucial for the translation of mRNAs that regulate ROS, the promotion of in vivo transformation, and the survival of cancer cells [28]. In addition to playing a part in translation, eIF4E can also modulate gene subsets related to key stress reactions in animals, including detoxifying ROS for normal cell function and controlling OS [29].

However, there are few studies investigating eIF4E expression and revealing its potential role in glioma. Thus, the motivation and novelty of this study are to demonstrate eIF4E overexpression and clarify the biological function of eIF4E under OS in glioma cells. In addition, this study aims to explore eIF4E gene expression in glioma and its sensitivity to OS.

2. Data and Methods

2.1. Database Analysis and Clinical Tissue Samples. eIF4E mRNA levels were analyzed with 163 GBM samples, 518 LGG samples, and 207 normal counterparts retrieved from the Gene Expression Profiling Interactive Analysis 2 (GEPIA2; URL: http://gepia2.cancer-pku.cn/#index).

In addition, clinical tissue (carcinoma tissues and adjacent counterparts) samples were collected from 36 pathologically confirmed glioma patients (age: 29–71, mean: 40.7 ± 13.8) presented to our hospital between July 2019 and September 2021. All cases enrolled were treatment-naive without any preoperative radiotherapy, chemotherapy, or biological therapy, with their specimens stored in −196°C liquid nitrogen. The hospital ethics committee approved this research, and all patients signed an informed consent form authorizing the use of their tissue specimens.

2.2. Cell Culture. Ordered from Shanghai Cell Bank, Chinese Academy of Sciences, human glioma cells (U87-MG, T98G, U251, and LN229) and human brain astrocytes HEB were all immersed in Dulbecco's modified Eagle's medium (DMEM, Gibco, USA) + 10% fetal bovine serum (FBS, Gibco, USA) + 100 U/mL penicillin + 100 μg/mL streptomycin for routine culture in an incubator under the conditions of 37°C and 5% CO_2, except that U87-MG, T98G, U251, and

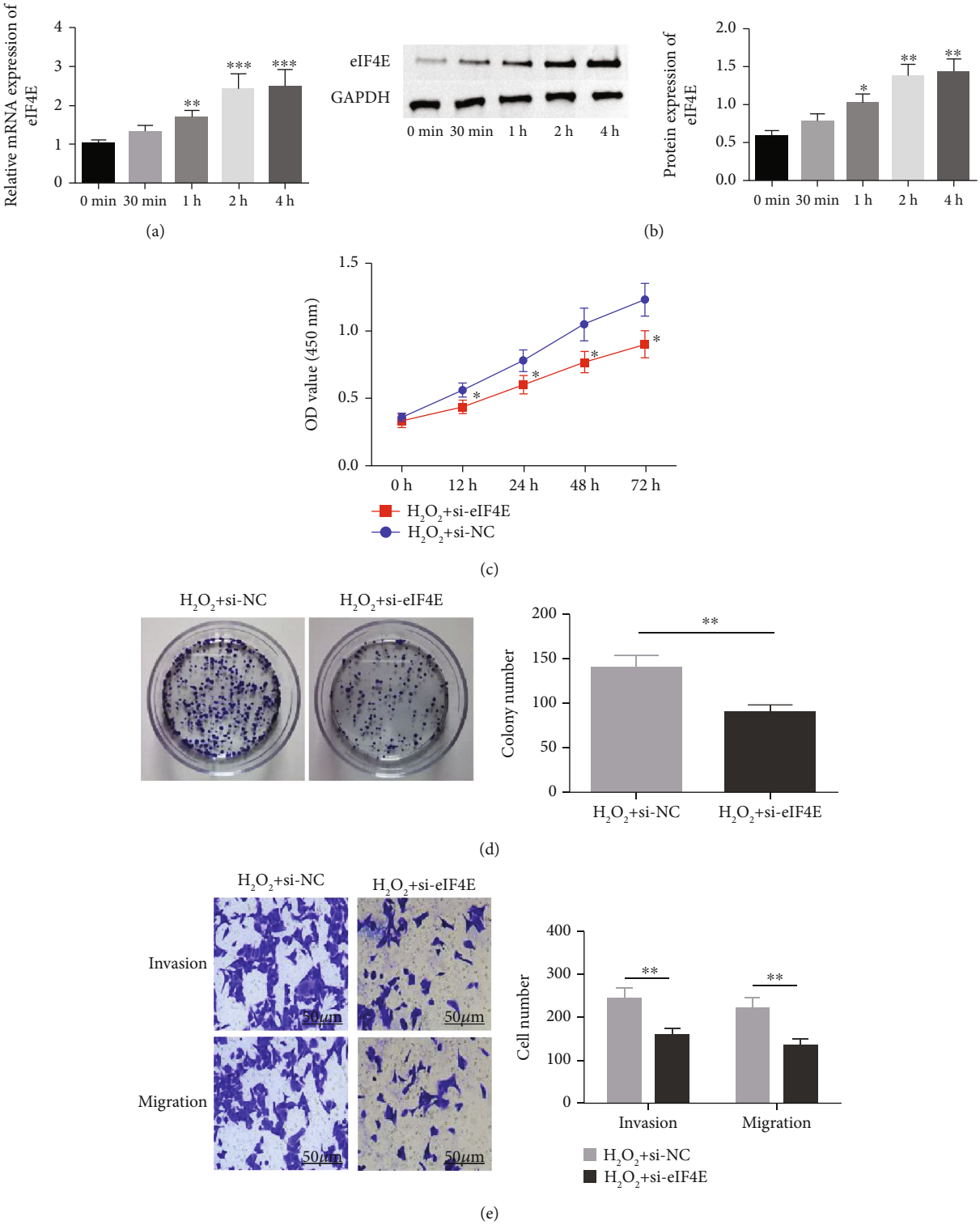

Figure 4: Continued.

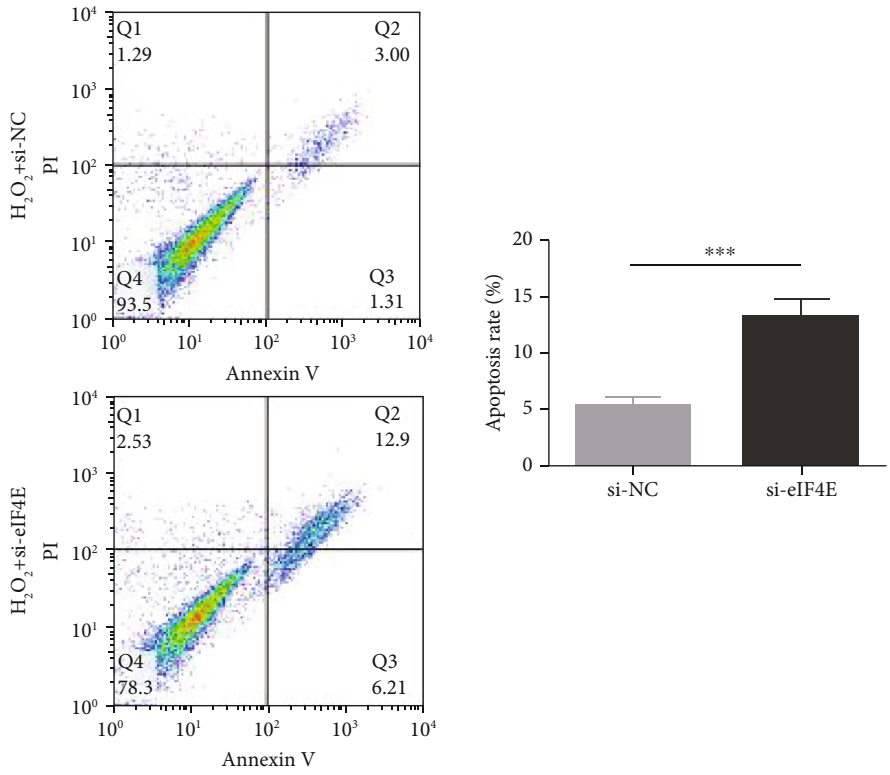

Figure 4: U251 cells' sensitivity to oxidative stress. (a: eIF4E mRNA in H_2O_2-induced U251 cells. b: eIF4E protein in U251 cells induced by H_2O_2. c: U251 cell proliferation after treatment. d: Number of U251 cell clones after treatment. e: Number of invading and migrating U251 cells after treatment. f: U251 cell apoptosis after treatment; $*P < 0.05$, $**P < 0.01$, $*** P < 0.001$.).

HEB were grown in high-glucose DMEM, while LN229 cells in low-glucose DMEM.

2.3. Cell Transfection and Intervention. RiboBio (Guangzhou) synthesized three different ATG4C small interfering RNAs (siRNAs) and a negative control siRNA. The exponentially growing cells were inoculated in the wells of 6 well plates for overnight culture. According to the Lipofectamine RNAiMAX reagent (Invitrogen, CA, USA) instructions, the designated siRNAs with a final concentration of 50 nM were transfected into 60–70% confluent plated cells. Lipofectamine 3000 reagent (Invitrogen, CA, USA) was used to transfect cells planted in the 6-well plates with RFP-GFP-LC3B plasmids (provided by Professor Cheng from Central South University) at 1.0 μg/well following the instructions. The medium was replaced with fresh medium + 10% FBS 6 hours post intervention, and the transfected cells were collected for further analysis.

2.4. Hydrogen Peroxide (H_2O_2) Treatment. Cell damage was induced by a certain concentration of H_2O_2, and the experimental cells were assigned to 3 groups: control, H_2O_2 (1 mM H_2O_2 intervention for 24 h), and si-eIF4E + H_2O_2 (1 mM H_2O_2 intervention for 24 h after eIF4E siRNA transfection).

2.5. qRT-PCR. After extraction by TRIzol reagent (Invitrogen), the total cell RNA underwent reverse transcription into cDNA with a Prime Script RT Reagent kit (Takara) by referring to the supplier's recommendations. Then, real-time PCR was carried out with the Stepone plus system (Applied Biosystems) as instructed by the SYBR Premix Ex Taq Kit (Takara) instructions, followed by PCR reactions using eIF4E as the primer: sense: 5′-TGCGGCTGATCTCCAA GTTTG-3′, anti-sense: 5′-CCCACATAGGCTCAATACC ATC-3′; GAPDH: sense: 5′-CTGGGCTACACTGAGC ACC-3′, anti-sense: 5′-AAGTGGTCGTTGAGGGCAATG-3. The internal reference was GAPDH. The $2^{-\Delta\Delta Ct}$ method was employed for the calculation of gene expression levels. All experiments were repeatedly determined three times.

2.6. Western Blot. Total cell proteins were extracted after cell lysis by RIPA. Protein concentration was determined by the BCA method, and the protein loading amount was 40 μg. The protein samples were shifted to a PVDF membrane post 12% SDS-PAGE. 5% skim milk powder was then used to seal at an ambient temperature for 1 h, and the primary antibody eIF4E (1 : 1000, Cell Signaling Technology, USA) was added to incubate at 4°C overnight. The next day, the second anti-horseradish peroxidase labeled antirabbit IgG antibody (1 : 2000, Cell Signaling Technology, USA) was added correspondingly. The electrochemiluminescence (ECL) method

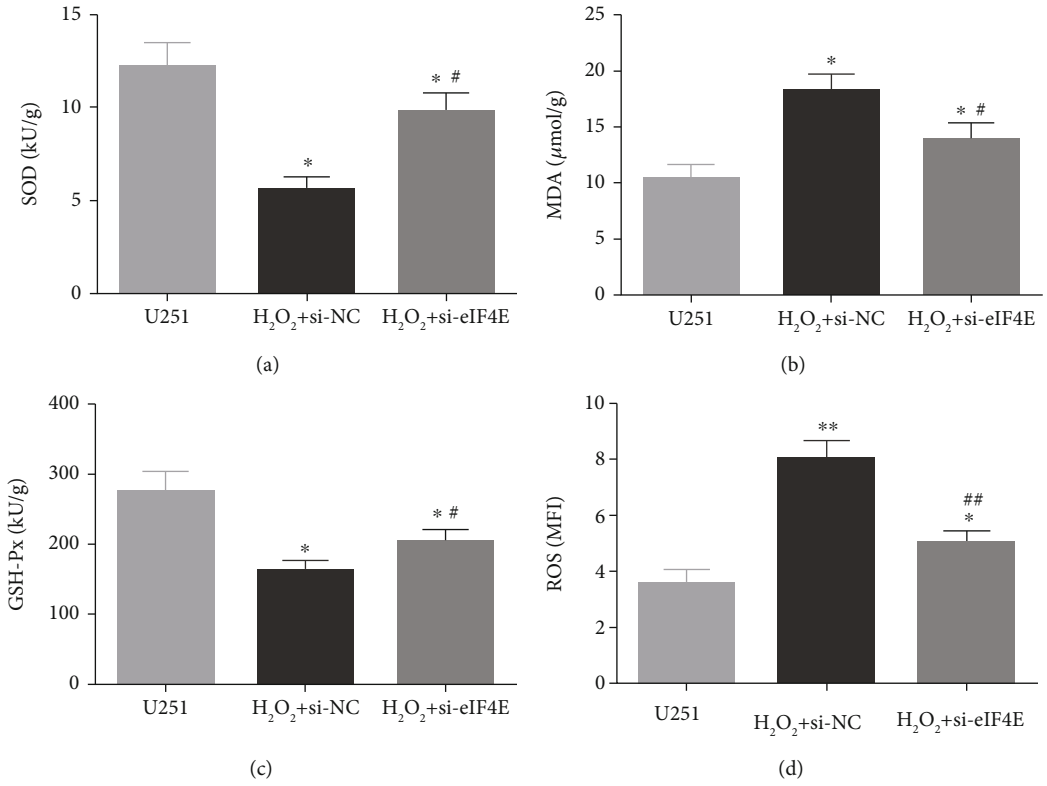

Figure 5: Impact of down-regulating eIF4E on oxidative stress indexes in U251 cells after H_2O_2 induction. (a: Comparison of SOD activity. b: Comparison of MDA content. c: Comparison of GSH-px content. d: Comparison of ROS content; $*P < 0.05$, $**P < 0.01$ *vs* U251 cells; $\#P < 0.05$, $\#\#P < 0.01$ *vs* H_2O_2 + si-NC.).

was adopted for color development. Images were collected by gel imaging system and processed by software Image J for gray level analysis. GAPDH was used as internal reference for semiquantitative protein analysis.

2.7. CCK-8. After entering the logarithmic growth phase (LGF), the cells (2×10^4/mL) were inoculated into the wells of a 96-well plate for a 24-hour culture under the conditions of 5% CO_2 and 37°C. Cells in each well were then added with CCK-8 reagent with a volume of 10 μl at 0, 12, 24, 48, and 72 h, respectively, and cultivated at indoor temperature for 2 hours, after which absorbance$_{450nm}$ was determined with a multifunctional microplate reader.

2.8. Cell Clone Formation. LGF cells of each group were digested and centrifuged, and evenly inoculated into 6-well plates after adjusting to 200 cells/mL by in a medium. After putting 1 mL cell suspension to each well, the 6-well plates were placed into an incubator (5% CO_2 and 37°C) for culture with the medium changed once every 4 days. When the number of cloned cells was more than 50, the culture was terminated, the supernatant was discarded, and the PBS solution was used for cleaning. After immobilization and cleaning with methanol, cells were added with crystal violet dyeing solution for dyeing in the dark for about 20 min, after which washing and drying of cells were performed. The number of cell clones with cells greater than 50 was analyzed and counted.

2.9. Transwell for Cell Invasiveness and Migration Detection. The transfected cells cultured to LGF were gathered, digested with trypsin, centrifuged, and thoroughly mixed with blank culture medium. Cells were laid (1×10^5 cells/well) on the upper Transwell chamber coated with Matrigel, while the lower chamber was pre-added with 500 μL of medium + 10% FBS. The upper chamber was then placed into a 24-well plate. After culturing in a cell incubator for 24 h, the medium was poured out, PBS-washed, air-dried, 4% paraformaldehyde-fixed, and 0.14% crystal violet-stained. The inverted microscope randomly selected five nonoverlapping fields for counting and photographing. The cell migration experiment did not need to spread Matrigel matrix glue in the upper chamber of Transwell chamber, and cell suspension was placed into the chamber for 24 h of culture. Other steps were basically the same as invasiveness detection.

2.10. OS Index Detection. Cells in each group were collected and lysed with cell lysate, and supernatant was collected to quantify SOD, MDA, and GSH-Px contents following kit manuals. Endogenous ROS fluorescence intensity was detected using the 2′,7′-dichlorofluorescein-diacetate (DCFH-DA) probe. Cells of each group (5×10^3 cells/mL) were inoculated into the wells of a 96-well plate for 48 hours of culture, and then, the fluorescent probe DCFH-DA (10 μmol/L) was added for incubator incubation (37°C, 20 min). After washing, the mean fluorescence intensity (MFI) of cells was detected by flow cytometry (FCM),

representing the intracellular ROS level. The excitation and emission wavelengths were 488 nm and 525 nm, respectively.

2.11. Apoptosis Detection. After 0.25% trypsin digestion, LGF cells were treated with 10 min of centrifugation (1000 rpm, 4°C), and three repeated rinsing. Single-cell suspension was prepared, and cells were suspended in 200 μL buffer and then incubated with 5 μL Annexin V-FITC and 10 μL PI in turn, after which FCM was performed to determine cell apoptosis.

2.12. Statistical Processing. SPSS25.0 processed the data. Mean values were obtained after three measurements of each test, and the data was denoted by the mean ± standard deviation. The Mann-Whitney U test was used to compare eIF4E expression between GBM, LGG samples, and normal samples. Comparisons between groups and among multiple groups were made by Student's t-test and one-way ANOVA plus Tukey post hoc test, respectively. The test level was $\alpha = 0.05$, and significance was determined at $P < 0.05$.

3. Results

3.1. Expression Profiling and Prognosis Significance of eIF4E in Glioma Patients. GEPIA2 was adopted to analyze eIF4E expression in LGG and GBM patients in the TCGA database. The results identified statistically elevated eIF4E expression in cancer tissues of LGG and GBM patients compared with normal counterparts ($P < 0.05$; Figure 1(a)). Consistent findings were obtained when detecting eIF4E in the obtained clinical tissue samples; namely, eIF4E was upregulated in carcinoma tissues compared with adjacent normal counterparts ($P < 0.05$; Figure 1(b)). Patients were grouped as high- and low-expression groups based on the median expression level. According to Kaplan-Meier survival analysis, patients with high eIF4E expression had obviously worse outcomes than those with low expression ($P < 0.05$; Figures 1(c) and 1(d)).

3.2. eIF4E Expression in Glioma Cells. qPCR and Western blot analyses revealed statistically regulated eIF4E mRNA and protein levels in glioma cell lines compared with HBE cells ($P < 0.05$), with the highest upregulation found in U251 cells (Figure 2).

3.3. Influence of down-Regulating eIF4E on U251 Cell Biological Function. The potential function of eIF4E in U251 cells was studied by transfecting si-eIF4E into U251 cells. Western blotting was performed to confirm that eIF4E was effectively downregulated by siRNA, and as expected, markedly reduced eIF4E protein was observed in U251 cells after si-eIF4E transfection ($P < 0.05$; Figure 3(a)). si-eIF4E transfection evidently prevented U251 cells from proliferating (Figure 3(b)) and reduced the number of cell clones (Figure 3(c)). Meanwhile, downregulating eIF4E validly suppressed the capacity of U251 cell to invade and migrate, and increased apoptosis (Figures 3(d) and 3(e)).

3.4. Downregulating eIF4E Enhances U251 Cells' Sensitivity to OS. To determine the protective action of eIF4E against OS in glioma cells, we treated U251 cells with H_2O_2. Under H_2O_2-induced OS, eIF4E increased with time at both mRNA and protein levels ($P < 0.05$; Figures 4(a) and 4(b)). After transfecting stimulated U251 cells with si-eIF4E, it was found that compared with the H_2O_2 + si-NC group, the proliferation rate of U251 in the H_2O_2 + si-eIF4E group decreased, the number of cell clones as well as invading and migrating cells declined, and the apoptosis rate elevated ($P < 0.05$; Figures 4(c)–4(f)). These results suggest that downregulating eIF4E may enhance glioma cells' sensitivity to OS.

3.5. Impact of Downregulating eIF4E on OS Indexes in U251 Cells after H_2O_2 Induction. The H_2O_2 + si-NC group exhibited statistically decreased SOD and GSH-Px and increased MDA and ROS than the U251 group ($P < 0.05$). Moreover, in comparison with the H_2O_2 + si-NC group, SOD and GSH-Px in U251 cells in the H_2O_2 + si-eIF4E group increased, while MDA and ROS decreased ($P < 0.05$; Figure 5).

4. Discussion

eIF4E activity abnormalities have been demonstrated in multiple human malignancies, and eIF4E overexpression is commonly observed in the breast, lung, stomach, colon, prostate, skin, and hematopoietic system. The elevation of eIF4E expression is related to the increase of disease grade [30–35]. However, it remains to define the correlation of eIF4E gene with glioma progression. This study is the first to demonstrate that eIF4E is overexpressed in glioma clinical samples and cells and that overexpression of eIF4E is significantly linked to adverse prognosis in such patients. Meanwhile, eIF4E knock-out prevented U251 cells from proliferating, invading, and migrating and increased the apoptosis rate. All these suggest the role of eIF4E gene as an attractive potential target for glioma therapy. Studies have shown that translation initiation depends primarily on eIF4E activity. Translational activation, as we know, is essential for carcinoma cell growth and survival, making translation a logical target for new anticancer treatments. Studies on different tumors indicated that eIF4E could be modulated at many levels by MAPK/MNK and PI3K/mTOR axis, like through serine 209 phosphorylation, transcription, and inhibitory interaction between binding proteins [36, 37]. Furthermore, elevated total eIF4E levels, together with 4EBP1 hyperphosphorylation, increased the effectiveness of eIF4E binding to eIF4G and enhanced cap-dependent translationa phenomenon found in breast and prostate carcinomas, while high eIF4E levels were associated with progression-free and overall survival reductions [38, 39].

We also found that in U251 cells, H_2O_2-induced OS injury stimulated eIF4E expression. eIF4E has been shown to regulate gene subsets related to key stress reactions, a function that is critical to cancer induction and progression and is usually linked to a substantial increase in eIF4E level to protect cells against ROS accumulation [40]. It has been reported that OS can activate eIF4E, and prolonging eIF4E activation contributes to proliferative responses [41, 42]. Previous reports have linked eIF4E to proliferation- and

survival-related protein translation [43, 44]. Furthermore, this study revealed that SOD and GSH-Px in U251 cells were significantly decreased, while MDA and ROS were increased after H_2O_2 stimulation. In addition, with the downregulation of eIF4E, the OS damage caused by H_2O_2 was rescued. SOD, a class of metalloproteins, is one of the most potent antioxidant enzymes [45]. The reduction in SOD activity is related to the destructive effect of O2-superoxide, a compound that accelerates the phosphorylation rate in many carcinogenic signaling processes through the deprotonation of serine or threonine residues, resulting in antiapoptosis effects and tumor progression [46]. GSH-Px is a selenium-dependent enzyme, presenting elevated levels in many cancers, including squamous cell carcinoma [47], colorectal cancer [48], and brain tumors [49]. This can be interpreted as a tumor having high levels of OS, and then, the levels of the body's antioxidant system increase correspondingly to compensate for the increased ROS levels as a natural defense against cancer [50]. When homeostasis is disturbed, lipid peroxides escape detoxification and produce toxic aldehydes, the most famous of which is malondialdehyde [51]. Moreover, high levels of ROS accumulation are shown to be closely related to programmed cell death. ROS can induce mitochondrial damage and initiate apoptosis. OS-induced cell death is an important factor in many diseases and cell death including cancer. While downregulating eIF4E decreased the ROS level, it promoted H_2O_2-induced apoptosis of glioma U251 cells. We believe that this may be an early self-protection effect in the process of H_2O_2-induced cell damage, which can reduce the ROS accumulation level through the degradation pathway.

However, there is still room for improvement in this study. The role of eIF4E in glioma is only simply revealed, and the underlying pathways and mechanisms are worthy of exploration. Besides, whether eIF4E can regulate the OS sensitivity of glioma in combination with autophagy and other pathways to regulate the apoptosis of glioma cells needs further research.

5. Conclusion

To sum up, this research is the first to demonstrate high eIF4E expression in cancer tissues of LGG and GBM patients and the close connection between high eIF4E levels with adverse prognosis of glioma patients. H_2O_2-induced OS can stimulate eIF4E expression in U251 cells, and downregulating eIF4E can prevent H_2O_2-induced glioma cells from proliferating, invading, and migrating and promote apoptosis.

Data Availability

The labeled dataset used to support the findings of this study are available from the corresponding author upon request.

Conflicts of Interest

The authors declare no competing interests.

Acknowledgments

This study received financial support from the Science and Technology Program of Shenzhen (GJHZ20190821161601670).

References

[1] S. Lapointe, A. Perry, and N. A. Butowski, "Primary brain tumours in adults," *The Lancet*, vol. 392, no. 10145, pp. 432–446, 2018.

[2] V. A. Cuddapah, S. Robel, S. Watkins, and H. Sontheimer, "A neurocentric perspective on glioma invasion," *Nature Reviews Neuroscience*, vol. 15, no. 7, pp. 455–465, 2014.

[3] F. Lang, Y. Liu, F.-J. Chou, and C. Yang, "Genotoxic therapy and resistance mechanism in gliomas," *Pharmacology & Therapeutics*, vol. 228, article 107922, 2021.

[4] J. Bi, S. Chowdhry, S. Wu, W. Zhang, K. Masui, and P. S. Mischel, "Altered cellular metabolism in gliomas – an emerging landscape of actionable co-dependency targets," *Nature Reviews Cancer*, vol. 20, no. 1, pp. 57–70, 2020.

[5] C. Hacioglu, F. Kar, S. Kacar, V. Sahinturk, and G. Kanbak, "Bexarotene inhibits cell proliferation by inducing oxidative stress, DNA damage and apoptosis via pparγ/nf-κb signaling pathway in c6 glioma cells," *Medical Oncology*, vol. 38, no. 3, pp. 1–11, 2021.

[6] I. M. Germano and E. Binello, "Gene therapy as an adjuvant treatment for malignant gliomas: from bench to bedside," *Journal of Neuro-Oncology*, vol. 93, no. 1, pp. 79–87, 2009.

[7] M. Lara-Velazquez, R. Al-Kharboosh, S. Jeanneret et al., "Advances in brain tumor surgery for glioblastoma in adults," *Brain Sciences*, vol. 7, no. 12, p. 166, 2017.

[8] P. Diamandis and K. D. Aldape, "Insights from molecular profiling of adult glioma," *Journal of Clinical Oncology*, vol. 35, no. 21, pp. 2386–2393, 2017.

[9] P. Jia, C. Dai, P. Cao, D. Sun, R. Ouyang, and Y. Miao, "The role of reactive oxygen species in tumor treatment," *RSC Advances*, vol. 10, no. 13, pp. 7740–7750, 2020.

[10] A. Görlach, E. Y. Dimova, A. Petry et al., "Reactive oxygen species, nutrition, hypoxia and diseases: problems solved?," *Redox Biology*, vol. 6, pp. 372–385, 2015.

[11] S. Reuter, S. C. Gupta, M. M. Chaturvedi, and B. B. Aggarwal, "Oxidative stress, inflammation, and cancer: how are they linked?," *Free Radical Biology and Medicine*, vol. 49, no. 11, pp. 1603–1616, 2010.

[12] H. Sies, "Oxidative stress: a concept in redox biology and medicine," *Redox Biology*, vol. 4, pp. 180–183, 2015.

[13] C. R. Reczek, K. Birsoy, H. Kong et al., "A crispr screen identifies a pathway required for paraquat-induced cell death," *Nature Chemical Biology*, vol. 13, no. 12, pp. 1274–1279, 2017.

[14] M. Dodson, R. Castro-Portuguez, and D. D. Zhang, "Nrf2 plays a critical role in mitigating lipid peroxidation and ferroptosis," *Redox Biology*, vol. 23, article 101107, 2019.

[15] M. Redza-Dutordoir and D. A. Averill-Bates, "Activation of apoptosis signalling pathways by reactive oxygen species," *Cell Research*, vol. 1863, no. 12, pp. 2977–2992, 2016.

[16] Q. Kong, J. Beel, and K. Lillehei, "A threshold concept for cancer therapy," *Medical Hypotheses*, vol. 55, no. 1, pp. 29–35, 2000.

[17] N. Sonenberg and A. G. Hinnebusch, "Regulation of translation initiation in eukaryotes: mechanisms and biological targets," *Cell*, vol. 136, no. 4, pp. 731–745, 2009.

[18] N. Siddiqui and N. Sonenberg, "Signalling to eif4e in cancer," *Biochemical Society Transactions*, vol. 43, no. 5, pp. 763–772, 2015.

[19] F. Pettersson, S. V. Del Rincon, A. Emond et al., "Genetic and pharmacologic inhibition of eif4e reduces breast cancer cell migration, invasion, and metastasis," *Cancer Research*, vol. 75, no. 6, pp. 1102–1112, 2015.

[20] B. Culjkovic and K. L. Borden, "Understanding and targeting the eukaryotic translation initiation factor eif4e in head and neck cancer," *Journal of Oncology*, vol. 2009, Article ID 981679, 12 pages, 2009.

[21] S. Jana, R. Deo, R. P. Hough et al., "Mrna translation is a therapeutic vulnerability necessary for bladder epithelial transformation," *JCI Insight*, vol. 6, no. 11, 2021.

[22] S. Wang, T. Pang, M. Gao et al., "Hpv e6 induces eif4e transcription to promote the proliferation and migration of cervical cancer," *FEBS Letters*, vol. 587, no. 6, pp. 690–697, 2013.

[23] S. Avdulov, S. Li, V. Michalek et al., "Activation of translation complex eif4f is essential for the genesis and maintenance of the malignant phenotype in human mammary epithelial cells," *Cancer Cell*, vol. 5, no. 6, pp. 553–563, 2004.

[24] T. P. Herbert, R. Fåhraeus, A. Prescott, D. P. Lane, and C. G. Proud, "Rapid induction of apoptosis mediated by peptides that bind initiation factor eif4e," *Current Biology*, vol. 10, no. 13, pp. 793–796, 2000.

[25] K. Dong, R. Wang, X. Wang et al., "Tumor-specific rnai targeting eif4e suppresses tumor growth, induces apoptosis and enhances cisplatin cytotoxicity in human breast carcinoma cells," *Breast Cancer Research and Treatment*, vol. 113, no. 3, pp. 443–456, 2009.

[26] Y. Ge, R. Cheng, Y. Zhou et al., "Cryptotanshinone induces cell cycle arrest and apoptosis of multidrug resistant human chronic myeloid leukemia cells by inhibiting the activity of eukaryotic initiation factor 4e," *Molecular and Cellular Biochemistry*, vol. 368, no. 1-2, pp. 17–25, 2012.

[27] Y.-S. Yao, W.-S. Qiu, R.-Y. Yao et al., "Mir-141 confers docetaxel chemoresistance of breast cancer cells via regulation of eif4e expression," *Oncology Reports*, vol. 33, no. 5, pp. 2504–2512, 2015.

[28] M. L. Truitt, C. S. Conn, Z. Shi et al., "Differential requirements for eif4e dose in normal development and cancer," *Cell*, vol. 162, no. 1, pp. 59–71, 2015.

[29] P. A. Gutierrez Sanchez, L. Babujee, H. Jaramillo Mesa et al., "Overexpression of a modified eif4e regulates potato virus y resistance at the transcriptional level in potato," *BMC Genomics*, vol. 21, no. 1, pp. 1–16, 2020.

[30] D. R. McClusky, Q. Chu, H. Yu et al., "A prospective trial on initiation factor 4e (eif4e) overexpression and cancer recurrence in node-positive breast cancer," *Annals of Surgery*, vol. 242, no. 4, pp. 584–592, 2005.

[31] C. N. Chen, F. J. Hsieh, Y. M. Cheng, P. H. Lee, and K. J. Chang, "Expression of eukaryotic initiation factor 4e in gastric adenocarcinoma and its association with clinical outcome," *Journal of Surgical Oncology*, vol. 86, pp. 22–27, 2004.

[32] I. B. Rosenwald, J.-J. Chen, S. Wang, L. Savas, I. M. London, and J. Pullman, "Upregulation of protein synthesis initiation factor eif-4e is an early event during colon carcinogenesis," *Oncogene*, vol. 18, no. 15, pp. 2507–2517, 1999.

[33] R. Wang, J. Geng, J. H. Wang, X. Y. Chu, H. C. Geng, and L. B. Chen, "Overexpression of eukaryotic initiation factor 4E (eIF4E) and its clinical significance in lung adenocarcinoma," *Lung Cancer*, vol. 66, no. 2, pp. 237–244, 2009.

[34] Z. Salehi, F. Mashayekhi, and F. Shahosseini, "Significance of eif4e expression in skin squamous cell carcinoma," *Cell Biology International*, vol. 31, no. 11, pp. 1400–1404, 2007.

[35] S. Wang, I. B. Rosenwald, M. J. Hutzler et al., "Expression of the eukaryotic translation initiation factors 4E and 2α in non-Hodgkin's lymphomas," *The American Journal of Pathology*, vol. 155, no. 1, pp. 247–255, 1999.

[36] P. M. Fischer, "Cap in hand: targeting eif4e," *Cell Cycle*, vol. 8, no. 16, pp. 2535–2541, 2009.

[37] Y. Jia, V. Polunovsky, P. B. Bitterman, and C. R. Wagner, "Cap-dependent translation initiation factor eIF4E: an emerging anticancer drug target," *Medicinal Research Reviews*, vol. 32, no. 4, pp. 786–814, 2012.

[38] J. R. Graff, B. W. Konicek, R. L. Lynch et al., "Eif4e activation is commonly elevated in advanced human prostate cancers and significantly related to reduced patient survival," *Cancer Research*, vol. 69, no. 9, pp. 3866–3873, 2009.

[39] L. Coleman, M. Peter, T. Teall et al., "Combined analysis of eif4e and 4e-binding protein expression predicts breast cancer survival and estimates eif4e activity," *British Journal of Cancer*, vol. 100, no. 9, pp. 1393–1399, 2009.

[40] R. Mittler, "Ros are good," *Trends in Plant Science*, vol. 22, no. 1, pp. 11–19, 2017.

[41] R. F. Duncan, H. Peterson, and A. Sevanian, "Signal transduction pathways leading to increased eif4e phosphorylation caused by oxidative stress," *Free Radical Biology and Medicine*, vol. 38, no. 5, pp. 631–643, 2005.

[42] L. Furic, L. Rong, O. Larsson et al., "Eif4e phosphorylation promotes tumorigenesis and is associated with prostate cancer progression," *Proceedings of the National Academy of Sciences*, vol. 107, no. 32, pp. 14134–14139, 2010.

[43] B. Culjkovic, I. Topisirovic, L. Skrabanek, M. Ruiz-Gutierrez, and K. L. Borden, "Eif4e promotes nuclear export of cyclin d1 mrnas via an element in the 3′ utr," *The Journal of Cell Biology*, vol. 169, no. 2, pp. 245–256, 2005.

[44] S. Li, T. Takasu, D. M. Perlman et al., "Translation factor eIF4E rescues cells from Myc-dependent apoptosis by inhibiting cytochrome c release∗," *Journal of Biological Chemistry*, vol. 278, no. 5, pp. 3015–3022, 2003.

[45] J.-F. Yi, Y.-M. Li, T. Liu et al., "Mn-sod and cuzn-sod polymorphisms and interactions with risk factors in gastric cancer," *World Journal of Gastroenterology: WJG*, vol. 16, no. 37, pp. 4738–4746, 2010.

[46] I. B. Bize, L. W. Oberley, and H. P. Morris, "Superoxide dismutase and superoxide radical in morris hepatomas," *Cancer Research*, vol. 40, no. 10, pp. 3686–3693, 1980.

[47] K. C. Deshpande, M. M. Kulkarni, and D. V. Rajput, "Evaluation of glutathione peroxidase in the blood and tumor tissue of oral squamous cell carcinoma patients," *Journal of Oral and Maxillofacial Pathology: JOMFP*, vol. 22, no. 3, p. 447, 2018.

[48] F. Lee, A. Vessey, E. Rofstad, D. Siemann, and R. Sutherland, "Heterogeneity of glutathione content in human ovarian cancer," *Cancer Research*, vol. 49, no. 19, pp. 5244–5248, 1989.

[49] H. Kudo, T. Mio, T. Kokunai, N. Tamaki, K. Sumino, and S. Matsumoto, "Quantitative analysis of glutathione in human brain tumors," *Journal of Neurosurgery*, vol. 72, no. 4, pp. 610–615, 1990.

[50] M. Strycharz-Dudziak, M. Kiełczykowska, B. Drop et al., "Total antioxidant status (tas), superoxide dismutase (sod), and glutathione peroxidase (gpx) in oropharyngeal cancer associated with ebv infection," *Oxidative Medicine and Cellular Longevity*, vol. 2019, Article ID 5832410, 15 pages, 2019.

[51] M. Singh, D. Shrivastava, and R. Kale, "Antioxidant potential of asparagus adscendens," *Antioxidant Enzyme*, vol. 323, 2012.

Hindawi
Oxidative Medicine and Cellular Longevity
Volume 2022, Article ID 4479905, 8 pages
https://doi.org/10.1155/2022/4479905

Research Article

Pathogenesis and Diagnostic Significance of EBV-miR-BARTs in Nasopharyngeal Carcinoma

Zhen Wu,[1] Xiaoling Zhang,[2] Pinjing Liu,[3] Aiyou Wei,[4] Wei Ouyang,[5] and Shengjun Xiao[6]

[1]*Xiangya Hospital, Central South University, Changsha, Hunan 410008, China*
[2]*Department of Physiology, Faculty of Basic Medical Science, Guilin Medical University, Guilin, Guangxi 541100, China*
[3]*Department of Hematology, Guigang People's Hospital, Guigang, Guangxi 537100, China*
[4]*Department of Obstetrics and Gynecology, The First Affiliated Hospital of Sun Yat-sen University, Guangzhou, Guangdong 510000, China*
[5]*College of Nursing, Guilin Medical University, Guilin, Guangxi 541100, China*
[6]*Department of Pathology, The Second Affiliated Hospital of Guilin Medical University, Guilin, Guangxi 541100, China*

Correspondence should be addressed to Shengjun Xiao; 168101007@csu.edu.cn

Received 15 July 2022; Revised 5 August 2022; Accepted 8 September 2022; Published 3 October 2022

Academic Editor: Shao Liang

Objective. Examining the role of EBV-miR-BARTs in nasopharyngeal cancer etiology and diagnosis. *Method*. As the subjects of this study, nasopharyngeal cancer cell lines were chosen and then randomly assigned to one of four groups: the control group, EBV-miR-BART5-3p NC, EBV-miR-BART5-3p mimics, and EBV-miR-BART5-3p inhibitor groups. Utilizing reverse transcription polymerase chain reaction, we determined the levels of gene expression in nasopharyngeal cancer cells that had been treated with EBV-miR-BART5-3p (RT-PCR). The MTT, Transwell, and scratch tests were used to determine the degree to which cells underwent apoptosis, invasion, and migration. The Western blotting method was used in order to examine the protein expression. *Result*. Compared with normal nasopharyngeal cells, P 0.05 showed that nasopharyngeal cancer cells had greater EBV-miR-BART5-3p expressions and proliferation rates in the control, EBV-miR-BART5-3p NC, and EBV-miR-BART5-3p No statistically significant differences were seen between the mimic groups ($P > 0.05$); compared with the control group, the proliferation rate of the EBV-miR-BART5-3p inhibitor group was lower with $P < 0.05$. At a significance threshold of P 0.05, there was no difference in the rates of apoptosis between the control group and the EBV-miR- BART5-3p NC group. Comparing the control group to the EBV-miR-BART5-3p mimics group and the EBV-miR-BART5-3p inhibitors group revealed that the rate of apoptosis was dramatically enhanced in the EBV-miR-BART5-3p inhibitors group but significantly decreased in the control group (P 0.05). When comparing the control group to the EBV-miR-BART5-3p NC group, there was no statistically significant change in the total number of invasive cells ($P > 0.05$). When comparing the EBV-miR-BART5-3p mimics group to the control group, we found a statistically significant increase in the former and a decrease in the latter (P 0.05). The migration rates of the control group, the EBV-miR-BART5-3p NC group, and the EBV-miR-BART5-3p mimics group did not vary from one another in a way that was statistically significant ($P > 0.05$). When compared to the control group, the migration rate was considerably (P 0.05) lower in the EBV-miR-BART5-3p inhibitor group. There were no discernible changes identified ($P > 0.05$) in the levels of Bcl-2 protein expression in the control group, the EBV-miR-BART5-3p NC group, and the EBV-miR-BART5-3p mimic group in a research that compared these three groups. Protein levels of BCL-2 were significantly decreased (P 0.05) in the EBV-miR-BART5-3p inhibitor group, in comparison to the control group. When comparing the control and EBV- miR-BART5-3p NC groups, we found no statistically significant differences in Bax and Caspase-3 protein expression levels ($P > 0.05$). The protein expressions of Bax and Caspase-3 were statistically significantly greater in the EBV-miR-BART5-3p contrast between the inhibitor and control groups. When comparing the protein expressions of MMP-2 and MMP-9 between the control group, the EBV-miR-BART5-3p NC group, and the EBV-miR-BART5-3p mimics group, there was no statistically significant change ($P > 0.05$). Protein levels of MMP-2 and MMP-9 were inhibited by EBV-miR-BART5-3p to a greater extent (P 0.05) in the experimental group compared to the control group. *Conclusion*. The understanding that inhibiting expression of EBV-miR-BART5-3p might reduce the risk of developing nasopharyngeal cancer may help direct clinical treatment for the condition.

1. Introduction

Nasopharyngeal carcinoma is caused by the canceration of epithelial cells of nasopharyngeal mucosa, which is mostly found in Southeast Asia and the Guangdong and Guangxi regions in southern China. The total incidence of nasopharyngeal carcinoma in China is 3.16/100,000 and the recurrence rate of the disease is high and has a poor prognosis of patients [1, 2]. It is very dangerous to people's lives, health, and wellbeing. Recent years have seen a surge in interest in the role that hereditary variables, environmental factors, Epstein-Barr virus (EBV), and other factors play in the development and progression of nasopharyngeal cancer, among which EBV is involved in the entire development of nasopharyngeal carcinoma [3, 4], especially existing largely in the early stage of epithelial tumor tissue of nasopharyngeal carcinom, stimulating the invasion and metastasis of tumor cells [5]. At present, there is still a lack of targeted drugs and new therapeutic methods that can effectively reduce the toxicity of EBV. The main treatment methods for patients with nasopharyngeal carcinoma are radiotherapy or chemotherapy drugs [6] . However, these treatments have high toxicity side effects and low cure rate, and many patients occurred the adverse reactions such as anemia and bone marrow suppression after treatment, which further increased the physical and psychological burden on patients. Therefore, finding specific and effective targets or biomarkers may be clinically significant since it holds the key to enhancing the disease's cure rate and prognostic consequences. Single-stranded, noncoding RNA microRNAs (miRNAs) are tiny molecules that may control gene expression. The research on the regulation mechanism of miRNA on tumor cells has gradually attracted attention in recent years. Based on the context, miRNAs may either promote or inhibit tumor growth. Which affects the proliferation and differentiation of tumor cells [7, 8]. EBV is a virus that can encode miRNA in host cells [9]. EBV-miR-BART survives in host cells, blocking immune response, whose cell biological behaviors have played a key role in cancer metabolism; the EBV-encoded miR-BART contributes to the onset and progression of nasopharyngeal cancer (includes BART5-5p, BART7-3p, BART5-3p, etc.). And Zheng et al. [10] found that upregulating the expression of EBV has shown that BART5-3p may both increase the number of nasopharyngeal cancer cells and prevent them from dying off naturally. So EBV-miRNA may become an effective target for the diagnosis and treatment of nasopharyngeal carcinoma by examining the expression of EBV-BART5-3p in nasopharyngeal cancer tissue and its influence on nasopharyngeal. This research was conducted to provide a scientific and clinical basis for the diagnosis and treatment of nasopharyngeal carcinoma, which is caused by carcinoma cells.

2. Materials and Methods

2.1. Cell Culture. The Chinese Academy of Sciences generously contributed both the normal nasopharyngeal cell line NP69 and CNE-2Z, a human nasopharyngeal carcinoma cell line. Cells were regularly grown and maintained in RPMI-1640 media with 10% fetal bovine serum, 100 U/ml penicillin, and 100 U/mL streptomycin, and the medium was changed every 3 days. Every other day, at a temperature of 37 degrees Celsius, a relative humidity of 95%, and a concentration of 5% carbon dioxide. When the subcultured cells were in the log phase, they were collected for harvesting.

Table 1: Comparison of EBV-miR-BART5-3p gene levels between nasopharyngeal carcinoma and nasopharyngeal mucosal inflammatory tissue samples ($\bar{\chi} \pm s$).

Grouping	n	EBV-miR-BART5-3p
Normal nasopharyngeal cells	3	0.69 ± 0.06
Nasopharyngeal carcinoma cells	3	5.16 ± 0.93
t		8.280
P		0.014

2.2. Reagents and Instruments. MMT reagent (Art. No. M2128, specification 1 g), methanol (Art. No. 34860, specification 1 L), Lipofectamine ™ 2000 transfection reagent (Art. No. 1 1668030, specification 0.3 mL), and Trizol reagent (Art. No. 1 5596018, specification 2 00 mL) were all purchased from Merck Sigma Co., USA; PBS buffer (Art. No. SNM491, specification 500 mL, Beijing Biolab Technology Co., Ltd.), rabbit monoclonal Bcl-2 primary antibody (Art. No. ab182773, specification 100μ L), rabbit monoclonal Bax primary antibody (Art. No. ab32124, specification 100 μL), rabbit monoclonal Caspase-3 (Art. No. ab32351, specification 100 μL), GAPDH rabbit monoclonal primary antibody (Art. No. ab181602, specification 100 μL), rabbit monoclonal MMP-2, and MMP9 (Art. No. ab92536, ab150077, specification 500 μg) were all purchased from Abcam Company, UK. A purchase was made from Shanghai Yisheng Biotechnology Co., Ltd. for an Annexin V-FITC/PI apoptosis detection kit with the item number 40302ES20; an ECL luminescence kit (Art. No. HR0338) from Beijing Biolab Technology Co., Ltd.; a QuantStudio 3 real-time fluorescence quantitative PCR instrument from Thermo Fisher; a CytoFLEX-type flow.

2.3. Experimental Method

2.3.1. Cell Transfection and Grouping. Logarithmically growing CNE-2Z cells were split into four groups. Control (nontransfected), EBV-miR-BART5-3p negative control (NC), Cells transfected with an inhibitor of EBV microRNA-BART5-3p (EBV-miR-BART5-3p inhibitor) were compared to cells expressing a mimic of this miRNA. Transfection was accomplished as described in the manual for the Lipofectamine TM 2000 transfection reagent.

2.3.2. RT-PCR Detects EBV-miR-BART5-3p Gene. Take the CNE-2Z cells transfected under 1.2.1, add Trizol reagent to lyse for 10 min, extract the total RNA in each group of cells and reverse transcribe into cDNA, and use a PCR instrument to measure content of EBV-miR-BART5-3p. The conditions were predenaturation at 95°C for 30 s, denaturation at 95°C for 10 s, annealing at 55°C for 30 s, and extension

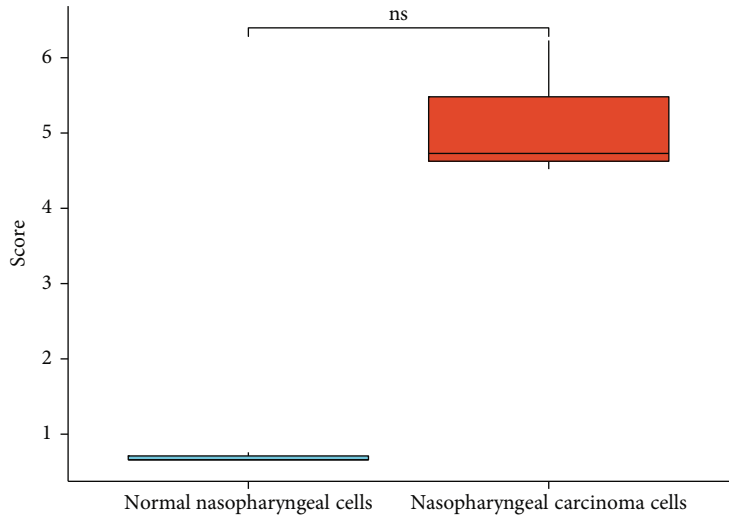

Figure 1: Comparison of EBV-miR-BART cells between the two groups.

Table 2: Comparison of cell proliferation rates in each group ($\bar{\chi} \pm s$).

Grouping	n	Proliferation rate (%)
Control group	3	88.52 ± 12.05
EBV-miR-BART5-3p NC group	3	87.14 ± 11.53
EBV-miR-BART5-3p mimics group	3	92.51 ± 8.69
EBV-miR-BART5-3p inhibitor group	3	35.80 ± 5.69*
F		22.482
P		<0.001

Note: Contrasted with the negative control group, *P 0.05.

Table 3: Comparison of apoptosis rates in each group ($\bar{\chi} \pm s$).

Grouping	n	Apoptosis rate (%)
Control group	3	16.85 ± 1.05
EBV-miR-BART5-3p NC group	3	16.09 ± 1.32
EBV-miR-BART5-3p mimic group	3	12.26 ± 1.63*
EBV-miR-BART5-3p inhibitor group	3	67.85 ± 3.59*
F		457.599
P		<0.001

Note: In contrast to the control group, *$P < 0.05$.

at 70°C for 10 s for a total of 30 cycles. The PCR reaction system used U6 as the internal reference, and the $2^{-\Delta\Delta Ct}$ method was used for calculation. EBV-miR-BART5-upstream 3p's primer was 5′-GTGGGCCGCTGTTCAC CT-3′, and its downstream primer was 5′-TGGTGTCGT GGAGTCG-3′; U6's upstream primer was 5′-CTCGCT TCGGCAGCACAT-3′, and its downstream primer was 5′-TTTGCGTGTCATCCTTGCG-3′.

2.3.3. MTT Test Detects Cell Proliferation. Using a 96-well plate with CNE-2Z cells transfected at a ratio of 1.2.1 : 1.0105, add 20 l of MTT solution to each well, add 200 μl of DMSO solution after shading cultured for 4 hours, and then shake to dissolve and after fully dissolving, detect the absorbance at 490 nm wavelength with a microplate reader and calculate the cell proliferative skill, and the procedure was performed three times. Formula: absorbance of cells in the experimental group/absorbance of cells in the control group = cell proliferation rate.

2.3.4. Detection of the Ability of Cell Apoptosis Ability by Flow Cytometry. Take the CNE-2Z cells transfected in 1.2.1, inoculate them, respectively, in 6-well plates, and wash them with precooled PBS buffer in the refrigerator. Annexin V-FITC/PI cell apoptosis detection reagent kit instructions were followed, and the apoptosis rate (in percentage) was measured using a flow cytometer. This study was repeated thrice.

2.3.5. Transwell Test Detects Cell Invasion. Take the CNE-2Z cells transfected in 1.2.1, digest the cells with trypsin and centrifuge, and then wash them once with PBS. First, set the cell concentration to 5 x 105 cells/mL. Transwell chambers covered with matrix gel were used to incubate 200 L of cells for 24 hours at 37 degrees Celsius, in a CO2 incubator. A cell culture plate containing 10% FBS medium was used to cultivate the cells. Subsequently, after removing the Transwell chamber, the matrix gel and cells within were cleaned with a cotton swab and preserved in a 4% formaldehyde solution for 10 minutes. The cells at the bottom of the well were stained for 10 minutes with 0.1% crystal violet solution before being rinsed and examined under a microscope.

2.3.6. Scratch Assay Was Used to Detect Cell Migration. The cells were collected to make the cells continue to grow in a monolayer adherent state until the confluence of cells reached 80% to 90%. Then, cells were scratched by keeping the pipette perpendicular to the well plate; consistent scratch width may be achieved. Then, to get rid of any leftover

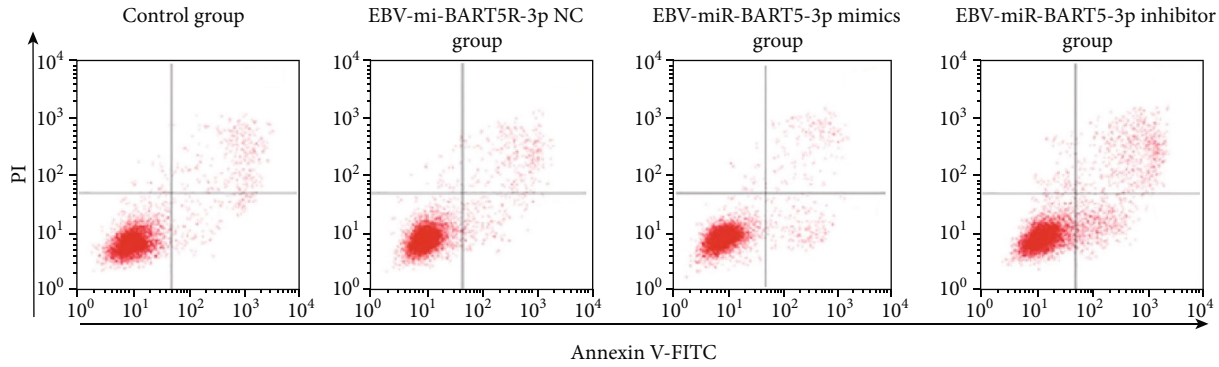

Figure 2: Comparison of each group's apoptosis rates.

Table 4: Comparison of the number of invasive cells in each group ($\bar{\chi} \pm s$).

Grouping	n	Number of invasive cells (pcs)
Control group	3	55.33 ± 6.11
EBV-miR-BART5-3p NC group	3	55.33 ± 6.51
EBV-miR-BART5-3p mimic group	3	69.00 ± 2.65*
EBV-miR-BART5-3p inhibitor group	3	30.33 ± 3.79*
F		30.878
P		<0.001

Note: Compared to the control subjects, $^*P < 0.05$.

debris, the cells were rinsed three times with PBS before being placed in an incubator set at 37 degrees Celsius and 5% carbon dioxide. Under the microscope, the resulting photos were taken at 0 hours and 48 hours after the experiment began. The formula for calculating the migration rate as a percentage is as follows: (24 hours minus 0 hours)/0 hours multiplied by 100 percent.

2.3.7. Western-Blot Was Used to Detect the Related Protein Expression in Nasopharyngeal Carcinoma Cells. The CNE-2Z cells transfected in 1.2.1 were added to the protein lysate and extracted cells of each group after the substance was tested using a BCA kit after being centrifuged at 12,000 rpm for 10 minutes at 4 degrees Celsius. kit for protein concentration. Following a 10-minute incubation in 0.1% crystal violet solution, the cells at the bottom of the well were washed and examined under a microscope. 30 μg protein was boiled and denatured in each group and made the electrophoresis in 10% polyacrylamide gel to transfer to blocked with 5% skim milk powder for 1 hour at room temperature on a PVDF membrane. The diluted Bcl-2 in primary antibodies of Bax, Caspase-3, MMP-2, and MMP-9 primary antibodies (1 : 1 000) were added and grew in a 4°C incubator overnight, rinsed three times in PBS buffer, adding diluted secondary antibodies (1 : 5000), a one-hour room temperature incubation followed by three further washings, adding ECL chemiluminescent reagent for color development, and using Quantity One software to calculate the relative expression of target protein (gray value of target protein/gray value of internal reference protein) with GAPDH as the internal reference.

2.4. Statistical Methods. Using SPSS22.0 software for data analysis, the measurement data conforming to the normal distribution was expressed in the form of ($\bar{\chi} \pm s$), and multiple pairwise comparisons and one-way analysis of variance (LSD-t test) were utilized to examine the data from the different groups. If the P value is less than 0.05, the results of the study may be considered reliable.

3. Results

Expressions of EBV-miR-BARTs in normal nasopharyngeal cells and nasopharyngeal carcinoma cells: Compared with normal nasopharyngeal cells, the Table 1 and Figure 1 reveal that EBV-miR-BART5-3p expression was significantly greater in nasopharyngeal cancer cells at P 0.05.

The effects of EBV-miR-BARTs on cell proliferation: There was no statistically significant difference between control, EBV-miR-BART5-3p NC, and EBV-miR-BART5-3p mimic groups in terms of proliferation rates ($P > 0.05$). The proliferation rate of the EBV-miR-BART5-3p inhibitor group was significantly lower than that of the control group (P 0.05; Table 2).

The effects of EBV-miR-BARTs on cell apoptosis: When comparing the control group and the EBV-miR-BART5-3p NC group, there was not a statistically significant difference in apoptotic rates between the control group and the EBV-miR-BART5-3p inhibitor group ($P > 0.05$), as shown in Table 3 and Figure 2. On the other hand, the apoptosis rate of the miR-BART5-3p mimic group was lower than that of the control group.

The effects of EBV-miR-BARTs on cell invasion: Counts of invasive cells from the control and EBV-miR-BART5-3p NC. None of the groups were statistically different from one another ($P > 0.05$), but Table 4 and Figure 3 show that the number of invasive number of EBV-infected cells in the EBV-miR-BART5-3p mimics and EBV-miR-BART5-3p inhibitor groups was significantly higher than in the control group. With a 0.05 cutoff for statistical significance, the study was considered to be statistically significant.

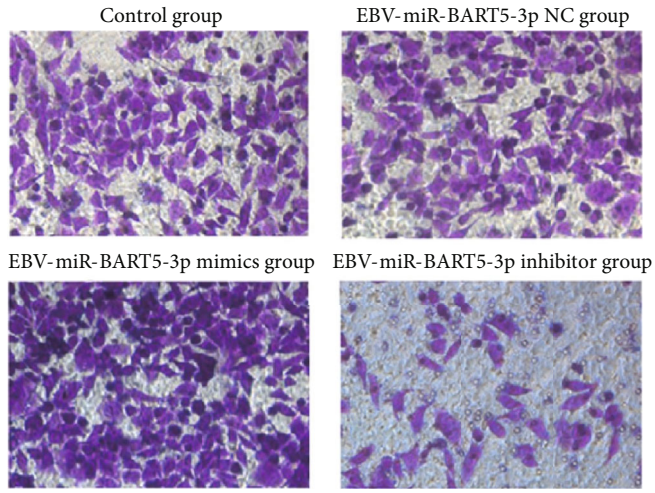

Figure 3: Comparison of the number of invasive cells in each group (×200).

Table 5: Comparison of cell migration rates in each group ($\bar{\chi} \pm s$).

Grouping	n	Mobility (%)
Control group	3	77.65 ± 8.52
EBV-miR-BART5-3p NC group	3	76.88 ± 8.03
EBV-miR-BART5-3p mimic group	3	89.53 ± 6.74
EBV-miR-BART5-3p inhibitor group	3	32.67 ± 5.96*
F		34.482
P		<0.001

Note: *P 0.05 vs. the control group.

Cell migration as affected by EBV-miR-BARTs: When comparing the control group, the EBV-miR-BART5-3p NC group, and the EBV-miR-BART5-3p mimic group, there was a significant difference in the migration rates; there was no statistically significant difference ($P > 0.05$); as shown in Table 5 and Figure 4, the migration rate of the EBV-miR-BART5-3p inhibitor group was significantly lower than that of the control group (P 0.05).

The effects of EBV-miR-BARTs on apoptosis proteins: Neither the control group nor the EBV-miR-BART5-3p NC group nor the EBV-miR-BART5-3p mimic group showed statistically significant differences in Bcl-2 expression levels ($P > 0.05$). The expression of BCL-2 protein was significantly decreased (P 0.05) When compared to the control group, Bax and Caspase-3 protein expressions were higher in the EBV-miR-BART5-3p inhibitor group, but there was no significant difference between the control and EBV-miR-BART5-3p NC groups ($P > 0.05$) (P 0.05), as shown by Table 6 and Figure 5.

The effects of EBV-miR-BARTs on invasion proteins: No discernable alterations in MMP-2 and MMP-9 protein expression were found between the control group, the EBV-miR-BART5-3p NC group, and the EBV-miR-BART5-3pa congregation of mimics. Protein expression levels of MMP-2 and MMP-9 were found to be considerably lower in the EBV-miR-BART5-3p inhibitor group compared to the control group (Figure 6 and Table 7).

4. Discussion

According to what its name says, nasopharyngeal carcinoma is a malignant epithelial tumor of the nasal and pharyngeal airways. The vast majority of cases have a pathological form that is a poorly differentiated, highly aggressive squamous cell carcinoma [11]. Because of this, it is of the utmost necessity to look into developing new treatment methods that can be used in the clinical care of patients who have this ailment. Numerous studies have shown that 44 different miR-BARTs are expressed in this disease. These miR-BARTs are responsible for oncogene or cancer suppressor gene functions, and they regulate the expressions of some EBV genes as well as host genes at the posttranscriptional level. This is an extremely important factor in the development, progression, and spread of the disease [12, 13]. Furthermore, miR-BART5-3p was shown to influence the development of the disease, but its specific mechanism is not clear, so this study took nasopharyngeal cancer cells as the research objects for analysis.

EBV-miR-BART5-3p expression was initially identified in nasopharyngeal carcinoma and normal nasopharyngeal cells. The data demonstrated that EBV-miR-BART5-3p expressions were greater in nasopharyngeal carcinoma cells compared to normal nasopharyngeal cells, suggesting that EBV-miR-BART 5-3p was really strongly expressed in the disease and was directly associated to the incidence of the illness. As we all know, the most typical and essential feature of cancer cells is proliferation, so controlling this feature can effectively prevent the occurrence of diseases. In addition, the most effective way to maintain basic cell activity is apoptosis, which is considered to be effective in eliminating cancer cells while causing very minimal damage to surrounding healthy tissue, which is also an important way for many chemotherapy drugs to clear tumor cell's way. Because it can participate in the ability of identifying the body and dealing with virus-infected cells in the body and inhibit the occurrence of cancer by regulating and improving damaged cells, so it is considered to be the key research direction of clinical treatment [14]. Therefore, this study

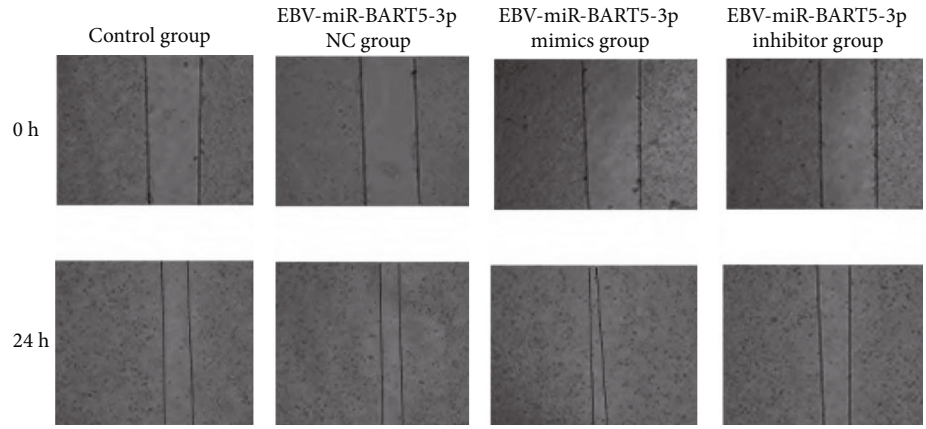

Figure 4: Comparison of cell migration rates in each group vs. the placebo group.

Table 6: Comparison of apoptosis proteins in each group ($\bar{\chi} \pm s$).

Grouping	n	Bcl-2	Bax	Caspase-3
Control group	3	1.55 ± 0.27	0.54 ± 0.03	0.58 ± 0.06
EBV-miR-BART5-3p NC group	3	1.52 ± 0.28	0.55 ± 0.08	0.58 ± 0.08
EBV-miR-BART5-3p mimic group	3	1.67 ± 0.24	0.28 ± 0.06*	0.29 ± 0.07*
EBV-miR-BART5-3p inhibitor group	3	0.34 ± 0.06*	1.58 ± 0.23*	1.64 ± 0.24*
F		23.377	61.282	58.928
P		<0.001	<0.001	<0.001

Note: Compared with the control group, $^*P < 0.05$.

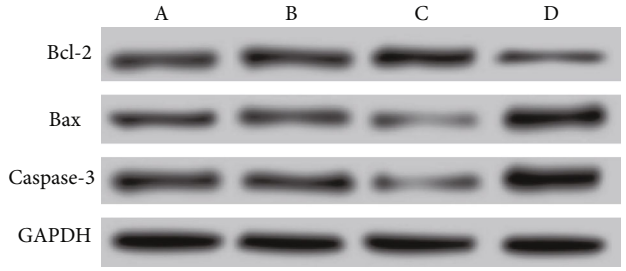

Figure 5: Comparison of apoptosis proteins in each group. Note: A is the control group; B is the EBV-miR-BART5-3p NC group; C is the EBV-miR-BART 5-3p mimic group; D is the EBV-miR-BART5-3p inhibitor group.

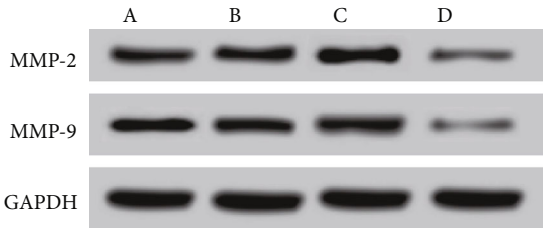

Figure 6: Comparison of cell invasion and apoptosis proteins in each group. Note: A is the control group; B is the EBV-miR-BART5-3p NC group; C is the EBV-miR-BART5-3p mimic group; D is the EBV-miR-BART5-3p inhibitor group.

detected the proliferative ability and apoptosis ability of nasopharyngeal carcinoma cells. According to the findings, the rates of cell proliferation in the control group, the EBV-miR-BART5-3p NC group, and the EBV-miR-BART5-3p mimic group did not significantly vary from one another. When the proliferation rate of EBV-miR-BART5-3p inhibitors was compared to that of the control group, it was shown to be lower. Flow cytometry analysis showed that comparison of apoptosis rates between the control and EBV-miR-BART5-3p NC groups revealed no statistically significant differences. While The EBV-miR-BART5-3p mimics group had considerably lower apoptosis than the control group, whereas the EBV-miR-BART5-3p inhibitors group had much more apoptosis than the control group. The fact that inhibiting its activity has the potential to effectively restrict the proliferation of nasopharyngeal carcinoma cells and promote the death of those cells demonstrates that EBV-miR-BART5-3p plays a role in the etiology of nasopharyngeal carcinoma. This is demonstrated by the fact that the inhibition of its activity has the potential to effectively restrict the proliferation of nasopharyngeal carcinoma cells. Moreover, the most harmful aspects of cancer are the disruption of the dynamic balance between cell proliferation and apoptosis, which leads to the creation and growth of malignant tumors, and life-threatening behavior of cancer cells is invasion and metastasis. It is not only a complex

Table 7: Comparison of cell invasion and apoptosis proteins in each group ($\bar{\chi} \pm s$).

Grouping	n	MMP-2	MMP- 9
Control group	3	1.75 ± 0.23	1.69 ± 0.27
EBV-miR-BART5-3p NC group	3	1.77 ± 0.28	1.68 ± 0.29
EBV-miR-BART5-3p mimic group	3	1.96 ± 0.31	1.98 ± 0.28
EBV-miR-BART5-3p inhibitor group	3	$0.51 \pm 0.11^*$	$0.49 \pm 0.10^*$
F		22.352	21.178
P		<0.001	<0.001

Note: Compared with the control group, $^*P < 0.05$.

behavior in the process but also interfered by many factors, so it is necessary to study the mechanisms of cancer cell proliferation, invasion, and apoptosis. Therefore, this is also one of the key research directions of clinical treatment, which can inhibit the disease by controlling or blocking these steps. Therefore, this study also detected the invasion and spread of nasopharyngeal cancer cells to other parts of the body. When invasive cell counts were compared between the control and EBV-miR-BART5-3p NC groups, the findings indicated no significant difference. According to the scratch test data, the number of invasive cells was more in the EBV-miR-BART5-3p reduction in the group that was treated with the EBV-miR-BART5-3p inhibitor in comparison to the group that received control treatment. Comparing the migration rates of the BART5-3p NC group, the EBV-miR-BART5-3p NC group, and the EBV-miR-BART5-3p mimic group, there was no statistically significant difference. As expected, migrating cells were less numerous in Epstein-Barr virus-specific inhibitors of the microRNA BART5-3p. Nasopharyngeal cancer cells were shown to invade and metastasize less when this miRNA was blocked, at least in comparison to the control group.

Studies [15, 16] believe that the Bcl-2 protein family produces the apoptosis-promoting proteins and plays a crucial part in the mitochondria-mediated death process, and the apoptosis-inhibiting proteins were playing a synergistic role to regulate cell apoptosis. In addition, since the initiation of apoptosis, often known as the process of programmed cell death, it requires the presence of the enzyme Caspase-3. Regulating the synthesis of the antiapoptotic protein Bcl-2 and the activation of downstream Caspase-3 is one possible method for avoiding the death of neurons. In order to do this, apoptosis-related protein expression was evaluated. The results showed that the expression of Bcl-2 protein did not vary significantly among the Ccontrol, EBV-miR-BART5-3p NC, and EBV-miR-BART5-3p mimic groups. While compared with the control group, the BCL-2 protein expression in the EBV-miR-BART5-3p inhibitor group was lower. It was found that there was no statistically significant difference between protein expression levels of Bax and Caspase-3 in the control vs. EBV-miR-BART5-3p NC groups compared with the Control group, Bax, and Caspase-3 protein. The expressions were found to be greater in the EBV-miR-BART5-3p inhibitor group. This suggests that inhibiting the expression of EBV-miR-BART5-3p can promote the apoptosis of nasopharyngeal carcinoma cells by downregulating Bcl-2 protein and upregulating Bax and Caspase-3 protein expressions. Besides, one of the basic loss of extracellular matrix is a necessary prerequisite for tumor spread. MMP is an extracellular matrix degradation enzyme whose main members MMP-2 and MMP-9 are the most critical proteins involved in tumor cell invasion, so the increased expression of MMPs may increase the invasion and metastasis of malignancies [17–19]. Therefore, additionally, invasion-related protein expression was detected, and the findings demonstrated that comparison of MMP-2 and MMP-9 protein expressions among the control, EBV-miR-BART5-3p NC, and EBV-miR-BART5-3p mimic groups revealed no statistically significant differences. The levels of protein expression for MMP-2 and MMP-9 were lower in the group that was given the EBV-miR-BART5-3p inhibitor compared to the group that was given the control. Based on these findings, it seems that EBV-miR-BART5-3p at low concentrations may limit MMP production, preventing cell invasion and metastasis by reducing MMP-2 and MMP-9 expression.

In conclusion, upregulating the EBV-miR-BART5-3p can regulate the occurrence and development of nasopharyngeal carcinoma cells, indicating that the mechanism through which EBV-miR-BARTs has a role in illness is still unknown. By making an impact on cell biology by controlling related apoptosis and invasion proteins. Blocking EBV-miR-BART5-3p expression reduces the risk of new cases of Epstein-Barr virus infection and further deterioration of nasopharyngeal carcinoma, suggesting that EBV-miR-BARTs may become a new biomarker for targeted therapy of nasopharyngeal carcinoma, which provides a certain reference for clinical treatment. However, its pathways and targets have not been fully elucidated, and further research is needed to reveal it.

Data Availability

The data used to support the findings of this study are included within the article and in the supplementary data file.

Conflicts of Interest

The authors declare that there are no conflicts of interest.

Acknowledgments

This work was supported by the National Natural Science Foundation of China (grant nos. 82060500, 81760491, and 81560441 to SJX) and the Natural Science Foundation of Guangxi Province of China (grant no. 2020GXNSFAA159040 to SJX).

References

[1] R. Chen, M. Zhang, Q. Li et al., "Retraction: the Epstein-Barr virus-encoded miR-BART22 targets MAP3K5 to promote host cell proliferative and invasive abilities in nasopharyngeal carcinoma," *Journal of Cancer*, vol. 8, no. 16, p. 3130, 2017.

[2] C. Jiang, J. Chen, S. Xie et al., "Evaluation of circulating EBV microRNA BART2-5p in facilitating early detection and screening of nasopharyngeal carcinoma," *International Journal of Cancer*, vol. 143, no. 12, pp. 3209–3217, 2018.

[3] H. Yang, G. Zhang, X. Che, and S. Yu, "Slug inhibition increases radiosensitivity of nasopharyngeal carcinoma cell line C666-1," *Experimental and Therapeutic Medicine*, vol. 15, no. 4, pp. 3477–3482, 2018.

[4] K. Xiao, Z. Yu, X. Li et al., "Genome-wide analysis of Epstein-Barr virus (EBV) integration and strain in C666-1 and raji Cells," *Journal of Cancer*, vol. 7, no. 2, pp. 214–224, 2016.

[5] X. Qiao, G. Hou, Y. L. He et al., "The novel regulatory role of the lncRNA-miRNA-mRNA axis in chronic inflammatory airway diseases," *Frontiers in Molecular Biosciences*, vol. 9, article 927549, 2022.

[6] S. F. Leung, K. C. Chan, B. B. Ma et al., "Plasma Epstein-Barr viral DNA load at midpoint of radiotherapy course predicts outcome in advanced-stage nasopharyngeal carcinoma," *Annals of Oncology*, vol. 25, no. 6, pp. 1204–1208, 2014.

[7] L. P. Tan, G. W. Tan, V. M. Sivanesan et al., "Systematic comparison of plasma EBV DNA, anti-EBV antibodies and miRNA levels for early detection and prognosis of nasopharyngeal carcinoma," *International Journal of Cancer*, vol. 146, no. 8, pp. 2336–2347, 2020.

[8] Q. Zhu, Q. Zhang, M. Gu et al., "MIR106A-5pupregulation suppresses autophagy and accelerates malignant phenotype in nasopharyngeal carcinoma," *Autophagy*, vol. 17, no. 7, pp. 1667–1683, 2021.

[9] X. Hong, N. Liu, Y. Liang et al., "Circular RNA CRIM1 functions as a ceRNA to promote nasopharyngeal carcinoma metastasis and docetaxel chemoresistance through upregulating FOXQ1," *Molecular Cancer*, vol. 19, no. 1, p. 33, 2020.

[10] X. Zheng, J. Wang, L. Wei et al., "Epstein-Barr virus microRNA miR-BART5-3p inhibits p53 expression," *Journal of Virology*, vol. 92, no. 23, article e01022, 2018.

[11] Y. Wang, Z. Guo, Y. Zhao et al., "Genetic polymorphisms of lncRNA-p53 regulatory network genes are associated with concurrent chemoradiotherapy toxicities and efficacy in nasopharyngeal carcinoma patients," *Scientific Reports*, vol. 7, no. 1, p. 8320, 2017.

[12] C. Lin, J. Zong, W. Lin et al., "EBV-miR-BART8-3p induces epithelial-mesenchymal transition and promotes metastasis of nasopharyngeal carcinoma cells through activating NF-κB and Erk1/2 pathways," *Journal of Experimental & Clinical Cancer Research*, vol. 37, no. 1, p. 283, 2018.

[13] L. Wu, J. Wang, D. Zhu et al., "Circulating Epstein-Barr virus microRNA profile reveals novel biomarker for nasopharyngeal carcinoma diagnosis," *Cancer Biomarkers*, vol. 27, no. 3, pp. 365–375, 2020.

[14] U. Sharma, T. S. Barwal, A. Malhotra et al., "Long non-coding RNA TINCR as potential biomarker and therapeutic target for cancer," *Life Sciences*, vol. 257, article 118035, 2020.

[15] W. Liao, J. Liu, B. Liu et al., "JIB-04 induces cell apoptosis via activation of the p53/Bcl-2/caspase pathway in MHCC97H and HepG2 cells," *Oncology Reports*, vol. 40, no. 6, pp. 3812–3820, 2018.

[16] A. Malki, M. Mohsen, H. Aziz et al., "New 3-Cyano-2-substituted pyridines induce apoptosis in MCF 7 breast cancer cells," *Molecules*, vol. 21, no. 2, p. 230, 2016.

[17] L. Rizzetto, F. Fava, K. M. Tuohy, and C. Selmi, "Connecting the immune system, systemic chronic inflammation and the gut microbiome: The role of sex," *Journal of Autoimmunity*, vol. 92, pp. 12–34, 2018.

[18] M. Laskowska, "Altered maternal serum matrix metalloproteinases MMP-2, MMP-3, MMP-9, and MMP-13 in severe early- and late-onset preeclampsia," *Biomed Research International*, vol. 2017, Article ID 6432426, p. 9, 2017.

[19] R. Guo, Y. P. Mao, L. L. Tang, L. Chen, Y. Sun, and J. Ma, "The evolution of nasopharyngeal carcinoma staging," *Journal de Radiologie*, vol. 92, no. 1102, article 20190244, 2019.

Hindawi
Oxidative Medicine and Cellular Longevity
Volume 2022, Article ID 5945828, 10 pages
https://doi.org/10.1155/2022/5945828

Research Article

Pursuing Diabetic Nephropathy through Aqueous Humor Proteomics Analysis

Huan Chen,[1,2] **Tan Wang**,[1,2] **Erqian Wang**,[1,2] **Ningning Li**,[3] **and Hanyi Min**[1,2]

[1]*Department of Ophthalmology, Peking Union Medical College Hospital, Chinese Academy of Medical Sciences and Peking Union Medical College, Beijing 100730, China*
[2]*Key Laboratory of Ocular Fundus Diseases, Chinese Academy of Medical Sciences and Peking Union Medical College, Beijing 100730, China*
[3]*Operating Room, Peking Union Medical College Hospital, Chinese Academy of Medical Sciences and Peking Union Medical College, Beijing 100730, China*

Correspondence should be addressed to Hanyi Min; 940871143@qq.com

Huan Chen and Tan Wang contributed equally to this work.

Received 20 July 2022; Revised 1 September 2022; Accepted 14 September 2022; Published 29 September 2022

Academic Editor: Shao Liang

In order to determine the possible aqueous humor (AH) proteins involved in diabetic nephropathy (DN) progression, we performed gel electrophoresis-liquid chromatography-tandem mass spectrometry protein profiling of AH samples from 5 patients with proliferative diabetic retinopathy (PDR) combined DN and 5 patients with PDR. Function enrichment analyses were carried out after the identification of differentially expressed proteins (DEPs). Protein-protein interaction networks were then built and the Search Tool for the Retrieval of Interacting Genes database and CytoNCA plugin in Cytoscape were utilized for module analysis. Ingenuity Pathway Analysis (IPA) was used to analyze disease and biological function, Tox function enrichment and upstream regulatory molecules/networks. Fifty-four DEPs were finally confirmed, whose enriched functions and pathways covered cell adhesion, extracellular exosome, complement activation, complement and coagulation cascades, etc. Nine hub genes were identified, including NCAM1, PLG, APOH, C3, PSAP, RBP4, CDH2, NUCB1, and GNS. IPA showed that C3 and PLG are involved in renal and urological system abnormalities. Conclusively, DEPs and hub proteins confirmed in this exploratory AH proteomic analysis may help us gain a deeper understanding of the molecular mechanisms involved in DN progression, providing novel candidate biomarkers for the early detection for diagnosis of DN.

1. Introduction

Diabetes mellitus is a chronic metabolic condition that can result in life-threatening complications [1–3]. Microvascular problems, like diabetic nephropathy (DN) and retinopathy (DR), are commonly associated with hyperglycemia and metabolic dysfunction in diabetes. Among microvascular complications, DN is a prime reason for end-stage renal failure globally. Currently, the clinical diagnosis of DN is based on proteinuria and/or altered glomerular filtration rate. DN progression is featured by a gradual increase in the rate of urinary albumin excretion, developing from normoalbuminuria to microalbuminuria and to macroalbuminuria. Nonetheless, due to considerable interindividual variability, conventional tests have significant limits for detection of DN in the early stages [4, 5]. Therefore, it is valuable to develop a more sensitive means to detect DN at an early stage.

Proteomics, which is based on mass spectrometry, has particular potential for identifying novel biomarkers in biofluids and could serve as the basis for new clinical testing. By analyzing the overall protein profiles in body fluids (urine, blood, etc.), proteomics can identify invaluable disease-specific biomarkers [6, 7]. In many patients with renal diseases, disease pathophysiology-related biomarkers have been identified

through urine and plasma proteomic analyses, with some of them put into practical clinical application [8–10].

Because DN often follows DR in the development of microvascular complications of diabetes, risk factors for DR include diabetes control and duration, elevated blood lipid levels, race, inflammatory cytokine levels in serum, and aqueous humor (AH) [11, 12]. Thus, it is worth to set DR combined with DN as the observation group and DN as the control group to explore the AH proteins modulated by DN. However, most studies usually perform quantitative proteomic analysis on urine and plasma specimens, and it is unclear whether differences in urine protein levels across cases in these analyses are due to differences in plasma protein levels or to elevated secreted protein levels caused by kidney injury [13]. To our knowledge, no proteomic study using AH has been performed to explore the key molecules.

This research employs the protein profiling method of gel electrophoresis plus liquid chromatography-tandem mass spectrometry (GeLC-MS/MS) and conducts bioinformatic analysis of proteins with markedly changed expression among groups and aims at identifying DN-modulated AH proteins in clinically well-defined diabetic populations while highlighting the biological processes underlying disease etiopathogenesis.

2. Materials and Method

2.1. Subjects. In this prospective case series research, 10 eyes from 10 diabetic patients (5 with PDR and 5 with PDR +DN), who were examined by the same internal medicine physician between March 2019 and October 2020 in the Peking Union Medical College Hospital, were analyzed. DN was confirmed by a 24-hour urinary albumin excretion of >300 mg, and PDR was confirmed by an ophthalmologist. Patients were clinically diagnosed with active PDR, presenting with repeated vitreous bleeding and/or retinal detachment as a result of fibrovascular membrane neovascularization. This study, after obtaining the approval from the Ethics Committee of our hospital and informed consent from all participants, was conducted strictly following the Declaration of Helsinki.

Patients all underwent pretreatment ocular examinations testing intraocular pressure (IOP), axial length, best-corrected visual acuity, and corneal endothelial cell counts, as well as ultrasound biomicroscopy of anterior and posterior segments.

Cases meeting any of the following were ruled out: (1) other retinal diseases besides DR; (2) other diseases of the eyes like glaucoma; (3) intraocular inflammation or infections; (4) intraocular surgery in the past 6 months; (5) previous penetrating ocular trauma; and (6) inability to receive eye operation because of recent myocardial infarction, uncontrolled diabetes/hypertension, cerebrovascular events, etc.

2.2. Sample Collection and Preparation. Following informed permission, patients received three days of prophylactic topical Levofloxacin instillation. Following topical anesthetic and sterilization of the operation field, patients were given an intravitreal anti-VEGF injection (Conbercept, Aflibercept, or Ranibizumab with a dosage of 0.05 mg, 2 mg, and 0.05 mg, respectively) via the superotemporal pars plana that was located 4 mm behind the limbus. Prior to anti-VEGF therapy, AH samples were taken from each patient for 10 minutes of centrifugation (13000 g, 4°C), followed by storage in tuberculin syringes and −80°C refrigeration.

Supernatants of AH samples obtained via centrifugation were placed into three KD ultrafiltration tubes. Then the protein solution was replaced with a lysis buffer that was composed of 2 M Thiourea (Sigma-Aldrich, USA) +7 M Urea (Amresco 0568-1Kg, USA) +0.1% 3-[(3-Cholamidopropyl) dimethylammonio]-1-propanesulfonate [CHAPS] + protease inhibitors.

Following ultrafiltration and centrifugation, we collected 10 μL of the sample and utilized the Bradford Protein Assay Kit (Thermo 23236, USA) for protein quantification. Proteins were then trypsin digested using the modified filter-aided sample preparation (FASP) technique [14, 15]. Briefly, lysate sample reduction was accomplished by incubating in dithiothretitol (DTT; 25 mM, Bio-Rad, USA) for 30 minutes at 60°C, and the subsequent 10 minutes of 50 mM iodoacetamide alkylation in the dark. After loading the samples onto a 10 kDa cutoff ultrafiltration membrane (Sartorius, Germany), they were incubated all night long at 37°C with trypsin (enzyme-to-protein ratio: 1 : 50). Following three 50 mM triethylammonium bicarbonate buffer (300 mL; Sigma T7408, USA) rinses, the samples were treated with 10 minutes of spinning at 12,000 g. Ziptip C18 pipette tips desalted peptides as instructed by the manufacturer's instructions.

After activation of the C18 solid phase extraction column and equilibration with ACN and 2% ACN, 0.1% FA, the sample loaded was pipetted 10 times, and then desalted and eluted with 2% and 50% ACN, 0.1% FA, respectively. After being collected into a rotary vacuum drier, the eluent was refrigerated at −80°C until use.

To build a data-independent acquisition (DIA) Spectral Library, dried peptides were subjected to 0.1% formic acid (FA; Thermo A117-50, USA) resuspension and the subsequent collection for sample dividing into samples with equal lysate quantities. The rest specimens were used with the Biognosys iRT kit, including the preparation of a 10 × iRT buffer and the subsequent addition of it to each sample at 9 : 1.

2.3. High-pH Reversed-Phase Fractionation. The digest samples were separated by additional high-pH reversed-phase chromatography. The RIGOL L-3000 system was utilized for the separation of mixed peptides in a 30 μg digest specimen using a reverse chromatography column (RIGOL, Beijing, China). After dissolution of peptides in mobile phase A (100 μL; 2% (v/v) acetonitrile (Thermo A955-4, USA), 98% (v/v) ddH_2O, pH 10), the mixture was spun down (14,000 g) for 20 minutes.

Then the mobile phase B (98% (v/v) acetonitrile, 2% (v/v) ddH_2O, pH 10) was injected into the supernatants at 1 mL/min in the column in a stepwise elution mode. Mobile phase B step gradients were used to acquire individual 15 minutes eluant fractions.

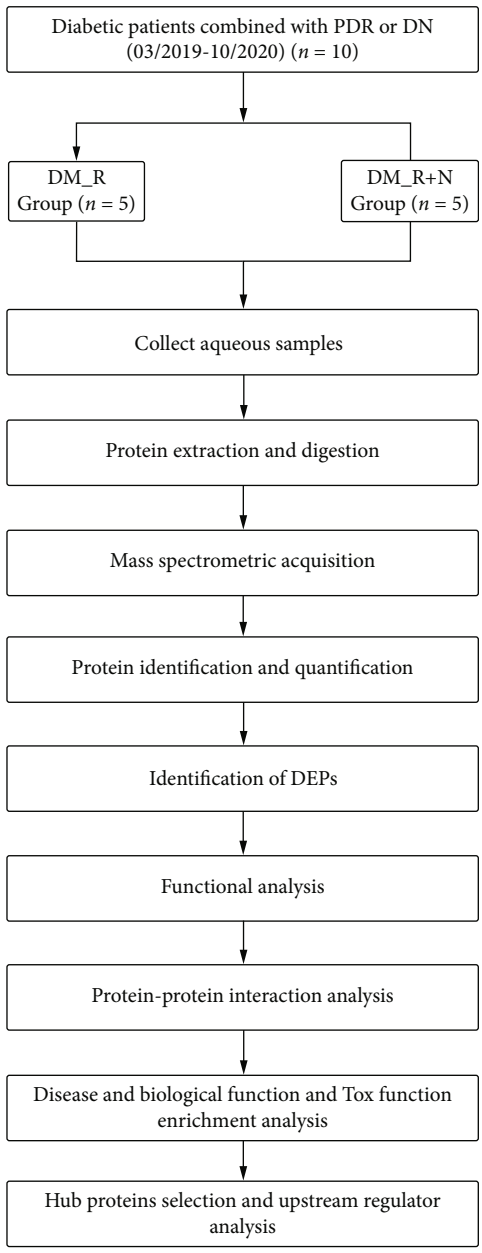

Figure 1: Research flowchart.

2.4. Mass Spectrometric (MS) Acquisition. For MS analysis, samples of 1 μg each volume were evaluated on an EASY-nLC1000 connected to an Orbitrap Fusion™ Tribrid™ MS instrument (Thermo Scientific) with the use of an internally prepared analytical column (150 μm ×150 mm, 1.9 μm). A binary solvent system, which was prepared by 0.1% FA in H_2O (A) and 0.1% FA in ACN (B), was adopted, and the linear gradient settings were as follows: 3-8% B/4 min, 8-22% B/65 min, 22-35% B/12 min, 35-90% B/4 min, and 90% B/5 min.

Using an EASY-Spray ion source, direct eluent introduction into the MS instrument was then carried out, with the spray voltage and capillary temperature set as 2.3 kV and 320°C, respectively. The whole MS scanning range was 300-1400 m/z for data-dependent acquisition- (DDA-) MS runs. With a resolution of 60,000, the MS had an under 3-stop-speed mode for 15,000 resolution MS/MS scans, while HCD had an isolation window and a normalized collision energy of 1.6 m/z and 32%, respectively. For DIA analyses, MS1 scans (automatic gain control (AGC) target 4e5 or 50 ms injection time) were performed from 300 to 1300 m/z, with DIA segmentation resolution of 30,000 (AGC target 5e5; for injection time). The collision energy was 32%, and the spectra were collected in profile mode.

2.5. Identification and Quantification of Proteins. DIA data analyses adopted Biognosys' Spectronaut pulsar programme [16]. The default software settings were employed for targeted data analyses, where dynamic iRT was utilized for retention time prediction types with window-based correction factors. Besides, local mass calibration, as well as limitless scrambled decoy generation, was utilized. We also employ an MS2-level interference connection for fragment elimination based on interference signals while retaining ≥3 for measurement. The false discovery rate (FDR) at peptide level was 1%.

Based on the principle of parsimony, the ID picker algorithm comes with the software package was used for proteomic inference. RAW images were converted to the Spectronaut file format when conducting spectral library-based studies and were calibrated according to the global spectral library's retention time dimension. After then, the files were used for spectrum analysis without any further retention time-based recalibration. To evaluate DDA data, Proteome Discoverer 2.3 with default settings (Trypsin/P (Promega, V5111, USA), two missed cleavages) was used. Cysteine carbamidomethylation and methionine and acetyl (protein N terminal) oxidation were used as the fixed modification and the variable modifications in the search criteria, respectively. The initial mass tolerances for precursor and fragment ions were set at 10 ppm and 0.02 Da, respectively [17]. UniProt human (uniprot_human_73940_20190731_iRT.fasta) and Biognosys' iRT peptides fasta (uploaded to the public repository) databases acted as references for DDA data retrieval.

2.6. Proteomic Analyses. After minimizing biases between experiments through median normalization, protein expression differences were then evaluated via a Student's t-test. Statistically significant differentially expressed proteins (DEPs) were defined using $p < 0.05$ and fold-change cut-offs of >1.5 and <0.667 (metabolite ratios >1.5 and <0.667 were classified as increased and decreased, respectively). Data normalization, DEPs, Gene Ontology (GO), and Kyoto Encyclopedia of Genes and Genomes (KEGG) analyses were performed in 'Wu Kong' platform (URL: https://www.omicsolution.com/wkomics/main/) [18]. Protein-protein interaction (PPI) networks of DEPs were constructed using the Search Tool for the Retrieval of Interacting Genes (STRING), with a combined score above 0.4 indicating statistical significance. Betweenness centrality was measured using CytoNCA plugin in Cytoscape v3.9.1 for the hub gene screening [19, 20]. "Without weight" was set as the parameter. IPA (Ingenuity Systems, USA) was utilized to discuss disease and biological function, Tox function enrichment and upstream regulatory molecules/networks.

Table 1: Subjects' characteristics*.

Variables	DM_R group ($n = 5$)	DM_R+N group ($n = 5$)	χ^2/t	$p^\dagger$
Age (y)	45.6 ± 15.4	42.2 ± 8.1	0.437	0.674
Male gender (%)	3 (60.0)	4 (80.0)	0.476	0.490
Right eye (number (%))	5 (100.0)	3 (60.0)	2.500	0.114
HbA1c (%)	8.1 ± 1.3	7.9 ± 0.4	0.329	0.751
Duration of diabetes (years)	9.2 ± 6.7	11.0 ± 5.0	0.615	0.556
Fasting blood glucose (mmol/L)	11.3 ± 6.0	7.4 ± 2.3	1.357	0.212
Indication for surgery				
Vitreous hemorrhage	5 (100.0)	5 (100.0)		—
Tractional retinal detachment	3 (60.0)	2 (40.0)	0.400	0.527

* Quantitative data and qualitative data were expressed as mean ± SD and number of people (%), respectively; $^\dagger p$ values refer to independent Student's t-test, Fisher's exact test, or the Chi-squared test exploring the difference of characteristics between groups.

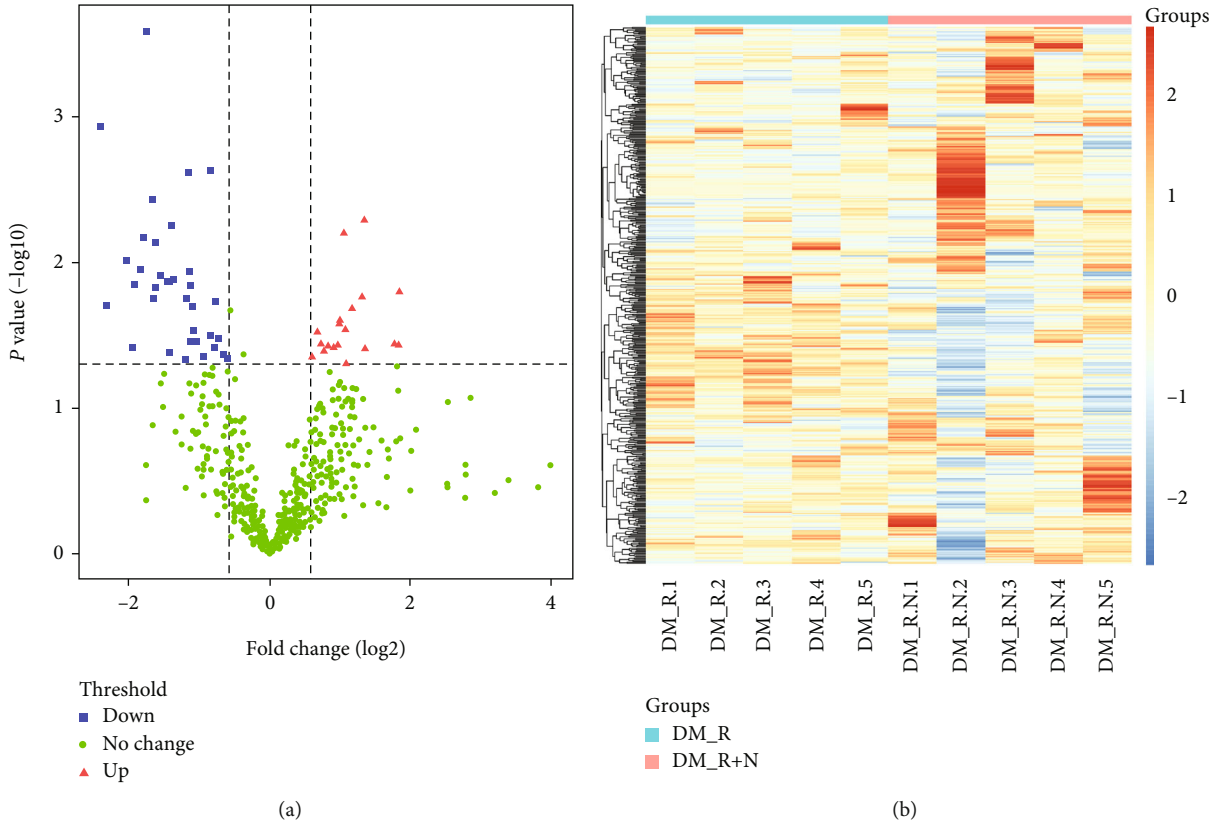

Figure 2: Differential expressed proteins analysis. (a) Valcano plot of the DEPs. (b) Heatmap of the DEPs.

2.7. Statistical Processing. A normality test was performed on all data. Continuous variables of normal distribution are expressed as mean ± standard deviation, and categorical variables are given numbers (percentages). Independent Student's t-test, Fisher's exact test or the Chi-squared test explored the intergroup difference of characteristics. A p value <0.05 was the significance level. R Statistical Software (RStudio, Inc., Boston, MA, USA; version 1.0.153) performed statistical analyses and plotting.

3. Results

3.1. Identification of DEPs. Figure 1 shows the workflow of our study. Table 1 shows patients' clinical features: PDR (DM_R) and PDR and nephropathy (DM_R+N) patients, 5 cases each with corresponding average ages 45.6 ± 15.4 and 42.2 ± 8.1 years ($p = 0.674$; Table 1). The two groups were statistically similar regarding gender ratio, age, HbA1c, duration of diabetes, fasting blood glucose (FBG), and

Table 2: Significantly differentially expressed proteins.

	Description	p.t. test	Fold-change	Express
A0A0A0MT36	Immunoglobulin kappa variable 6D-21 (nonfunctional)(IGKV6D-21)	0.036955223	3.57463889	Upregulate
A0A0C4DH25	Immunoglobulin kappa variable 3D-20 (IGKV3D-20)	0.049493681	2.128066835	Upregulate
A0A286YEY1	Immunoglobulin heavy constant alpha 1 (IGHA1)	0.028949107	2.110253625	Upregulate
B4E1Z4	Complement factor B (ENSP00000410815)	0.026456377	1.992205397	Upregulate
E7ES19	Thrombospondin 4 (THBS4)	0.017307964	2.481397525	Upregulate
P00742	Coagulation factor X (F10)	0.037825362	1.773541552	Upregulate
P00747	Plasminogen (PLG)	0.036283396	1.661644313	Upregulate
P01008	Serpin family C member 1 (SERPINC1)	0.030104627	1.601734876	Upregulate
P01024	Complement C3 (C3)	0.04465175	1.521368772	Upregulate
P01602	Immunoglobulin kappa variable 1-5 (IGKV1-5)	0.025182741	2.001283426	Upregulate
P01709	Immunoglobulin lambda variable 2-8 (IGLV2-8)	0.040265165	1.711371053	Upregulate
P02749	Apolipoprotein H (APOH)	0.039317619	2.55723495	Upregulate
P02753	Retinol binding protein 4 (RBP4)	0.038694982	1.88456551	Upregulate
P07357	Complement C8 alpha chain (C8A)	0.037286856	1.950270583	Upregulate
P22314	Ubiquitin like modifier activating enzyme 1 (UBA1)	0.036426384	3.419798742	Upregulate
P25311	Alpha-2-glycoprotein 1, zinc-binding (AZGP1)	0.006282018	2.078922885	Upregulate
P80188	Lipocalin 2 (LCN2)	0.020689034	2.250249072	Upregulate
Q15828	Cystatin E/M (CST6)	0.015888421	3.585016053	Upregulate
Q5T123	SH3 domain binding glutamate rich protein like 3 (SH3BGRL3)	0.005080205	2.546679302	Upregulate
A0A087WX77	Neural cell adhesion molecule 1 (NCAM1)	0.013520081	0.362177114	Downregulate
A0A087X0M8	Cell adhesion molecule L1 like (CHL1)	0.002396942	0.447154673	Downregulate
A0A087X0S5	Collagen type VI alpha 1 chain (COL6A1)	0.002327337	0.556691701	Downregulate
A0A087X1J7	Glutathione peroxidase 3 (GPX3)	0.042604595	0.636518049	Downregulate
A0A2R8Y7U1	Tripeptidyl peptidase 1 (TPP1)	0.007284898	0.324649629	Downregulate
C9IZG4	cutA divalent cation tolerance homolog (CUTA)	0.014864747	0.323983214	Downregulate
C9JIZ6	Prosaposin (PSAP)	0.044621913	0.51799473	Downregulate
C9JYY6	Neuronal cell adhesion molecule (NRCAM)	0.011508226	0.450951245	Downregulate
E9PF17	Versican (VCAN)	0.038360004	0.257367031	Downregulate
F6S8M0	Glucosamine (N-acetyl)-6-sulfatase (GNS)	0.012224358	0.341371268	Downregulate
F6VDH7	ST13 Hsp70 interacting protein (ST13)	0.019827016	0.200673989	Downregulate
H0YF95	Seizure related 6 homolog (SEZ6)	0.013350489	0.371791006	Downregulate
K7ELL7	Protein kinase C substrate 80 K-H (PRKCSH)	0.017635437	0.43953481	Downregulate
O43505	Beta-1,4-glucuronyltransferase 1 (B4GAT1)	0.045900429	0.662871362	Downregulate
O60575	Serine peptidase inhibitor Kazal type 4 (SPINK4)	0.046274131	0.436778293	Downregulate
O75882	Attractin (ATRN)	0.032912143	0.603382567	Downregulate
O95445	Apolipoprotein M (APOM)	0.011195521	0.27929918	Downregulate
P10745	Retinol binding protein 3 (RBP3)	0.000256535	0.294947516	Downregulate
P12110	Collagen type VI alpha 2 chain (COL6A2)	0.041236514	0.371699968	Downregulate
P15291	Beta-1,4-galactosyltransferase 1 (B4GALT1)	0.03477554	0.458653103	Downregulate
P19022	Cadherin 2 (CDH2)	0.029216973	0.468621717	Downregulate
P20849	Collagen type IX alpha 1 chain (COL9A1)	0.00669932	0.287809307	Downregulate
P23471	Protein tyrosine phosphatase receptor type Z1 (PTPRZ1)	0.005534332	0.378623205	Downregulate
P43251	Biotinidase (BTD)	0.018418073	0.582873713	Downregulate
Q02818	Nucleobindin 1 (NUCB1)	0.035050498	0.482356964	Downregulate
Q14563	Semaphorin 3A (SEMA3A)	0.017746065	0.317266926	Downregulate
Q15223	NECTIN cell adhesion molecule 1 (NECTIN1)	0.001170444	0.188635993	Downregulate
Q15904	ATPase H+ transporting accessory protein 1 (ATP6AP1)	0.003694191	0.314344708	Downregulate
Q6UX71	Plexin domain containing 2 (PLXDC2)	0.031813223	0.559106065	Downregulate

Table 2: Continued.

	Description	p.t. test	Fold-change	Express
Q8WXD2	Secretogranin III (SCG3)	0.014293057	0.455315443	Downregulate
Q96JP9	Cadherin related family member 1 (CDHR1)	0.014155971	0.262671062	Downregulate
Q99784	Olfactomedin 1 (OLFM1)	0.013202271	0.386150368	Downregulate
Q9BRK5	Stromal cell derived factor 4 (SDF4)	0.009752638	0.243429438	Downregulate
Q9BTY2	Alpha-L-fucosidase 2 (FUCA2)	0.038217313	0.576768404	Downregulate
Q9HAT2	Sialic acid acetylesterase (SIAE)	0.020162057	0.466031421	Downregulate

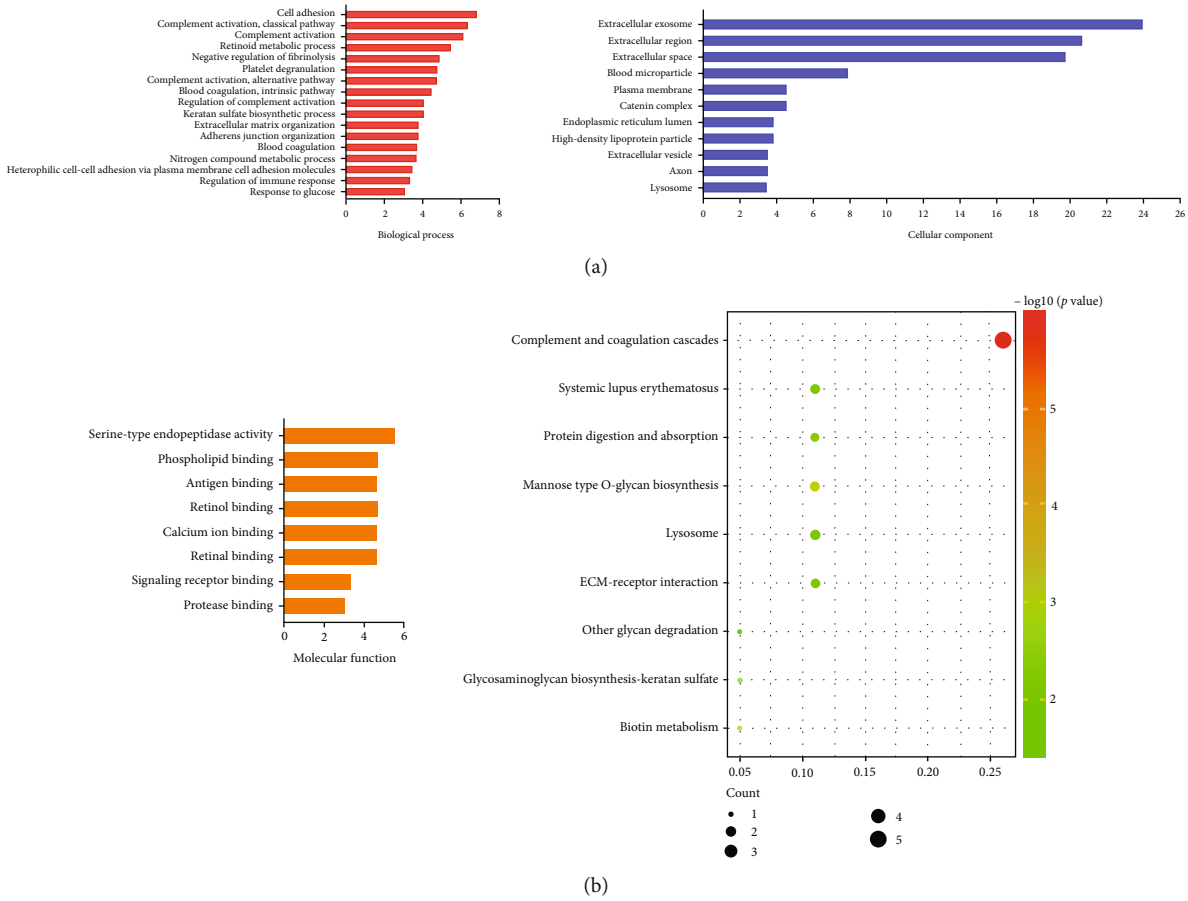

Figure 3: Functional enrichment pathway analysis. (a) Go enrichment. (b) KEGG enrichment.

Table 3: Differentially expressed proteins with Betweenness centrality above 10.

	Proteins	Betweenness centrality
1	NCAM1	Betweenness: 62.5
2	PLG	Betweenness: 44.5
3	APOH	Betweenness: 40.833332
4	C3	Betweenness: 19.833334
5	PSAP	Betweenness: 16.0
6	RBP4	Betweenness: 11.0
7	CDH2	Betweenness: 10.166667
8	NUCB1	Betweenness: 10.0
9	GNS	Betweenness: 10.0

indication for surgery. Macroalbuminuria was present in the DM_R+N group (>300 mg/24 h).

Large-scale LC-MS/MS analysis of all gel bands retrieved 692 unique proteins (Table S1). Filter by 0.5 missing ratio in each group, and after filling by the global minimum method, 496 common to all cases were further studied, identifying 54 statistically significant DEPs, 19 that were upregulated and 35 that were downregulated statistically significant DEPs (volcano plot Figure 2(a), heatmap Figure 2(b)) (Table 2).

3.2. GO and KEGG Pathway Enrichment Analysis. DEPs GO was categorized as biological processes, cellular components, and molecular functions (Figure 3(a)). In the top 3 biological process group, DEPs were dominantly enriched in cell adhesion, complement activation, and classical pathway. DEPs in

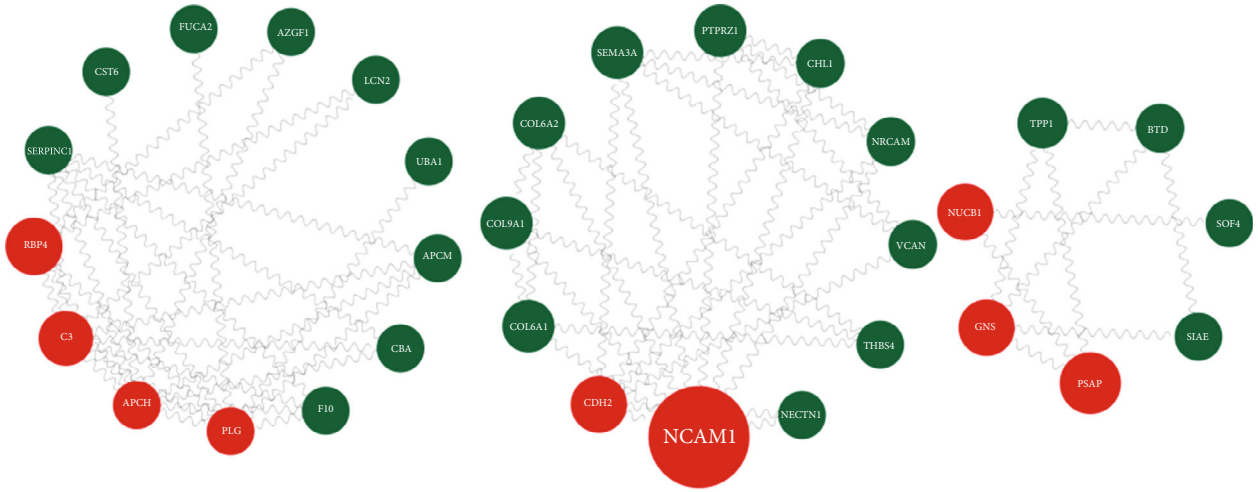

Figure 4: PPI network demonstrates the relationships between proteins.

the top 3 cellular component group were primarily enriched in extracellular exosome/area/space. The top 3 molecular function group DEPs were dominantly enriched in cell adhesion, complement activation, and classical pathway. DEGs were predominantly enriched in complement and coagulation cascades, as indicated by KEGG enrichment analysis in Figure 3(b).

3.3. Protein Networks. To better understand the relationship between DEPs, we utilized the STRING database for PPI analysis. The PPI can be classified as either known interaction (curated databases and experimental determination of literature), predicted interaction (gene-neighborhood, gene fusion, and gene cooccurrence), or others (text mining, coexpression, and protein homology). See Table S2 for detailed information. There were 34 (63.0%) proteins interacting with other proteins in the 54 DEPs. Proteins with betweenness centrality above 10 include NCAM1, PLG, APOH, C3, PSAP, RBP4, CDH2, NUCB1, and GNS (Table 3, Figure 4).

Red indicated the differentially expressed proteins with betweenness centrality above 10; green indicated differentially expressed proteins with betweenness centrality below 10.

3.4. Disease and Biological Function and Tox Function Enrichment Analyses. We performed disease and biological function and Tox function enrichment analyses for 54 DEPs with the QIAGEN IPA (QIAGEN, USA; URL: http://www.qiagen.com/ingenuity).

As shown in Table 4, DEPs were enriched to 15 functional categories involving renal and urological disease with statistical significance, including renal vein thrombosis, migration, atypical hemolytic uremic syndrome (aHUS), failure, biotinidase deficiency, septic acute kidney injury, staghorn calculus, susceptibility to aHUS type 5, end stage renal disease (ESRD), aHUS, adhesion, acute tubular necrosis, C3 glomerulopathy, nephrosis, and membranoproliferative glomerulonephritis. The corresponding diseases or function annotations were renal vein thrombosis, migration of kidney cell lines, aHUS, failure of kidney, biotinidase deficiency, septic acute kidney injury, staghorn calculus, susceptibility to aHUS type 5, ESRD, acute phase aHUS, adhesion of kidney cell lines, acute tubular necrosis, C3 glomerulopathy, nephrosis, and membranoproliferative glomerulonephritis, respectively.

As shown in Table 5, DEPs were enriched to 11 Tox functional categories involving renal and urological system abnormalities with statistical significance. The specific diseases or functions annotation involved include failure of kidney, ESRD, acute tubular necrosis, C3 glomerulopathy, nephrosis, ischemic acute renal failure, membranoproliferative glomerulonephritis, steroid-dependent nephrotic syndrome, and IgA nephropathy.

DEPs involved in renal and urological system abnormalities include C3, F10, BTD, LCN2, PLG, SEMA3A, SERPINC1, CHL1, and RBP3. Among them, C3 and PLG were also the selected hub proteins in PPI networks of all DEPs with betweenness centrality above 10.

3.5. Analysis of Upstream Regulators. Upstream regulator analysis, in which IPA was used to statistically enrich upstream regulators, was used to identify candidate upstream regulators of proteins (Table S3).

Upstream factors statistically affecting C3 included IL1B, PPARA, TWIST1, Tnf receptor, estrogen receptor, EZH2, NR1H2, C3AR1, miR-291a-3p (and other miRNAs w/seed AAGUGCU), EHMT1, CD46, and IL6. Upstream factors statistically affecting PLG included JINK1/2, Jnk, Akt, and IL6.

4. Discussion

DN has become the prime culprit for ESRD in both the developed and developing countries [21, 22]. However, because of the complicated etiology of DN as well as ethnic differences, its molecular mechanism remains uncharacterized. Many DN patients are diagnosed late and are difficult to cure with conventional therapy [23], which largely underlies DN patients' adverse renal outcomes. Hence, there is an

Table 4: Functional enrichment involving renal and urological disease for differentially expressed proteins.

Categories	Functions	Diseases or functions annotation	p value	Molecules	# molecules
Cardiovascular disorders, hematological diseases, organismal injuries and abnormalities, and renal and urological disease	Renal vein thrombosis	Renal vein thrombosis	0.0000364	F10, SERPINC1	2
Cellular movement and renal and urological system development and function	Migration	Migration of kidney cell lines	0.000108	C3, CHL1, F10, RBP3	4
Cardiovascular disorders, cell death and survival, connective tissue disorders, hematological diseases, organismal injuries and abnormalities, and renal and urological disease	Atypical hemolytic uremic syndrome	Atypical hemolytic uremic syndrome	0.000907	C3, PLG	2
Organismal injuries and abnormalities and renal and urological disease	Failure	Failure of kidney	0.00237	C3, F10, SERPINC1, LCN2	4
Developmental disorder, hereditary disorder, metabolic disease, organismal injuries and abnormalities, and renal and urological disease	Biotinidase deficiency	Biotinidase deficiency	0.00249	BTD	1
Organismal injuries and abnormalities and renal and urological disease	Septic acute kidney injury	Septic acute kidney injury	0.00249	LCN2	1
Organismal injuries and abnormalities and renal and urological disease	Staghorn calculus	Staghorn calculus	0.00249	PLG	1
Cardiovascular disorders, cell death and survival, connective tissue disorders, hematological diseases, organismal injuries and abnormalities, and renal and urological disease	Susceptibility to atypical hemolytic uremic syndrome type 5	Susceptibility to atypical hemolytic uremic syndrome type 5	0.00249	C3	1
Organismal injuries and abnormalities and renal and urological disease	End stage renal disease	End stage renal disease	0.00318	C3, F10, SERPINC1	3
Cardiovascular diseases, cell death and survival, connective tissue disorders, hematological diseases, organismal injuries and abnormalities, and renal and urological disease	Atypical hemolytic uremic syndrome	Acute phase atypical hemolytic uremic syndrome	0.00497	C3	1
Cell-to-cell signaling and interaction and renal and urological system development and function	Adhesion	Adhesion of kidney cell lines	0.00664	C3, F10	2
Organismal injuries and abnormalities and renal and urological disease	Acute tubular necrosis	Acute tubular necrosis	0.00745	LCN2	1
Organismal injuries and abnormalities and renal and urological disease	C3 glomerulopathy	C3 glomerulopathy	0.00745	C3	1
Organismal injuries and abnormalities and renal and urological disease	Nephrosis	Nephrosis	0.00861	C3, F10, SERPINC1	3
Immunological disease, inflammatory disease, inflammatory response, organismal injuries and abnormalities, andrenal and urological disease	Membranoproliferative glomerulonephritis	Membranoproliferative glomerulonephritis	0.00992	C3	1

urgent need for potential markers that can facilitate early diagnosis and targeted therapies. Because DN often follows DR in the development of microvascular complications of diabetes, it is worth to set DR combined with DN as the observation group and DN as the control group to explore the AH proteins modulated by DN.

In the present study, proteins in AH samples of 5 patients with PDR combined DN and 5 patients with PDR were quantified, and the DEPs between two groups were identified. Then, GO and KEGG pathway enrichment were analyzed (Figures 3(a) and 3(b)). Moreover, PPI was analyzed and hub proteins were selected, including NCAM1, PLG, APOH, C3, PSAP, RBP4, CDH2, NUCB1, and GNS. To further search for hub proteins associated with renal and urological disease, IPA was used. C3 and PLG were selected as hub proteins associated with renal and urological disease.

C3 is central in complement system activation. The proteolytic cleavage of C3 by C3 convertases is the key reaction in both classical and alternative pathways of complement. Following activation, C3b can perform covalent binding to cell surface carbohydrates or immune aggregates through its reactive thioester. PLG can dissolve blood clot fibrin and functions as a proteolytic factor in embryonic development, tissue remodeling, neoplasm invasiveness, inflammation, and many other processes. It is also capable of

Table 5: Tox functional categories involving renal and urological system abnormalities for differentially expressed proteins.

Categories	Functions	Diseases or functions annotation	p value	Molecules	# molecules
Kidney failure	Failure	Failure of kidney	0.00237	C3,F10,SERPINC1,LCN2	4
Kidney failure	End stage renal disease	End stage renal disease	0.00318	C3,F10,SERPINC1	3
Kidney failure	Acute tubular necrosis	Acute tubular necrosis	0.00745	LCN2	1
Glomerular injury	C3 glomerulopathy	C3 glomerulopathy	0.00745	C3	1
Nephrosis	Nephrosis	Nephrosis	0.00861	C3,F10,SERPINC1	3
Kidney failure and renal damage	Ischemic acute renal failure	Ischemic acute renal failure	0.00992	LCN2	1
Glomerular injury, renal inflammation, renal nephritis	Membranoproliferative glomerulonephritis	Membranoproliferative glomerulonephritis	0.00992	C3	1
Nephrosis	Steroid-dependent nephrotic syndrome	Steroid-dependent nephrotic syndrome	0.0295	C3	1
Glomerular injury, renal inflammation, and renal nephritis	IgA nephropathy	IgA nephropathy	0.0882	C3	1
Glomerular injury, renal inflammation, and renal nephritis	Lupus nephritis	Lupus nephritis	0.412	C3	1
Renal necrosis/cell death	Apoptosis	Apoptosis of kidney cell lines	0.478	RBP4	1

activating urokinase-type plasminogen activators and collagenases, as well as complement zymogens like C1 and C5. And fibronectin and laminin cleavage results in cell detachment and apoptosis.

Several studies have found that C3 and PLG are essential in the pathogenesis of DN. Zhao et al. found C3 correlated negatively with annual estimated glomerular filtration rate decline [24]. Moreover, C3 has also been identified as possibly involved in diabetic tubulointerstitial injury by Zeng et al. [25]. And PLG was determined by Wang et al. to be critical in regulating the occurrence of DN [26]. Caseiro et al. analyzed alterations in urine proteomes in T1DM patients with and without complications (e.g., DR and DN) and identified that ephrin type-B receptor 4 and vitamin K-dependent protein Z were feasible markers for advanced T1DM complicated by DR or DN [27]. However, this study did not analyze the differentially coexpressed proteins between the DR combined DN group and DR group, nor did the betweenness centrality use to screen hub proteins, and IPA was not used to select proteins associated with renal and urological disease.

Advances in analytical techniques and database search programs have substantially supported the proteomic research on DR and DN. The identification of DEPs is the key to revealing specific pathological processes. Proteins of particular interest that occupy a place in the PDR combined DN/PDR DEP list may be the candidate biomarkers for early-stage DN [28]. The limitations of this work mainly lie in the following two aspects: one is the absence of verification of DEPs, for which orthogonal analyses, including western blotting, radioimmunoassay, Enzyme-Linked Immunosorbent Assays (ELISA), and immunohistochemistry should be carried out for validation [29, 30]; the other is the limited samples included that cannot contribute to a meaningful evaluation, requiring further research with expanded sample size.

5. Conclusion

This research, as far as we are aware, is the first to analyze the mechanism of progression of DN on the basis of PDR in AH samples. The findings offer novel insights into alterations of AH proteomes in PDR combined DN patients and further validation of key proteins previously found in other tissue samples such as urine and blood [25, 31]. The selected hub proteins may interfere with the regulation of PDR comorbid DN from PDR in AH, especially for C3 and PLG, but further work for validation of this hypothesis is warranted.

Data Availability

The datasets generated during the current study are available from the corresponding author on reasonable request.

Conflicts of Interest

The authors declare that they have no competing interests.

Authors' Contributions

Huan Chen and Tan Wang contributed equally to this work and are co-first authors. HM designed the research. TW, HC, BQ, and NL conducted the research and analyzed the data. HM, TW, EW, and HC wrote the paper. HM had primary responsibility for the final content. All authors read and approved the final manuscript.

Supplementary Materials

Supplementary 1. Table S1: Unique proteins were detected by the large-scale LC-MS/MS analysis.

Supplementary 2. Table S2: Protein-protein interaction analysis results using the STRING database.

Supplementary 3. Table S3: Statistically significant upstream regulators from IPA.

References

[1] A. Soggiu, C. Piras, L. Bonizzi, H. Hussein, S. Pisanu, and P. Roncada, "A discovery-phase urine proteomics investigation in type 1 diabetes," *Acta Diabetologica*, vol. 49, no. 6, pp. 453–464, 2012.

[2] S. Banon and D. Isenberg, "Rheumatological manifestations occurring in patients with diabetes mellitus," *Scandinavian Journal of Rheumatology*, vol. 42, no. 1, pp. 1–10, 2013.

[3] K. Shikata, T. Ninomiya, and Y. Kiyohara, "Diabetes mellitus and cancer risk: review of the epidemiological evidence," *Cancer Science*, vol. 104, no. 1, pp. 9–14, 2013.

[4] P. Zürbig, G. Jerums, P. Hovind et al., "Urinary proteomics for early diagnosis in diabetic nephropathy," *Diabetes*, vol. 61, no. 12, pp. 3304–3313, 2012.

[5] Y.-M. Sun, Y. Su, J. Li, and L.-F. Wang, "Recent advances in understanding the biochemical and molecular mechanism of diabetic nephropathy," *Biochemical and Biophysical Research Communications*, vol. 433, no. 4, pp. 359–361, 2013.

[6] P. E. Geyer, L. M. Holdt, D. Teupser, and M. Mann, "Revisiting biomarker discovery by plasma proteomics," *Molecular Systems Biology*, vol. 13, no. 9, p. 942, 2017.

[7] A. Beasley-Green, "Urine proteomics in the era of mass spectrometry," *International Neurourology Journal*, vol. 20, Supplement 2, pp. S70–S75, 2016.

[8] J. P. Schanstra and H. Mischak, "Proteomic urinary biomarker approach in renal disease: from discovery to implementation," *Pediatric Nephrology*, vol. 30, no. 5, pp. 713–725, 2015.

[9] J. Siwy, P. Zürbig, A. Argiles et al., "Noninvasive diagnosis of chronic kidney diseases using urinary proteome analysis," *Nephrology Dialysis Transplantation*, vol. 32, pp. 2079–2089, 2017.

[10] T. Fiseha and Z. Tamir, "Urinary markers of tubular injury in early diabetic nephropathy," *International Journal of Nephrology*, vol. 2016, Article ID 4647685, 10 pages, 2016.

[11] C. I. Bondor, A. R. Potra, D. Moldovan et al., "Relationship of adiponectin to markers of oxidative stress in type 2 diabetic patients: influence of incipient diabetes-associated kidney disease," *International Urology and Nephrology*, vol. 47, no. 7, pp. 1173–1180, 2015.

[12] W.-L. Liao, Y.-H. Chen, C.-C. Chen et al., "Effect of adiponectin level and genetic variation of its receptors on diabetic retinopathy: a case–control study," *Medicine*, vol. 98, no. 11, article e14878, 2019.

[13] A. Araumi, T. Osaki, K. Ichikawa et al., "Urinary and plasma proteomics to discover biomarkers for diagnosing between diabetic nephropathy and minimal change nephrotic syndrome or membranous nephropathy," *Biochemistry and Biophysics Reports*, vol. 27, article 101102, 2021.

[14] J. R. Wiśniewski, A. Zougman, N. Nagaraj, and M. Mann, "Universal sample preparation method for proteome analysis," *Nature Methods*, vol. 6, no. 5, pp. 359–362, 2009.

[15] J. R. Wiśniewski, "Quantitative evaluation of filter aided sample preparation (fasp) and multienzyme digestion fasp protocols," *Analytical Chemistry*, vol. 88, no. 10, pp. 5438–5443, 2016.

[16] F. Zhang, W. Ge, G. Ruan, X. Cai, and T. Guo, "Data-independent acquisition mass spectrometry-based proteomics and software tools: a glimpse in 2020," *Proteomics*, vol. 20, no. 17-18, article 1900276, 2020.

[17] L. Leng, M. Li, W. Li et al., "Sera proteomic features of active and recovered covid-19 patients: potential diagnostic and prognostic biomarkers," *Signal Transduction and Targeted Therapy*, vol. 6, pp. 1–3, 2021.

[18] H. Yu, H. Luo, L. Chang et al., "The nedd8-activating enzyme inhibitor mln4924 reduces ischemic brain injury in mice," *Proceedings of the National Academy of Sciences*, vol. 119, no. 6, article e2111896119, 2022.

[19] Y. Tang, M. Li, J. Wang, Y. Pan, and F.-X. Wu, "Cytonca: a cytoscape plugin for centrality analysis and evaluation of protein interaction networks," *Biosystems*, vol. 127, pp. 67–72, 2015.

[20] M. E. Smoot, K. Ono, J. Ruscheinski, P.-L. Wang, and T. Ideker, "Cytoscape 2.8: new features for data integration and network visualization," *Bioinformatics*, vol. 27, no. 3, pp. 431-432, 2011.

[21] L. Zhang, J. Long, W. Jiang, Y. Shi, X. He, and Z. Zhou, "Trends in chronic kidney disease in China," *New England Journal of Medicine*, vol. 375, pp. 905-906, 2016.

[22] W. E. Mitch, "Treating diabetic nephropathy—are there only economic issues?," *New England Journal of Medicine*, vol. 351, no. 19, pp. 1934–1936, 2004.

[23] D. Fineberg, K. A. Jandeleit-Dahm, and M. E. Cooper, "Diabetic nephropathy: diagnosis and treatment," *Nature Reviews Endocrinology*, vol. 9, no. 12, pp. 713–723, 2013.

[24] L. Zhao, Y. Zhang, F. Liu et al., "Urinary complement proteins and risk of end-stage renal disease: quantitative urinary proteomics in patients with type 2 diabetes and biopsy-proven diabetic nephropathy," *Journal of Endocrinological Investigation*, vol. 44, no. 12, pp. 2709–2723, 2021.

[25] M. Zeng, J. Liu, W. Yang et al., "Multiple-microarray analysis for identification of hub genes involved in tubulointerstial injury in diabetic nephropathy," *Journal of Cellular Physiology*, vol. 234, no. 9, pp. 16447–16462, 2019.

[26] Y. Z. Wang, W. W. Xu, D. Y. Zhu et al., "Specific expression network analysis of diabetic nephropathy kidney tissue revealed key methylated sites," *Journal of Cellular Physiology*, vol. 233, no. 10, pp. 7139–7147, 2018.

[27] A. Caseiro, A. Barros, R. Ferreira et al., "Pursuing type 1 diabetes mellitus and related complications through urinary proteomics," *Translational Research*, vol. 163, no. 3, pp. 188–199, 2014.

[28] C. Schori, C. Trachsel, J. Grossmann, I. Zygoula, D. Barthelmes, and C. Grimm, "The proteomic landscape in the vitreous of patients with age-related and diabetic retinal disease," *Investigative Ophthalmology & Visual Science*, vol. 59, no. 4, pp. AMD31–AMD40, 2018.

[29] L. J. Cehofski, N. Mandal, B. Honoré, and H. Vorum, "Analytical platforms in vitreoretinal proteomics," *Bioanalysis*, vol. 6, no. 22, pp. 3051–3066, 2014.

[30] S. Walia, A. C. Clermont, B.-B. Gao, L. P. Aiello, and E. P. Feener, "Vitreous proteomics and diabetic retinopathy," *Seminars in Ophthalmology*, vol. 25, pp. 289–294, 2010.

[31] G. Baydas, V. S. Nedzvetskii, P. A. Nerush, S. V. Kirichenko, and T. Yoldas, "Altered expression of NCAM in hippocampus and cortex may underlie memory and learning deficits in rats with streptozotocin-induced diabetes mellitus," *Life Sciences*, vol. 73, no. 15, pp. 1907–1916, 2003.

Hindawi
Oxidative Medicine and Cellular Longevity
Volume 2022, Article ID 9993319, 15 pages
https://doi.org/10.1155/2022/9993319

Research Article

Integrated Analysis of Multiomics Data Identified Molecular Subtypes and Oxidative Stress-Related Prognostic Biomarkers in Glioblastoma Multiforme

Yawen Ma and Zhuo Xi

Department of Neurosurgery, Shengjing Hospital of China Medical University, Shenyang, Liaoning 11000, China

Correspondence should be addressed to Zhuo Xi; neurosurgeon_xz@163.com

Received 7 July 2022; Revised 12 August 2022; Accepted 24 August 2022; Published 22 September 2022

Academic Editor: Shao Liang

Glioblastoma multiforme (GBM) is a glioma in IV stage, which is one of the most common primary malignant brain tumors in adults. GBM has the characters of high invasiveness, high recurrence rate, and low survival rate and with a poor prognosis. GBM implicates various genetic changes and epigenetic and gene transcription disorders, which are crucial in developing GBM. With the progression and enhancement of high-throughput sequencing technologies, the acquirement and administering approaches of diverse biological omics data on distinctive levels are developing more advanced. However, the research of GBM with multiomics remains largely unknown. We identified GBM-related molecular subtypes by integrated multiomics data and exploring the connections of gene copy number variation (CNV) and methylation gene (MET) change data. The expression of CNV and MET genes was examined through cluster integration analysis. The present study confirmed three clusters (iC1, iC2, and iC3) with distinctive prognosis and molecule peculiarities. We also recognized three oxidative stress protecting molecules (OSMR, IGFBP6, and MYBPH) by contrasting gene expression, MET, and CNV in the three subtypes. OSMR, IGFBP6, and MYBPH were differentially expressed in the clusters, suggesting they might be recognized as characteristic markers for the three clusters in GBM. Through integrative investigation of genomics, epigenomics, and transcriptomics, we offer novel visions into the multilayered molecules of GBM and facilitate the accuracy remedy for GBM sufferers.

1. Introduction

Glioblastoma multiforme (GBM) is one of the central nervous system's most common and highly malignant primary tumors [1]. The incidence rate of GBM in men is higher than that in women, with a tendency for family aggregation [2]. Previous studies suggest that the average onset of GBM is about 60 years old; however, the patients showed a younger trend in recent years. The common symptoms of GBM are progressive somatosensory and motor dysfunction, headache, dizziness, and convulsions [3, 4]. At present, surgical resection is the standard method for treating GBM. Postoperative temozolomide concurrent radiotherapy and chemotherapy followed by temozolomide oral chemotherapy were the primary treatment for GBM. However, even after active treatment, the prognosis of GBM is still inferior [5]. In recent years, the development of high-throughput technology and bioinformatics analysis has dramatically increased the amount of biological data for research and provided new ideas for exploring the etiology, pathogenesis, and new drug treatment targets of GBM [6, 7].

High throughput technology is applied to various "omics," mainly including (1) genomics, which is used to detect DNA mutations; (2) transcriptomics, which is used to detect mRNA expression; (3) epigenomics which studies the effect of DNA modification on mRNA expression without changing the sequence; (4) proteomics, which is used to detect protein components; and (5) metabonomics, used to determine the level of metabolites [8]. Omics technology could evaluate and integrate omics data of tissues and cells, accurately exhibit the biological process of disease, and facilitate the realization of personalized precision medicine

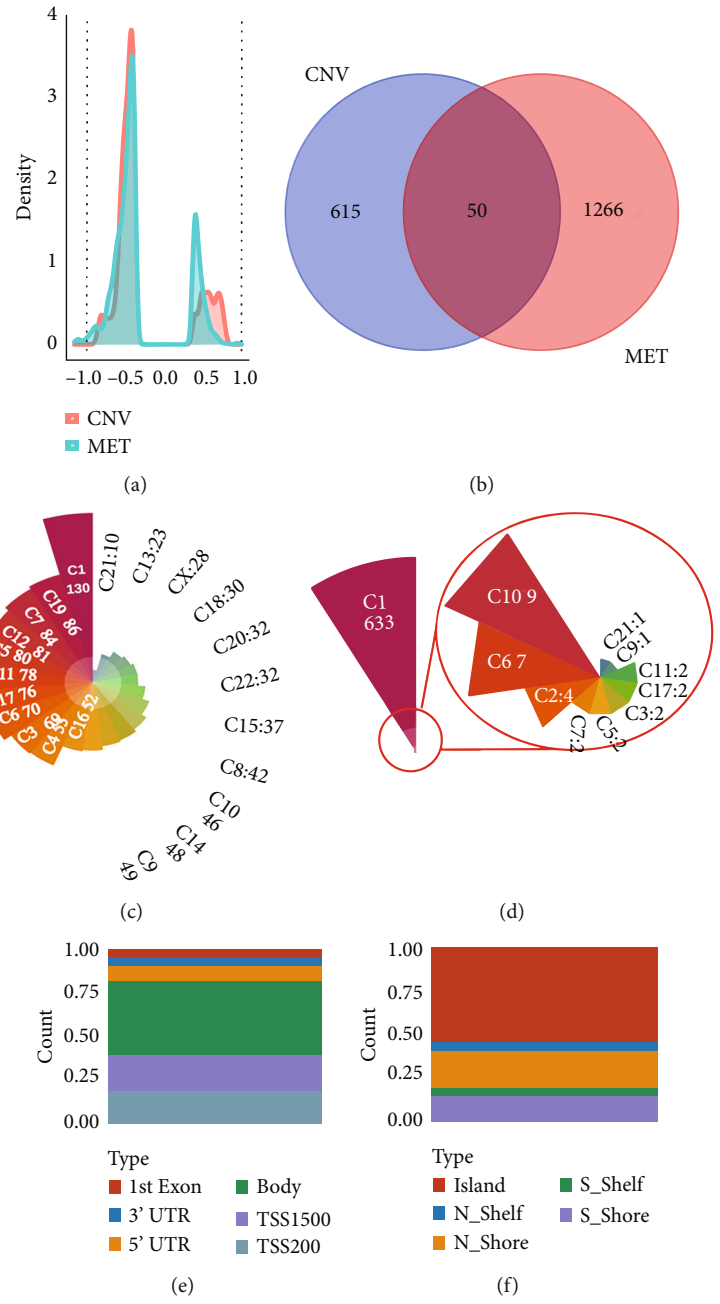

Figure 1: Correlation analysis for MET-Gs and CNV-Gs. (a) Correlation analysis between MET-Gs and CNV-Gs in a z-score distribution. (b) CNV-G and MET-G overlap. (c) Distribution of CNV-Gs on chromosomes. (d) Distribution of MET-Gs on chromosomes. (e) The proportional frequency of CpG sites in the promoter based on the existence of CpG island. (f) The proportional frequency of CpG sites in the promoter is based on their distance from genomic regions.

[9]. Genomic change resulting from gene CNV and single-nucleotide mutations (SNPs) might accelerate the progression of cancers [10]. CNV plays a crucial supervisory role in GBM development, and transcriptional dysregulation resulting from copy number alterations was future actions in GBM development [11]. In addition, exploration of DNA MET has validated the massive heterogeneousness of epigenome obstacles in GBM and various cancers. Emerging evidence shows that DNA methylation facilitates heterogeneous biologic activities and is implicated in GBM development. The multiomics profiles enable it feasible to carry out an integrated exploration based on genomics, epigenomics, and transcriptomics to enhance GBM prognosis [12].

In this study, we evaluated gene expressions using genomic and epigenetic patterns using a multi-omics combination. We also determined distinctive molecular subtypes markedly related to GBM outcome. Three oxidative stress-related prognostic biomarkers for patients with GBM were identified based on CNV, MET, and gene expressions.

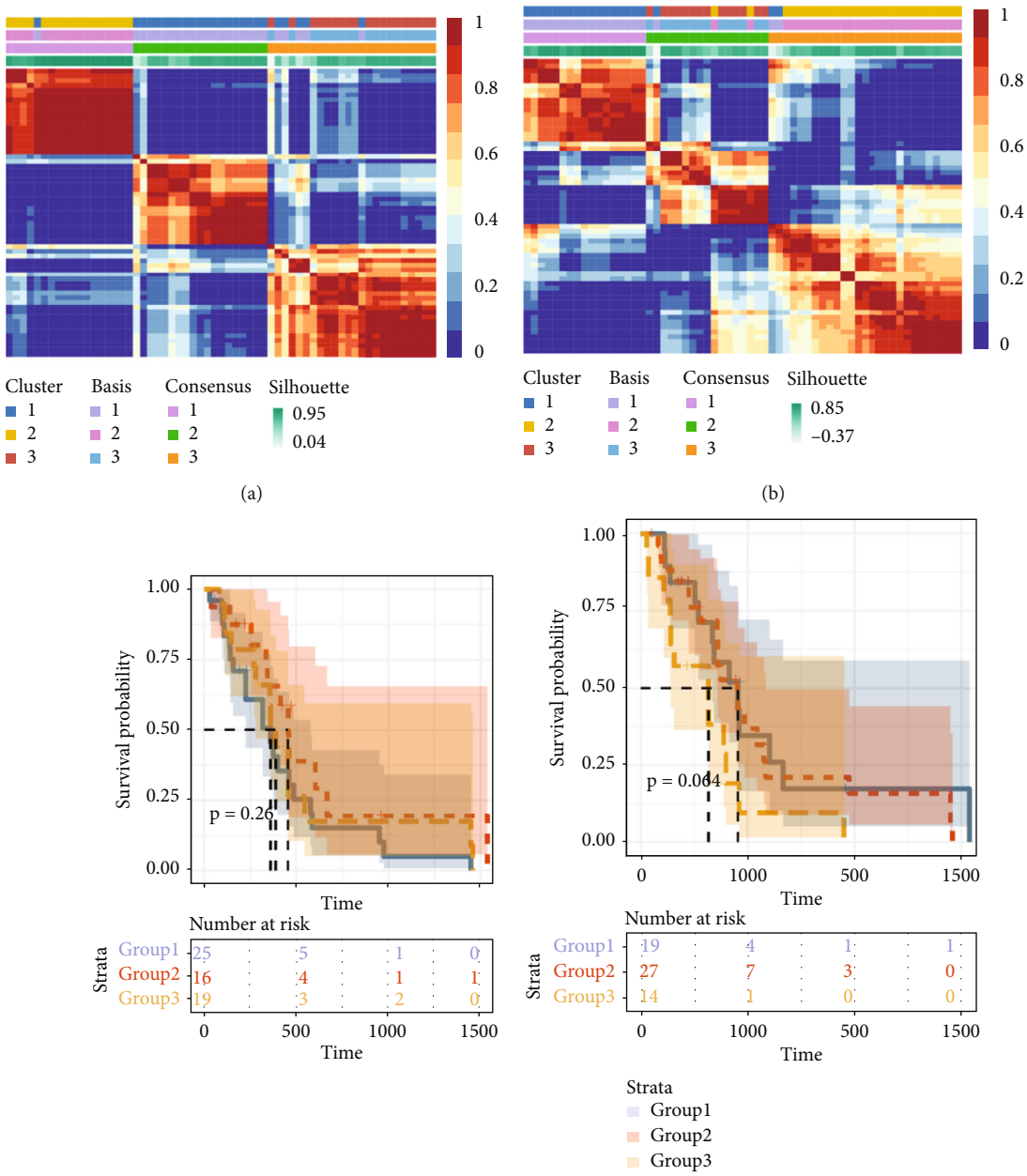

Figure 2: Continued.

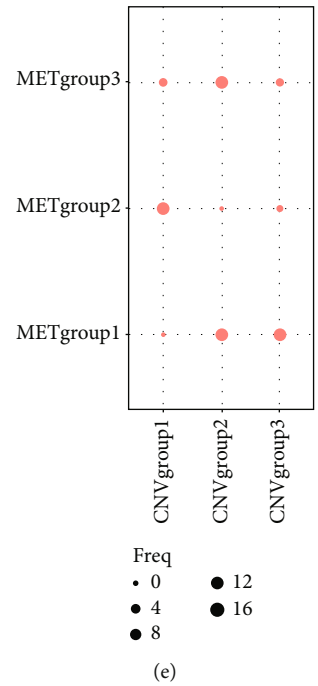

Figure 2: CNV-Gs and MET-Gs gene set-based molecular subtype detection. (a) NMF clustering consequences for CNV-Gs. (b) NMF clustering consequences for MET-Gs. (c) The survival analysis for CNV-G subclasses. (d) The survival analysis for MET-G subclasses. (e) The overlapped subtypes recognized from CNV-G and MET-G clusters.

2. Methods

2.1. Data Origination. R software was employed to analyze the clinical data, RNA-seq, methylation, and CNV from The Cancer Genome Atlas (TCGA) GBM cohorts. At the same time, SNV data from TCGA GBM is also obtained. We next sought datasets about the GBM miRNA expressions from the Gene Expression Omnibus (GEO) database. The microarray dataset GSE4271, including GBM clinical patients, was selected for our subsequent analysis.

2.2. Data Processing. About the arrangement of CNV probes, two intervals with 50% overlap were regarded as equivalent, whereas the number of coverages probes less than five intervals was uninvolved. They were mapping CNV probes to corresponding genes using GTF of GENCODE. The GRh38's Gencode.v22 was used for CNV intervals mapping to the related gene. About RNA-seq statistics, the low expression genes in each trial were uninvolved (the proportion of samples with 0 per kilobase of transcript per million mapped reads (FPKM) per million mapping reads to the total sample was <0.5), whereas the gene set with advanced expression was reserved. About chip statistics, directly load the standardized expression profile (EXP) matrix and reach the probe with the gene consistent with the note of the platform. The median level of multiple probes matched to a similar gene was established as the gene expression, whereas probes matched to compound genes were detached. For the methylation data, exceeding 70% of the trials existed omitted spots, which were replaced with values created through the KNN (k-Nearest Neighbor) approach. Using GRh38's Gencode.v22 comment preserved TSS probes of 200 bp downstream and 2 kb upstream and further recorded their genes.

2.3. Detection of CNV-G and MET-G Gene Set. This study used the Pearson correlation coefficient (R) to evaluate the correlation among RNA-seq, DNA methylation, and CNV. The correlation coefficient is transformed to a Z value conferring to $\ln((1+r)/(1-r))$. The genes that scored $P < 0.05$ in the correlation coefficient assessment established a gene set drastically associated with (CNV genes) CNV-Gs and another gene set associated with MET-Gs (methylation genes).

2.4. The Molecular Subtype Identification. The iClusterPlus package and nonnegative matrix factorization (NMF) in R software were used to discover the genomics-based molecular subtypes between the expressions of CNV-G/MET-G gene sets. To observe the association between the CNV-G/MET-G gene sets and phenotypes, the trials were clustered by the NMF technique. The clinical characteristics of the samples and the connection between the molecular subtypes were studied. Cluster K was established as 2-10. According to the correlation coefficient, the ideal clusters of molecular subgroups were established based on CNV-Gs and molecular subgroups based on MET-Gs.

2.5. Association between Molecular Subtypes and Tumor Microenvironment. TIMER is an approach used to systematically evaluate the clinical effect of diverse immune cells on different tumors. The CIBERSORT method was applied to assess the distribution of immune cells in all tumor trials,

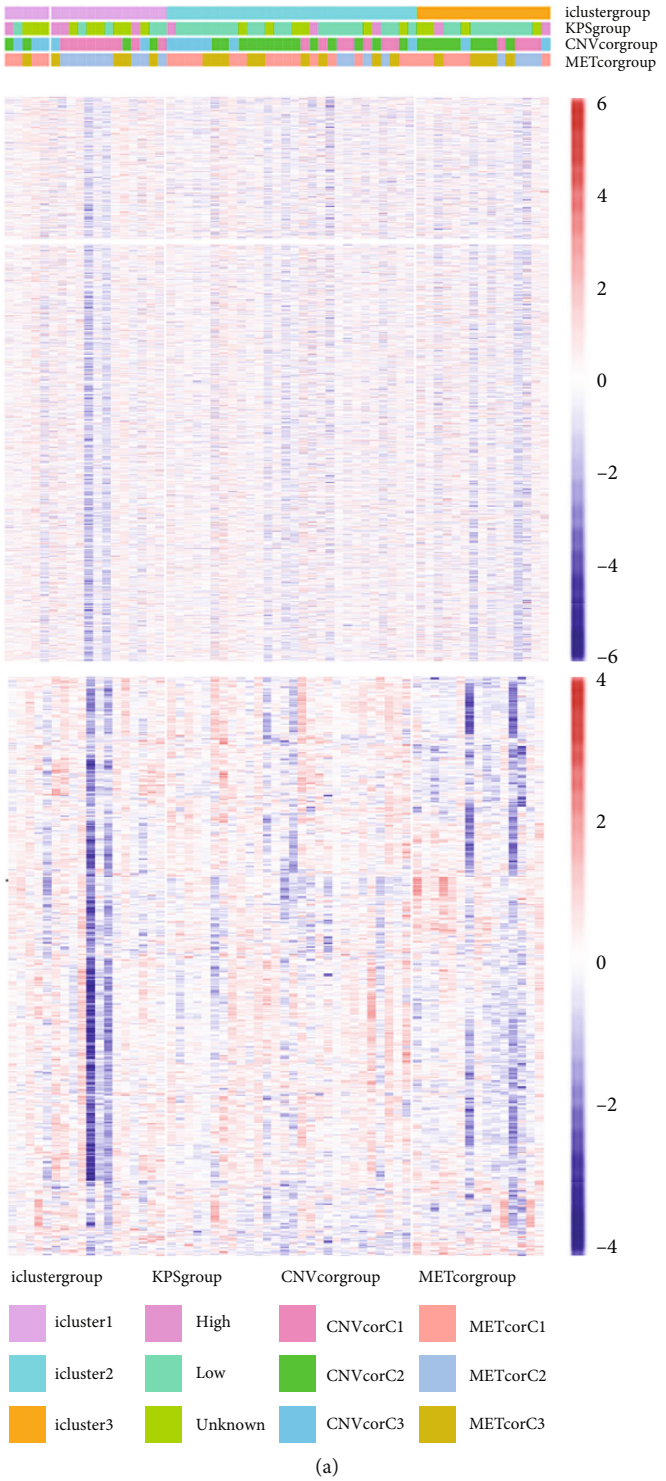

(a)

Figure 3: Continued.

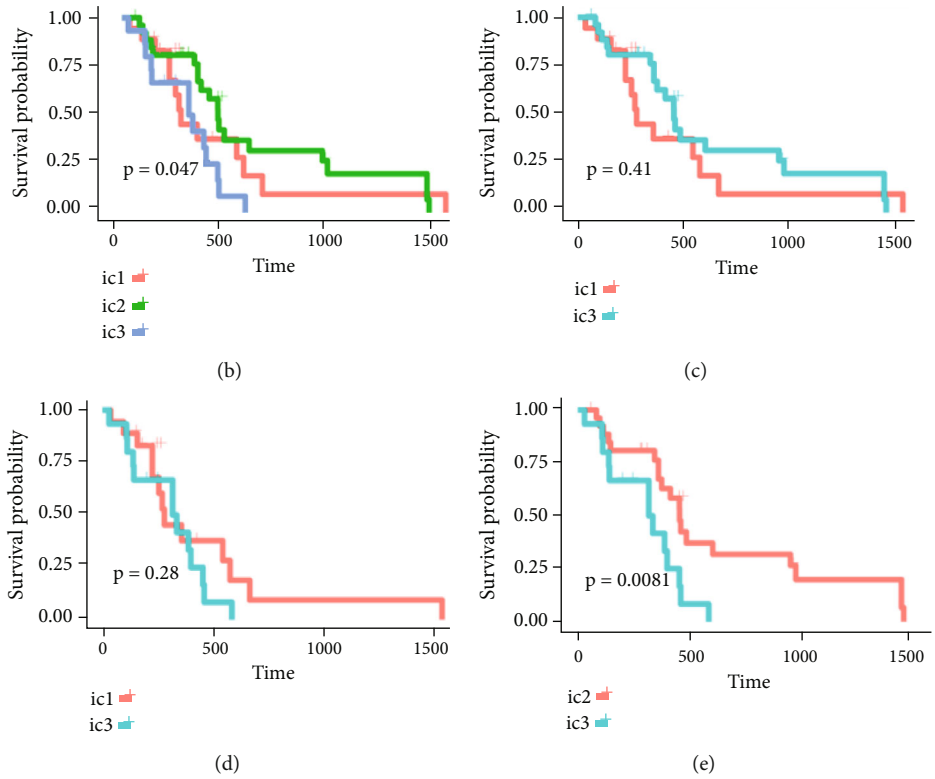

Figure 3: Integrated cluster sampling of CNV, EXP, and MET. (a) Heatmap of the expression of subtypes CNV-Gs and MET-Gs. (b) The difference of OS time between the three subtypes. (c) The difference of OS time between iC1 and iC2 subtypes. (d) The difference of OS time between iC1 and iC3 subtypes. (e) The difference of OS time between iC2 and iC3 subtypes.

and when the samples with $P < 0.05$ were elected for correlation analysis between immune cells and target genes.

2.6. Exploration of Genetic Alterations in Molecular Subtypes. Genetic differences in distinctive molecular subtypes were assessed. DESeq2 was applied to explore variances in gene expressions between diverse molecular subtypes, and two-fold difference criteria plus FDR < 0.05 was chosen as the threshold to distinguish genetic differences across molecular subtypes.

2.7. Association between Genomic Variation and Molecular Subtypes. To uncover the association between genomic deviation and molecular subtypes, TCGA-GBM statistics were examined. Fisher's exact test was applied to examine the differentially expressed genomic. $P < 0.05$ was chosen to detect mutational variances.

2.8. Statistical Analysis. Spss20.0 statistical analysis software was used for data analysis, and the Pearson linear correlation test was applied to examine the correlation. Log-rank and Kaplan–Meier (KM) tests were used for survival analysis. $P < 0.05$ was considered statistically significant.

3. Results

3.1. Comparison of CNV-Gs and MET-Gs. 664 CNV-Gs and 1316 MET-Gs were identified using correlation analysis with $P < 0.05$. As shown in Figure 1(a), the correlation of CNV-Gs markedly transferred to the right, whereas the correlation of MET-Gs transferred to the left. Furthermore, the association between CNV and gene expressions was evaluated, and we observed the overall correlation coefficient > 0, implying that CNV was positively connected to gene expressions (Figure 1(a)). A comparison of CNV-Gs and MET-Gs gene sets observed 50 overlapping genes (Figure 1(b)). We found a notable difference in the distribution of CNV-Gs on chromosomes 1 and 2 (Figure 1(c)). Similarly, we also observed a marked difference in the MET-G distribution on chromosomes 1 and 2 (Figure 1(d)). We observed marked differences in the frequency of DNA methylation in vivo and at the transcription initiation site (Figure 1(e)). In addition, most MET-Gs were observed in the open sea regions than in CpG islands ($P < 0.001$, Figure 1(f)).

3.2. CNV-G and MET-G Gene Set-Based Molecular Subtype Detection. To distinguish molecular subtypes that exposed the multiomics forms of the CNV-G and MET-G gene sets, the genomic statistics of CNV, MET, and RNA expressions were integrated through the iCluster. Three clusters (iC1, iC2, and iC3) were identified for CNV-Gs by the NMF method (Figure 2(a)). Similarly, three ideal clusters (iC1, iC2, and iC3) were obtained for MET-Gs (Figure 2(b)). As shown in Figure 2(c), marked prognostic changes were detected in the three CNV-G subtypes. Moreover, the three MET-G subtypes detected marked prognostic differences (Figure 2(d)). Most importantly, we found an apparent overlap among the three CNV-G subtypes and three MET-G subtypes (Figure 2(e)).

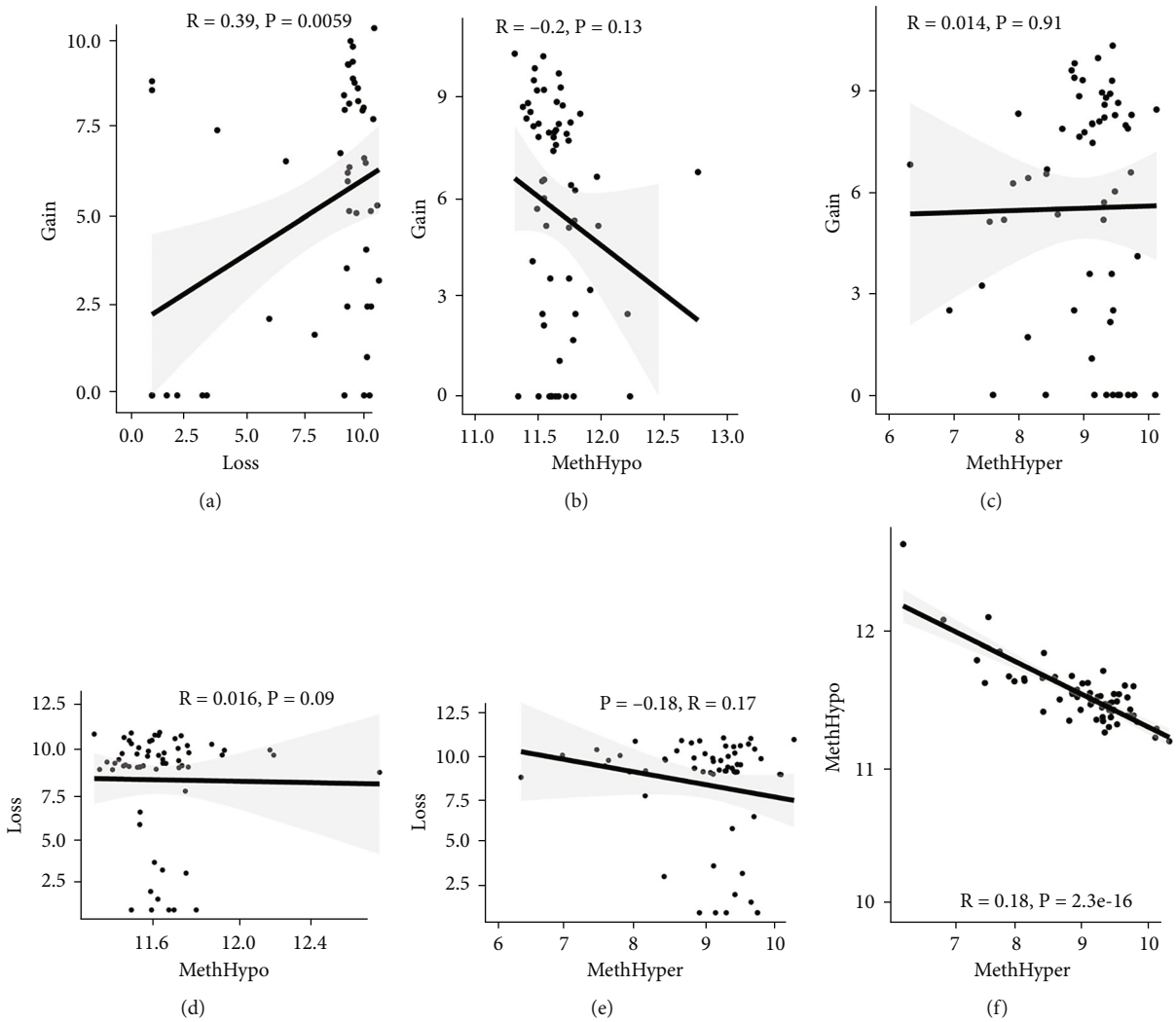

Figure 4: DNA CNV abnormalities were accordant with MET abnormalities. (a) Frequency scattering of gain and loss in CNV. (b) Frequency scattering of gain and MetHyper in CNV. (c) CNV gain and MetHypo distribution (d) CNV loss and MetHyper distribution and MetHypo. (e) CNV loss and MetHypo distribution. (f) Frequency scattering of MetHyper and MetHypo.

3.3. MET, CNV, and EXP Data Were Integrated into Cluster Samples. By clustering the omics data, we obtained three subtypes (iC1, iC2, and iC3) with noticeably altered OS times. A heatmap was screened to exhibit the RNA gene expression of CNV-G and MET-G clusters (Figure 3(a)). Moreover, it is determined that the OS time of the three subtypes (iC1, iC2, and iC3) was considerably different, and iC3 had the worst OS among the three clusters (Figure 3(b)). Figure 3(c) shows iC2 had a markedly better OS than iC1. Furthermore, iC1 had a markedly better OS than iC3 (Figure 3(d)). iC2 had a markedly better OS than iC3 (Figure 3(e)). These results implied that iC2 had the best OS time in the three subtypes.

3.4. DNA CNV Abnormalities Were Accordant with MET Abnormalities. To assess the association between CNV and methylation aberrations, CNV > 0.3 was considered gain, CNV < −0.3 was considered loss, the β value of MET > 0.8 was classified as MetHypo, and MET < 0.2 was classified as MetHypo. As shown in Figure 4(a), a marked correlation existed between CNV loss and gain. However, the correlation between Gain and MetHype/MetHypo, loss, and MetHyper/MetHypo was not statistically different (Figures 4(b)–4(e)). In addition, MetHypo is negatively connected to methyper (Figure 4(f)).

3.5. Analysis of Tumor Immune Cell Infiltration in Molecular Subtypes. The CIBERSORT algorithm was applied to compare tumor immune cell infiltration in subtypes and determine the proportions of the tumor-infiltrating immune cells in distinctive subtypes (Figure 5(a)). The percentage of tumor immune cell infiltration in tissue samples from patients with GBM was determined (Figure 5(b)). Most importantly, we observed an increased percentage of neutrophils in the iC2 subtype compared to other subtypes (Figure 5(c)).

3.6. Molecular Characteristics of the Three GBM Subtypes. According to the findings of iCluster, gene expression changes between the three subtypes with prognostic

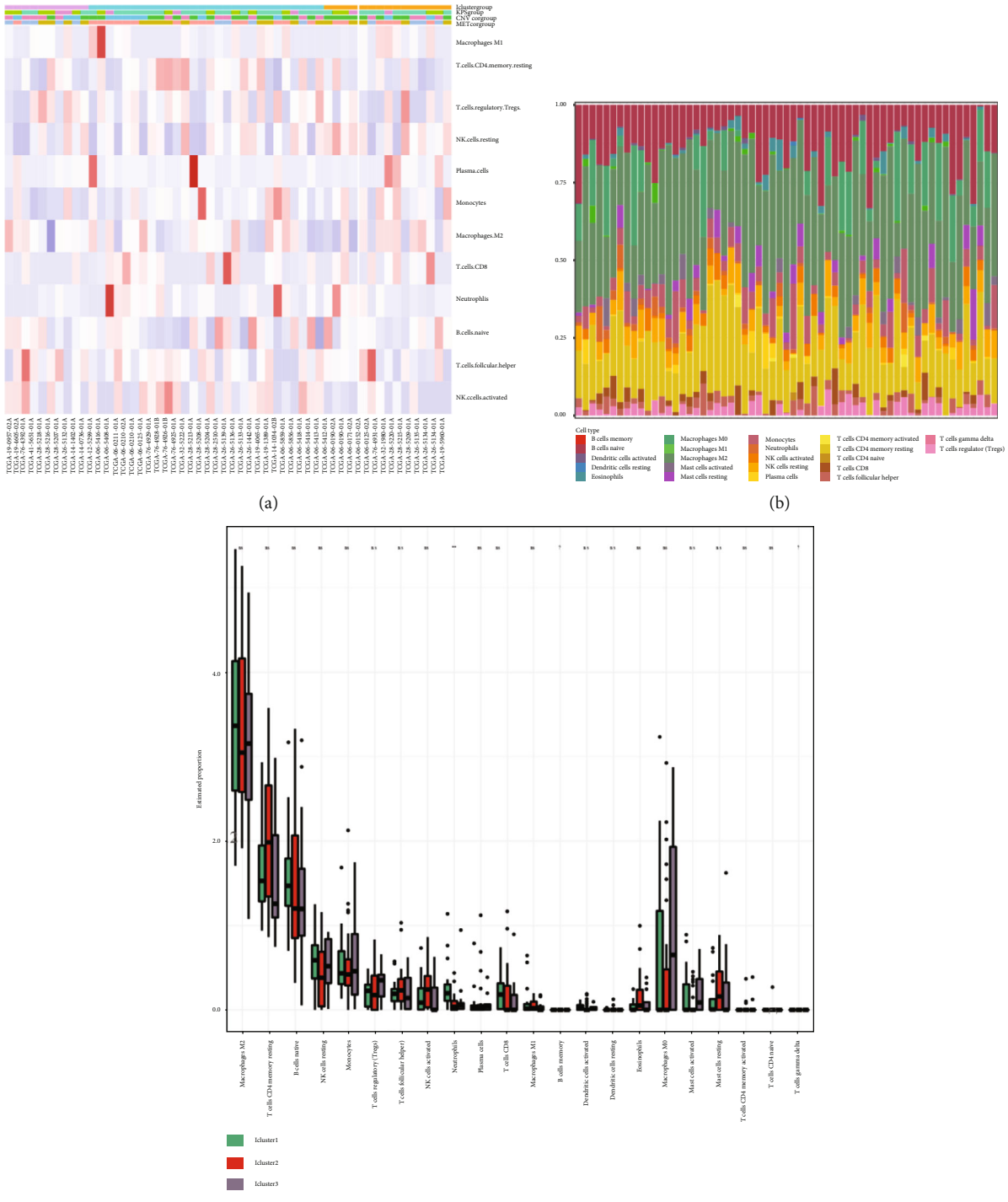

FIGURE 5: Analysis of tumor immune cell infiltration in molecular subtypes. (a) Comparison of tumor immune cell infiltration in molecular subtypes. (b) The proportion of infiltrating immune cells in tissue samples. (c) Immunosignature scores of immune cells in molecular subtypes.

distinctions were compared, and 564 DEGs were identified, followed by the removal of low-expressed genes (Figure 6(a)). The methylation incidence of DEGs in iC2 was markedly enhanced compared with that of iC1 and iC3, implying that methylation exhibited specific impacts on GBM prognosis (Figure 6(b)). When assessing the relationship between gene expression, MET, and CNV, we observed that the gene expression of DEGs in trials with MET was markedly enhanced (Figure 6(c)). The GO enrichment evaluation showed that the DEGs were markedly enriched in an extracellular matrix organization, angiogenesis cell differential, and regulation of nervous development

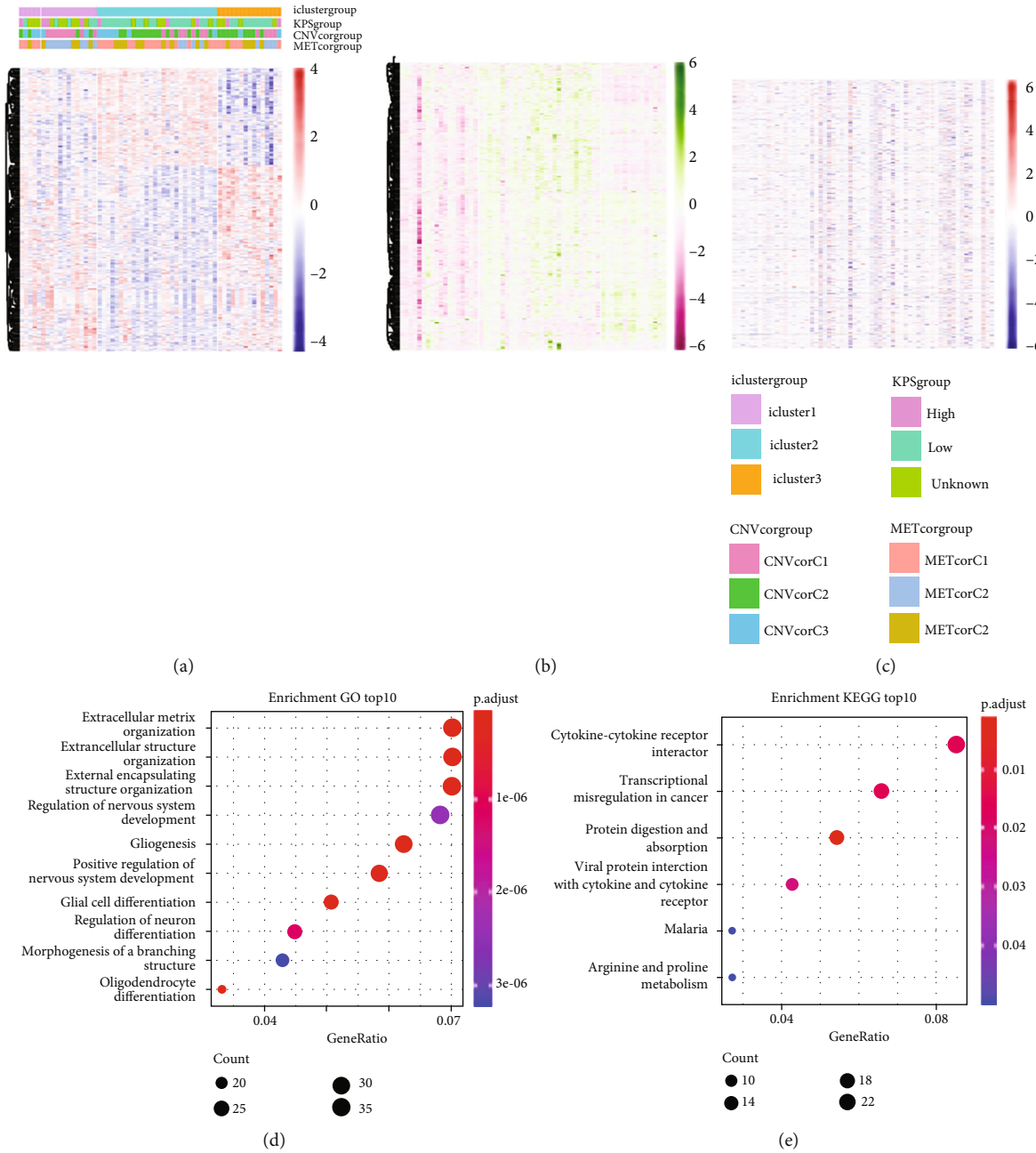

Figure 6: Subtype characterizations. (a) Distribution of CNV in the three subtypes. (b) Distribution of MET in the three subtypes. (c) Heatmap of DEGs in the three subtypes. (d) GO enrichment analysis for DEGs in three subtypes. (e) KEGG enrichment analysis for DEGs in three subtypes.

(Figure 6(d)). Similarly, the enriched KEGG pathways of the DEGs are demonstrated in Figure 6(e).

3.7. Association between Gene Expressions and CNV/MET. To explore the association between gene expressions and CNV-Gs/MET-Gs, the survival analysis was performed to recognize the differentially expressed genes among three subtypes. Three genes, OSMR, MYBPH, and IGFBP6, were markedly connected to prognosis. The expression of MYBPH and the IGFBP6 gene were negatively correlated with MET (Figures 7(b) and 7(d)). However, there was no difference between the expression of MYBPH and IGFBP6 genes and CNV (Figures 7(a) and 7(c)). MYBPH and IGFBP6 were markedly advanced in iC2 with the wickedest prognosis than iC1 and iC3 (Figures 7(e) and 7(f)). In addition, we uncovered that the expression of MYBPH and IGFBP6 expression was appreciably connected to tumor prognosis (Figures 7(g) and 7(h)).

3.8. Mutation Spectrum of the Three GMB Subtypes. We studied whether the mutation spectrum of the three GBM subtypes is different. To detect the top 50 genes, the

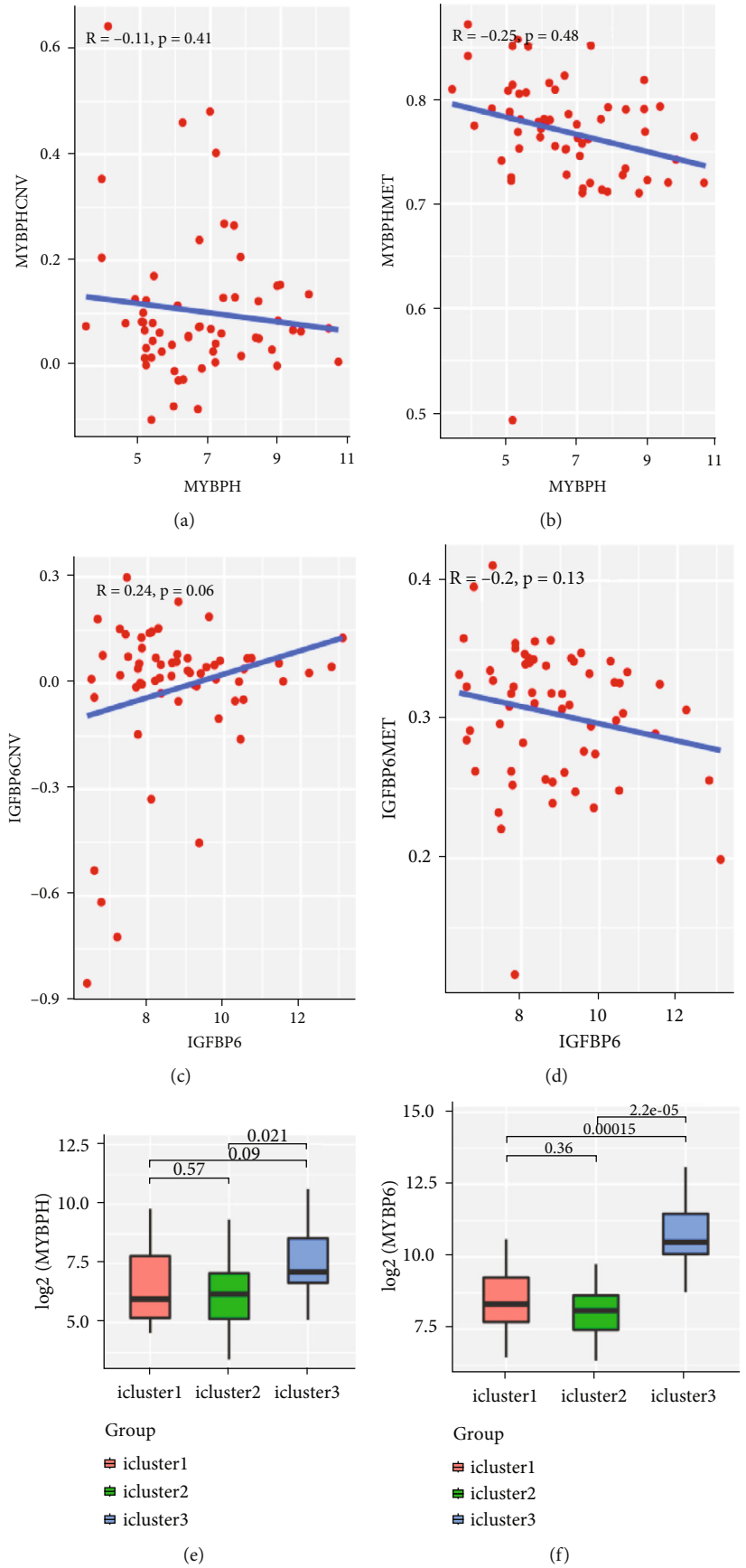

Figure 7: Continued.

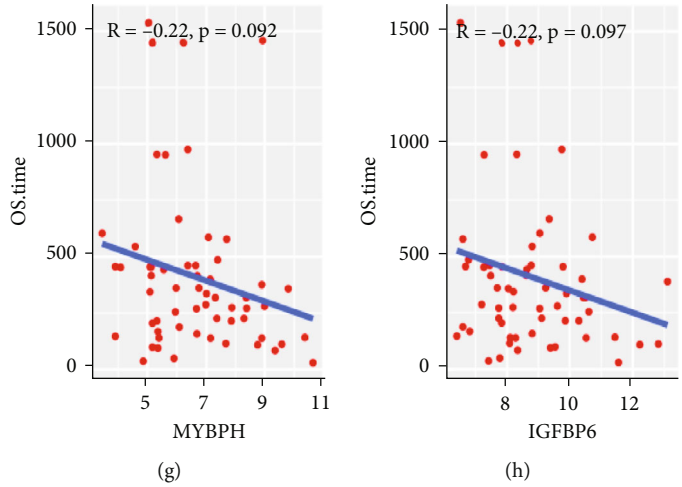

Figure 7: Association between gene expressions and CNV/MET. (a) Correlation between MYBPH CNV and expression in subtypes. (b) Correlation between IGFBP6 CNV and expression in subtypes; methylation and expression of the MYBPH gene. (c) Correlation between MYBPH MET and expression in subtypes. (d) Correlation between IGFBP6 MET and expression in subtypes. (e) The expression distribution of MYBPH in subtypes. (f) The expression distribution of IGFBP6 in subtypes. (g) The overall survival was examined for MYBPH. (h) The overall survival was examined for IGFBP6.

mutation spectrum of different subtypes was evaluated (Figures 8(a) and 8(b)). Through evaluating the mutation spectrum variances, we uncovered that the gain/loss of CNV in iC2 was much more marked higher than in iC1 and iC3 subtypes (Figure 8(c)). By comparing the iC2 subtype with the other two subtypes, we found that TP53, PTEN, NF1, EGFR, AHNAK TTN, MUC16, and AHNAK2 were the top eight common mutant genes (Figures 8(d) and 8(e)).

4. Discussion

Glioblastoma multiforme (GBM) belongs to grade IV glioma and accounts for 12% to 15% of all intracranial tumors. It has the highest malignant degree and the worst prognosis in gliomas, and the 5-year survival rate is only 5% [13]. Similar to other malignant tumors, glioblastoma has the characteristics of high invasion, resistance to radiotherapy and chemotherapy, immunosuppression in the microenvironment, and a high recurrence rate [14]. Operation combined with radiotherapy and chemotherapy is the standard treatment for GBM [15]. However, despite the increasing understanding of glioblastoma, there is still a lack of practical progress in treating this disease. Therefore, there is an urgent need to make new progress in studying the exact molecular mechanisms and reliable therapeutic targets of GBM.

Emerging evidence indicates that cancer results from abnormal genetic and epigenetic events [16]. The epigenetic mechanism is a stable genetic feature that changes in DNA sequence could not explain [17]. Like histone modification, DNA methylation does not affect the genome DNA sequence but adds a methyl (CH3) group to CG dinucleotide cytosine [18]. According to the abnormal changes in DNA methylation, diagnosing and treating tumors and predicting biomarkers are considered broad prospects [19]. In recent years, most of the studies have focused on the kinetics of aberrant promoter methylation in GBM, and there are also a few studies on enhancer methylation. Aberrant methylation enhancers can lead to various diseases, including abnormal gene expression in various cancers [20, 21].

An in-depth understanding of genetic and epigenetic variations might assist in elucidating the pathogenesis of GBM. In the current study, we used multiomics data from TCGA GBM and GSE4271 datasets to identify the molecular subtypes and oxidative stress-related prognostic biomarkers in glioblastoma multiforme. We evaluated the association between epigenetics and CNV and detected that DNA CNV deviations were constant with MET aberrations. Through multiomics relationship investigation, CNV-C and MET-C gene sets were recognized, and the association between CNV and MET was created with the gene expressions. According to multiomics clusters constructed with gene expression, MET, and CNV, three molecular subtypes were obtained; iC2 was related to the poorest clinical results. Additionally, we recognized three prognostic gene indicators and validated them as well.

The immunophenotype of the tumor microenvironment functions a critical role in tumor occurrence and progress and is crucial for the prognosis and success of immunotherapy [22]. GBM microenvironment contains various immune cell categories, such as regulatory T cells (Tregs), tumor-associated macrophages (TAM), microglia, and suppressor cells from bone marrow [23]. Evidence has indicated that the expression of proinflammatory cytokines (IL-12, IL-18, and TNF-γ) was reduced, while soluble inhibitory molecules (IL-10 and VEGF) were enhanced in GBM [24, 25]. Glioma cells could also inhibit the antitumor immune response by regulating the activity of immune cells [26]. This study examined the significant variances in the immune microenvironment of three subtypes. We observed an increased percentage of neutrophils in iC2 compared to other subtypes. In

(a)

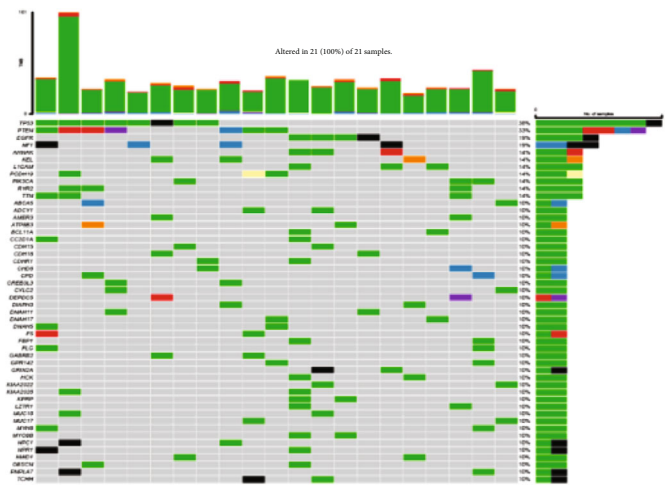

(b)

(c)

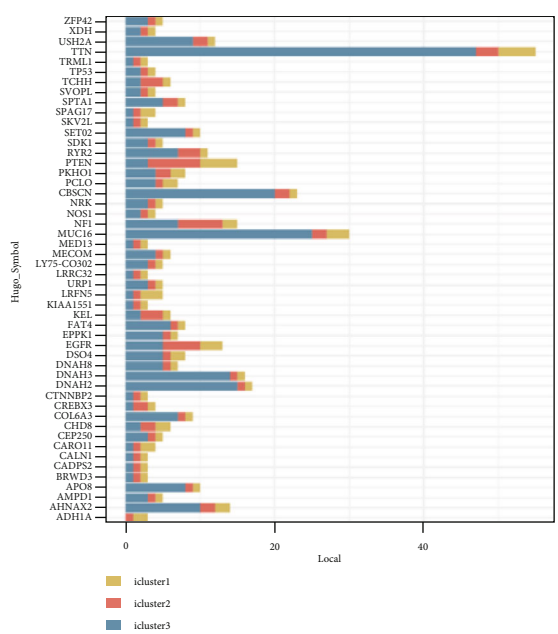

(d)

Figure 8: Continued.

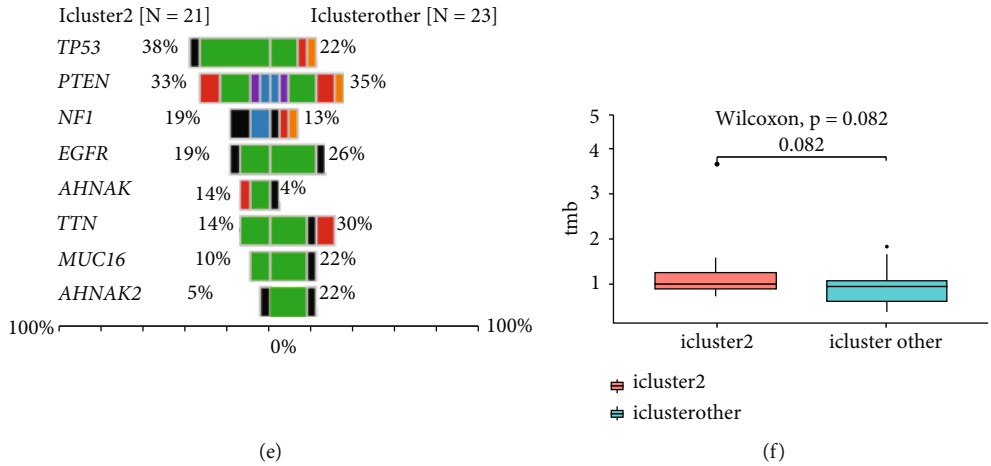

Figure 8: Mutation spectrum of the three GMB subtypes. (a–c) The top 50 mutated genes in the iC1, iC2, and iC3 subtypes. (d) Number of mutations in the top 50 genes. (e) Mutation spectrum of the first ten genes in the iC2 subtype.

the end, the three subtypes exhibited distinct immune microenvironmental characteristics. This change might be associated with their heterologous clinical consequences and therefore was prospective marks for BMG immunotherapy.

In addition, through contrasting the molecular characters, three illustrative markers (OSMR, IGFBP6, and MYBPH) were recognized and confirmed in the three subtypes. Myosin binding protein H (MYBPH) comprises 477 amino acids, and its molecular weight is 55 kDa [27]. The myosin-binding protein family contains two subtypes of MYBPH and MYBPC, which have apparent homology at the carboxyl end and have the same sequence and structural similarity [28]. Emerging evidence indicates that elevated MYBPH has been associated with a poor prognosis and recurrent in GBM [29]. Moreover, the deletion of MYBPH could inhibit the migration of glioma cells [30].

IGFBP is a group of multifunctional proteins with similar structure and function, and it has a high affinity with IGFs. IGFBP is vital in regulating physiological and pathological processes in vivo through IGF-dependent or IGF-independent mechanisms [31]. IGFBP-6 is a critical member of the IGF family and widely exists in human tissues, cells, and body fluids; it can bind to IGF-2 and inhibit the physiological function of promoting cell growth, proliferation, and differentiation mediated by IGF-2 [32]. IGFBP-6 could promote cell migration and regulate neutrophil activity, which suggests regulating inflammatory immune response and oxidative stress [33, 34]. Some studies have indicated that IGFBP-6 could inhibit tumor angiogenesis in multiple systems through the IGF-2-independent pathway [35].

The Oncostatin M receptor (OSMR) is a member of the interleukin-6 receptor family, performing various cellular functions, including regulating homeostasis, cell growth, and differentiation [36]. OSMR binds with gp130 to form a high-affinity receptor for its main ligand cytokine, antitumor M (OSM). OSM is mainly secreted by T lymphocytes, neutrophils, and macrophages and was initially used as an anticancer drug [37]. However, in some cases, OSM can promote tumor progression. Overexpression of OSM and OSMR has been detected in various cancers, including gastric, colorectal, breast, and glioma [38, 39]. OSM-OSMR signal transduction plays a vital role in inflammation, oxidative stress, hematopoiesis, and development and is increasingly considered an essential factor in tumor progression [40].

We observed that MYBPH and IGFBP6 were markedly connected to GBM diagnosis among the three genes. MYBPH and IGFBP6 were increased in iC3 and negatively connected to MET and prospective marks for BMG diagnosis.

In conclusion, we investigated underlying mechanisms of glioblastoma multiforme by multiomics exploration for genomics, epigenomics, and transcriptomics. We revealed that DNA CNV and MET change function critical roles in GBM. Moreover, we recognized three molecular subtypes of GBM and found three oxidative stress-related biomarkers. These findings might sustain the progression of exact diagnostic evaluations and therapies for GBM patients.

Data Availability

The labeled dataset used to support the findings of this study is available from the corresponding author upon request.

Conflicts of Interest

The authors declare no competing interests.

Acknowledgments

This research was supported by 345 Talent Project of Shengjing Hospital (No. M0730).

References

[1] B. M. Schmitt, A. S. Boewe, C. Götz et al., "CK2 activity mediates the aggressive molecular signature of glioblastoma multiforme by inducing nerve/glial antigen (NG)2 expression," *Cancers*, vol. 13, no. 7, p. 1678, 2021.

[2] Y. H. Hsieh, J. P. Tsai, C. L. Yu, C. C. Lee, J. C. Hsu, and J. C. Chen, "Overexpression of lipocalin-2 inhibits proliferation and invasiveness of human glioblastoma multiforme cells by

activating ERK targeting cathepsin D expression," *Biology*, vol. 10, no. 5, p. 390, 2021.

[3] S. Z. Du, C. Chen, L. Qin, and X. L. Tang, "Bioinformatics analysis of immune infiltration in glioblastoma multiforme based on data using a methylation chip in the GEO database," *Cancer Research*, vol. 10, no. 3, pp. 1484–1491, 2021.

[4] S. Daniele, V. La Pietra, R. Piccarducci et al., "CXCR4 antagonism sensitizes cancer cells to novel indole-based MDM2/4 inhibitors in glioblastoma multiforme," *European Journal of Pharmacology*, vol. 897, no. 2, article 173936, 2021.

[5] S. Yang, C. Xie, T. Guo et al., "Simvastatin inhibits tumor growth and migration by mediating caspase-1-dependent pyroptosis in glioblastoma multiforme," *World Neurosurgery*, 2022.

[6] X. Chen, Y. Pan, M. Yan, G. Bao, and X. Sun, "Identification of potential crucial genes and molecular mechanisms in glioblastoma multiforme by bioinformatics analysis," *Molecular Medicine Reports*, vol. 22, no. 2, pp. 859–869, 2020.

[7] J. Zhu, J. Ye, L. Zhang et al., "Differential expression of circular RNAs in glioblastoma multiforme and its correlation with prognosis," *Translational Oncology*, vol. 10, no. 2, pp. 271–279, 2017.

[8] C. Xu, J. Yang, A. Kosters, B. R. Babcock, P. Qiu, and E. E. B. Ghosn, "Comprehensive multi-omics single-cell data integration reveals greater heterogeneity in the human immune system," *BioRxiv*, vol. 165, pp. e12–e21, 2022.

[9] N. Yoosuf, M. Maciejewski, D. Ziemek et al., "Early prediction of clinical response to anti-TNF treatment using multi-omics and machine learning in rheumatoid arthritis," *Rheumatology*, vol. 61, no. 4, pp. 1680–1689, 2021.

[10] H. Zhang, K. Cui, S. Yao, Y. Yin, D. Liu, and Z. Huang, "Comprehensive molecular and clinical characterization of SLC1A5 in human cancers," *Pathology-Research and Practice*, vol. 3, article 153525, 2021.

[11] L. Nobre, M. Johnson, R. Siddaway et al., "LGG-61. Cerebrospinal fluid as a source for liquid biopsy in pediatric gliomas," *Neuro-Oncology*, vol. 24, no. 1, pp. i102–i102, 2022.

[12] J. N. Poynter, J. R. B. M. Bestrashniy, K. A. T. Silverstein et al., "Cross platform analysis of methylation, miRNA and stem cell gene expression data in germ cell tumors highlights characteristic differences by tumor histology," *BMC Cancer*, vol. 15, article 769, 2015.

[13] M. Stella, L. Falzone, A. Caponnetto et al., "Serum extracellular vesicle-derived circHIPK3 and circSMARCA5 are two novel diagnostic biomarkers for glioblastoma multiforme," *Pharmaceuticals*, vol. 14, no. 7, p. 618, 2021.

[14] U. Pagalay, A. Syamsuadi, and M. D. Ismansyah, "Numerical solution model of brain tumors glioblastoma multiforme with treatment effect using Runge Kutta Fehlberg methods," in *Proceedings of the International Conference on Engineering, Technology and Social Science* of *Advances in Social Science, Education and Humanities Research*, pp. 767–776, Indonesia, 2021.

[15] F. Sabir, R. Ismail, G. Katona, and I. Csóka, "Nose to brain delivery of n-propylgallte loaded lipid nanoparticles for targeting glioblastoma multiforme via QbD approach," in *III. Symposium of Young Researchers on Pharmaceutical Technology, Biotechnology and Regulatory Science*, vol. 3, p. 50, Szeged Hungary, 2021.

[16] N. Tawil, C. Spinelli, R. Bassawon, and J. Rak, "Genetic and epigenetic regulation of cancer coagulome - lessons from heterogeneity of cancer cell populations," *Thrombosis Research*, vol. 191, pp. S99–S105, 2020.

[17] H. Haque, F. Arifin, S. Adilina, M. Rafsanjani, and S. Shatabda, "SubFeat: feature subspacing ensemble classifier for function prediction of DNA, RNA and protein sequences," *BioRxiv*, 2020.

[18] E. Martinez-Balibrea, A. Martínez-Cardús, A. Ginés et al., "Tumor-related molecular mechanisms of oxaliplatin resistance," *Molecular Cancer Therapeutics*, vol. 14, no. 8, pp. 1767–1776, 2015.

[19] I. K. Mensah, A. B. Norvil, L. AlAbdi et al., "Misregulation of the expression and activity of DNA methyltransferases in cancer," *Cancer*, vol. 3, no. 4, 2021.

[20] A. D. Dekker, P. D. Deyn, and M. G. Rots, "Epigenetics: the neglected key to minimize learning and memory deficits in Down syndrome," *Neuroscience & Biobehavioral Reviews*, vol. 45, pp. 72–84, 2014.

[21] L. Ding, L. Yang, C. Ren et al., "A review of aberrant DNA methylation and epigenetic agents targeting DNA methyltransferases in endometriosis," *Current Drug Targets*, vol. 21, no. 11, pp. 1047–1055, 2020.

[22] C. Chu, K. Yao, J. Lu et al., "Immunophenotypes based on the tumor immune microenvironment allow for unsupervised penile cancer patient stratification," *Cancers*, vol. 12, no. 7, p. 1796, 2020.

[23] H. Bi and C. Zhang, "Extrinsic factors associated with the response to immunotherapy in glioblastoma," *Cancer Letters*, vol. 511, pp. 47–55, 2021.

[24] R. B. Sartor and F. Hoentjen, "Proinflammatory cytokines and signaling pathways in intestinal innate immune cells," *Mucosal Immunology*, pp. 681–701, 2005.

[25] R. A. Kore and E. C. Abraham, "Inflammatory cytokines, interleukin-1 beta and tumor necrosis factor-alpha, upregulated in glioblastoma multiforme, raise the levels of CRYAB in exosomes secreted by U373 glioma cells," *Biochemical & Biophysical Research Communications*, vol. 453, no. 3, pp. 326–331, 2014.

[26] M. Qing, J. Zhou, W. Chen, and L. Cheng, "Highly expressed CYBRD1 associated with glioma recurrence regulates the immune response of glioma cells to interferon," *Evidence-Based Complementary and Alternative Medicine*, vol. 2021, Article ID 2793222, 12 pages, 2021.

[27] P. A. Trevisoli, G. C. Moreira, C. Boschiero et al., "A missense mutation in the MYBPH gene is associated with abdominal fat traits in meat-type chickens," *Frontiers in Genetics*, vol. 12, article 698163, 2021.

[28] J. M. Mouton, L. van der Merwe, A. Goosen et al., "MYBPH acts as modifier of cardiac hypertrophy in hypertrophic cardiomyopathy (HCM) patients," *Human Genetics*, vol. 135, no. 5, pp. 477–483, 2016.

[29] Y. K. Banasavadi-Siddegowda, S. Namagiri, Y. Otani et al., "Targeting protein arginine methyltransferase 5 sensitizes glioblastoma to trametinib. Neuro-Oncology," *Neuro-Oncology Advances*, vol. 4, no. 1, 2022.

[30] H. K. Lee, S. Finniss, S. Cazacu et al., "Mesenchymal stem cells deliver synthetic microRNA mimics to glioma cells and glioma stem cells and inhibit their cell migration and self-renewal," *Oncotarget*, vol. 4, no. 2, pp. 346–361, 2013.

[31] C. Chen, F. W. Huang, S. S. Huang, and J. S. Huang, "IGFBP-3 and TGF-β inhibit growth in epithelial cells by stimulating type V TGF-β receptor (TβR-V)-mediated tumor suppressor

signaling," *FASEB BioAdvances*, vol. 3, no. 9, pp. 709–729, 2021.

[32] A. Liso, N. Capitanio, R. Gerli, and M. Conese, "From fever to immunity: a new role for IGFBP-6?," *Journal of Cellular and Molecular Medicine*, vol. 22, no. 10, pp. 4588–4596, 2018.

[33] J. Xie, C. Zhao, Q. Han, H. Zhou, Q. Li, and X. Diao, "Effects of pyrene exposure on immune response and oxidative stress in the pearl oyster, _Pinctada martensii_," *Pinctada martensii. Fish & Shellfish Immunology*, vol. 63, pp. 237–244, 2017.

[34] M. Conese, L. Pace, N. Pignataro et al., "Insulin-like growth factor binding protein 6 is secreted in extracellular vesicles upon hyperthermia and oxidative stress in dendritic cells but not in monocytes," *International Journal of Molecular Sciences*, vol. 21, no. 12, p. 4428, 2020.

[35] C. Zhao, X. Zhu, G. Wang, W. Wang, S. Ju, and X. Wang, "Decreased expression of IGFBP6 correlates with poor survival in colorectal cancer patients," *Pathology - Research and Practice*, vol. 216, no. 5, article 152909, 2020.

[36] D. van Keulen, I. D. van Koeverden, A. Boltjes et al., "Common variants associated with OSMR expression contribute to carotid plaque vulnerability, but not to cardiovascular disease in humans," *Frontiers in Cardiovascular Medicine*, vol. 8, article 658915, 2021.

[37] Y. Li, F. Chen, Y. Xie et al., "Feiyangchangweiyan capsule protects against ulcerative colitis in mice by modulating the OSM/OSMR pathway and improving gut microbiota," *Phytomedicine*, vol. 80, article 153372, 2021.

[38] A. M. Araujo, A. Abaurrea, P. Azcoaga et al., "Stromal oncostatin M cytokine promotes breast cancer progression by reprogramming the tumor microenvironment," *Journal of Clinical Investigation*, vol. 132, no. 7, 2022.

[39] S. C. Dinca, D. Greiner, K. Weidenfeld, L. Bond, D. Barkan, and C. L. Jorcyk, "Novel mechanism for OSM-promoted extracellular matrix remodeling in breast cancer: LOXL2 upregulation and subsequent ECM alignment," *Breast Cancer Research*, vol. 23, no. 1, pp. 1–8, 2021.

[40] J. Smigiel, J. G. Parvani, I. Tamagno, K. Polak, and M. W. Jackson, "Breaking the oncostatin M feed-forward loop to suppress metastasis and therapy failure," *The Journal of Pathology*, vol. 245, no. 1, pp. 6–8, 2018.

Hindawi
Oxidative Medicine and Cellular Longevity
Volume 2022, Article ID 2238985, 7 pages
https://doi.org/10.1155/2022/2238985

Research Article

The Prediction Value of D-Dimer on Prognosis in Intensive Care Unit among Old Patients (≥65 Years): A 9-Year Single-Center Retrospective Study of 9261 Cases

Hui Lian,[1] Huacong Cai,[2] Hongmin Zhang,[3] Xin Ding,[3] Xiaoting Wang,[1,3] and Shuyang Zhang[4]

[1]*Department of Health Care, Peking Union Medical College Hospital, Chinese Academy of Medical Sciences and Peking Union Medical College, Beijing, China*
[2]*Department of Hematology, Peking Union Medical College Hospital, Chinese Academy of Medical Sciences and Peking Union Medical College, Beijing, China*
[3]*Department of Critical Care Medicine, Peking Union Medical College Hospital, Chinese Academy of Medical Sciences and Peking Union Medical College, Beijing, China*
[4]*Department of Cardiology, Peking Union Medical College Hospital, Chinese Academy of Medical Sciences, Beijing 100730, China*

Correspondence should be addressed to Xiaoting Wang; icuting@163.com and Shuyang Zhang; shuyangzhang103@163.com

Received 13 July 2022; Revised 29 August 2022; Accepted 8 September 2022; Published 22 September 2022

Academic Editor: Shao Liang

Background. D-dimer (DD) has been indicated as a potential indicator due to its connection with the prognosis of the COVID-19 pandemic. Aging is linked to elevated DD levels in coagulation activation. However, few studies have investigated the correlation of DD with prognosis, especially in the old population. Therefore, this study aims **at** investigat**ing** the correlation of DD with prognosis in shock and perioperative populations over 65 years of age. *Methods*. We analyzed 9261 old patients admitted to intensive care units (ICUs) with either confirmed shock or in perioperative period of high-risk surgery, with 8813 of them had DD levels determined on admission. In-hospital mortality, length of ICU stay and ventilation time (VT) associated variables were assessed using generalized linear models. *Results*. Although DD levels had no positive correlations with in-hospital mortality (RR, 1.006; 95% CI, 0.998-1.014) and length of ICU stay (RR, 1.012; 95% CI, 0.997-1.028) in Model 3, they were strongly correlated with VT (RR, 1.577; 95% CI, 1.024-2.064). Higher DD levels in females (RR, 1.804; 95% CI, 1.116-2.602), those who used antibiotics (RR, 1.736; 95% CI, 1.092-2.453), those with surgery (RR, 1.640; 95% CI, 1.273-2.114), and those with shock (RR, 1.740; 95% CI, 1.001-2.687) had stronger correlation with longer VT than the counterparts. While patients who were between 65 and 74 years old (RR, 1.023; 95% CI, 1.003–1.043), with no use of antibiotics (RR, 1.007; 95% CI, 1.001–1.013) nor shock (RR, 1.011; 95% CI, 1.002–1.021), but had undergone surgical procedures (RR, 1.030; 95% CI, 1.012–1.048) were correlated with a longer ICU length of stay. *Conclusion*. DD levels at ICU admission are highly related to increased VT and length of ICU stay in the old population with either confirmed shock or after high-risk surgery, indicating the strong potential of DD as a marker with prognostic utility for all ICU patients in the future.

1. Introduction

The proportion of old patients (≥65 years) in the Intensive Care Unit (ICU) has significantly increased as a result of population aging [1–3]. Aging leads to deterioration of organ function, which is usually correlated with imbalances in oxygen supply and demand, endothelial dysfunction, and coagulopathy [4]. D-dimer (DD), as a fibrin degradation product, has been extensively used in clinical detection of coagulation disorders. A DD value less than 0.55 mg/L FEU is usually considered normal detected by means of immunoturbidimetry. DD has received growing attention since the outbreak of the coronavirus disease 2019 (COVID-19) pandemic, because of its pathological deterioration with the aggravation of cytokine

storms, thrombosis, and disseminated intravascular coagulation (DIC) [5].

Aging is associated with the elevation of plasma levels of a wide variety of molecular markers, including DD, during coagulation activation [6]. In addition, increased DD levels are commonly found in various clinical settings such as inflammation, congestive cardiac failure, pneumonia, septicemia, terminal cancer, surgical procedure, pregnancy, and advanced age [7]. Further studies have taken DD as a potential indicator for its correlation with the prognosis of COVID-19, as well as community-acquired pneumonia in multiple studies [8]. However, little research has delved into the correlation of DD with patient prognosis, especially in the old population. Therefore, the motivation and novelty of the study is to explore the connection between DD and prognosis in shock and perioperative populations over 65 years of age.

2. Materials and Methods

2.1. Study Design and Research Population. This single-center retrospective study included 9,261 old patients (≥65 years of age) with either confirmed shock or in perioperative period of high-risk surgery hospitalized between January 2013 and December 2021 in ICUs of the Peking Union Medical College Hospital, a top tertiary hospital in China. We defined the study population because perioperative patients and septic shock patients were the most common populations with coagulation abnormalities in the ICU. Participants were either discharged or died prior to data acquisition.

2.2. Data Collection. We obtained demographic, clinical, laboratory, medication, and outcome data from the electronic medical records system for analysis. Demographic data covered gender, age, activity of daily living scale, etc. Laboratory results included blood routine examination, coagulation function related parameters (e.g., DD, fibrinogen, thromboplastin time, activated partial thromboplastin time, prothrombin time, prothrombin activity, and fibrin degradation products), inflammatory cytokines (ICs) on ICU admission (e.g., interleukin [IL]-6, C reactive protein [CRP], serum ferritin, procalcitonin, erythrocyte sedimentation rate [ESR], and lactate dehydrogenase), other assessments (hepatorenal function, myocardial enzymes and electrolytes), and multiple blood gas analyses. In our hospital, DD was measured using immunoturbidimetry. A DD level within the range of 0-0.55 mg/L FEU was considered normal. Clinical and medication data included outcomes, antibiotics, vasopressors, operations, ventilation time (VT), and length of ICU stay. The testing frequency was adjusted based on disease progression as assessed by the attending physician. Personal information was removed to protect privacy. Two physicians independently extracted the data using a standardized collection. Data accuracy was reviewed and confirmed by a third physician. Approval from the ethics committee of Peking Union Medical College Hospital (S-K360) has been obtained for this research, and all procedures were in compliance with relevant guidelines and regulations.

2.3. Endpoints. The primary endpoint was in-hospital mortality, while the secondary ones included length of ICU stay and VT.

2.4. Statistics and Analysis. The continuous data were denoted by median (interquartile range [IQR]) because none of them are normally distributed after the Kruskal-Wallis test. Categorical variables, tested by the Chi-square or the Fisher's exact test, were presented as number of cases (percentages). Mortality conforms to the Poisson distribution because it is a relatively low probability event. Multivariant analysis was performed using the Generalized Linear Model. Model 1 was univariant analysis. Model 2 was adjusted for gender, age, and the Sequential Organ Failure Assessment (SOFA) score according to previous study [9] and our preliminary analysis. Model 3 was adjusted for gender, age, SOFA score, operation, shock (defined as lactate increased with requirement for vasopressors), and antibiotics. The significance level was $p < 0.05$. All data was processed by SPSS 26.0 (IBM Corporation, Armonk, NY, USA).

3. Results

3.1. Demographic and Clinical Features. In general, 9261 patients were finally included, with 5026 (54.3%) of them being males; as to the age groups, 5145 (55.6%) and 3368 (36.4%) aged 65-74 and 75-84, respectively, while only 748 (8%) were very old patients (VOPs, ≥85 years old). DD elevations were common, with 89.9% of the tested patients above the upper limit of normal (ULN). 6288 (67.9%) of them had undergone operation, almost half were treated with antibiotics, and around one third were diagnosed with shock. The median SOFA score was 4 in the studied population.

In terms of the outcomes, 129 died in hospital. Most patients stayed in ICU for no less than 2 days. The median VT was 14 hours. See Table 1 for details.

3.2. DD Level on ICU Admission and Correlation with Serum Biomarkers. 8813 of the patients had the DD level tested on ICU admission, with a median DD value of 2.18 mg/L (reference range 0-0.55 mg/L) and a normal DD found in only 975 (11%). Among those with an abnormal DD, 17.6% of them were between 1 and 2 ULN, 21.9% were between 2.1-4 ULN, 20.9% were between 4.1-8 ULN and 28.6% were more than 8 ULN (Table 2). Pearson correlation analyses were conducted among potential correlated factors, such as platelet (PLT), lactate dehydrogenase (LDH), DD, lymphocyte (L#), and white blood cells (WBC), by referring to previous research [9]. The correlation coefficient is listed in Table 2. As indicated by Table 3, statistical significance is present between DD and PLT, Fibrinogen, L# and WBC, but the correlation is relatively low.

3.3. DD Level at ICU Admission and Correlation with in-Hospital Mortality. Univariant analysis (Model 1) showed that higher DD levels were linked to a higher possibility of

Table 1: Demographic and clinical characteristics (including D-dimer level) of the study population.

ITEM	*N*	%
AGE		
65-74	5145	55.6
75-84	3368	36.4
≥85	748	8
Gender		
Male	5026	54.3
Female	4235	45.7
Operation		
Yes	6288	67.9
No	2973	32.1
Shock		
Yes	3069	33.1
No	6192	66.9
Antibiotics		
Yes	4913	53.1
No	4348	46.9
D-dimer		
Normal	975	11.1
1-2 ULN	1546	17.6
2.1-4 ULN	1928	21.9
4.1-8 ULN	1837	20.9
>8 ULN	2523	28.6
Mortality	129	1.4

Note: ULN: upper limits of normal.

death (risk ratio [RR], 1.014; 95% confidence interval [CI], 1.009-1.020). However, after adjusting for demographics and SOFA score (Model 2), the associations became insignificant (RR, 1.005; 95% CI, 0.998–1.012). Nonsignificant significance was found in Model 3 (RR, 1.006; 95% CI, 0.998–1.014). (Figure 1).

Sensitivity analyses were performed for various age groups, gender, antibiotics, operation, and shock. All models were adopted. No statistical significance was found between the above factors and in-hospital mortality in these analyses. (Figure 2).

3.4. DD Llevel at ICU Aadmission and Ccorrelation with Llength of ICU Sstay. Model 1 showed that higher DD levels were correlated with longer ICU stay (RR, 1.066; 95% CI, 1.049-1.083). Model 2 slightly attenuated these associations (RR, 1.047; 95% CI, 1.030-1.065). The associations become insignificant in Model 3, a further adjusted model (RR, 1.012; 95% CI, 0.997–1.028). (Figure 1).

Sensitivity analyses showed interesting results. Taking Model 3 as an example, people who were between 65 and 74 years old (RR, 1.023; 95% CI, 1.003–1.043), without antibiotics (RR, 1.007; 95% CI, 1.001–1.013) nor shock (RR, 1.011; 95% CI, 1.002–1.021), but with surgical procedures (RR, 1.030; 95% CI, 1.012–1.048) were correlated with a longer ICU stay. While a correlation between a higher DD level and a shorter ICU stay was determined in VOPs (RR, 0.936; 95% CI, 0.888–0.985). There was no statistical significance in those aged between 75 and 84 (RR, 1.027; 95% CI, 0.996–1.058). (Figure 3).

3.5. DD Level on ICU Admission and Correlation with VT. Univariant analysis showed that higher DD levels were associated with longer VT (RR, 3.364; 95% CI, 2.563-4.417). Model 2 slightly attenuated these associations (RR, 2.666; 95% CI, 2.007-3.541), and Model 3 further attenuated these associations (RR, 1.577; 95% CI, 1.024-2.064). (Figure 1).

In Model 3, higher DD levels in females (RR, 1.804; 95% CI, 1.116-2.602), those who used antibiotics (RR, 1.736; 95% CI, 1.092-2.453), and those with operation (RR, 1.640; 95% CI, 1.273-2.114), and those with shock (RR, 1.740; 95% CI, 1.001-2.687) had a stronger correlation with longer VT than their counterparts. Those aged between 65 and 74 also showed a strong correlation (RR, 2.166; 95% CI, 1.491-2.864), while neither VOPs nor those between 75 and 84 had correlations with VT. (Figure 4).

4. Discussion

This is the first ever study investigating the impact of DD elevations on outcomes of the old population hospitalized in ICUs. Although DD levels were found to have no positive correlations with in-hospital mortality and length of ICU stay, they were strongly correlated with VT. Higher levels of DD in females, those who used antibiotics, those with operation and shock had stronger correlation with longer VT than the counterparts. Interestingly, the VOPs showed different trends from the younger age groups. Patients who were between 65 and 74 years old, without antibiotics, had undergone surgical procedures or without shock were correlated with a longer ICU stay.

4.1. DD Level and Clinical Outcomes. DD elevation, which represents the activation of coagulation and fibrinolysis systems, has been indicated as one of the most commonly seen laboratory abnormalities, as can be seen in malignant diseases, postoperative conditions, inflammation and infections [10]. DD had not been widely recognized as a prognostic biomarker until the COVID-19 pandemic. However, recent studies have reported higher DD levels in severe COVID-19 patients compared with mild counterparts [11]. A meta-analysis of COVID-19 patients showed that upregulated DD on admission is correlated with an evidently elevated possibility of all-cause death (RR, 4.77; 95% CI, 3.02–7.54) [12]. A DD level of 0.5 μg/ml on admission was recommended as the cutoff for the risk of death for COVID-19 patients.

In our study, statistical significance was found between DD and VT, but not between DD and mortality or length of ICU stay. There might be some possible mechanisms for the close relationship between VT and DD. The entire lung vascular system is covered by the endothelial surface layer, which is responsible for vascular homeostasis [13]. For both perioperative and septic shock patients, inflammation can lead to increased levels of endothelial dysfunction that

Table 2: Demographic, serum biomarkers and clinical features of the study population.

	N	Minimun	25th percentile	Median	75th percentile	Maximun
Age	9261	65	69	73	79	105
D-dimer	8813	0.2	0.99	2.18	4.83	297.2
L#	9183	0	0.49	0.73	1.12	29
SOFA score	8763	0	1	4	7	21
Length of ICU stay	9261	1	2	2	4	248
Ventilation time	7004	1	7	14	21	2637

Note: L#: lymphocyte count; SOFA: Sequential Organ Failure Assessment.

Table 3: Pearson correlation analyses among serum biomarkers.

	PLT	LDH	Fibrinogen	D-dimer	L#	WBC
PLT	1	-0.041	0.357*	-0.078*	0.16*	0.138*
LDH		1	-0.068	0.036	0.057	0.009
Fibrinogen			1	0.051*	0.032*	0.09*
D-dimer				1	-0.004	0.07*
L#					1	0.142*
WBC						1

Note: Bold text indicates the presence of statistical significance. PLT: platelet; LDH: lactate dehydrogenase; L#: lymphocyte; WBC: white blood cells. * $P < 0.05$.

induces a prothrombotic state, resulting in relatively high incidence of lung injury in both groups [14, 15]. At the same time, endothelial dysfunction has been demonstrated to lead to prolonged ventilation [16], which in turn causes the reduction of endothelial cell density, thus prolonging VT and inducing more severe endothelial cell loss [17]. DD bind to endothelial cells though a series of receptors, such as ICAM-1 and integrins. It has been demonstrated that DD levels increased during inflammation, which suggested the presence of micro and macrovascular thrombosis in arteriovenous circulation [18]. Thrombotic complications were observed in 31% of ICU patients with COVID-19 infections [19]. There is also research reporting elevated DD and fibrin degradation products, as well as increased prothrombin time and activated partial thromboplastin time in COVID-19 nonsurvivors [20]. The rise in DD has been shown to be positively related to fibrin accumulating in the alveoli as a result of lung injury [21]. So, it is reasonable that higher DD levels led to longer VT, which is also a good explanation for the correlation between increased DD levels and longer length of ICU stay.

After adjusting for age, gender and SOFA, DD alone had little impact on mortality. Sensitivity analyses showed statistical significance in none of the groups, which was different from the recent studies conducted on COVID-19 patients [20, 22, 23]. According to an observational cohort study, biomarkers of epithelial cell damage and acute-phase proteins (soluble receptor for advanced glycation end-products [sRAGE], soluble tumor necrosis factor receptor 1 [sTNFR-1], etc.), rather than endothelial dysfunction-associated biomarkers, were linked to COVID-19 critical illness [24]. Further studies are warranted to explore whether epithelium or endothelium plays a dominant role in disease severity. And epithelial-associated biomarkers on mortality should be explored if the association between epithelial cells and disease severity is confirmed.

4.2. DD Level and the Impact of Aging. This study focused on the old population, because the median age of the entire ICU population may be already above 65 years as the population ages. The VOP population may be the fastest growing subgroup among ICU patients. And until recently, most ICU physicians have been reluctant to admit these VOPs. The outcomes for this group may be different from the younger counterparts [25]. Unlike many previous studies, our study fails to demonstrate a correlation between DD and the outcomes of VOPs [26, 27]. We even concluded that DD elevations were linked to a shorter ICU stay in VOPs in Model 3, which is hard to explain and may be attributed to a number of factors. Only 19 out of the 749 VOPs died in hospital, which can demonstrate that the admission and discharge policy for VOPs are more flexible in clinical activities. The average SOFA score of the VOPs was 4.08 (standard deviation [SD], 3.55), which means that these VOPs are highly feasible for the study; they consented to risky procedures; anesthetists and surgeons agree to perform the surgeries, and very few VOPs have limitations on life-support treatment [28, 29]. Most of the VOPs did not undergo major surgery or experienced severe septic shock. Several factors like end-of-life decisions and ICU quality of care also influence their outcomes. All the above "confounding factors" affect the ultimate result. Another possible explanation is that higher DD levels mean more severe endothelial dysfunction [30], which means more severe disease and shorter time to outcome. While in patients aged 65-74, both the reaction and the therapy were more similar to those aged 18-64. The results might be more reasonable.

4.3. DD Level and the Impact of Antibiotics, Surgery Procedure and Shock. In previous studies, multiple factors, such as old age, male, shortness of breath, hypertension, diabetes mellitus, coronary heart disease, cerebrovascular disease, gastrointestinal reactions, psychiatric symptoms, renal dysfunction, and traumatic fractures have been confirmed to affect DD levels and patient outcomes [31]. In this study, we proved that higher DD levels in females, those who used antibiotics, those with operation, and those with shock had a close correlation with longer VT than the counterparts. The results are reasonable, as infections, operation, and shock are all risk factors that promote inflammation that aggravates

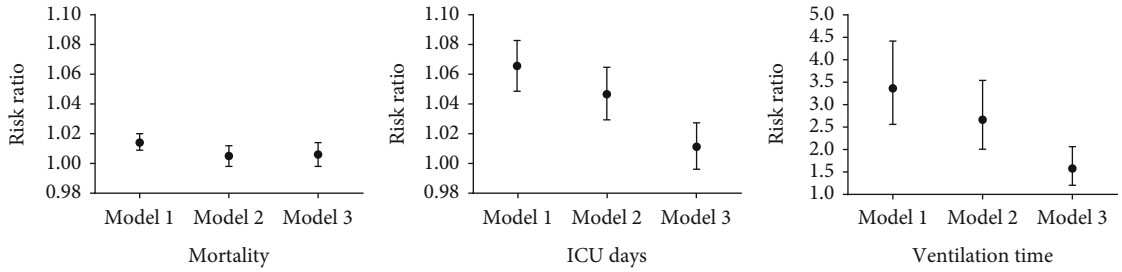

Figure 1: DD levels at ICU admission and correlation with mortality, length of ICU stay and VT. DD: D-dimer; VT: ventilation time.

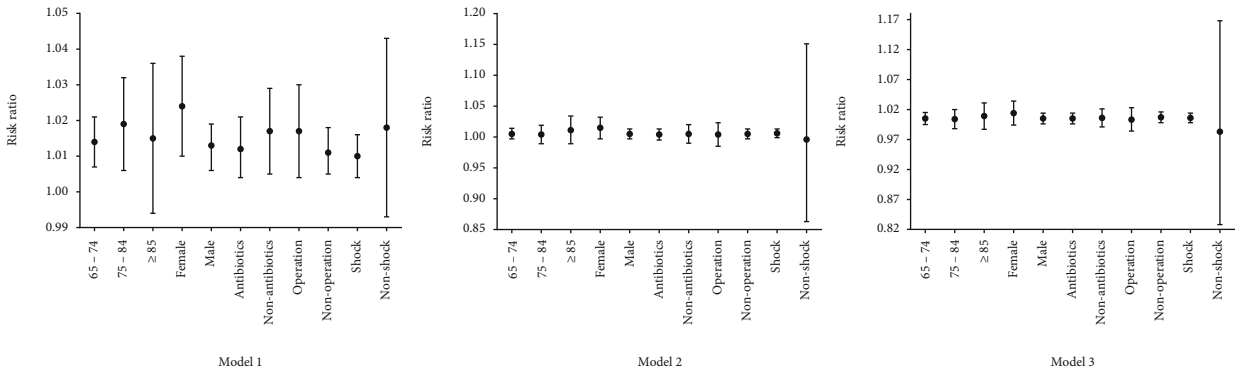

Figure 2: Sensitivity analysis of DD levels at ICU admission and correlation with mortality. DD: D-dimer.

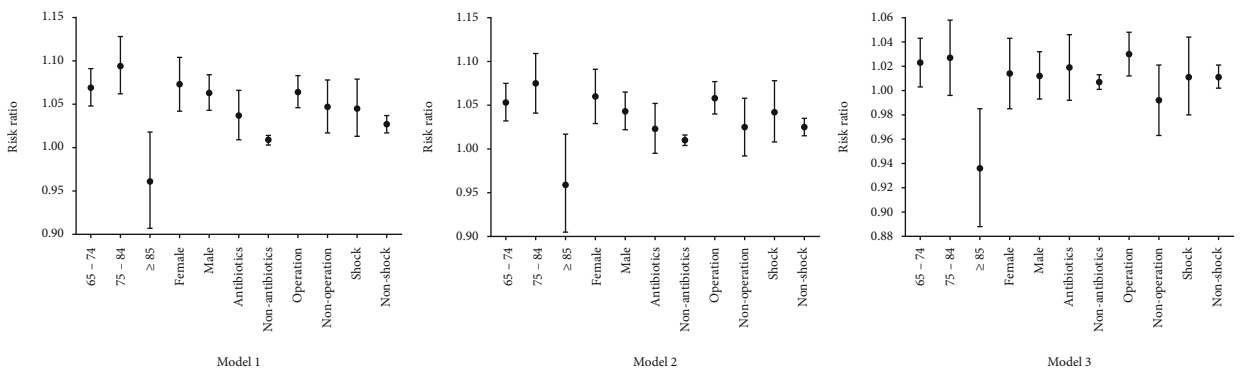

Figure 3: Sensitivity analysis of DD levels at ICU admission and correlation with length of ICU stay. DD: D-dimer.

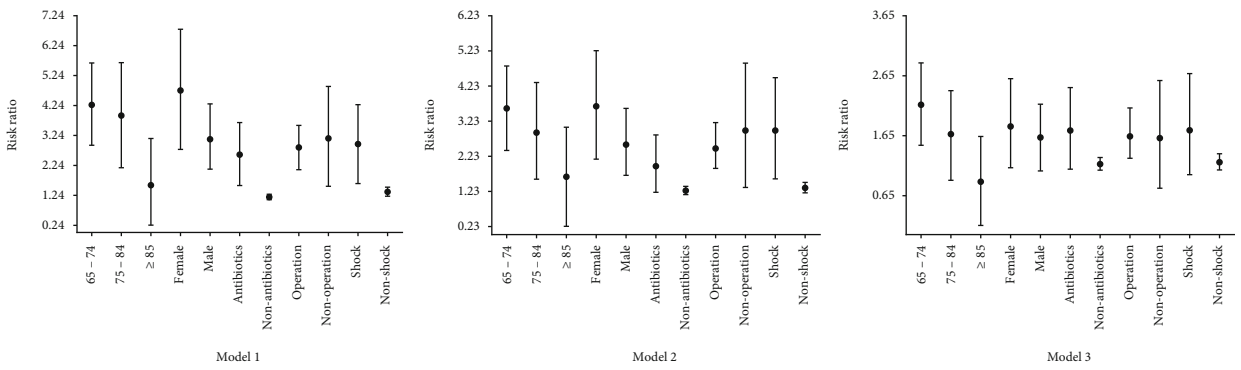

Figure 4: Sensitivity analysis: DD levels at ICU admission and correlation with VT. DD: D-dimer; VT: ventilation time.

endothelial injury. (1) All kinds of infections can cause the release of pro-ICs, including IL-2, IL-6, IL-7, MCP-1, and TNF-α [32]. This is followed by high activation of macrophages, T cells, and natural killer cells, releasing more than 150 kinds of ICs [33]. Endothelial cells become dysfunctional when there is a cytokine storm, leading to an abnormally activated coagulation system [34]. (2) Surgery itself is a stress response as well as a general inflammatory response that promotes the production of catecholamine and glucocorticoid [35]. Stress response also includes sympathetic activation and increased shear stress on the vessel wall. A systematic review on endothelial dysfunction after noncardiac surgery showed immediately decreased endothelial function after surgery, which might be improved 1 month later [36]. (3) In shock patients, hypoperfusion, microcirculation impairment, and endothelial dysfunction promote each other, with endothelial dysfunction playing a vital part in hemodynamic homeostasis imbalance. All the above factors can affect the DD levels, as well as VT [37]. In conclusion, infection, operation, and shock are the risk factors for prolonged VT.

In this paper, we also determined that in noninfection, nonshock, and operation patients, DD elevations were correlated with length of ICU stay. Although insignificant, the infection group has a higher RR than the noninfection counterpart. This is similar to the interpretation for VT above.

4.4. Limitations of the Study. The study has several limitations, though it has a relatively large sample size. While some correlations have been found through statistical analyses in this single-center retrospective study, the results obtained require larger-scale validation. We believe that the correlation between DD levels and patient outcomes is related to the endothelial dysfunction caused by multiple factors, but we have not tested that theory. In the future, we will design prospective studies to verify this hypothesis. Second, only DD levels at the time of ICU admission were available. As a result, we were unable to assess alterations in DD levels over time, let alone the impacts of these alterations on clinical outcomes. Third, as we mentioned above, the admission and discharge policy are more flexible in clinical activities with age, which improved individual heterogeneity. Clinical studies aimed that VOPs may address this issue.

5. Conclusions

Elevated DD levels at ICU admission are linked to an increased risk of VT and prolonged length of ICU stay in the old population with either confirmed shock or after high-risk surgery, indicating the potential role of DD as a warning sign to predict disease severity, as well as a marker of prognostic utility for all ICU patients in the future.

Data Availability

Data and materials are available from the corresponding author on reasonable request.

Ethical Approval

This study has been approved by ethics committee of Peking Union Medical College Hospital (S-K360). Written informed consent has been obtained from all the participants.

Consent

Written informed consent for publication was obtained from all participants.

Conflicts of Interest

The authors have no conflicts of interest to declare.

Authors' Contributions

Xiaoting Wang and Hui Lian were responsible for the conceptualization. Hui Lian and Huacong Cai were tasked for the data curation. Hui Lian, Huacong Cai, and Hongmin Zhang were assigned for the formal analysis. Hui Lian, Huacong Cai, Hongmin Zhang, and Xin Ding were charged for the investigation. Xiaoting Wang, Shuyang Zhang, and Hui Lian were assigned for the project administration. Xiaoting Wang, Shuyang Zhang, and Hongmin Zhang were responsible for the supervision: Hui Lian and Huacong Cai were tasked for the writing of the original draft. Xiaoting Wang, Shuyang Zhang, Hui Lian, and Hongmin Zhang did the reviewing and editing. Hui Lian and Huacong Cai contributed equally to this work and are co-first authors.

Acknowledgments

This study is supported by Key Project of Central Health Care Scientific Research (2020ZD08). We thank Professor Dawei Liu, Bin Du, and Bin Peng for their contribution to this work.

References

[1] F. Wang, X. Wu, S.-y. Hu et al., "Type 2 myocardial infarction among critically ill elderly patients in the intensive care unit: the clinical features and in-hospital prognosis," *Aging Clinical and Experimental Research*, vol. 32, no. 9, pp. 1801–1807, 2020.

[2] M. Burstow, I. Civil, and L. Hsee, "Trauma in the elderly: demographic trends (1995-2014) in a major New Zealand trauma centre," *World Journal of Surgery*, vol. 43, no. 2, pp. 466–475, 2019.

[3] C.-C. Lai, C.-H. Ho, C.-L. Chang et al., "Critical care medicine in Taiwan from 1997 to 2013 under national health insurance," *Journal of Thoracic Disease*, vol. 10, no. 8, pp. 4957–4965, 2018.

[4] A. J. Donato, D. R. Machin, and L. A. Lesniewski, "Mechanisms of dysfunction in the aging vasculature and role in age-related disease," *Circulation Research*, vol. 123, no. 7, pp. 825–848, 2018.

[5] H. Asakura and H. Ogawa, "Covid-19-associated coagulopathy and disseminated intravascular coagulation," *International Journal of Hematology*, vol. 113, no. 1, pp. 45–57, 2021.

[6] C. Haase, M. Joergensen, C. Ellervik, M. K. Joergensen, and L. Bathum, "Age- and sex-dependent reference intervals for D-dimer: evidence for a marked increase by age," *Thrombosis Research*, vol. 132, no. 6, pp. 676–680, 2013.

[7] J. I. Weitz, J. C. Fredenburgh, and J. W. Eikelboom, "A test in context: D-dimer," *Journal of the American College of Cardiology*, vol. 70, no. 19, pp. 2411–2420, 2017.

[8] A. Poudel, Y. Poudel, A. Adhikari et al., "D-dimer as a biomarker for assessment of covid-19 prognosis: D-dimer levels on admission and its role in predicting disease outcome in hospitalized patients with covid-19," *PLoS One*, vol. 16, no. 8, article e0256744, 2021.

[9] S. A. Short, S. Gupta, S. K. Brenner et al., "D-dimer and death in critically ill patients with coronavirus disease 2019," *Critical Care Medicine*, vol. 49, no. 5, pp. e500–e511, 2021.

[10] M. Rostami and H. Mansouritorghabeh, "D-dimer level in covid-19 infection: a systematic review," *Expert Review of Hematology*, vol. 13, no. 11, pp. 1265–1275, 2020.

[11] H. Sivaloganathan, E. E. Ladikou, and T. Chevassut, "Covid-19 mortality in patients on anticoagulants and antiplatelet agents," *British Journal of Haematology*, vol. 190, pp. e192–e195, 2020.

[12] D. M. Simadibrata and A. M. Lubis, "D-dimer levels on admission and all-cause mortality risk in covid-19 patients: a meta-analysis," *Epidemiology & Infection*, vol. 148, p. e202, 2020.

[13] N. M. Goldenberg and W. M. Kuebler, "Endothelial cell regulation of pulmonary vascular tone, inflammation, and coagulation," *Comprehensive Physiology*, vol. 5, pp. 531–559, 2015.

[14] F. Brettner, V. von Dossow, and D. Chappell, "The endothelial glycocalyx and perioperative lung injury," *Current Opinion in Anesthesiology*, vol. 30, no. 1, pp. 36–41, 2017.

[15] E. C. Goligher, M. Dres, B. K. Patel et al., "Lung- and diaphragm-protective ventilation," *American Journal of Respiratory and Critical Care Medicine*, vol. 202, no. 7, pp. 950–961, 2020.

[16] M. Matthay, R. Zemans, G. Zimmerman et al., "Acute respiratory distress syndrome," *Nature Reviews. Disease Primers*, vol. 5, no. 1, 2019.

[17] J. A. Margo, M. F. Whiting, C. H. Brown, C. K. Hoover, and W. M. Munir, "The effect of chronic pulmonary disease and mechanical ventilation on corneal donor endothelial cell density and transplant suitability," *American Journal of Ophthalmology*, vol. 183, pp. 65–70, 2017.

[18] J. Zhang, K. M. Tecson, and P. A. McCullough, "Endothelial dysfunction contributes to covid-19-associated vascular inflammation and coagulopathy," *Reviews in Cardiovascular Medicine*, vol. 21, no. 3, pp. 315–319, 2020.

[19] F. Klok, M. Kruip, N. Van der Meer et al., "Incidence of thrombotic complications in critically ill icu patients with covid-19," *Thrombosis Research*, vol. 191, pp. 145–147, 2020.

[20] N. Tang, D. Li, X. Wang, and Z. Sun, "Abnormal coagulation parameters are associated with poor prognosis in patients with novel coronavirus pneumonia," *Journal of Thrombosis and Haemostasis*, vol. 18, no. 4, pp. 844–847, 2020.

[21] B. J. Hunt and M. Levi, "Re the source of elevated plasma d-dimer levels in covid-19 infection," *British Journal of Haematology*, vol. 190, no. 3, pp. e133–e134, 2020.

[22] L. Zhang, X. Yan, Q. Fan et al., "D-dimer levels on admission to predict in-hospital mortality in patients with covid-19," *Journal of Thrombosis and Haemostasis*, vol. 18, no. 6, pp. 1324–1329, 2020.

[23] A. Alonso-Fernandez, N. Toledo-Pons, B. G. Cosio et al., "Prevalence of pulmonary embolism in patients with covid-19 pneumonia and high d-dimer values: a prospective study," *PLoS One*, vol. 15, no. 8, article e0238216, 2020.

[24] P. K. Bhatraju, E. D. Morrell, L. Zelnick et al., "Comparison of host endothelial, epithelial and inflammatory response in icu patients with and without covid-19: a prospective observational cohort study," *Critical Care*, vol. 25, p. 148, 2021.

[25] H. Flaatten, D. De Lange, A. Artigas et al., "The status of intensive care medicine research and a future agenda for very old patients in the icu," *Intensive Care Medicine*, vol. 43, no. 9, pp. 1319–1328, 2017.

[26] L. Naymagon, N. Zubizarreta, J. Feld et al., "Admission d-dimer levels, d-dimer trends, and outcomes in covid-19," *Thrombosis Research*, vol. 196, pp. 99–105, 2020.

[27] F. Qeadan, B. Tingey, L. Y. Gu, A. H. Packard, E. Erdei, and A. I. Saeed, "Prognostic values of serum ferritin and d-dimer trajectory in patients with covid-19," *Viruses*, vol. 13, no. 3, p. 419, 2021.

[28] H. Flaatten, M. Beil, and B. Guidet, "Elderly patients in the intensive care unit," *Seminars in Respiratory and Critical Care Medicine*, vol. 42, pp. 10–19, 2021.

[29] B. Guidet, H. Flaatten, A. Boumendil et al., "Withholding or withdrawing of life-sustaining therapy in older adults (≥80 years) admitted to the intensive care unit," *Intensive Care Medicine*, vol. 44, no. 7, pp. 1027–1038, 2018.

[30] L. Tran, B. Pannier, P. Lacolley et al., "A case-control study indicates that coagulation imbalance is associated with arteriosclerosis and markers of endothelial dysfunction in kidney failure," *Kidney International*, vol. 99, no. 5, pp. 1162–1172, 2021.

[31] X. He, F. Yao, J. Chen et al., "The poor prognosis and influencing factors of high d-dimer levels for covid-19 patients," *Scientific Reports*, vol. 11, no. 1, article 81300, pp. 1–7, 2021.

[32] B. G. Chousterman, F. K. Swirski, and G. F. Weber, "Cytokine storm and sepsis disease pathogenesis," *Seminars in Immunopathology*, vol. 39, pp. 517–528, 2017.

[33] P. Mehta, D. F. McAuley, M. Brown et al., "Covid-19: consider cytokine storm syndromes and immunosuppression," *The Lancet*, vol. 395, no. 10229, pp. 1033-1034, 2020.

[34] M. Gaestel, A. R. Nebreda, and M. B. Yaffe, *Cytokine storm*, Massachusetts Medical Society, 2021.

[35] C. Finnerty, N. Mabvuure, A. Ali, R. Kozar, and D. Herndon, "The surgicall y induced stress response, JPEN-J," *Journal of Parenteral and Enteral Nutrition*, vol. 37, Supplement 5, pp. 21s–29s, 2013.

[36] E. Søndergaard, S. Fonnes, and I. Gögenur, "Endothelial dysfunction after non-cardiac surgery: a systematic review," *Acta Anaesthesiologica Scandinavica*, vol. 59, no. 2, pp. 140–146, 2015.

[37] S. Opal and T. Van Der Poll, "Endothelial barrier dysfunction in septic shock," *Journal of Internal Medicine*, vol. 277, no. 3, pp. 277–293, 2015.

Hindawi
Oxidative Medicine and Cellular Longevity
Volume 2022, Article ID 3972272, 21 pages
https://doi.org/10.1155/2022/3972272

Research Article

Identification of Monocyte-Associated Genes Related to the Instability of Atherosclerosis Plaque

Wentao Qin,[1] **Fu Gan**,[2] **Riguan Liang**,[3] **Jing Li**,[4] **Xiaomei Lai**,[5] **Yongfa Dai**,[6,7] **and Jie Liu**[6,7]

[1]*Department of Bone and Joint, The First Affiliated Hospital of Guangxi Medical University, Nanning, Guangxi 530021, China*
[2]*Department of Urology Surgery, The Affiliated Hospital of Youjiang Medical University for Nationalities, Baise, China*
[3]*Department of Joint Surgery and Sports Medicine, Baise People's Hospital, Baise 533000, China*
[4]*Department of Nuclear Medicine, The First Affiliated Hospital of Guangxi Medical University, Nanning, Guangxi 530021, China*
[5]*Department of Cardiovascular Medicine, The First Affiliated Hospital of Guangxi Medical University, Nanning, Guangxi 530021, China*
[6]*Department of Cardiovascular Medicine, The First People's Hospital of Nanning, Nanning, Guangxi 530016, China*
[7]*Department of Cardiovascular Medicine, The Fifth Affiliated Hospital of Guangxi Medical University, Nanning, Guangxi 530016, China*

Correspondence should be addressed to Yongfa Dai; yoinffa@outlook.com and Jie Liu; gxnnliujie@163.com

Received 6 July 2022; Revised 5 August 2022; Accepted 12 August 2022; Published 21 September 2022

Academic Editor: Shao Liang

Background. Atherosclerotic plaque instability is a common cause of stroke and ischemic infarction, and identification of monocyte-associated genes has become a prominent feature in cardiovascular research as a contributing/predictive marker. *Methods*. Whole genome sequencing data were downloaded from GSE159677, GSE41571, GSE120521, and GSE118481. Single-cell sequencing data analysis was conducted to cluster molecular subtypes of atherosclerotic plaques and identify specific genes. Differentially expressed genes (DEGs) between normal subjects and patients with unstable atheromatous plaques were screened. Weighted gene coexpression network analysis (WGCNA) was performed to find key module genes. In addition, GO and KEGG enrichment analyses explored potential biological signaling pathways to generate protein interaction (PPI) networks. GSEA and GSVA demonstrated activations in plaque instability subtypes. *Results*. 239 monocyte-associated genes were identified based on bulk and single-cell RNA-sequencing, followed by the recognition of 1221 atherosclerotic plaque-associated DEGs from the pooled matrix. GO and KEGG analyses suggested that DEGs might be related to inflammation response and the PI3K-Akt signaling pathway. Eight no-grey modules were obtained through WGCNA analysis, and the turquoise module has the highest correlation with unstable plaque ($R^2 = 0.40$), which contained 1323 module genes. After fetching the intersecting genes, CXCL3, FPR1, GK, and LST1 were obtained that were significantly associated with plaque instability, which had an intense specific interaction. Monocyte-associated genes associated with atherosclerotic plaque instability have certain diagnostic significance and are generally overexpressed in this patient population. In addition, 11 overlapping coexpressed genes (CEG) might also activated multiple pathways regulating inflammatory responses, platelet activation, and hypoxia-inducible factors. GSVA showed that the corresponding pathways were significantly activated in high expression samples. *Conclusions*. Overexpression of CXCL3, GK, FPR1, and LST1 was advanced recognition and intervention factors for unstable plaques, which might become targets for atherosclerosis rupture prevention. We also analyzed the potential mechanisms of CEG from inflammatory and oxidative stress pathways.

1. Introduction

Atherosclerosis (AS) is a common cardiovascular disease with a high mortality and morbidity rate due to chronic inflammatory changes caused by the accumulation of cholesterol on the walls of blood vessels over time. Atherosclerosis mainly occurs in medium and large arteries, characterized by the formation of multifocal atherosclerotic plaques on the inner wall of arteries [1–4]. Atherosclerotic plaques are mainly composed of lipids, necrotic cells, and some inflammatory factors, which are divided into stable and unstable plaques according to the stability of the plaques. The rupture of unstable atherosclerotic plaques often leads to serious consequences, including ischemic stroke and acute myocardial infarction. Some studies have found that more than 70% of fatal coronary thrombosis is caused by the rupture of unstable plaques [5, 6]. In-depth elucidation of the molecular mechanism of unstable plaque formation to achieve early recognition and intervention is of great significance to prevent severe clinical complications. However, the specific molecular mechanisms involved in the instability of atherosclerotic plaques are very complicated and have not been fully reported. It is imperative to conduct in-depth research on it.

Currently, only a few studies have reported the possible factors involved in the formation and rupture of unstable plaques. For example, Bao et al.'s study suggested that CD5L, S100A12, and CKB were involved in regulating the stability of atherosclerotic plaques [7]. Other studies reported that visfatin could act as an inflammation mediator and ultimately aggravated the instability of atherosclerotic plaques [8, 9]. Liu et al. reported the downregulation of IGFBP6 expression in unstable carotid atherosclerotic plaques and indicated that it might be an available prediction marker for vulnerable plaques [10]. Besides, a previous study has confirmed that EFEMP1, BGN, and RILP may have potential diagnostic value for atherosclerotic plaque rupture [11]. Another study suggested that the stability of atherosclerotic plaques may be related to oxidative stress of cells, and the oxidative stress caused by excessive reactive oxygen species in cells plays an important role in atherosclerosis. In carotid plaques, SIRT6 can promote the occurrence of oxidative stress through various ways, and it is obviously overexpressed in unstable carotid plaques, suggesting that the process of oxidative stress is a dangerous factor in the stability of plaques. Summarily, many studies have identified various factors that may contribute to plaque instability. However, it is worth noting that the above research and analysis on plaque instability are mostly limited to the transcriptome level. Existing studies have confirmed the difference in cell composition between ruptured and stable plaques [12–14]. Also, the underlying mechanism of macrophages and foam cells involved in atherosclerotic plaque instability and rupture has been partially characterized [15, 16]. Numerous studies have reported that monocytes play an essential role in atherosclerotic, but monocyte-associated genes' effect on plaque instability is still not very clear [17–21]. Therefore, it is essential to explore the clinical significance and potential mechanisms of monocyte-associated genes in atherosclerotic plaque instability through the combined single-cell sequencing and transcriptomics data analysis.

In this study, we combined single-cell sequencing data analysis, differential expression analysis, and WGCNA analysis to obtain significant monocyte-associated candidate genes related to atherosclerotic plaque instability. Furthermore, we detected the expression status of the obtained candidate genes in monocytes and unstable plaques and explored its diagnostic significance. Finally, GSEA, GSVA, coexpression analysis, etc., were used to explore the underlying mechanism preliminarily.

2. Materials and Methods

2.1. Data Acquisition and Preprocessing. The datasets (single-cell sequencing data: GSE159677 with 6 qualified samples; transcriptome data: GSE41571, GSE120521, and GSE118481 with 11, 8, and 16 qualified samples, respectively) included in this study were all obtained from GEO databases (https://www.ncbi.nlm.nih.gov/geo/). The transcriptome data were proceeded by log2 conversion and normalization, then used for subsequent analysis. Due to the small sample size, the SVA software package is used to integrate GSE41571 and GSE120521 datasets into a merged dataset containing ten stable plaque samples and nine unstable plaque samples, and batch correction between the two datasets is also solved.

2.2. Single-Cell Sequencing Data Analysis. To obtain monocyte-associated genes in atherosclerotic plaque, the GSE159677 dataset, which contained 6 matched samples, was used for single-cell sequencing data analysis through the Seurat and SingleR packages. We integrated the data of 6 samples and performed data normalization. Hereafter, data quality control was carried out. Briefly, cells with less than 50 genes and more than 5 percent of mitochondrial genes will be removed. The number of highly variable genes was set at 1500. Principal component analysis (PCA) was performed on the top 1500 variable genes to visualize transcriptional variability. T-SNE method was used for further dimensional reduction of the principal components (p value < 0.05), and then, cells were clustered. Monocyte-related genes were extracted using the FindAllMarkers function.

2.3. Weighted Coexpression Network Analysis (WGCNA). WGCNA analysis was performed on the GSE118481 dataset to find gene module genes significantly associated with plaque instability. An appropriate soft threshold was reasonably selected as the degree of scale independence reached 0.9. Besides, the min module size is set to 30, and modules with a similarity over 0.8 will be merged. Genes in modules that most significantly correlated with unstable plaque were considered crucial genes associated with plaque instability.

2.4. Identification of Significant Monocyte-Associated Candidate Genes Related to Plaque Instability. We performed differential expression analysis on the merged dataset using the limma package. $|\text{logFC}| > 1$ and adj.p-value < 0.05 were used as the threshold to identify differentially expressed

genes (DEGs). LogFC < −1 and logFC > 1 represented genes downregulated and upregulated in unstable plaques, respectively. Overlapping genes identified by single-cell sequencing data analysis, differential expression analysis, and WGCNA analysis were considered to be significant monocyte-associated candidate genes related to plaque instability. These overlapping candidate genes will be used for further analysis.

2.5. Determination of Expression and Diagnostic Value of Candidate Genes. To determine the candidate genes' ability to distinguish the stable from unstable plaques, we performed receiver operating characteristic (ROC) curve analysis in the R software (version 3.6.3) using the pROC package (for analysis) and the ggplot2 package (for visualization). Subsequently, we measured the area under the ROC curve (AUC) to evaluate the candidate genes' diagnosing capability. Moreover, we also extracted the expression profile data of candidate genes and then drew the violin plot to determine their expression patterns.

2.6. Functional Enrichment Analysis of DEGs. The DAVID database (https://david.ncifcrf.gov/) was widely used in bioinformatics analysis [22]. In our study, we used the DAVID database to carry out functional enrichment analysis to gain an in-depth understanding of the potential mechanisms of DEGs in plaque instability. Briefly, we carried out two functional enrichment analyses, including Gene Ontology (GO) analysis and the Kyoto Encyclopedia of Genes and Genomes (KEGG) pathway analysis. The analysis results were shown in the form of bubble charts.

2.7. Gene Set Enrichment Analysis (GSEA). It was critical to explore the as-yet-undiscovered pathways associated with plaque instability. Therefore, based on the merged dataset, we performed GSEA and result visualization using the R packages clusterProfile and enrichplot, respectively. For this analysis, we used "h.all.v7.4.symbols.gmt" as the reference gene set.

2.8. Identification and Functional Analysis of Overlapping Coexpressed Genes (CEGs) of Candidate Genes. Using the merged dataset, we performed coexpression analysis on candidate genes, and genes with a Pearson correlation coefficient r greater or equal to 0.70 were considered as CEGs. GeneMANIA (http://www.genemania.org) was an online database that provided functional analysis services [23]. In our study, GeneMANIA was implemented to explore the molecular function of overlapping CEGs. In addition, we analyzed the related genes in GeneMANIA database in STRING database (https://cn.string-db.org/) at protein level.

2.9. Functional Similarity Analysis of Candidate Genes and Correlation Analysis of PI3K-ATK Pathway-Related Genes. We used GoSemSim package to analyze the interaction between protein of the candidate genes and scored their similarities. The scores were used to judge the functional effect. Finally, we selected the gene with the highest score and made a correlation analysis with PI3KR5 and other candidate genes.

2.10. Gene Set Variation Analysis (GSVA) and Identification of Correlations between the Candidate Genes. GSVA was performed using the R package "GSVA" to identify signaling pathways associated with candidate genes. Specifically, we performed the above analysis by dividing the samples into high and low expression groups according to the median expression values of candidate genes. Besides, "h.all.v7.4.-symbols.gmt" was the reference gene set of GSVA. Meanwhile, we calculated the Pearson correlation coefficient between the candidate genes based on the merged dataset to explore their relationship.

2.11. Statistical Analysis. Statistical analysis involved in this study was completed on the R (version 3.6.3) platform. Comparison of candidate gene expression in stable and unstable plaques was performed using independent sample t-tests. Unless otherwise stated, p values less than 0.05 were considered statistically significant.

3. Results

3.1. Extraction of Monocyte-Related Genes. To obtain monocyte-related genes in atherosclerotic plaques, we first integrated and quality-controlled the single-cell sequencing data from the six samples included in GSE159677. The top 1500 variable genes are shown (Figure 1(a)). Further, the normalization of single-cell sequencing data was carried out, and 15 principal components (p value < 0.05) were used for subsequent analysis (Figures 1(b) and 1(c)). This study identified 10 cell clusters using the Seurat package, and cluster 2 was classified as monocytes (Figure 1(d)). We subsequently extracted cell cluster-associated specific genes and presented the top 10 genes for each cell cluster in a heatmap (Figure 1(e)). The extracted 239 monocyte-related genes will be used in subsequent studies.

3.2. Extraction of Genes Associated with Plaque Instability Phenotype. We utilized WGCNA analysis to identify modules significantly associated with the phenotype of unstable atherosclerotic plaques. Module genes were considered to be significantly associated with plaque instability. The parameters were set as follows: (1) MergeHeightCut = 0.25, (2) scale-free $R^2 = 0.9$, (3) minimum size of module genes = 30, and (4) soft-thresholding power = 11. Ultimately, we obtained eight nongrey modules, among which the turquoise module containing 1323 genes had the strongest positive correlation with the unstable plaque phenotype ($R^2 = 0.40$, p-value = $5.3e-52$) (Figures 2(a)–2(d)). Genes included in this module will be selected for conducting further analysis.

3.3. Identification of 4 Significant Monocyte-Associated Candidate Genes Related to Plaque Instability. PCA analysis revealed significant differences in gene expression between stable and unstable plaques (Figure 3(a)). In our current study, a total of 1221 DEGs were identified from the merged dataset, which may play an important role in the development of unstable plaques (Figure 3(b)). The heatmap showed the top 20 upregulated and downregulated genes (Figure 3(c)). Only overlapping genes identified in single-

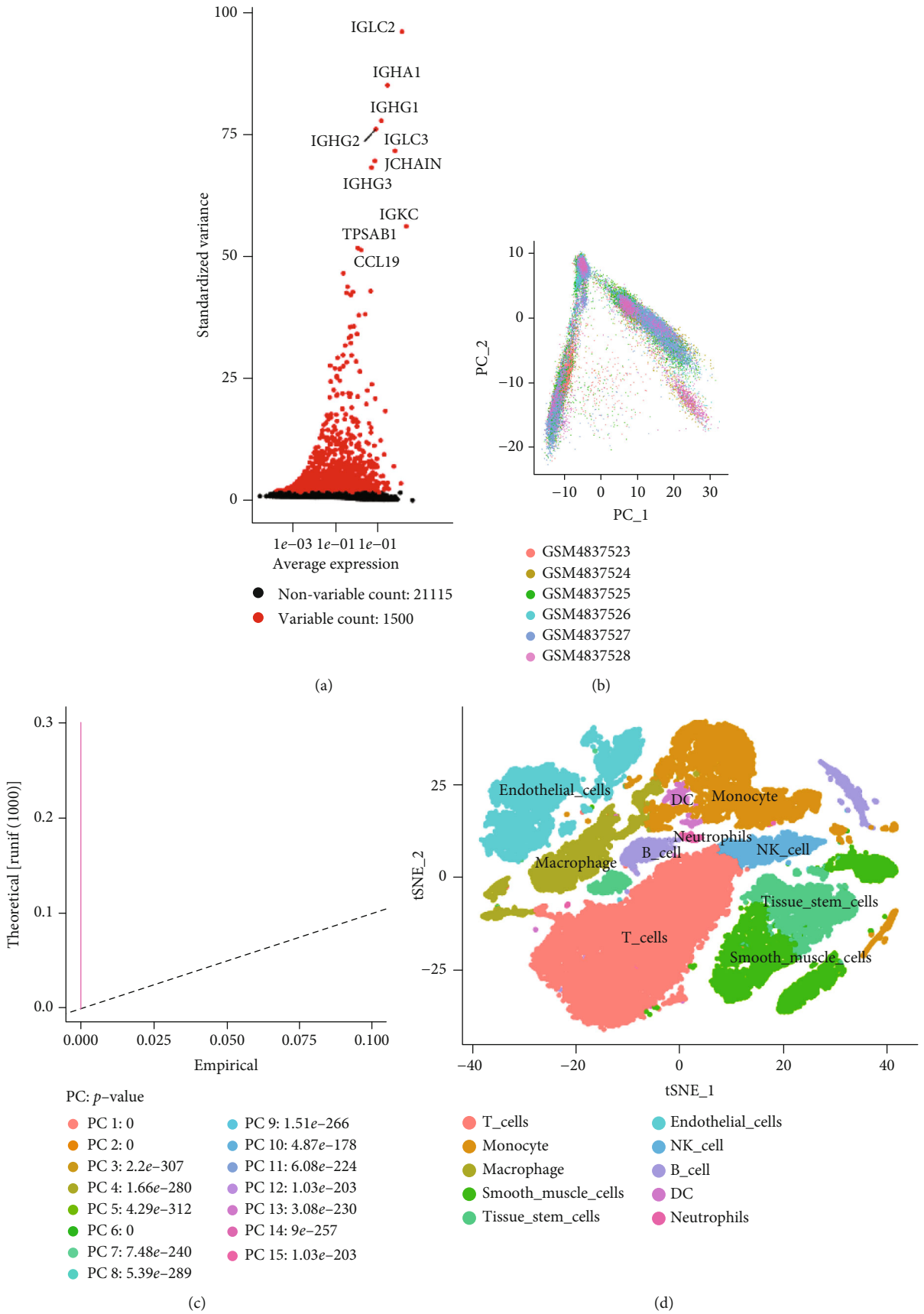

Figure 1: Continued.

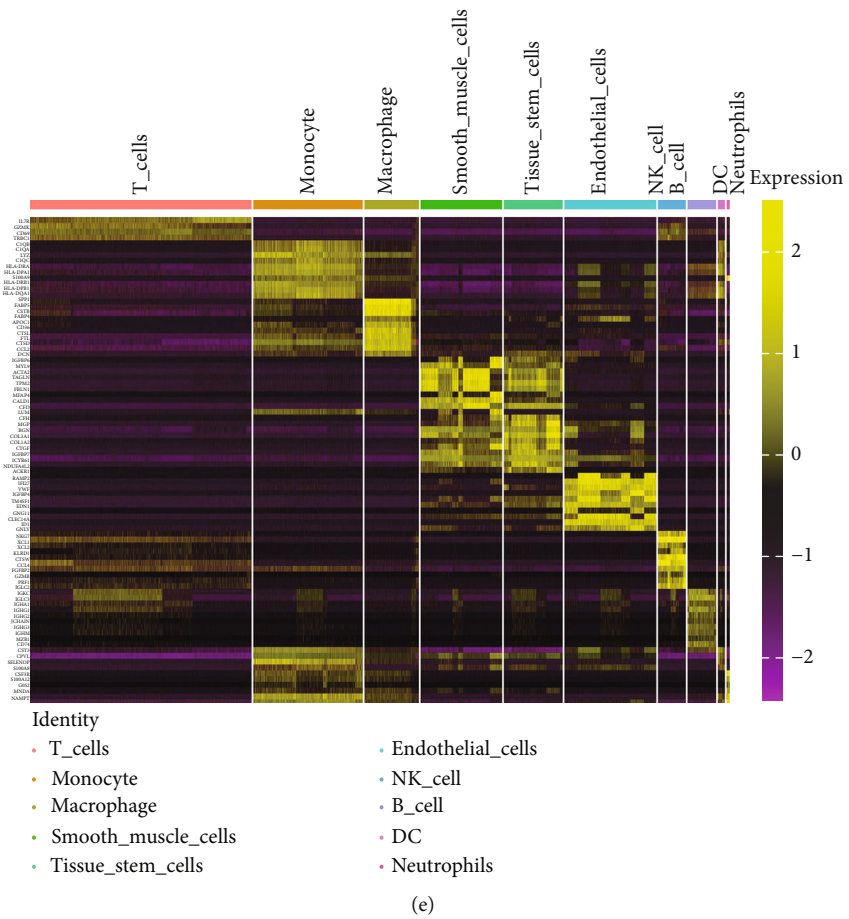

(e)

Figure 1: Extraction of monocyte-related genes by single-cell sequencing data analysis. (a) Gene filtering. (b, c) Principal component analysis (PCA) plot colored by various samples. (d) T-SNE plot colored by cell types. (e) Identification of various cell cluster-associated specific genes.

cell sequencing data analysis, WGCNA analysis, and differential expression analysis will be considered significant monocyte-associated candidate genes related to plaque instability. We intersected the genes identified by the three approaches to obtain 4 overlapping genes, including CXCL3, FPR1, GK, and LST1, which will be used as candidate genes for follow-up research (Figure 3(d)).

3.4. Overexpression of Four Candidate Genes and Its Promising Diagnostic Significance. In our study, we determined the expression status of four candidate genes (CXCL3, FPR1, GK, and LST1) and corresponding diagnostic significance in unstable plaques. Our study showed that these candidate genes had moderate and above discriminative capability and could effectively discriminate between stable and unstable plaques. Besides, we detected the overexpression of the candidate genes in unstable atherosclerotic plaques in the merged dataset (Figures 4(a)–4(d)). Not only that, but we also detected their upregulated expression in monocytes (Figures 5(a)–5(d)). In conclusion, our study suggested that the expression of four candidate genes was significantly upregulated, which has a certain diagnostic value for unstable plaques.

3.5. Functional Enrichment Analysis of DEGs. We performed GO enrichment analysis and KEGG pathway analysis through the online DAVID database. GO enrichment analysis had three parts, including cellular components (CC), biological process (BP), and molecular function (MF). For BP, DEGs were mainly enriched in signal transduction, inflammatory response, immune response, etc. (Figure 6(a)). Regarding CC, DEGs were mainly enriched in the plasma membrane, integral component of membrane, etc. (Figure 6(b)). In terms of MF, DEGs were significantly enriched in protein binding, protein homodimerization activity, etc. (Figure 6(c)). In addition, KEGG pathway analysis showed that these genes were particularly related to the PI3K-Akt signaling pathway, pathways in cancer, and focal adhesion (Figure 6(e)).

3.6. Gene Set Enrichment Analysis (GSEA). Herein, GSEA was carried out to explore underlying pathways involved in the development of unstable plaques, which may participate in the regulation of plaque instability. Our results suggest that multiple signaling pathways may be involved, including "HALLMARK_INFLAMMATORY_RESPONSE" and "HALLMARK_PI3K_AKT_MTOR_SIGNALING" (Figure 7).

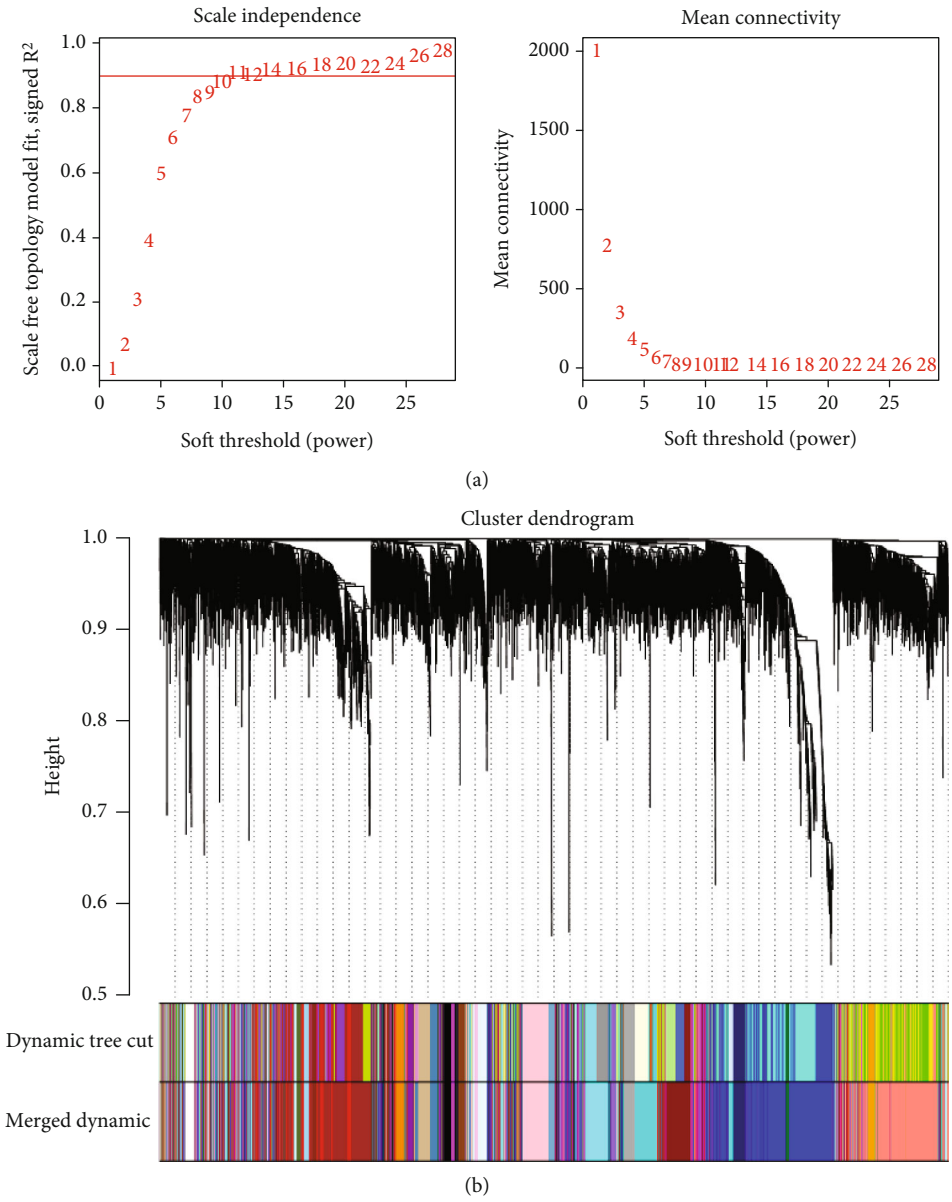

Figure 2: Continued.

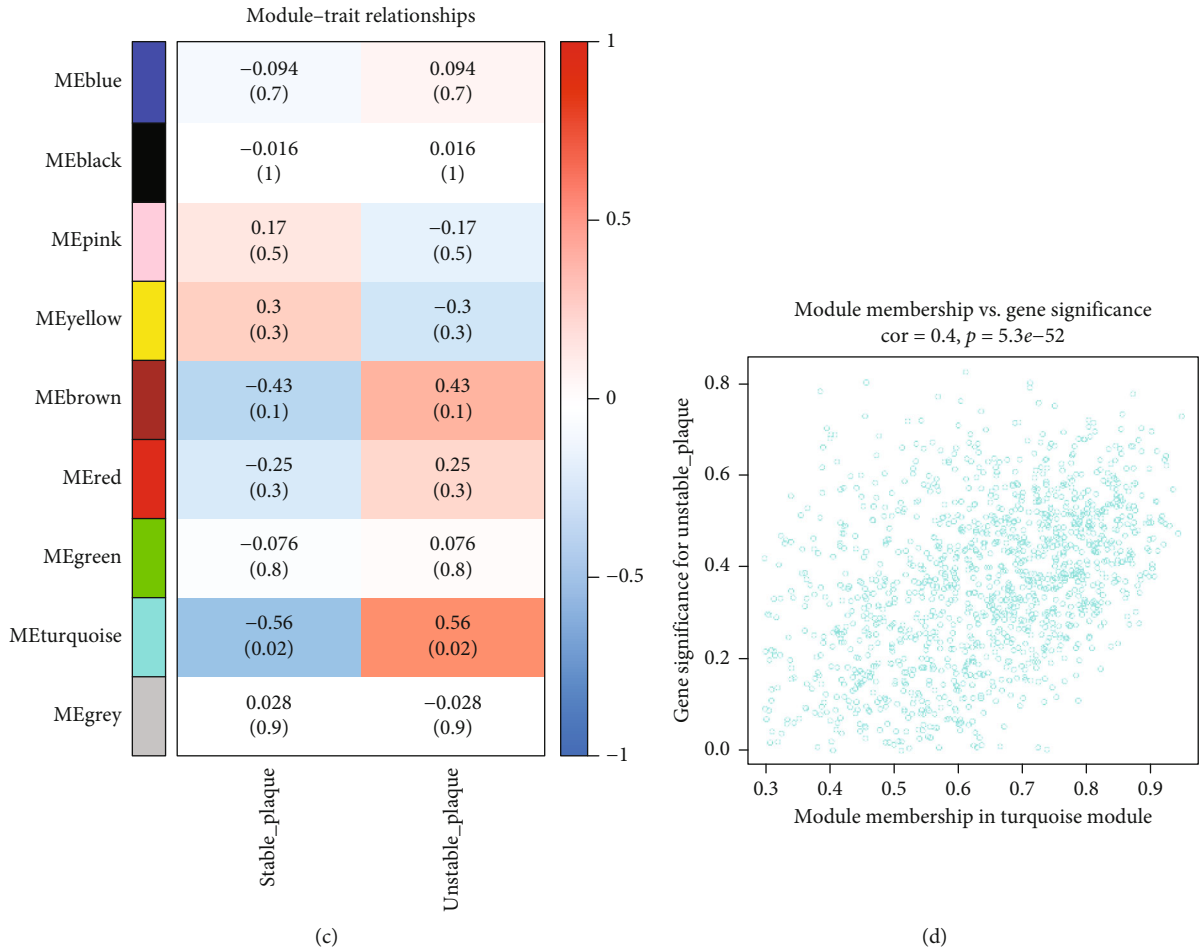

Figure 2: Identification of the crucial genes related to atherosclerotic plaque instability phenotype through weighted coexpression network analysis (WGCNA). (a) Scale-free fit parameters of different soft-thresholding powers and according to average connectivity of different soft-thresholding powers. (b) Cluster dendrogram obtained in this study. (c) The heatmap showed the correlation of modules and phenotypes and annotated the correlation coefficient and p value. (d) Gene significances of the selected turquoise module.

3.7. Identification and Functional Analysis of Overlapping Coexpressed Genes (CEGs) of Candidate Genes. We identified 11 overlapping CEGs of the candidate genes (CXCL3, FPR1, GK, and LST1) in the merged dataset. Figure 8 shows the correlation between the candidate genes and 11 overlapping CEGs. Further, functional analysis from the GeneMANIA database suggested that these genes were closely related to regulating inflammatory responses (Figure 9(a)). From the protein interaction analysis of STRING database, we can see that there is a close relationship between related genes (Figure 9(b)).

3.8. Gene Set Variation Analysis (GSVA) and Identification of Correlations between Candidate Genes. Our study found that there was a significant positive correlation between these candidate genes (CXCL3, FPR1, GK, and LST1) (Figure 9(c)). Then, we conducted GSVA to explore signaling pathways associated with the candidate genes in unstable plaques. This study revealed that multiple pathways, including "HALLMARK_PI3K_AKT_MTOR_SIGNALING" and "HALLMARK_INFLAMMATORY_RESPONSE," were significantly activated in the samples with high expression of the candidate genes (Figures 9(d)–9(g)). Notably, this result was consistent with that of the GSEA.

3.9. Evaluation of Protein Interaction and Correlation Analysis of PIK3R5 Gene. We analyzed each candidate gene at the level of biological process (BP) and cellular component (CC) and got the protein similarity score of the candidate genes. In the box diagram, the line in the box indicates the median value of functional similarity, and it can be seen that the score of FPR1 is the highest (Figure 10(a)). In the correlation analysis diagram, FPR1 is positively correlated with PIK3R5 and other overlapping genes significantly (Figures 10(b)–10(e)).

4. Discussion

Atherosclerosis (AS) is an occlusive artery disease that usually occurs in middle-aged and older adults, which seriously threatens patients' health and life quality [24, 25]. In particular, unstable atherosclerotic plaques rupture, leading to blood embolism, which can lead to a series of serious clinical consequences that can be fatal for patients [26, 27]. It is

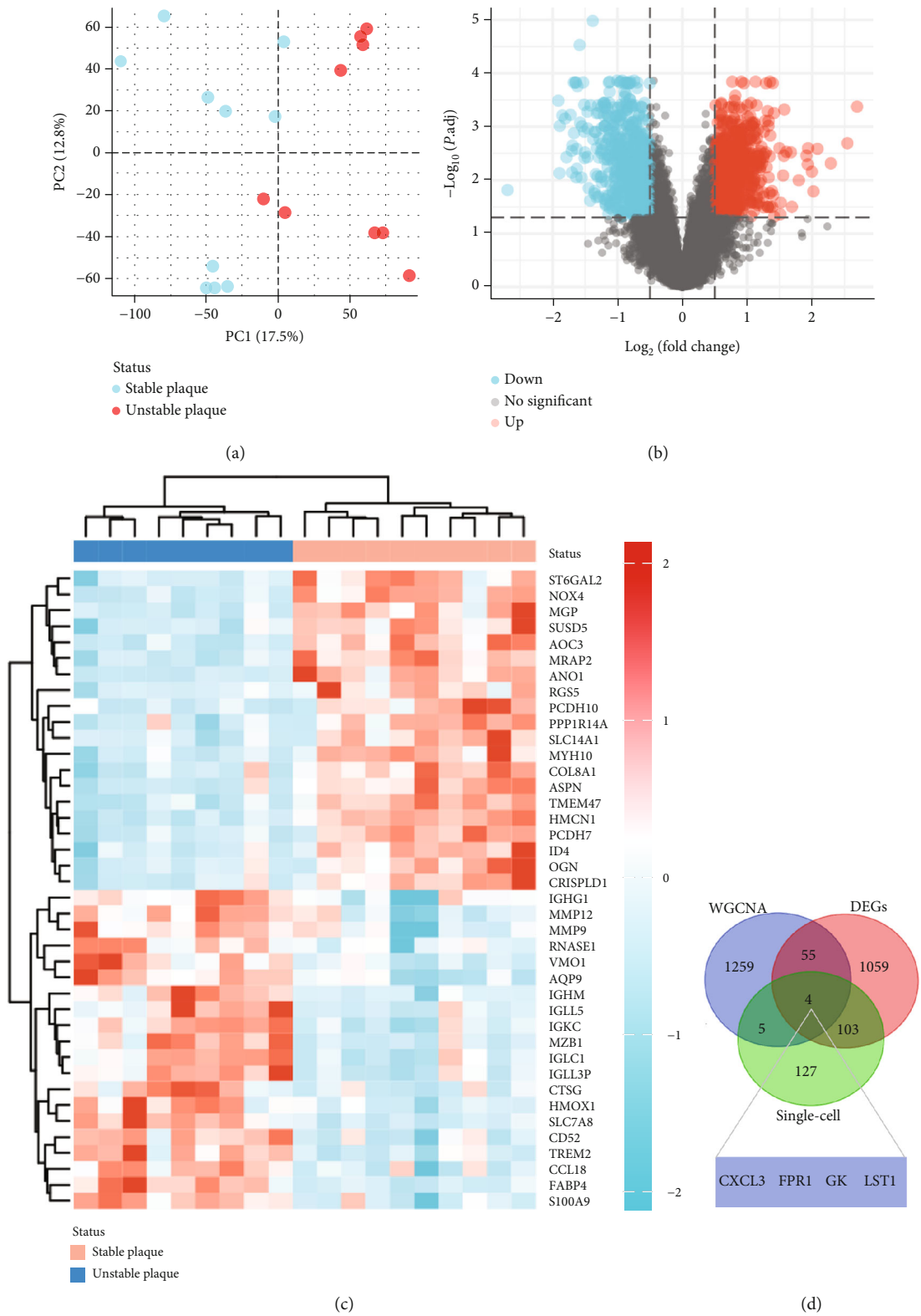

Figure 3: Differential expression analysis and identification of significant monocyte-associated candidate genes related to plaque instability. (a) Two-dimensional PCA cluster plot of the merged dataset; blue represented the stable sample, and red represented the unstable plaque sample. (b) Volcano plot of differentially expressed genes (DEGs), red represents upregulated genes, blue represents downregulated genes, and grey represents no significantly differentially expressed genes. (c) A heatmap of the most 20 upregulated and downregulated genes. (d) Venn diagram showed the obtained four overlapping significant monocyte-associated candidate genes (CXCL3, FPR1, GK, and LST1) related to plaque instability.

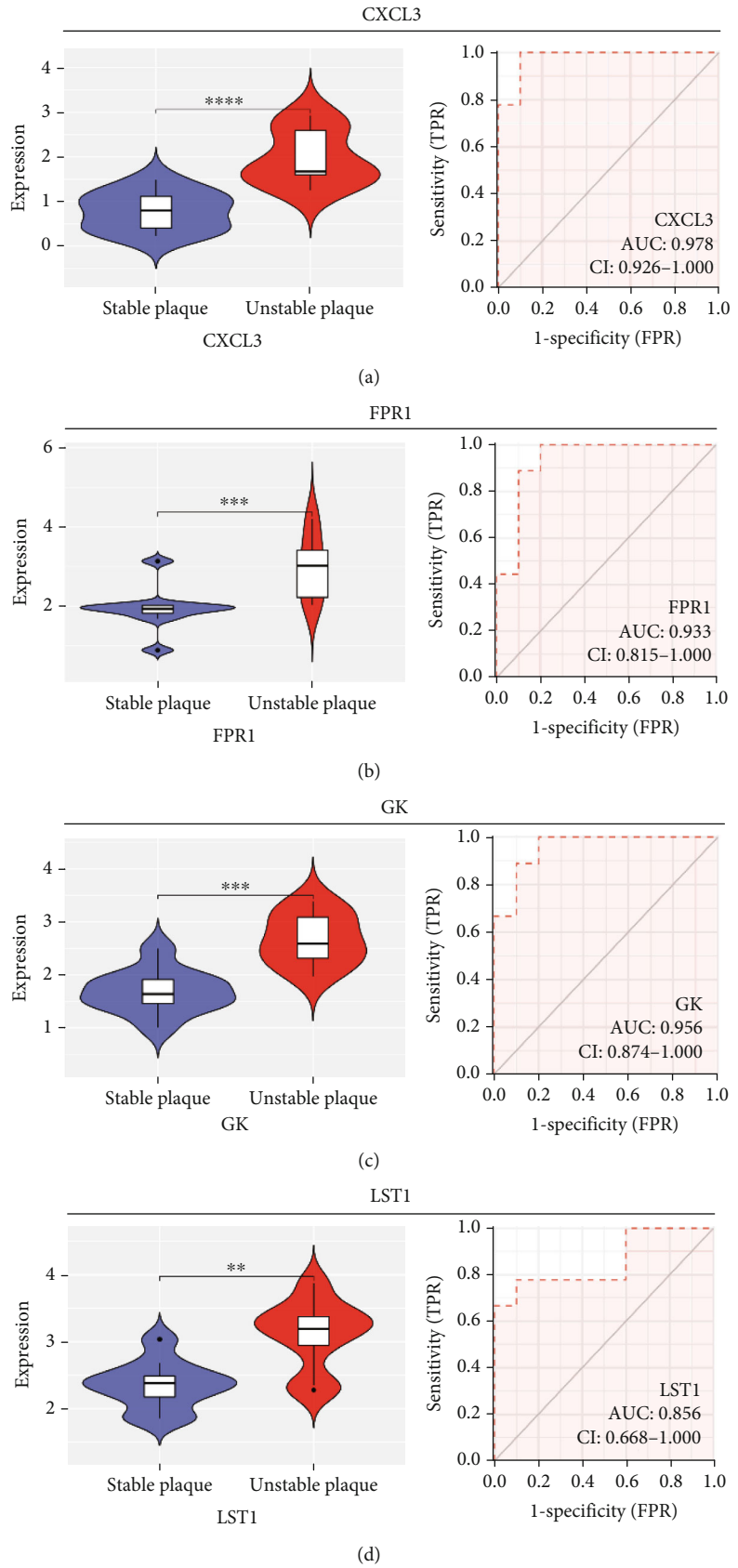

Figure 4: Expression level and diagnostic ability of the candidate genes in merged dataset. (a) CXCL3. (b) FPR1. (c) GK. (d) LST1 ($^{*}p < 0.05$, $^{**}p < 0.01$, $^{***}p < 0.001$, $^{****}p < 0.0001$).

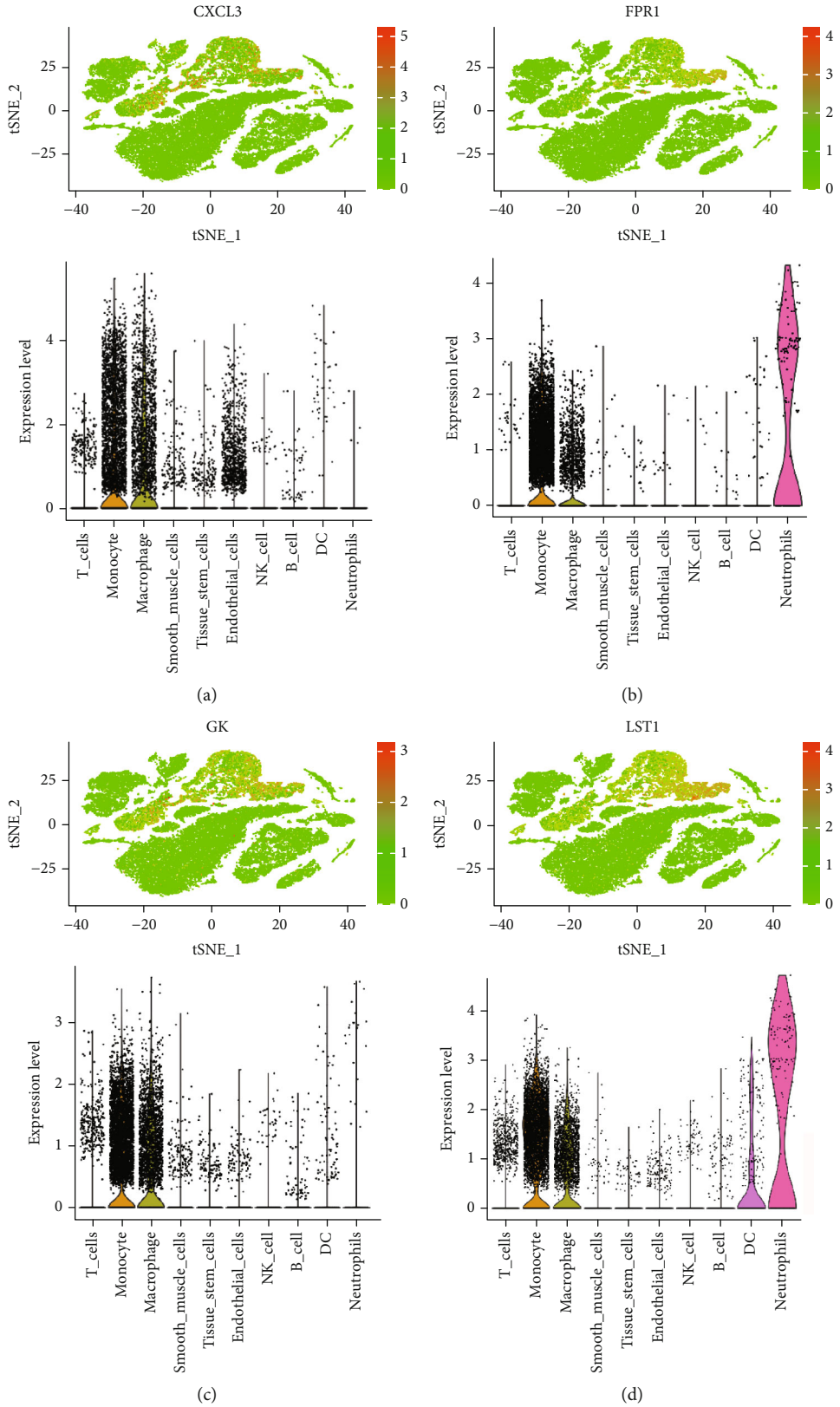

Figure 5: The expression level of the candidate genes at the single-cell level was shown in t-SNE and violin plots. The redder the color represented the higher expression level. (a) CXCL3. (b) FPR1. (c) GK. (d) LST1.

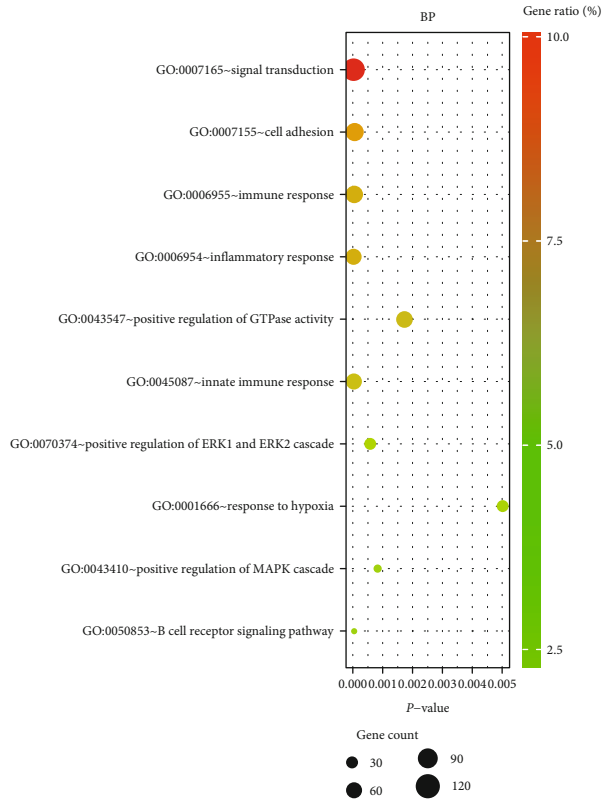

(a)

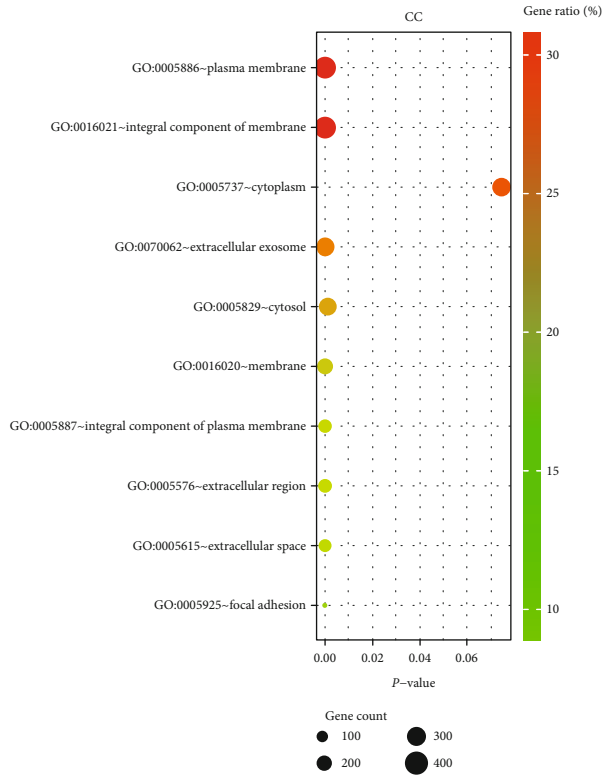

(b)

Figure 6: Continued.

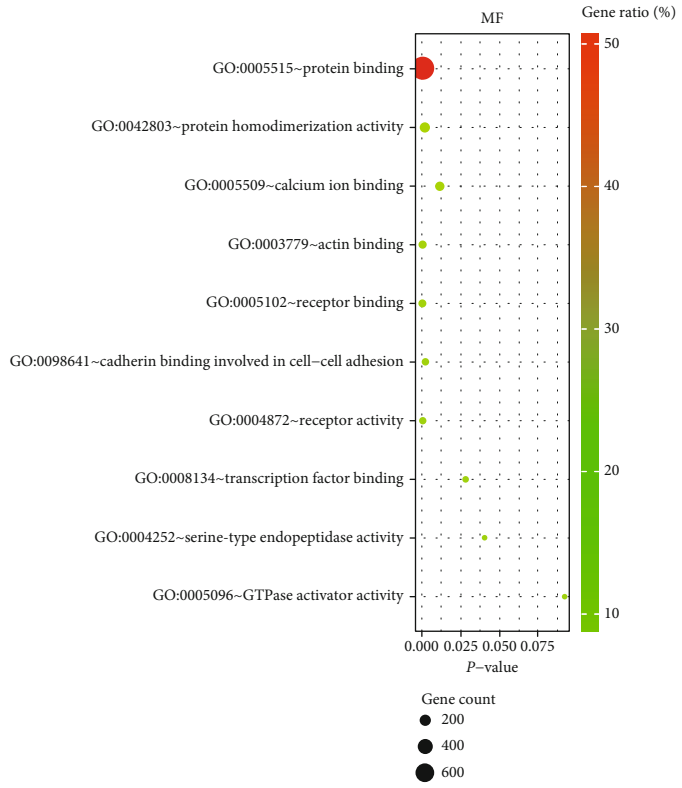

(c)

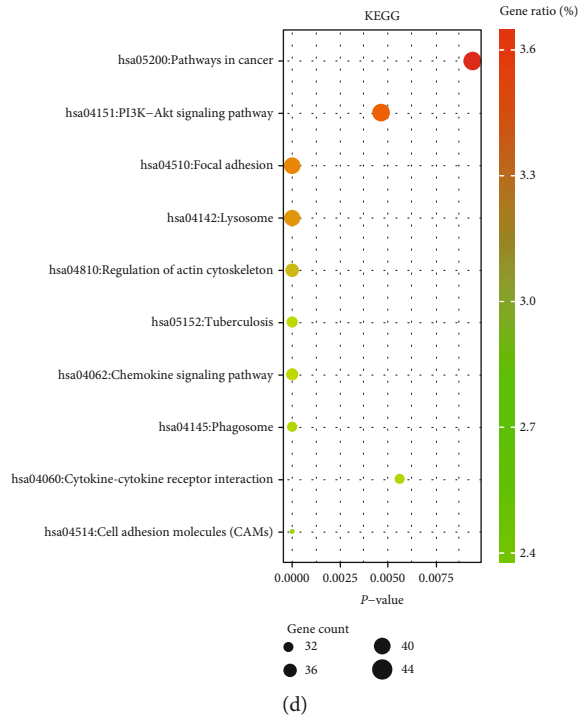

(d)

Figure 6: Functional enrichment analysis of 1221 differentially expressed genes (DEGs) by DAVID database: (a) biological process (BP); (b) cellular component (CC); (c) molecular function (MF); (d) KEGG pathway analysis.

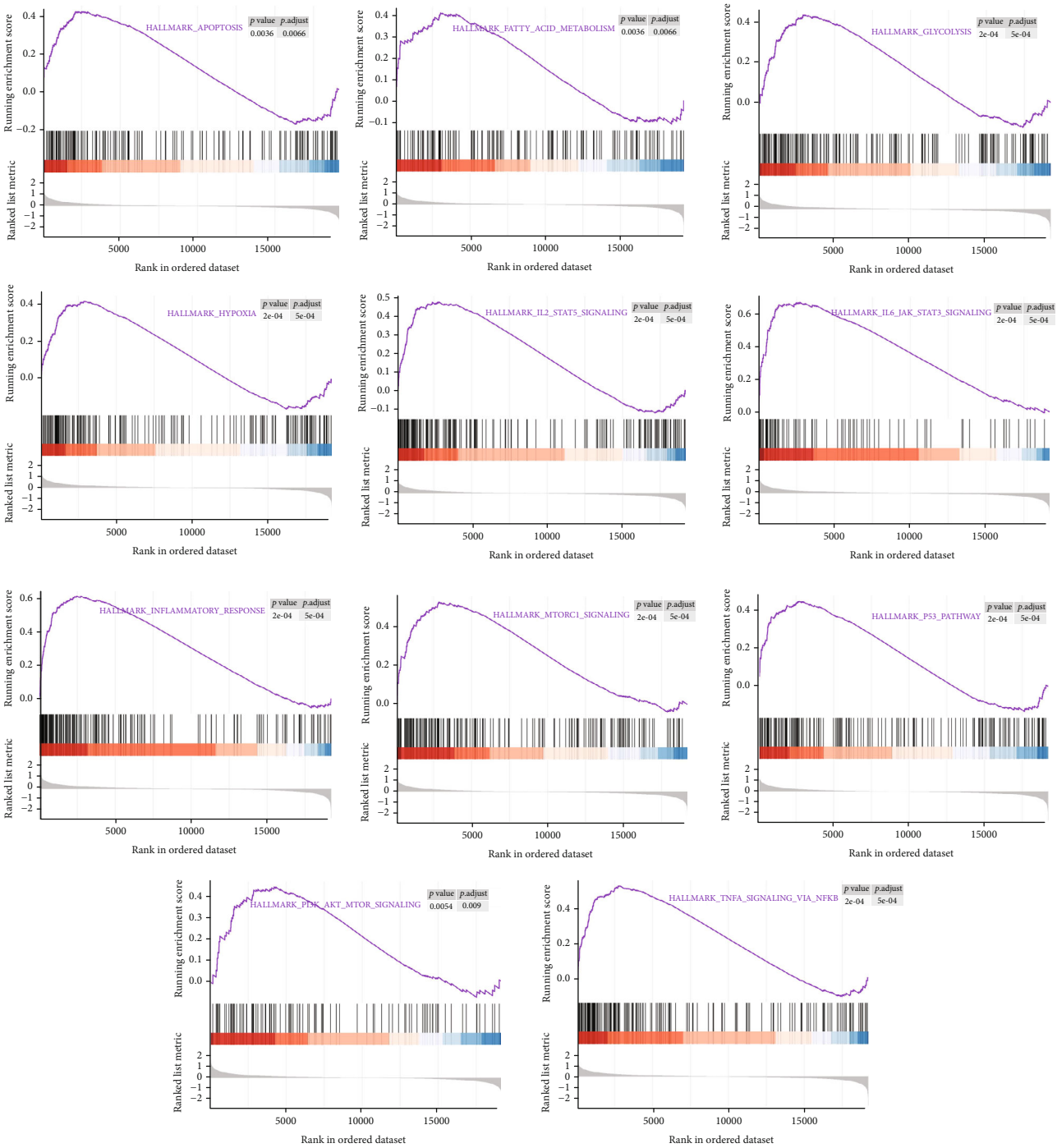

Figure 7: GSEA plot showed that multiple signaling pathways may be involved in the regulation of plaque instability, including "HALLMARK_INFLAMMATORY_RESPONSE" and "HALLMARK_PI3K_AKT_MTOR_SIGNALING."

therefore critical to explore biomarkers associated with plaque instability and to take targeted interventions and preventive measures to reduce fatal clinical complications. In this study, we sought to combine single-cell sequencing data with transcriptome data to elucidate the clinical significance and potential mechanisms of monocyte-associated genes in atherosclerotic plaque instability.

As we all know, monocyte recruitment in the vascular wall plays an important role in the development of atherosclerosis [28, 29]; however, there are relatively few studies about the role of monocyte-associated genes on atherosclerosis. Our current study identified four (CXCL3, FPR1, GK, and LST1) significant monocyte-associated candidate genes related to atherosclerotic plaque instability using single-cell sequencing data analysis, WGCNA analysis, and differential expression analysis methods. We found that these candidate genes were significantly overexpressed in unstable plaques compared with stable plaques. Single-cell

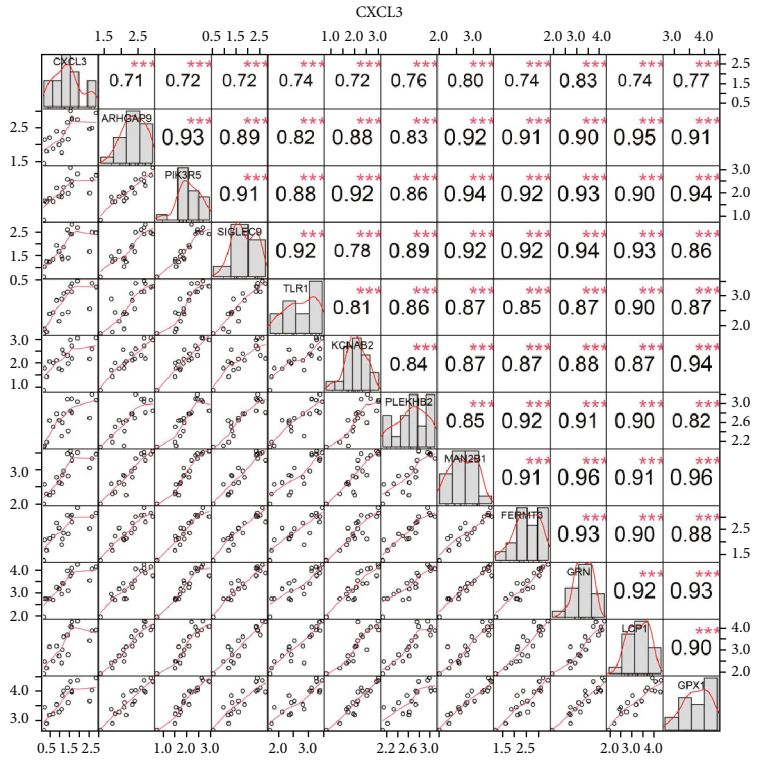

(a)

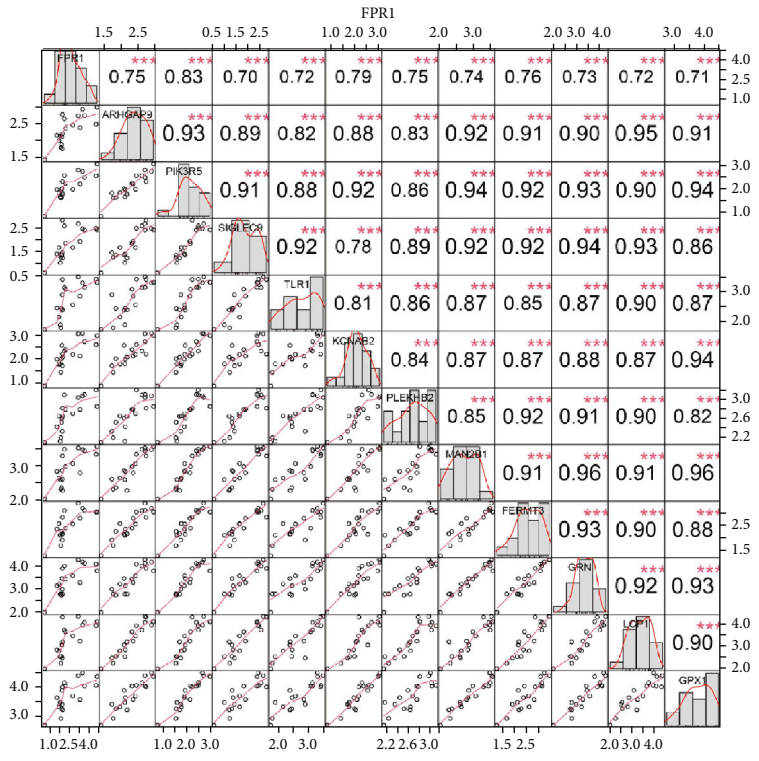

(b)

Figure 8: Continued.

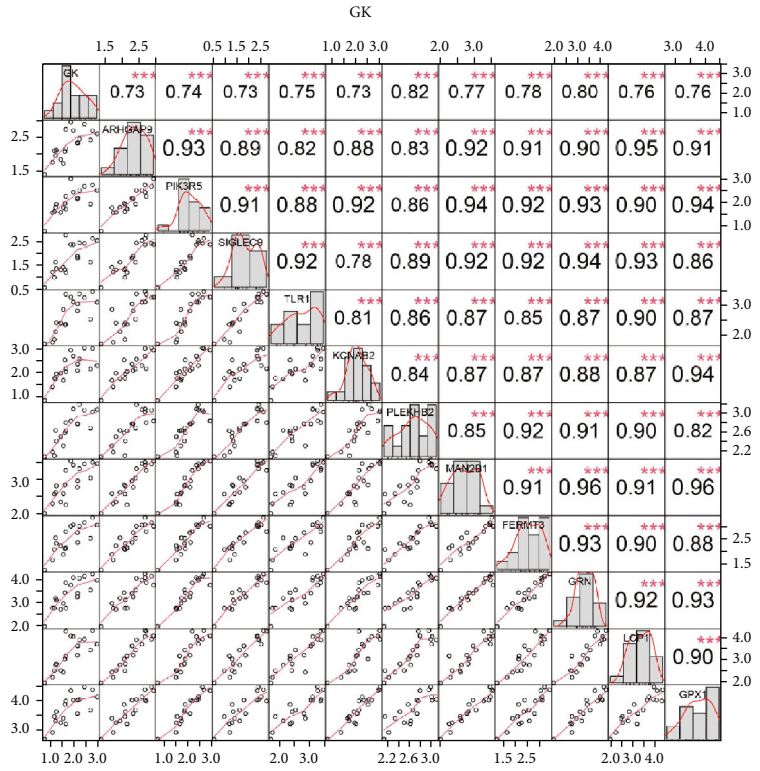

(c)

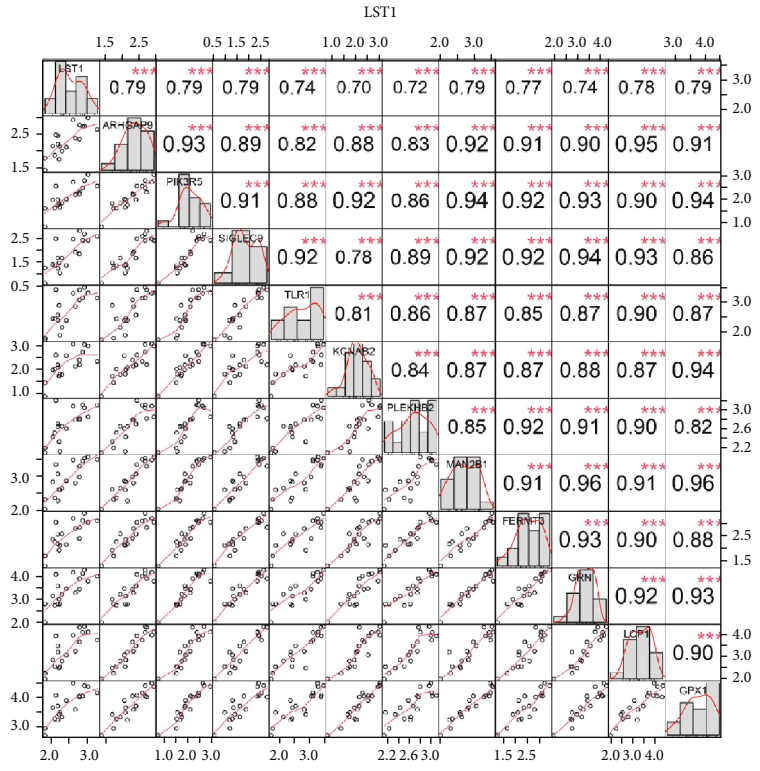

(d)

Figure 8: Correlations between the candidate genes and 11 overlapping coexpressed genes (CEGs): (a) CXCL3; (b) FPR1; (c) GK; (d) LST1.

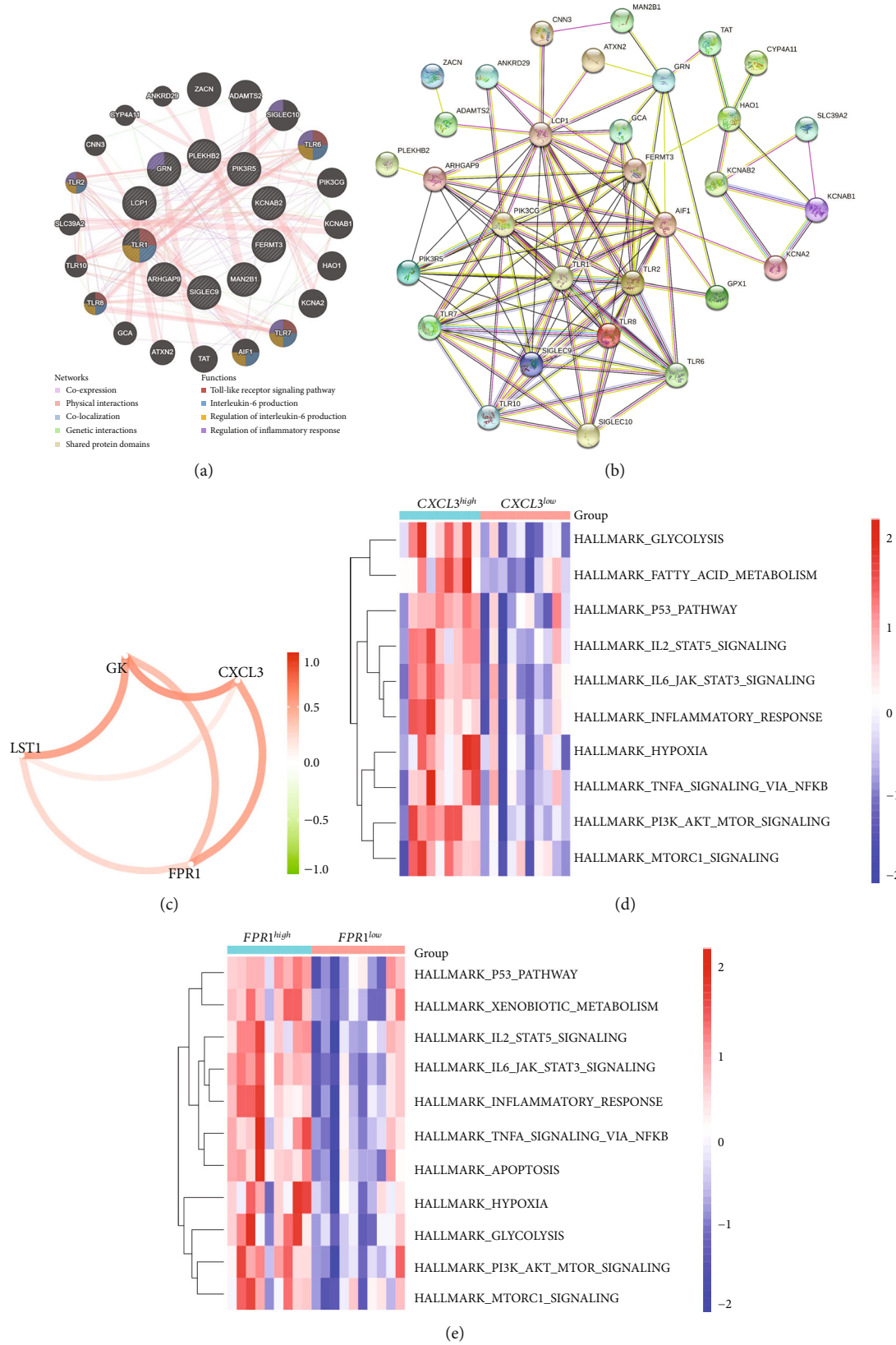

Figure 9: Continued.

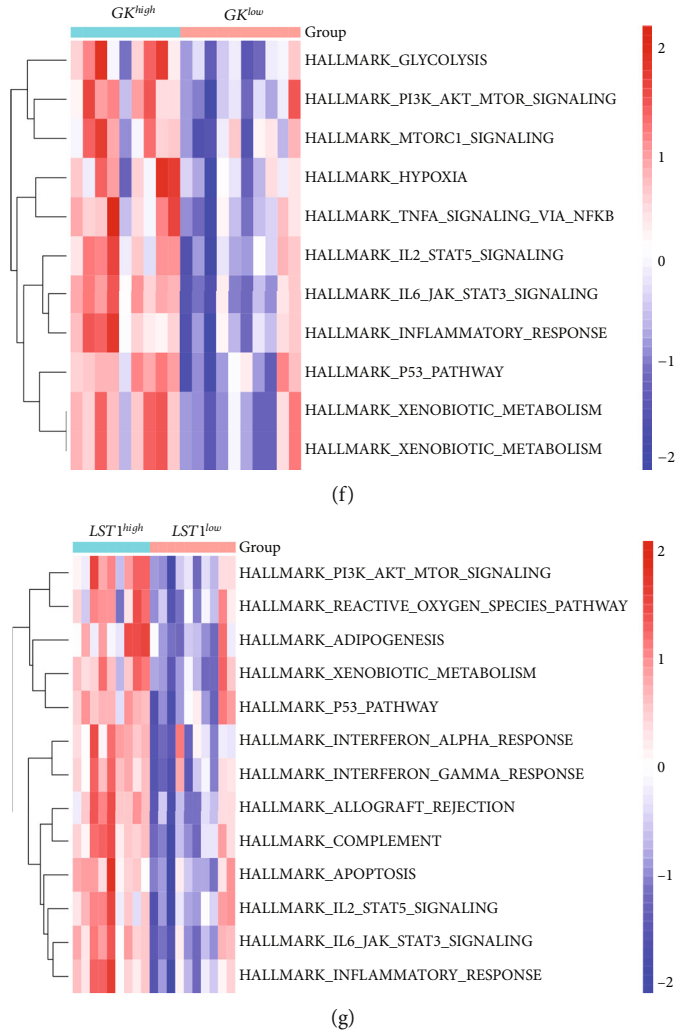

Figure 9: (a) Functional analysis of 11 coexpressed genes from the GeneMANIA database. (b) Protein interaction analysis network diagram of related genes on STRING database. (c) Correlation between the candidate genes. (d–g) Four heatmaps showed the results of gene set variation analysis (GSVA) of the candidate genes, arranged by CXCL3, FPR1, GK, and LST1.

sequencing data analysis indicated that the expression of these genes was upregulated in monocytes. There are some other studies that support our findings. Gargalovic et al. found that CXCL3 might contribute to the inflammatory effects of oxidized1-palmitoyl-2-arachidonyl-sn-3-glycerophosphorylcholine in the atherosclerotic lesion, which is crucial for the recruitment of monocytes [30]. Autoradiography and immunohistochemical analysis in one study has confirmed abundant FPR1 expression in atherosclerotic lesions [31]. Many studies have shown that GK is an essential enzyme in the formation of triacylglycerol [32, 33], which contributes to the development and progression of atherosclerosis [34, 35]. Furthermore, it was found that the candidate genes have the upper-middle ability to distinguish the stable and unstable plaques (AUC > 0.850 for all), which suggests that the four upregulated monocyte-associated candidate genes may be underlying biomarkers for early identification and intervention of unstable plaques.

Meanwhile, our study was also devoted to exploring the underlying mechanisms of the candidate genes in atherosclerotic plaque instability. Previous studies have reported that CXCL3, FPR1, and LST1 were closely associated with inflammation and oxidative stress, while GK played a central role in adipogenesis and gluconeogenesis [25–28]. CXCL3 is a well-known proinflammatory gene [36, 37]. FPR1 serves as a receptor that mediates oxidative stress signaling in the mammalian cell [38, 39, 40]. A study found that LST1 regulates inflammatory response in a model of inflammatory disease [41]. As for GK, it also shows a potential relationship with oxidative stress [42]. Previous studies have reported that these candidate genes were closely associated with inflammation and oxidative stress. It is consistent with our previous study that a high functional similarity was found among the candidate genes, which indicates that these candidate genes may act on several similar pathways. In our study, GO and KEGG analyses suggested that DEGs might be related to inflammation response and the PI3K-Akt signaling pathway. GSEA indicated that multiple pathways, including "HALLMARK_PI3K_AKT_MTOR_SIGNALING" and "HALLMARK_INFLAMMATORY_RESPONSE,"

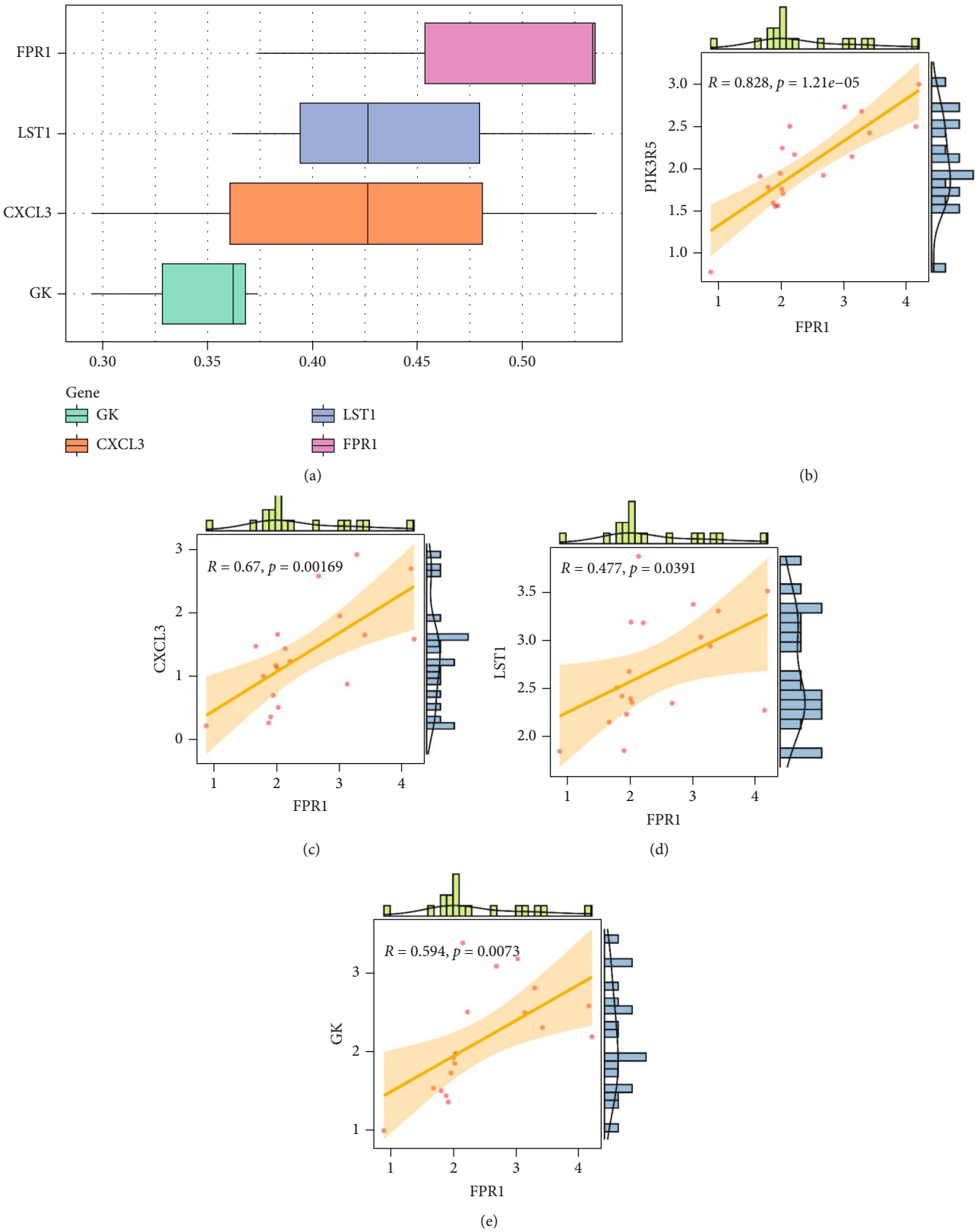

Figure 10: (a) Summary of protein functional similarity of overlapping genes. (b–e) Correlation analysis between FPR1 gene and PIK3R5 and other overlapping genes.

were excessively activated in unstable plaque. GSVA showed that these two pathways were also significantly activated in high expression samples of the candidate genes. Furthermore, coexpression analysis suggested that these candidate genes may be related to regulating inflammatory response. In conclusion, existing evidence showed that the candidate genes were likely to affect the atherosclerotic plaque instability through the inflammatory response and PI3K/Akt/mTOR signaling pathways, a well-known pathway relating to oxidative stress. Previous studies have shown that inflammation played an important role in the progression of atherosclerosis, which may be involved in driving plaque instability [43–46]. Another study showed that it could affect the initial recruitment of white blood cells to the final rupture of unstable atherosclerotic plaques [47]. In addition, numerous studies have reported its crucial role in the rupture of atherosclerotic plaque [48–51]. Similarly, our current study also indicated that the candidate genes were closely related to the excessive activation of inflammatory response in unstable plaques, which may be one of the potential mechanisms that aggravated the instability of atherosclerotic plaques. From the existing evidence, we speculate that the crosstalk between the candidate genes and PI3K/Akt/mTOR signaling pathway may activate inflammatory response leading to atherosclerotic plaque instability.

However, it was undeniable that our study conclusions may also have certain limitations due to the insufficient sample size, which required further in vivo and in vitro experimental verification.

5. Conclusions

Taken together, this study shows that the upregulated CXCL3, GK, FPR1, and LST1 may be effective biomarkers for early identification and intervention of unstable atherosclerotic plaques. Besides, we speculate that they may play a synergistic role with CEGs in regulating inflammation and PI3K/AKT/mTOR signaling pathways, thereby aggravating the instability of atherosclerotic plaques and promoting plaque rupture.

Data Availability

All the data used to support the findings of the study can be found in the article.

Conflicts of Interest

The authors declare that they have no competing interests.

Authors' Contributions

YF Dai and J Liu conceived and designed the study. WT Qin, RG Liang, and YF Dai were responsible for the data analysis. WT Qin and F Gan were responsible for writing the draft. J Li and XM Lai made contributions to data collecting and collating. YF Dai and Jie Liu revised and proofread the manuscript. All of the authors have reviewed and approved the final manuscript. Wentao Qin, Fu Gan, and Riguan Liang contributed equally to this work.

References

[1] F. Dehghan, R. Soori, K. Gholami et al., "Purslane (Portulaca oleracea) seed consumption and aerobic training improves biomarkers associated with atherosclerosis in women with type 2 diabetes (T2D)," *Scientific Reports*, vol. 6, no. 1, article 37819, 2016.

[2] S. Honda, K. Ikeda, R. Urata, E. Yamazaki, N. Emoto, and S. Matoba, "Cellular senescence promotes endothelial activation through epigenetic alteration, and consequently accelerates atherosclerosis," *Scientific Reports*, vol. 11, no. 1, p. 14608, 2021.

[3] K. Ahmad Nazri, N. Fauzi, F. Buang et al., "*Gynura procumbens* standardised extract reduces cholesterol levels and modulates oxidative status in postmenopausal rats fed with cholesterol diet enriched with repeatedly heated palm oil," *Evidence-based Complementary and Alternative Medicine*, vol. 2019, Article ID 7246756, 15 pages, 2019.

[4] H. Yan, S. Wang, Z. Li et al., "Rspo2 suppresses CD36-mediated apoptosis in oxidized low density lipoprotein-induced macrophages," *Molecular Medicine Reports*, vol. 14, no. 4, pp. 2945–2952, 2016.

[5] S. Fumagalli, C. Perego, R. Zangari et al., "Lectin pathway of complement activation is associated with vulnerability of atherosclerotic plaques," *Frontiers in Immunology*, vol. 8, p. 288, 2017.

[6] E. Biros, C. Moran, P. Norman et al., "Association between the advanced glycosylation end product-specific receptor gene and cardiovascular death in older men," *PLoS One*, vol. 10, no. 7, article e0134475, 2015.

[7] M. Bao, R. Zhang, X. Huang et al., "Transcriptomic and proteomic profiling of human stable and unstable carotid atherosclerotic plaques," *Frontiers in Genetics*, vol. 12, article 755507, 2021.

[8] T. Dahl, A. Yndestad, M. Skjelland et al., "Increased expression of visfatin in macrophages of human unstable carotid and coronary atherosclerosis: possible role in inflammation and plaque destabilization," *Circulation*, vol. 115, no. 8, pp. 972–980, 2007.

[9] M. Landecho, C. Tuero, V. Valentí, I. Bilbao, M. de la Higuera, and G. Frühbeck, "Relevance of leptin and other adipokines in obesity-associated cardiovascular risk," *Nutrients*, vol. 11, no. 11, p. 2664, 2019.

[10] Y. Liu, W. Huan, J. Wu, S. Zou, and L. Qu, "IGFBP6 is downregulated in unstable carotid atherosclerotic plaques according to an integrated bioinformatics analysis and experimental verification," *Journal of Atherosclerosis and Thrombosis*, vol. 27, no. 10, pp. 1068–1085, 2020.

[11] B. Xu, R. Liu, C. Huang et al., "Identification of key genes in ruptured atherosclerotic plaques by weighted gene correlation network analysis," *Scientific Reports*, vol. 10, no. 1, p. 10847, 2020.

[12] S. Melzer, R. Ankri, D. Fixler, and A. Tarnok, "Nanoparticle uptake by macrophages in vulnerable plaques for atherosclerosis diagnosis," *Journal of Biophotonics*, vol. 8, no. 11-12, pp. 871–883, 2015.

[13] E. Karlöf, T. Seime, N. Dias et al., "Correlation of computed tomography with carotid plaque transcriptomes associates

calcification with lesion-stabilization," *Atherosclerosis*, vol. 288, pp. 175–185, 2019.

[14] A. V. Finn, M. Nakano, J. Narula, F. D. Kolodgie, and R. Virmani, "Concept of vulnerable/unstable plaque," *Arteriosclerosis, Thrombosis, and Vascular Biology*, vol. 30, no. 7, pp. 1282–1292, 2010.

[15] H. Wang, D. Liu, and H. Zhang, "Investigation of the underlying genes and mechanism of macrophage-enriched ruptured atherosclerotic plaques using bioinformatics method," *Journal of Atherosclerosis and Thrombosis*, vol. 26, no. 7, pp. 636–658, 2019.

[16] K. Zhang, X. Qin, X. Zhou et al., "Analysis of genes and underlying mechanisms involved in foam cells formation and atherosclerosis development," *PeerJ*, vol. 8, article e10336, 2020.

[17] Y. Ding, R. Yin, S. Zhang et al., "The combined regulation of long non-coding RNA and RNA-binding proteins in atherosclerosis," *Frontiers in Cardiovascular Medicine*, vol. 8, article 731958, 2021.

[18] L. Tomas, F. Prica, and C. Schulz, "Trafficking of mononuclear phagocytes in healthy arteries and atherosclerosis," *Frontiers in Immunology*, vol. 12, article 718432, 2021.

[19] H. Xu, Y. Ni, and Y. Liu, "Mechanisms of action of MiRNAs and LncRNAs in extracellular vesicle in atherosclerosis," *Frontiers in Cardiovascular Medicine*, vol. 8, article 733985, 2021.

[20] L. Jin, Z. Deng, Y. Bai, and P. Ye, "Functions of monocytes and macrophages and the associated effective molecules and mechanisms at the early stage of atherosclerosis," *Acta Cardiologica Sinica*, vol. 37, no. 5, pp. 522–533, 2021.

[21] K. Krychtiuk, M. Lenz, P. Hohensinner et al., "Circulating levels of proprotein convertase subtilisin/kexin type 9 (PCSK9) are associated with monocyte subsets in patients with stable coronary artery disease," *Journal of Clinical Lipidology*, vol. 15, no. 3, pp. 512–521, 2021.

[22] G. Zhang, X. Liu, Z. Sun et al., "A2M is a potential core gene in intrahepatic cholangiocarcinoma," *BMC Cancer*, vol. 22, no. 1, p. 5, 2022.

[23] D. Warde-Farley, S. Donaldson, O. Comes et al., "The GeneMANIA prediction server: biological network integration for gene prioritization and predicting gene function," *Nucleic Acids Research*, vol. 38, supplement 2, pp. W214–W220, 2010.

[24] X. Zeng, H. Zhu, W. Liu, J. Zhong, and J. Luo, "Electrocardiogram-based R wave pulse wave index for assessment of carotid atherosclerosis," *Medical Science Monitor*, vol. 26, article e919606, 2020.

[25] S. Hehir, N. Plourde, L. Gu et al., "Carbohydrate composition of amphiphilic macromolecules influences physicochemical properties and binding to atherogenic scavenger receptor A," *Acta Biomaterialia*, vol. 8, no. 11, pp. 3956–3962, 2012.

[26] P. Siegel, L. Sander, A. Fricke et al., "P_2Y_{12} receptor blockers are anti-inflammatory drugs inhibiting both circulating monocytes and macrophages including THP-1 cells," *Scientific Reports*, vol. 11, no. 1, p. 17459, 2021.

[27] X. Zhang, J. Li, J. Qin et al., "Oncostatin M receptor β deficiency attenuates atherogenesis by inhibiting JAK2/STAT3 signaling in macrophages," *Journal of Lipid Research*, vol. 58, no. 5, pp. 895–906, 2017.

[28] G. Eelen, P. de Zeeuw, L. Treps, U. Harjes, B. W. Wong, and P. Carmeliet, "Endothelial cell metabolism," *Physiological Reviews*, vol. 98, no. 1, pp. 3–58, 2018.

[29] P. Libby, "Inflammation in atherosclerosis," *Nature*, vol. 420, no. 6917, pp. 868–874, 2002.

[30] P. S. Gargalovic, N. M. Gharavi, M. J. Clark et al., "The unfolded protein response is an important regulator of inflammatory genes in endothelial cells," *Arteriosclerosis, Thrombosis, and Vascular Biology*, vol. 26, no. 11, pp. 2490–2496, 2006.

[31] Y. Zhang, B. Kundu, M. Zhong et al., "PET imaging detection of macrophages with a formyl peptide receptor antagonist," *Nuclear Medicine and Biology*, vol. 42, no. 4, pp. 381–386, 2015.

[32] L. Rahib, N. K. MacLennan, S. Horvath, J. C. Liao, and K. M. Dipple, "Glycerol kinase deficiency alters expression of genes involved in lipid metabolism, carbohydrate metabolism, and insulin signaling," *European Journal of Human Genetics*, vol. 15, no. 6, pp. 646–657, 2007.

[33] F. Y. Xu, W. A. Taylor, J. A. Hurd, and G. M. Hatch, "Etomoxir mediates differential metabolic channeling of fatty acid and glycerol precursors into cardiolipin in H9c2 cells," *Journal of Lipid Research*, vol. 44, no. 2, pp. 415–423, 2003.

[34] S. Raposeiras-Roubin, X. Rosselló, B. Oliva et al., "Triglycerides and residual atherosclerotic risk," *Journal of the American College of Cardiology.*, vol. 77, no. 24, pp. 3031–3041, 2021.

[35] J. Peng, F. Luo, G. Ruan, R. Peng, and X. Li, "Hypertriglyceridemia and atherosclerosis," *Lipids in Health and Disease*, vol. 16, no. 1, p. 233, 2017.

[36] C. F. Hu, S. P. Wu, G. J. Lin et al., "Microglial Nox2 plays a key role in the pathogenesis of experimental autoimmune encephalomyelitis," *Frontiers in Immunology*, vol. 12, 2021.

[37] F. Dastmalchi, A. Karachi, C. Yang et al., "Sarcosine promotes trafficking of dendritic cells and improves efficacy of antitumor dendritic cell vaccines via CXC chemokine family signaling," *Journal for Immunotherapy of Cancer*, vol. 7, no. 1, p. 321, 2019.

[38] C. Y. Chen, Y. F. Tsai, W. J. Huang, S. H. Chang, and T. L. Hwang, "Propofol inhibits endogenous formyl peptide-induced neutrophil activation and alleviates lung injury," *Free Radical Biology and Medicine*, vol. 129, pp. 372–382, 2018.

[39] R. Fusco, E. Gugliandolo, R. Siracusa et al., "Formyl peptide receptor 1 signaling in acute inflammation and neural differentiation induced by traumatic brain injury," *Biology*, vol. 9, no. 9, p. 238, 2020.

[40] Y. Xiao, W. Zhu, M. He, H. Nie, W. Chen, and Q. Huang, "High c-di-GMP promotes expression of fpr-1 and katE involved in oxidative stress resistance in Pseudomonas putida KT2440," *Applied Microbiology and Biotechnology*, vol. 103, no. 21-22, pp. 9077–9089, 2019.

[41] M. Fabisik, J. Tureckova, N. Pavliuchenko et al., "Regulation of inflammatory response by transmembrane adaptor protein LST1," *Frontiers in Immunology*, vol. 12, article 618332, 2021.

[42] R. Sivaramakrishnan and A. Incharoensakdi, "Enhancement of lipid production in *Synechocystis* sp. PCC 6803 overexpressing glycerol kinase under oxidative stress with glycerol supplementation," *Bioresource Technology*, vol. 267, pp. 532–540, 2018.

[43] L. Galiuto, L. Leccisotti, G. Locorotondo et al., "Coronary plaque instability assessed by positron emission tomography and optical coherence tomography," *Annals of Nuclear Medicine*, vol. 35, no. 10, pp. 1136–1146, 2021.

[44] J. Budzianowski, K. Pieszko, P. Burchardt, J. Rzeźniczak, and J. Hiczkiewicz, "The role of hematological indices in patients with acute coronary syndrome," *Disease Markers*, vol. 2017, Article ID 3041565, 9 pages, 2017.

[45] B. Ren, Z. Song, L. Chen, X. Niu, and Q. Feng, "Long non-coding RNA UCA1 correlates with elevated disease severity, Th17 cell proportion, inflammatory cytokines, and worse prognosis in acute ischemic stroke patients," *Journal of Clinical Laboratory Analysis*, vol. 35, no. 3, article e23697, 2021.

[46] S. Margetic, "Inflammation and haemostasis," *Biochemia Medica*, vol. 22, no. 1, pp. 49–62, 2012.

[47] J. Fragoso-Lona, J. Ramírez-Bello, D. Cruz-Robles, O. Pérez-Méndez, A. de la Peña, and G. Vargas-Alarcón, "Pro-inflammatory and anti-inflammatory markers in coronary artery disease and acute ischemic coronary syndrome," *Archivos de cardiologia de Mexico*, vol. 79, no. 1, pp. 54–62, 2009.

[48] E. Meester, E. de Blois, B. Krenning et al., "Autoradiographical assessment of inflammation-targeting radioligands for atherosclerosis imaging: potential for plaque phenotype identification," *EJNMMI Research*, vol. 11, no. 1, p. 27, 2021.

[49] E. Profumo, B. Buttari, and R. Riganò, "Oxidative stress in cardiovascular inflammation: its involvement in autoimmune responses," *International Journal of Inflammation*, vol. 2011, Article ID 295705, 6 pages, 2011.

[50] A. Lin, M. Kolossváry, J. Yuvaraj et al., "Myocardial infarction associates with a distinct pericoronary adipose tissue radiomic phenotype: a prospective case-control study," *JACC Cardiovascular Imaging*, vol. 13, no. 11, pp. 2371–2383, 2020.

[51] M. Saneipour, K. Ghatreh-Samani, E. Heydarian, E. Farrokhi, and N. Abdian, "Adiponectin inhibits oxidized low density lipoprotein-induced increase in matrix metalloproteinase 9 expression in vascular smooth muscle cells," *Arya Atherosclerosis*, vol. 11, no. 3, pp. 191–195, 2015.

Hindawi
Oxidative Medicine and Cellular Longevity
Volume 2022, Article ID 1129062, 20 pages
https://doi.org/10.1155/2022/1129062

Research Article

Combined Evaluation of mRNA and Protein Expression, Promoter Methylation, and Immune Infiltration of UBE2I in Pan-Digestive System Tumors

Shuai Huang, Xiangkun Wang, Kai Luo, Xudong Zhang, Zhongyuan Liu, and Renfeng Li

Department of Hepatobiliary and Pancreatic Surgery, The First Affiliated Hospital of Zhengzhou University, Zhengzhou, 450052 Henan, China

Correspondence should be addressed to Renfeng Li; z17263883982@163.com

Received 9 July 2022; Revised 1 August 2022; Accepted 9 August 2022; Published 20 September 2022

Academic Editor: Shao Liang

Background. Digestive system tumors (DSTs) have high morbidity and mortality worldwide. This study explored the potential value of ubiquitin-conjugating enzyme E2 I (*UBE2I*) in pan-digestive system tumors (pan-DSTs). *Methods*. Differential expression, tumor stages, and survival outcomes of *UBE2I* in pan-DSTs were determined using the GEPIA database. The TIMER database was used to confirm the correlation of *UBE2I* expression with pan-DSTs and immune infiltrates. Differential analyses of *UBE2I* promoter methylation and protein levels were performed using the UALCAN database. The underlying mechanisms of *UBE2I* involvement in pan-DSTs were visualized using interaction networks. The diagnostic value of *UBE2I* in pan-DSTs was identified using the Oncomine database. *Results*. *UBE2I* was differentially and highly expressed in cholangiocarcinoma (CHOL), pancreatic adenocarcinoma (PAAD), colon adenocarcinoma (COAD), rectal adenocarcinoma (READ), liver hepatocellular carcinoma (LIHC), and stomach adenocarcinoma (STAD). According to survival analysis, upregulated *UBE2I* was associated with adverse overall and disease-free survival in PAAD and favorable overall survival in READ. *UBE2I* expression was partially linked to the purity of immune infiltration in COAD, LIHC, PAAD, READ, and STAD, as indicated by the immune infiltration analysis. Promoter methylation analysis showed differential and high methylation of *UBE2I* in PAAD as well as stratified analysis by gender, nodal metastasis, and race. Protein expression analysis in colon cancer revealed that *UBE2I* had differential and high expression in tumors as well as stratified analysis by gender, tumor histology, race, and tumor stage. Mechanism explorations demonstrated that in COAD and PAAD, *UBE2I* was involved in spliceosomal snRNP complex, Notch signaling pathway, etc. Diagnostic analysis indicated that *UBE2I* had consistent diagnostic value for COAD and PAAD. *Conclusions*. Upregulated *UBE2I* may be a diagnostic and surveillance predictive signature for PAAD and COAD. The potential significance of immune infiltrates and promoter methylation in PAAD and COAD needs further exploration.

1. Introduction

The term digestive system tumor (DST) describes a group of tumors that affect diverse digestive system tissues, involving esophagus, stomach, liver, pancreas, colon, and rectum [1]. The majority of these neoplasms are carcinomas (>90%) [2]. DST remains a leading cause of tumor-related mortality, causing approximately three million deaths worldwide each year [3, 4]. In recent years, the number of DST cases has significantly increased, highlighting the urgent requirement for more effective treatment strategies [5]. Despite significant advances in molecular medicine in disease prevention, diagnosis, and treatment, the prognosis of DSTs remains poor due to their increasing prevalence, diagnosis at advanced stages, tumor recurrence, and drug resistance [6]. Identification of novel molecular targets for DSTs may therefore provide insights into the development of effective therapeutic drugs.

SUMOylation is a reversible protein posttranslational modification process in which small ubiquitin-like modifier (SUMO) proteins are covalently bound to target proteins'

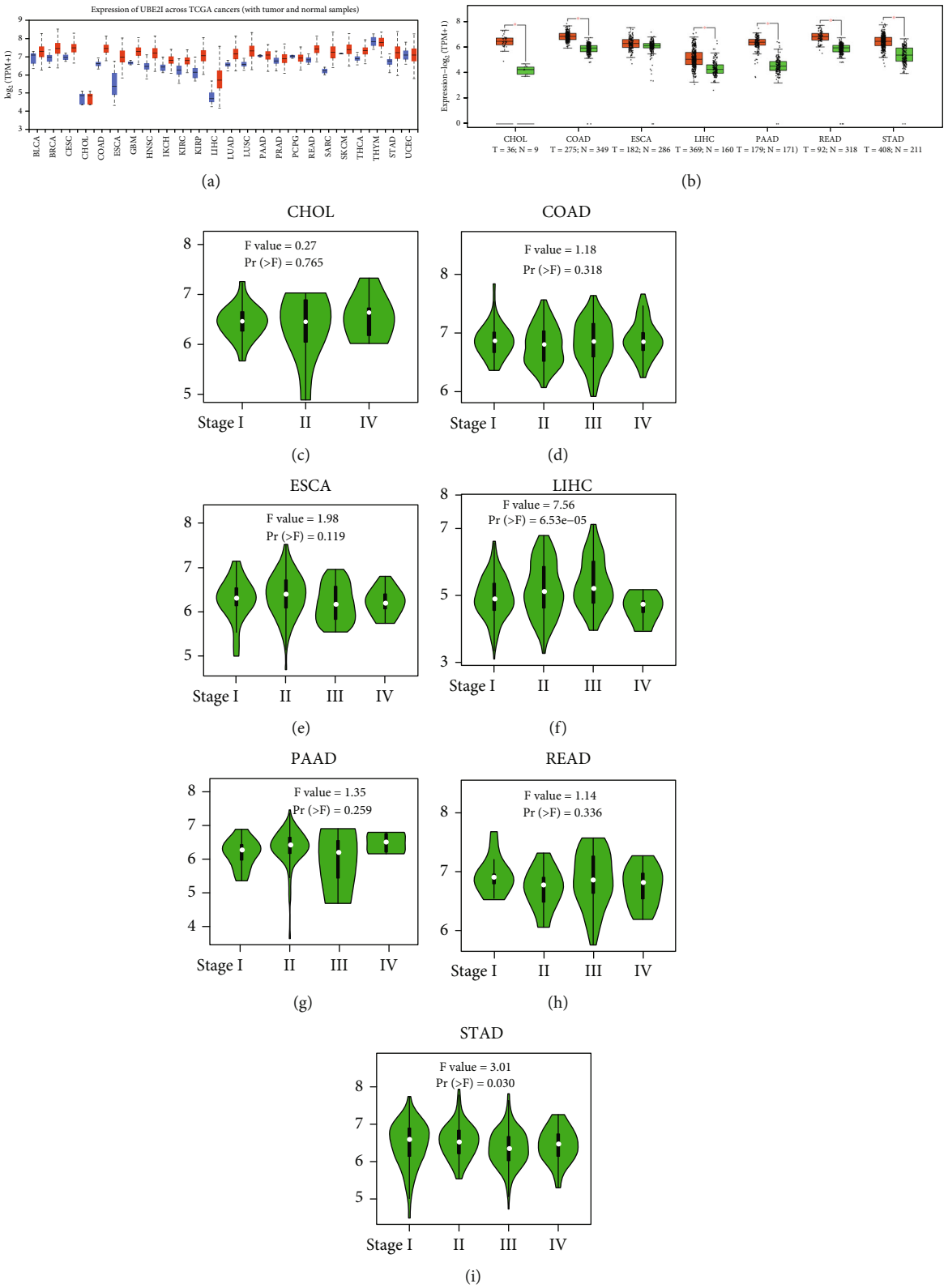

Figure 1: Differentialexpression and disease progression plots of *UBE2I* in pan-DSTs. (a) Differential expression patterns of *UBE2I* in pan-DSTs from TCGA. (b) Differential expression patterns of *UBE2I* in pan-DSTs. (c–i) Disease progression plots between *UBE2I* expression and tumor stage in CHOL, COAD, ESCA, LIHC, PAAD, READ, and STAD.

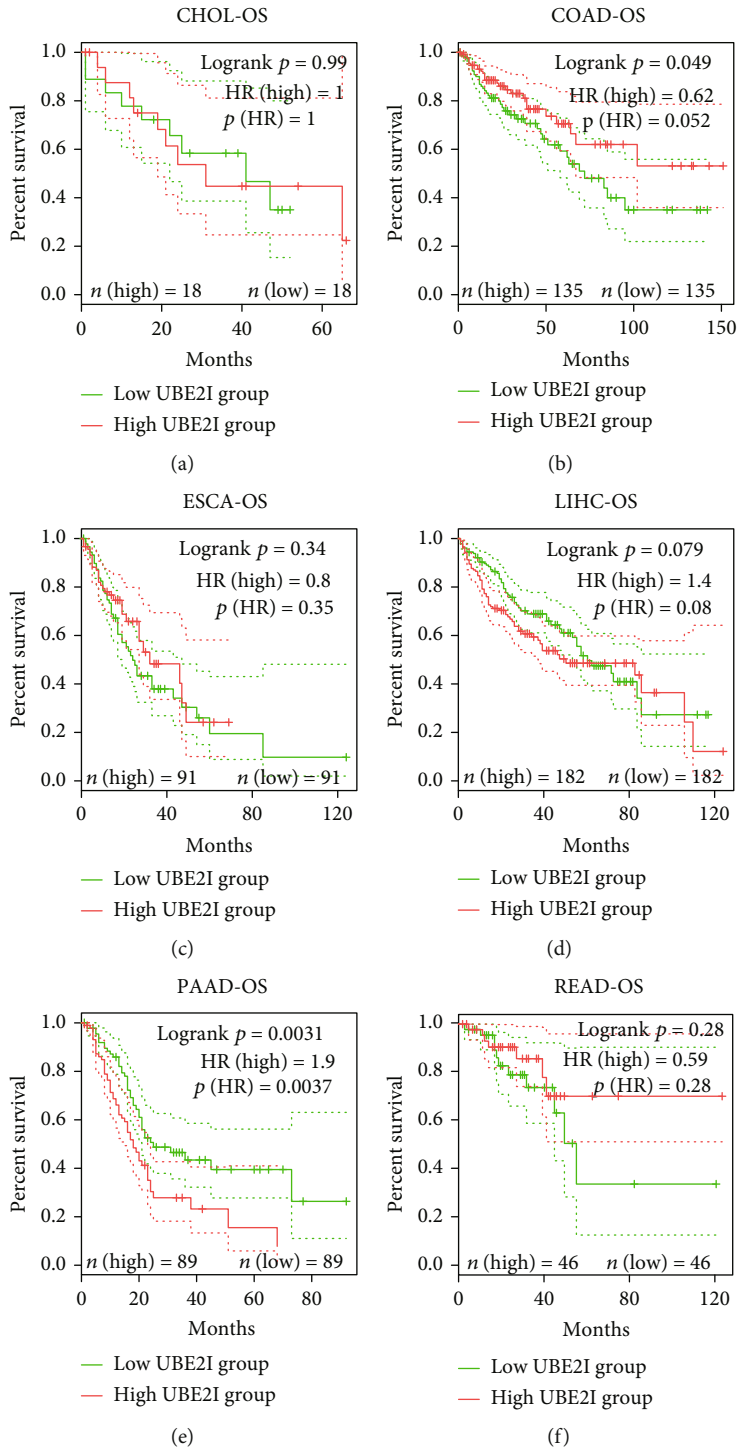

Figure 2: Continued.

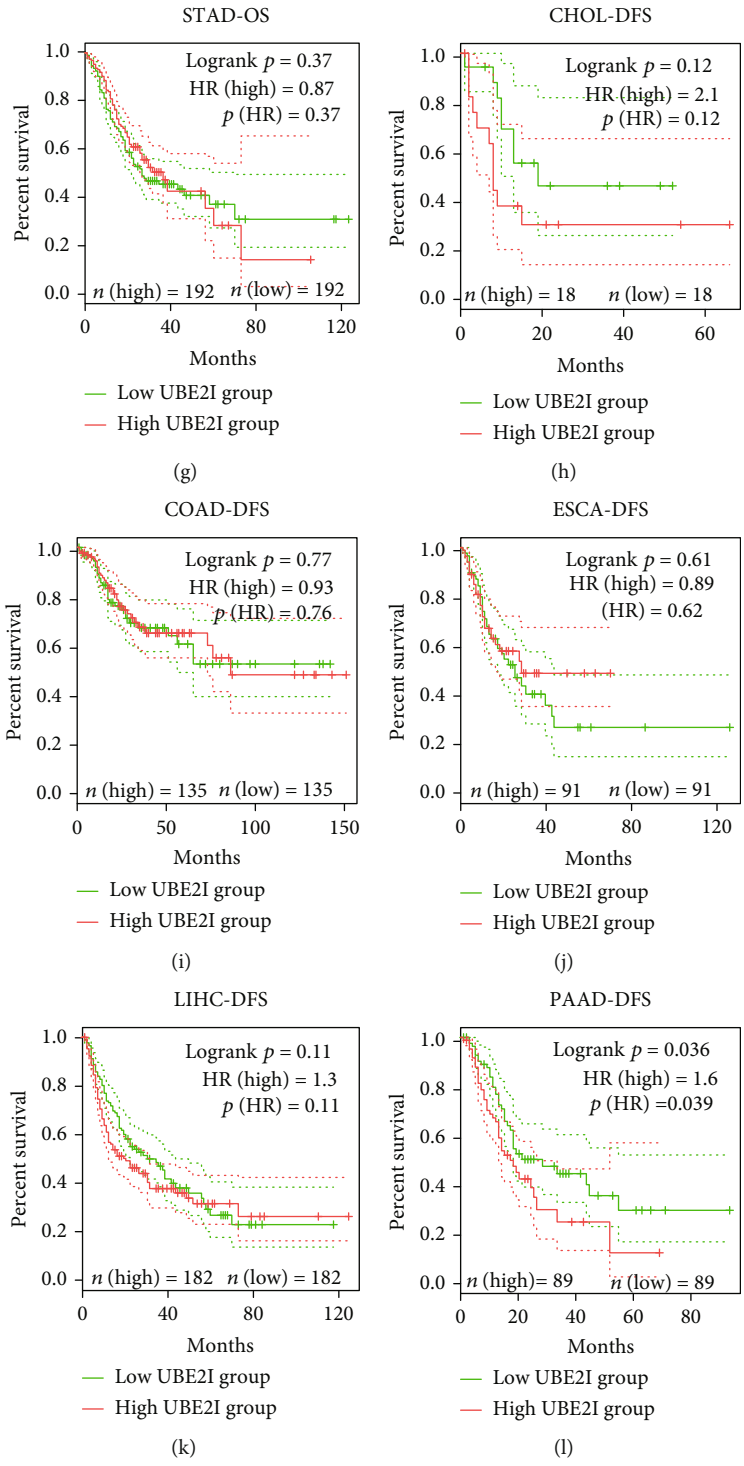

Figure 2: Continued.

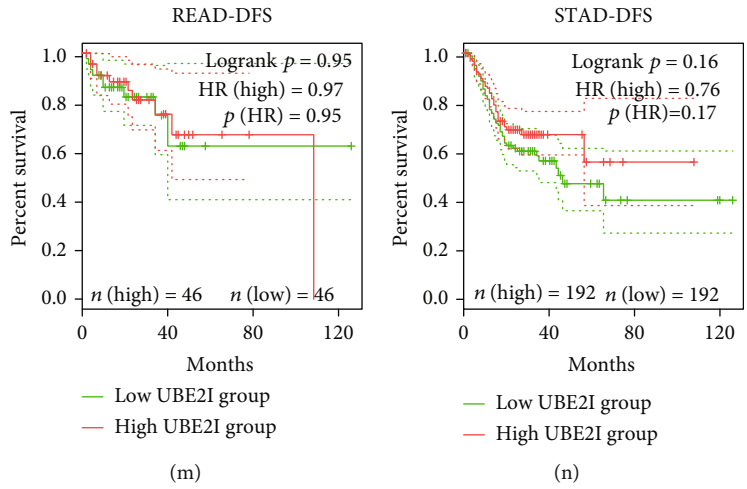

Figure 2: Overall and disease-free survival plots in relation to *UBE2I* expression in pan-DSTs. (a–g) Overall survival plots based on *UBE2I* expression in CHOL, COAD, ESCA, LIHC, PAAD, READ, and STAD. (h–n) Disease-free survival plots based on *UBE2I* expression in CHOL, COAD, ESCA, LIHC, PAAD, READ, and STAD.

lysine residues [7]. The SUMO system modulates a wide range of cellular processes, including cell division, chromatin segregation, transcription, signal transduction, protein stability, and translocation [7]. Ubiquitin conjugating enzyme E2 I (*UBE2I*) is a crucial component of this system, augmenting the ubiquitination and proteasomal flux of target proteins [7]. SUMOylation is an important posttranslational modification that fine-tunes almost all cellular functions and pathological processes, playing an important role in human tumorigenesis [8]. The SUMO pathway can induce cell proliferation, antiapoptosis, and metastatic potential by regulating proteins involved in carcinogenesis [9–13].

siRNA-mediated suppression of *UBE2I* is reported to inhibit LC3-II, an autophagy marker protein, and conversely promote the expression of SQSTM1/p62, which translocates ubiquitinated proteins to the proteasome and the autophagosome precursor—phagophore [7]. Furthermore, increased SUMOylation exerts a cardioprotective effect and decreases morbidity in proteotoxic cardiac disease [7]. *UBE2I* was significantly downregulated in patients with chromosome 9 open reading frame 72 and neurological progranulin mutations as well as sporadic frontotemporal dementia and age-matched controls [14]. Knockdown of *UBE2I*, also known as *UBC9*, impairs Notch 1-activated breast epithelial cell proliferation, indicating the potential value of *UBE2I* in targeted treatment of Notch-driven breast cancer [15]. In addition, differentially expressed *UBE2I* was observed in all four (clear cell, endometrioid, mucinous, and serous) subtypes of epithelial ovarian cancer [16]. Another study by Poleshko et al. [17] demonstrated that enzymes of the SUMO pathway are critical for the maintenance of epigenetic silencing. Furthermore, *UBE2I* upregulation was reported to be linked to disease development in a mouse model of necrotizing enterocolitis [18]. However, limited knowledge is available regarding the expression patterns and functions of *UBE2I* in digestive disorders, in particular, DSTs. Accordingly, the motivation and novelty of the study is to investigate the potential roles played by *UBE2I* and its underlying mechanism in pan-DSTs.

2. Materials and Methods

2.1. UBE2I Expression Patterns in Different Types of Cancers and Normal Tissue Specimens. *UBE2I* mRNA levels in pan-cancerous and normal tissue specimens from the UALCAN database (http://ualcan.path.uab.edu/) [19], a comprehensive, user-friendly, and interactive web resource for cancer omics data analyses, were examined. Then, the Gene Expression Profiling Interactive Analysis (GEPIA; URL: http://gepia2.cancer-pku.cn/#index) [20], a newly developed server for RNA sequencing expression data analyses of 9736 carcinoma tissues and 8587 normal counterparts from the TCGA and GTEx projects, was utilized to determine differential expression patterns of *UBE2I* in pan-DSTs using standard processing pipelines. Correlations of *UBE2I* expression patterns with tumor stages in pan-DSTs from the GEPIA database were further explored.

2.2. Survival and Immune Infiltrate Analyses in Pan-DSTs. Survival analyses, including overall survival (OS) and disease-free survival (DFS), of pan-DSTs from the GEPIA database were conducted. *UBE2I* expression in pan-DST samples was subdivided into either low or high group based on the median value. Next, we analyzed immune infiltrates in pan-DSTs in terms of gene expression, survival outcomes, and somatic copy number alterations (SCNAs) using the Tumor Immune Estimation Resource (TIMER; URL: https://cistrome.shinyapps.io/timer/) database [21, 22]. Specifically, the gene module mainly focused on the correlation of *UBE2I* expression with the abundance of immune infiltrates (B, $CD4^+$ T, and $CD8^+$ T cells, as well as neutrophils (NP), macrophages (MP) and dendritic cells (DC)), the survival module primarily discussed the correlation of survival outcomes with *UBE2I* expression and immune

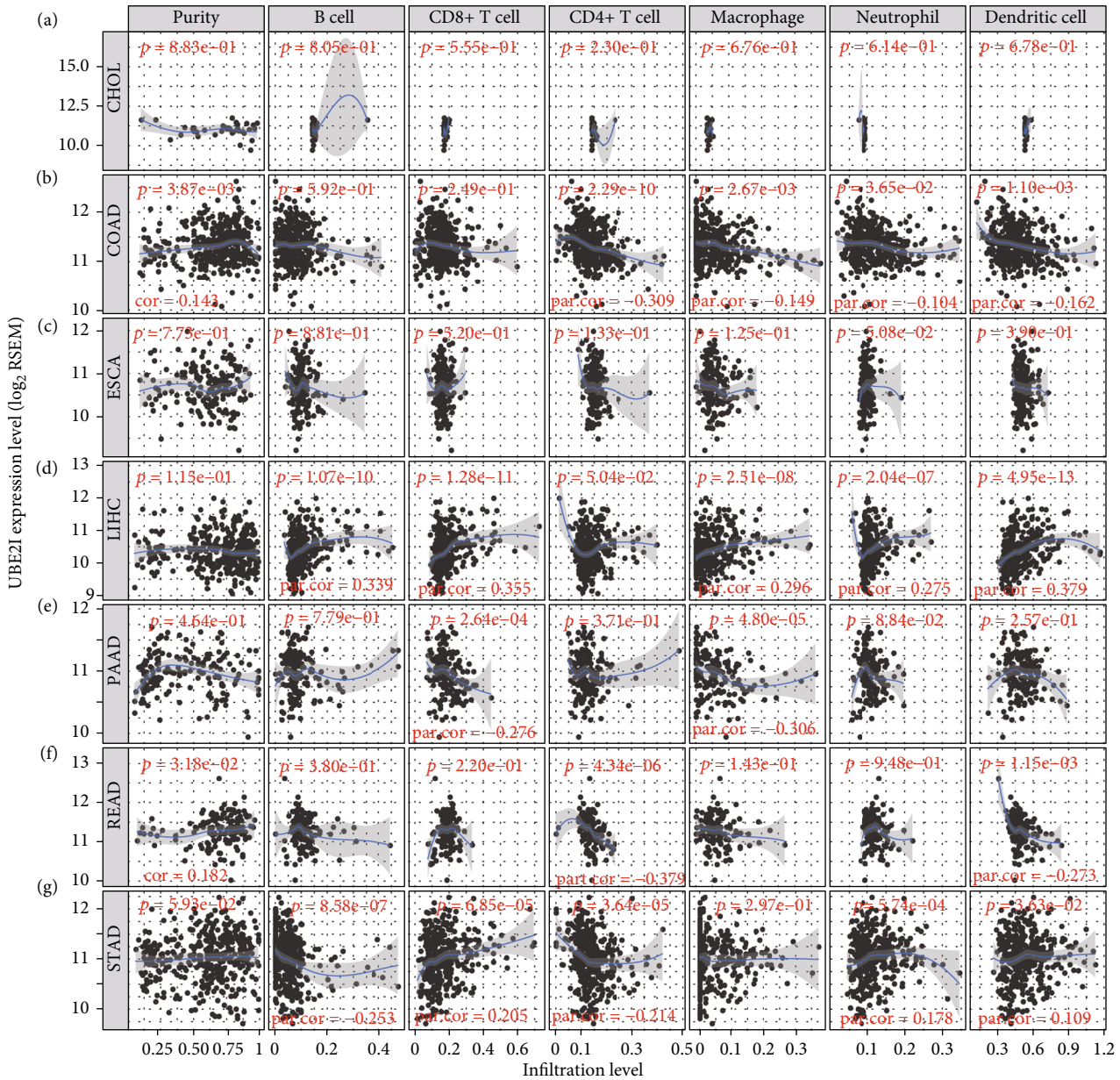

Figure 3: Correlation analysis of *UBE2I* expression with immune infiltrates. (a–g) Correlations of *UBE2I* with immune infiltrates (purity, B cells, $CD8^+$ T cells, $CD4^+$ T cells, MP, NP, and DC) in CHOL, COAD, ESCA, LIHC, PAAD, READ, and STAD.

infiltrate abundance, and the SCNA module mainly investigated the correlation of somatic CNA with immune infiltrate abundance.

2.3. Promoter Methylation and Protein Expression Analyses in Pan-DSTs. Differential promoter methylation of *UBE2I* was evaluated by types as well as stratified analyses additionally conducted by gender, race and nodal metastasis in pan-DSTs. Subsequently, protein levels of *UBE2I* were analyzed by types and stratification of colon cancer by gender, race, tumor stage, and tumor histology (information on other pan-DSTs was not available from the database).

2.4. Interaction Networks Involving UBE2I in Pan-DSTs. The potential mechanisms underlying the prognostic significance of *UBE2I* in pan-DSTs were further explored. Related genes coexpressed with *UBE2I* in these tumors were identified from the cBioPortal database (URL: https://www.cbioportal.org/), and the top 100 were used for interaction network construction [23, 24]. Interaction networks of pathways (bioprocesses, cellular composition, molecular functions, immune processes, KEGG pathways, reactome pathways, and diseases, etc.) were generated with ClueGO plugin of Cytoscape software *v*3.7.2 [25, 26]. Gene-gene interaction (GGI) as well as protein-protein interaction (PPI) networks

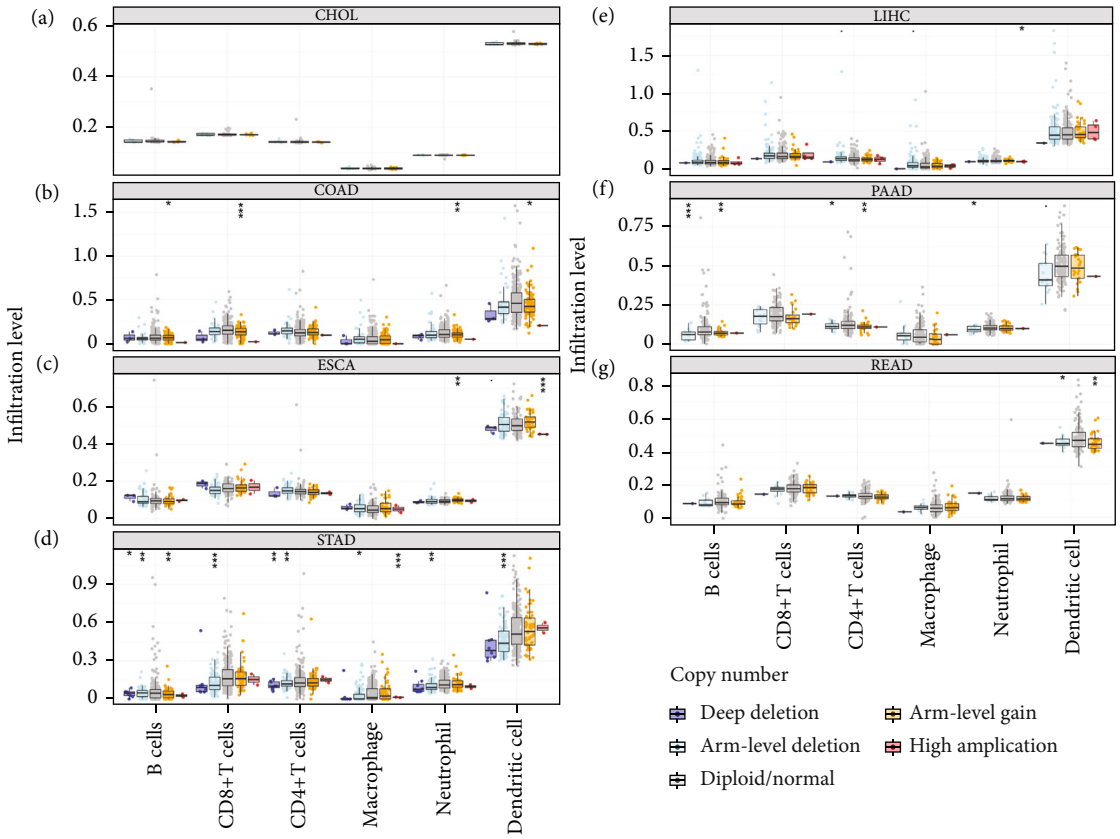

Figure 4: Analysis of associations between SCNAs of *UBE2I* and immune infiltrates of pan-DSTs. (a–g) Analysis of the correlation of SCNAs of *UBE2I* with immune infiltrates (B cells, $CD8^+$ T cells, $CD4^+$ T cells, MP NP, and DC) in CHOL, COAD, ESCA, LIHC, PAAD, READ, and STAD.

were constructed to explore potential interactions at gene and protein levels using geneMANIA (URL: http://genemania.org/) [27] and STRING (URL: https://string-db.org/) [28] databases, respectively.

2.5. Diagnostic Significance of UBE21 in Survival of DSTs. The diagnostic significance of *UBE2I* was determined based on the expression of *UBE2I* in pan-DSTs obtained from the Oncomine database (URL: https://www.oncomine.org/resource/main.html). Specifically, diagnostic significance was evaluated via receiver operating characteristic (ROC) curves constructed using both tumor and nontumor data. The criteria for the identification of potential diagnostic biomarkers were as follows: (1) those showing differential expression in tumor and nontumors and (2) those with an area under curve (AUC) ≥ 0.700 and a $P \leq 0.050$. The Cancer Genome Atlas (TCGA) datasets, including COAD and PAAD, Alon colon cancer [29], and Logsdon pancreas [30] datasets, were used for evaluating the diagnostic value of *UBE2I*.

2.6. Statistical Analysis. One-way ANOVA was applied for gene expression analysis of *UBE2I* in different tumor stages. Analyses of differential expression patterns of *UBE2I* between carcinoma specimens and normal counterparts, as well as promoter methylation between groups, including differences between tumor and normal, male and female, different races, node metastasis and tumor grade categories, were performed via the Mann–Whitney *U* test. Survival analysis and the correlation of *UBE2I* expression with immune infiltrates were made via the log-rank test and the Spearman's correlation coefficients, respectively. The Cox proportional hazard ratio (HR) with a 95% confidence interval (95% CI) was calculated from the survival plots. $P \leq 0.05$ indicated the presence of statistical significance.

3. Results

3.1. Differential UBE2I mRNA Expression in Pan-DSTs. From the TCGA database, we obtained data of 7 different types of digestive system cancers, namely, cholangiocarcinoma (CHOL), colon adenocarcinoma (COAD), esophageal carcinoma (ESCA), liver hepatocellular carcinoma (LIHC), pancreatic adenocarcinoma (PAAD), rectal adenocarcinoma (READ), and stomach adenocarcinoma (STAD). Evaluation of *UBE2I* mRNA expression across TCGA cancers revealed upregulated *UBE2I* in carcinomas, versus normal counterparts, in most cases (Figure 1(a)). Except ESCA, differentially expressed *UBE2I* was observed across all other pan-DST types (all $P \leq 0.05$, Figure 1(b)). Evaluation of expression by pan-DST staging showed that *UBE2I* was differentially expressed in the diver stage in LIHC and STAD

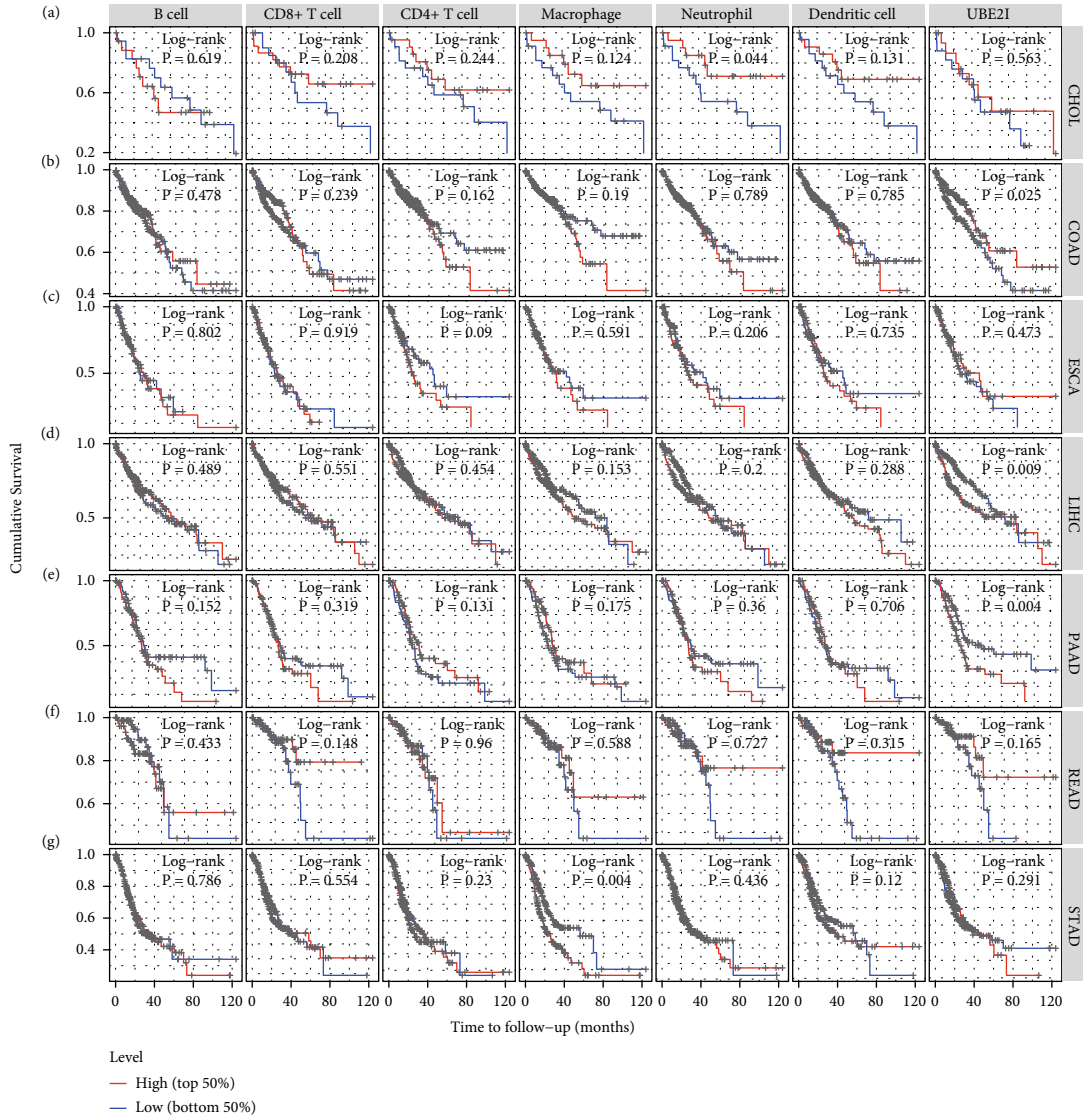

Figure 5: Immune infiltrate-related survival and *UBE2I* expression in pan-DSTs. (a–g) Immune infiltrate-related survival and *UBE2I* expression in CHOL, COAD, ESCA, LIHC, PAAD, READ, and STAD.

($P < 0.0001$, 0.030; Figures 1(f) and 1(i)) but not in other DST types (all $P > 0.05$, Figures 1(c)–1(e), 1(g), and 1(h)). Specifically, *UBE2I* expression was increased in stages I-III while decreased in stage IV in LIHC; however, the converse expression pattern was observed in STAD.

3.2. Survival Analysis of UBE2I in Pan-DSTs. Survival analyses, including OS and DFS, were carried out to determine the role of *UBE2I* expression in the prognosis of pan-DSTs. We observed favorable prognostic significance of *UBE2I* for OS in COAD and PAAD (log-rank [11] $P = 0.049$, HR (high) $= 0.620$; LR $P = 0.003$, HR (high) $= 1.900$; Figures 2(b) and 2(e)) but not in other DSTs examined (all LP $P > 0.050$; Figures 2(a), 2(c), 2(d), 2(f), and 2(g)). In terms of DFS, *UBE2I* showed favorable prognostic significance in PAAD only (LP $P = 0.036$, HR (high) $= 1.600$; Figure 2(l)). It suggests that upregulated *UBE2I* is beneficial for COAD but not for PAAD in terms of both OS and DFS.

3.3. Immune Infiltrate Analysis of UBE21 in Pan-DSTs. Spearman's correlation coefficients were used to evaluate the correlation of *UBE2I* expression with immune infiltrates in a range of pan-DSTs. The data showed no connection between *UBE2I* expression and purity or immune infiltrates (B cells, $CD4^+$, and $CD8^+$ T cells, as well as NP, MP, and DC) in CHOL and ESCA (all $P > 0.050$, Figures 3(a) and 3(c)). In COAD, *UBE2I* was positively associated with purity but negatively with $CD4^+$ T cells, MP, NP, and DC (all $P < 0.050$, $R = 0.143$, -0.309, -0.149, -0.104, and -0.162; Figure 3(b)). In LIHC, a positive association between *UBE2I* and B cells, $CD8^+$ T cells, MP, NP, and DC was determined (all $P < 0.050$, $R = 0.339$, 0.355, 0.296, 0.275, and 0.379; Figure 3(d)). In PAAD, an inverse connection was found between *UBE2I* and $CD8^+$ T cells and MP (both $P < 0.050$, $R = -0.276$ and -0.306; Figure 3(e)). In READ, *UBE2I* was positively linked to purity but negatively to $CD4^+$ T and DC (all $P < 0.050$, $R = 0.182$, -0.37, and -0.273; Figure 3(f)).

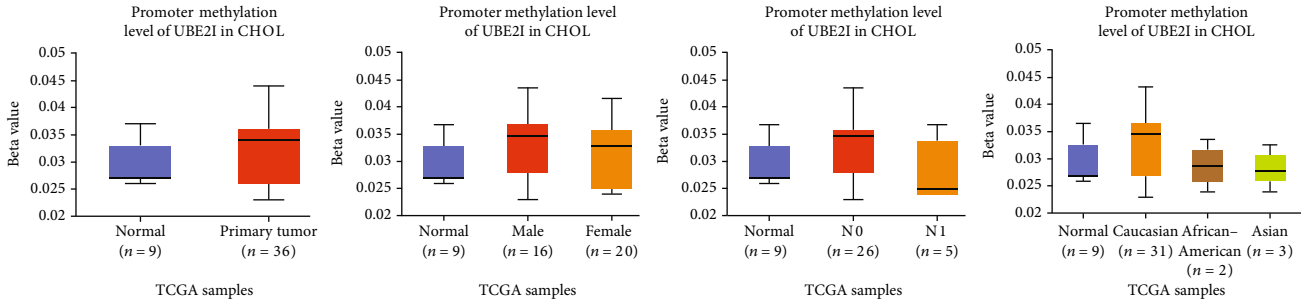

(a)

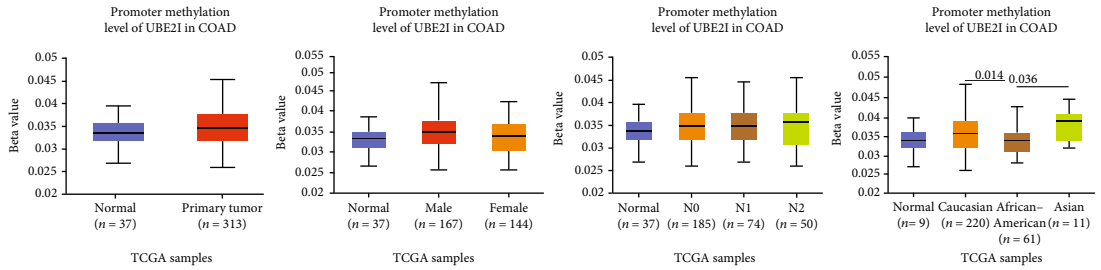

(b)

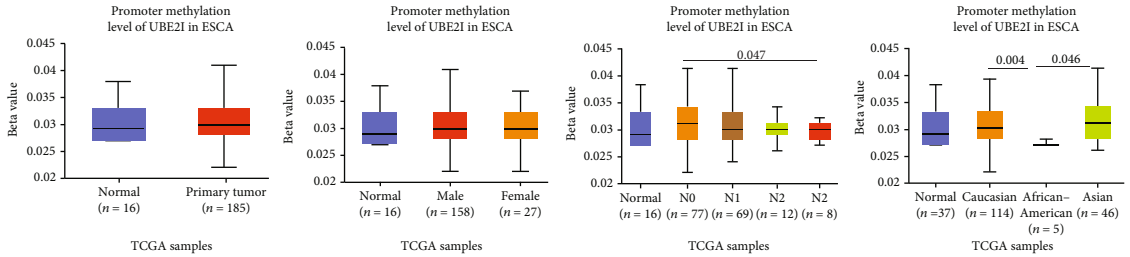

(c)

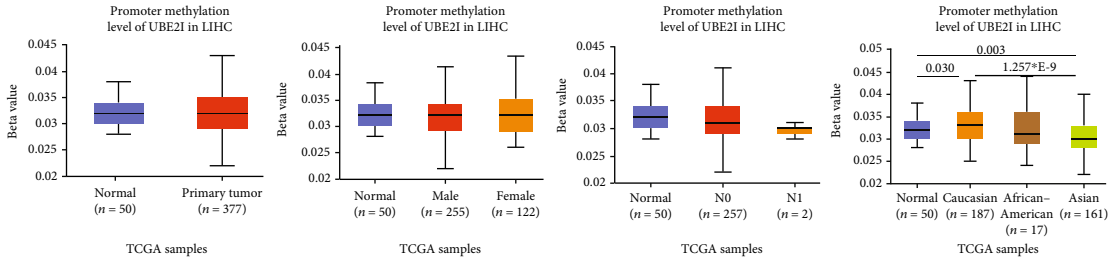

(d)

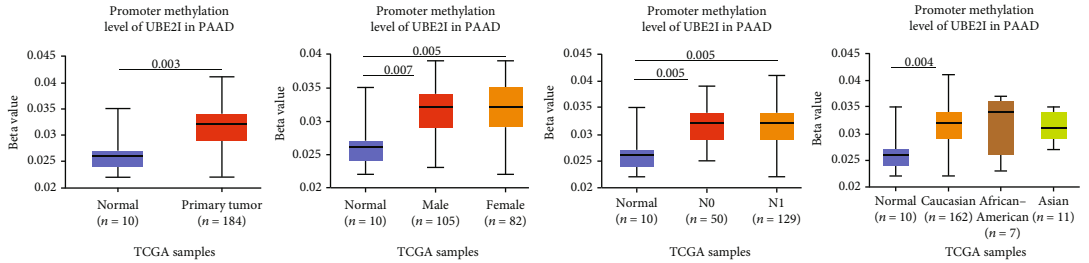

(e)

Figure 6: Continued.

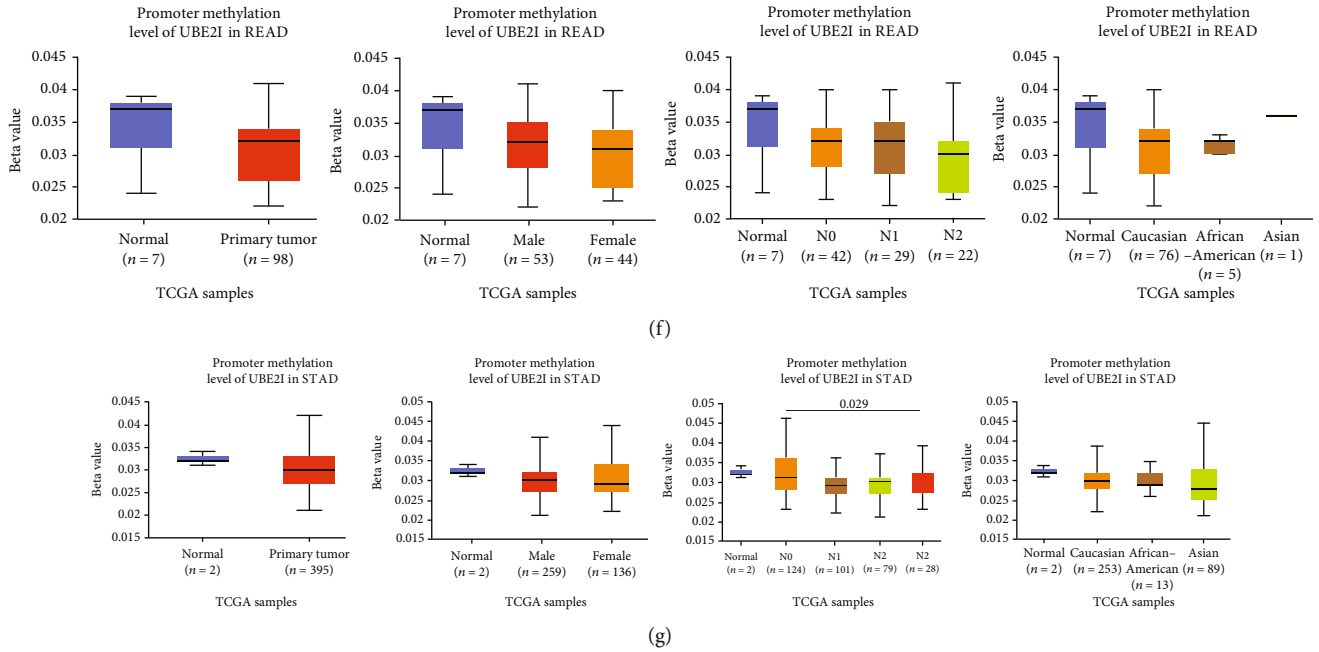

Figure 6: Promoter methylation analysis of *UBE2I* in pan-DSTs and stratified analyses by gender, lymph node, and race. (a–g) Promoter methylation analysis of *UBE2I* in pan-DSTs and stratified analyses by gender, lymph node, and race in CHOL, COAD, ESCA, LIHC, PAAD, READ, and STAD.

And in STAD, *UBE2I* was found to be positively correlated with $CD8^+$ T cells, NP, and DC but had an inverse association with B and $CD4^+$ T cells (all $P < 0.050$, $R = 0.205$, 0.178, 0.109, -0.253, and -0.214; Figure 3(g)).

The potential connection between SCNAs of *UBE21* and immune infiltrates was further examined. Notably, no significant associations were observed between *UBE21* and all the six types of immune infiltrates (B cells, $CD4^+$ T cells, $CD8^+$ T cells, NP, MP, and DC) in CHOL (Figure 4(a)). In contrast, SCNAs of *UBE2I* (deep deletion, arm-level deletion and arm-level gain) were strongly linked to all the above six immune infiltrate types in STAD (Figure 4(g)). While in LIHC, SCNAs of *UBE2I* were significant only in relation to neutrophil amplification (Figure 4(d)). In READ, SCNAs of *UBE2I* (arm-level deletion and gain) showed statistical significance in relation to DC (Figure 4(f)). In COAD, SCNAs of *UBE2I* were strongly related to B cells, $CD8^+$ T cells, NP, and DC in terms of arm-level gain (Figure 4(b)). In PAAD, a close connection between the arm-level deletion and gain of *UBE2I* and B cells, $CD8^+$ T cells, and NP was determined (Figure 4(e)). In ESCA, arm-level gain of *UBE2I* showed a significant correlation with the high amplification of NP and DC (Figure 4(c)).

Next, prognostic analysis was performed based on immune infiltrates and *UBE2I* expression in pan-DSTs. The results showed that neutrophil infiltration was significantly correlated with CHOL while macrophage infiltration was correlated with STAD (log-rank $P = 0.044$, 0.004; Figures 5(a) and 5(g)). *UBE2I* expression showed favorable prognostic value in COAD, LIHC, and PAAD (log-rank $P = 0.025$, 0.009, and 0.004; Figures 5(b), 5(d), and 5(e)), but not in other cancer types.

3.4. Promoter Methylation Analysis of UBE2I in Pan-DSTs. Promoter methylation analysis was initially applied to validate differential expression of *UBE2I* in tumor and normal samples. Differential methylation of *UBE2I* was observed in PAAD, with high methylation in tumor and low methylation in normal cells ($P = 0.003$; Figure 6(e)), but not in other DSTs (all $P > 0.050$; Figures 6(a)–6(d), 6(f), and 6(g)). Furthermore, upon stratification by gender, differential methylation of *UBE2I* was consistently observed in the PAAD subtype, with high methylation levels in both male and female populations, compared to their control counterparts ($P = 0.007$, 0.005; Figure 6(e)). Stratified analysis by nodal metastasis showed differential methylation of *UBE2I* in ESCA, PAAD, and STAD. Consistently, differential levels of methylated *UBE2I* were detected in nodal metastasis groups of ESCA and STAD, with high methylation at N0 and low methylation at N3 ($P = 0.047$, 0.029; Figures 6(c) and 6(g)). In PAAD, high methylated *UBE2I* levels were observed at both N0 and N1 stages, compared to normal samples (both $P = 0.005$; Figure 6(e)). Upon stratification by race, differential methylation of *UBE2I* was detected in COAD, ESCA, LIHC, and PAAD subtypes. Specifically, *UBE2I* methylation levels in COAD and ESCA were significantly higher in Asians and Caucasians than in African-Americans ($P = 0.014$, 0.036; 0.004, 0.046; Figures 6(b) and 6(c)). Higher methylation in Caucasians and lower methylation in Asians with LIHC were detected, compared to the corresponding control groups ($P = 0.030$, 0.003), with significant differences between the two races ($P = 1.257 * E - 9$; Figure 6(d)). The Caucasian subgroup of PAAD displayed high *UBE2I* methylation, compared to the corresponding control group ($P = 0.004$; Figure 6(e)).

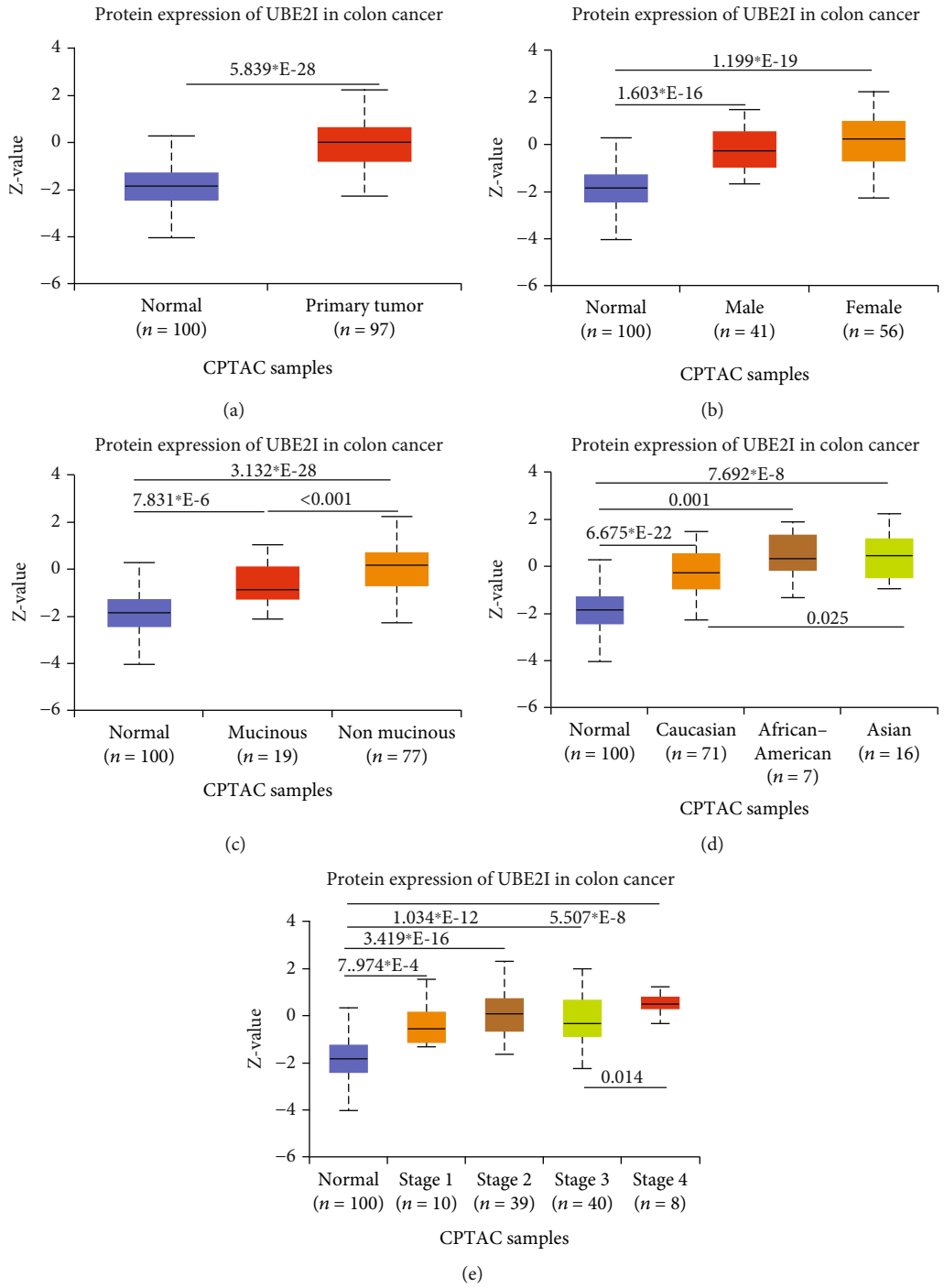

Figure 7: Protein expression analysis of *UBE2I* in tumors. (a–e) Stratified analyses by gender, race, tumor stage, and tumor histology in colon cancer.

3.5. Protein Expression Analysis of UBE2I in Colon Cancer. *UBE2I* was highly expressed in primary colon tumors, versus normal counterparts ($P = 5.839^{*}E - 28$, Figure 7(a)). Stratified analyses by gender, tumor histology, race, and tumor staging consistently disclosed higher expression in tumor versus normal tissue. Both sexes in the tumor groups displayed higher UBE21 expression than their control counterparts ($P = 1.603^{*}E - 16$, $1.199^{*}E - 19$; Figure 7(b)). High expression was detected in both mucinous and nonmucinous types, compared to normal tissue ($P = 7.831^{*}E - 6$, $3.132^{*}E - 28$; Figure 7(c)), which was more marked in nonmucinous than mucinous tumors ($P < 0.001$). We also detected high expression in Caucasian, Franco-American, and Asian populations with colon cancer, compared to their control counterparts ($P = 6.675^{*}E - 22$, 0.001, $7.692^{*}E - 8$; Figure 7(d)), with even higher expression in Asians versus Caucasians ($P = 0.025$). *UBE21* was upregulated in tumor stages I-IV ($P = 7.974^{*}E - 4$, $3.419^{*}E - 16$, $1.034^{*}E - 12$,

Table 1: Coexpression-related genes of *UBE2I* in COAD.

Correlated gene	Cytoband	Spearman's correlation	*P* value	*q* value
RNPS1	16p13.3	0.652	$4.92E-73$	$9.85E-69$
NDUFAB1	16p12.2	0.639	$2.76E-69$	$2.77E-65$
JPT2	16p13.3	0.626	$7.87E-66$	$5.25E-62$
PAM16	16p13.3	0.552	$1.81E-48$	$9.05E-45$
C16ORF91	16p13.3	0.542	$1.40E-46$	$5.59E-43$
NIP7	16q22.1	0.531	$2.23E-44$	$7.45E-41$
FOPNL	16p13.11	0.518	$5.71E-42$	$1.63E-38$
HSBP1	16q23.3	0.516	$1.35E-41$	$3.37E-38$
DNAJA2	16q11.2	0.516	$1.52E-41$	$3.39E-38$
KCTD5	16p13.3	0.512	$6.05E-41$	$1.21E-37$
PMM2	16p13.2	0.509	$2.88E-40$	$4.81E-37$
LYRM1	16p12.3	0.509	$2.88E-40$	$4.81E-37$
DNAJA3	16p13.3	0.507	$6.38E-40$	$9.82E-37$
CFAP20	16q21	0.506	$7.81E-40$	$1.12E-36$
KARS	16q23.1	0.5	$1.07E-38$	$1.43E-35$
RSL1D1	16p13.13	0.498	$1.95E-38$	$2.44E-35$
NDUFB4	3q13.33	0.496	$4.52E-38$	$5.32E-35$
GINS2	16q24.1	0.495	$5.90E-38$	$6.57E-35$
NUTF2	16q22.1	0.493	$1.58E-37$	$1.67E-34$
MRPS34	16p13.3	0.491	$3.54E-37$	$3.54E-34$
NUBP2	16p13.3	0.488	$1.07E-36$	$1.02E-33$
POMP	13q12.3	0.487	$1.52E-36$	$1.39E-33$
TOMM6	6p21.1	0.484	$5.17E-36$	$4.50E-33$
SNRPC	6p21.31	0.483	$6.16E-36$	$5.14E-33$
PSMB1	6q27	0.48	$1.68E-35$	$1.35E-32$
EEF2KMT	16p13.3	0.475	$1.24E-34$	$9.55E-32$
EXOSC8	13q13.3	0.473	$2.57E-34$	$1.91E-31$
NAE1	16q22.1	0.471	$4.38E-34$	$3.13E-31$
EP300	22q13.2	-0.47	$7.31E-34$	$5.05E-31$
HEBP2	6q24.1	0.467	$2.00E-33$	$1.33E-30$
METTL9	16p12.2	0.467	$2.09E-33$	$1.33E-30$
CMC2	16q23.2	0.467	$2.13E-33$	$1.33E-30$
MSRB1	16p13.3	0.465	$4.67E-33$	$2.83E-30$
CENPN	16q23.2	0.465	$5.04E-33$	$2.97E-30$
METTL26	16p13.3	0.464	$5.65E-33$	$3.23E-30$
CLIC1	6p21.33	0.463	$9.56E-33$	$5.32E-30$
MRPL18	6q25.3	0.462	$1.03E-32$	$5.59E-30$
RPS15A	16p12.3	0.459	$4.01E-32$	$2.11E-29$
EMC8	16q24.1	0.457	$8.05E-32$	$4.13E-29$
HERC1	15q22.31	-0.454	$1.65E-31$	$8.28E-29$
NDUFB10	16p13.3	0.454	$2.01E-31$	$9.84E-29$
THOC7	3p14.1	0.454	$2.13E-31$	$1.02E-28$
CIAO2B	16q22.1	0.452	$3.81E-31$	$1.77E-28$
CYB5B	16q22.1	0.451	$4.67E-31$	$2.12E-28$
TSR3	16p13.3	0.451	$5.35E-31$	$2.38E-28$
NOTCH2	1p12	-0.45	$6.77E-31$	$2.95E-28$
FAM192A	16q13	0.45	$7.97E-31$	$3.39E-28$
MTMR3	22q12.2	-0.45	$8.43E-31$	$3.52E-28$
PSMD13	11p15.5	0.449	$8.87E-31$	$3.62E-28$
NBPF10	1q21.1	-0.449	$1.12E-30$	$4.47E-28$
UCHL3	13q22.2	0.449	$1.17E-30$	$4.61E-28$
POLR2C	16q21	0.448	$1.70E-30$	$6.56E-28$
TMEM208	16q22.1	0.447	$2.03E-30$	$7.66E-28$
MRPS15	1p34.3	0.446	$2.62E-30$	$9.72E-28$
HMGB1	13q12.3	0.446	$3.08E-30$	$1.12E-27$
DIP2A	21q22.3	-0.444	$5.29E-30$	$1.89E-27$
ZSWIM8	10q22.2	-0.444	$6.15E-30$	$2.16E-27$
NDUFAF4	6q16.1	0.443	$7.55E-30$	$2.61E-27$
ARPC4	3p25.3	0.442	$9.40E-30$	$3.19E-27$
PI4KA	22q11.21	-0.442	$1.02E-29$	$3.39E-27$
MRPL47	3q26.33	0.442	$1.12E-29$	$3.69E-27$
ZNF263	16p13.3	0.441	$1.67E-29$	$5.40E-27$
STUB1	16p13.3	0.44	$1.81E-29$	$5.75E-27$
RPUSD1	16p13.3	0.44	$2.17E-29$	$6.69E-27$
FAM168A	11q13.4	-0.44	$2.17E-29$	$6.69E-27$
UBE2C	20q13.12	0.439	$2.65E-29$	$8.04E-27$
ZFYVE1	14q24.2	-0.438	$3.28E-29$	$9.80E-27$
SRSF3	6p21.31-p21.2	0.438	$3.62E-29$	$1.07E-26$
PRDX1	1p34.1	0.437	$4.54E-29$	$1.32E-26$
PSENEN	19q13.12	0.436	$6.31E-29$	$1.80E-26$
BCL7C	16p11.2	0.436	$7.23E-29$	$2.04E-26$
TMEM186	16p13.2	0.434	$1.56E-28$	$4.35E-26$
UTP4	16q22.1	0.434	$1.61E-28$	$4.42E-26$
PPIH	1p34.2	0.433	$1.84E-28$	$4.97E-26$
BFAR	16p13.12	0.432	$2.31E-28$	$6.17E-26$
LSM2	6p21.33	0.431	$3.36E-28$	$8.86E-26$
GLRX3	10q26.3	0.431	$3.72E-28$	$9.67E-26$
BANF1	11q13.1	0.429	$5.85E-28$	$1.50E-25$
BCL2L2	14q11.2	-0.429	$6.01E-28$	$1.52E-25$
COX7A2	6q14.1	0.429	$6.73E-28$	$1.68E-25$
MRPL28	16p13.3	0.429	$7.08E-28$	$1.75E-25$
DCTPP1	16p11.2	0.429	$7.54E-28$	$1.84E-25$
PTMA	2q37.1	0.427	$1.44E-27$	$3.48E-25$
ATP5F1C	10p14	0.426	$1.58E-27$	$3.78E-25$
DYNC1H1	14q32.31	-0.425	$2.13E-27$	$5.02E-25$

Table 1: Continued.

Correlated gene	Cytoband	Spearman's correlation	P value	q value
RPS7	2p25.3	0.425	$2.24E-27$	$5.21E-25$
MCRIP2	16p13.3	0.424	$3.50E-27$	$8.07E-25$
ZNF236	18q23	-0.423	$3.76E-27$	$8.56E-25$
TFAP4	16p13.3	0.422	$5.43E-27$	$1.22E-24$
AKAP13	15q25.3	-0.422	$5.96E-27$	$1.33E-24$
ZFYVE26	14q24.1	-0.421	$7.79E-27$	$1.71E-24$
GOT2	16q21	0.421	$8.77E-27$	$1.91E-24$
COPS9	2q37.3	0.42	$1.19E-26$	$2.57E-24$
TECPR2	14q32.31	-0.419	$1.41E-26$	$3.00E-24$
HECTD4	12q24.13	-0.419	$1.67E-26$	$3.52E-24$
CIAO3	16p13.3	0.418	$1.69E-26$	$3.52E-24$
FYCO1	3p21.31	-0.418	$1.76E-26$	$3.63E-24$
MRPL48	11q13.4	0.418	$1.97E-26$	$4.02E-24$
LSM3	3p25.1	0.417	$2.53E-26$	$5.12E-24$
ANKRD52	12q13.3	-0.417	$2.58E-26$	$5.16E-24$

and $5.507^{*}E-8$; Figure 7(e)), with higher expression in stage IV, compared to stage III carcinoma ($P = 0.014$).

3.6. Interaction Networks of Potential Pathways Involving UBE2I in COAD and PAAD. *UBE2I* coexpressed genes in the cBioPortal database were first identified for analysis. The top 100 genes related to *UBE2I* in COAD and PAAD are presented in Tables 1 and 2, respectively, based on which the interaction networks involving *UBE2I* in COAD were constructed (Figure 8). Associated genes were found to be involved in preribosome, transport of mature mRNAs derived from intron-containing transcripts, spliceosomal snRNP complexes, Notch signaling, mitochondrial protein complexes, small ribosomal subunits, and Alzheimer's disease. The interaction network of *UBE2I* in PAAD included genes involved in ruffle membrane, regulation of cellular senescence, spliceosomal snRNP complex, gene, and protein expression by JAK-STAT axis after interleukin-12 stimulation, protein phosphatase inhibitor activity, and HIV infection (Figure 9). Finally, GGI and PPI networks were constructed to visualize these relationships. GGI analysis showed physical, coexpression, pathway, and genetic interactions of *UBE21* with *SUMO1*, *SUMO3*, *RANBP2*, *SYCE2*, *SYCE1*, *PIAS3*, *PIAS4*, *RAD51*, and *RAD52* (Figure 10(a)). In PPI analysis, physical, coexpression, pathway, and genetic interactions of UBE21 with SUMO1-3, SAE1, PIAS1, PIAS3, UBA2, and RWDD3 were detected (Figure 10(b)).

3.7. Diagnostic Value of UBE2I in Pan-DSTs. In view of the prognostic significance of *UBE2I* in COAD and PAAD, its diagnostic value in these cancer types was further explored. *UBE2I* displayed differential expression and favorable diagnostic value in COAD of TCGA colorectal and Alon datasets (AUC = 0.766 and 0.978, $P = 0.002$, <0.001, <0.001, and

Table 2: Coexpression-related genes of UBE2I in PAAD.

Correlated gene	Cytoband	Spearman's correlation	P value	q value
TMSB10	2p11.2	0.75	$3.44E-33$	$6.87E-29$
PTMA	2q37.1	0.678	$3.91E-25$	$2.75E-21$
EIF6	20q11.22	0.677	$4.13E-25$	$2.75E-21$
PPIA	7p13	0.673	$1.13E-24$	$5.10E-21$
MFSD2B	2p23.3	0.672	$1.28E-24$	$5.10E-21$
PFDN2	1q23.3	0.671	$1.53E-24$	$5.10E-21$
SNRPA1	15q26.3	0.671	$1.82E-24$	$5.20E-21$
PPP4C	16p11.2	0.664	$6.75E-24$	$1.69E-20$
NUTF2	16q22.1	0.66	$1.71E-23$	$3.80E-20$
CFL1	11q13.1	0.657	$3.06E-23$	$6.12E-20$
RNF181	2p11.2	0.653	$7.23E-23$	$1.31E-19$
PPIH	1p34.2	0.652	$9.20E-23$	$1.53E-19$
RNPS1	16p13.3	0.649	$1.61E-22$	$2.48E-19$
PSMD13	11p15.5	0.638	$1.20E-21$	$1.71E-18$
S100A16	1q21.3	0.638	$1.35E-21$	$1.80E-18$
BANF1	11q13.1	0.634	$2.74E-21$	$3.43E-18$
KANK1	9p24.3	-0.633	$3.12E-21$	$3.67E-18$
CLASP2	3p22.3	-0.632	$3.82E-21$	$4.02E-18$
NOP10	15q14	0.632	$3.82E-21$	$4.02E-18$
S100A11	1q21.3	0.629	$6.69E-21$	$6.68E-18$
CKS1B	1q21.3	0.626	$1.19E-20$	$1.13E-17$
HMGA1	6p21.31	0.626	$1.24E-20$	$1.13E-17$
BOLA2	16p11.2	0.62	$3.42E-20$	$2.97E-17$
NUDT1	7p22.3	0.619	$4.09E-20$	$3.41E-17$
PPP1R14B	11q13.1	0.618	$4.66E-20$	$3.73E-17$
MRGBP	20q13.33	0.618	$5.15E-20$	$3.96E-17$
SNRPG	2p13.3	0.617	$5.81E-20$	$4.30E-17$
MBLAC2	5q14.3	-0.617	$6.18E-20$	$4.41E-17$
RALY	20q11.22	0.617	$6.40E-20$	$4.41E-17$
KCTD5	16p13.3	0.616	$6.81E-20$	$4.54E-17$
NCOA1	2p23.3	-0.611	$1.57E-19$	$9.87E-17$
S100A10	1q21.3	0.611	$1.58E-19$	$9.87E-17$
UBE2C	20q13.12	0.61	$1.87E-19$	$1.13E-16$
ZNF420	19q13.12	-0.61	$2.01E-19$	$1.18E-16$
ICA1L	2q33.2	-0.61	$2.12E-19$	$1.21E-16$
FNDC3A	13q14.2	-0.609	$2.44E-19$	$1.36E-16$
ELOB	16p13.3	0.608	$3.02E-19$	$1.63E-16$
CHMP4B	20q11.22	0.606	$3.92E-19$	$2.06E-16$
METTL7A	12q13.12	-0.605	$4.38E-19$	$2.25E-16$
C16ORF91	16p13.3	0.605	$4.53E-19$	$2.26E-16$
CPEB4	5q35.2	-0.604	$5.29E-19$	$2.58E-16$
STX4	16p11.2	0.604	$5.56E-19$	$2.65E-16$
TMEM189	20q13.13	0.602	$7.50E-19$	$3.48E-16$

Table 2: Continued.

Correlated gene	Cytoband	Spearman's correlation	*P* value	*q* value
SYNJ1	21q22.11	-0.602	8.40*E* − 19	3.82*E* − 16
CKS2	9q22.2	0.599	1.33*E* − 18	5.87*E* − 16
CIB1	15q26.1	0.599	1.35*E* − 18	5.87*E* − 16
ZNF471	19q13.43	-0.597	1.70*E* − 18	7.21*E* − 16
FAM122A	9q21.11	-0.597	1.91*E* − 18	7.95*E* − 16
AMIGO1	1p13.3	-0.596	2.13*E* − 18	8.69*E* − 16
PTTG1	5q33.3	0.595	2.32*E* − 18	9.28*E* − 16
ZNF37A	10p11.1	-0.595	2.58*E* − 18	9.93*E* − 16
SMARCA2	9p24.3	-0.595	2.58*E* − 18	9.93*E* − 16
PSMA7	20q13.33	0.594	2.83*E* − 18	1.07*E* − 15
THOC6	16p13.3	0.593	3.49*E* − 18	1.29*E* − 15
TNFRSF12A	16p13.3	0.592	3.73*E* − 18	1.34*E* − 15
RNF7	3q23	0.592	3.74*E* − 18	1.34*E* − 15
RNF180	5q12.3	-0.591	4.38*E* − 18	1.54*E* − 15
WASF3	13q12.13	-0.59	5.81*E* − 18	1.98*E* − 15
SCNM1	1q21.3	0.59	5.84*E* − 18	1.98*E* − 15
PSMD4	1q21.3	0.589	6.07*E* − 18	2.02*E* − 15
PSMA1	11p15.2	0.589	6.15*E* − 18	2.02*E* − 15
BCL2L12	19q13.33	0.588	7.19*E* − 18	2.32*E* − 15
MRPL28	16p13.3	0.588	7.80*E* − 18	2.48*E* − 15
REV3L	6q21	-0.587	8.64*E* − 18	2.70*E* − 15
NBEA	13q13.3	-0.586	9.74*E* − 18	3.00*E* − 15
TSTD2	9q22.33	-0.586	9.96*E* − 18	3.02*E* − 15
HCFC2	12q23.3	-0.586	1.13*E* − 17	3.37*E* − 15
ACADSB	10q26.13	-0.585	1.22*E* − 17	3.59*E* − 15
SETBP1	18q12.3	-0.585	1.30*E* − 17	3.78*E* − 15
C19ORF33	19q13.2	0.583	1.64*E* − 17	4.68*E* − 15
ZNF429	19p12	-0.583	1.72*E* − 17	4.79*E* − 15
ACACB	12q24.11	-0.583	1.73*E* − 17	4.79*E* − 15
PKMYT1	16p13.3	0.583	1.77*E* − 17	4.85*E* − 15
ANXA2	15q22.2	0.582	1.83*E* − 17	4.94*E* − 15
EIF3M	11p13	0.582	1.94*E* − 17	5.17*E* − 15
FTSJ1	Xp11.23	0.582	2.09*E* − 17	5.48*E* − 15
KAT2B	3p24.3	-0.581	2.32*E* − 17	6.01*E* − 15
CTTNBP2	7q31.31	-0.58	2.78*E* − 17	7.12*E* − 15
SLC2A13	12q12	-0.58	2.86*E* − 17	7.23*E* − 15
LONRF2	2q11.2	-0.579	2.98*E* − 17	7.35*E* − 15
ANKFY1	17p13.2	-0.579	2.98*E* − 17	7.35*E* − 15
TAF10	11p15.4	0.579	3.08*E* − 17	7.50*E* − 15
ADAMTSL3	15q25.2	-0.578	3.51*E* − 17	8.41*E* − 15
MRPS6	21q22.11	0.578	3.53*E* − 17	8.41*E* − 15
MAML3	4q31.1	-0.578	3.69*E* − 17	8.67*E* − 15
ZBED3	5q13.3	-0.576	4.61*E* − 17	1.06*E* − 14
LEMD1	1q32.1	0.576	4.62*E* − 17	1.06*E* − 14
TRMT112	11q13.1	0.576	4.81*E* − 17	1.09*E* − 14
PEG3	19q13.43	-0.576	4.92*E* − 17	1.10*E* − 14
OST4	2p23.3	0.576	4.93*E* − 17	1.10*E* − 14
APC	5q22.2	-0.575	5.37*E* − 17	1.17*E* − 14
LYPLA2	1p36.11	0.575	5.38*E* − 17	1.17*E* − 14
SF3B6	2p23.3	0.575	5.72*E* − 17	1.23*E* − 14
KLHDC1	14q21.3	-0.575	5.91*E* − 17	1.26*E* − 14
SELENOH	11q12.1	0.575	6.09*E* − 17	1.28*E* − 14
ULK2	17p11.2	-0.574	6.44*E* − 17	1.34*E* − 14
TALDO1	11p15.5	0.574	6.61*E* − 17	1.36*E* − 14
PREPL	2p21	-0.574	6.70*E* − 17	1.37*E* − 14
APPBP2	17q23.2	-0.574	6.80*E* − 17	1.37*E* − 14
KCNJ3	2q24.1	-0.573	7.98*E* − 17	1.59*E* − 14

<0.001; Figures 11(a)–11(d)). Moreover, *UBE2I* showed differential expression and good diagnostic value in PAAD of TCGA pancreas and Logsdon datasets (AUC = 0.986 and 0.849, $P = 0.003$, 0.002, <0.001, and <0.001; Figures 11(e)–11(h)).

4. Discussion

The current research explored the potential correlation of *UBE2I* expression with a range of pan-DSTs, including CHOL, COAD, ESCA, LIHC, PAAD, READ, and STAD. Our data preliminary revealed differential expression of *UBE2I*, with higher expression in all tumor types, except ESCA. Interestingly, survival analysis indicated that high *UBE2I* expression was associated with adverse OS and DFS in PAAD but improved OS in READ. In immune infiltrate analysis, *UBE2I* expression was partially associated with purity or B cells, $CD8^+$ and $CD4^+$ T cells, MP, NP, and DC in COAD, LIHC, PAAD, READ, and STAD. Evaluation of the correlation between SCNAs and immune infiltrates revealed that *UBE2I* was associated with all six immune infiltrate types in STAD but partially associated with specific immune cell types in the other five pan-DST types. Differential promoter methylation of *UBE2I* was observed in PAAD only, with high methylation in tumor and low methylation in normal tissues. Consistently, stratified analyses by gender, nodal metastasis, and race showed differential methylation in PAAD, which was also partially observed in COAD, ESCA, and STAD. In colon cancer, differential UBE2I protein expression was observed as well as following stratification by gender, tumor histology, race, and tumor stage. Analysis of the interaction networks of potential pathways disclosed involvement of *UBE2I* in the spliceosomal snRNP complex, Notch signaling pathway, mitochondrial protein complex, small ribosomal subunit, Alzheimer's disease, protein phosphatase inhibitor activity, and HIV infection in

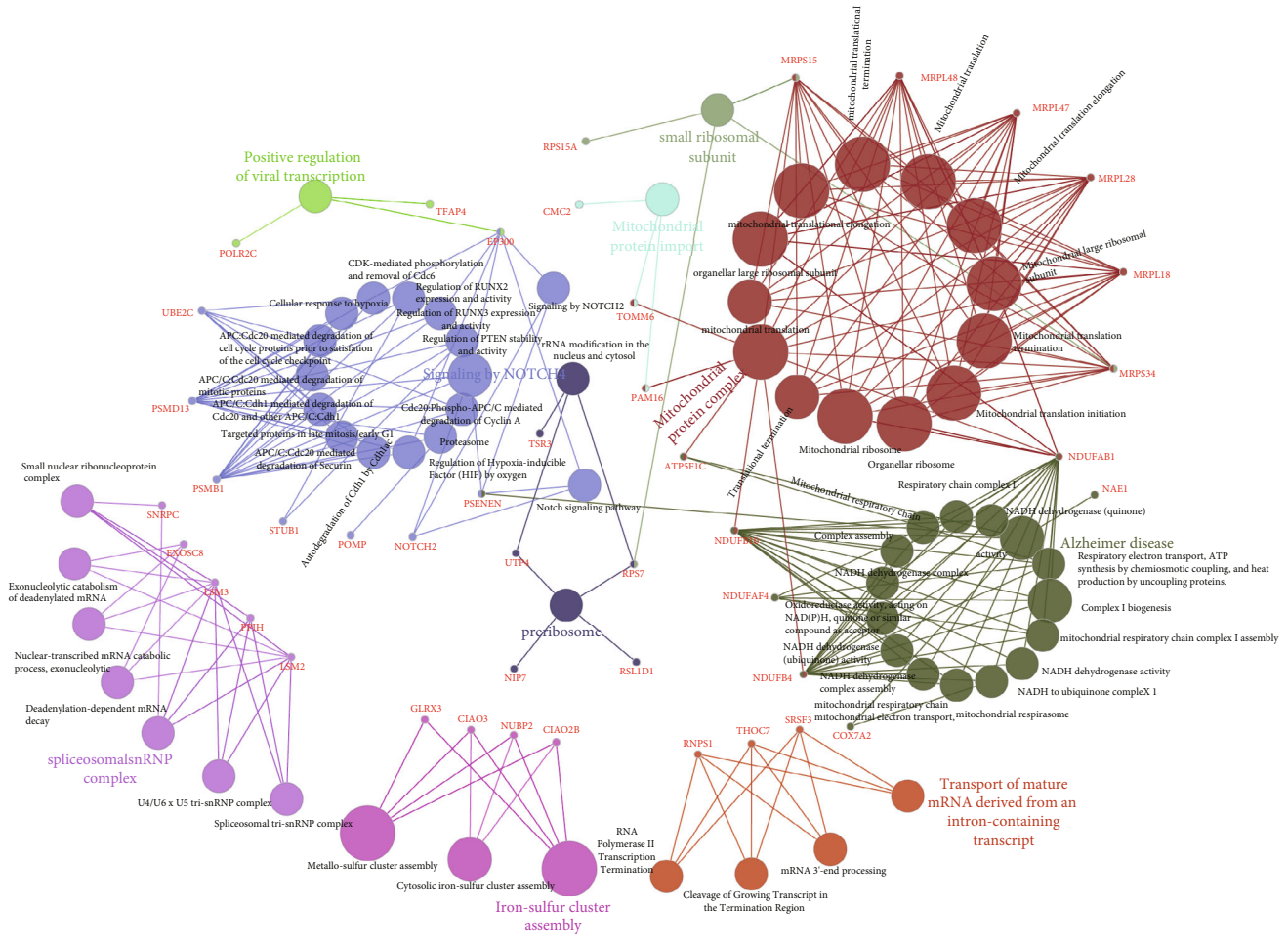

Figure 8: Illustration of functional enrichment pathways of *UBE2I* and coexpressed genes involved in COAD.

COAD and PAAD. Furthermore, *UBE2I* showed differential expression and favorable diagnostic value in COAD and PAAD from two separate datasets.

Digestive system carcinomas comprise many types of neoplasms including esophageal cancer, gastric cancer, small and large bowel cancers, and cancers from liver and bile duct system, pancreas, and anal regions [31], which are reported to contribute to more than 3.2 billion deaths worldwide [2]. In addition, digestive system malignancies account for ~40% of cancer-related deaths worldwide with substantial adverse effects on both developed and developing countries [4]. Thus, identifying novel biomarkers for early diagnosis and survival surveillance for high-risk populations and post-surgical patients remains an urgent medical requirement. Digestive system carcinoma subtypes in the TCGA database include CHOL, ESCA, LIHC, PAAD, COAD, READ, and STAD. To our knowledge, no studies to date have determined the expression profiles and clinical implications of *UBE2I*, also known as *UBC9*, in these pan-DSTs.

UBC9, the unique E2-conjugating enzyme needed for SUMOylation, is a core modulator of essential cellular functions and changes frequently in cancer, contributing substantially to the progression of human tumors [32]. Mattoscio and Chiocca [33] previously suggested that upregulation of *UBC9* in HGSOC cells with *BRCA1* mutations leads to loss of caveolin-1 and induction of vascular epithelial growth factor, supporting a pathway linking *BRCA1* mutation in HGSOC with peritoneal permeability and ascites formation. The same group reported that knockdown of *UBC9* in BRCA1 mutant triple-negative breast cancer and HGSOC cells inhibited cell proliferation and migration, indicating the pivotal role of *UBC9* in endothelial-mesenchymal transition in such cancer type [34]. Epithelial-mesenchymal transition is a biological phenomenon whereby epithelial cells show enhanced migration ability to distal sites, facilitating tumor metastasis [35]. These findings support critical roles of *UBC9* expression and dependent pathways in metastasis of triple-negative breast cancer. Similarly, our results suggest association of high *UBC9* expression with poor prognosis in PAAD as well as differential levels (low in normal samples) of promoter methylation concerning lymph node metastasis. The role of *UBC9* in PAAD in our study is consistent with that reported in other studies across diverse tumor types, including lung, colorectal, prostate, ovarian, and breast cancers as well as melanoma [36–41]. In addition, we determined the diagnostic potential of UBE2I in PAAD and COAD, which has rarely been reported in cancers. Our data showed favorable prognostic value of *UBE2I* in COAD but

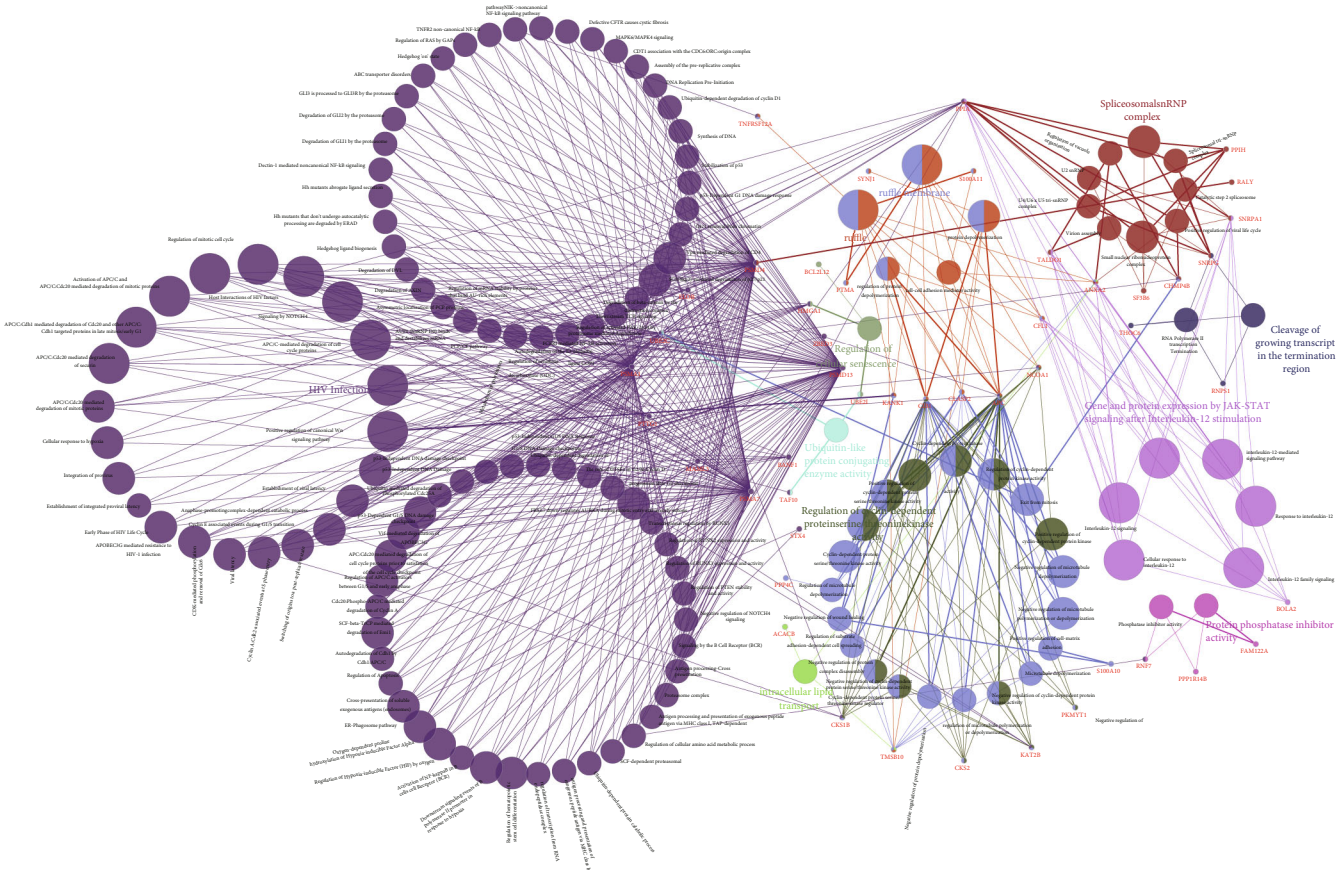

FIGURE 9: Illustration of interaction networks of *UBE2I* and coexpressed genes involved in PAAD.

(a) (b)

FIGURE 10: Gene-gene and protein-protein interaction networks. (a) Gene-gene interaction networks of *UBE2I* and related genes. (b) Protein-protein interaction networks of UBE2I and related proteins.

not in PAAD. A previous study on 602 early-stage colorectal cancer patients by Fridman et al. [42] revealed the presence of high memory T-cell (CD45RO$^+$ and CD8$^+$) infiltrates in tumors. In our experiments, *UBE2I* expression was positively correlated with purity and inversely with CD4$^+$ T cells, MP, NP, and DC rather than CD8$^+$ T cells, regardless of tumor

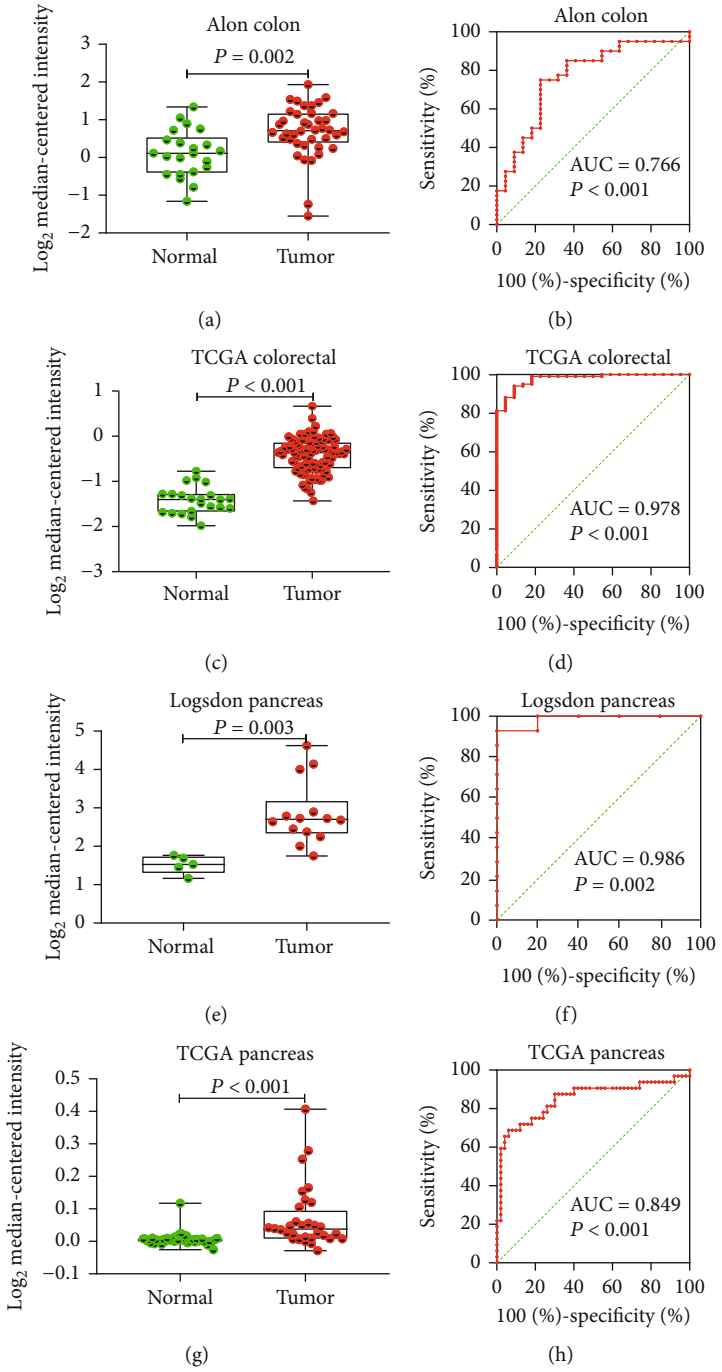

Figure 11: Differential expression and diagnostic ROC curves of *UBE2I* in COAD and PAAD. (a, c) Differential expression of *UBE2I* in COAD. (b, d) Diagnostic ROC curve of *UBE2I* in COAD. (e, g) Differential expression of *UBE2I* in PAAD. (f, h) Diagnostic ROC curve of *UBE2I* in PAAD.

stages. However, whether this inconsistency is associated with tumor staging or other influencing factors is yet to be elucidated.

Promoter methylation is the most extensively characterized type of epigenetic alteration; in particular, DNA methylation in CpG islands is predominantly present in the upstream promoter region that takes responsibility for inhibitory protein complex recruitment, inducing transcriptional repression of downstream genes [43]. There was once a proposal that DNA methylation alterations may contribute to oncogenesis, as the cytosine base of DNA was initially found to be methylated to 5-methylcytosine, or the fifth base [44]. Recent evidence has shown that 5-methylcytosine distribution alterations can help effectively differentiate cancer from normal cells, with focal hypermethylation of tumor suppressor gene promoters identified as one of the main mechanisms [44]. Homeostasis alterations of epigenetic mechanisms are crucial to the development of human

cancers [44]. Consistently, our experiments showed increased promoter hypermethylation of *UBE2I* in PAAD tumors relative to control, which retained significance upon stratification by gender, race, and nodal metastasis, supporting the involvement of *UBE2I* hypermethylation in the development of PAAD. However, no data on methylation levels and prognostic significance on *UBE2I* were available for other pan-DST types.

Marked advances in tumor immunotherapy have been attributed to the increasing awareness of the importance of the tumor immune microenvironment in inhibiting antitumor immunity [45]. Overcoming the ability of cancer cells to evade immune detection allows the available treatment approaches for multiple cancer types to attack tumors via harnessing the "non-self"-directed specificity of the immune system [45]. One of the most promising therapeutic strategies for antitumor immunity reactivation is pharmacological manipulation of physiological immune checkpoints [45]. Exploiting immune checkpoint pathways is a major mechanism for tumors to escape immune surveillance, so immune checkpoint blockade underlies the antineoplasmic activity of most approved agents targeting CTLA-4, as well as programmed cell death protein-1/ligand-1 [46]. Additionally, a number of predictive biomarkers, such as abundance and location of tumor-infiltrating lymphocytes, have been explored for immune-oncology applications [42]. Established findings suggest that local inflammation significantly affects tumor progression. The group further showed that highly adaptive immune infiltrates of intratumoral lymphocytes present a crucial prognostic marker for solid tumors [42].

Solid tumors are often infiltrated by immune cells, including T and B lymphocytes, natural killer cells, DC, MP, NP, eosinophils, and mast cells [42]. Dunn and coworkers reported an association of immune deficiency with tumor proliferation and aggressiveness in a mouse model [47]. Clinical, experimental and epidemiological studies have indicated chronic inflammation as an important inducer of various cancer types [48], such as *Helicobacter pylori* infection in gastric cancer [49] and mucosal lymphoma [50]. The presence of lymphocytes in large quantities, especially T cells, in contrast to infiltration of cells responsible for chronic inflammation, is considered a beneficial prognostic marker for diverse cancer types, including melanoma, non-Hodgkin's lymphoma, head-and-neck cancer, non-small-cell lung cancer, and breast, ovarian, esophageal, and urothelial carcinomas [42, 51–53]. Data from the current study indicate that *UBE2I* expression is associated with six immune infiltrate cell types and purity in COAD, LIHC, PAAD, READ, and STAD. Similar to earlier findings, a high NP count was associated with favorable prognosis in CHOL while a high MP count indicated adverse prognosis in STAD. Further research is warranted to explain this differential prognostic relevance.

This study has a number of limitations that should be taken into consideration. First, the findings obtained require further validation in other cohorts on a larger scale. Second, it is essential to clarify the mechanisms of *UBE2I* in COAD and PAAD *in vivo* and *in vitro*. Third, clinical translation needs to be explored for optimizing therapeutic application.

Data Availability

The authors confirm that the data supporting the findings of this study are available within the article.

Conflicts of Interest

The authors declare no competing interests.

Authors' Contributions

Shuai Huang and Xiangkun Wang contributed equally to this work and are co-first authors.

Acknowledgments

This work was supported by the Henan Province Key R&D and Promotion Special Support Project and Henan Province Medical Science and Technology Joint Construction Project (LHGJ20220317).

References

[1] L. Lin, L. Xia, D. Tang, Y. Dai, and W. Chen, "Analysis of autophagy-related genes and associated noncoding rnas and transcription factors in digestive system tumors," *Future Oncology*, vol. 15, no. 36, pp. 4141–4154, 2019.

[2] A. Stenzinger and W. Weichert, "Genetic profiling of cancers of the digestive system: biological insights and clinical implications," *Pathobiology*, vol. 84, no. 6, pp. 306–322, 2018.

[3] M. L. Bacigalupo, P. Carabias, and M. F. Troncoso, "Contribution of galectin-1, a glycan-binding protein, to gastrointestinal tumor progression," *World Journal of Gastroenterology*, vol. 23, no. 29, pp. 5266–5281, 2017.

[4] L. Torre, F. Bray, R. Siegel, J. Ferlay, J. Lortet-Tieulent, and A. Jemal, "Global cancer statistics, 2012," *CA: a Cancer Journal for Clinicians*, vol. 65, no. 2, pp. 87–108, 2015.

[5] S. Lu, Z. Su, W. Fu, Z. Cui, X. Jiang, and S. Tai, "Altered expression of long non-coding rna gas5 in digestive tumors," *Bioscience Reports*, vol. 39, no. 1, 2019.

[6] F. Bray, J. Ferlay, I. Soerjomataram, R. L. Siegel, L. A. Torre, and A. Jemal, "Global cancer statistics 2018: Globocan estimates of incidence and mortality worldwide for 36 cancers in 185 countries," *CA: a Cancer Journal for Clinicians*, vol. 68, no. 6, pp. 394–424, 2018.

[7] M. K. Gupta and J. Robbins, "Making the connections: autophagy and post-translational modifications in cardiomyocytes," *Autophagy*, vol. 12, no. 11, pp. 2252-2253, 2016.

[8] Z.-J. Han, Y.-H. Feng, B.-H. Gu, Y.-M. Li, and H. Chen, "The post-translational modification, sumoylation, and cancer (review)," *International Journal of Oncology*, vol. 52, no. 4, pp. 1081–1094, 2018.

[9] S. Bergink and S. Jentsch, "Principles of ubiquitin and sumo modifications in DNA repair," *Nature*, vol. 458, no. 7237, pp. 461–467, 2009.

[10] T. M. Thomson and M. Guerra-Rebollo, "Ubiquitin and sumo signalling in DNA repair," *Biochemical Society Transactions*, vol. 38, no. 1, pp. 116–131, 2010.

[11] H. D. Ulrich, "Ubiquitin and sumo in DNA repair at a glance," *Journal of Cell Science*, vol. 125, no. 2, pp. 249–254, 2012.

[12] S. P. Jackson and D. Durocher, "Regulation of DNA damage responses by ubiquitin and sumo," *Molecular Cell*, vol. 49, no. 5, pp. 795–807, 2013.

[13] P. Sarangi and X. Zhao, "Sumo-mediated regulation of DNA damage repair and responses," *Trends in Biochemical Sciences*, vol. 40, no. 4, pp. 233–242, 2015.

[14] M. Serpente, C. Fenoglio, S. M. Cioffi et al., "Profiling of ubiquitination pathway genes in peripheral cells from patients with frontotemporal dementia due to c9orf72 and grn mutations," *International Journal of Molecular Sciences*, vol. 16, no. 1, pp. 1385–1394, 2015.

[15] M. L. H. Katayama, F. S. Pasini, M. A. A. K. Folgueira, I. M. L. Snitcovsky, and M. M. Brentani, "Molecular targets of $1,25(OH)_2D_3$ in HC11 normal mouse mammary cell line," *The Journal of Steroid Biochemistry and Molecular Biology*, vol. 84, no. 1, pp. 57–69, 2003.

[16] Y. Guo, P. Fu, H. Zhu et al., "Correlations among ercc1, xpb, ube2i, egf, tal2 and ilf3 revealed by gene signatures of histological subtypes of patients with epithelial ovarian cancer," *Oncology Reports*, vol. 27, no. 1, pp. 286–292, 2012.

[17] A. Poleshko, A. V. Kossenkov, N. Shalginskikh et al., "Human factors and pathways essential for mediating epigenetic gene silencing," *Epigenetics*, vol. 9, no. 9, pp. 1280–1289, 2014.

[18] K. Jung, J.-H. Kim, H. S. Cheong et al., "Gene expression profile of necrotizing enterocolitis model in neonatal mice," *International Journal of Surgery*, vol. 23, no. Part A, pp. 28–34, 2015.

[19] D. S. Chandrashekar, B. Bashel, S. A. H. Balasubramanya et al., "Ualcan: a portal for facilitating tumor subgroup gene expression and survival analyses," *Neoplasia*, vol. 19, no. 8, pp. 649–658, 2017.

[20] Z. Tang, C. Li, B. Kang, G. Gao, C. Li, and Z. Zhang, "Gepia: a web server for cancer and normal gene expression profiling and interactive analyses," *Nucleic Acids Research*, vol. 45, no. W1, pp. W98–W102, 2017.

[21] T. Li, J. Fan, B. Wang et al., "Timer: a web server for comprehensive analysis of tumor-infiltrating immune cells," *Cancer Research*, vol. 77, no. 21, pp. e108–e110, 2017.

[22] B. Li, E. Severson, J.-C. Pignon et al., "Comprehensive analyses of tumor immunity: implications for cancer immunotherapy," *Genome Biology*, vol. 17, no. 1, pp. 1–16, 2016.

[23] J. Gao, B. A. Aksoy, U. Dogrusoz et al., "Integrative analysis of complex cancer genomics and clinical profiles using the cbioportal," *Science Signaling*, vol. 6, no. 269, p. pl1, 2013.

[24] E. Cerami, J. Gao, U. Dogrusoz et al., "The cbio cancer genomics portal: an open platform for exploring multidimensional cancer genomics data," *Cancer Discovery*, vol. 2, no. 5, pp. 401–404, 2012.

[25] G. Bindea, B. Mlecnik, H. Hackl et al., "Cluego: a cytoscape plug-in to decipher functionally grouped gene ontology and pathway annotation networks," *Bioinformatics*, vol. 25, no. 8, pp. 1091–1093, 2009.

[26] P. Shannon, A. Markiel, O. Ozier et al., "Cytoscape: a software environment for integrated models of biomolecular interaction networks," *Genome Research*, vol. 13, no. 11, pp. 2498–2504, 2003.

[27] D. Warde-Farley, S. L. Donaldson, O. Comes et al., "The genemania prediction server: biological network integration for gene prioritization and predicting gene function," *Nucleic Acids Research*, vol. 38, suppl_2, pp. W214–W220, 2010.

[28] D. Szklarczyk, A. L. Gable, D. Lyon et al., "String v11: protein–protein association networks with increased coverage, supporting functional discovery in genome-wide experimental datasets," *Nucleic Acids Research*, vol. 47, no. D1, pp. D607–D613, 2019.

[29] U. Alon, N. Barkai, D. A. Notterman et al., "Broad patterns of gene expression revealed by clustering analysis of tumor and normal colon tissues probed by oligonucleotide arrays," *Proceedings of the National Academy of Sciences*, vol. 96, no. 12, pp. 6745–6750, 1999.

[30] C. D. Logsdon, D. M. Simeone, C. Binkley et al., "Molecular profiling of pancreatic adenocarcinoma and chronic pancreatitis identifies multiple genes differentially regulated in pancreatic cancer," *Cancer Research*, vol. 63, no. 10, pp. 2649–2657, 2003.

[31] F. T. Bosman, F. Carneiro, R. H. Hruban, and N. D. Theise, *WHO Classification of Tumours of the Digestive System*, World Health Organization, 2010.

[32] D. Mattoscio, C. Casadio, C. Miccolo et al., "Autophagy regulates ubc9 levels during viral-mediated tumorigenesis," *PLoS Pathogens*, vol. 13, no. 3, article e1006262, 2017.

[33] D. Mattoscio and S. Chiocca, "Sumo pathway components as possible cancer biomarkers," *Future Oncology*, vol. 11, no. 11, pp. 1599–1610, 2015.

[34] A. Desai, J. Xu, K. Aysola et al., "Molecular mechanism linking brca1 dysfunction to high grade serous epithelial ovarian cancers with peritoneal permeability and ascites," *Journal of Gynecology Research*, vol. 1, no. 1, p. 1, 2015.

[35] J. Xu, A. Footman, Y. Qin et al., "Brca1 mutation leads to deregulated ubc9 levels which triggers proliferation and migration of patient-derived high grade serous ovarian cancer and triple negative breast cancer cells," *International Journal of Chronic Diseases & Therapy*, vol. 2, no. 3, pp. 31–38, 2016.

[36] J. Xu, C. Shumate, Y. Qin et al., "A novel ubc9-dependent pathway regulates sirt1-er-α axis and brca1-associated tnbc lung metastasis," *Integrative Molecular Medicine*, vol. 4, no. 4, p. 4, 2017.

[37] Y.-Y. Mo, Y. Yu, E. Theodosiou, P. Rachel Ee, and W. T. Beck, "A role for ubc9 in tumorigenesis," *Oncogene*, vol. 24, no. 16, pp. 2677–2683, 2005.

[38] S.-F. Chen, C. Gong, M. Luo, H.-R. Yao, Y.-J. Zeng, and F.-X. Su, "Ubc9 expression predicts chemoresistance in breast cancer," *Chinese Journal of Cancer*, vol. 30, no. 9, pp. 638–644, 2011.

[39] S. J. Moschos, D. M. Jukic, C. Athanassiou et al., "Expression analysis of ubc9, the single small ubiquitin-like modifier (sumo) e2 conjugating enzyme, in normal and malignant tissues," *Human Pathology*, vol. 41, no. 9, pp. 1286–1298, 2010.

[40] S. Moschos, A. Smith, M. Mandic et al., "Sage and antibody array analysis of melanoma-infiltrated lymph nodes: identification of ubc9 as an important molecule in advanced-stage melanomas," *Oncogene*, vol. 26, no. 29, pp. 4216–4225, 2007.

[41] F. Wu, S. Zhu, Y. Ding, W. T. Beck, and Y.-Y. Mo, "MicroRNA-mediated regulation of ubc9 expression in cancer cells," *Clinical Cancer Research*, vol. 15, no. 5, pp. 1550–1557, 2009.

[42] J. Galon, M. Dieu-Nosjean, E. Tartour, C. Sautes-Fridman, and W. Fridman, "Immune infiltration in human tumors: a prognostic factor that should not be ignored," *Oncogene*, vol. 29, no. 8, pp. 1093–1102, 2010.

[43] A. Meeker and C. Heaphy, "Gastroenteropancreatic endocrine tumors," *Molecular and Cellular Endocrinology*, vol. 386, no. 1-2, pp. 101–120, 2014.

[44] S. B. Baylin and P. A. Jones, "Epigenetic determinants of cancer," *Cold Spring Harbor Perspectives in Biology*, vol. 8, no. 9, article a019505, 2016.

[45] P. Danaher, S. Warren, R. Lu et al., "Pan-cancer adaptive immune resistance as defined by the tumor inflammation signature (tis): results from the cancer genome atlas (tcga)," *Journal for Immunotherapy of Cancer*, vol. 6, no. 1, pp. 1–17, 2018.

[46] W. Ma, B. M. Gilligan, J. Yuan, and T. Li, "MicroRNA-26a suppresses epithelial-mesenchymal transition in human hepatocellular carcinoma by repressing enhancer of zeste homolog 2," *Journal of Hematology & Oncology*, vol. 9, no. 1, pp. 1–21, 2016.

[47] G. P. Dunn, L. J. Old, and R. D. Schreiber, "The three es of cancer immunoediting," *Annual Review of Immunology*, vol. 22, no. 1, pp. 329–360, 2004.

[48] B. Liu, C. Lu, Y.-X. Song et al., "The role of pleomorphic adenoma gene-like 2 in gastrointestinal cancer development, progression, and prognosis," *International Journal of Clinical and Experimental Pathology*, vol. 7, no. 6, pp. 3089–3100, 2014.

[49] P. Hohenberger and S. Gretschel, "Gastic cancer," *The Lancet*, vol. 362, no. 9380, pp. 305–315, 2003.

[50] M. Stolte, E. Bayerdörffer, A. Morgner et al., "Helicobacter and gastric malt lymphoma," *Gut*, vol. 50, Supplement 3, pp. iii19–iii24, 2002.

[51] C. G. Clemente, M. C. Mihm Jr., R. Bufalino, S. Zurrida, P. Collini, and N. Cascinelli, "Prognostic value of tumor infiltrating lymphocytes in the vertical growth phase of primary cutaneous melanoma," *Cancer*, vol. 77, no. 7, pp. 1303–1310, 1996.

[52] K. Schumacher, W. Haensch, C. Röefzaad, and P. M. Schlag, "Prognostic significance of activated cd8+ t cell infiltrations within esophageal carcinomas," *Cancer Research*, vol. 61, no. 10, pp. 3932–3936, 2001.

[53] L. Zhang, J. R. Conejo-Garcia, D. Katsaros et al., "Intratumoral t cells, recurrence, and survival in epithelial ovarian cancer," *New England Journal of Medicine*, vol. 348, no. 3, pp. 203–213, 2003.

Hindawi
Oxidative Medicine and Cellular Longevity
Volume 2022, Article ID 8385456, 11 pages
https://doi.org/10.1155/2022/8385456

Research Article

Cefazolin/BMP-2-Loaded Mesoporous Silica Nanoparticles for the Repair of Open Fractures with Bone Defects

Mingkui Shen, Lulu Wang, Li Feng, Chuangye Xu, Yi Gao, Sijing Li, Yulan Wu, and Guoxian Pei

School of Medicine, Southern University of Science and Technology, Shenzhen, 518055 Guangdong, China

Correspondence should be addressed to Guoxian Pei; peigx@sustech.edu.cn

Received 6 July 2022; Revised 20 August 2022; Accepted 28 August 2022; Published 20 September 2022

Academic Editor: Shao Liang

The study aimed to explore the feasibility of a nanodrug delivery system to treat open fractures with bone defects. We developed a cefazolin (Cef)/bone morphogenetic protein 2 (BMP-2)@mesoporous silica nanoparticle (MSN) delivery system; meanwhile, Cef/MBP-2@ poly(lactic-co-glycolic acid) (PLGA) was also developed as control. For the purpose of determining the osteogenic and anti-inflammatory actions of the nanodelivery system, we cultured bone marrow mesenchymal stem cells (BMSCs) and constructed a bone defect mouse model to evaluate its clinical efficacy. After physicochemical property testing, we determined that MSN had good stability and did not easily accumulate or precipitate and it could effectively prolong the Cef's half-life by nearly eight times. In BMSCs, we found that compared with the PLGA delivery system, MSNs better penetrated into the bone tissue, thus effectively increasing BMSCs' proliferation and migration ability to facilitate bone defect repair. Furthermore, the MSN delivery system could improve BMSCs' mineralization indexes (alkaline phosphatase [ALP], osteocalcin [OCN], and collagen I [Col I]) to effectively improve its osteogenic ability. Moreover, the MSN delivery system could inhibit inflammation in bone defect mice, which was mainly reflected in its ability to reduce the release of IL-1β and IL-4 and increase IL-10 levels; it could also effectively reduce apoptosis of $CD4^+$ and $CD8^+$ T cells, thus improving their immune function. Furthermore, the percentage of new bones, bone mineral density, trabecular volume, and trabecular numbers in the fracture region were improved in mice treated with MSN, which allowed better repair of bone defects. Hence, Cef/BMP-2@MSN may be feasible for open fractures with bone defects.

1. Introduction

Recent years have witnessed a rising incidence of multiple and compound injuries that are mostly complicated with open limb fractures due to increasing traffic accidents [1]. As patients' fracture ends are combined with bone defects and are easily polluted, delayed healing and even chronic osteomyelitis may occur at the fracture end during the long-term healing process [2]. To achieve stable fixation effects and promote rapid recovery from the disease, it is often necessary to select appropriate materials to fill the bone defects. At present, mainly autologous and allogeneic bones are used for filling, with which good clinical results have been achieved [3]. However, there are also deficiencies. For example, autologous bone transplantation can cause injuries on the bone removal site [4], whereas transplantation of allogeneic bone may lead to rejection [5]. Therefore, the development of filling materials with bone induction and bone conduction ability would be key to treating open fractures complicated by bone defects. In addition, although these wounds have been thoroughly debrided, in large and deep wounds, a few foreign bodies might accumulate in both soft and bone tissue, resulting in wound inflammation and even osteomyelitis later in the healing process [6]. Therefore, if the filling material would have antibacterial effects or could include antibiotics, it could have an effective sterilizing effect in the marrow cavity and could effectively promote wound healing. Recent progress in tissue bioengineering has allowed solving the above issues.

In tissue bioengineering, seed cells, scaffold materials, and associated growth factors are often combined to repair

bone defects [7]. Bone marrow mesenchymal stem cells (BMSCs), with potent repair ability and multidirectional differentiation potential, are commonly used as seed cells for bone repair [8]. Therefore, stimulating the effective BMSC differentiation into osteoblasts (OBs) is the key to promoting the repair of bone defects [9]. Bone morphogenetic protein 2 (BMP-2) has been reported to effectively shorten the healing time of fractured mice and increase bone mineral density (BMD) and trabecular thickness at the bone defect [10]. In a follow-up study, the BMP-2-activated SMDA signaling pathway was found to promote related functional protein levels, thus enabling BMSCs' differentiation into OBs, the initiation of the entire osteogenesis process [11, 12]. Therefore, the combination of BMP-2 and BMSCs can effectively enhance the proliferative and osteogenic ability of BMSCs, which could, in turn, promote bone defect healing [13, 14].

To effectively colonize BMP-2 in the marrow cavity and to achieve continuous release, we chose mesoporous silica nanoparticles (MSNs) as BMP-2's transmission carrier. MSN has a large spatial structure inside, which can effectively load BMP-2 [15]. Simultaneously, its adjustable pore structure can well regulate the release rate of BMP-2 to be continuous in the marrow cavity [16]. In addition, MSN has good modifiability [17]. By modifying a variety of superficial functional groups, MSN can achieve pH response characteristics and anti-inflammatory effects [18, 19] to further improve the transmission efficiency and curative effect of the loaded drugs.

In addition, chronic inflammation will stimulate osteoclasts to increase their activity, inhibiting the formation of a new bone [20]. Due to deep wound and serious tissue pollution, bacterial infection is easy to occur in the therapy of open fracture with bone defect; therefore, systemic antibiotic treatment is required at the same time. Cefazolin (Cef), as the first generation β-lactam antibiotics, can destroy the bacterial cell wall to kill them. Cef has good sensitivity to varieties of G^+ bacteria and can also inhibit G^- bacterial infection, which is one of the representative antibiotics in clinic and has a wide range of clinical indications. Unfortunately, the systemic use of antibiotics can hardly reach an effective inhibitory concentration in the marrow cavity. A previous study reported Cef concentration in infected bone tissue approximately 10 times lower than that in serum [21]. In addition, bacteria will adhere to the implant surface to form a biofilm to further resist the penetration of Cef, thereby reducing the clinical therapeutic effect. To overcome the above limitations of Cef and minimize the risk of treatment failure, we loaded Cef into MSN, which can effectively reduce losses during transportation and can reduce the adverse reactions caused by excessive systemic use. Conversely, it is more conducive to reaching effective inhibitory concentration in the marrow cavity and effectively inhibits the inflammatory reaction, which could increase the treatment outcome of the MSN delivery system for open fractures complicated by bone defects [22]. In this study, we investigated the role of Cef and BMP-2-loaded MSN in repairing open fractures complicated by bone defects.

2. Data and Methods

2.1. Cef/BMP-2@MSN Preparation

2.1.1. MSN Synthesis. After dissolving hexadecyltrimethylammonium bromide (CTAB) (3 g; H5882-100G, Sigma-Aldrich, USA) in 300 mL of dH_2O, the pH of the solution was prepared to 11 by adding NaOH. Following 15 min of stirring that maintained at 50°C, tetraethyl orthosilicate (TEOS) (3 g; 333859-25ML, Sigma-Aldrich) was further placed to the above mixture for another 2 h of stirring. The supernatant was removed after centrifugation (3,000 rpm), and the resulting precipitate was treated with two rinses with dH_2O and alcohol. Then, the CTAB in the above particles were removed by continuous thermal (550°C) degradation for 4 h. After vacuum drying, MSNs were collected and its FTIR spectrum was measured by ATR.

2.1.2. Cef and BMP-2 Loading into MSNs. Cef (20 mg) was dissolved in acetate buffer at pH 5 and adjusted to 10 mg/mL. Then, 200 mg of MSN was dissolved in 4 mL of the above configuration solution. After magnetic stirring (300 rpm) for 2 h at 26°C, Cef was loaded into MSN using the concentrated solution adsorption method, and then, 1 mL of BMP-2 solution (10 mg/mL; ab80798, Abcam, USA) was put into the above mixture. After ultrasonic emulsification for 5 min, Cef/BMP-2@MSNs were obtained by vacuum drying, and they were washed twice with PBS (Figure 1). Cef/BMP-2@MSN was then freeze-dried and finally stored at 4°C.

Meanwhile, based on the conventional protocol, we assembled poly(lactic-co-glycolic acid) (PLGA) (S24436, Shanghai Yuanye Bio-Technology Co., Ltd) with Cef and BMP-2 to build the BMP-2@PLGA delivery system as a control. Briefly, 20 mg of Cef was dissolved in methanol solution (1:2) and added to PLGA liquid dissolved in dichloromethane (270997, Sigma-Aldrich). After magnetic stirring (35000 rpm, 40 s), the above polymer solution was added into PVA (0.5%, 3 mL, 38534, Sigma-Aldrich) for further emulsification, and then, 1 mL of BMP-2 solution (10 mg/mL) was placed to the above mixture. After further emulsification of the mixture for 5 minutes, dichloromethane was wiped off with the help of rotary evaporation (RV-211M, Shanghai Yiheng Scientific Instrument Co., Ltd., China) [23, 24]. At last, the above emulsion solution was vacuum dried to obtain Cef/BMP-2@PLGA, and they were washed three times with dH_2O and freeze-dried at 4°C.

2.2. Cell Culture. Mice BMSCs (MUBMX-01001, Cyagen, Guangzhou, China) planted in the wells of 24-well plates were cultivated for 24 h with mice BMSC specific medium (MUXMX-90011, Cyagen) placed in a cell incubator (51032124, Thermo Fisher Scientific, Waltham, MA, USA) under 5% CO_2 and at 37°C. The cultured cells were then diluted to a 4×10^4/mL solution for further use.

2.3. Bone Defect Mouse Model Building. Nine 8-week-old male C56BL/6 J mice (Jiangsu Jicui Yaokang Biotech, China), weighting 120–150 g, were purchased for bone defect animal model building. After anesthesia with

ketamine, a 2 cm incision was created on the mouse thigh skin and the femur was fully exposed through layer-by-layer cutting of the subcutaneous tissue. The middle femur was cut off with a wire saw, and the space between fracture ends was expanded. Then, a 25 g needle was inserted into the femoral marrow cavity for fixation, and the wound was sutured layer by layer. Postoperatively, the mice were kept warm on a heating pad until they could move again. Eventually, bone defect mice were successfully modeled. The above mouse models were further assigned to the control, PLGA, and MSN groups, for saline, Cef/BMP-2@PLGA, and Cef/BMP-2@MSN injection into the lesion site every three days for 2 weeks, respectively. The experiment, ratified by the Experimental Animal Ethics Committee of Medical College of South University of Science and Technology, was carried out following the Chinese guidelines for the care and use of laboratory animals.

2.4. Physicochemical Characterization of Cef/BMP-2@MSN

2.4.1. Stability Test. The stability of an in vivo nanodelivery system is important for smooth drug delivery to the target. In this study, Cef/BMP-2@MSN was immersed in PBS and PBS + 10% serum to simulate the in vivo environment, and the size of the Cef/BMP-2@MSN particles was observed under a scanning electron microscope (SP8, Leica, Wetzlar, Germany). Further, to better show the in vivo stability of the MSN delivery system, Cef/BMP-2@MSNs were coupled with Cy5 and dissolved in PBS + 10% serum. Then, to test the production of sediment, their fluorescence intensity was observed at 0, 24, 48, and 72 h.

2.4.2. Cef's Half-Life Determination. To determine the half-life of Cef, 20 mg of Cef/BMP-2@MSN and Cef/BMP-2@PLGA was mixed with PBS at 37°C and centrifuged (1,000 rpm) to collect the supernatant. Cef concentration was determined by HPLC.

2.4.3. Permeability Test. Before testing Cef/BMP-2@MSNs' therapeutic effects, we tested their permeability in bone tissue by observing the fluorescence intensity of Cef/BMP-2@MSN-Cy5. Eight-week-old male C56BL/6J mice were divided into the MSN and PLGA groups that were subjected to Cef/BMP-2@MSN-Cy5 and Cef/BMP-2@PLGA-Cy5 injection into the bone marrow cavity of the mouse femoral shaft, respectively. After 24 h, the injection site was dissected for observation of Cy5-labeled cells under a confocal microscope (FV3000, OLYMPUS, Japan). Stronger infiltration capacity is indicated if the cells are more brightly labeled.

2.5. Cell Viability and Apoptosis Assays. The ability of BMSCs in repairing bone defects can be evaluated by detecting their proliferation activity and apoptosis. BMSCs, 1 mL of dilution as prepared in Section 2.2, were added to a 12-well plate with mouse BMSC specific medium and split into the control, PLGA, and MSN groups that were given no treatment, Cef/BMP-2@PLGA, and Cef/BMP-2@MSN, respectively. After culturing in a cell incubator for 24 h, we first observed the cell density under a differential interference contrast (DIC) microscope (MX8R, Dongguan Beitesen Precision Instrument Co., Ltd., China). Then, anti-ki67 and anti-caspase-3 (Abcam, USA; ab15580, ab32351) were used to label the active cells in each group and mark apoptotic BMSCs, respectively. Cell viability was observed with a confocal microscope.

2.6. Cell Migration Detection. To detect BMSC migration in the different groups, 1 mL of BMSC dilution from Section 2.2 was added to a 12-well plate with mouse BMSC specific medium and groups as the control, PLGA, and MSN groups for no treatment, Cef/BMP-2@PLGA intervention, and Cef/BMP-2@MSN intervention, respectively. After culturing in a cell incubator for 24 h, a pipette gun was used to scratch the cell layer, and then, the BMSCs on the scratch were washed out with PBS. After culturing with serum-free medium (10743011, Thermo Fisher Scientific, USA) for another 24 h, BMSC migration at the scratch was observed microscopically, and the total number of migrating BMSCs was calculated.

2.7. Mineralization and Osteogenesis Characterization. During bone repair, the mineralization and osteogenesis of BMSCs also play a vital part. Therefore, we measured their mineralization ability by immunofluorescence (IF) of alkaline phosphatase (ALP), osteocalcin (OCN), and collagen I (Col I). AP-TNAP ALPL polyclonal antibody Cy3 conjugated and OCN antibody FITC conjugated (both from Nanjing Chuanbo Biotech, China; C03321Cy3, C05448F) as well as anti-collagen I/FITC (Shanghai Weimeng Biotech, China) were used for staining on days 4 and 7 after culture, and the fluorescence intensity was observed using a confocal microscope. ALP, OCN, and Col I mRNA levels of each group were quantified by PCR. In brief, the total RNA of the above indicators in cells was isolated first, and then reverse transcribed into cDNA. β-Actin was chosen as the internal parameter of ALP, OCN, and Col I, and their relative expressions were calculated by $2^{-\triangle\triangle Ct}$ method. See Table 1 for the primer information.

2.8. Detection of Immunoinflammatory Responses in Our Mouse Model. To evaluate the inflammatory response in bone defect mouse models, tail venous blood of mice was extracted on the 4th day after treatment. The supernatant was collected via centrifugation (1,000 rpm) to detect IL-1β, IL-4, and IL-10 levels by ELISA. Mouse IL-1 beta ELISA Kit (ab197742), Mouse TNF alpha ELISA Kit (ab100747), and Mouse IL-10 ELISA Kit (ab255729) were purchased from Abcam. For immune function detection, the blood samples of mice were collected to separate peripheral blood mononuclear cells (PBMC) by density gradient centrifugation, and PBMC concentration was adjusted to 1×10^6/mL with binding buffer solution. A PBMC suspension (100 μL) was transferred to a 5 mL PE tube, and PE Anti-CD4 antibody [EPR20122] (ab252151) and Alexa Fluor® 647 anti-CD8 alpha antibody [EPR21769] (ab237365) were used to separately label CD4 and CD8. Then, 5 μL of annexin V-FITC and 5 μL of propidium iodide were placed to the above mixture solution. After mixing and incubating in the dark for

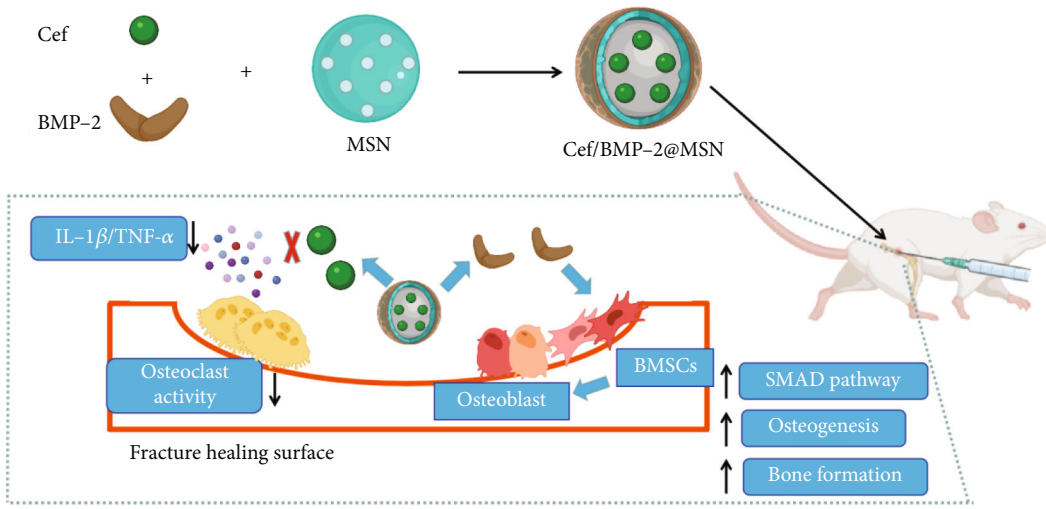

Figure 1: Schematic diagram of the assembly process and mechanism of Cef/BMP-2@MSN.

Table 1: Primer information of PCR.

	F primer	R primer
ALP	5′-AACCCAGACACAAGCATTCC-3′	5′-CCAGCAAGAAGAAGCCTTTG-3′
OCN	5′-CAGGGCAGTAACTTATCTTG-3′	5′-CCTGAACCAAGCCTTACTCA-3′
Col I	5′-CACCCTCAAGAGCCTGAGTC-3′	5′-CGGGCTGATGTACCAGTTCT-3′
β-Actin	5′-CTGGCACCACACCTTCTACA-3′	5′-GGTACGACCAGAGGCATACA-3′

15 min, flow cytometry (Attune CytPix, Thermo Fisher Scientific) was used to detect lymphocyte apoptosis.

2.9. Therapeutic Effect Detection of Cef/BMP-2@MSN. Four and seven weeks after treatment, mice were killed and their femurs were excised and stored at −20°C. First, a macroscopic image of the specimen was observed, including callus formation and fracture line healing at the fracture end. Second, femoral specimens were scanned with microcomputed tomography (CT, Skyscan 1272, Bruker, Belgium), and the plane pixel resolution was set to 2,048 × 2,048, with a layer spacing of 16 μm. The proximal fracture (a thickness of 0.5 mm) from scanned images was selected for detection, and the percentage of new bones, BMD, trabecular volume (TBV), and average trabecular number (TB.N) were observed. The BMD and percentage of new bones were obtained indirectly by voxel quantitation of CT scanning images.

2.10. Statistical Methods. SPSS 23.0 and prism were used for data processing. The inter-group differences of measurement data, denoted by ($\bar{x} \pm s$), were tested by the t test, with $P < 0.05$ indicating the presence of significance.

3. Results and Discussion

3.1. Characteristics of the Cef/BMP-2@MSN Delivery System. The FTIR spectrum of synthesized MSN showed that there were absorption peaks at 1095 cm^{-1} and 905 cm^{-1}, which were anti-symmetric and symmetric stretching vibrations of Si-O-Si; meanwhile, the absorption peak at 968 cm^{-1} was the bending vibration of Si-OH, which was consistent with the FTIR spectrum of MSN previously reported [25]. The stability of the nanodelivery system can significantly improve drug delivery efficiency. As shown in Figure 2(a), the Cef/BMP-2@MSN was about 240 nm in size, with the ability to maintain a stable size in both the PBS and serum; only a few precipitates could be detected after fluorescein binding (Figure 2(b)). Otherwise, Cef's half-life significantly influenced the dosage and duration of drug administration. The nanodelivery system effectively prolonged Cef's half-life by eight times in the MSN group (Figure 2(c)). Thus, MSN can remain stable while improving the half-life of Cef during in vivo delivery.

3.2. Cef/BMP-2@MSN Could Penetrate the Bone Tissue. The permeability of nanodelivery systems in bone tissue is key to improve drug efficacy. As shown in Figures 3(a) and 3(b), more MSNs permeated the bone tissue than PLGA. Quantitatively, MSN showed higher fluorescence intensity than PLGS in bone tissue (Figure 3(c)). Therefore, MSN could better transfer Cef and BMP-2 to the bone tissue.

3.3. Cef/BMP-2@MSN Could Increase BMSC Activity. A high BMSC activity can improve the efficiency of bone repair. As shown in Figures 4(a)–4(c), we found that BMSCs proliferated more and arranged more closely under DIC. Moreover, PLGA and MSN-treated BMSCs, especially MSN-treated ones, showed higher fluorescence intensity than the control

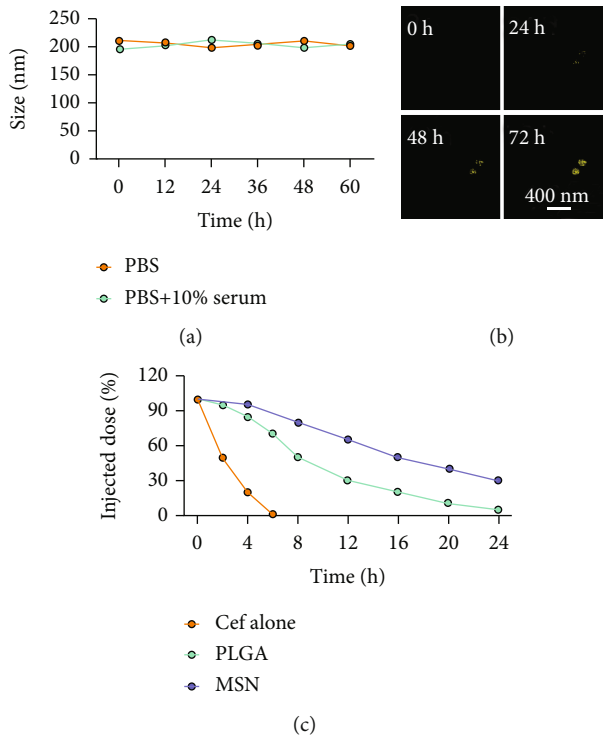

Figure 2: Physicochemical characterization of Cef/BMP-2@MSN. (a) Cef/BMP-2@MSN stability in different media. (b) Precipitate numbers of Cef/BMP-2@MSN-Cy5 standing in serum for certain hours. (c) Half-life period test of Cef in MSN and PLGA.

group (Figures 4(d)–4(f)). The above results suggest a higher ability of MSN to promote BMSC proliferation.

3.4. Cef/BMP-2@MSN Could Reduce BMSC Apoptosis. The apoptotic degree of BMSCs can reflect the repair ability of bone defects. The PLGA and MSN groups exhibited higher fluorescence intensities than the control group, especially the MSN group (Figure 5), demonstrating the ability of MSN to better suppress BMSC apoptosis.

3.5. Cef/BMP-2@MSN Could Increase BMSC Mobility. BMSC mobility can reflect the bone induction and bone conduction ability of nanodelivery systems. Compared with the control group (Figure 6(a)), more BMSCs migrated to the scratch area in the PLGA and MSN groups, especially in the MSN group (Figures 6(b) and 6(c)). Quantitative analysis showed that the MSN group had a higher number of migrating BMSCs and area of displacement than the control group (Figures 6(d) and 6(e)).

3.6. BMSC Mineralization and Osteogenesis Significantly Increased in the MSN Group. BMSC mineralization and osteogenesis can effectively reflect the maturity of OBs. Hence, we evaluated the osteogenic capacity of the MSN delivery system by measuring the levels of osteogenic genes (ALP, OCN, and Col I). After 7 days of culture, the MSN group showed higher fluorescence intensities of those markers than the control and PLGA groups (Figures 7(a)–7(i)). Quantitative analysis also determined higher ALP,

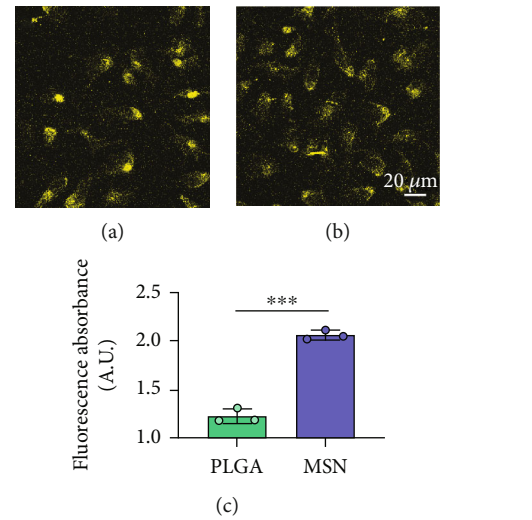

Figure 3: Infiltration of Cef/BMP-2@MSN in bone marrow tissue. (a) Infiltration of PLGA. (b) Infiltration of MSN. (c) Quantitative fluorescence evaluation of PLGA-Cy5 and MSN-Cy5 in bone tissue. $*** P < 0.001$.

OCN, and Col I mRNA levels in the MSN group (Figures 7(j)–7(l)). It indicates that MSN can better increase the osteogenic capacity of BMSCs.

3.7. The Immune Function of Mice Significantly Improved in the MSN Group. For the treatment of open fractures, inhibiting inflammatory reactions and improving immunity are important for promoting bone repair. IL-1β and TNF-α levels were lower, while IL-10 was higher in the MSN group compared with the control group (Figures 8(a)–8(c)). In terms of immune function, the levels of apoptotic $CD4^+$ and $CD8^+$ lymphocytes clearly decreased in the MSN and PLGA groups versus the control group (Figures 8(d) and 8(e)). Therefore, MSN is able to better transport Cef to bone tissue to inhibit inflammation and enhance immune function.

3.8. MSN Delivery System Could Better Accelerate Bone Defect Repair. We developed bone defect mouse models to further evaluate MSN's repair ability. As shown in Figure 9(a), MSN could better promote callus formation at the fracture end of bone defect mice and could blur the fracture line, and PLGA could only partly improve the lesions. Otherwise, we quantitatively evaluated the bone defect repair ability of MSN by the percentage of new bones, BMD, TBV, and TB.N, and found them improved in mice models treated with MSN (Figures 9(b)–9(e)). Therefore, MSN can better speed up bone defect repair.

4. Discussion

The development of bioengineering technology allows new therapeutic options for a variety of diseases, including open fractures with bone defects [26]. Biomaterials can be implanted into bone defects and can serve as a scaffold for osteoblast adhesion while improving bone induction and conduction [27]. Moreover, biomaterials can be loaded with

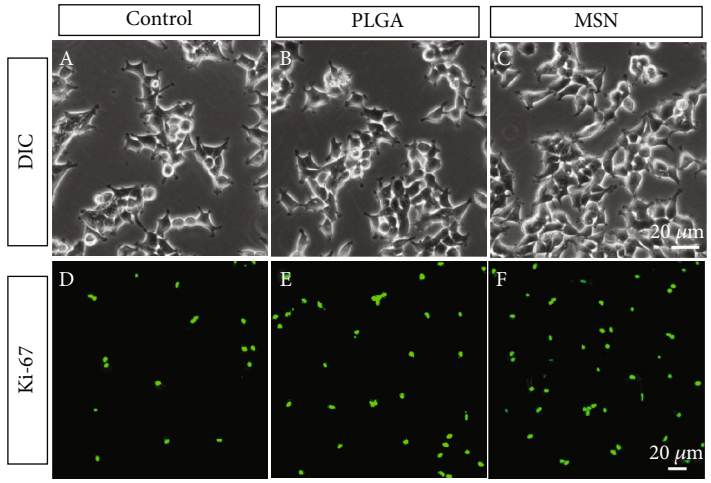

Figure 4: BMSC viability assessment. (a–c) DIC image of BMSCs in the control, PLGA, and MSN groups on day 7. (d–f) Anti-Ki67 expression pattern in the control, PLGA, and MSN groups on the 7th day.

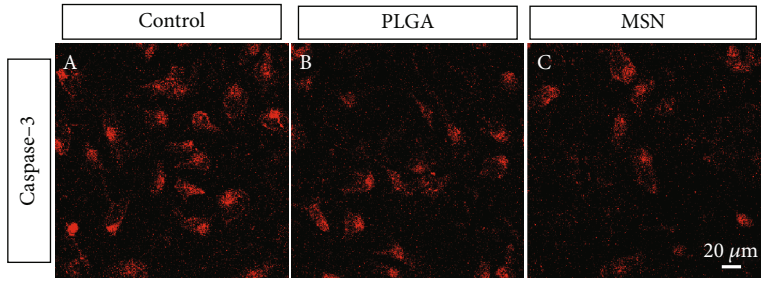

Figure 5: BMSC apoptosis detection. Expression patterns of anti-caspase-3 in the control group (a), PLGA group (b), and MSN group (c).

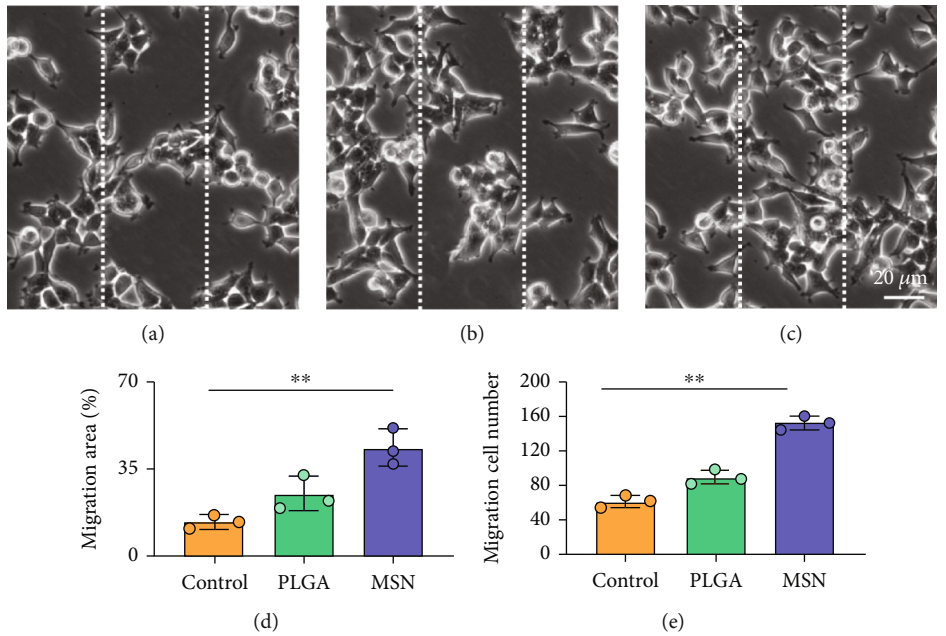

Figure 6: Scratch test of BMSCs in different groups. (a) BMSCs without any treatment. (b) BMSCs treated with PLGA. (c) BMSCs treated with MSN. (d) Quantitative evaluation of BMSC migration range in the three groups. (e) Quantitative evaluation of BMSC migration number in the three groups. $**P < 0.01$.

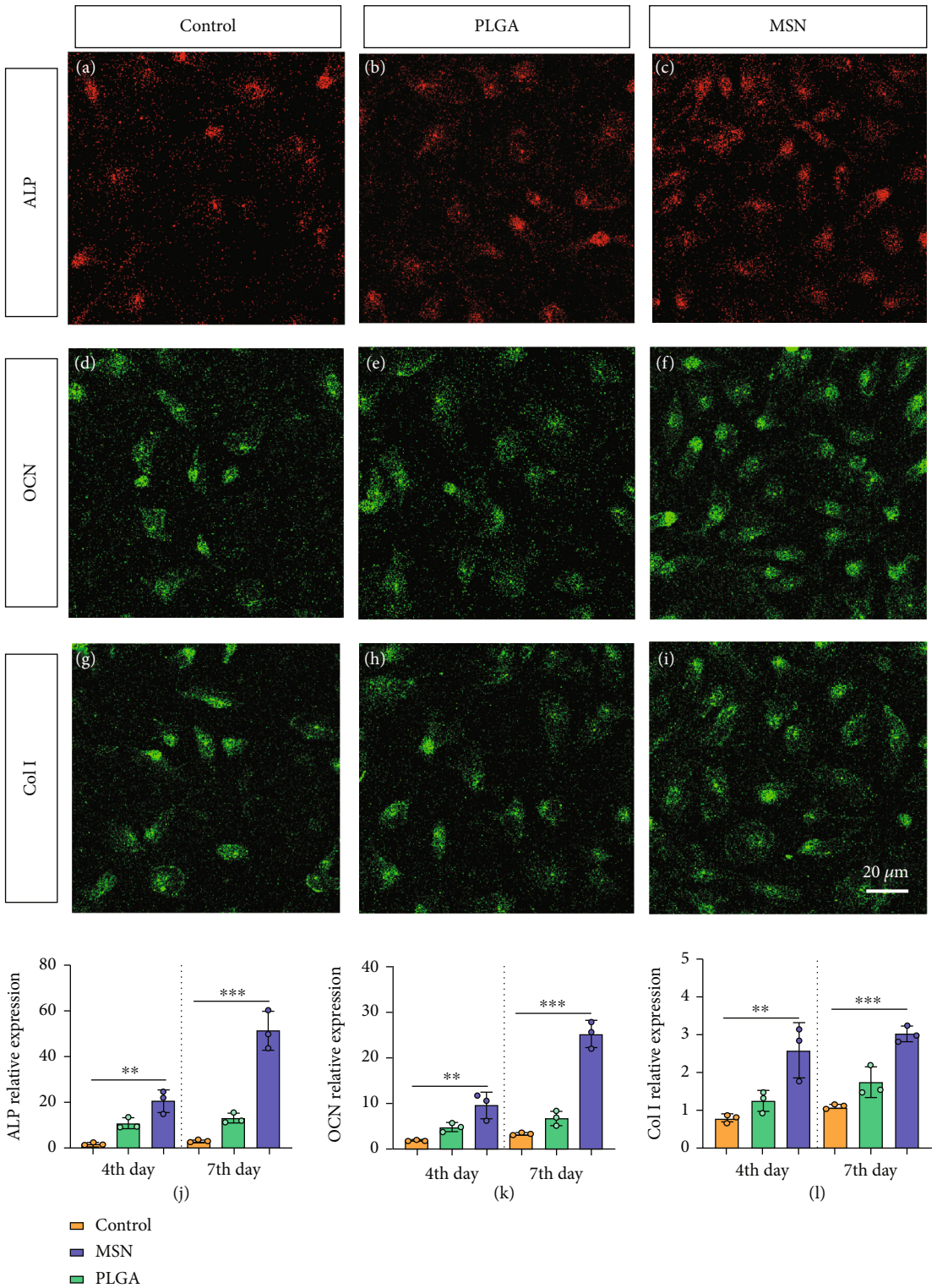

Figure 7: Osteogenic gene measurements. (a–c) ALP fluorescent staining. (d–f) OCN fluorescent staining. (g–i) Col I fluorescent staining. (j–l) Quantification of ALP, OCN, and Col I relative expression in the control, PLGA, and MSN groups. $^{**}P < 0.01$; $^{***}P < 0.001$.

antibiotics and growth factors according to the treatment needs to enhance the antibacterial and osteogenic effects of scaffold materials [28]. For example, Chatzipetros et al. [29] used composite scaffold material made of nanohydroxyapatite (nHA)/chitosan to fill and repair rat calvarial defects model. At 4 weeks after operation, a large number of new bones were found to form around the scaffold, which can promote the fusion of scaffold material and host bone and further ensure its stability. At 8 weeks after operation, massive new bone formed in the scaffold material, which

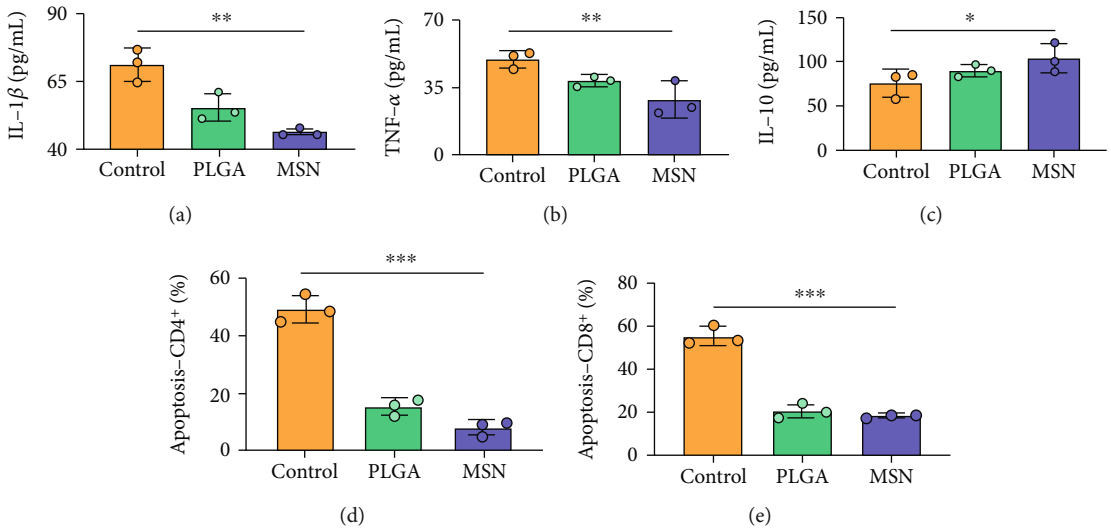

Figure 8: Immunoinflammatory response in mouse models. (a) Comparison of serum IL-1β. (b) Comparison of serum TNF-α. (c) Comparison of serum IL-10. (d) Comparison of $CD4^+$ T cell apoptosis. (e) Comparison of serum $CD8^+$ T cell apoptosis. $*P < 0.05$; $**P < 0.01$; $***P < 0.001$.

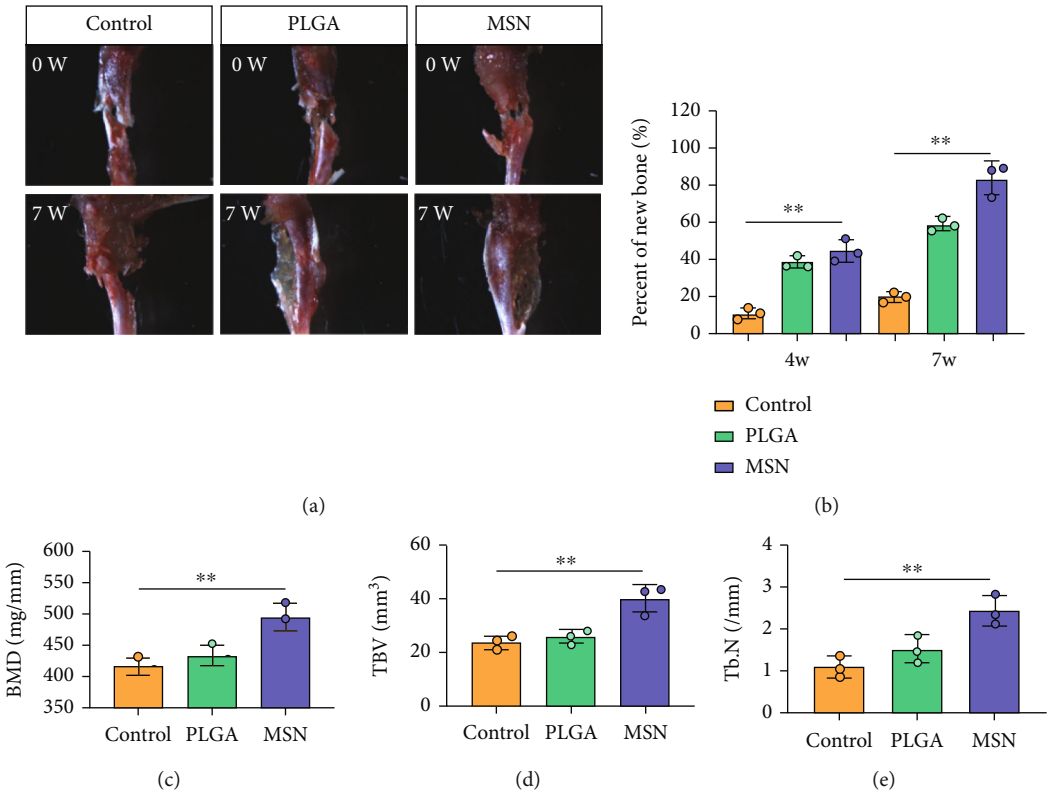

Figure 9: Therapeutic effects of Cef/BMP-2@MSN on bone defects. (a) Macroscopic findings of lesions in bone defect mice treated with saline, PLGA, or MSN. (b) Percentage of new bones at the fracture end in bone defect mice treated with saline, PLGA, or MSN. (c) BMD of lesions in bone defect mice treated with saline, PLGA, or MSN. (d) TBV of lesions in bone defect mice treated with saline, PLGA, or MSN. (e) TB.N of lesions in bone defect mice treated with saline, PLGA, or MSN. $**P < 0.01$.

further confirmed its bone induction and osteogenesis. In vitro test, Kuang et al. [30] further loaded levofloxacin on the three-dimensional composite scaffold made of MSN/nHA/polyurethane, which effectively improved the anti-infection ability of the scaffold and reduced the adhesion of bacteria, so as to give better play to its effect in bone defect repair. Therefore, biomaterials provide a new direction for treating open fractures complicated by bone defects.

In this study, we used MSN loaded BMP-2 and Cef to form composite scaffolds for bone defect treatment, and Cef/BMP-2@MSN was found to have good stability in serum and did not easily deposit, which could improve the delivery efficiency of Cef and BMP-2 in vivo. Therefore, Cef/BMP-2@MSN could better achieve the action target, which could better promote the differentiation of BMSCs and could inhibit the occurrence of an inflammatory reaction. In addition, the use of MSN increased the half-life of Cef by nearly eight times, which could effectively reduce the Cef dosage while ensuring its anti-inflammatory effects, while effectively reducing adverse reactions by drug overdose. Furthermore, MSN could better penetrate bone tissue, allowing BMP-2 to better promote BMSC differentiation into mature OBs. At the same time, it helped in reaching an effective inhibitory concentration of Cef in the bone tissue to better avoid the occurrence of osteomyelitis.

The good proliferative activity of BMSCs is conducive to better repair bone defects. In the MSN group, we found that BMSCs were more proliferative and closely arranged, and had stronger migration ability, which consists with the research results of Liu et al. [10]. The reason may be that compared with PLGA, MSN can better load BMP-2 and improve its targeted delivery function, so that BMP-2 can better penetrate bone tissue and exert its bone induction and bone conduction ability [31–33]. As a result, BMSCs in MSN group can be promoted to better differentiate into mature OBs, which is conducive to accelerating bone defect repair time and improving curative effects [34, 35]. To better quantify the degree of osteoblast differentiation and maturation, we evaluated the mineralization ability of BMSCs in terms of ALP, OCN, and Col I, and the levels of the above indicators increased significantly in the MSN group, indicating that the MSN delivery system could better play the osteogenic function of BMP-2 to accelerate bone repair.

In addition, the inflammatory response in mouse models treated with MSN was more effectively controlled, as shown by significantly lower IL-1 and IL-4 releases and a higher IL-10 release. Further, symptoms of congestion and edema at the fracture site of mice treated with MSN were better controlled. Szewczyk et al. [36] found that in osteomyelitis therapy, Cef@MSN drug delivery system had a better antibacterial effect on *Staphylococcus aureus* strains, which is consistent with our results. This is mainly due to the fact that MSN can better target and deliver the loaded Cef to bone tissue, so as to effectively increase the concentration of antibiotics around the scaffold to reduce the incidence of infection caused by open fracture. Moreover, the control of inflammation is helpful to reduce osteoclast stimulation and promoting bone defect repair. After CT scanning, the percentage of new bones at the fracture end in the MSN group was higher, so as BMD, TBV, and mean TB.N, which further confirmed that Cef/BMP-2@MSN had a significant effect on the repair of open fractures with bone defects.

This research was limited in that it only studied the proliferative activity and mineralization ability of BMSCs after BMP-2 stimulation but did not deeply explore its underlying mechanisms. In addition, the effects of different scaffolds on the repair of bone defects were not discussed. Therefore, the above deficiencies need to be further improved in follow-up research.

5. Conclusion

With favorable in vivo stability, the Cef/BMP-2@MSN delivery system can validly prolong the half-life of Cef. In addition, it can better penetrate bone tissue. Therefore, MSN can effectively reduce the dosage of Cef while ensuring good anti-inflammatory effects and improving the activity, migration ability, and mobility of BMSCs. In bone defect, the mouse that models the MSN delivery system alleviates inflammation and enhances immunity while promoting bone repair. Therefore, Cef/BMP-2@MSN may be a good choice for treating open fractures complicated by bone defects.

Data Availability

The labeled dataset used to support the findings of this study are available from the corresponding author upon request.

Conflicts of Interest

The authors declare no competing interests.

Authors' Contributions

Mingkui Shen and Lulu Wang contributed equally to this work and are co-first authors.

Acknowledgments

This work was supported by the Research Startup Fund of Southern University of Science and Technology (Y01416214).

References

[1] M. H. Brem, M. Blanke, A. Olk et al., "Der Vacuum-assisted closure and instillation- (VAC™-Instill-)Verband," *Der Unfallchirurg*, vol. 111, no. 2, pp. 122–125, 2008.

[2] P. X. Zhang, F. Xue, Y. Dang et al., "Clinical effect of distal radius fracture treated with open reduction and internal plate fixation," *Chinese Medical Journal*, vol. 125, no. 1, pp. 140–143, 2012.

[3] C. H. Zhou, Y. Ren, H. J. Song et al., "One-stage debridement and bone transport versus first-stage debridement and second-stage bone transport for the management of lower limb post-traumatic osteomyelitis," *Journal of Orthopaedic Translation*, vol. 28, pp. 21–27, 2021.

[4] B. K. Rai, R. Vaishya, and A. K. Agarwal, "Spontaneous bone regeneration in an open segmental fracture of the forearm with extruded middle segment," *Cureus*, vol. 8, no. 9, pp. e772(1)–e772(6), 2016.

[5] H. Hasturk, A. Kantarci, T. Ohira et al., "RvE1 protects from local inflammation and osteoclastmediated bone destruction in periodontitis," *FASEB Journal*, vol. 20, no. 2, pp. 401–403, 2006.

[6] D. Mehrabani, A. Khodakaram-Tafti, H. Shaterzadeh-Yazdi, B. Zamiri, and M. Omidi, "Comparison of the regenerative effect of adipose-derived stem cells, fibrin glue scaffold, and

autologous bone graft in experimental mandibular defect in rabbit," *Dental Traumatology*, vol. 34, no. 6, pp. 413–420, 2018.

[7] H. Saeed and M. Iqtedar, "Bone marrow stromal cell (BMSC) and skeletal aging: role of telomerase enzyme," *Pakistan Journal of Pharmaceutical Sciences*, vol. 27, no. 2, pp. 321–333, 2014.

[8] D. Kou, M. Du, X. Hou et al., "Centimeter-sized biomimetic bone constructs fabricated via CBD-BMP2-collagen microcarriers and BMSC-gelatin microspheres," *Journal of Materials Chemistry B*, vol. 4, no. 3, pp. 461–470, 2016.

[9] L. Liao, B. Shi, H. Chang et al., "Heparin improves BMSC cell therapy: anticoagulant treatment by heparin improves the safety and therapeutic effect of bone marrow-derived mesenchymal stem cell cytotherapy," *Theranostics*, vol. 7, no. 1, pp. 106–116, 2017.

[10] D. B. Liu, C. Sui, T. T. Wu, L. Z. Wu, Y. Y. Zhu, and Z. H. Ren, "Association of bone morphogenetic protein (BMP)/Smad signaling pathway with fracture healing and osteogenic ability in senile osteoporotic fracture in humans and rats," *Medical Science Monitor*, vol. 24, pp. 4363–4371, 2018.

[11] Y. Pan, J. Chen, Y. Yu, K. Dai, J. Wang, and C. Liu, "Enhancement of BMP-2-mediated angiogenesis and osteogenesis by 2-N,6-O-sulfated chitosan in bone regeneration," *Biomaterials Science*, vol. 6, no. 2, pp. 431–439, 2018.

[12] J. D. Glaeser, K. Salehi, L. E. A. Kanim et al., "Anti-inflammatory peptide attenuates edema and promotes BMP-2-induced bone formation in spine fusion," *Tissue Engineering Part A*, vol. 24, no. 21-22, pp. 1641–1651, 2018.

[13] L. D. Loozen, A. Vandersteen, A. H. Kragten et al., "Bone formation by heterodimers through non-viral gene delivery of BMP-2/6 and BMP-2/7," *European Cells and Materials*, vol. 35, pp. 195–208, 2018.

[14] P. Zhou, J. Wu, Y. Xia et al., "Loading BMP-2 on nanostructured hydroxyapatite microspheres for rapid bone regeneration," *International Journal of Nanomedicine*, vol. 13, pp. 4083–4092, 2018.

[15] N. Bara, M. Eshwarmoorthy, K. Subaharan, and G. Kaul, "Mesoporous silica nanoparticle is comparatively safer than zinc oxide nanoparticle which can cause profound steroidogenic effects on pregnant mice and male offspring exposed in utero," *Toxicology and Industrial Health*, vol. 34, no. 8, pp. 507–524, 2018.

[16] Y. Hu, L. Ke, H. Chen et al., "Natural material-decorated mesoporous silica nanoparticle container for multifunctional membrane-controlled targeted drug delivery," *International Journal of Nanomedicine*, vol. 12, pp. 8411–8426, 2017.

[17] R. Rosenbrand, D. Barata, P. Sutthavas et al., "Lipid surface modifications increase mesoporous silica nanoparticle labeling properties in mesenchymal stem cells," *International Journal of Nanomedicine*, vol. 13, pp. 7711–7725, 2018.

[18] H. Wen, J. Guo, B. Chang, and W. Yang, "pH-responsive composite microspheres based on magnetic mesoporous silica nanoparticle for drug delivery," *European Journal of Pharmaceutics and Biopharmaceutics*, vol. 84, no. 1, pp. 91–98, 2013.

[19] L. Sun, X. Zhang, C. Zheng, Z. Wu, and C. Li, "A pH gated, glucose-sensitive nanoparticle based on worm-like mesoporous silica for controlled insulin release," *The Journal of Physical Chemistry: B*, vol. 117, no. 14, pp. 3852–3860, 2013.

[20] P. T. Tran, D. H. Park, O. Kim, S. H. Kwon, B. S. Min, and J. H. Lee, "Desoxyrhapontigenin inhibits RANKL-induced osteoclast formation and prevents inflammation-mediated bone loss," *International Journal of Molecular Medicine*, vol. 42, no. 1, pp. 569–578, 2018.

[21] B. Spellberg and B. A. Lipsky, "Systemic antibiotic therapy for chronic osteomyelitis in adults," *Clinical Infectious Diseases*, vol. 54, no. 3, pp. 393–407, 2012.

[22] W. F. Rodrigues, M. F. M. Madeira, T. A. da Silva et al., "Low dose of propranolol down-modulates bone resorption by inhibiting inflammation and osteoclast differentiation," *British Journal of Pharmacology*, vol. 165, no. 7, pp. 2140–2151, 2012.

[23] C. Vilos, L. A. Velasquez, P. I. Rodas et al., "Preclinical development and in vivo efficacy of Ceftiofur-PLGA microparticles," *PLoS One*, vol. 10, no. 4, pp. 1–19, 2015.

[24] Y. Ji, G. P. Xu, Z. P. Zhang, J. J. Xia, J. L. Yan, and S. H. Pan, "BMP-2/PLGA delayed-release microspheres composite graft, selection of bone particulate diameters, and prevention of aseptic inflammation for bone tissue engineering," *Annals of Biomedical Engineering*, vol. 38, no. 3, pp. 632–639, 2010.

[25] D. X. Huo, D. D. Cheng, R. J. Li, J. Liu, Y. L. Gu, and X. J. Lv, "Preparation and drug loading properties of mesoporous silicananopartical solid dispersions," *Journal of Inner Mongolia Medical University*, vol. 43, no. 5, pp. 449–460, 2021.

[26] K. Ando, S. Imagama, K. Kobayashi et al., "Effects of a self-assembling peptide as a scaffold on bone formation in a defect," *PLoS One*, vol. 13, no. 1, pp. 1–12, 2018.

[27] R. L. Stewart, J. T. Cox, D. Volgas et al., "The use of a biodegradable, load-bearing scaffold as a carrier for antibiotics in an infected open fracture model," *Journal of Orthopaedic Trauma*, vol. 24, no. 9, pp. 587–591, 2010.

[28] A. Decambron, A. Fournet, M. Bensidhoum et al., "Low-dose BMP-2 and MSC dual delivery onto coral scaffold for critical-size bone defect regeneration in sheep," *Journal of Orthopaedic Research*, vol. 35, no. 12, pp. 2637–2645, 2017.

[29] E. Chatzipetros, S. Damaskos, K. I. Tosios et al., "The effect of nano-hydroxyapatite/chitosan scaffolds on rat calvarial defects for bone regeneration," *Implant Dentistry*, vol. 7, no. 1, pp. 40(1)–40 (11), 2021.

[30] Z. Kuang, G. Dai, R. Wan et al., "Osteogenic and antibacterial dual functions of a novel levofloxacin loaded mesoporous silica microspheres/nano-hydroxyapatite/polyurethane composite scaffold," *Genes and Diseases*, vol. 8, no. 2, pp. 193–202, 2021.

[31] D. Gan, M. Liu, T. Xu, K. Wang, H. Tan, and X. Lu, "Chitosan/biphasic calcium phosphate scaffolds functionalized with BMP-2-encapsulated nanoparticles and RGD for bone regeneration," *Journal of Biomedical Materials Research: Part A*, vol. 106, no. 10, pp. 2613–2624, 2018.

[32] L. Yin, S. Yang, M. He et al., "Physicochemical and biological characteristics of BMP-2/IGF-1-loaded three-dimensional coaxial electrospun fibrous membranes for bone defect repair," *Journal of Materials Science: Materials in Medicine*, vol. 28, no. 6, pp. 1–5, 2017.

[33] Y. S. Lin and C. L. Haynes, "Impacts of mesoporous silica nanoparticle size, pore ordering, and pore integrity on hemolytic activity," *Journal of the American Chemical Society*, vol. 132, no. 13, pp. 4834–4842, 2010.

[34] F. Geiger, H. Lorenz, W. Xu et al., "VEGF producing bone marrow stromal cells (BMSC) enhance vascularization and resorption of a natural coral bone substitute," *Bone*, vol. 41, no. 4, pp. 516–522, 2007.

[35] Y. Liu, L. Ming, H. Luo et al., "Integration of a calcined bovine bone and BMSC-sheet 3D scaffold and the promotion of bone regeneration in large defects," *Biomaterials*, vol. 34, no. 38, pp. 9998–10006, 2013.

[36] A. Szewczyk, A. Skwira, A. Konopacka, R. Sądej, G. Walker, and M. Prokopowicz, "Mesoporous silica pellets as bifunctional bone drug delivery system for cefazolin," *International Journal of Pharmaceutics*, vol. 588, 2020.

Hindawi
Oxidative Medicine and Cellular Longevity
Volume 2022, Article ID 1592786, 7 pages
https://doi.org/10.1155/2022/1592786

Research Article

Effects of Antibiotics on Weight in Obese Patients after Sleeve Gastrectomy

Yisen Hou,[1] Xinzhe Zhai,[1] Xiaotao Wang,[1] Yi Wu,[1] Zhigan Lv,[2] Peng Ma,[1] Rui Yang,[1] Haoliang Zhao,[1] and Jianli Han[1]

[1]*Department of Thyroid & Bariatric Metabolic Surgery, Third Hospital of Shanxi Medical University, Shanxi Bethune Hospital, Shanxi Academy of Medical Sciences, Taiyuan, 030032 Shanxi, China*
[2]*Department of Anesthesia, Third Hospital of Shanxi Medical University, Shanxi Bethune Hospital, Shanxi Academy of Medical Sciences, Taiyuan, 030032 Shanxi, China*

Correspondence should be addressed to Jianli Han; hjl13803456545@126.com

Received 11 July 2022; Revised 29 August 2022; Accepted 8 September 2022; Published 19 September 2022

Academic Editor: Shao Liang

Obese patients can significantly reduce weight and have a positive impact on obesity-related diseases. However, the risk of infection complications in obese people is higher than that in normal people, especially the surgical site infection. This research investigates the effect of antibiotics on weight change of obese patients after laparoscopic sleeve gastrectomy (LSG). A retrospective analysis was performed on 131 morbidly obese patients or obese patients with complications who received LSG treatment in the Third Hospital of Shanxi Medical University from 2013 to 2020. Patients were separated into the antibiotic group (59 cases) and the normal group (72 cases) according to whether antibiotics were used after surgery. The differences of postoperative weight-related indexes, inflammation-related indexes, and short-term complications were compared between the two groups. At 12-month follow-up, the % excess weight loss (%EWL) in the antibiotic group was statistically abated than that in the normal group (92.99 ± 28.60, $P < 0.01$). In addition, the percentage of total weight loss (%total weight loss (%TWL)) was abated in the antibiotic group than in the normal group, but it was not significant ($P > 0.05$). White blood cell count and neutrophil count in the antibiotic group were statistically raised than those in the in normal group ($P < 0.05$), but neutrophil/lymphocyte ratio (NLR) showed no significant difference. Comparison of short-term postoperative complications between the two groups showed that the number of abdominal wall wound infection, body temperature > 38°C, and abdominal pain > 3 days in the antibiotic group were abated, but they were not statistically significant ($P > 0.05$). Short-term antibiotic exposure after sleeve gastrectomy had an adverse effect on postoperative weight loss, with no significant improvement in short-term complications.

1. Introduction

According to the World Health Organization (WHO), obesity affects 13% of population, which means that the body mass index (BMI) of 650 million people is more than $30\,kg/m^2$ [1]. Obesity can lead to type 2 diabetes, hypertension, hyperlipidemia, high uric acid hematic disease, and other diseases. LSG is the basic weight loss surgery; obese patients can significantly reduce weight and have a positive impact on obesity-related diseases [2]. However, the risk of infection complications in obese people is higher than that in normal people, especially the surgical site infection [3]. The Guiding Principles for Clinical Application of Antibiotics [4] pointed out that type II incision infection may exist, and antibacterial drugs should be used for prevention. The main purpose of the use of postoperative antibiotics is to prevent postoperative infection, which can reduce postoperative infection and mortality. In addition, it can avoid excessive consumption of medical resources. But some scholars at home and abroad think sleeve shape after gastrectomy antimicrobial drug use will exist for weight loss [5, 6]. Therefore, this article intends to explore the laparoscopic sleeve shape

in gastric resection of antimicrobial drug use effect on the patient's body weight changes and inflammatory indexes, providing reference for clinical use antimicrobial drugs.

2. Clinical Data

2.1. The General Information. Refer to the guide [7, 8] to develop inclusion and exclusion criteria. Inclusion criteria: (1) clear diagnosis, obesity BMI > 32.5 kg/m^2; (2) BMI > 27.5 kg/m^2, the traditional treatment of poorly controlled and conform to at least two metabolic syndrome, or there are complications; (3) there is no history of chronic mental illness, no history of psychiatric drugs abuse, and no past surgical history of gastrointestinal surgery. Exclusion criteria: (1) physical cause or other medicines cause of obesity, including increased cortisol disease, hypothyroidism, and drug obesity; (2) there is a clear operation contraindication; (3) during pregnancy and lactation; and (4) date for any reason within six months before and after the surgery patients exposed to antibiotics.

According to inclusion and exclusion standard, from 2013 to 2020, retrospectively analyzed in Shanxi Medical University Third Hospital treated obese or morbidly obese with complications and a total of 131 patients accepting LSG, male 38 cases, and 93 cases of female. All of the patients' clinical data are complete. According to the postoperative use of antibiotics or not, they were divided into the antibiotic groups ($n = 59$) and the normal group ($n = 72$). The clinical data all came from the patient's admission review and follow-up, and all obtained the informed consent of the patients and their families.

2.2. Surgical Method. Surgical method reference guide is in [7, 8]. After the success of the anesthesia, regular disinfection shop towels, four-hole method operation, umbilical along the placement on the puncture outfit, establish CO_2 pneumoperitoneum, 10 cm above the umbilicus left collarbone midline, right collarbone midline and xiphoid process under the puncture outfit were inserted into ultrasonic knife pliers, no damage. After laparoscopic exploration, along the greater curvature stomach, from broken retinal tissue, ultrasonic knife close to the wall of the stomach to cardia. His horn on the left, next to the pylorus to 4 cm, place 36 Fr stomach tube through the mouth. From the pylorus to 5 cm, use linear cutting closer against gastric tube to remove the greater curvature side of the stomach tissue, nail warehouse 5 until the bottom of the stomach, the residual stomach cavity is about 100 mL tube, using agnail can absorb line continuous slurry muscularis suture cut edge. Intraoperative protection of abdominal viscera, take out to remove the stomach tissue, no such active bleeding, gauze instruments correctly counted, eliminate pneumoperitoneum, pull out the puncture outfit, using membrane suture closure in the incision.

2.3. Observation Index. The basic information and weight changes of the two groups of patients before and after 1, 3, 6, and 12 months were recorded, and the changes of inflammatory indexes within 7 days were recorded. Basic information includes age, gender, height, weight, BMI, blood pressure, blood glucose, and obesity complications. Patients after discharge for 1, 3, 6, and 12 months of follow-up returned to court record these patients' body weight, BMI, %, %EWL, blood pressure, and blood sugar. Among them %TWL = (baseline weight real − time weight)/(baseline weight) by 100%; %EWL = [(baseline weight − real − time weight)]/(baseline weight − target weight) by 100%; the target weight %EWL is calculated by BMI = 25 corresponding weight value. Patients have postoperative 1-, 3-, and 7-day leukocyte count, neutrophil count, lymphocyte count, and NLR.

2.4. Statistical Methods. We analyzed using SPSS 21.0 software. Conform to the normal distribution of continuous numerical variables using mean difference of +/- standard deviation ($\bar{x} \pm s$), with comparison between the two groups using independent sample t-test. Count data to [cases (%)], said line is compared between groups with chi-square test. $P < 0.05$ was statistically significant.

3. Results

3.1. Patients with General Data Comparison between Two Groups. This research included 59 patients (21 males and 38 females) in the antibiotic group and 72 patients (17 males and 55 females) in the normal group. Fasting blood sugar and glycated hemoglobin were statistically raised in the antibiotic group than in the normal group. There were no statistical differences in gender, age, height, weight, preoperative BMI, systolic pressure, diastolic pressure, 2 h PG, fasting insulin, fasting C-peptide, and hospitalization duration, as shown in Table 1.

3.2. Comparison of Weight-Related Indexes between the Two Groups. Comparing the antibiotic group with the normal group, 1, 3, 6, and 12 months after, the weight difference has no statistical significance. Antibiotic %TWL was abated in the antibiotic group than in the normal group from 1 month to 12 months after operation, but it was not significant ($P > 0.05$). BMI was statistically raised; %EWL was statistically abated in the antibiotic group 6 months after surgery. But BMI was no difference at postoperative 1 month and 3 months. %EWL was no difference at 1 month and 6 months after operation of two groups, as shown in Table 2.

3.3. Comparison of Inflammatory Indexes between Two Groups. Leukocyte and neutrophil count between two groups raised statistically in postoperative day 1, with obvious statistical significance difference. In addition, white blood cell count in postoperative day 3 difference is statistically significant. Seven days after surgery, there is no difference in leukocyte and neutrophil count between two groups. Lymphocyte count has no difference between two groups after 1, 3, and 7 days of operation. NLR between the two groups is statistically significant 7 days after surgery, as shown in Table 3.

3.4. Comparison of Short-Term Postoperative Complications between the Two Groups. In the antibiotic group and the normal group, postoperative gastrointestinal leakage,

Table 1: Patients with general data comparison between two groups.

	Antibiotic group ($n = 59$)	Normal group ($n = 72$)	t value	P value
Gender (male/female)	21 (16.03%)/38 (29.01%)	17 (12.98%)/55 (41.98%)	2.261	0.133
Age (year)	33.39 ± 10.61	33.78 ± 7.31	-1.487	0.140
Height (m)	1.68 ± 0.09	1.67 ± 0.08	0.513	0.609
Preoperative weight (kg)	116.53 ± 23.20	110.09 ± 23.88	1.555	0.122
BMI	41.22 ± 6.66	39.16 ± 6.38	1.798	0.074
Preoperative hypertension	27 (20.61%)	28 (21.37%)		
Systolic pressure (mmHg)	158.19 ± 10.14	156.93 ± 10.28	0.456	0.650
Diastolic pressure (mmHg)	97.19 ± 10.22	99.07 ± 9.48	-0.710	0.481
Preoperative diabetes	44 (33.59%)	31 (23.66%)		
Fasting blood glucose (mmol/L)	8.74 ± 3.03	7.45 ± 1.72	2.33	0.023
2 h PG (mmol/L)	15.08 ± 5.18	13.3 ± 3.79	1.976	0.052
Glycosylated hemoglobin	7.46 ± 1.47	6.63 ± 1.09	2.812	0.006
Fasting insulin (mU/L)	36.04 ± 54.02	33.61 ± 33.43	0.222	0.825
Fasting C-peptide (nmol/L)	5.16 ± 5.11	5.31 ± 2.18	-0.155	0.877
Hospitalization time (day)	5.61 ± 1.53	5.04 ± 2.17	1.694	0.093

Table 2: Comparison of weight-related indexes between the two groups.

Index	Group	Preoperative	1 month after operation	3 months after operation	6 months after operation	12 months after operation
Weight (kg)	Antibiotic group	116.53 ± 23.20	105.24 ± 19.73	95.24 ± 16.52	88.26 ± 15.51	81.89 ± 14.36
	Normal group	110.09 ± 23.88	99.38 ± 21.66	90.48 ± 20.43	82.92 ± 18.60	76.63 ± 16.98
BMI	Antibiotic group	41.22 ± 6.66	37.24 ± 5.53	33.73 ± 4.67	31.27 ± 4.42*	28.98 ± 3.80*
	Normal group	39.16 ± 6.38	35.36 ± 5.85	32.19 ± 5.58	29.52 ± 5.18*	27.30 ± 4.85*
%TWL	Antibiotic group		9.43 ± 2.75	17.71 ± 5.07	23.62 ± 6.52	28.95 ± 7.97
	Normal group		9.69 ± 2.62	17.81 ± 3.98	24.57 ± 5.20	30.14 ± 6.45
%EWL	Antibiotic group		25.70 ± 7.02*	48.35 ± 12.91*	64.86 ± 19.12**	79.28 ± 22.95**
	Normal group		29.91 ± 11.51*	55.09 ± 18.43*	75.83 ± 23.49**	92.99 ± 28.60**

*Comparison between the antibiotic group and the normal group, $P < 0.05$; **comparison between the antibiotic group and the normal group, $P < 0.01$.

bleeding, venous thromboembolism, and anastomotic stenosis were not present; in the antibiotic group, abdominal wound infection, temperature > 38°C, and abdominal pain > 3 days are smaller but not significant than those in the normal group, as shown in Table 4.

4. Discussion

This study retrospectively analyzed 131patients with morbidly obese or obese patients with complications who received LSG in the Third Hospital of Shanxi Medical University from 2013 to 2020. According to whether antibiotics were used after surgery, the patients were separated into the antibiotic group (59 cases) and the normal group (72 cases) to explore the effect of antibiotics on the weight changes of obese patients after LSG. Our data show that there is no significant difference in total body weight in obese patients at 1, 3, 6, and 12 months after short-term exposure to antibiotics. However, the %EWL in the antibiotic group is lower than that in the normal group at 1 month after surgery and last until 12 months. In addition, the BMI in the antibiotic group is significantly higher than that in the normal group at 6 months after surgery. Therefore, we think that short-term antibiotic exposure after LSG has an adverse effect on postoperative %EWL reduction. As in previous studies, it has been found that antibiotics can destroy the intestinal flora; the negative impact of weight loss and the influence has nothing to do with the food intake, sports activities, or

Table 3: Comparison of inflammatory indexes between two groups.

Index	Group	Preoperative	1 day after operation	3 days after operation	7 days after operation
White blood cells (10^9/L)	Antibiotic group	8.16 ± 1.93	14.57 ± 3.98**	10.85 ± 2.79*	8.33 ± 2.02
	Normal group	7.80 ± 1.59	13.04 ± 2.03	9.97 ± 1.36	8.31 ± 1.19
Neutrophils (10^9/L)	Antibiotic group	5.04 ± 1.62	12.24 ± 3.63**	7.99 ± 2.22	5.56 ± 1.68
	Normal group	4.58 ± 1.26	10.73 ± 1.88	7.37 ± 1.27	5.31 ± 1.02
Lymphocyte (10^9/L)	Antibiotic group	2.51 ± 0.72	1.28 ± 0.46	1.83 ± 0.63	2.11 ± 0.72
	Normal group	2.49 ± 0.66	1.26 ± 0.41	1.80 ± 0.47	2.29 ± 0.53
NLR	Antibiotic group	2.12 ± 0.79	10.65 ± 4.33	4.72 ± 1.67	2.94 ± 1.46*
	Normal group	1.95 ± 0.82	9.42 ± 3.41	4.39 ± 1.52	2.44 ± 0.83

*Comparison between the antibiotic group and the normal group, $P < 0.05$; **comparison between the antibiotic group and the normal group, $P < 0.01$.

energy consumption [9–12]. Also, in a retrospective study [5, 6], it was found that patients treated with levofloxacin/metronidazole had significantly less weight loss than patients treated with cefoxitin 6 months after surgery, and this trend continued 12 months after surgery. However, in this clinical study, only the types of antibiotics are grouped, and there is no blank control group, so we can only speculate that the types of antibiotics will have different effects on body weight. In our study, patients who were treated with cefoxitin or cefmonate after surgery were selected as the antibiotic group and patients without exposure to antibiotics as the normal group. Compared with previous studies, the effect of antibiotic on weight change is demonstrated more scientifically.

Obesity is considered to be a chronic and systemic inflammatory disease, and its plasma clinical inflammatory markers are elevated at baseline before operation. We have the same findings in our study, which is also a reason for the prophylactic use of antibiotics. Based on this, in this study's antibiotic group with all the prophylactic use of antibiotics in the day after surgery, we found that in the first postoperative day, the antibiotic and normal group white blood cells and neutrophils were significantly elevated, and the increase in the antibiotic group was more obvious ($P < 0.05$). Lymphocytes decreased obviously. And this change will improve 7 days after surgery. Normal group of white blood cells increase associated with postoperative acute trauma, and antibiotics leukocyte and neutrophil count and the normal group rise for unknown reasons. Studies have shown that [13, 14] at postoperative day 1 WBC $> 12.15 \times 10^3$ μ/L with LSG 3.34 times associated with an increased incidence of complications, postoperative day 1 NLR 10 or higher and prolonged hospitalization, total complications, and mainly the high incidence of complications. But our data do not support this prediction model. In our observation, in both the antibiotic and normal groups, the WBC were higher than this value, the antibiotic group of postoperative day 1 NLR > 10, and normal group NLR < 10 . The number of short-term postoperative complications in the antibiotic group (10 case) was less than that in the normal group (17 cases). The length of hospital stay in the antibiotic group (5.61 ± 1.53) was longer than that in the normal group (5.04 ± 2.17) ($P > 0.05$). However, some studies have shown that [15] preoperative NLR is the only risk factor for postoperative complications. In our study, there was no significant difference in preoperative NLR and postoperative complications between the antibiotic group and the normal group. Our study seems to support the conclusions of this later study.

Surgical site infection (SSI) is the most common postoperative complication [11]. According to the report, laparoscopic decrease heavy hand about 4% incidence of postoperative SSI, the most common cause of SSI microbes to *Staphylococcus aureus* and coagulase negative *Staphylococcus aureus*. Therefore, beta-lactam class antibiotics are antibiotics to prevent a line [3]. Cefoxitin is one of the most commonly used; because it is against *Staphylococcus aureus*, gram-negative bacteria and anaerobic bacteria are antimicrobial spectrum. But there is literature, which points out that the most advocate preventive gastroduodenal surgery is cefazolin [12, 16, 17]. In our study, the main antibiotics were cefamandole axetil and cefoxitin. Our study also supports this conclusion. We find that there are 7 patients (5.34%) with abdominal wound infection after surgery, including 2 (1.53%) in the antibiotic group and 5 (3.82%) in the normal group. However, there is no significant difference between the two groups ($P > 0.05$). Therefore, we believe that the use of postoperative antibiotics has no significant improvement on postoperative complications in obese patients.

There are important limitations in our research. First of all, [14, 16–18] poor postoperative body weight factors include age, male, high BMI earlier onset age, obesity, high blood pressure, and diabetes. In our study, these indicators are layered, which may affect the accuracy of experimental results. Secondly, our study did not explore the mechanism of weight change. It is reported that [10, 12, 18, 19] prophylactic use of antimicrobial drugs affects postoperative body weight change mechanism which may be associated with intestinal flora changes and bile acid. We plan to detect the intestinal flora of the patients before surgery and reexamine regularly at 1, 3, 6, and 12 months after surgery to observe the changes of intestinal flora. The changes of bile acid

Table 4: Comparison of short-term postoperative complications between the two groups.

Group	Gastrointestinal leakage	Hemorrhage	Venous thromboembolism	Anastomotic stenosis	Abdominal wound infection	Body temperature > 38°C	Abdominal pain > 3 days	Total number of complications
Antibiotic group	0	0	0	0	2 (1.53%)	3 (2.29%)	5 (3.82%)	10 (7.63%)
Normal group	0	0	0	0	5 (3.82%)	5 (3.82%)	7 (5.34%)	17 (12.98%)
χ^2 value					0.260	0.006	0.061	0.880
P value					0.610	0.940	0.805	0.348

*Comparison between the antibiotic group and the normal group, $P < 0.05$; **comparison between the antibiotic group and the normal group, $P < 0.01$.

spectrum in serum and feces will be detected at the same time. Then, we were followed up for only 1 year, while it was reported that the effect of antibiotics on intestinal flora after LSG lasted for 1 year, that is, the intestinal flora returned to preoperation 1 year after operation. We plan to expand the follow-up period to 2 years after surgery to observe the postoperative weight changes of obese patients. Finally, the sample size of our study is insufficient, which is more obvious in the number of postoperative complications.

5. Conclusion

To sum up, our research suggests that LSG antibiotic use of postoperative after weight loss has an adverse effect, especially for %EWL; its mechanism may be associated with intestinal flora changes and bile acid. Postoperative antibiotic use will increase white blood cell count and neutrophil count, but no obvious improvement for short-term complications.

6. Summary

This research adopts the single factor analysis and comparison of antibiotic use on the sleeve shape, the influence of weight obesity patients after gastrectomy. It is found that in short-term exposure to antibiotics postoperatively, obese patients' %EWL is decreased obviously, and the overall weight change was not significant. Patients with inflammatory indexes compared with no antibiotics, leukocyte count and neutrophil count increased obviously. There was no evident difference whether use of antibiotics and short-term complications. Problems of this study were less samples, not for stratified patients with preoperative body weight. In the subsequent studies with larger sample sizes, they were divided into high BMI and low BMI groups, a longer follow-up period, and more reliable conclusions. In addition, this study did not explore the mechanism of change; in the subsequent research, we can explore the antibiotic effects on intestinal flora and bile acid changes.

Data Availability

The labeled dataset used to support the findings of this study is available from the corresponding author upon request.

Conflicts of Interest

The authors declare no competing interests.

Acknowledgments

This study was funded by the Shanxi Province 136 Revitalization Medical Project Construction Funds.

References

[1] P. Woźniewska, I. Diemieszczyk, and H. R. Hady, "Complications associated with laparoscopic sleeve gastrectomy - a review," *Gastroenterology Review/Przegląd Gastroenterologiczny*, vol. 16, no. 1, pp. 5–9, 2021.

[2] S. Grönroos, M. Helmiö, A. Juuti et al., "Effect of laparoscopic sleeve gastrectomy vs Roux-en-Y gastric bypass on weight loss and quality of life at 7 years in patients with morbid obesity: the SLEEVEPASS randomized clinical trial," *JAMA Surgery*, vol. 156, no. 2, pp. 137–146, 2021.

[3] T. Belveyre, J. Scala-Bertola, M. Esposito, A. Luc, J. Lipman, and E. Novy, "Influence of the obesity phenotype on the adequacy of antibiotic prophylaxis with cefoxitin for obese patients undergoing bariatric surgery: lessons learnt and future considerations," *European Journal of Drug Metabolism and Pharmacokinetics*, vol. 46, no. 4, pp. 479–485, 2021.

[4] The clinical application of antibacterial drugs guiding principles revised working group, *Clinical application of antibacterial drugs guiding principles: 2015 edition*, vol. 8, no. 6, 2015People's Health Publishing House, 2015.

[5] R. Jacobson, S. Terranella, C. Booker, S. Khalid, A. Torquati, and P. Omotosho, "The impact of perioperative antibiotic prophylaxis on weight loss following laparoscopic sleeve gastrectomy," *Journal of Laparoendoscopic & Advanced Surgical Techniques. Part A*, vol. 30, no. 9, pp. 998–1000, 2020.

[6] Y. Gu, P. Zhang, Y. Wang, L. Y. Zhu, and Z. Y. Dong, "Chinese expert consensus on ambulatory laparoscopic sleeve gastriectomy(2021 edition)," *Chinese Journal of Practical Surgery*, vol. 42, pp. 17–23, 2022.

[7] Y. Wang, C. C. Wang, S. H. Zhu, P. Zhang, and H. Liang, "China's obesity and type 2 diabetes surgery guide," *Chinese Journal of Practical Surgery*, vol. 42, no. 1, pp. 17–23, 2022.

[8] M. Shimonov, L. Leibou, E. Davidov, O. Bernadsky, J. Wainstein, and E. Leibovitz, "Effects of helicobacter pylori colonization/infection on the metabolic profile of obese persons undergoing sleeve gastrectomy surgery for weight reduction," *The Israel Medical Association Journal*, vol. 18, no. 7, pp. 401–403, 2016.

[9] H. Nalluri, S. Kizy, K. Ewing et al., "Peri-operative antibiotics acutely and significantly impact intestinal microbiota following bariatric surgery," *Scientific Reports*, vol. 10, no. 1, p. 20340, 2020.

[10] C. Jahansouz, C. Staley, S. Kizy et al., "Antibiotic-induced disruption of intestinal microbiota contributes to failure of vertical sleeve gastrectomy," *Annals of Surgery*, vol. 269, no. 6, pp. 1092–1100, 2019.

[11] Á. A. Ferraz, F. Santa-Cruz, and C. E. Edmiston Jr., "Antibiotic prophylaxis in bariatric surgical procedures: is there an ideal antimicrobial agent?," *Surgical Infections*, vol. 21, no. 8, pp. 654–658, 2020.

[12] J. J. Patz, M. C. Helm, R. M. Higgins, M. I. Goldblatt, J. C. Gould, and T. L. Kindel, "Peri-operative, intravenous clindamycin may improve the resolution rate of hypertension after Roux-en-Y gastric bypass in morbidly obese patients," *Surgical Endoscopy*, vol. 33, no. 12, pp. 3984–3989, 2019.

[13] M. Wysocki, P. Małczak, M. Wierdak et al., "Utility of inflammatory markers in detection of perioperative morbidity after laparoscopic sleeve gastrectomy, laparoscopic Roux-en-Y gastric bypass, and one-anastomosis gastric bypass-multicenter study," *Obesity Surgery*, vol. 30, no. 8, pp. 2971–2979, 2020.

[14] J. E. Contreras, C. Santander, I. Court, and J. Bravo, "Correlation between age and weight loss after bariatric surgery," *Obesity Surgery*, vol. 23, no. 8, pp. 1286–1289, 2013.

[15] G. Bora Makal and O. Yıldırım, "Are the C-reactive protein/albumin ratio (CAR), neutrophil-to-lymphocyte ratio (NLR), and platelet-to-lymphocyte ratio (NLR) novel inflammatory biomarkers in the early diagnosis of postoperative complications after laparoscopic sleeve gastrectomy," *Obesity Research & Clinical Practice*, vol. 14, no. 5, pp. 467–472, 2020.

[16] X. Chen, C. E. Brathwaite, A. Barkan et al., "Optimal cefazolin prophylactic dosing for bariatric surgery: no need for higher doses or intraoperative redosing," *Obesity Surgery*, vol. 27, no. 3, pp. 626–629, 2017.

[17] B. Mayir, "Practices concerning sleeve gastrectomy in Turkey: a survey of surgeons," *World Journal of Gastrointestinal Surgery*, vol. 13, no. 5, pp. 452–460, 2021.

[18] C. Y. Chen, C. H. Lee, H. M. Lee et al., "Check point to get adequate weight loss within 6-months after laparoscopic sleeve gastrectomy for morbid obesity in Asian population," *Scientific Reports*, vol. 10, no. 1, p. 12788, 2020.

[19] A. Vrieze, C. Out, S. Fuentes et al., "Impact of oral vancomycin on gut microbiota, bile acid metabolism, and insulin sensitivity," *Journal of Hepatology*, vol. 60, no. 4, pp. 824–831, 2014.

Hindawi
Oxidative Medicine and Cellular Longevity
Volume 2022, Article ID 1275141, 10 pages
https://doi.org/10.1155/2022/1275141

Research Article

miR-342-3p Inhibits Acute Myeloid Leukemia Progression by Targeting SOX12

Ying Wang, Xiaonan Guo, Lihua Wang, Lina Xing, Xiaolei Zhang, and Jinhai Ren

Department of Hematology, The Second Hospital of Hebei Medical University, Shijiazhuang, 050000 Hebei, China

Correspondence should be addressed to Jinhai Ren; jinhai1966@yeah.net

Received 12 July 2022; Revised 12 August 2022; Accepted 20 August 2022; Published 8 September 2022

Academic Editor: Shao Liang

Background. It is well known that microRNAs (miRNAs) interfere with the progression of various human malignancies. This article is aimed at exploring the regulating role of miR-342-3p in acute myeloid leukemia (AML) and its mechanism. *Methods*. We used the Gene Expression Omnibus (GEO) database to determine miR-342-3p differential expression patterns in AML patients' plasma and cells as well as healthy individuals' plasma and T cells. Quantitative real-time PCR and Western blotting were performed for plasma and cell miR-342-3p and SRY-related high-mobility-group box (SOX12) expression quantification, and cell counting kit-8 assay and flow cytometry were used for the determination of AML cell growth, cycle, and apoptosis. A dual-luciferase reporter gene assay was further carried out to identify the targeted association between miR-342-3p and SOX12 mRNA 3′UTR after prediction by a bioinformatics website. Pearson's correlation analysis was performed to analyze the connection between miR-342-3p and SOX12 expressions. The LinkedOmics database was utilized to explore the downstream pathways in which SOX12 was enriched. *Results*. Evidently downregulated plasma miR-342-3p and markedly elevated SOX12 were observed in AML patients versus healthy individuals. miR-342-3p mimics suppressed AML cell growth, enhanced apoptosis, and induced G0/G1 phase arrest; conversely, enhanced capacity of AML cells to proliferate, suppressed apoptosis, and accelerated cell cycle were observed after treatment with miR-342-3p inhibitors. SOX12 was confirmed as miR-342-3p's target gene. Overexpressing or knocking down SOX12 reversed miR-342-3p's impacts on AML cell growth, apoptosis, and cycle. Upregulated SOX12 was positively related to DNA replication and RNA polymerase signaling pathways. *Conclusion*. miR-342-3p affects apoptosis of AML cells and their ability to proliferate via targeted regulation of SOX12.

1. Introduction

Known as a highly heterogeneous and hematological malignancy, acute myeloid leukemia (AML) features undifferentiated bone marrow (BM) progenitor cells accumulated in the peripheral blood and BM [1]. Stem cell transplantation and chemotherapy remain the current mainstays of treatment for AML, but the treatment effect is unsatisfactory for those at advanced stages with recurrence and metastasis [2]. There are studies suggesting an association of gene mutations and abnormal expression of malignancy-related genes with the occurrence of AML [3, 4]. In this context, delving into possible mechanisms by which AML occurs and progresses is crucial for providing novel therapeutic targets for the disease.

As a kind of small endogenous noncoding RNAs widely present in eukaryotes that participate extensively in numerous biological processes (cell growth, differentiation, apoptosis, etc.) [5], microRNAs (miRNAs) are strongly linked to the genesis and development of multiple tumors, such as leukemia [6], gastric carcinoma [7], thyroid carcinoma [8], and hepatic carcinoma [9]. A large amount of research has indicated underexpressed miR-342-3p in lung carcinoma [10], pancreatic carcinoma [11], colon carcinoma [12], and other malignancies, with its expression highly correlated to disease staging, metastasis, and prognosis. For instance, underexpressed miR-342-3p in non-small-cell lung carcinoma is linked to poor patient outcomes, and overexpressing miR-342-3p markedly represses tumor cells' capacity to proliferate and migrate, demonstrating miR-342-3p's role as a candidate diagnostic biomarker and therapeutic target [13]. We learned through bioinformatics analysis that in AML patients, plasma miR-342-3p is abnormally

underexpressed, yet it is still unclear about the mechanism underlying disease occurrence and development.

Being a member of the SOX gene family, SRY-related high-mobility-group box (SOX12) is a key transcription factor that is capable of maintaining the self-renewing and proliferation capacities of many tissue-specific stem cells (SCs) like embryonic SCs [14]. Over the past few years, increasing research has demonstrated the crucial role of SOX12 in tumor occurrence, growth, proliferation, invasion, and metastasis, with different biological behaviors in different types of tumors [15]. Reportedly, SOX12 is a tumor-promoting gene in hepatocellular cancer [16] and breast carcinoma [17]. However, in colorectal cancer [18], it is a tumor-suppressing gene. There has also been research suggesting that SOX12 is significantly highly expressed in AML, and SOX12 knockdown represses THP1 cell viability, reduces cell colonies, and induces G1 phase cell cycle arrest, indicating that SOX12 can be a new potential target for AML [15]. Bioinformatics prediction showed that SOX12 may be miR-342-3p's target. It is found that miR-342-3p overexpression in liver cancer SCs leads to reduced tumor volume, as well as lower Sox2 at mRNA and protein levels [19]. Due to the unknown mechanism of miR-342-3p and its target SOX12 in AML, the motivation and novelty of this research is to survey the possible mechanisms by which miR-342-3p influences AML cell multiplication and apoptosis via targeting SOX12, aiming to decipher new mechanisms of AML genesis and development and provide a theoretical basis for seeking novel targeted therapies.

2. Data and Methods

2.1. Collection of Plasma Samples. Forty-seven AML plasma samples collected in this experiment were obtained from patients hospitalized between February 2018 and May 2020. All AML cases were confirmed by BM cell morphology and FCM examinations. The control group consisted of 47 healthy pregnant women who had normal full-term delivery in the hospital during the same period, from whom umbilical cord blood samples were collected. The current research was endorsed by the Hospital's Ethics Committee and conducted following the *Declaration of Helsinki* and the ethics committee guidelines. Every participant signed informed consent.

2.2. Cultivation and Transfection of Cells. The AML cells (HL-60, THP-1, KG-1, CCRF-CEM, and MOLT-3) used in this study were all supplied by the American Type Culture Collection (Manassas, USA). First, we selected healthy people undergoing physical examinations in the hospital. Next, Ficoll liquid (Solarbio, Beijing, China) was used to separate their BM primary leukocytes. The culture medium of KG-1 and HL-60 was 10% fetal bovine serum supplemented Roswell Park Memorial Institute Medium 1640 (RPMI1640; both from Gibco, Carlsbad, CA, USA), which was placed in a 5% CO_2, 37°C incubator. When the cells grew to about 90% confluency, they were subjected to 0.25% trypsin (Roche, Basel, Switzerland) digestion, centrifugation, and passage. This was followed by trypsinization of logarithmic-phase KG-1 and HL-60 cells and their subsequent inoculation at 1×10^6 cells/well into the wells of 6-well plates. After being incubated overnight, they were transfected with the following oligonucleotides and plasmids (all from RiboBio, Guangzhou, China): miR-342-3p mimics (miR mimics), mimics control (mimics NC), inhibitors (miR inhibitors), and negative control inhibitors NC, as well as SOX12 and si-SOX12, following the instructions of the Lipofectamine™ 2000 (Invitrogen, Carlsbad, CA, USA) transfection reagent. Quantitative real-time polymerase chain reaction (qRT-PCR) determined the transfection efficiency 48 h after transfection for further analysis.

2.3. qRT-PCR. TRIzol (Invitrogen, Shanghai, China) extracted cell and tissue total RNA, after which reverse transcription of the total RNA into cDNA was carried out employing a reverse transcription kit ordered from Qiagen, Hilden, Germany. qRT-PCR was then carried out with the use of a SYBR® Premix Ex Taq™ (Takara, Kusatsu, Shiga, Japan) and the ABI7500 system (Applied Biosystems, San Francisco, CA, USA). SOX12 mRNA and miR-342-3p levels, relative to U6 and GAPDH, respectively, were quantified by the $2^{-\Delta\Delta Ct}$ formula. Three independent replicates were performed for each experiment. The following are the primer sequences: miR-342-3p sense (5′-3′): GGGTCTCACAC AGAAATCGC and antisense (5′-3′), CAGTGCGTGTC GTGGAGT; SOX12 sense: AGGAAGGTGAAGAGGA GACG and antisense, ATCATCTCGGTAACCTCGGG; GAPDH sense, CACCCACTCCTCCACCTTTG and antisense, CCACCACCCTGTTGCTGTAG; and U6 sense: CGCGCTTCGGCAGCACATATACT and antisense, ACGCTTCACGAATTTGCGTGTC.

2.4. Cell Counting Kit-8 (CCK-8) Assay. KG-1 and HL-60 transfected 48 h later were inoculated at 2000 cells/well in 96-well plates. We set 5 replicate wells, into which 10 μL/well CCK-8 solution (Invitrogen, Shanghai, China) was placed on days 1, 2, and 3 for another 2 h of cultivation in the incubator. Each well's absorbance $(OD)_{450\ nm}$ was determined using a microplate reader (Multiskan, Thermo, USA).

2.5. Flow Cytometry (FCM). We followed the manufacturer's instructions of Annexin V Apoptosis Detection Kit I and PI (BD Biosciences) to measure cell apoptosis. For each group of transfected cells, they were suspended in a 500 μL binding buffer and then mixed with Annexin V-FITC/PI double-labeled staining reagent (5 μL). In the dark, the mixture was treated with ice incubation and PI solution (5 μL) cultivation with, both for 20 min. Cell detection was performed within 1 h with a flow cytometer. A Cell Cycle and Apoptosis Analysis Kit was utilized to determine the cell cycle. In brief, the collected cells were treated with a PI-RNase mixed solution, and FCM (BD FACSCanto™ II) was carried out to for fluorescence analysis. For each sample, at least 10^4 cells were required for analysis. Each experiment was repeated 3 times.

2.6. Dual-Luciferase Reporter (DLR) Gene Assay. A Lipofectamine™ 2000 kit was utilized to cotransfect wild-type (WT) or mutant (MUT) DLR vectors (WT-SOX12 or

MUT-SOX12; RiboBio, Guangzhou, China) and miR mimics or mimics NC into KG-1 cells and to cotransfect WT-SOX12 or MUT-SOX12 and miR inhibitors or inhibitors NC into HL-60. Luciferase activity was determined 48 h later under the instructions of the DLR gene detection kit (Promega, Madison, WI, USA). The ratio of the luminescence intensity of ranilla luciferase/firefly luciferase was the binding intensity of SOX12 to miR-342-3p.

2.7. Western Blot (WB) Analysis. Cell culturing was terminated 48-72 h posttransfection, after which total protein isolation from cells was conducted using RIPA lysis buffer (Pierce, Rockford, IL, USA) +1% protease inhibitors. Samples with an equal amount were isolated via polyacrylamide gel electrophoresis (10%) and then electrotransferred onto a PVDF membrane. Following 1 h of 5% skim milk blocking on a shaker at an ambient temperature, it was incubated with an anti-SOX12 primary antibody (Product No.: SAB1412152; dilution: 1 : 1000; Sigma-Aldrich; Merck KGaA) overnight at 4°C on a shaker. After three rinses in TBST, it was incubated (1 h) with a secondary antibody anti-GAPDH antibody (Product No.: ab6789; Abcam, Shanghai, China) diluted at 1 : 5000, also at an ambient temperature. After 3 rinses in TBST and development, the protein bands were analyzed by a gel imaging system. The target protein's relative expression = $OD_{\text{target protein}}/OD_{\text{internal control}}$.

2.8. Pathway Enrichment Analysis. Further, we performed KEGG pathway enrichment analysis using DAVID to explore the biological functional roles of the downstream target gene set of miR-342-3p.

2.9. Gene Set Enrichment Analysis (GSEA). Samples were grouped (high/low expression groups) based on median SOX12 expression value, and the influences of gene expression profiling on tumors were investigated by GSEA (screening criteria: FDR < 0.25 and $P < 0.05$).

2.10. Statistics and Analysis. The statistical processing and drawing software were SPSS 22.0 (SPSS Inc., Chicago, IL, USA) and GraphPad Prism 9 software (GraphPad Software, La Jolla, CA), respectively. The limma package analyzed the differential expression of each dataset. $|\log(FC)| \geq 1$ and adj. P value < 0.05 were used as the screening criteria for differentially expressed genes (DEGs). The results of all measurement experiments, denoted by mean ± standard deviation, were compared between groups and among multiple groups via independent sample t-test and single factor analysis of variance, respectively, with $P < 0.05$ indicating a difference of statistical significance.

3. Results

3.1. Plasma and Cell miR-342-3p in AML Patients. To understand miR-342-3p expression characteristics, we used the Gene Expression Omnibus (GEO) database (URL: https://www.ncbi.nlm.nih.gov/gds/) to download gene chip datasets GSE31629 [20] and GSE51908 [21, 22] to analyze changes in plasma and cell miRNA expression in AML patients. In the GSE31629 dataset, 771 downregulated and 17 upregulated miRNAs were identified; in the dataset GSE51908, 40 miRNAs were downregulated and 47 were upregulated (Figures 1(a) and 1(b)). Subsequently, we utilized qRT-PCR to quantify miR-342-3p levels in AML patients' plasma and found remarkably downregulated expression in AML patients as compared to the normal group (Figure 1(c)). Similarly, miR-342-3p expression in AML cell strains (THP-1, HL-60, KG-1, CCRF-CEM, and MOLT-3) was dramatically reduced compared with primary leukocytes (Figure 1(d)).

3.2. Biological Functions of miR-342-3p in AML. miR-342-3p showed the lowest expression in KG-1 and the highest expression in HL-60 among the five AML cell strains. Therefore, we transfected KG-1 with miR-342-3p mimics and mimics NC and HL-60 with miR-342-3p inhibitors and inhibitors NC, separately. qRT-PCR verified the success of transfection (Figure 2(a)). The changes in cell viability were examined through CCK-8 assay. It showed dramatically suppressed KG-1 cell viability by miR-342-3p mimics and markedly enhanced HL-60 viability by miR-342-3p inhibitors, versus the control group (Figure 2(b)). Next, we performed FCM to determine miR-342-3p's impacts on cell apoptosis and cycle. As demonstrated by Figures 2(c) and 2(d), enhanced apoptosis and blocked cell cycle were observed following miR-342-3p mimic intervention, while restrained cell apoptosis and accelerated cell cycle were found after miR-342-3p inhibitors transfection.

3.3. SOX12 Is miR-342-3p's Direct Downstream Target. To delve deeper into the mechanism by which miR-342-3p affects AML, we performed downstream target prediction of miR-342-3p utilizing bioinformatics websites TargetScan (TargetScanHuman 7.2) and StarBase (URL: http://starbase.sysu.edu.cn/index.php) (Figure 3(a)), as well as enrichment analysis of miR-342-3p's downstream target genes using the Kyoto Encyclopedia of Genes and Genomes (KEGG) database. The results identified strong correlations of the above target genes with the Ras signaling pathway and the mRNA surveillance pathway (Figure 3(b)). SOX12 is an important target gene, and there are binding loci between miR-342-3p and SOX12 mRNA 3′UTR, which is shown in Figure 3(c). Upregulating miR-342-3p remarkably suppressed WT-SOX12's luciferase activity, and inhibiting miR-342-3p statistically enhanced WT-SOX12's luciferase activity, versus the control group, as indicated by the DLR gene assay; there was no significant effect on that of the MUT-SOX12 group (Figure 3(d)). WB indicated that miR-342-3p mimics can lower SOX12 expression, and conversely, miR-342-3p inhibitors can elevate SOX12 expression (Figure 3(e)). Through qRT-PCR, we found noticeably increased SOX12 mRNA expression in the AML group versus the normal group (Figure 3(f)) and an inverse connection between miR-342-3p expression and SOX12 mRNA (Figure 3(g)).

3.4. SOX12 Can Reverse miR-342-3p's Impacts on AML. Further, to probe into the influences of SOX12 and miR-342-3p

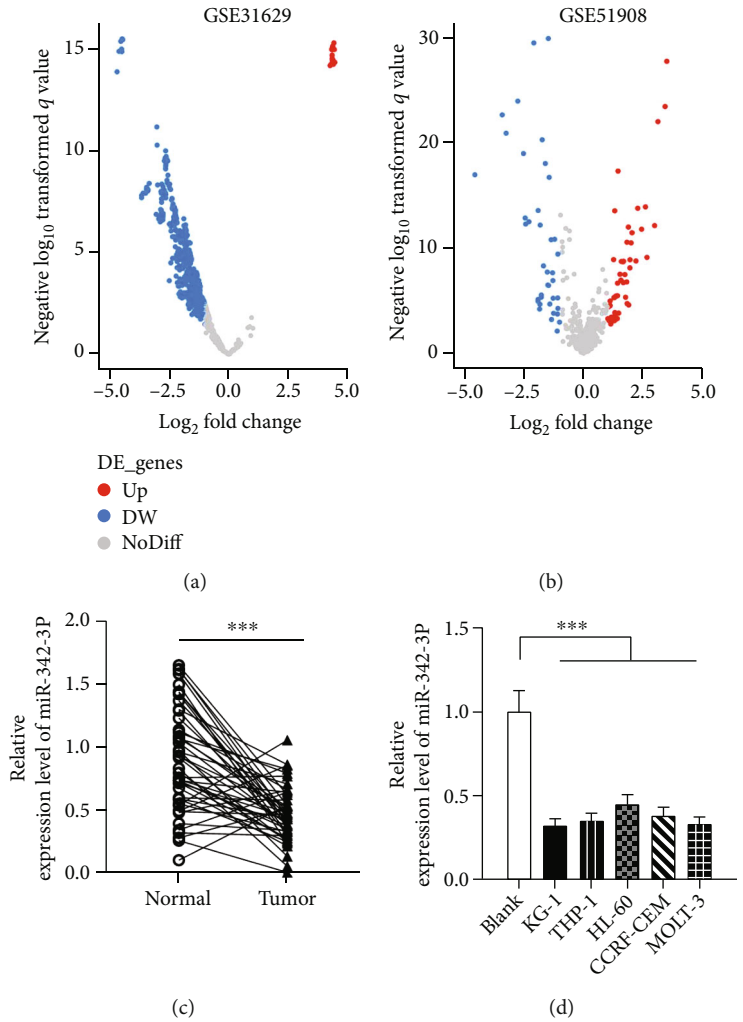

Figure 1: Plasma and cell miR-342-3p expression in AML patients. (a and b) Microarray datasets, downloaded from the GEO database, were utilized to analyze miRNAs' expression differences, and the volcano plots display differentially expressed miRNAs in AML plasma samples. (c) miR-342-3p expression in 47 cases of AML plasma and normal plasma by qRT-PCR. (d) miR-342-3p expression in primary leukocytes and AML cell lines (HL-60, THP-1, KG-1, CCRF-CEM, and MOLT-3) by qRT-PCR. $^{***}P < 0.001$.

on AML cell growth, apoptosis, and cycle, we cotransfected miR mimics, mimics NC, SOX12 and miR inhibitors, inhibitor NC, and si-SOX12 into KG-1 and HL-60 cells, respectively. qRT-PCR validated the success of all transfections (Figure 4(a)). Then, according to CCK-8 assay and FCM, miR-342-3p mimics dramatically suppressed the ability of cells to proliferate, induced cell apoptosis, and blocked cell cycle processes versus control cells, whereas SOX12 overexpression reversed these effects (Figures 4(b)–4(d)). miR-342-3p inhibitors markedly facilitated cell growth, inhibited apoptosis, and accelerated cell cycle processes, while knocking down SOX12 restored these effects (Figures 4(b)–4(d)).

3.5. SOX12 Activates DNA Replication and RNA Polymerase Signaling Pathways. GSEA was further employed for signaling pathway enrichment analysis, so as to elucidate the mechanism underlying SOX12's regulation of AML cells' biological functions; it identified that high SOX12 expression was positively related to DNA replication and the activation of RNA polymerase signaling pathways (Figures 5(a) and 5(b)). Next, WB was employed to detect the roles played by SOX12 and miR-342-3p in DNA replication and the expression of cell cycle-related proteins (Ki-67, pHH3, and PCNA) (Figures 5(c) and 5(d)). It was suggested that SOX12 overexpression led to enhanced expression of pHH3, Ki-67, and PCNA, and SOX12 knockdown resulted in decreased expression of these genes, while miR-342-3p mimics and inhibitors reversed the above mentioned effects, respectively. All the evidence demonstrates the inhibitory action of miR-342-3p/SOX12 against DNA replication and cell cycle signaling axis.

4. Discussion

AML, primarily manifesting as anemia, bleeding, fever, and infection, is a hematopoietic malignancy with high cytogenetic or molecular heterogeneity that is clinically characterized by acute and severe onset, difficulty in control, easy relapse, and poor prognosis, which seriously threaten human life and health [23, 24]. According to cell

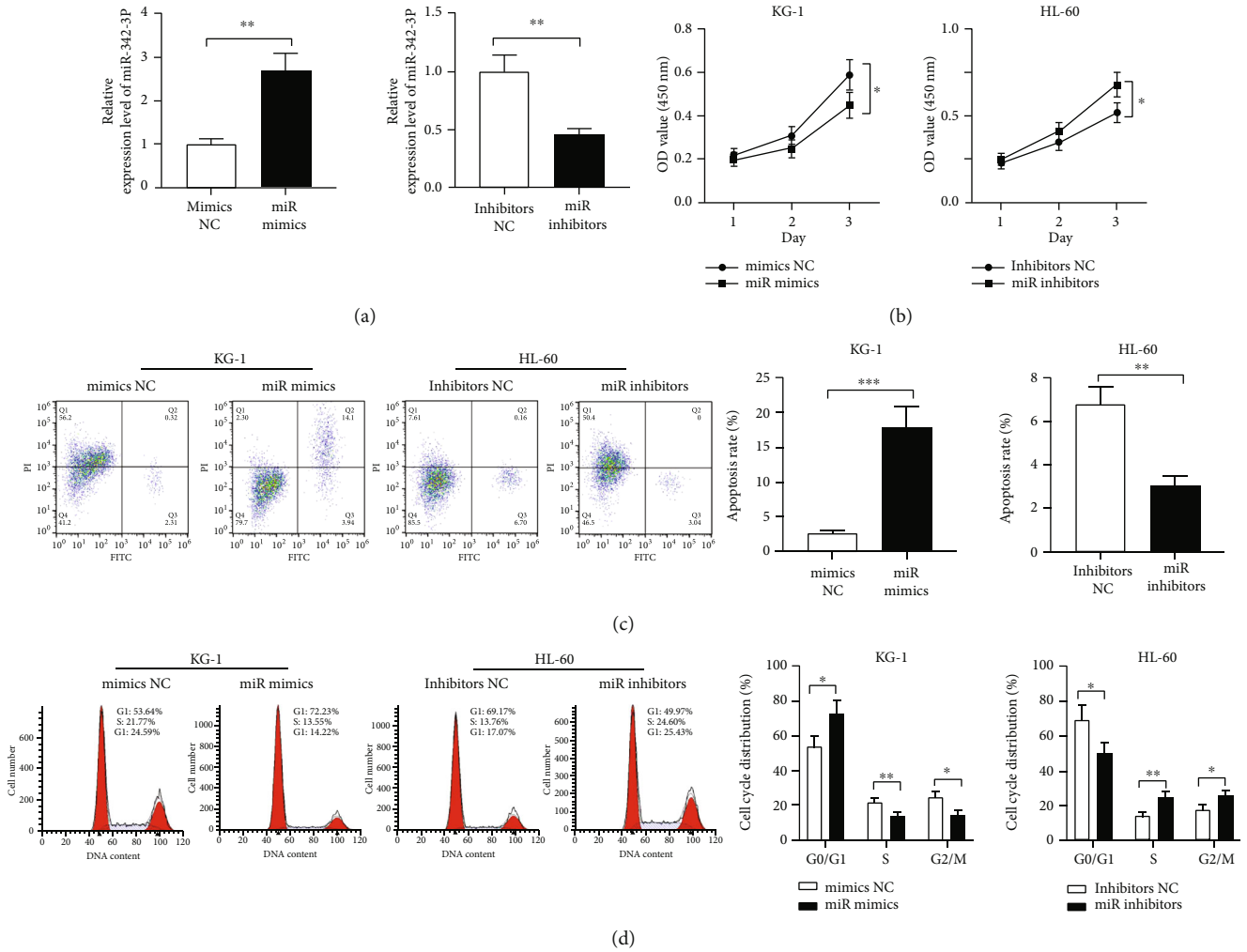

Figure 2: Impacts of miR-342-3p on AML cell growth, apoptosis, and cycle. (a) qRT-PCR was performed to verify transfection efficiency after transfecting mimics NC and miR mimics into KG-1 and inhibitors NC and miR inhibitors into HL-60. (b) CCK-8 assay was carried out posttransfection to determine KG-1 and HL-60 cell viability. (c and d) Flow cytometry was conducted to measure posttransfection KG-1 and HL-60 cell apoptosis and cycle changes. $^{*}P < 0.05$, $^{**}P < 0.01$, and $^{***}P < 0.001$.

morphological and histochemical characteristics, AML can be classified as FAB, MIC, and other types [23, 24]. Except for acute promyelocytic leukemia, the complete response rate of combined chemotherapy for AMI is only 65-75%, and the long-term disease-free survival rate (leukemia-free survival) is 20-30%; the five-year survival is only 40% for those aged under 60 [25, 26]. Despite dramatic advances in the treatment of AML, there are still quite a few AML patients who have a poor prognosis. To improve patients' outcomes, it is highly significant to delve into the nosogenesis of AML and its treatment.

miRNAs, as a kind of highly conserved 20-24 nucleotide length-long noncoding RNAs, are capable of binding to the incomplete complementary locus in mRNA 3′UTR to inhibit gene expression after transcription [27]. As cancer promoters or tumor suppressors, they can participate in modulating multiple biological processes (cell cycle progression, growth, apoptosis, etc.) in malignancies [28]. Evidence in recent years has revealed that miRNAs are strongly linked to AML occurrence and development and play a crucial regulatory role in AML occurrence by regulating their target genes. There is a study indicating that in AML, miR-12462 is low-expressed and inhibits AML cell growth both in vivo and in vitro and enhances AML cell chemotherapy sensitivity via targeting SLC9A1, thus playing a tumor-suppressing role [29]. miR-212-5p keeps at a low level in AML cells, and overexpressing miR-212-5p can suppress AML cell growth and promote apoptosis [30]. miR-342-3p, once called miR-342, is a 23-base single-stranded small RNA that is located on chromosome 14q32. miR-342-3p is located in the intron of the EVL gene, its host gene. A number of experiments have shown that miR-342-3p shows consistent expression with EVL's mRNA expression [31]. The involvement of miR-342-3p in cancer occurrence and development as a tumor suppressor and kinase regulator has been well documented. For example, miR-342-3p, expressing at low levels in hepatocellular carcinoma, restrains the capacities of tumor cells to growth and migrate through negative

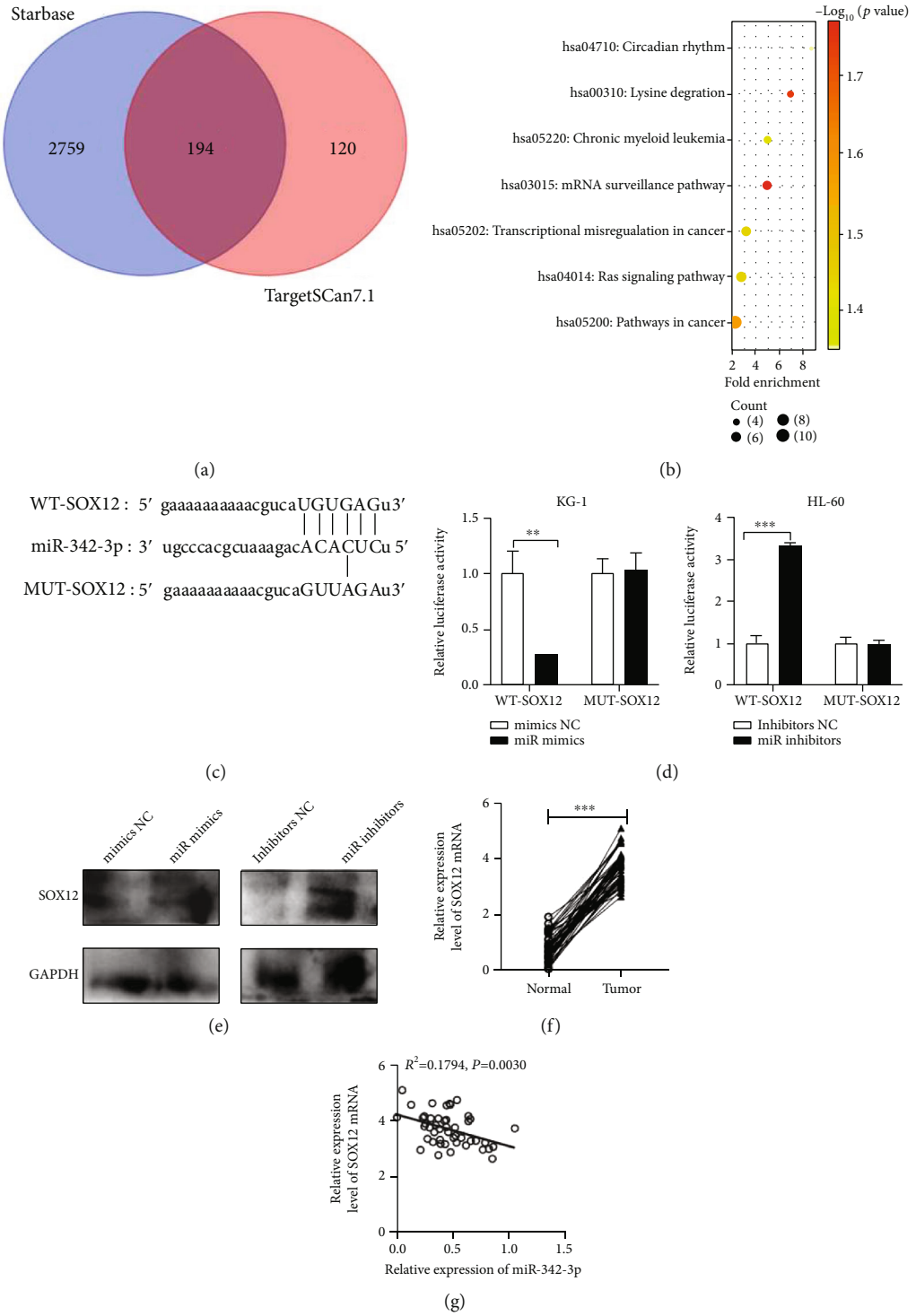

Figure 3: SOX12 is miR-342-3p's direct downstream target. (a) StarBase (URL: http://starbase.sysu.edu.cn/index.php) and TargetScan (URL: TargetScanHuman 7.2) were employed to predict miR-342-3p's downstream targets and a Venn diagram was drawn. (b) Pathway enrichment analysis of miR-342-3p's downstream target gene sets using the KEGG database. (c) The binding sequences of SOX12 mRNA 3′UTR WT and MUT to miR-342-3p. (d) Impacts of miR-342-3p overexpression on WT-SOX12 and MUT-SOX12 luciferase activity by dual-luciferase reporter gene assay. (e) Impacts of miR-342-3p mimics or inhibitors on SOX12 protein expression by Western blot. (f) qRT-PCR detection of SOX12 mRNA expression in the plasma of 47 AML patients and healthy individuals. (g) Pearson correlation analysis of the correlation between SOX12 mRNA and miR-342-3p expression in AML plasma. $^{*}P < 0.05$, $^{**}P < 0.01$, and $^{***}P < 0.001$.

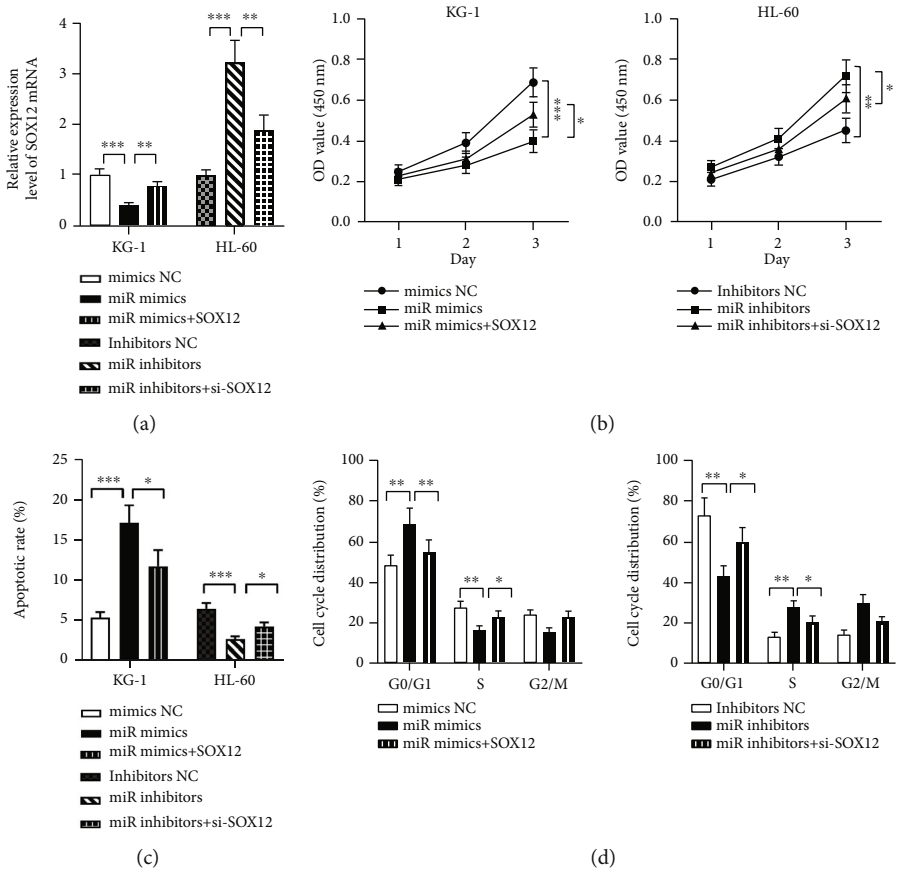

Figure 4: SOX12 can reverse miR-342-3p's impacts on AML cell growth, apoptosis, and cycle. (a) qRT-PCR was performed to verify transfection efficiency after transfecting miR mimics+SOX12 into KG-1 and miR inhibitors and si-SOX12 into HL-60. (b) KG-1 and HL-60 cell viability detected by CCK-8 assay posttransfection. (c and d) KG-1 and HL-60 cell apoptosis and cycle changes measured by flow cytometry posttransfection. $^{*}P < 0.05$, $^{**}P < 0.01$, and $^{***}P < 0.001$.

regulation of MCT1 [32]. In glioma tissues and cells, miR-342-3p is regulated by circ_ARF1, forming a feedback loop composed of U2AF2, ARF1, ISL2, and miR-342-3p, which modulates glioma development [33]. In ovarian cancer tissues and cell lines, underexpressed miR-342-3 is linked to patients' poor clinicopathological markers; miR-342-3 overexpression inhibits tumor cell migration and invasion [34]. miR-342-3p underexpression in acute leukemia [35] and a strong correlation of miR-342-3p expression with the therapeutic effect of acute leukemia and chronic leukemia have also been demonstrated [36, 37]. This study first discovered downregulated miR-342-3p in AML patient's plasma. Further research suggested that miR-342-3p mimics suppressed AML cell growth, accelerated apoptosis, and induced G0/G1 cell cycle arrest, while inhibiting miR-342-3p contributed to the opposite effects.

SOX12 is a member of the SOX family, which is a newly discovered supergene family to encode transcription factors, and is mainly characterized by its product having an HMG-box conserved motif that can specifically bind to DNA sequences to modulate other genes' expression, thereby playing an important part in animal development and the maintenance of cell characteristics [38, 39]. Recent evidence has also revealed that the SOX gene family members may feature prominently in cell proliferation and even cancerization and the stage transformation of malignancies; moreover, the mutation, deletion, and overexpression of SOX genes are strongly linked to the genesis and development of various malignancies [40]. There are studies demonstrating the correlation of SOX12 expression dysregulation with the occurrence and development of colon carcinoma [41], squamous cell carcinoma of the esophagus [42], renal carcinoma [43], and AML [44]. Research has indicated that after SOX12 knockdown, β-catenin mRNA, and protein levels are dramatically reduced, and TCF/Wnt activity is reduced, which leads to G1 phase cell cycle arrest and decreased cell colonies, indicating that SOX12 may regulate β-catenin expression to interfere with the TCF/Wnt pathway and participate in leukemia progression [15]. SOX12 is significantly highly expressed in AML cells, and miR-625-5p targets SOX12 directly to suppress AML cell growth and apoptosis [45]. Additionally, SOX12 knockdown inhibits AML cell proliferation via repressing Wnt/β-catenin axis activity, whereas miR-489-3p can reverse the effect of SOX12 [44], which is similar to our observations. We discovered the role of SOX12 as a downstream target of miR-342-3p, and that miR-342-3p inactivates the DNA replication pathway through targeted regulation of SOX12, thus suppressing the growth of AML cells while inducing apoptosis and G0/G1 cell cycle arrest. However, there is still room

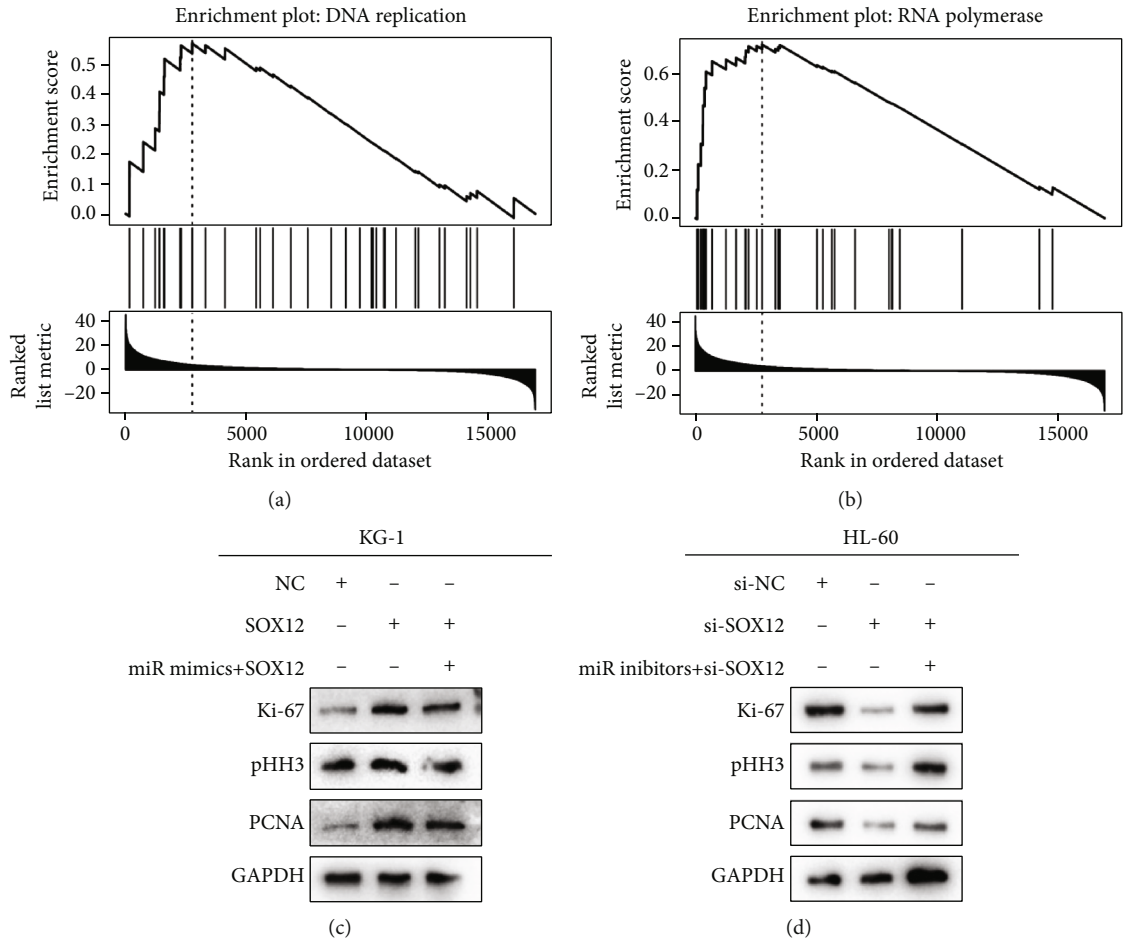

Figure 5: SOX12 activates DNA replication and RNA polymerase signaling pathways. (a and b) The GSEA plot shows a positive connection between SOX12 expression and DNA replication and RNA polymerase pathways. (c and d) Western blot analysis of Ki-67, pHH3, and PCNA expressions.

for improvement in this study. Although we found that miR-342-3p inactivates the DNA replication pathway through targeted regulation of SOX12, some other downstream pathways were not further investigated. Furthermore, besides SOX12, there may be other important downstream targets of miR-342-3p that we have missed. Thus, more experiments are needed to further reveal the mechanisms underlying the action of miR-342-3p against AML.

5. Conclusion

To sum up, miR-342-3p mimics can suppress AML cell proliferation. Furthermore, miR-342-3p negatively regulates SOX12 expression at the protein and mRNA levels, thereby modulating DNA replication signaling pathways and ultimately inhibiting cell proliferation. All these suggest that miR-342-3p and SOX12 may be targets for AML treatment.

Data Availability

The labeled datasets used to support the findings of this study are available from the corresponding author upon request.

Conflicts of Interest

The authors declare no competing interests.

References

[1] I. De Kouchkovsky and M. Abdul-Hay, "Acute myeloid leukemia: a comprehensive review and 2016 update," *Blood Cancer Journal*, vol. 6, no. 7, p. e441, 2016.

[2] M. S. Infante, M. Á. Piris, and J. Á. Hernández-Rivas, "Alteraciones moleculares en leucemia mieloide aguda y sus implicaciones clinicas y terapeuticas," *Medicina Clínica (English Edition)*, vol. 151, no. 9, pp. 362–367, 2018.

[3] C. W. Elgarten and R. Aplenc, "Pediatric acute myeloid leukemia: updates on biology, risk stratification, and therapy," *Current Opinion in Pediatrics*, vol. 32, no. 1, pp. 57–66, 2020.

[4] J. Prada-Arismendy, J. C. Arroyave, and S. Röthlisberger, "Molecular biomarkers in acute myeloid leukemia," *Blood Reviews*, vol. 31, no. 1, pp. 63–76, 2017.

[5] L. Zhang, Y. Liao, and L. Tang, "Microrna-34 family: a potential tumor suppressor and therapeutic candidate in cancer," *Journal of Experimental & Clinical Cancer Research*, vol. 38, no. 1, pp. 1–13, 2019.

[6] L. Liu, W. Ren, and K. Chen, "Mir-34a promotes apoptosis and inhibits autophagy by targeting hmgb1 in acute myeloid leukemia cells," *Cellular Physiology and Biochemistry*, vol. 41, no. 5, pp. 1981–1992, 2017.

[7] S. Hu, Q. Zheng, H. Wu, C. Wang, T. Liu, and W. Zhou, "Mir-532 promoted gastric cancer migration and invasion by targeting nkd1," *Life Sciences*, vol. 177, pp. 15–19, 2017.

[8] S. Bian, "miR-4319 inhibited the development of thyroid cancer by modulating FUS- stabilized SMURF1," *Journal of Cellular Biochemistry*, vol. 121, no. 1, pp. 174–182, 2020.

[9] T. Fang, H. Lv, G. Lv et al., "Tumor-derived exosomal mir-1247-3p induces cancer-associated fibroblast activation to foster lung metastasis of liver cancer," *Nature Communications*, vol. 9, no. 1, pp. 1–13, 2018.

[10] Q. Shen, Y. Sun, and S. Xu, "Linc01503/mir-342-3p facilitates malignancy in non-small-cell lung cancer cells via regulating lasp1," *Respiratory Research*, vol. 21, no. 1, pp. 1–12, 2020.

[11] X. Meng, J. Ma, B. Wang, X. Wu, and Z. Liu, "Long noncoding RNA OIP5-AS1 promotes pancreatic cancer cell growth through sponging mir-342-3p via AKT/ERK signaling pathway," *Journal of Physiology and Biochemistry*, vol. 76, no. 2, pp. 301–315, 2020.

[12] L. Zhou, J. Li, Y. Tang, and M. Yang, "Exosomal LncRNA LINC00659 transferred from cancer-associated fibroblasts promotes colorectal cancer cell progression via miR-342-3p/ANXA2 axis," *Journal of Translational Medicine*, vol. 19, no. 1, pp. 1–14, 2021.

[13] X. Xue, X. Fei, W. Hou, Y. Zhang, L. Liu, and R. Hu, "Mir-342-3p suppresses cell proliferation and migration by targeting AGR2 in non-small cell lung cancer," *Cancer Letters*, vol. 412, pp. 170–178, 2018.

[14] S. Zou, C. Wang, J. Liu et al., "Sox12 is a cancer stem-like cell marker in hepatocellular carcinoma," *Molecules and Cells*, vol. 40, p. 847, 2017.

[15] H. Wan, J. Cai, F. Chen, J. Zhu, J. Zhong, and H. Zhong, "SOX12: a novel potential target for acute myeloid leukaemia," *British Journal of Haematology*, vol. 176, no. 3, pp. 421–430, 2017.

[16] P. Yuan, L. Meng, and N. Wang, "SOX12 upregulation is associated with metastasis of hepatocellular carcinoma and increases CDK4 and IGF2BP1 expression," *European Review for Medical and Pharmacological Sciences*, vol. 21, no. 17, pp. 3821–3826, 2017.

[17] J. Xu, J. Zhang, L. Li, J. Mao, T. You, and Y. Li, "SOX12 expression is associated with progression and poor prognosis in human breast cancer," *American Journal of Translational Research*, vol. 12, no. 12, pp. 8162–8174, 2020.

[18] J. Li, Y. Zheng, X. Li et al., "UCHL3 promotes proliferation of colorectal cancer cells by regulating SOX12 via AKT/mTOR signaling pathway," *American Journal of Translational Research*, vol. 12, no. 10, pp. 6445–6454, 2020.

[19] C. Xu, W. Sun, J. Liu, H. Pu, and Y. Li, "MiR-342-3p inhibits LCSC oncogenicity and cell stemness through HDAC7/PTEN axis," *Inflammation Research*, vol. 71, no. 1, pp. 107–117, 2022.

[20] M. Yamagishi, K. Nakano, A. Miyake et al., "Polycomb-mediated loss of miR-31 activates NIK-dependent NF-κB pathway in adult T cell leukemia and other cancers," *Cancer Cell*, vol. 21, no. 1, pp. 121–135, 2012.

[21] Y. S. Tan, M. Kim, T. J. Kingsbury, C. I. Civin, and W.-C. Cheng, "Regulation of RAB5C is important for the growth inhibitory effects of MiR-509 in human precursor-B acute lymphoblastic leukemia," *PLoS One*, vol. 9, no. 11, p. e111777, 2014.

[22] J. Candia, S. Cherukuri, Y. Guo et al., "Uncovering low-dimensional, miR-based signatures of acute myeloid and lymphoblastic leukemias with a machine-learning-driven network approach," *Convergent Science Physical Oncology*, vol. 1, no. 2, p. 025002, 2015.

[23] P. Bose, P. Vachhani, and J. E. Cortes, "Treatment of relapsed/refractory acute myeloid leukemia," *Current Treatment Options in Oncology*, vol. 18, no. 3, pp. 1–30, 2017.

[24] E. H. Estey, "Acute myeloid leukemia: 2019 update on risk-stratification and management," *American Journal of Hematology*, vol. 93, no. 10, pp. 1267–1291, 2018.

[25] H. Döhner, D. J. Weisdorf, and C. D. Bloomfield, "Acute myeloid leukemia," *New England Journal of Medicine*, vol. 373, no. 12, pp. 1136–1152, 2015.

[26] C. DiNardo and C. Lachowiez, "Acute myeloid leukemia: from mutation profiling to treatment decisions," *Current Hematologic Malignancy Reports*, vol. 14, no. 5, pp. 386–394, 2019.

[27] B. Simonson and S. Das, "MicroRNA therapeutics: the next magic bullet?," *Mini Reviews in Medicinal Chemistry*, vol. 15, no. 6, pp. 467–474, 2015.

[28] J. Krol, I. Loedige, and W. Filipowicz, "The widespread regulation of microRNA biogenesis, function and decay," *Nature Reviews Genetics*, vol. 11, no. 9, pp. 597–610, 2010.

[29] Y. Jia, W. Liu, H.-E. Zhan et al., "Roles of hsa-miR-12462 and SLC9A1 in acute myeloid leukemia," *Journal of Hematology & Oncology*, vol. 13, no. 1, pp. 1–5, 2020.

[30] J. Lin, H. Zeng, and J. Zhao, "Mir-212-5p regulates the proliferation and apoptosis of AML cells through targeting FZD5," *European Review for Medical and Pharmacological Sciences*, vol. 22, no. 23, pp. 8415–8422, 2018.

[31] M. H. Radfar, W. Wong, and Q. Morris, "Computational prediction of intronic microRNA targets using host gene expression reveals novel regulatory mechanisms," *PLoS One*, vol. 6, no. 6, p. e19312, 2011.

[32] R.-M. Komoll, Q. Hu, O. Olarewaju et al., "Microrna-342-3p is a potent tumour suppressor in hepatocellular carcinoma," *Journal of Hepatology*, vol. 74, no. 1, pp. 122–134, 2021.

[33] Y. Jiang, J. Zhou, J. Zhao et al., "The U2AF2/circRNA ARF1/miR-342–3p/ISL2 feedback loop regulates angiogenesis in glioma stem cells," *Journal of Experimental & Clinical Cancer Research*, vol. 39, no. 1, pp. 1–22, 2020.

[34] C. Wang, W. Zhang, S. Xing, Z. Wang, J. Wang, and J. Qu, "Mir-342-3p inhibits cell migration and invasion through suppressing forkhead box protein Q1 in ovarian carcinoma," *Anti-Cancer Drugs*, vol. 30, no. 9, pp. 917–924, 2019.

[35] E. Coskun, M. Neumann, C. Schlee et al., "Microrna profiling reveals aberrant microrna expression in adult ETP-ALL and functional studies implicate a role for miR-222 in acute leukemia," *Leukemia Research*, vol. 37, no. 6, pp. 647–656, 2013.

[36] N. Mosakhani, R. Räty, A. Tyybäkinoja, M.-L. Karjalainen-Lindsberg, E. Elonen, and S. Knuutila, "MicroRNA profiling in chemoresistant and chemosensitive acute myeloid leukemia," *Cytogenetic and Genome Research*, vol. 141, no. 4, pp. 272–276, 2013.

[37] S. Li, H. F. Moffett, J. Lu et al., "MicroRNA expression profiling identifies activated B cell status in chronic lymphocytic leukemia cells," *PLoS One*, vol. 6, no. 3, p. e16956, 2011.

[38] D. Grimm, J. Bauer, P. Wise et al., "The role of sox family members in solid tumours and metastasis," *Presented at Seminars in Cancer Biology*, vol. 67, no. 1, pp. 122–153, 2020.

[39] A. Sarkar and K. Hochedlinger, "The sox family of transcription factors: versatile regulators of stem and progenitor cell fate," *Cell Stem Cell*, vol. 12, no. 1, pp. 15–30, 2013.

[40] M. Ashrafizadeh, S. Taeb, K. Hushmandi et al., "Cancer and sox proteins: new insight into their role in ovarian cancer progression/inhibition," *Pharmacological Research*, vol. 161, p. 105159, 2020.

[41] F. Du, J. Chen, H. Liu et al., "SOX12 promotes colorectal cancer cell proliferation and metastasis by regulating asparagine synthesis," *Cell Death & Disease*, vol. 10, no. 3, pp. 1–19, 2019.

[42] C. Li, M. Zhu, J. Zhu et al., "SOX12 contributes to the activation of the JAK2/STAT3 pathway and malignant transformation of esophageal squamous cell carcinoma," *Oncology Reports*, vol. 45, no. 1, pp. 129–138, 2021.

[43] Z. Chen, K. Xiao, S. Chen, Z. Huang, Y. Ye, and T. Chen, "Circular RNA hsa_circ_001895 serves as a sponge of microRNA-296-5p to promote clear cell renal cell carcinoma progression by regulating SOX12," *Cancer Science*, vol. 111, no. 2, pp. 713–726, 2020.

[44] C. Li, Q. Gao, M. Wang, and H. Xin, "LncRNA SNHG1 contributes to the regulation of acute myeloid leukemia cell growth by modulating miR-489-3p/SOX12/Wnt/β-catenin signaling," *Journal of Cellular Physiology*, vol. 236, no. 1, pp. 653–663, 2021.

[45] Z. Shang, X. Ming, J. Wu, and Y. Xiao, "Downregulation of circ 0012152 inhibits proliferation and induces apoptosis in acute myeloid leukemia cells through the miR-625-5p/sox12 axis," *Hematological Oncology*, vol. 39, no. 4, pp. 539–548, 2021.

Hindawi
Oxidative Medicine and Cellular Longevity
Volume 2022, Article ID 4622520, 19 pages
https://doi.org/10.1155/2022/4622520

Research Article

KDM3A Attenuates Myocardial Ischemic and Reperfusion Injury by Ameliorating Cardiac Microvascular Endothelial Cell Pyroptosis

Bofang Zhang, Gen Liu, Bing Huang, Huafen Liu, Hong Jiang, Zheng Hu, and Jing Chen

Department of Cardiology, Renmin Hospital of Wuhan University, Cardiovascular Research Institute, Wuhan University, Hubei Key Laboratory of Cardiology, Wuhan 430000, China

Correspondence should be addressed to Jing Chen; chenjing1982@whu.edu.cn

Received 13 July 2022; Accepted 22 August 2022; Published 2 September 2022

Academic Editor: Shao Liang

Cardiac microvascular endothelial cell ischemia-reperfusion (CMEC I/R) injury occurs in approximately 50% of acute myocardial infarction patients subjected to successful revascularization therapy. This injury leads to cardiac microcirculatory system dysfunctions, which seriously affect cardiac functions and long-term prognostic outcomes. Previously, we elucidated the role of lysine-specific demethylase 3A (KDM3A) in protecting cardiomyocytes from I/R injury; however, its roles in CMEC I/R injuries have yet to be fully established. In this study, hypoxia/reoxygenation (H/R) treatment significantly impaired CMEC functions and induced their pyroptosis, accompanied by KDM3A downregulation. Then, gain- and loss-of-function assays were performed to investigate the roles of KDM3A in CMEC H/R injury *in vitro*. KDM3A knockout enhanced CMEC malfunctions and accelerated the expressions of pyroptosis-associated proteins, such as NLRP3, cleaved-caspase-1, ASC, IL-1β, GSDMD-N, and IL-18. Conversely, KDM3A overexpression developed ameliorated alternations in CMEC H/R injury. *In vivo*, KDM3A knockout resulted in the deterioration of cardiac functions and decreased the no-reflow area as well as capillary density. Mechanistically, KDM3A activated the PI3K/Akt signaling pathway and ameliorated I/R-mediated CMEC pyroptosis. In conclusion, KDM3A is a promising treatment target for alleviating CMEC I/R injury.

1. Introduction

During the last decades, acute myocardial infarction (AMI) incidences have markedly declined as a result of the progressive implementation of preventive therapies and strict control of relative risk factors. However, AMI is among the main causes of mortality as well as morbidity worldwide [1]. Biologically, AMI results from abrupt occlusion of the coronary artery, leading to acute myocardial ischemia and irreversible damage to cardiomyocytes [2]. Therapeutic approaches that are aimed at ameliorating ischemic injuries have been integrated into clinical practice, and timely resumption of blood flow to ischemic myocardium has become a standard therapy [3, 4]. However, reperfusion may cause additional damage to the myocardium and compromise the therapeutic benefits, which is termed ischemic and reperfusion (I/R) injury [5]. This outcome exacerbates postinfarction maladaptive cardiac remolding and heart failure [6, 7]. The pathophysiology of I/R injury is multifactorial and is yet to be fully elucidated, and cardiac microcirculatory system dysfunction has emerged as a strong contributor.

As a highly structured organ, the heart consists of various cell types, such as cardiomyocytes, cardiac microvascular endothelial cells (CMECs), fibroblasts, and inflammatory cells [8]. This multicellularity enables intercellular communication within the heart, which then optimizes its functions [9]. Previous studies assessed the pathologic changes and associated mechanisms in cardiomyocytes during I/R injury. As the main component of the cardiac microcirculatory system, the specific

contributions of CMECs to cardiomyocyte protection against I/R injury have drawn considerable attention. Indeed, CMECs are the most abundant cell types in the heart. Cardiomyocytes are surrounded by a capillary network that is pivotal for maintaining a sustained supply of oxygen and nutrients [10]. Effective revascularization of the infarct-associated artery does not imply sufficient perfusion of the ischemic myocardium, an outcome that is attributed to the myocardial "no-reflow" phenomenon (also known as microcirculatory I/R injury) [11]. Reperfusion induces swelling, deformation, and even death of CMECs, followed by distal embolization, microvascular plugging, and platelet aggregation, resulting in microvascular obstruction (MVO) [12]. The crosstalk between CMECs and cardiomyocytes plays a key role in regulating cardiac functions [13]. During I/R injury, insult to CMECs is the initial factor in cardiomyocyte damage [14, 15]. Therefore, elucidation of the molecular mechanisms involved in microcirculatory I/R injury will inform on maintenance of the normal functions of CMECs to treat myocardial I/R injury.

The complex pathophysiology of MVO is highly associated with inflammation and death of CMECs [16]. Pyroptosis is a unique form of inflammatory programmed cell death that is mediated in a NOD-like receptor thermal protein domain associated protein 3 (NLRP3) inflammasome/caspase-1-dependent manner [17]. Compared to apoptosis and necrosis, pyroptosis is characterized by rapid cell lysis, DNA damage, and massive release of intracellular contents, leading to violent proinflammatory responses [17–19]. Pyroptosis-associated cell death is significant in the myocardial I/R injury process [20, 21]. Besides, the NLRP3 inflammasome is a critical arbitrator of endothelial dysfunction-related inflammatory diseases, such as atherosclerosis, myocardial I/R injury, coronary arteritis, and ischemic stroke [22, 23]. Recently, Sun et al. reported that inhibition of the NLRP3/caspase-1 pathway ameliorates reperfusion injury-induced CMEC pyroptosis, thereby increasing capillary formations, mitigating inflammatory reactions, and attenuating infarct sizes [24]. Therefore, investigation of the key targets that regulate CMEC pyroptosis during I/R injury has therapeutic implications.

Lysine-specific demethylase 3A (KDM3A), which is also referred to as Jumonji domain-containing 1A (JMJD1A), is a member of the Jumonji c domain-containing protein family that functions as a histone demethylase to specifically demethylate the dimethylated histone H3 lysine 9 (H3K9me2) [25]. H3K9 methylation is deemed as a transcriptionally repressive mark; upregulation of KDM3A levels may inhibit H3K9me2 demethylation and activate the transcription of its specific target genes [26]. It has been reported that KDM3A has a role in various biological processes, such as cell proliferation, migration, tumor cell infiltration, and angiogenesis [27, 28]. It also has pathophysiological significance in diabetic vascular complications, AMI, and cardiac hypertrophy [29–31]. Therefore, KDM3A is pivotal in the regulatory network of cardiovascular diseases. In our latest study, KDM3A protected the myocardium from I/R injury and regulated inflammatory reactions as well as death of cardiomyocytes [26]. Nevertheless, the potential significance of KDM3A in CMEC I/R injury has not been conclusively established. We evaluated the roles of KDM3A in pathologic processes of CMEC I/R injury and elucidated on associated mechanisms.

2. Materials and Methods

2.1. Isolation of Primary CMECs and Establishment of Hypoxia/Reoxygenation Models In Vitro. Isolation of CMECs from wild-type (WT) and KDM3A global knockout rats (male, 20 days old) with SD backgrounds was done using the enzyme dissociation method as previously reported [26]. CMECs were cultured in an endothelial cell culture medium, and at a confluence of 80-90%, cells were subjected to anoxic and reoxygenation treatments. To simulate a hypoxic environment, an ischemic buffer (20 mM sodium lactate, 1 mM NaH_2PO_4, 0.5 mM sodium EDTA·$2H_2O$, 24 mM $NaHCO_3$, 118 mM NaCl, 2.5 mM $CaCl_2$·$2H_2O$, and 16 mM KCL) was supplemented to the culture medium. Incubation of cells was done in a trigas incubator that was filled with 5% CO_2 and 95% N_2 for 30 min. To mimic the reperfusion process, the ischemic buffer was replaced by a normal complete medium with further incubation for 6 h in a normoxic environment. To establish if the PI3K/Akt signaling pathway has a role in protective effects of KDM3A on CMECs, the specific PI3K/Akt signaling pathway inhibitor (LY294002 (No. HY-10108, MCE, 20 μM)), was added 1 h before hypoxic and reoxygenation treatments.

2.2. Establishment of KDM3A Knockout Rats. The KDM3A global knockout rats were generated using the CRISPR/Cas9 gene-editing technology as previously described [26, 30]. We designed and created one single guide RNA (sgRNA) flanked exon 5 of the KDM3A gene in rats. After purifying and mixing the sgRNA and Cas9 mRNA, microinjections were performed on embryos. In order to determine the exact indel mutations of the generated founders, the PCR products were TA cloned and sequenced. Thereafter, the F1 heterozygote (KDM3A+/-) was obtained by mating the founder rat (the breeding line) with the WT (KDM3A+/+) SD rat strain. Screening of the KDM3A-KO strain was achieved via sibling mating of heterozygous F1 offspring.

2.3. Adenovirus Transduction. Adenoviral vectors encoding KDM3A (Ad-KDM3A) and control Ad-green fluorescent protein (GFP) (Ad-GFP) were constructed by GeneChem Co., Ltd. (Shanghai, China). At 50%-60% cell confluence, equal amounts of Ad-KDM3A or Ad-GFP at 50 MOI were dissolved into a serum-free medium and transfected for 4 h, respectively. Thereafter, the supernatant containing the adenovirus was abandoned and replaced with complete medium, followed by incubation for another 12 h. Successful transduction of the adenovirus was confirmed by the assessment of GFP expressions under fluorescent microscopy. The Ad-KDM3A-induced upregulation of the KDM3A protein was assessed by the Western blot assay.

2.4. Cell Proliferation and Migration Analyses. Proliferative abilities of CMECs in different groups were assessed by the cell counting kit-8 (CCK-8) assay. Cells were inoculated into 96-well plates (2×10^3 cells/well), incubated, and supplemented

with 20 μL of the CCK-8 reagent (Dojindo Molecular Technologies, Inc., Japan) in every well followed by incubation for 4 h. Optical density (OD) value for all wells were obtained at 450 nm by the spectrophotometry system (Bio-Rad Laboratories, Inc., CA, USA).

The migration capacity of CMECs in each group was evaluated by the Transwell chamber (Corning Inc., Corning, NY, USA) and wound healing assays. Briefly, cells (1×10^5) were inoculated into the upper chamber with serum-free medium (200 μL) while 600 μL medium with FBS (10%) was perfused into the lower chamber followed by 12 h of incubation. Nonmigrating cells on the upper side of the membrane were gently wiped off while cells that had migrated to the lower membrane surface were formaldehyde (4%)-fixed and stained with crystal violet (0.5%) in the dark. At least three wells from each group were selected, and one random field of each well was chosen to count the cells that were on the lower surface of the membrane by light microscopy (Olympus Corporation, Tokyo, Japan). Wound healing assays were performed using culture inserts (No. 81176, Cat., USA). In this assay, 70 μL of CMEC suspension containing 1×10^4 cells was inoculated into each side of the inserts and incubated for 12 h. The culture insert was gently removed when the cell layer reached confluency. One mL of endothelial cell medium was extracted to fill the dishes, after which the CMECs were incubated for another 12 h. Representative images were obtained by light microscopy, and the wound closure rate for each group was calculated using the ImageJ software.

2.5. Tube Formation and Sprouting Assay. After various treatments, angiogenesis abilities of CMECs were measured by tube formation and sprouting assays. Briefly, 80 μL liquid Matrigel was infused into each well of 96-well plates and sat still for 1 h to solidify. Then, trypsinized CMECs were resuspended into the complete medium and seeded into Matrigel-coated wells (1×10^4 cells/well). After 8 h, capillary-like tube structures were determined by light microscopy; total tube length and tube loops for each well in one high-power field were evaluated by ImageJ software. For the sprouting assay, trypsinized CMECs were resuspended in 0.2% methylcellulose and adjusted to 1000 cells/spheroid per 25 μL. Using a multichannel pipette (25 μL), droplets were placed on the cover of 15 mL plates, covered with the plate, flipped upright, and incubated overnight. 12 h later, 10 mL of PBS with 10% FBS was pipetted onto the cover plates to collect the spheroids that were centrifuged for 5 min at 300 g. A collagen matrix was used to resuspend the spheroids, after which 500 μL was transferred to each well of the 24-well plate. Subsequently, 0.5 mL endothelial cell culture medium was added on top of the collagen matrix followed by incubation for another 12 h. At the end of the experiment, spheroids were imaged for quantification of sprout counts and determination of sprout length.

2.6. Cell Death Analysis. In vitro, CMEC vitality was assessed using Hoechst 33342/PI double fluorescent staining. Briefly, CMECs at a density of 5×10^5 were seeded onto coverslips and subjected to corresponding treatments. Then, cells in different groups were incubated with Hoechst 33342 for 10 min and PI for 25 min away from light. Stained cells were observed by microscopy. The percentage of Hoechst 33342/PI dual-positive cells was measured to determine the apoptotic rate. To measure *in vivo* cell death ratios, TUNEL staining was performed as instructed by the manufacturer. The myocardium (red) was marked by the anti-α-actinin antibody, while DAPI and green fluorescent dye was used to label entire (blue) and apoptotic (green) nuclei, respectively. The apoptotic index (AI) was determined as the ratio of TUNEL-positive cells (green) to total cells (blue).

2.7. Secretory Capacity Assay. To measure the secretory capacity of CMECs in different groups *in vitro*, levels of Nitric Oxide (NO) in the cell culture supernatants were assayed by the enzyme-linked immunosorbent assay (ELISA; Nanjing Jiancheng Biology Engineering Institute, China) as instructed by the manufacturer. eNOS activities were determined by the conversion of L-[14C] arginine to L-[14C] citrulline in the cell lysate of each group (Cayman Chemical, MI).

2.8. Establishment of Rat I/R Injury Models and Assessment of Myocardial Infarct Sizes. The myocardial I/R model was established as reported [26]. Rats (male, 6-8 weeks, 220-250 g) were anaesthetized via intraperitoneal administration of pentobarbital sodium (40 mg/kg) (Sigma-Aldrich, USA), and a left parasternal incision was performed. Then, left anterior descending (LAD) ligation was performed for 30 min on rats, followed by reperfusion for 24 h. Sham-operated rats underwent the same operations, minus LAD occlusion or reperfusion.

Evans blue and TTC staining were done to detect myocardial infarct sizes. At 24 h after I/R injury, LAD was religated at the site of prior occlusion, and Evans blue (2.0%, 1 mL) (Sigma-Aldrich, USA) was administered into the aorta. Hearts from each rat group were collected, transected at the papillary muscle plane, and incubated with 1% TTC. White areas (negatively stained) denoted the infarcted myocardium. The proportion of myocardial infarct was determined as infarcted areas/total left ventricle (LV) areas $\times$ 100%.

2.9. Evaluation of Cardiac Functions. An echocardiography assay was conducted to assess cardiac LV functions at baseline and at 24 h after reperfusion. Ultrasound images were obtained from the parasternal short axis at the midpapillary muscle level, after which left ventricular fractional shortening (LVFS) and left ventricular ejection fraction (LVEF) were subsequently calculated.

2.10. Determination of No-Reflow Area and Capillary Density. The no-reflow area of each group after I/R treatment was measured by thioflavin-S and Evan's blue dual-staining. At 24 h after reperfusion, thioflavin-S (4%) was administered via the inferior vena cava and stained for 5 min. Then, LAD was religatured at the same occlusion location, and 3% Evan's blue was administered to the nonschemic myocardium via the jugular vein for staining. Thereafter, rat hearts were obtained from every group, transected at the papillary muscle plane, and exposed to ultraviolet

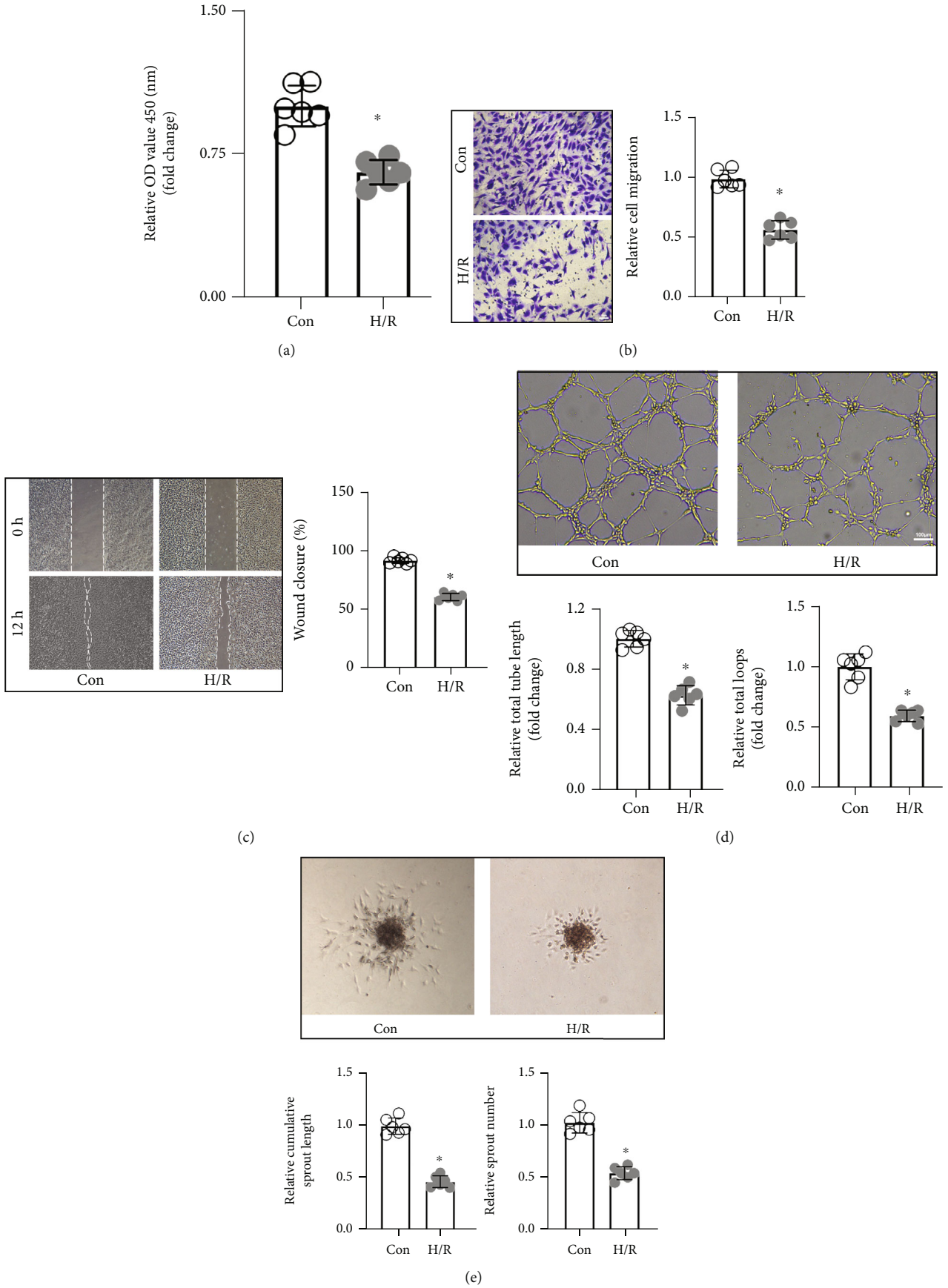

Figure 1: Continued.

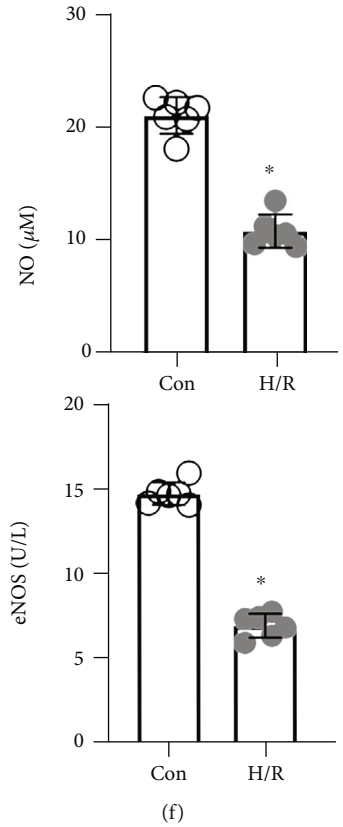

Figure 1: H/R treatment resulted in CMEC injury and dysfunction. (a) The proliferative capacity of CMECs was assessed by the CCK-8 assay, and the OD value was the quantitative indicator ($n = 6$, $^*p < 0.05$, relative to the Con group). The migration capacity of CMECs was measured by the transwell chamber assay (b) and wound healing assay (c), respectively. The number of cells on the lower membrane surface (scale bar = 50 μm) and wound closure rate of each group were calculated ($n = 6$, $^*p < 0.05$, relative to the Con group). The neovascularization capacity of CMECs was measured by tube formation (d) and sprouting assays (e). Total tube length and total loops (scale bar = 50 μm), as well as cumulative sprouts and sprout counts for each group, were evaluated ($n = 6$, $^*p < 0.05$, relative to the Con group). (f) To detect the synthesis and secretion capacities of CMECs, eNOS and NO levels in supernatants of every group were determined ($n = 6$, $^*p < 0.05$, relative to the Con group).

light. Myocardium tissues with blue fluorescence indicated normal perfusion. Areas with no-reflow (attenuated or absent thioflavin-S fluorescence) were determined by the software of ImageJ and presented as a ratio of LV.

To investigate capillary densities of different groups, representative sections of different groups were stained with the CD31 antibody as previously described [32].

2.11. Western Blot Assay. In this assay, CMECs and myocardial tissue samples were lysed using the RIPA lysis buffer for protein extraction as instructed by the manufacturer. Then, 4.5 μg/μL total proteins from each group were separated by 10% SDS-PAGE, transferred onto polyvinylidene fluoride membranes (Millipore, MA, USA), blocked using 5% nonfat dried milk, and incubated overnight with primary antibodies against KDM3A, p-Akt, NLRP3, ASC, IL-1β, GSDMD-N, cleaved-caspase-1, and IL-18. Further incubation was performed with appropriate secondary antibodies. An enhanced chemiluminescence system (Thermo Fisher Scientific, Inc.) was used to visualize the protein bands. GAPDH was the internal control. BandScan 4.30 (Glyko, Novato, CA, USA) was used to semiquantify the blots.

2.12. Statistical Analysis. Continuous variables are presented as the mean ± SD. Student's t-test was used for between-group comparisons of means while one-way analysis of variance (ANOVA) was used for among-group comparisons, followed by the Student-Newman-Keuls (SNK) q tests for pairwise comparisons. $p \leq 0.05$ denoted significance. The SPSS 19.0 and GraphPad Prism (Version 8.2.1) software were used for analyses.

3. Results

3.1. H/R Treatment Induced CMEC Injury and Dysfunction. The capacities of CMECs for proliferation, migration, angiopoiesis, and secretion were determined before and after H/R treatment. Figure 1(a) shows that cell proliferative potential in the H/R group was markedly reduced, relative to the control group. Findings from the transwell chamber assay indicated that there were fewer cells that had migrated to the lower membrane surface in the H/R group (Figure 1(b)). The wound healing rate of the H/R group was also reduced, relative to the control group (Figure 1(c)). Migration capacities of CMECs were impaired after H/R treatment.

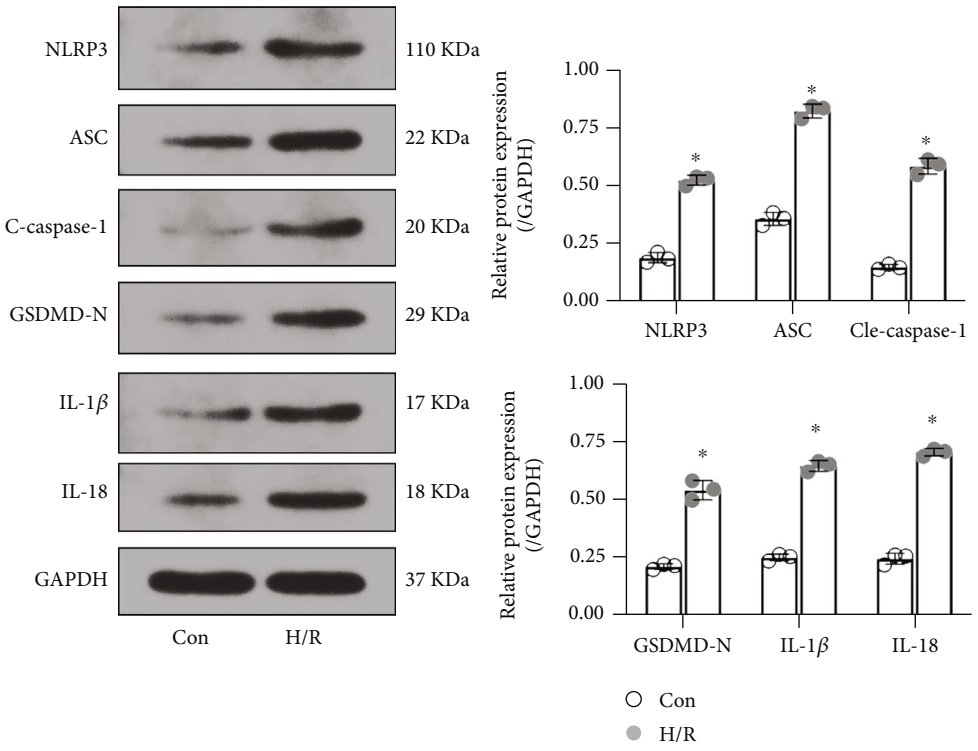

(a)

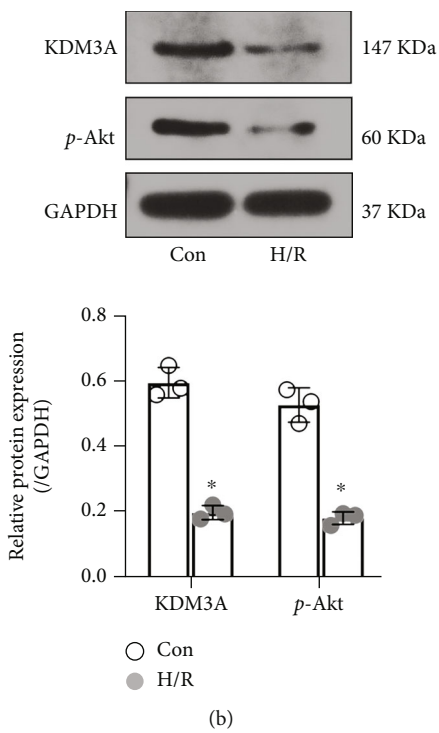

(b)

Figure 2: Continued.

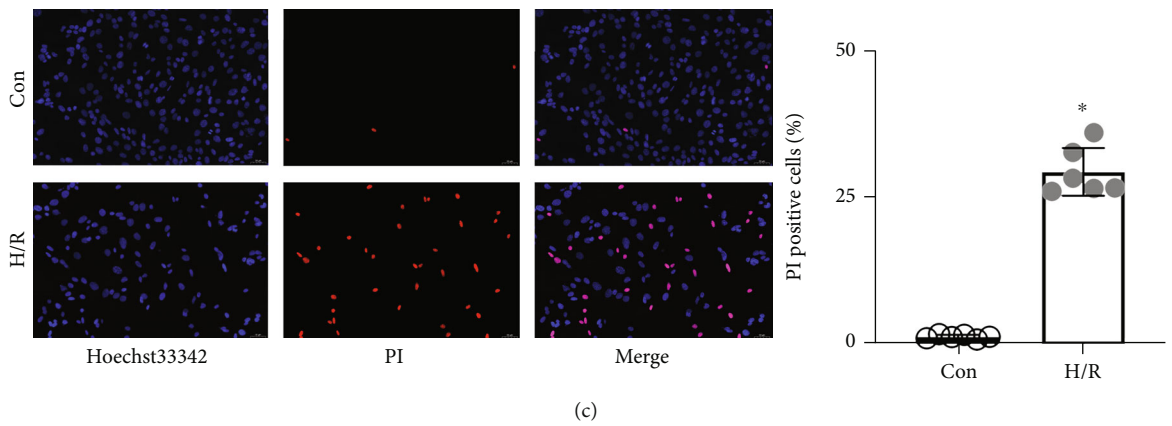

(c)

Figure 2: H/R treatment induced CMEC pyroptosis accompanied by downregulation of KDM3A and p-Akt. (a) The Western blot assay was conducted to evaluate the levels of pyroptosis-related proteins, including NLRP3, GSDMD-N, cleaved-caspase-1, ASC, IL-1β, and IL-18 ($n = 3$, $^*p < 0.05$, relative to the Con group). (b) The expressions of KDM3A and p-Akt before and after H/R treatments were also detected by Western blot assay ($n = 3$, $^*p < 0.05$, relative to the Con group). (c) Hoechst 33342/PI double fluorescent staining was performed to detect cell death *in vitro*, and the percentage of PI-positive cells was calculated in each group ($n = 6$, $^*p < 0.05$, relative to the Con group).

Neovascularization is a vital ability of endothelial cells. In Figure 1(d), total tube length and total vascular loop number of CMECs in the H/R group were less than those of the control group. Moreover, sprout numbers and sprout length of CMECs were decreased after H/R treatment (Figure 1(e)). Then, eNOS and NO levels in the supernatant were measured to assess cell synthesis and secretion capacities for each group. It was found that eNOS and NO levels were markedly suppressed in the H/R group (Figure 1(f)). As a result, H/R treatment led to CMEC injury and cellular dysfunction.

3.2. H/R Treatment Induced CMEC Pyroptosis and Altered KDM3A Expressions. NLRP3/caspase-1-dependent pyroptosis is positively associated with I/R injury [20, 21, 24]. To determine if pyroptosis was induced in CMECs during H/R, key pyroptosis-associated indicators, such as NLRP3, ASC, cleaved-caspase-1, GSDMD-N, IL-1β, and IL-18, were detected by Western blotting. In Figure 2(a), expressions of the above indicators were significantly enhanced in response to H/R treatment, relative to the control group. There was an obvious increase in the number of Hoechst 3342/PI dual-stained positive cells in the H/R-treated group. However, as a crucial mediator in cardiovascular diseases, expressions of KDM3A and its downstream target (p-Akt) were downregulated after H/R treatment. These findings imply that CMEC pyroptosis is involved in H/R and KDM3A is an important contributor during the process.

3.3. KDM3A Knockout Exacerbated H/R-Induced CMEC Injury and Dysfunction. To establish the effects of KDM3A on CMECs after H/R treatment, loss-of-function assays were conducted. The KDM3A-KO rat strain was established, and KDM3A gene deleted CMECs were isolated. Determination of whether KDM3A gene knockout affected CMEC functions under normoxic conditions revealed that there were no marked differences between the WT and KDM3A-KO groups with regard to their capacities for cell proliferation, migration, angiogenesis, and secretion (Supplementary Figure 1). Thereafter, the cellular functions were measured again after cells had been subjected to H/R treatments. In Figure 3(a), proliferation capacities of cells in the KDM3A-KO+H/R group were markedly weakened, relative to the WT+H/R group. Besides, H/R markedly inhibited the migration capacities of CMECs, which were exacerbated by KDM3A knockout (Figures 3(b) and 3(c)). Data from tube formation and sprouting assays showed that KDM3A knockout impaired the angiogenic potency of CMECs, as manifested by reduced tube length and total tube loop number as well as the reduced sprout numbers and sprout length in the KDM3A-KO+H/R group (Figures 3(d) and 3(e)). Regarding cell secretion functions, Figure 3(f) shows that KDM3A gene deficiency inhibited the secretion of protective cytokines. These findings imply that KDM3A knockout aggravates H/R-induced CMEC malfunctions.

3.4. KDM3A Knockout Deteriorates H/R-Induced CMEC Pyroptosis and Suppressed p-Akt Levels. To establish whether KDM3A can regulate CMEC pyroptosis during H/R-mediated injury and to investigate the underlying mechanisms, we assessed the levels of pyroptosis-associated proteins and p-Akt levels before and after KDM3A knockout. In Figure 4(a), KDM3A knockout upregulated NLRP3, cleaved-caspase-1, ASC, GSDMD-N, IL-1β, and IL-18 levels. Moreover, the increase in the number of Hoechst 3342/PI dual-staining positive cells implies that KDM3A knockout promoted cell death. However, p-Akt protein levels were markedly decreased after KDM3A gene deletion, suggesting that KDM3A knockout exacerbated H/R-induced CMEC pyroptosis by suppressing the PI3K/Akt signaling pathway.

3.5. KDM3A Overexpression Ameliorated H/R-Induced CMEC Injury and Dysfunction, while LY294002 Treatment Reversed These Effects. To validate the putative function of KDM3A, gain-of-function experiments were also performed. We tried to construct CMECs-specific KDM3A

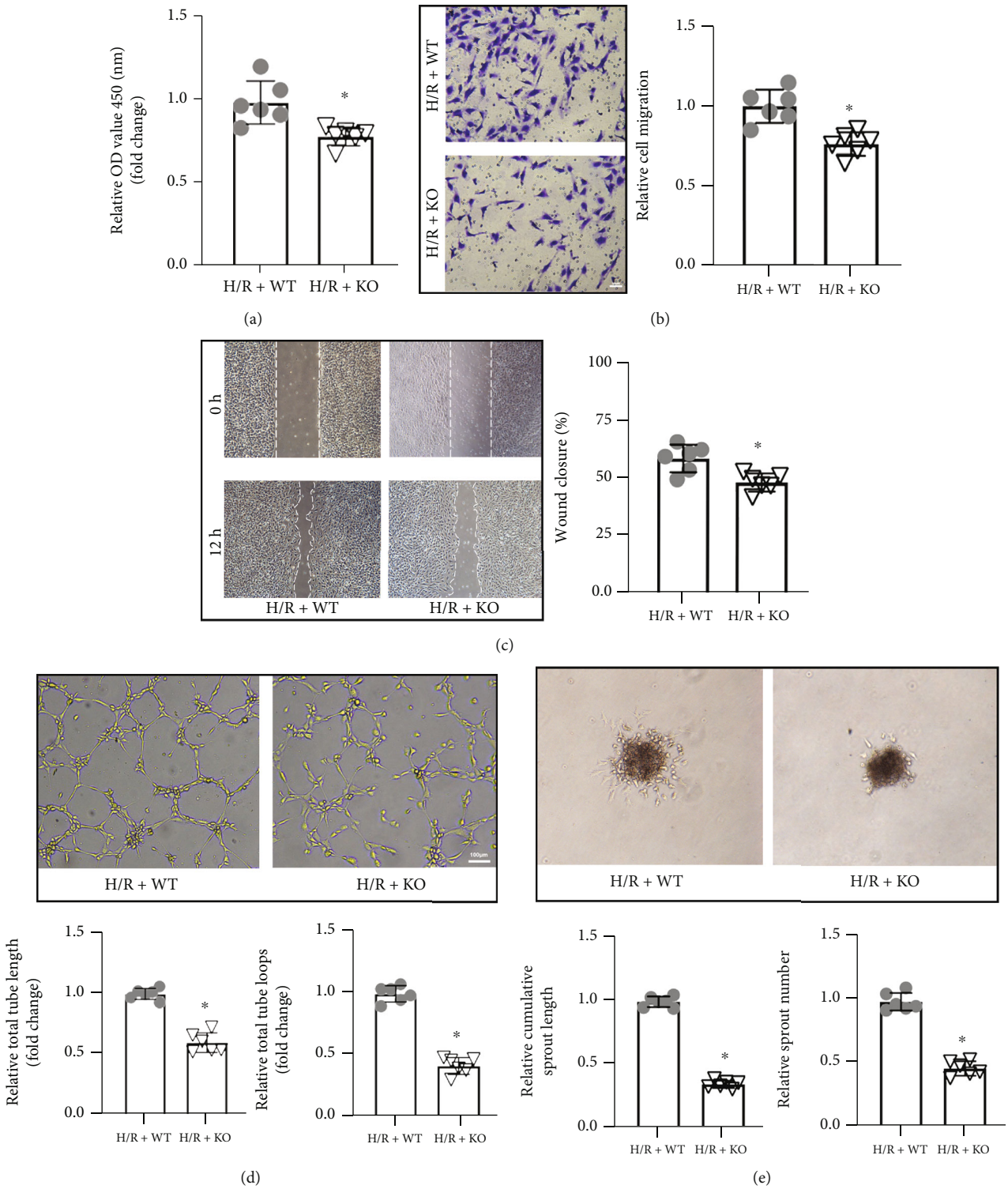

Figure 3: Continued.

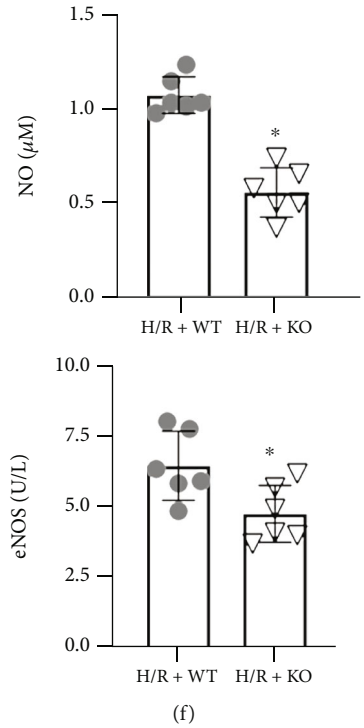

Figure 3: KDM3A knockout exaggerated H/R-induced CMEC injury and dysfunction. (a) The CCK-8 assay was used to estimate the proliferative abilities of WT CMECs and KDM3A-KO CMECs during H/R ($n = 6$, $^*p < 0.05$, compared to the H/R+WT group). (b, c) Transwell chamber and wound healing assays were conducted to assess the migration capacities of CMECs before and after KDM3A knockout during H/R ($n = 6$, $^*p < 0.05$ relative to the H/R+WT group). (d, e) Tube formation and sprouting assays were performed to investigate the neovascularization capacities of CMECs in the H/R+WT and H/R+KO groups ($n = 6$, $^*p < 0.05$, relative to the H/R+WT group). (f) Levels of eNOS and NO in supernatants were measured to assess the synthesis and secretion capacities of CMECs in every group after H/R treatment ($n = 6$, $^*p < 0.05$, relative to the H/R+WT group).

overexpression rats; unfortunately, the embryo does not survive. As a result, Ad-KDM3A recombinant adenovirus vector was constructed as an alternative and transfected into CMECs to upregulate KDM3A protein levels. Proliferative capacities of CMECs in different groups were evaluated by the CCK-8 assay. In Figure 5(a), KDM3A overexpression attenuated the H/R-induced impairment of proliferation capacities. However, pretreatment with LY294002, a specific PI3K/Akt signaling pathway inhibitor, ameliorated the advantage of KDM3A upregulation. Similarly, KDM3A overexpression improved the migration capacity of CMECs after H/R treatment, as manifested by the migration of more cells to the lower membrane surface and enhanced wound healing rate in the Ad-KDM3A+H/R group. LY294002 treatment ameliorated these beneficial effects (Figures 5(b) and 5(c)). Consistently, to a large extent, Ad-KDM3A transfection compensated for the adverse effects of hypoxia on angiogenic functions of CMECs. Tube length and total tube loop number as well as sprout numbers and sprout length in the Ad-KDM3A+H/R group were markedly increased, relative to the Ad-GFP+H/R group. Variations of these parameters were reversed by suppression of the PI3K/Akt signaling pathway (Figures 5(d) and 5(e)). Regarding cell synthesis and secretion functions, Figure 5(f) shows that overexpressed KDM3A significantly enhances the secretion of eNOS and NO in response to H/R, whereas LY294002 eliminates these beneficial effects. Collectively, these findings show that KDM3A has significant roles in the repair of impaired CMECs' functions. Its multiple protective effects against H/R might be associated with the PI3K/Akt signaling pathway.

3.6. KDM3A Overexpression Mitigated H/R-Induced CMEC Pyroptosis via PI3K/Akt Signaling Pathway Activation. Given that KDM3A deletion aggravated H/R-induced CMEC pyroptosis, we evaluated the effects of overexpressed KDM3A. In Figure 6(a), Ad-KDM3A transfections markedly inhibited the H/R-induced upregulation of pyroptosis-associated proteins. PI3K/Akt signaling pathway suppression by LY294002 ameliorated these beneficial effects. Consistent with these results, KDM3A upregulation markedly reduced H/R injury-induced cell death, while LY294002 pretreatment reversed these outcomes. Meanwhile, treatment with LY294002 suppressed KDM3A overexpression-induced PI3K/Akt signaling pathway activation. Evidence from the gain- and loss-of-function assays confirmed that KDM3A could regulate CMEC pyroptosis by regulating the PI3K/Akt signaling pathway.

3.7. KDM3A Knockout Exacerbated I/R-Induced Cardiac Function Deterioration and Reduced the Perfusion of Coronary Microcirculation. We aimed to validate our *in vitro* findings

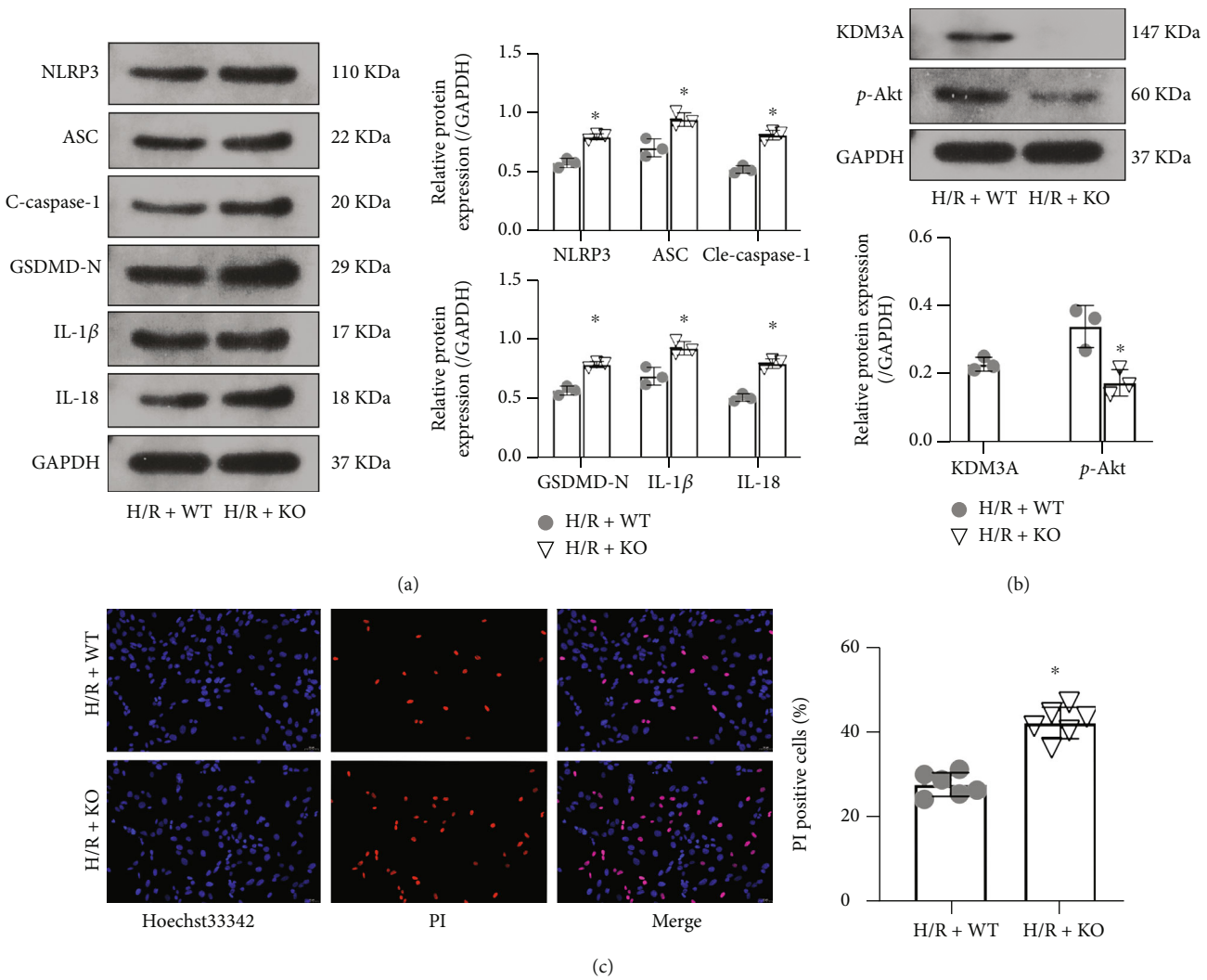

Figure 4: KDM3A knockout promoted H/R-induced CMEC pyroptosis and suppressed p-Akt levels. (A) Western blotting was performed to determine the levels of pyroptosis-related proteins, such as NLRP3, GSDMD-N, cleaved-caspase-1, ASC, IL-1β, and IL-18 ($n = 3$, $^*p < 0.05$ relative to the H/R+WT group). (b) Western blotting was also performed to verify the effects of KDM3A knockout and to detect p-Akt levels after KDM3A knockout during H/R stimulation ($n = 3$, $^*p < 0.05$, relative to H/R+WT group). (c) CMECs that had lost their vitality in the H/R+WT and H/R+KO groups were analyzed by Hoechst 33342/PI double fluorescent staining ($n = 6$, $^*p < 0.05$, compared to the H/R+WT group).

in vivo using wild-type and KDM3A gene globe-knockout rats. Echocardiography was performed to evaluate cardiac functions for each group. In Figure 7(a) and Supplementary Figure 2, KDM3A knockout reduced the percentage of LVEF and LVFS, compared to the WT group in response to I/R injury. Besides, KDM3A gene deletion enlarged the myocardial infarct sizes (Figure 7(b)). In addition, I/R injury significantly increased the no-reflow area, accompanied by a marked decrease in capillary density. However, the situation is getting worse as manifested by an enlarged no-reflow area and reduced fluorescence intensities of CD31 in the KDM3A-KO +I/R group (Figures 7(c) and 7(d)). Moreover, the I/R insult resulted in massive cell death in the myocardial tissue, which was further exacerbated by KDM3A knockout. TUNEL-positive cells were increased in the KDM3A-KO+I/R group, relative to the KDM3A-WT+I/R group (Figure 7(e)). Thus, the evidence above indicates that KDM3A alleviates I/R injury by remediating coronary microcirculation dysfunction.

4. Discussion

Although KDM3A protects cardiomyocytes from I/R injury, its involvement and potential molecular mechanisms in alleviating CMEC I/R injury have yet to be fully established. To elucidate the cause-effect relationship between KDM3A and CMEC I/R injury, we created CMEC I/R injury models and tried to decipher its significance. The KDM3A levels in CMECs were markedly reduced in response to H/R. KDM3A knockdown further impaired the proliferation, migration, and angiogenesis capacities of CMECs after H/R treatment. Besides, KDM3A deletion exacerbated H/R-induced inflammatory

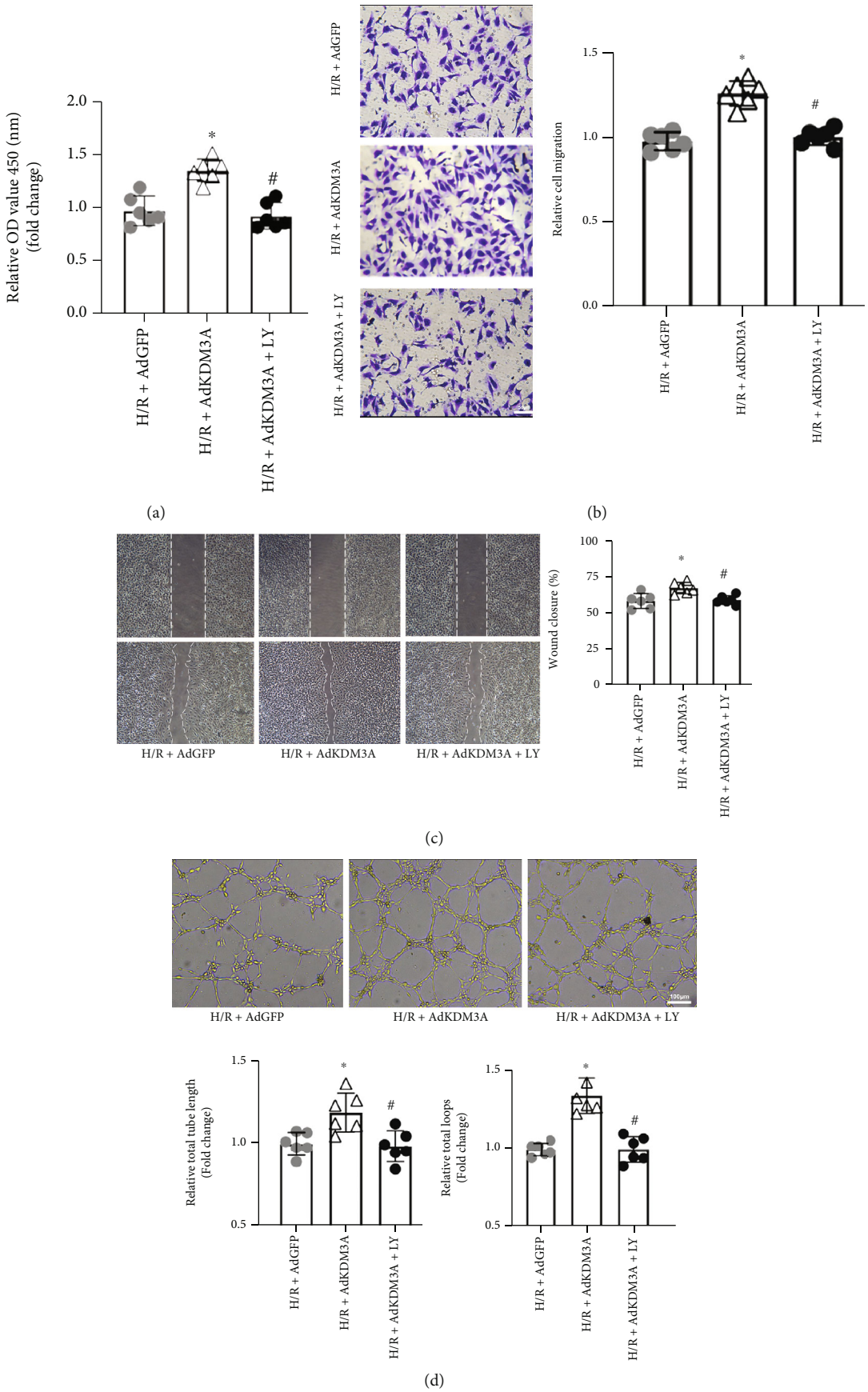

Figure 5: Continued.

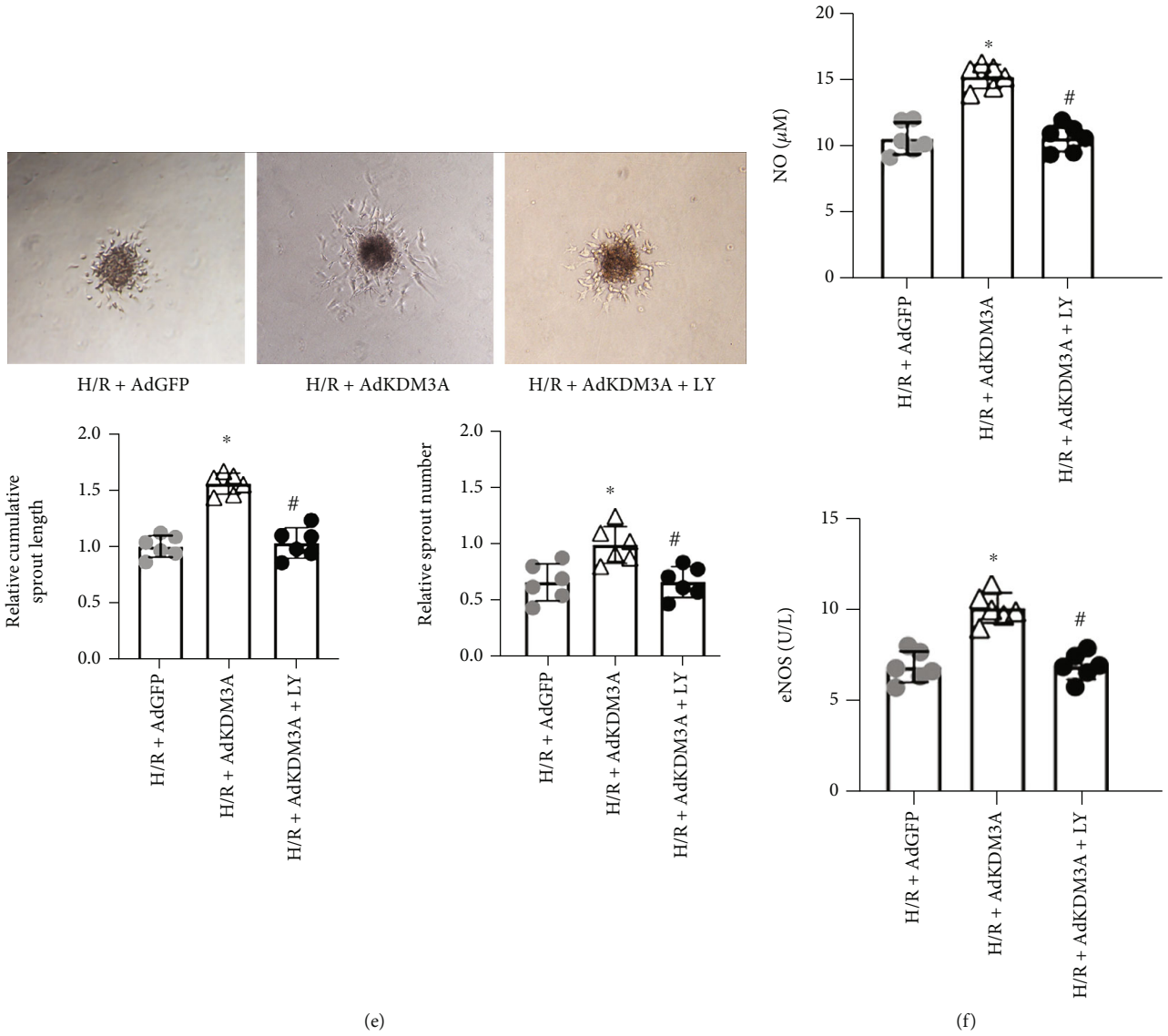

Figure 5: KDM3A overexpression ameliorated H/R-induced CMEC injury and dysfunctions, while suppression of the PI3K/Akt signaling pathway reversed these beneficial effects. (a) The CCK-8 assay was conducted to measure the proliferative abilities of CMECs in each group ($n = 6$, $^{*}p < 0.05$, relative to the H/R+Ad-GFP group, $^{\#}p < 0.05$, compared to the H/R+Ad-KDM3A group). (b, c) Migration abilities of CMECs after KDM3A overexpression or/and PI3K/Akt inhibition were detected by transwell chamber and wound healing assays ($n = 6$, $^{*}p < 0.05$, compared to the H/R+Ad-GFP group, $^{\#}p < 0.05$, compared to the H/R+Ad-KDM3A group). (d, e) Images of tube formation and sprouting assay for each group. Neovascularization capacities of CMECs after KDM3A overexpression or/and PI3K/Akt signaling pathway inhibition were evaluated. (f) eNOS and NO levels in supernatants of each group were measured to determine the synthesis and secretion capacities of CMECs ($n = 6$, $^{*}p < 0.05$, compared to the H/R+Ad-GFP group; $^{\#}p < 0.05$, compared to the H/R +Ad-KDM3A group).

responses in CMECs and cell death, accompanied by marked upregulations of pyroptosis-associated cytokines. However, these negative outcomes were reversed by KDM3A upregulation. Notably, pretreatment with LY294002, a PI3K/Akt pathway inhibitor, partially reduced the beneficial effects of KDM3A upregulation. *In vivo*, KDM3A knockout exacerbated cardiac functions as well as myocardial damage and reduced the density of the capillary network during I/R injury. This is the first study to establish that KDM3A inhibits CMEC I/R injury, supporting the notion that KDM3A can mitigate I/R-induced CMEC pyroptosis via PI3K/Akt signaling pathway activation.

Fresh blood supply to ischemic tissues is the most efficient way of reducing ischemia-induced cardiomyocyte damage or death [3]. Nevertheless, microvascular I/R injury occurs in about 50% of patients, including those with successful revascularization treatment [33]. Despite blood flow of the epicardial artery being restored rapidly and effectively if microvascular I/R injury occurs, capillaries that nourish cardiomyocytes are ineffectively infused [11, 12]. This phenomenon emerges

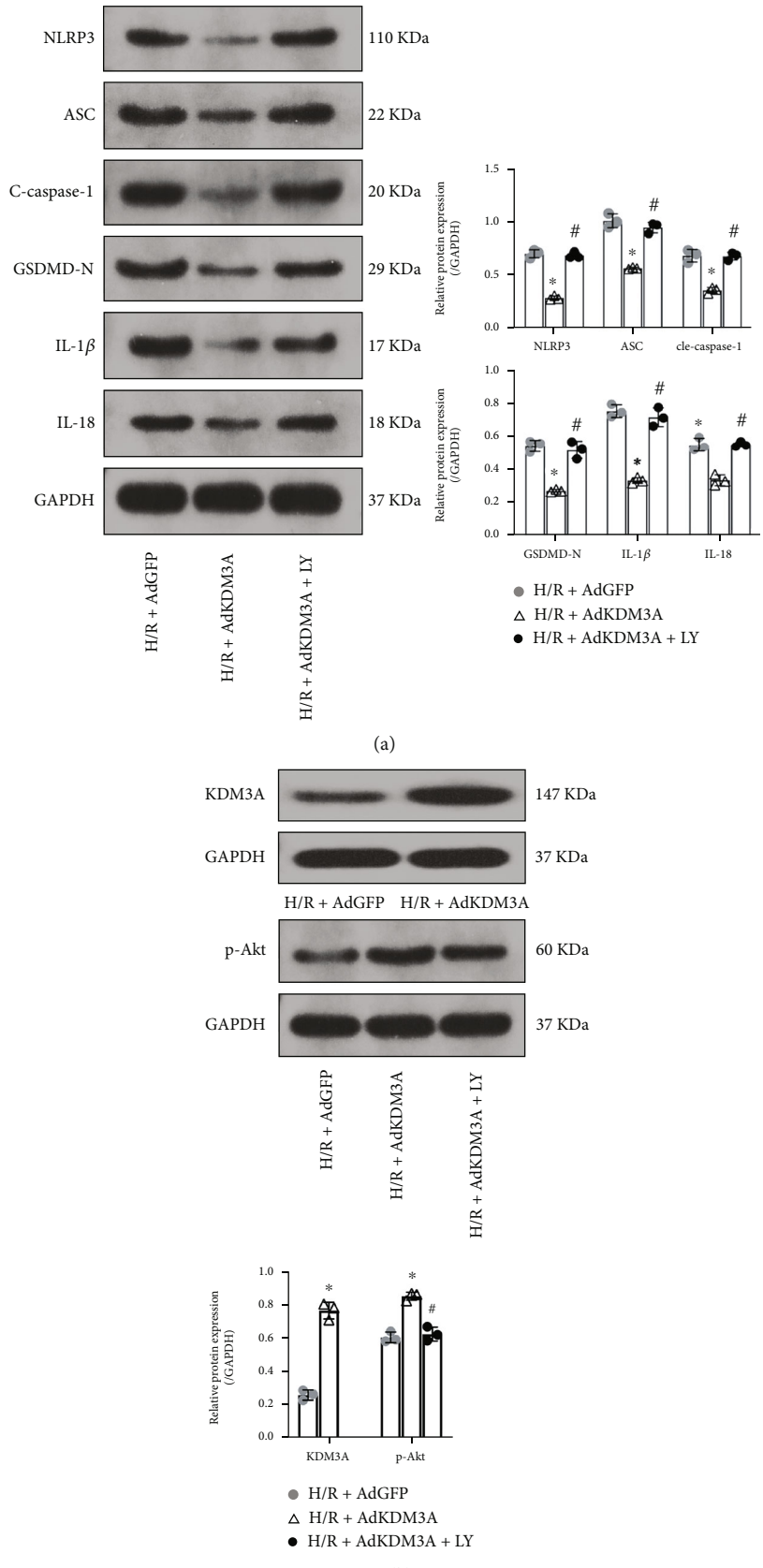

Figure 6: Continued.

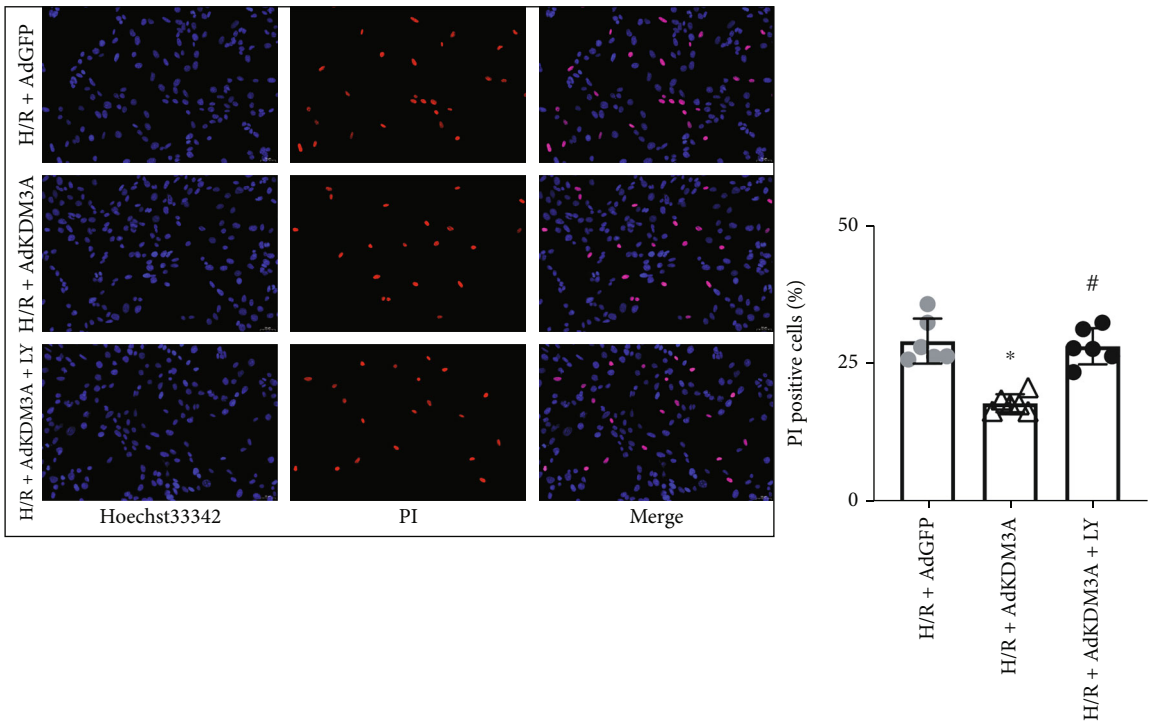

(c)

Figure 6: KDM3A overexpression mitigated H/R-induced CMEC pyroptosis through activating PI3K/Akt signaling pathway. (a) Protein levels of NLRP3, ASC, GSDMD-N, cleaved-caspase-1, IL-1β, and IL-18 were analyzed by Western blot assay. KDM3A overexpression significantly downregulated the expressions of pyroptosis-associated proteins while LY294002 treatment ameliorated these beneficial effects in the setting of H/R ($n = 3$, $^{*}p < 0.05$, compared to the H/R+Ad-GFP group, $^{\#}p < 0.05$, compared to the H/R+Ad-KDM3A group). (b) Western blot assay was also performed to verify the transfection effects of Ad-KDM3A and to detect the expressions of p-Akt after KDM3A overexpression or/and PI3K/Akt inhibition under the condition of H/R stimulation. (c) Hoechst 33342/PI double fluorescent staining was conducted to assess cell death in each group ($n = 6$, $^{*}p < 0.05$, compared to the H/R+Ad-GFP group, $^{\#}p < 0.05$, compared to the H/R+Ad-KDM3A group).

within several minutes after revascularization and lasts for a few weeks. Epidemiologically, microvascular injury is an independent predictive risk factor for in-hospital mortality and one-year major adverse cardiovascular events [34]. There is an intimate physiological association between CMECs and cardiomyocytes. Anatomically, each cardiomyocyte is surrounded by 3–4 CMECs [35]. The microcirculatory network formed by CMECs is far from merely being the interface between epicardial vessels and cardiomyocytes and also provides oxygen and nutrition, which are necessary for cardiomyocytes to survive. Moreover, under physiological conditions, CMECs are involved in cardiac metabolism, contractile performance, growth, and rhythmicity [14, 36, 37]. It has been reported that CMECs are the first responder cells to cardiac I/R injury, and their malfunctions exacerbate the impairment of cardiomyocytes, acting as dynamic sensors and modulators for myocardial functions [13, 38]. Therefore, there is a need to decipher the underlying mechanisms in microvascular I/R injury and to determine effective therapeutic targets for the efficient amelioration of the no-reflow phenomenon.

As a newly recognized pattern of inflammation-associated cell death, pyroptosis is implicated in cardiovascular disease development, especially atherosclerosis, AMI, and myocardial I/R injuries [20, 39, 40]. In stressful environments, myocardial reperfusion injury-induced danger-associated molecular patterns activate the NLRP3 inflammasome, which is a representative multimeric protein complex that acts as the innate immune signal receptor to sense multiple stimuli and induce inflammatory responses under pathological and physiological states. The specific pyroptotic caspase-1 is recruited to the NLRP3 inflammasome and converted into its active form via autocatalysis. Precursors of IL-1β as well as IL-18 are cleaved into their mature form by activated caspase-1, which also separates the C- and N-terminals of GSDMD. Consequently, numerous nanopore holes are formed on the cell membrane, leading to elevated secretion of proinflammatory cytokines and induction of secondary inflammation cascades, resulting in cell swell, lysis, and pyroptotic death [40–42]. Inhibiting NLRP3 inflammasome activation in the early reperfusion period can ameliorate AMI-induced deterioration of cardiac performance and minimize the infarct size [43]. Besides, Bai et al. reported on intimate interactions between endothelial dysfunctions and NLRP3 inflammasome-associated pathways. Moreover, they highlighted the significance of the NLRP3 inflammasome in endothelial dysfunction-associated inflammatory diseases [23]. Sun et al. reported that myocardial I/R injury provoked the canonical NLRP3/caspase-1-depended pyroptosis pathway. However, gastrodin treatment inhibited CMEC pyroptosis and proinflammatory cascades, reducing

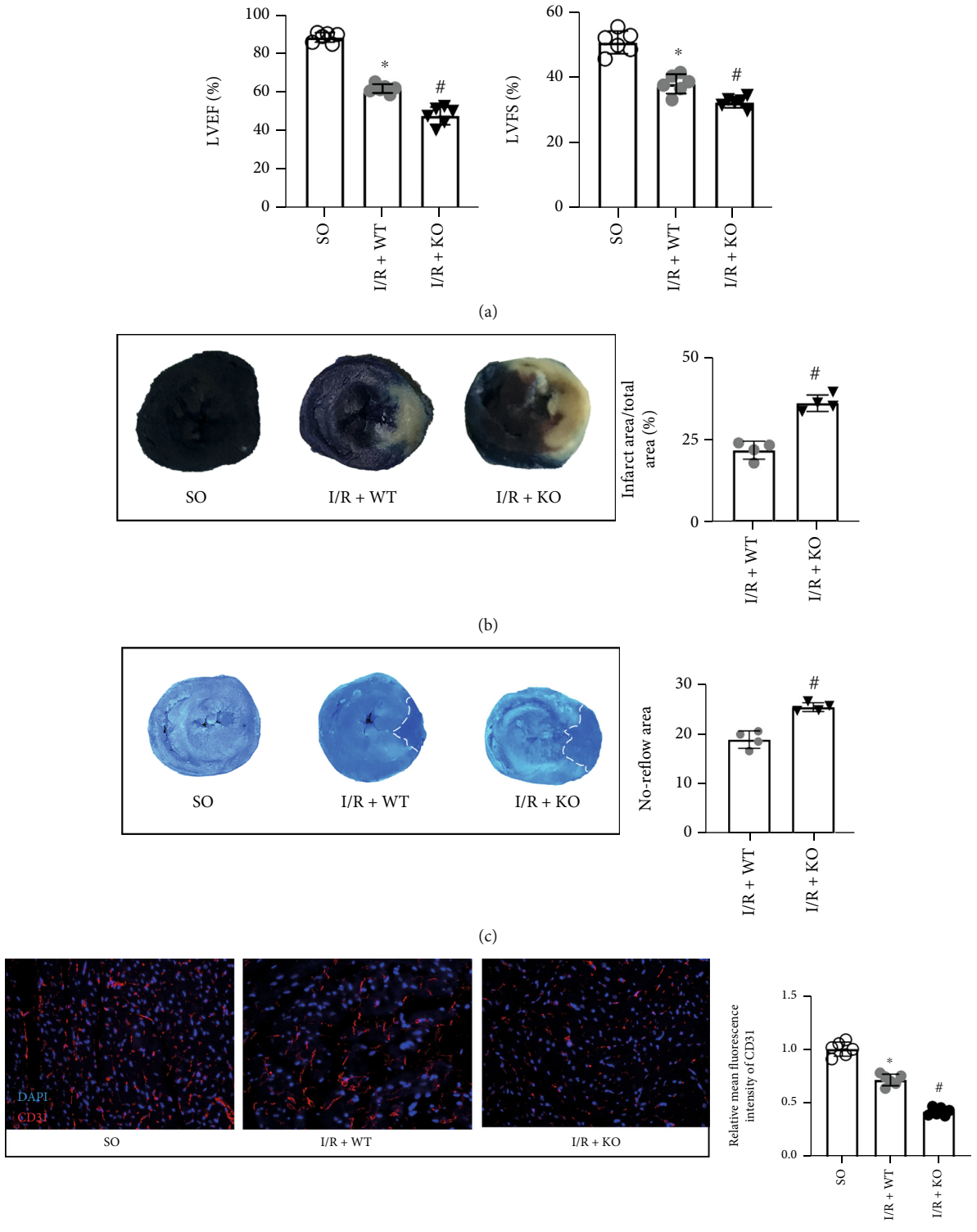

Figure 7: Continued.

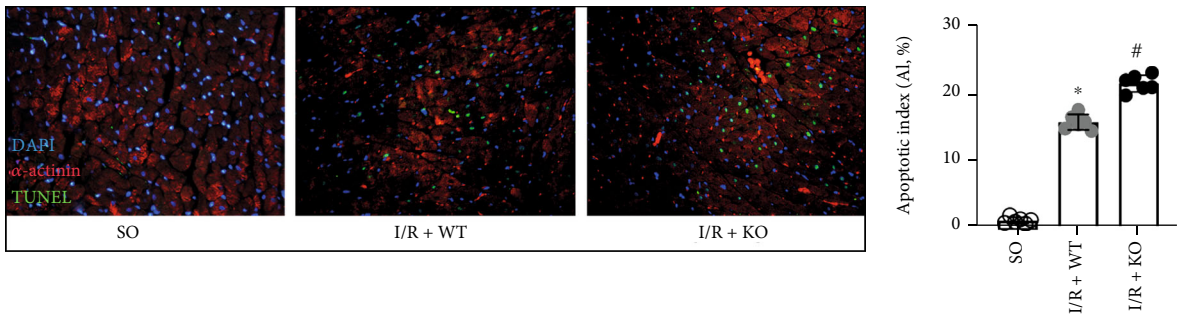

(e)

Figure 7: KDM3A knockout further exacerbates the deteriorated cardiac function and myocardial injury induced by I/R injury as well as reduces the perfusion of coronary microcirculation. (a) The changes in cardiac function, including LVEF and LVFS, were evaluated by echocardiography in rats of different groups ($n = 6$, $^{*}p < 0.05$, as compared to the SO group; $^{\#}p < 0.05$, as compared to the H/R+WT group). (b) Representative images of the myocardial infarction area of each group, and the ratio of the infarction area to the total left ventricular area was calculated ($n = 4$, $^{*}p < 0.05$, as compared to the SO group; $^{\#}p < 0.05$, as compared to the H/R+WT group). (c) Representative images of thioflavin-S and Evan's blue dual-staining were performed to detect the no-reflow area after I/R injury of each group ($n = 4$, $^{*}p < 0.05$, as compared to the SO group; $^{\#}p < 0.05$, as compared to the H/R+WT group). (d) Representative images of CD31 fluorescence staining were conducted to estimate the capillary density. Scale bar = 20 μm. (e) Representative images and averaged data of the apoptotic index in rat heart tissue of each group. TUNEL staining (green) indicates apoptotic nuclei; DAPI counterstaining (blue) indicates total nuclei. Scale bar = 20 μm. The apoptotic index (AI) is presented as the percentage of TUNEL-positive nuclei to the total number of nuclei ($n = 6$, $^{*}p < 0.05$, as compared to the SO group; $^{\#}p < 0.05$, as compared to the H/R+WT group).

myocardial infarct size, alleviating inflammatory cell infiltration, and increasing capillary formation [24]. Consistently, our findings indicated that the proliferation, migration, angiogenesis, and secretory capacities of CMECs after H/R treatment were significantly compromised, accompanied by upregulations of the NLRP3/caspase-1 signaling pathway-related inflammatory molecules and augmentation of CMEC pyroptosis. Findings from the subsequent *in vivo* experiment affirmed that I/R injury-induced CMEC pyroptosis exacerbates cardiac malfunction and maladaptive remodeling. Therefore, the development of novel preventive methods and effective treatment strategies to inhibit CMEC pyroptosis is a potential therapeutic approach for ameliorating myocardial I/R injury.

Phosphoinositide 3-kinases (PI3K)/serine/threonine kinase (Akt) is a ubiquitous signaling pathway in multiple cell biological processes and promotes cell survival [44]. Akt is a key downstream mediator of PI3K, and its activation form (phosphorylated Akt, p-Akt) can interact with various important regulatory factors that mediate different pathological processes, including inflammation, apoptosis, and oxidative stress [44, 45]. The PI3K/Akt pathway is a vital mediator in protecting diverse types of cells from pyroptosis during I/R injury. Diao et al. documented that hypothermia treatment protects hippocampal neurons against neuronal I/R-mediated pyroptosis by activating the PI3K/Akt pathway [46]. They also found that treatment with a specific NLRP3 inflammasome inhibitor, which is the downstream element of PI3K/Akt, results in comparable protective effects on cellular viability. Li et al. reported that docosahexaenoic acid (DHA) ameliorates liver ischemia-reperfusion injury by downregulating the levels of pyroptosis-related proteins (NLRP3 as well as cleaved caspase-1) and reducing the secretion of proinflammatory cytokines. However, incubation with LY294002 significantly abolished these beneficial effects [45]. In rat myocardial I/R injury models, Xu et al. unravelled that Aesculin attenuated reperfusion arrhythmias and myocardial damage, improved the hemodynamic functions, and remitted the inflammatory responses as well as cardiomyocyte pyroptosis. However, Aesculin-mediated cardioprotective and NLRP3 inflammasome suppression effects were blocked by the Akt inhibitor [47]. In this study, compared to the enhanced CMEC pyroptosis and upregulation of NLRP3/caspase-1 signaling pathway-related molecules, expressions of p-Akt were significantly suppressed in CMEC H/R injury models. Therefore, the PI3K/Akt signaling pathway might be a vital mediator of CMEC pyroptosis and a potential candidate for the regulation of CMEC I/R injury.

Our findings inform on the development of protective approaches against myocardial I/R injury in a KDM3A-dependent ETS1 enhancement through impacting multipathogenetic episodes including apoptosis, inflammation, and ROS [26]. However, it has not been established whether and how KDM3A attenuates CMEC I/R injury. As a histone demethylase, the biochemical features of KDM3A have been characterized, but its physiological role in different diseases has yet to be conclusively determined. KDM3A was originally found to be elevated and had a vital role in hypoxia [48]. Studies on KDM3A have majorly focused on cancer, where it enhances tumor cell proliferation, migration, invasion, and angiogenesis. Therefore, KDM3A is regarded as a poor prognostic marker [27, 28]. In recent years, epigenetic modulations were considered to be a crucial factor in the pathogenesis of cardiovascular diseases, and the functions of KDM3A have been explored [29, 30]. In our unpublished study of cardiac metabolic memory injury under diabetic conditions, KDM3A was found to be an upstream modulator of NF-κB/p65 and a regulator of cardiomyocyte injury by disturbing apoptosis, inflammation, and ROS. Our findings confirm the protective roles of KDM3A against AMI-induced myocardial injury and maladaptive cardiac remodeling [30]. KDM3A is also involved in cardiac

hypertrophy as well as fibrosis [31] and is a crucial upstream regulator of the PI3K/Akt signaling pathway [31, 49]. We assessed the significance and mechanisms of KDM3A in CMEC I/R injury in the present study. It was established that KDM3A upregulation attenuated H/R-induced CMEC malfunctions, accompanied by a marked increase in p-Akt levels. However, expressions of cleaved caspase-1, IL-1β, NLRP3, and IL-18 were remarkably downregulated. On the contrary, KDM3A knockout exacerbated these abnormalities. However, LY294002 partially blocked the beneficial effects of KDM3A overexpression. *In vivo*, KDM3A knockout aggravated cardiac dysfunction, increased the infarct size, reduced capillary density, and enhanced pyroptosis-associated protein expressions by inactivating the PI3K/Akt signaling pathway.

In summary, KDM3A protects CMECs from H/R injury-induced pyroptosis via PI3K/Akt signaling pathway activation. Therefore, interventional strategies that selectively regulate KDM3A are potential candidates for mitigation of I/R injury. Future studies should investigate the roles of endogenous upstream targets of KDM3A, including specific microRNAs, lncRNAs, and/or circRNAs in CMECs, by alternatively regulating KDM3A expressions, which may also represent a novel modality for protecting CMECs against I/R injury.

Data Availability

The original contributions presented in the study are included in the article; further inquiries can be directed to the corresponding author upon reasonable request.

Ethical Approval

The animal study was approved by the Animal Care and Use Committee of Wuhan University.

Conflicts of Interest

The authors declare that they have no conflict of interest.

Authors' Contributions

BZ, GL, and HL conceived the study and drafted the manuscript. JC, BZ, GL, and HL designed and performed the experiments. BZ, JC, GL, ZH, HJ, and BH made substantial contributions to collecting, collating, and analyzing data. JC, BZ, and BH edited and proofread the manuscript. All authors read and approved the final manuscript. Bofang Zhang, Gen Liu, and Bing Huang contributed equally to this work.

Acknowledgments

We wish to thank Dr. Qi Hu, Dr. Shuo Yang, and Dr. Jing Zhang for their helpful advice and discussion. This work was financially funded and supported by the National Natural Science Foundation of China (Nos. 81570331 and 82100287) and the National Natural Science Foundation of Hubei Province (2021CFB110).

Supplementary Materials

Supplementary Figure 1: KDM3A deletion exerts no obvious influence on CMECs' function under normoxic conditions. Supplementary Figure 2: echo raw data and time point zero heart function of each group. Supplementary Figure 3: uncropped blot corresponding to Figures 2(a) and 2(b). Supplementary Figure 4: uncropped blot corresponding to Figures 4(a) and 4(b). Supplementary Figure 5: uncropped blot corresponding to Figures 6(a) and 6(b). *(Supplementary Materials)*

References

[1] Y. Y. Xiong, Z. T. Gong, R. J. Tang, and Y. J. Yang, "The pivotal roles of exosomes derived from endogenous immune cells and exogenous stem cells in myocardial repair after acute myocardial infarction," *Theranostics*, vol. 11, no. 3, pp. 1046–1058, 2021.

[2] A. A. Damluji, S. van Diepen, J. N. Katz et al., "Mechanical complications of acute myocardial infarction: a scientific statement from the American Heart Association," *Circulation*, vol. 144, no. 2, pp. e16–e35, 2021.

[3] J. Heger, C. Hirschhäuser, J. Bornbaum et al., "Cardiomyocytes-specific deletion of monoamine oxidase B reduces irreversible myocardial ischemia/reperfusion injury," *Free Radical Biology & Medicine*, vol. 165, pp. 14–23, 2021.

[4] S. M. Davidson, P. Ferdinandy, I. Andreadou et al., "Multitarget Strategies to Reduce Myocardial Ischemia/Reperfusion Injury:," *Journal of the American College of Cardiology*, vol. 73, no. 1, pp. 89–99, 2019.

[5] Q. Fan, R. Tao, H. Zhang et al., "Dectin-1 contributes to myocardial ischemia/reperfusion injury by regulating macrophage polarization and neutrophil infiltration," *Circulation*, vol. 139, no. 5, pp. 663–678, 2019.

[6] R. Gao, L. Wang, Y. Bei et al., "Long noncoding RNA cardiac physiological hypertrophy-associated regulator induces cardiac physiological hypertrophy and promotes functional recovery after myocardial ischemia-reperfusion injury," *Circulation*, vol. 144, no. 4, pp. 303–317, 2021.

[7] X. Ge, Q. Meng, L. Wei et al., "Myocardial ischemia-reperfusion induced cardiac extracellular vesicles harbour proinflammatory features and aggravate heart injury," *J Extracell Vesicles*, vol. 10, no. 4, article e12072, 2021.

[8] V. F. M. Segers, D. L. Brutsaert, and G. W. De Keulenaer, "Cardiac remodeling: endothelial cells have more to say than just no," *Frontiers in Physiology*, vol. 9, p. 382, 2018.

[9] T. Kamo, H. Akazawa, and I. Komuro, "Cardiac nonmyocytes in the hub of cardiac hypertrophy," *Circulation Research*, vol. 117, no. 1, pp. 89–98, 2015.

[10] A. R. Pinto, A. Ilinykh, M. J. Ivey et al., "Revisiting cardiac cellular composition," *Circulation Research*, vol. 118, no. 3, pp. 400–409, 2016.

[11] C. Li, Q. Ma, S. Toan, J. Wang, H. Zhou, and J. Liang, "SERCA overexpression reduces reperfusion-mediated cardiac microvascular damage through inhibition of the calcium/MCU/mPTP/necroptosis signaling pathways," *Redox Biology*, vol. 36, article 101659, 2020.

[12] I. Eitel, S. de Waha, J. Wöhrle et al., "Comprehensive prognosis assessment by CMR imaging after ST-segment elevation myocardial infarction," *Journal of the American College of Cardiology*, vol. 64, no. 12, pp. 1217–1226, 2014.

[13] T. M. Leucker, M. Bienengraeber, M. Muravyeva et al., "Endothelial-cardiomyocyte crosstalk enhances pharmacological cardioprotection," *Journal of Molecular and Cellular Cardiology*, vol. 51, no. 5, pp. 803–811, 2011.

[14] B. Ibáñez, G. Heusch, M. Ovize, and F. Van de Werf, "Evolving therapies for myocardial ischemia/reperfusion injury," *Journal of the American College of Cardiology*, vol. 65, no. 14, pp. 1454–1471, 2015.

[15] X. Wu, M. R. Reboll, M. Korf-Klingebiel, and K. C. Wollert, "Angiogenesis after acute myocardial infarction," *Cardiovascular Research*, vol. 117, no. 5, pp. 1257–1273, 2021.

[16] R. A. Montone and G. La Vecchia, "Interplay between inflammation and microvascular obstruction in ST-segment elevation myocardial infarction: The importance of velocity," *International Journal of Cardiology*, vol. 339, pp. 7–9, 2021.

[17] P. Yu, X. Zhang, N. Liu, L. Tang, C. Peng, and X. Chen, "Pyroptosis: mechanisms and diseases," *Signal Transduction and Targeted Therapy*, vol. 6, no. 1, p. 128, 2021.

[18] B. E. Burdette, A. N. Esparza, H. Zhu, and S. Wang, "Gasdermin D in pyroptosis," *Acta Pharmaceutica Sinica B*, vol. 11, no. 9, pp. 2768–2782, 2021.

[19] D. Frank and J. E. Vince, "Pyroptosis versus necroptosis: similarities, differences, and crosstalk," *Cell Death and Differentiation*, vol. 26, no. 1, pp. 99–114, 2019.

[20] H. Shi, Y. Gao, Z. Dong et al., "GSDMD-mediated cardiomyocyte pyroptosis promotes myocardial I/R injury," *Circulation Research*, vol. 129, no. 3, pp. 383–396, 2021.

[21] X. Ye, Y. Hang, Y. Lu et al., "CircRNA circ-NNT mediates myocardial ischemia/reperfusion injury through activating pyroptosis by sponging miR-33a-5p and regulating USP46 expression," *Cell Death Discov*, vol. 7, no. 1, p. 370, 2021.

[22] C. Jia, H. Chen, J. Zhang et al., "Role of pyroptosis in cardiovascular diseases," *International Immunopharmacology*, vol. 67, pp. 311–318, 2019.

[23] B. Bai, Y. Yang, Q. Wang et al., "NLRP3 inflammasome in endothelial dysfunction," *Cell Death & Disease*, vol. 11, no. 9, p. 776, 2020.

[24] W. Sun, H. Lu, L. Lyu et al., "Gastrodin ameliorates microvascular reperfusion injury-induced pyroptosis by regulating the NLRP3/caspase-1 pathway," *Journal of Physiology and Biochemistry*, vol. 75, no. 4, pp. 531–547, 2019.

[25] P. Dandawate, C. Ghosh, K. Palaniyandi et al., "The histone demethylase KDM3A, increased in human pancreatic tumors, regulates expression of DCLK1 and promotes tumorigenesis in mice," *Gastroenterology*, vol. 157, no. 6, pp. 1646–1659.e11, 2019.

[26] X. Guo, B. F. Zhang, J. Zhang, G. Liu, Q. Hu, and J. Chen, "The histone demthylase KDM3A protects the myocardium from ischemia/reperfusion injury via promotion of ETS1 expression," *Commun Biol*, vol. 5, no. 1, p. 270, 2022.

[27] M. Sechler, J. K. Parrish, D. K. Birks, and P. Jedlicka, "The histone demethylase KDM3A, and its downstream target MCAM, promote Ewing sarcoma cell migration and metastasis," *Oncogene*, vol. 36, no. 29, pp. 4150–4160, 2017.

[28] H. Lin, X. Zhu, G. Chen et al., "KDM3A-mediated demethylation of histone H3 lysine 9 facilitates the chromatin binding of Neurog2 during neurogenesis," *Development*, vol. 144, no. 20, pp. 3674–3685, 2017.

[29] J. Chen, J. Zhang, J. Yang et al., "Histone demethylase KDM3a, a novel regulator of vascular smooth muscle cells, controls vascular neointimal hyperplasia in diabetic rats," *Atherosclerosis*, vol. 257, pp. 152–163, 2017.

[30] B. F. Zhang, H. Jiang, J. Chen et al., "LncRNA H19 ameliorates myocardial infarction-induced myocardial injury and maladaptive cardiac remodelling by regulating KDM3A," *Journal of Cellular and Molecular Medicine*, vol. 24, no. 1, pp. 1099–1115, 2020.

[31] Q. J. Zhang, T. A. T. Tran, M. Wang et al., "Histone lysine dimethyl-demethylase KDM3A controls pathological cardiac hypertrophy and fibrosis," *Nature Communications*, vol. 9, no. 1, p. 5230, 2018.

[32] B. F. Zhang, H. Jiang, J. Chen, Q. Hu, S. Yang, and X. P. Liu, "Silica-coated magnetic nanoparticles labeled endothelial progenitor cells alleviate ischemic myocardial injury and improve long-term cardiac function with magnetic field guidance in rats with myocardial infarction," *Journal of Cellular Physiology*, vol. 234, no. 10, pp. 18544–18559, 2019.

[33] M. van Kranenburg, M. Magro, H. Thiele et al., "Prognostic value of microvascular obstruction and infarct size, as measured by CMR in STEMI patients," *JACC: Cardiovascular Imaging*, vol. 7, no. 9, p. 930, 2014.

[34] V. R. Taqueti, S. D. Solomon, A. M. Shah et al., "Coronary microvascular dysfunction and future risk of heart failure with preserved ejection fraction," *European Heart Journal*, vol. 39, no. 10, pp. 840–849, 2018.

[35] N. Kaneko, R. Matsuda, M. Toda, and K. Shimamoto, "Three-dimensional reconstruction of the human capillary network and the intramyocardial micronecrosis," *American Journal of Physiology. Heart and Circulatory Physiology*, vol. 300, no. 3, pp. H754–H761, 2011.

[36] X. B. Zhao, Y. Qin, Y. L. Niu, and J. Yang, "Matrine inhibits hypoxia/reoxygenation-induced apoptosis of cardiac microvascular endothelial cells in rats _via_ the JAK2/STAT3 signaling pathway," *Biomedicine & Pharmacotherapy*, vol. 106, pp. 117–124, 2018.

[37] W. Sun, H. Lu, S. Dong et al., "Beclin1 controls caspase-4 inflammsome activation and pyroptosis in mouse myocardial reperfusion-induced microvascular injury," *Cell Communication and Signaling: CCS*, vol. 19, no. 1, p. 107, 2021.

[38] H. Zhou, Y. Zhang, S. Hu et al., "Melatonin protects cardiac microvasculature against ischemia/reperfusion injury via suppression of mitochondrial fission-VDAC1-HK2-mPTP-mitophagy axis," *Journal of Pineal Research*, vol. 63, no. 1, p. e12413, 2017.

[39] X. He, X. Fan, B. Bai, N. Lu, S. Zhang, and L. Zhang, "Pyroptosis is a critical immune-inflammatory response involved in atherosclerosis," *Pharmacological Research*, vol. 165, article 105447, 2021.

[40] W. Liu, J. Shen, Y. Li et al., "Pyroptosis inhibition improves the symptom of acute myocardial infarction," *Cell Death & Disease*, vol. 12, no. 10, p. 852, 2021.

[41] Z. Zhaolin, L. Guohua, W. Shiyuan, and W. Zuo, "Role of pyroptosis in cardiovascular disease," *Cell Proliferation*, vol. 52, no. 2, article e12563, 2019.

[42] Y. Zhang, X. Liu, X. Bai et al., "Melatonin prevents endothelial cell pyroptosis via regulation of long noncoding RNA MEG3/miR-223/NLRP3 axis," *Journal of Pineal Research*, vol. 64, no. 2, p. e12449, 2018.

[43] S. Toldo and A. Abbate, "The NLRP3 inflammasome in acute myocardial infarction," *Nature Reviews. Cardiology*, vol. 15, no. 4, pp. 203–214, 2018.

[44] S. Xu, J. Wang, J. Jiang et al., "TLR4 promotes microglial pyroptosis via lncRNA-F630028O10Rik by activating PI3K/

AKT pathway after spinal cord injury," *Cell Death & Disease*, vol. 11, no. 8, p. 693, 2020.

[45] Z. Li, F. Zhao, Y. Cao et al., "DHA attenuates hepatic ischemia reperfusion injury by inhibiting pyroptosis and activating PI3K/Akt pathway," *European Journal of Pharmacology*, vol. 835, pp. 1–10, 2018.

[46] M. Y. Diao, Y. Zhu, J. Yang et al., "Hypothermia protects neurons against ischemia/reperfusion-induced pyroptosis via m6A-mediated activation of PTEN and the PI3K/Akt/GSK-3β signaling pathway," *Brain Research Bulletin*, vol. 159, pp. 25–31, 2020.

[47] X. N. Xu, Y. Jiang, L. Y. Yan et al., "Aesculin suppresses the NLRP3 inflammasome-mediated pyroptosis via the Akt/GSK3β/NF-κB pathway to mitigate myocardial ischemia/reperfusion injury," *Phytomedicine*, vol. 92, article 153687, 2021.

[48] S. Wellmann, M. Bettkober, A. Zelmer et al., "Hypoxia upregulates the histone demethylase JMJD1A via HIF-1," *Biochemical and Biophysical Research Communications*, vol. 372, no. 4, pp. 892–897, 2008.

[49] X. Guo, J. Chen, B. F. Zhang, H. Jiang, H. Qi, and Y. Shuo, *Abstract 19689: Kdm3a protects myocardium from ischemia/reperfusion injury through targeting Akt-dependent signaling pathways*, American Heart Association (AHA) Scientific Sessions, Anaheim, California, 2017.

Hindawi
Oxidative Medicine and Cellular Longevity
Volume 2022, Article ID 4560609, 10 pages
https://doi.org/10.1155/2022/4560609

Research Article

Investigating Causal Relations between Genetic-Related Intermediate Endophenotype and Risk of Chronic Prostatitis: Mendelian Randomization Study

Shengfeng Zhang,[1,2,3] Xing Xie,[1] Lei Yu,[1] Nili Jiang,[1] Xihuan Wei,[1] and Yanling Hu[1]

[1]*Department of Biochemistry and Molecular Biology, School of Pre-Clinical Medicine, Guangxi Medical University, Nanning, 53002 Guangxi, China*
[2]*Department of Intensive Care Unit, The People's Hospital of Guangxi Zhuang Autonomous Region & Research Center of Intensive Care Unit, Nanning, 530021 Guangxi, China*
[3]*Guangxi Academy of Medical Sciences, Nanning, 530021 Guangxi, China*

Correspondence should be addressed to Yanling Hu; ylhupost@163.com

Received 7 July 2022; Revised 4 August 2022; Accepted 13 August 2022; Published 28 August 2022

Academic Editor: Shao Liang

Objective. Prostatitis is a common disease of the male genitourinary system, which seriously disturbs the physical and mental health of male patients. It is related to many factors such as living habits, age, and race, but the etiology has not been fully elucidated. This study investigated whether there is a causal relationship between clinical biochemical indicators (i.e., intermediate phenotype) and prostatitis through Mendelian randomization. The subjects of the study were prostatitis patients and related SNPs in the Guangxi Fangchenggang health examination cohort. *Methods*. According to the requirements of Mendelian randomization (MR), the single nucleotide polymorphisms (SNPs) related to prostatitis patients and 29 common SNPs related to clinical biochemical indicators were analyzed by linkage disequilibrium, and the calculated SNPs were selected. Finally, the related SNPs were analyzed by Mendelian randomization method. *Results*. 15 biochemical indicators such as complement C4, FOL, CRP, HCY, and estradiol have shared chronic prostatitis SNP sites, and five qualified SNPs were finally screened for complement C4. Finally, complement C4 was obtained by Mendelian randomization method ($P = 0.039$), which was statistically significant. The other 28 clinical endophenotypes were all negative. *Conclusion*. The results show that there was a causal relationship between complement C4 and prostatitis, and the more consistent SNP is rs2075799.

1. Introduction

Prostatitis is the third most common urinary system disease that threatens men's health after benign prostatic hyperplasia and prostate cancer [1]. Overall, it is estimated that 4.5%-9% of the male population is diagnosed with prostatitis, and the recurrence rate is as high as 50% in elderly patients [2]. Prostate symptoms can lead to depression and decreased quality of life [3]. Inflammation has adverse consequences on sperm quality [4] and finally leads to infertility [5], which affects the health of human offspring. This is also the most serious consequence. It is caused by the interaction of various stimulating factors [6]. The causes of its occurrence are varied [7]. Chronic prostatitis (CP)/chronic pelvic pain syndrome (CPPS) is closely related to lifestyle, diet, smoking, gastrointestinal or anorectal diseases, and impaired sexual function [8]. It has even been suggested that high-level spare-time sports activities can reduce the incidence of CP/CPPS. Some people believe that age, race, and geographical area are also important risk factors for chronic prostatitis [9], while others believe that body mass index (BMI) is also a risk factor [10]. The history of moderate to severe lower urinary tract symptoms (LUTS) and prostatic hypertrophy (BPH) is significantly related to prostatitis [11]. Studies have shown that prostatitis-like symptoms are a multifactorial problem closely related to drinking,

smoking, frequent sexual intercourse, fatigue, stress, and lack of sleep [7]. Although the results of some observational studies show that lifestyle factors affect CP/CPPS risks, so far, such studies are still few in general [10]. At present, there is no report on the relationship between clinical biochemical indicators and prostatitis. Therefore, our research group conducted linkage disequilibrium (LDSC) analysis on the relationship between prostatitis and clinical in the early stage and found that complement C4 and C3 have significant correlation with prostatitis, but it is not clear whether there is a causal relationship. And Mendelian randomization method is a popular and accurate epidemiological method to study causality. This method can select single nucleotide polymorphisms (SNP) as an instrumental variable, which can avoid the influence of confounding factors such as environmental factors on the relationship between exposure factors and outcomes [12, 13]. Therefore, it is necessary to conduct Mendelian randomization analysis on whether there is a causal relationship between clinical endophenotype and prostatitis.

2. Materials and Methods

2.1. The Sources of Data

2.1.1. Case Group. The samples were from six large-scale tertiary grade A hospitals in Guangxi. This study received consent and approval from the Medical Ethics Committee of Guangxi Medical University. The diagnosis of CP was carried out according to the CP classification standard of the National Institutes of Health (NIH) [14], and the inclusion and exclusion criteria of samples were established. (1) Inclusion criteria: complaints of long-term and repeated pain or discomfort in the pelvic area, lasting for more than 3 months, may be accompanied by different degrees of urination symptoms and sexual dysfunction, which seriously affects the quality of life of patients; routine examination of prostatitis EPS/semen/urine VB3 bacterial culture after prostate massage was negative. (2) Exclusion criteria: excluding patients with neurogenic bladder, urethral stricture, benign prostatic hyperplasia, prostate cancer, testicular epididymis and spermatic cord diseases, overactive bladder, interstitial cystitis, sexually transmitted diseases, bladder tumors, urinary tuberculosis, stones, and other diseases affecting urination, as well as severe diabetes, cardiovascular diseases, liver and kidney insufficiency, psychosis, habitual diarrhea or inflammatory intestinal diseases, lumbar diseases, central, and peripheral neuropathy, etc.

2.1.2. Control Group. The inclusion criteria were matched by age and sex; normal subjects were selected from unrelated areas in the same area as CP patients. The exclusion criteria were no urinary system-related diseases or tumors and cardiovascular diseases, no diabetes, psychosis, hepatic and renal insufficiency, inertial diarrhea or patients with inflammatory intestinal diseases, lumbar diseases, central, and peripheral neuropathy, etc.

2.2. Genome-Wide SNP Genotyping. The first phase of male health samples from the First People's Hospital of Fangchenggang was genotyped on DNA samples using Human Omni 1-Quad chip from Illumina company in the United States. The second phase of male urology outpatient samples from six large-scale tertiary grade A hospitals in Guangxi was genotyped on DNA samples using Human Omni ZhongHua-8 chip from Illumina company in the United States. The brief procedure of the experiment was as follows: amplification of whole genome DNA → endonuclease digestion to fragment DNA → isopropanol precipitation of DNA → DNA resuspension → DNA hybridization with chip → washing → single base extension → staining. After scanning the fluorescence signal by Illumina iScan chip scanning system, the data were obtained according to the different fluorescence emitted by the fluorescent groups represented by different deoxyribose bases. The obtained fluorescence data were analyzed by Genome Studio software to obtain SNP typing data files.

2.3. Genotyping Data Filtering. The genotyping data were filtered using PLINK 1.07 software, and strict quality control was performed on the obtained SNPs data, with the following data exclusion criteria: call rate < 0.95, minor allele frequency (MAF) < 0.01, and Hardy-Weinberg equilibrium (HWE) < 1×10^{-3}.

2.4. Genotyping Data Filling. According to the linkage disequilibrium (LD) rules based on Hapmap Phase II Han Chinese in Beijing (CHB) population release#24 panel, the IMPUTE 5 software was to fill the genome of SNP sites that had not been typed, and the sites with a posterior probability greater than 90% were reserved. And based on the same exclusion criteria as above, fill the SNP data after genome filling again.

2.5. Selection of Instrumental Variables. In order to better investigate the causal relationship between clinical biochemical indicators and CP, the SNPs we selected need to meet the following criteria: (1) high association between SNPs and clinical biochemical indicators with genome-wide study significance, i.e., $P < 5 \times 10^{-8}$. (2) SNPs were independent of each other to avoid the bias caused by linkage disequilibrium (LD), when R^2 of LD > 0.01, one of them was eliminated [15].

2.6. Evaluation of Instrumental Variables. To ensure that the correlation between instrumental variables and exposure factors was strong, the F value of each SNP is usually used to determine the strength of the correlation and to avoid bias from weak instrumental variables, and bias from weak instrumental variables was generally considered to be absent when the F value was greater than 10 [16]. The statistical power of the MR analysis of CP was calculated for each SNP using an online tool (http://cnsgenomics.com/shiny/mRnd/). In Mendelian randomization, it was important to ensure that instrumental variables and confounding factors are independent of each other and cannot be indirectly linked to outcome variables through confounding factors. Therefore, SNPs associated with confounding factors were excluded by whether they were associated with confounding factors or not.

2.7. Two-Sample Mendelian Randomization. Mendelian randomization estimates the relationship between genetically related intermediate endophenotypes and CP by the following three MR methods: inverse-variance weighted (IVW), MR-Egger regression, and weighted median (WM). IVW is one of the commonly used methods, but it presupposes that all instrumental variables are valid, and as long as one SNP does not satisfy the assumptions of instrumental variables, this method will be biased. Although multiple genetic variants can enhance the statistical power of Mendelian randomization analysis, due to the existence of pleiotropy, the causal relationship with CP is biased when some genetic variants do not satisfy the assumption of instrumental variables [16]. However, when 50% of SNPs are effective instrumental variables, WM can obtain estimates consistent with the final effect [17]. Under the internal assumption that instrumental variables are independent of direct effects, the MR-Egger regression provides a valid effect estimate even if all SNPs are invalid instrumental variables [18].

2.8. Sensitivity Analysis and Heterogeneity Test. To further evaluate the effect of heterogeneity on the causal estimation, Cochran's Q test was used to evaluate the heterogeneity test of the instrumental variables [19], while one SNP in turn was excluded and the remaining SNPs were continued to be analyzed by the Mendelian randomization method, i.e., leave one out (LOO) for sensitivity analysis of the results [20]. Statistical analysis was performed using the "TwoSampleMR" package in R software (v3.6.1 https://www.r-project.org), and differences were considered statistically significant at $P < 0.05$.

3. Results

3.1. Screening of Mendelian Randomization Instrumental Variables (Shared SNP Sites). The overall situation of the respective shared SNP sites associated with 29 clinical biochemical indicators of chronic prostatitis is shown in Table 1; 15 biochemical indicators such as complement C4 and FOL have shared SNP sites with CP, with the number of shared sites ranging from 1286. 14 biochemical indicators such as IgA and BUN have no shared SNP sites with CP. Shared SNP sites of chronic prostatitis and 15 clinical biochemical indicators are shown in Table 1. Chronic prostatitis has a total of 286 shared SNP sites associated with complement C4, and after a chain imbalance analysis, there are five SNP sites that can be used as instrumental variables (as shown in Table 2), with F values ranging from two to 12, partially biased by weak instrumental variables.

3.2. Estimation Results of Mendelian Randomization Method. Inverse-variance weighted results showed that there was a causal relationship between exposure (complement C4) and chronic prostatitis (OR = 1.040, $P = 0.039$), as shown in Figure 1. The remaining four methods: weighted median estimator (OR = 1.154, 95% CI: 0.192~6.940, $P = 0.143$), Mendelian randomization Egger regression (OR = 1.067, 95% CI: 0.452~2.520, $P = 0.077$), simple mode (OR = 1.209, 95% CI: 0.457~3.201, $P = 0.193$), and weighted mode (OR = 1.212, 95% CI: 0.470~3.122, $P = 0.165$), settled with a P value > 0.05 (as shown in Table 3). Among them, 15 clinical biochemical indicators (exposure) and chronic prostatitis (outcome) shared SNPs (after linkage disequilibrium correction) ranging from one to two. Clinical biochemical indicators include complement C4, complement C3, immunoglobulin M (IgM), C-type reactive protein (CRP), alpha-fetoprotein (AFP), ferritin (FERR), vitamin B12, low-density lipoprotein (LDL), high-density lipoprotein (HDL), follicle-stimulating hormone (FSH), estradiol, uric acid, sex hormone-binding globulin (SHBG), FOL (folic acid), and HCY (homocysteine). Using six Mendelian randomization statistical methods, the calculation results of the causal effect of 14 clinical biochemical indicators on CP are negative; that is, there is no causal relationship with CP (outcome), as shown in Table 4.

3.3. Sensitivity Analysis. To ensure the credibility of this study, the MR-Egger method was used to test the instrumental variables. As shown in Figure 2, genetic pleiotropy does not bias the results. Meanwhile, less heterogeneity among SNPs was observed with the IVW method ($Q = 0.88$, $P = 0.64$). In the sensitivity analysis, we eliminated one SNP in turn and analyzed the remaining SNPs, and there was no one SNP that had a significant effect on the outcome effect, as shown in Figure 3.

4. Discussion

Mendelian randomization (MR) is an important epidemiological method that can be used for causal reasoning [21–23]. It uses SNP site data as an instrumental variable to explore the causal relationship between exposure factors and results. Compared with traditional observation and study, it reduces the bias caused by confounding factors and reverse causality and improves its accuracy and scientificity [24]. Compared with randomized controlled trials, it is called a natural randomized control by the epidemiological community. Genetic variation is usually inherited independently, which means that they are usually in a specific relationship [25]. Even if there are unmeasured confusing factors, Mendelian can be used for causal inference [10]. Mendelian randomization studies using biochemical indicators (including inflammatory markers) for chronic prostatitis have not been reported so far. In this study, we used six statistical methods (MR-Egger, weighted median, inverse-variance weighted, simple mode, weighted mode, and Wald ratio) of MR to estimate the causal relationship between 29 commonly used clinical biochemical indicators and prostatitis. Among the 29 biochemical indicators, only 15 clinical indicators met the aforementioned hypothesis of MR, and the remaining 14 did not meet the conditions and were excluded.

Complement C4, complement C3, CRP, and IL-6 are commonly used in clinic to evaluate inflammation, but no causal relationship between C3, CRP, IL-6, and prostatitis was found in this study. However, Hartwig et al. [26] calculated that sIL-6R was positively correlated with the occurrence of schizophrenia through Mendelian randomization

Table 1: Clinical biochemical indicator shared SNP sites with chronic prostatitis.

Exposure (indicators)	Outcome (CP) number of shared SNP	Exposure (indicators)	Outcome (CP) number of shared SNP	Exposure (indicators)	Outcome (CP) number of shared SNP
Complement C4	286	FSH	2	IgA	0
FOL	20	IgM	1	BUN	0
CRP	15	LDL	1	IgE	0
HCY	15	FERR	1	Insulin	0
Estradiol	15	SHBG	1	ALT	0
Uric acid	4	TG	0	TE	0
Complement C3	3	Cholesterol	0	Creatinine	0
B12	2	BMI	0	Glucose	0
HDL	2	ASO	0	Triglyceride	0
AFP	2	IgG	0		

Note: CP: chronic prostatitis; FOL: folic acid; CRP: C-type reactive protein; HCY: homocysteine; B12: vitamin B12; HDL: high-density lipoprotein; AFP: alpha-fetoprotein; FSH: follicle-stimulating hormone; LDL: low-density lipoprotein; FERR: ferritin; SHBG: sex hormone-binding globulin; TG: triglyceride; BMI: body mass index; ASO: antistreptolysin O; IgG: immunoglobulin G; IgA: immunoglobulin A; IgE: immunoglobulin E; BUN: blood urea nitrogen; ALT: alanine transaminase; SNP: single-nucleotide polymorphism.

Table 2: Exposure (complement C4) and outcome (CP) instrumental variable SNP sites.

SNP ID	SE	*P* value	Exposure	*F*
rs12660700	0.288	0.044	$1.51E-38$	9.13
rs17201248	0.150	0.164	$1.91E-36$	8.61
rs2075799	0.159	0.197	$2.33E-49$	11.58
rs4112312	-0.048	0.350	$4.83E-08$	2.36
rs9268577	-0.177	0.099	$1.19E-16$	4.20

Note: SE is standard error.

method and also pointed out that some effects were mediated by CRP [26]. Our study results show that there was no causal relationship between most clinical indicators and prostatitis. Considering the possibility of weak instrumental variables leading to bias or the presence of genetic pleiotropy that was excluded. Of course, it is also true that many of the 29 indicators included in this study (except procalcitonin, high-sensitivity C-reactive protein, and IL-6) have not been proven to be directly related to prostatitis inflammation in the clinical, meaning that the results of the observational study are consistent with the results of our Mendelian randomization study in this project.

Prospective studies have shown that genetic susceptibility to CRP levels is positively associated with the risk of infection in adults [27, 28]. At present, many literatures have confirmed that complement C4 and C3 are related to inflammation [29, 30]. They are important clinical biochemical markers of the human immune system, and changes in their levels can reflect the state of immunity. Complement C4 and C3 can represent the level of inflammation. For example, the levels of complement C4 and C3 in noncritical and critical patients with covid-19 are different. It is reported that in children with stable asthma, the level of complement C3 was significantly higher than that in the normal control group, and there was no significant difference in the level of complement C4 [31]. It was considered that complement C3 is positively correlated with asthma [31]. It was also considered that the complement C3 of asthmatic children was significantly higher than that of the control group, and there was no significant difference in complement C4 [32]. Studies have confirmed that inflammation and immune factors (IgE, complement C4, complement C3, CRP, ASO, and RF) and hormone elements (Osteoc, FSH, testosterone, and insulin) are significantly related to the occurrence of prostatitis [33]. It showed that this study was highly consistent with the previous research results of Chen et al. [33]. There were five SNP sites with a positive causal association between complement C4 and chronic prostatitis in this study. Among them, s2075799 ($F = 11.58$), rs12660700 ($F = 9.13$), rs17201248 ($F = 8.61$), rs2075799 ($F = 11.58$), rs4112312 ($F = 2.36$), and rs9268577 ($F = 4.20$), only the F value of rs2075799 is 11.58. According to the ideal state, the F value was greater than 10, there was no weak instrumental variable, while it was consistent with the result resolution consistency of multiple randomization methods. Among them, rs2075799 ($F = 11.58$) was the ideal SNP site that meets the above criteria. The SNP of rs2075799 exist in the MHC II region of 2-mb on the chromosome, and this SNP site is highly correlated with the level of complement C4. rs2075799-related genes are related to schizophrenia, but there is no literature reported that it was related to chronic prostatitis. In MR-Egger analysis of complement C4, its intercept was close to zero, the P value was less than 0.005, and there was no horizontal pleiotropy, which was consistent with the results of inverse-variance weighted operation. The statistical results of the two are consistent, which makes it clear that the results are credible. With the development of MR methodology, a multivariate MR Egger regression analysis method for adjusting multieffects has been proposed, which was beyond the range that can be explained by genetically estimated exposure factors and has the same direction,

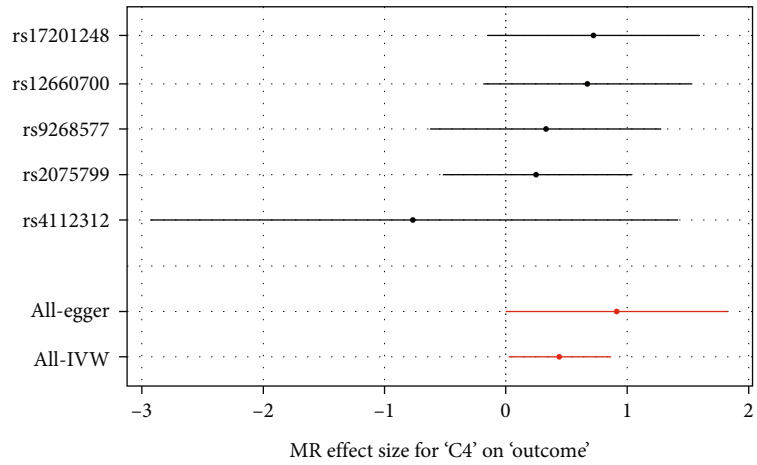

Figure 1: Results of Mendelian randomization method for complement C4 and chronic prostatitis (CP).

Table 3: Mendelian randomization to estimate the values of causal effect of complement C4 on chronic prostatitis (CP).

Exposure (indicators)	Outcome (CP) shared SNP	Statistical method	β value	SE value	P value	OR value	CI value
Complement C4	5	MR-Egger	0.915	0.464	0.143	1.154	0.192~6.940
		Weighted median (WM)	0.439	0.248	0.077	1.067	0.452~2.520
		Inverse-variance weighted (IVW)	0.441	0.214	0.039	1.040	0.438~2.468
		Simple mode (SM)	0.497	0.317	0.193	1.209	0.457~3.201
		Weighted mode (WM)	0.483	0.285	0.165	1.212	0.470~3.122

but it was larger and more complex [18]. These studies indicated that complement C4 can be used as a biochemical marker for causal inference of chronic prostatitis. This will be of great significance to the diagnosis, treatment, and prevention of prostatitis. As we all know, acute prostatitis can be diagnosed by comprehensive clinical manifestations, biochemical examination of prostatic fluid, and examinations such as CT. However, the diagnosis is confirmed by prostate finger examination, prostate biopsy, and pathology of surgical resection; these invasive operations will bring great pain and risks to the patient. However, it has been reported that prostatitis is positively correlated with prostate cancer, which is an important high-risk factor for the development of prostate cancer [34]. The potential continuous stimulation of chronic inflammation, the immune status of the prostate, the inflammatory mediators and cytokines of the prostate, and proliferative inflammation and atrophy were high-risk factors for prostate cancer, which suggested that local inflammation of prostate and damage of prostate in systemic inflammatory reaction may lead to the occurrence or progress of prostate cancer [35]. Some also believe that the prostate was cancerous through oxidative stress and reactive oxygen species. Inflammation and atrophic hyperplasia were high-risk factors for prostate cancer, and that inflammation was a possible factor for the generation or development of cancer [36]. Therefore, early intervention of chronic prostatitis will also be of great significance to the prevention of chronic prostatitis [37]. If a noninvasive, accurate, safe, effective, fast, and convenient detection method for early diagnosis can be found, it will bring great benefits to many patients and is also the key to early prevention and treatment of early prostatitis.

From the perspectives of statistics, genetics, and epidemiology, we used a two-sample Mendelian randomization method for the first time to analyze the causal relationship between clinical indicators and CP, which confirmed that there is a causal relationship between complementC4 and CP.

Although the sample size of this research group is not large, the sample comes from the same region and has a certain regional representation, which reduces the bias caused by different populations. The study of Mendelian randomization method is very strict with the standards of exposure factors and causal correlation. There are more Mendelian randomization study methods, each with its own basic conditions, and each method has its own advantages and disadvantages. The application of MR methods must require that any single SNP site must be strongly correlated with exposure factors, not weakly correlated and correlated with confounding factors, and it must be a unidirectional positive relationship, and there must be no multiple effects and reverse causality. It has been suggested that various methods such as sample size calculation and model hypothesis can be used to solve potential methodological problems [32]. There are many determinants of the effect of MR, including the frequency of using genetic variation, the size of the impact of variation on risk factors, the strength of genetic instrument

Table 4: Mendelian randomization to estimate causal effect values for 14 clinical biochemical indicators of CP.

Exposure (indicators)	Outcome (CP) shared SNP	Statistical method	β value	SE value	P value
LDL	1	MR-Egger	/	/	/
		Weighted median	/	/	/
		Inverse-variance weighted	/	/	/
		Simple mode	/	/	/
		Weighted mode	/	/	/
		Wald ratio	-0.164	0.249	0.510
SHBG	1	MR-Egger	/	/	/
		Weighted median	/	/	/
		Inverse-variance weighted	/	/	/
		Simple mode	/	/	/
		Weighted mode	/	/	/
		Wald ratio	0.793	0.654	0.225
Uric acid	1	MR-Egger	/	/	/
		Weighted median	/	/	/
		Inverse-variance weighted	/	/	/
		Simple mode	/	/	/
		Weighted mode	/	/	/
		Wald ratio	-0.005	0.003	0.078
Estradiol	2	MR-Egger	/	/	/
		Weighted median	/	/	/
		Inverse-variance weighted	0.093	0.839	0.912
		Simple mode	/	/	/
		Weighted mode	/	/	/
		Wald ratio	/	/	/
FERR	1	MR-Egger	/	/	/
		Weighted median	/	/	/
		Inverse-variance weighted	/	/	/
		Simple mode	/	/	/
		Weighted mode	/	/	/
		Wald ratio	0.000	0.001	0.840
FSH	1	MR-Egger	/	/	/
		Weighted median	/	/	/
		Inverse-variance weighted	/	/	/
		Simple mode	/	/	/
		Weighted mode	/	/	/
		Wald ratio	0.887	0.477	0.063
HDL	1	MR-Egger	/	/	/
		Weighted median	/	/	/
		Inverse-variance weighted	/	/	/
		Simple mode	/	/	/
		Weighted mode	/	/	/
		Wald ratio	-0.869	0.693	0.210
IgM	1	MR-Egger	/	/	/
		Weighted median	/	/	/
		Inverse-variance weighted	/	/	/
		Simple mode	/	/	/

Table 4: Continued.

Exposure (indicators)	Outcome (CP) shared SNP	Statistical method	β value	SE value	P value
		Weighted mode	/	/	/
		Wald ratio	0.248	0.573	0.665
B12	1	MR-Egger	/	/	/
		Weighted median	/	/	/
		Inverse-variance weighted	/	/	/
		Simple mode	/	/	/
		Weighted mode	/	/	/
		Wald ratio	0.002	0.001	0.164
CRP	1	MR-Egger	/	/	/
		Weighted median	/	/	/
		Inverse-variance weighted	/	/	/
		Simple mode	/	/	/
		Weighted mode	/	/	/
		Wald ratio	-0.102	0.164	0.537
AFP	1	MR-Egger	/	/	/
		Weighted median	/	/	/
		Inverse-variance weighted	/	/	/
		Simple mode	/	/	/
		Weighted mode	/	/	/
		Wald ratio	-0.925	0.634	0.145
Complement C3	1	MR-Egger	/	/	/
		Weighted median	/	/	/
		Inverse-variance weighted	/	/	/
		Simple mode	/	/	/
		Weighted mode	/	/	/
		Wald ratio	-1.389	1.165	0.233
FOL	20	MR-Egger	0.334	0.233	0.168
		Weighted median	0.008	0.027	0.763
		Inverse-variance weighted	0.007	0.021	0.734
		Simple mode	0.010	0.047	0.832
		Weighted mode	0.010	0.043	0.815
		Wald ratio	/	/	/
HCY	15	MR-Egger	0.008	0.022	0.742
		Weighted median	-0.005	0.010	0.635
		Inverse-variance weighted	-0.004	0.008	0.590
		Simple mode	-0.009	0.016	0.591
		Weighted mode	-0.004	0.014	0.749
		Wald ratio	/	/	/

Note: CP: chronic prostatitis; LDL: low-density lipoprotein; FOL: folic acid; CRP: C-type reactive protein; HCY: homocysteine; B12: vitamin B12; HDL: high-density lipoprotein; AFP: alpha-fetoprotein; FSH: follicle-stimulating hormone; FERR: ferritin; SHBG: sex hormone-binding globulin; IgM: immunoglobulin M.

and the size of the study sample, and the strength of the relationship between exposure factors and outcomes [38, 39]. The best way to improve the reliability of the study results is to increase the study sample further.

With the development of genome-wide association studies and the continuous increase of genetic association-related data and the opening of public data, the current application of Mendelian randomization has a basis of data sources and gradually appears to be relatively simple and more widely used. However, it is still difficult to obtain reliable results from database surveys, because in the traditional inverse-variance weighting, all genetic variations must be effective instrumental variables to obtain consistent results. So sensitivity analysis of genetic variation was carried out by median

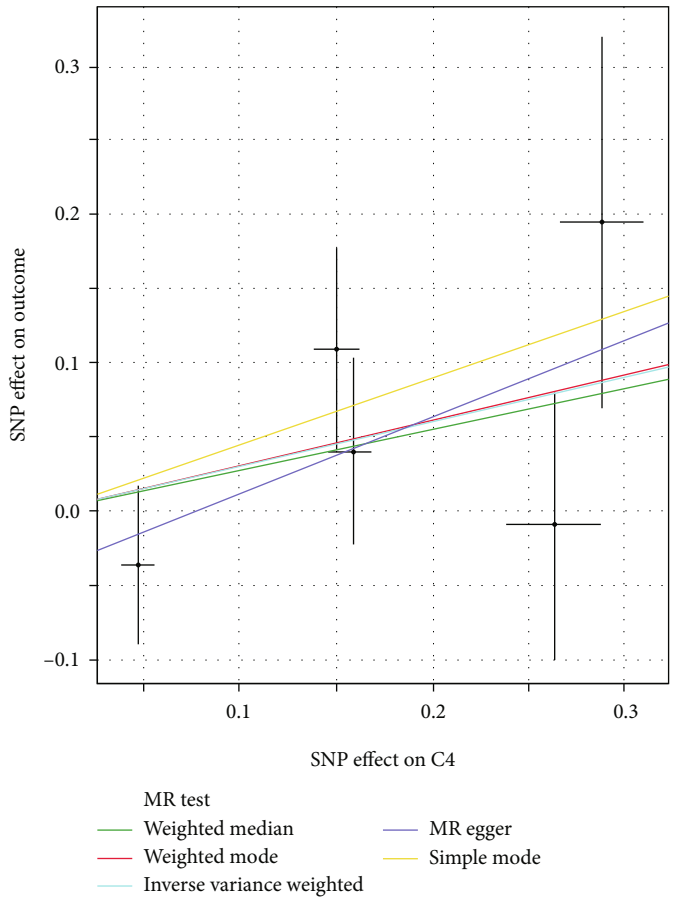

Figure 2: IVW, MR-Egger regression, and WM scatter plot to study the effect of C4 on CP.

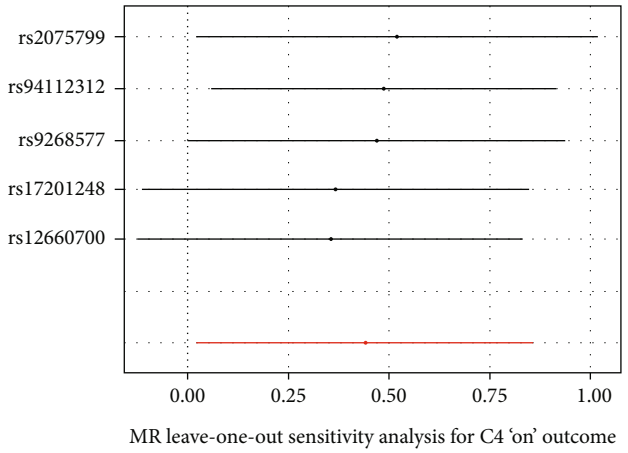

Figure 3: Sensitivity analysis of the leave-one-out method.

regression method and MR-Egger regression method in Mendelian randomization study [40].

This study is still deficient in that only a few of the 29 clinical endophenotypes have one to two shared SNP sites, especially when there are less than five SNP sites. Except IVW method, other methods should be inconclusive. This may lead to false negatives. This may be due to the relatively small sample size.

However, this is based on the original data provided by the current GWAS study, which is a retrospective study, and the existing statistical data does not increase the number of SNP sites by increasing the number of samples. In the future, when more sample data are added and the relevant SNP sites are expanded, subsequent researchers can conduct MR analysis of these intermediate endophenotypes again.

5. Conclusion

In a word, MR can find the causal relationship between exposure factors and genetic variation of outcome from molecular mechanism. The MR study of complement C4 and CP in this study shows that there is a causal relationship between complement C4 and CP, which can provide a new idea and method for the molecular mechanism and immune mechanism of prevention and treatment of chronic prostatitis. If further study can confirm, it is of great significance in the early treatment and prevention of chronic prostatitis and even in the prevention of prostate cancer.

Data Availability

The labeled dataset used to support the findings of this study is available from the corresponding author upon request.

Conflicts of Interest

The authors declare no competing interests.

Acknowledgments

The source of the unit data is the Genomics and Individualization Research Center of Guangxi Medical University. The authors would like to express their gratitude for the support from the National Natural Science Foundation of China (Project Contract No. 82160537).

References

[1] F. U. Khan, A. U. Ihsan, H. U. Khan et al., "Comprehensive overview of prostatitis," *Biomed Pharmacother*, vol. 94, pp. 1064–1076, 2017.

[2] J. Rees, M. Abrahams, A. Doble, A. Cooper, and the Prostatitis Expert Reference Group (PERG), "Diagnosis and treatment of chronic bacterial prostatitis and chronic prostatitis/chronic pelvic pain syndrome: a consensus guideline," *BJU International*, vol. 116, no. 4, pp. 509–525, 2015.

[3] W. Häuser, G. Schmutzer, A. Hinz, and E. Brähler, "Prävalenz und prädiktoren urogenitaler schmerzen des manns," *Schmerz*, vol. 26, no. 2, pp. 192–199, 2012.

[4] R. A. Condorelli, G. I. Russo, A. E. Calogero, G. Morgia, and S. La Vignera, "Chronic prostatitis and its detrimental impact on sperm parameters: a systematic review and meta-analysis," *Journal of Endocrinological Investigation*, vol. 40, no. 11, pp. 1209–1218, 2017.

[5] F. M. Wagenlehner, T. Diemer, K. G. Naber, and W. Weidner, "Chronic bacterial prostatitis (NIH type II): diagnosis, therapy and influence on the fertility status," *Andrologia*, vol. 40, no. 2, pp. 100–104, 2008.

[6] M. E. Karlovsky and M. A. Pontari, "Theories of prostatitis etiology," *Current Urology Reports*, vol. 3, no. 4, pp. 307–312, 2002.

[7] N. M. Anichkov and I. V. Kniaz'kin, "Chronic prostatitis: (1) etiology, pathogenesis, modeling, classification," *Advances in Gerontology*, vol. 11, pp. 84–92, 2003.

[8] R. Zhang, A. K. Chomistek, J. D. Dimitrakoff et al., "Physical activity and chronic prostatitis/chronic pelvic pain syndrome," *Medicine and Science in Sports and Exercise*, vol. 47, no. 4, pp. 757–764, 2015.

[9] B. Riegel, C. A. Bruenahl, S. Ahyai, U. Bingel, M. Fisch, and B. Löwe, "Assessing psychological factors, social aspects and psychiatric co-morbidity associated with chronic prostatitis/chronic pelvic pain syndrome (CP/CPPS) in men — a systematic review," *Journal of Psychosomatic Research*, vol. 77, no. 5, pp. 333–350, 2014.

[10] X. Chen, C. Hu, Y. Peng et al., "Association of diet and lifestyle with chronic prostatitis/chronic pelvic pain syndrome and pain severity: a case-control study," *Prostate Cancer and Prostatic Diseases*, vol. 19, no. 1, pp. 92–99, 2016.

[11] J. C. Nickel, "Role of α1-blockers in chronic prostatitis syndromes," *BJU International*, vol. 101, Supplement 3, pp. 11–16, 2008.

[12] D. A. Lawlor, R. M. Harbord, J. A. Sterne, N. Timpson, and G. Davey Smith, "Mendelian randomization: using genes as instruments for making causal inferences in epidemiology," *Statistics in Medicine*, vol. 27, no. 8, pp. 1133–1163, 2008.

[13] J. Zheng, D. Baird, M. C. Borges et al., "Recent developments in Mendelian randomization studies," *Current epidemiology reports*, vol. 4, no. 4, pp. 330–345, 2017.

[14] M. S. Litwin, M. McNaughton-Collins, F. J. Fowler Jr. et al., "The National Institutes of Health chronic prostatitis symptom index: development and validation of a new outcome measure. Chronic Prostatitis Collaborative Research Network," *The Journal of Urology*, vol. 162, no. 2, pp. 369–375, 1999.

[15] Z. Zhao, J. Zhang, J. He, and G. Zeng, "Clinical utility of the UPOINT phenotype system in Chinese males with chronic prostatitis/chronic pelvic pain syndrome (CP/CPPS): a prospective study," *PLoS One*, vol. 8, no. 1, article e52044, 2013.

[16] M. J. Brion, K. Shakhbazov, and P. M. Visscher, "Calculating statistical power in Mendelian randomization studies," *International Journal of Epidemiology*, vol. 42, no. 5, pp. 1497–1501, 2013.

[17] J. Bowden, G. Davey Smith, P. C. Haycock, and S. Burgess, "Consistent estimation in Mendelian randomization with some invalid instruments using a weighted median estimator," *Genetic Epidemiology*, vol. 40, no. 4, pp. 304–314, 2016.

[18] J. Bowden, G. Davey Smith, and S. Burgess, "Mendelian randomization with invalid instruments: effect estimation and bias detection through egger regression," *International Journal of Epidemiology*, vol. 44, no. 2, pp. 512–525, 2015.

[19] M. F. Greco, C. Minelli, N. A. Sheehan, and J. R. Thompson, "Detecting pleiotropy in Mendelian randomisation studies with summary data and a continuous outcome," *Statistics in Medicine*, vol. 34, no. 21, pp. 2926–2940, 2015.

[20] S. Burgess, J. Bowden, T. Fall, E. Ingelsson, and S. G. Thompson, "Sensitivity analyses for robust causal inference from Mendelian randomization analyses with multiple genetic variants," *Epidemiology*, vol. 28, no. 1, pp. 30–42, 2017.

[21] G. D. Smith and S. Ebrahim, "'Mendelian randomization': can genetic epidemiology contribute to understanding environmental determinants of disease?," *International Journal of Epidemiology*, vol. 32, no. 1, pp. 1–22, 2003.

[22] L. Paternoster, K. Tilling, and G. Davey Smith, "Genetic epidemiology and Mendelian randomization for informing disease therapeutics: conceptual and methodological challenges," *PLoS Genetics*, vol. 13, no. 10, article e1006944, 2017.

[23] T. J. Vander Weele, E. J. Tchetgen Tchetgen, M. Cornelis, and P. Kraft, "Methodological challenges in Mendelian randomization," *Epidemiology*, vol. 25, no. 3, pp. 427–435, 2014.

[24] G. Davey Smith and G. Hemani, "Mendelian randomization: genetic anchors for causal inference in epidemiological studies," *Human Molecular Genetics*, vol. 23, no. R1, pp. R89–R98, 2014.

[25] S. Burgess, D. S. Small, and S. G. Thompson, "A review of instrumental variable estimators for Mendelian randomization," *Statistical Methods in Medical Research*, vol. 26, no. 5, pp. 2333–2355, 2017.

[26] F. P. Hartwig, M. C. Borges, B. L. Horta, J. Bowden, and G. Davey Smith, "Inflammatory biomarkers and risk of schizophrenia: a 2-sample Mendelian randomization study," *JAMA Psychiatry*, vol. 74, no. 12, pp. 1226–1233, 2017.

[27] K. A. Kaspersen, K. M. Dinh, L. T. Erikstrup et al., "Low-grade inflammation is associated with susceptibility to infection in healthy men: results from the Danish Blood Donor Study (DBDS)," *PLoS One*, vol. 11, no. 10, article e0164220, 2016.

[28] J. Zacho, T. Benfield, A. Tybjærg-Hansen, and B. G. Nordestgaard, "Increased baseline C-reactive protein concentrations

are associated with increased risk of infections: results from 2 large Danish population cohorts," *Clinical Chemistry*, vol. 62, no. 2, pp. 335–342, 2016.

[29] M. Copenhaver, C. Y. Yu, and R. P. Hoffman, "Complement components, C3 and C4, and the metabolic syndrome," *Current Diabetes Reviews*, vol. 15, no. 1, pp. 44–48, 2019.

[30] M. Ohno, M. Hasegawa, A. Hayashi et al., "Lipopolysaccharide O structure of adherent and invasive *Escherichia coli* regulates intestinal inflammation via complement C3," *PLoS Pathogens*, vol. 16, no. 10, article e1008928, 2020.

[31] F. I. Najam, A. S. Giasuddin, and A. H. Shembesh, "Complement components (C3, C4) in childhood asthma," *Indian Journal of Pediatrics*, vol. 72, no. 9, pp. 745–749, 2005.

[32] M. Abdel Fattah, M. El Baz, A. Sherif, and A. Adel, "Complement components (C3, C4) as inflammatory markers in asthma," *Indian Journal of Pediatrics*, vol. 77, no. 7, pp. 771–773, 2010.

[33] Y. Chen, J. Li, Y. Hu et al., "Multi-factors including inflammatory/immune, hormones, tumor-related proteins and nutrition associated with chronic prostatitis NIH IIIa+b and IV based on *FAMHES* project," *Scientific Reports*, vol. 7, no. 1, p. 9143, 2017.

[34] C. M. Porter, E. Shrestha, L. B. Peiffer, and K. S. Sfanos, "The microbiome in prostate inflammation and prostate cancer," *Prostate Cancer and Prostatic Diseases*, vol. 21, no. 3, pp. 345–354, 2018.

[35] K. S. Sfanos and A. M. De Marzo, "Prostate cancer and inflammation: the evidence," *Histopathology*, vol. 60, no. 1, pp. 199–215, 2012.

[36] K. S. Sfanos, S. Yegnasubramanian, W. G. Nelson, and A. M. De Marzo, "The inflammatory microenvironment and microbiome in prostate cancer development," *Nature Reviews Urology*, vol. 15, no. 1, pp. 11–24, 2018.

[37] A. M. De Marzo, E. A. Platz, S. Sutcliffe et al., "Inflammation in prostate carcinogenesis," *Nature Reviews Cancer*, vol. 7, no. 4, pp. 256–269, 2007.

[38] C. A. Emdin, A. V. Khera, and S. Kathiresan, "Mendelian randomization," *JAMA*, vol. 318, no. 19, pp. 1925-1926, 2017.

[39] N. M. Davies, M. V. Holmes, and G. Davey Smith, "Reading Mendelian randomisation studies: a guide, glossary, and checklist for clinicians," *BMJ*, vol. 362, article k601, 2018.

[40] D. A. Lawlor, "Commentary: two-sample Mendelian randomization: opportunities and challenges," *International Journal of Epidemiology*, vol. 45, no. 3, pp. 908–915, 2016.